I. R. IRAN

ISSN: 1728-144X
e-ISSN: 1735-9244

International Journal of Engineering

Journal Homepage: www.ije.ir

MERC

TRANSACTIONS B: APPLICATIONS

Volume 39, Number 08, August 2026

Materials and Energy Research Center

In the Name of God

INTERNATIONAL JOURNAL OF ENGINEERING
Transactions B: Applications

DIRECTOR-IN-CHARGE
H. Omidvar

EDITOR IN CHIEF
G. D. Najafpour

ASSOCIATE EDITOR
A. Haerian

EDITORIAL BOARD

S.B. Adeloju, Charles Sturt University, Wagga, Australia
K. Badie, Iran Telecomm. Research Center, Tehran, Iran
M. Balaban, Massachusetts Ins. of Technology (MIT), USA
M. Bodaghi, Nottingham Trent University, Nottingham, UK
E. Clausen, Univ. of Arkansas, North Carolina, USA
W.R. Daud, University Kebangsaan Malaysia, Selangor, Malaysia
M. Ehsan, Sharif University of Technology, Tehran, Iran
J. Faiz, Univ. of Tehran, Tehran, Iran
H. Farrahi, Sharif University of Technology, Tehran, Iran
K. Firoozbakhsh, Sharif Univ. of Technology, Tehran, Iran
A. Haerian, Sajad Univ., Mashhad, Iran
H. Hassanpour, Shahrood Univ. of Tech., Shahrood, Iran
W. Hogland, Linnaeus Univ, Kalmar Sweden
A.F. Ismail, Univ. Tech. Malaysia, Skudai, Malaysia
M. Jain, University of Nebraska Medical Center, Omaha, USA
M. Keyanpour rad, Materials and Energy Research Center, Karaj, Iran
A. Mahmoudi, Bu-Ali Sina University, Hamedan, Iran
O.P. Malik, University of Calgary, Alberta, Canada
G.D. Najafpour, Babol Noshirvani Univ. of Tech., Babol, Iran
F. Nateghi-A, Int. Ins. Earthquake Eng. Seis., Tehran, Iran
S. E. Oh, Kangwon National University, Korea
M. Osanloo, Amirkabir Univ. of Tech., Tehran, Iran
M. Pazouki, MERC, Karaj, Iran
J. Rashed-Mohassel, Univ. of Tehran, Tehran, Iran
S. K. Sadrnezhaad, Sharif Univ. of Tech, Tehran, Iran
R. Sahraeian, Shahed University, Tehran, Iran
A. Shokuhfar, K. N. Toosi Univ. of Tech., Tehran, Iran
R. Tavakkoli-Moghaddam, Univ. of Tehran, Tehran, Iran
T. Teng, Univ. Sains Malaysia, Gelugor, Malaysia
P. Tiong, Nanyang Technological University, Singapore
X. Wang, Deakin University, Geelong VIC 3217, Australia
H. Omidvar, Amirkabir Univ. of Tech., Tehran, Iran

EDITORIAL ADVISORY BOARD

S. T. Akhavan-Niaki, Sharif Univ. of Tech., Tehran, Iran
M. Amidpour, K. N. Toosi Univ of Tech., Tehran, Iran
M. Azadi, Semnan university, Semnan, Iran
M. Azadi, Semnan University, Semnan, Iran
F. Behnamfar, Isfahan University of Technology, Isfahan
R. Dutta, Sharda University, India
M. Eslami, Amirkabir Univ. of Technology, Tehran, Iran
H. Hamidi, K.N.Toosi Univ. of Technology, Tehran, Iran
S. Jafarmadar, Urmia Univ., Urmia, Iran
A. Kheyroddin, Semnan Univ., Semnan, Iran
N. Latifi, Mississippi State Univ., Mississippi State, USA
H. Oraee, Sharif Univ. of Tech., Tehran, Iran
S. M. Seyed-Hosseini, Iran Univ. of Sc. & Tech., Tehran, Iran
M. T. Shervani-Tabar, Tabriz Univ., Tabriz, Iran
E. Shirani, Isfahan Univ. of Tech., Isfahan, Iran
A. Siadat, Arts et Métiers, France
C. Triki, Hamad Bin Khalifa Univ., Doha, Qatar

TECHNICAL STAFF
M. Khavarpour; M. Mohammadi; V. H. Bazzaz, R. Esfandiar; T. Ebadi

DISCLAIMER

The publication of papers in International Journal of Engineering does not imply that the editorial board, reviewers or publisher accept, approve or endorse the data and conclusions of authors.

International **J**ournal of **E**ngineering *Transactions A: Basics* (ISSN 1728-1431) (EISSN 1735-9244)
International **J**ournal of **E**ngineering *Transactions B: Applications* (ISSN 1728-144X) (EISSN 1735-9244)
International **J**ournal of **E**ngineering *Transactions C: Aspects* (ISSN 2423-7167) (EISSN 1735-9244)
Web Sites: www.ije.ir & www.ijeir.info E-mails: ije.editor8@gmail.com, Tel: (+9821) 88771578, Fax: (+9821) 88773352
Materials and Energy Research Center (MERC)

ISSN: 1728-144X, e-ISSN: 1735-9244

International Journal of Engineering, Volume 39, Number 08, August 2026

CONTENTS

Transactions B: Applications

H. Tamadon Ghareghieh, M. Yazdi, D. Yousefi Kebria, H. Aminirad	Effect of Different Non-aqueous Phase Liquids on Geoenvironmental Properties of Sandy Soils Stabilized with Bentonite	1790-1801
D. V. Gloukhov, D. V. Suchkov, A. P. Altukhova, D. R. Smirnov	Modeling of Dust Content Control System for Industrial Enterprises in the Mineral Resource Sector	1802-1811
A. Dey, S. Biswas, A. Gupta, M. Debnath	Multi-head Spectral-attentive Residual Generative Adversarial Network: A High-fidelity Generative Adversarial Network Based Model for Image Haze Removal	1812-1820
A. A. Bondarenko, M. K. Rogachev, A. S. Skvortsov, K. V. Dmitriev	Catalytic Conversion of Heavy Oil Using Molybdenum Based Water-soluble Catalyst	1821-1828
A. Faraji, M. R. Rahimipour, M. Farvizi, H. Omidvar	Behavior of a Next-Generation Nickel Super Alloy Turbine Component under Direct Exposure to Gas Heat from Combustion in a Long-term Operation	1829-1842
M. N. Abd-Al Ameer, I. S. Kareem, A. A. Ismaeel	Performance of Peltier-Based Thermal Management System: Impact of Multiple Modules on Cooling Efficiency and Energy Consumption	1843-1854
K. Reza Kashyzadeh, M. A. Ganjabi, S. Moghbeli, A. N. Ramzi Hassan, S. V. Khlopkov, M. Laad	Effects of Surface-level Defects on Tensile and Fatigue Strength of Spot Weld Bonding – Three-sheet Steel	1855-1864
I. I. Rastvorova, V. M. Filatov, S. A. Vilkov	Reduction of Optical Density in Highly Viscous Oils through Ultrasonic Treatment within The Infrared Wavelength Range	1865-1877
H. Yaghobi	A Modified Impedance-Based Loss of Field Detection Method of Synchronous Generator in the Presence of Series Capacitor and its Over-voltage Devices	1878-1892
Y. Guo, W. Qi, H. Zhou, G. Zhang, H. Liu	Geological Evaluation of Undersea Tunnel Excavation in Fault Fracture Zones Based on On-Site Drilling Tests	1893-1907
O. M. Prischepa, Y. V. Nefedov, A. V. Loginov, I. V. Tokarev, N. N. Vostrikov, A. M. Yashmolkin, A. M. Zharkov	Geochemical Characterization of Paleozoic Source Rocks in Nerutinskaya-3 Well, Timan-Pechora Petroleum Province	1908-1917

ISSN: 1728-144X, e-ISSN: 1735-9244

International Journal of Engineering, Volume 39, Number 08, August 2026

F. B. Khurshid, M. S. Izhar, N. Islam, N. A. Khan	Effect of Foundation Flexibility on Seismic Energy Dissipation in RC Bridges Subjected to Fling-step Ground Motions	1918-1932
N. Safaeian Hamzehkolaei, B. Karimi Ferezghi	An Interpretable Hybrid Shapley Additive Explanations Brown Bear Optimization Algorithm Predictive Models for End Bearing Capacity of Rock Socketed Piles	1933-1952
S. K. Mousavi, S. A. Hosseini, H. R. Vosoughifar, R. Barandoust, G. Mohammadi	A Multi-objective Optimization Model for Intelligent Information Management in Resource-Constrained Road and Transportation Projects	1953-1975
S. Shojaee Barjoee, V. Rodionov, R. Babkin, M. Tumanov, B. Shojaee Barjoee	An Integrated Modified Failure Mode Effects Analysis Shannon Entropy Combined Compromise Solution Approach to Safety Risk Assessment in Stone Crusher Unit of Ceramic Sector	1976-1987
M. Asgari, A. M. Boroujerdian	Evaluation of Optimal Turns Configuration at Intersections in Urban Roads Network Based on Safety and Congestion indices using Non-dominated Sorting Genetic Algorithm-2	1988-2011
B. Rahimpour Cami, H. Hassanpour, H. Mashayekhi	A Preference-based User Similarity to Construct a Collaborative Recommender System	2012-2021
A. A. Salman Al-Taai, W. A. Waryosh	Influence of Load Eccentricity on Structural Response of Slender Hybrid Self-compacting Concrete Columns with Reactive Powder Concrete Shells under Uniaxial Loading	2022-2034
R. Amiri, J. Karimpour, H. Izadkhah	Enhancing Smart Contract Access Control via Digital Identity Management and Machine Learning	2035-2048
S. Ojaghi, S. Jafarmadar, S. Khalilarya	Assessment of using Soybean Biodiesel Fuel on Performance and Exhaust Emission Characteristics of a Common-rail Diesel Engine (OM355)	2049-2062

IJE TRANSACTIONS B: Applications Vol. 39, No. 08, (August 2026) 1790-1801

International Journal of Engineering

Journal Homepage: www.ije.ir

Effect of Different Non-aqueous Phase Liquids on Geoenvironmental Properties of Sandy Soils Stabilized with Bentonite

H. Tamadon Ghareghieh[a], M. Yazdi*[a], D. Yousefi Kebria[b], H. Aminirad[b]

[a] *Department of Civil Engineering, CT.C., Islamic Azad University, Tehran, Iran*
[b] *Environmental Engineering Department, Faculty of Civil Engineering, Babol Noshirvani University of Technology, Babol, Iran*

PAPER INFO

Paper history:
Received 01 July 2025
Received in revised form 14 August 2025
Accepted 27 August 2025

Keywords:
Soil Microstructure Analysis
Non-aqueous Phase Liquid Contamination
Bentonite-Amended Sandy Soil
Geoenvironmental Engineering
Hydraulic and Shear Behavior

ABSTRACT

Energy requirements for remediation of petroleum-contaminated soils and strategy selection are essential from both environmental and geotechnical perspectives. The effectiveness of clay minerals and other stabilizers in enhancing the geotechnical properties of sandy soils contaminated with light non-aqueous phase liquids (LNAPLs) was confirmed in previous research. However, the combined impact of bentonite to sand ratio (BSR), and type and concentration of LNAPL simultaneously on geotechnical and environmental properties has not been thoroughly investigated and remains poorly understood. In this study, the influence of diesel and benzene with different concentrations (100, 150, 200, and 250 g LNAPLs/kg dry soil) on the geoenvironmental characteristics of sandy soils stabilized and improved using different BSRs (0, 0.2, 0.4, and 0.6) were comperehesllly evaluated. The results indicated an increase in maximum dry density (MDD) and a reduction in optimum moisture content (OMC) during the compaction tests. Additionally, a decrease in cohesion and a decrease in the friction angle were observed in soils with higher concentrations of LNAPLs and BSR, with diesel exhibiting more pronounced effects than benzene. An increase in MDD and a decrease in OMC were also noted with escalating concentrations of both LNAPLs. Based on the results, BSR = 0.4 was found to be the optimal value that the soil mixture exhibits high MDD, low permeability (1×10^{-9}–7×10^{-9} cm/s), significantly increased cohesion (>50 kPa), and acceptable internal friction angles (~20–22°), at the concentrations of 150–200 g/kg. Analytical techniques, including FTIR, EDAX, XRF, and XRD were confirmed these results, providing insights into the mechanisms of contaminant retention in bentonite-amended sandy soils. The findings of this study can inform the geotechnical design of structures on LNAPL-contaminated soils and guide the selection of appropriate remediation methods.

***doi**: 10.5829/ije.2026.39.08b.01*

Graphical Abstract

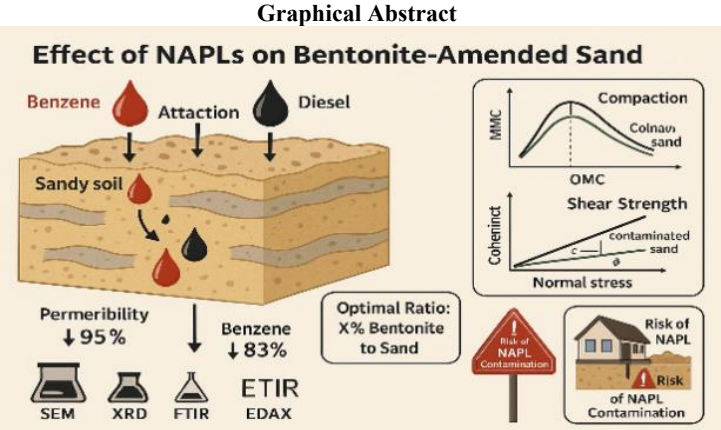

* Corresponding Author Email: mar.yazdi@iau.ac.ir (M. Yazdi)

Please cite this article as: Tamadon Ghareghieh H, Yazdi M, Yousefi Kebria D, Aminirad H. Effect of Different Non-aqueous Phase Liquids on Geoenvironmental Properties of Sandy Soils Stabilized with Bentonite. International Journal of Engineering, Transactions B: Applications. 2026;39(08):1790-801.

1. INTRODUCTION

Soil contamination by petroleum hydrocarbons in coastal sandy areas, as highlighted in various studies and reports by the USEPA and UN environmental programs, poses significant environmental risks and challenges for civil engineering projects. Remediation of petroleum-contaminated sandy soils via thermal desorption methods typically requires up to 5,000–6,000 kJ/kg (1.4–1.7 kWh/kg), while electrochemical methods have reported specific energy consumption in the range of 1.6–2.9 kWh/kg, depending on contamination levels and scale (1, 2).

Recent studies have supported the efficacy of bentonite-enhanced bioremediation observed by Adams et al. (3). TPH concentration was reduced by approximately 55% after 28.8 months. However, Qv et al. (4) demonstrated that adding bentonite to aerobic composting of petroleum-contaminated soil improved hydrocarbon removal efficiency from 45% to 79%. Similarly, Li et al. (5) confirmed that advanced oxidation processes combined with mineral additives significantly enhanced hydrocarbon degradation, aligning with the stabilization trends reported in earlier field-scale studies.

Improving the geoenvironmental properties of these soils is crucial to ensure both environmental safety and structural stability in infrastructure development. Light Non-Aqueous Phase Liquids (LNAPLs), such as diesel and benzene with different Physicochemical characteristics, are among the most pervasive organic pollutants adversely affecting groundwater and soil systems on a global scale (6). Due to their low water solubility and high hydrophobicity, LNAPLs tend to persist in the subsurface environment, leading to long-term pollution and posing Substantial risks to human health and ecosystems (7, 8). Sandy soils, w ith large pore spaces and high permeability, facilitate rapid LNAPL migration, which complicates remediation methods and increases the potential for widespread contamination (9). Consequently, improving the geotechnical and geoenvironmental characterization of sandy soils to limit contaminant migration has become an essential research concern.

Sandy soil stabilization using bentonite with high swelling capacity and cation exchange capacity has been widely adopted as an effective method to enhance geoenvironmental engineering properties (10, 11), because it is enable to fill soil voids, adsorb NAPLs, and reduce contaminant migration (12, 13).

Physical and biochemical remediation of petroleum hydrocarbons contaminated soil, as well as the use of bentonite as a stabilization agent to stabilize the sandy soil contaminated with NAPLs, has been widely investigated and reported by our group, which has shown promising results in enhancing soil remediation and stabilization methods and reducing leaching of contaminated fields (14-19). Furthermore, Several studies have demonstrated that bentonite amendments can significantly enhance soil cohesion and decrease hydraulic conductivity, providing both structural reinforcement and environmental containment (20-22).

Also, statistical and numerical modeling have been used in related studies. De Medeiros et al. (22) used ANOVA to evaluate the influence of moisture content and emulsion type on the stiffness of stabilized soil and found that moisture content and emulsion type significantly affect soil stiffness, with certain emulsions performing best at optimal moisture. Zheng et al. (23) employed numerical modeling and showed that a confined sand cell reduces vibration transmission and improves damping. Kassem et al. (24) reported that cemented phosphogypsum enhances strength and durability, especially under cyclic loading.

Moreover, most other investigations have focused on either geotechnical improvements or contaminant adsorption separately, with limited integrated analysis of how LNAPL contamination influences the mechanical and environmental behavior of bentonite-stabilized sandy soils (25). For example, Safehian et al. (26) showed that increasing diesel concentration (from 100 to 250 g /kg dry soil) in fine-grained soil resulted in a decrease in maximum dry density (MDD), uniaxial strength, internal friction angle, and cohesion, while increasing compressibility and OMC. Similarly, the results of Al-Aghbari et al. (27)demonstrate that the Atterberg limits and cohesion of sandy soils contaminated with diesel fuel and gasoline (at concentrations of 0%, 5%, and 10%) were enhanced, while the angle of internal friction, permeability, and OMC were reduced. These findings aligned with Nasehi et al. (28), who Indicated a decrease in MDD, OMC, and internal friction angle, while cohesion and Atterberg limits increased in fine-grained soil.

Hanaei et al. (29) investigated the effect of varying contamination levels (0%, 5%, 10%, and 15%) of diesel and benzene on two types of sandy soils. The results revealed a reduction in permeability of the contaminated soils, as well as a decline in MDD and OMC. Moreover, direct shear tests showed increased cohesion and decreased internal friction angle following contamination.

To comprehensively evaluate the impact of LNAPL contamination on the engineering and chemical behavior of bentonite-stabilized sandy soils, this research employed several advanced characterization experiments, including Fourier Transform Infrared Spectroscopy (FTIR), Energy Dispersive X-ray Spectroscopy (EDX), X-Ray Fluorescence (XRF), and X-Ray Diffraction (XRD) were used to explain the microstructural and chemical modifications and

interaction between LNAPLs and soils. Moreover, the synergistic effects and coupled impacts of type and concentration of LNAPL, and bentonite content (BSR) on geotechnical and environmental behavior were assessed to determine the optimal BSR that balances practical and economic factors. Because too much bentonite can reduce soil structure or increase costs without sufficient benefits.

2. MATERIALS AND METHODS

2. 1. Sand-Bentonite Mixture The sandy soil was collected from the southern coastline of the Caspian Sea (Iran). The particle size distribution was determined in accordance with ASTM D422 (30). The specific gravity was measured to be 2.75 g/cm³, following the procedures outlined in ASTM D854 (31). According to the results of grain size analysis and the Unified Soil Classification System (USCS), the sand and bentonite samples were classified as SP (poorly graded sand) and CH (clay with high plasticity), respectively. To identify the dominant mineralogical composition of the bentonite, XRD analysis was performed using a diffractometer equipped with Cu-Kα radiation (λ = 0.154 nm). The analysis revealed montmorillonite as the primary clay mineral. Additionally, quartz, clinoptilolite, cristobalite, and calcite were identified as minor constituents (see Figure 1). The key physical properties of the sand and bentonite used in this study are summarized in Table 1.

Furthermore, Table 2 presents the chemical composition of both materials, as determined through XRF analysis. To ensure homogeneity across all test specimens, the required soil quantities were first sieved through a No. 4 mesh and subsequently oven-dried at 105 °C for 24 hours. Diesel and benzene—procured from the Tehran Oil Refinery—were selected as the representative petroleum-based contaminants due to their widespread presence in petroleum-contaminated soils globally and in the Caspian coastal region, as documented by the U.S. Environmental Protection Agency (USEPA) in large-scale spill assessments.

The dried soil was then mixed with sodium bentonite at different BSRs (0, 0.2, 0.4, and 0.6), and separately contaminated different concentrations of diesel and benzene (100, 150, 200, and 250 g /kg dry soil), following the approach by Sarmadi et al. (32). The applied concentrations with observed TPH ranges reported in sediments and soils affected by major spills.

To achieve uniform distribution and stabilization of the mixtures, the prepared samples were conditioned at at standard laboratory ambient temperature, assumed to be approximately 25 °C (33).

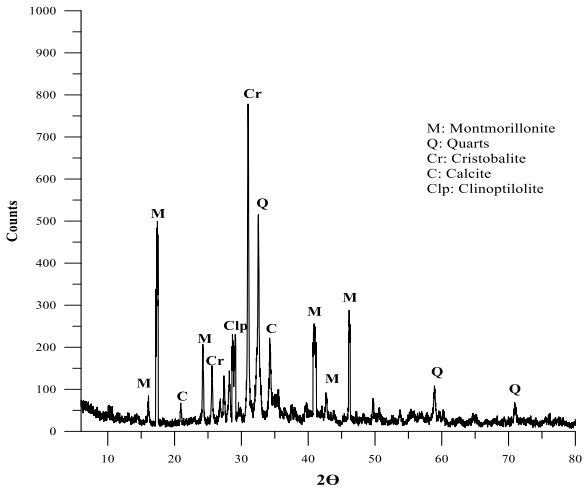

Figure 1. XRD pattern of bentonite

TABLE 1. Parameters of soil characteristics

Parameter	Sand	Bentonite
Classification (USCS)	SP	CH
Specific gravity (*Gs*)	2.75	2.7
Liquid Limit (%)	-	135
Plastic Limit (%)	-	40
Plasticity Index (%)	-	95
Maximum dry density (gr/cm^3)	1.77	1.48
Minimum dry density (gr/cm^3)	1.5	1.31
D_{50} (mm)	0.22	-
e_{min}	0.53	-
e_{max}	0.8	-
C_u	1.6	
C_s	1.1	

TABLE 2. Element Data of sand and bentonite sample

Soil	Compound (%)											
	SiO_2	Al_2O_3	Fe_2O_3	TiO_2	CaO	MgO	Na_2O	K_2O	SO_3	MnO	P_2O_5	LOI
Sand	93.5	0.82	1.26	-	1.43	0.223	0.061	0.095	0.27	-	-	1.04
Bentonite	61.4	13	2.5	0.25	4.7	1.24	2.7	0.6	0.45	0.04	0.07	12

2. 2. Methods A comprehensive suite of experimental procedures was employed to evaluate the geotechnical and chemical characteristics of the contaminated and treated soil specimens. Standard Proctor compaction tests, conducted in accordance with ASTM D698 (34), were used to determine the MDD and OMC of each soil mix. Shear strength parameters, including cohesion and internal friction angle, were obtained through direct shear tests following the ASTM D3080 (35) standard. To evaluate the hydraulic behavior of the specimens, constant head permeability tests were performed in line with ASTM D2434(36). In addition to mechanical characterization, the chemical alterations induced by hydrocarbon contamination and bentonite treatment were assessed using FTIR, conducted in accordance with ASTM D5477 (37). This integrative testing approach enabled a robust analysis of the physical, hydraulic, and chemical response of the sand–bentonite mixtures under varying contaminant levels.

2. 2. 1. Compaction Test Each sample was prepared using a cylindrical mold with a diameter of 4 inches and an approximate volume of 945 cm³. The soil was placed in five equal layers, and each layer was compacted by applying 25 uniform blows using a 10-pound hammer dropped from a height of 18 inches. Upon completion of compaction, the specimens' dry densities and moisture contents were determined. For hydrocarbon-contaminated specimens, the moisture content was calculated using a modified approach that accounts for the residual hydrocarbons present after drying, as proposed by Khamehchiyan et al. (38). The calculation is expressed by Equation 1:

$$W(\%) = (1 + mn)\frac{\mathrm{Wt}}{\mathrm{Wd}} - (1 + n) \quad (1)$$

where W_t is Weight of the moist contaminated soil, W_d is Weight of the dry contaminated soil, m is Percentage of residual contaminant after drying and n (%) is Initial percentage of contaminant before drying.

This correction ensures accurate determination of water content in samples where hydrocarbons may evaporate or partially remain during the drying process.

2. 2. 2. Direct Shear Test Direct shear tests were carried out in accordance with ASTM D3080 (39) to determine the shear strength parameters of the soil Mixture, specifically the internal friction angle (ϕ) and cohesion (c). A direct shear apparatus equipped with a shear box of dimensions 100 × 100 mm² was utilized for this purpose. Specimens were compacted into the shear box in three to four uniform layers using Plexiglas frames, each with dimensions of 10 cm × 10 cm × 3.3 cm, to ensure the final specimen volume matched the box capacity. The compaction was performed at the OMC corresponding to the previously determined MDD of each mix. Shear testing was conducted under constant normal stresses of 50, 100, 150, 200, and 250 kPa, with a controlled horizontal displacement rate of 0.7 mm/min. This setup allowed for accurate determination of the stress–strain behavior and failure envelopes of the contaminated and treated soil specimens.

2. 2. 3. Permeability Test Constant head permeability tests were performed in accordance with ASTM D2434 (36) to evaluate the hydraulic conductivity of the soil specimens. To enhance the accuracy of the results, each test was repeated three times per specimen, and the average value was recorded as the final result. The testing apparatus included a cylindrical mold with an internal diameter of 8 cm and a height of 22 cm. Hydraulic conductivity (K) in the vertical direction was calculated using the following equation:

$$K = \frac{Q \times L}{t \times A \times h} \quad (2)$$

where Q is volume of water discharged, L is length of the soil specimen, t: Duration of flow, A is cross-section area of the soil specimen and h is constant head.

2. 2. 4. FTIR Analysis Fourier Transform Infrared Spectroscopy (FTIR) analyses were conducted in accordance with ASTM D5477 (37) and ASTM E168-16 (39) to investigate chemical interactions and changes in functional groups within the soil specimens. The FTIR technique detects molecular vibrations, including stretching (changes in bond length), bending (changes in bond angle), or a combination of both, to infer the presence and type of chemical bonds. Analyses were performed using a Spectrum 100 spectrometer (PerkinElmer, USA) with a scanning range of 1450–4000 cm^{-1}. Solid samples were finely ground and analyzed either in powder form or as potassium bromide (KBr) pellets to ensure spectral accuracy. FTIR provided insights into the alteration of soil chemistry induced by hydrocarbon contaminants and bentonite stabilization.

3. RESULTS AND DISCUSSION

3. 1. Energy Dispersive X-ray Spectroscopy (EDX) To investigate the elemental composition and morphology of the bentonite used, the EDX spectrum of the bentonite sample was employed, as illustrated in Figure 2. The analysis revealed that oxygen was the most abundant element (45% by weight), followed by silicon (39.4%), aluminum (13.2%), and sodium (2.7%). These findings confirm the mineralogical signature of bentonite, characterized by high silica and alumina content, consistent with the presence of montmorillonite as the dominant mineral phase. Aluminum is an essential

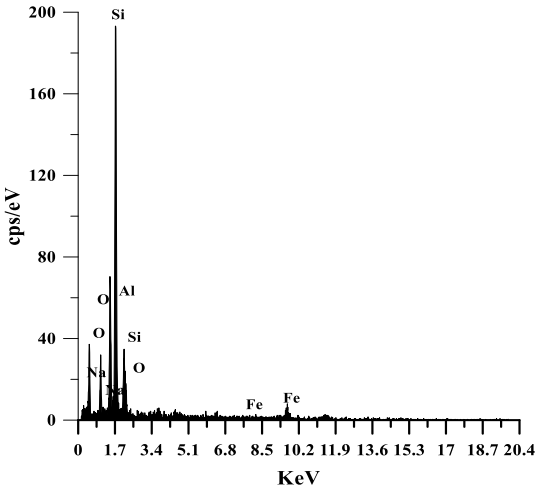

Figure 2. EDX pattern of bentonite

component of the tetrahedral/octahedral sheets in montmorillonite, contributing to the cation exchange capacity (CEC).

3. 2. Compaction Characteristics of Contaminated Specimens Figures 3 and 4 presents the results of the standard compaction tests conducted on soil specimens containing various BSR (0, 0.2, 0.4, and 0.6), with varying levels of diesel and benzene contamination, respectively. As illustrated, at a constant bentonite content, increasing the proportion of hydrocarbon contaminants results in a noticeable increase in MDD and a corresponding decrease in OMC.

This trend can be attributed to the lubricating effect of diesel and benzene, both of which exhibit relatively low polarity and high viscosity. As the contamination level increase, a greater fraction of the soil surface becomes coated with hydrocarbons. This coating reduces interparticle friction and facilitates particle slippage and rearrangement, leading to a denser particle packing. This effect, indirectly evidenced by the observed increase in MDD and decrease in OMC, is consistent with previous studies (32, 38) that reported reduced void ratio and pore volume in TPH-contaminated soils.

Moreover, both diesel and benzene are hydrophobic in nature, forming a nonpolar film around soil particles that inhibits water-soil interaction. This hydrophobic barrier limits the soil's water absorption capacity, thereby reducing the amount of moisture required to achieve optimum compaction. The combination of reduced interparticle resistance and decreased water demand results in a compaction curve that shifts toward higher densities and lower moisture contents compared to uncontaminated conditions.

3. 3. Influence of NAPLs and BSR on Compaction Behavior The interaction between soil particles and NAPLs alters the physicochemical structure of the soil matrix, particularly through the reduction of the diffuse double layer surrounding clay minerals. This contraction of the double layer brings particles closer together, thereby enhancing intergranular contact under a given compaction effort. As a result, the MDD increases due to improved particle coherence—an effect previously reported by Meegoda and Ratnaweera (40) and Al-Sanad et al. (41).

The findings of the present study demonstrate that increasing hydrocarbon contamination leads to a consistent reduction in OMC, accompanied by an increase in MDD, which aligns well with earlier research. The lubricating properties of hydrocarbons, particularly diesel and benzene, contribute to this outcome by reducing interparticle friction and facilitating denser packing during compaction. Furthermore, the hydrophobic nature of these contaminants restricts water-soil interaction, lowering the amount of water needed to reach optimum compaction.

At a constant contamination level, increasing the bentonite content results in a further increase in MDD, suggesting that the addition of bentonite enhances soil structure through its high specific surface area and water absorption capacity. Consequently, the OMC also increase, as more water is required to hydrate the bentonite particles and achieve the desired compaction response.

Notably, the observed rate of change in compaction parameters was more pronounced in diesel-contaminated samples compared to those treated with benzene. This can be attributed to the higher viscosity of diesel, which intensifies its lubricating effect—a trend corroborated by previous studies such as those by Hanaei et al. (29), Shin and Das (42). Similarly, Kermani and Ebadi (43) observed that increasing hydrocarbon content from 4% to 12% led to a progressive increase in dry density and concurrent decrease in moisture content. However, some studies have reported contrasting behavior; for instance, Al-Sanad et al. (41) noted a decrease in dry density at contamination levels between 4% and 6%. These variations underline the complex interplay between contaminant type, viscosity, and soil mineralogy in governing compaction characteristics.

Based on the results, both diesel and benzene increase MDD and reduce OMC of soil mixtures, but benzene shows a significantly weaker effect. At the concentration of 200–250 g/kg dry soil, MDD increases less in benzene-contaminated soils due to lower polarity, and lighter molecular structure. Increasing BSR higher volatility, content mitigates both effects, but it is more effective against diesel than benzene. This is likely due to bentonite's higher affinity for heavier hydrocarbons like diesel. Overall, benzene impairs compaction more severely, necessitating enhanced stabilization strategies for affected soils.

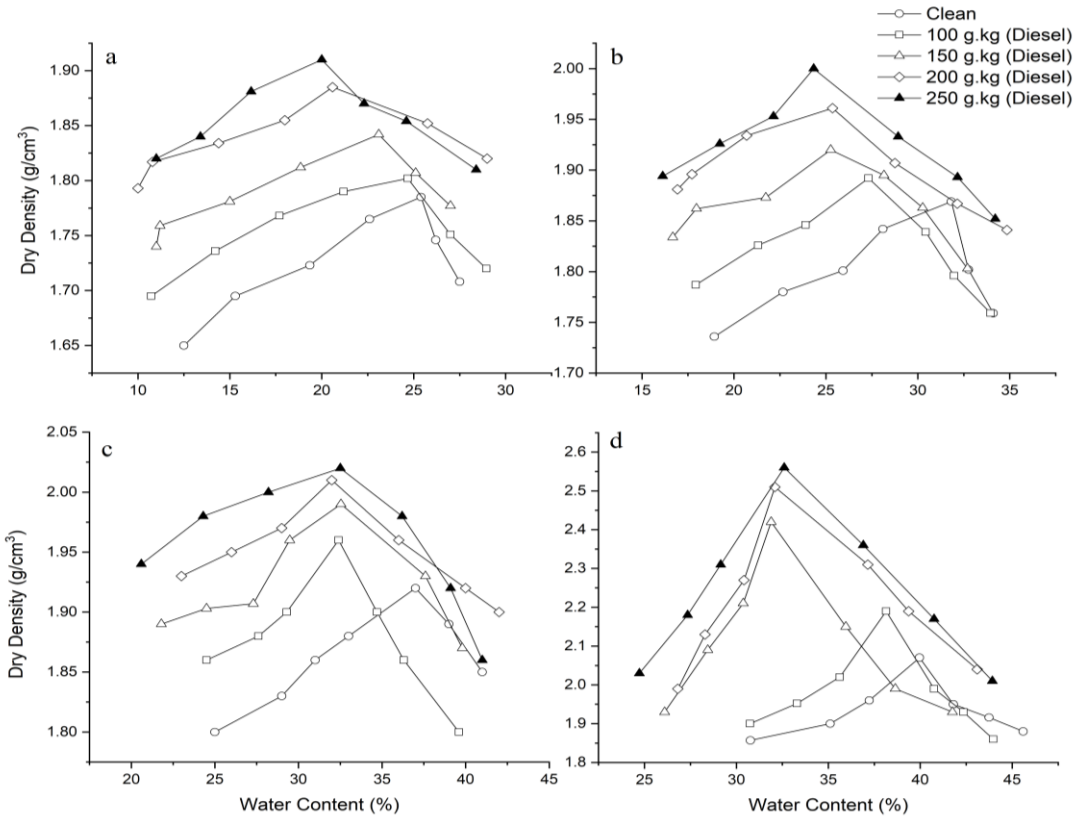

Figure 3. The influence of diesel concentration on dry density curves and water content in soil mixture with different BSR a) 0, b) 0.2, c) 0.4, and d) 0.6

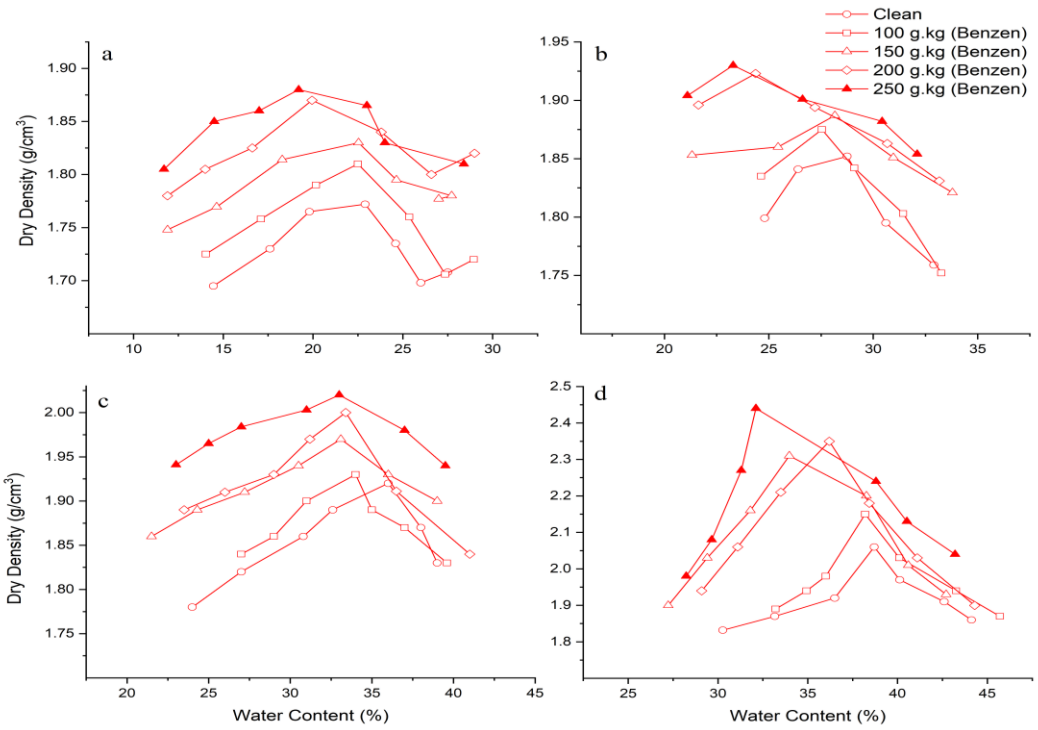

Figure 4. The influence of benzene concentration on dry density curves and water content in soil mixture with different BSR a) 0, b) 0.2, c) 0.4, and d) 0.6

3. 4. Variation in Soil Cohesion and Internal Friction Angle Figures 5 and 6 present the variation in soil cohesion (c) and internal friction angle (ϕ) with different BSR and contaminant concentration.

The test results indicate that cohesion in both diesel- and benzene-contaminated soils increases with increasing BSR. At BSR = 0.0, cohesion values are minimal, ranging from 1 to 9 kPa depending on contaminant type and concentration. However, as the BSR increases to 0.6, cohesion sharply increases and reaches between 45 and 75 kPa. The cohesion gain is attributed to the interparticle binding effect of bentonite, which promotes electrochemical attractions and reduces void ratio. Overall, cohesion was observed to increase with bentonite addition, due to the intrinsic cohesive properties of bentonite and its high viscosity and surface area, which contribute to the formation of interparticle bonds (44). Conversely, increasing the concentration of diesel or benzene contamination led to a decline in cohesion. On average, sand–bentonite mixtures contaminated with NAPLs exhibited a 45% increase in cohesion compared to clean sand, although this gain diminished with increasing contaminant concentration. The observed reduction in cohesion due to hydrocarbon exposure is likely the result of diminished cation exchange capacity, replacement of adsorbed water by contaminant molecules, and a reduction in the soil's effective specific surface area (38). In essence, while bentonite enhances cohesion, NAPLs tend to offset this effect, particularly at higher concentrations.

These trends are consistent with those reported by Mohammadi and Ebadi (44), who found that at a fixed bentonite level, increasing NAPL content reduces the angle of internal friction while marginally increasing or stabilizing cohesion. Similarly, Shin and Das (42) and Khamehchiyan et al. (38) reported significant reductions in ϕ in poorly graded or silty sands subjected to oil contamination. The extent of changes in both ϕ and c appears to be strongly influenced by the viscosity of the NAPL contaminant. More viscous fluids, such as diesel, exhibit a stronger lubricating effect and promote more significant reductions in internal friction angle, a finding supported by Khosravi et al. (45) and other researchers.

At BSR=0, diesel consistently exhibit higher cohesion than benzene. This pattern can be explained by the viscous, adhesive nature of diesel, which coats soil particles and enhances apparent cohesion, whereas benzene (with more volatile and less interactive) has a weaker bonding effect. Similar this results Taheri et al. (46) observed diesel contamination increased cohesion in sand–bentonite soil due to flocculation and particle agglomeration. In contrast, Hanaei et al. (29) found that the effect of benzene on cohesion was more less intense and primarily dependent on bentonite content.

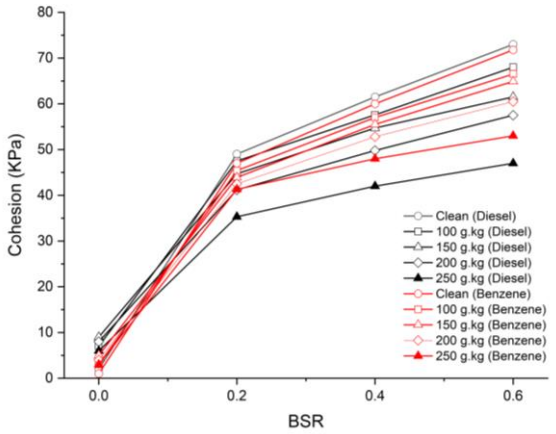

Figure 5. Cohesion function variation of soil mixture contaminated with diesel and benzene at different BSR

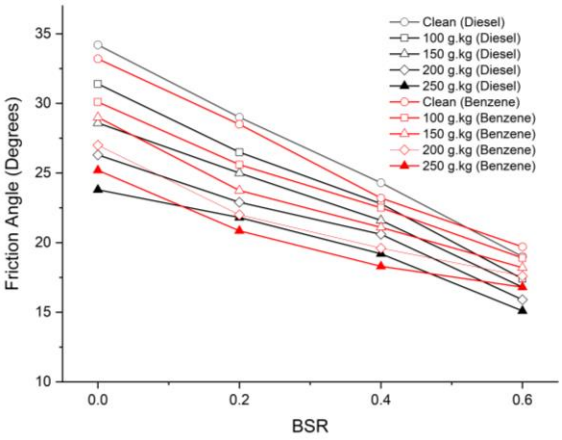

Figure 6. The change of the internal friction angle in diesel and benzene contaminated soil mixture at different BSR

3. 5. Permeability Response to NAPL Contamination and Bentonite Content Figure 7 illustrates the variation in the coefficient of permeability (k) for sand–bentonite mixtures subjected to diesel and benzene contamination at different concentrations of various BSR (0, 0.2, 0.4, and 0.6). The data indicate a clear decreasing trend in hydraulic conductivity with increasing proportions of both NAPL contaminants and bentonite specifically, for specimens contaminated with 200 g benzene/kg dry soil, the permeability was reduced by 31.4%, 61.1%, and 45% at BSRs of 0.2, 0.4, and 0.6, respectively. In comparison, the corresponding reductions for diesel-contaminated specimens were more pronounced—46.2%, 66.8, and 63.5% at the same bentonite contents. These findings suggest that diesel exerts a greater sealing and pore-blocking effect than benzene, which is attributable to its higher viscosity and more significant interaction with soil particles.

Based on the results, the permeability of soil mixtures contaminated with diesel and benzene decreases consistently with increasing contaminant concentration (0–250 g/kg dry soil), and the extent of this reduction is more pronounced with higher bentonite-to-sand ratios (BSR). The most substantial decline in permeability was observed at BSR = 0.6, where the coefficient of permeability dropped below 1×10^{-9} cm/s, indicating nearly impermeable conditions suitable for engineered barrier systems. However, this observation does not contradict the more pronounced percentage reduction in permeability caused by diesel at identical BSRs. The apparent lower absolute permeability in benzene-contaminated soils may stem from deeper infiltration into the bentonite layers, resulting in increased tortuosity and longer flow paths, despite its lower viscosity. Thus, while diesel exhibits stronger pore-blocking due to its viscous nature, benzene's molecular-scale interaction with bentonite contributes to finer microstructural occlusions, leading to distinct permeability behavior. These findings highlight the dual role of bentonite in both reducing hydraulic conductivity and mitigating contaminant transport.

The observed reduction in permeability can be explained by the partial to full filling of pore spaces by NAPL molecules, which obstruct water flow pathways and reduce the effective porosity of the soil matrix. Moreover, the lamellar and swelling characteristics of bentonite amplify this effect by closing off microvoids and increasing soil plasticity. These mechanisms are in agreement with previous studies such as Shin and Das (42) and Al-Aghbari et al. (27), who reported that NAPLs with greater kinematic viscosity cause more severe permeability declines.

Supporting evidence can also be found in earlier works by Khamehchiyan et al. (38)and Hanaei et al. (29), who observed that diesel and benzene contamination in sandy and silty soils significantly reduced permeability, particularly when bentonite was introduced as a sealing agent. These reductions were attributed to decreased pore connectivity and increased interparticle adhesion. Similarly, Sarmadi et al. (32) and Oyediran et al. (47) confirmed that NAPL contamination leads to reduced permeability, lower internal friction angle, and increased apparent cohesion in treated sandy soils.

The role of soil gradation was also emphasized in studies such as Al-Sanad et al. (41), who demonstrated a steady decline in permeability for poorly graded sands exposed to hydrocarbons. Additionally, Khamehchiyan et al. (38) attributed the continued decrease in permeability of silty sands to reduced effective porosity following hydrocarbon exposure.

Collectively, these findings confirm that the permeability reduction in contaminated soil is governed by a combination of fluid viscosity, contaminant content, soil structure, and bentonite-enhanced sealing, all of which are crucial in predicting fluid transport behavior in polluted geotechnical systems.

3. 6. FTIR Analysis Figure 8 depicts the FTIR spectrum of the soil before and after contamination with diesel and benzene for different BSRs (0, 0.2, 0.4, and 0.6). FTIR analysis reveals molecular interactions and functional groups through changes in absorption and transmission intensity. In addition to the higher wavenumber regions, the 400–1450 cm^{-1} fingerprint region was also analyzed to capture key hydrocarbon and clay-related vibrations.

Within the fingerprint region, major peaks were identified at 1030–1056 cm^{-1} (Si–O stretching in bentonite, C–O stretching in alcohols/phenols), 1160–1180 cm^{-1} (C–O–C asymmetric stretching in ethers/esters), 1260–1300 cm^{-1} (COOH bending/CH_2 twisting), 1375–1385 cm^{-1} (CH_3 symmetric bending), and 1450 cm^{-1} (CH_2 bending). Quantitatively, the intensity of these peaks decreased by approximately 60–75 % as the BSR increased from 0 to 0.6, indicating reduced abundance of polar functional groups due to bentonite–LNAPL interactions.

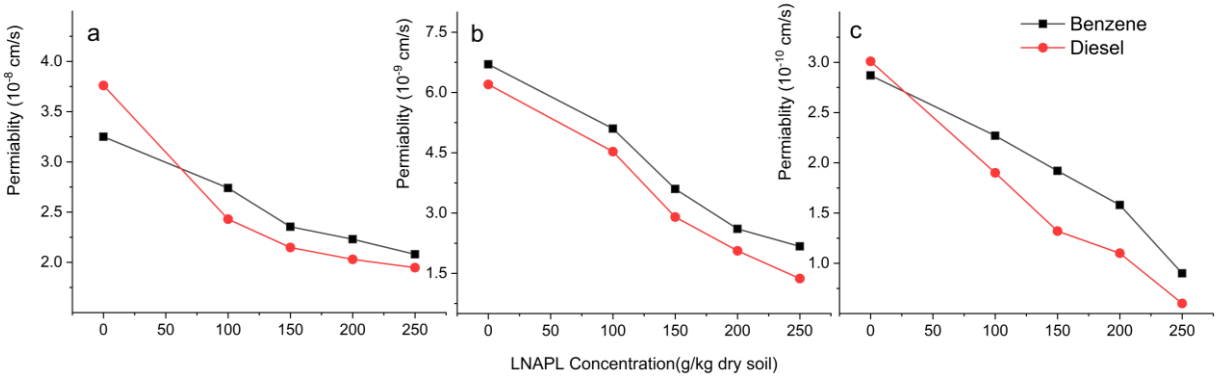

Figure 7. Variation of Permeability contaminated soil with different NAPL and BSR: a) 0.2, b) 0.4, c) 0.6

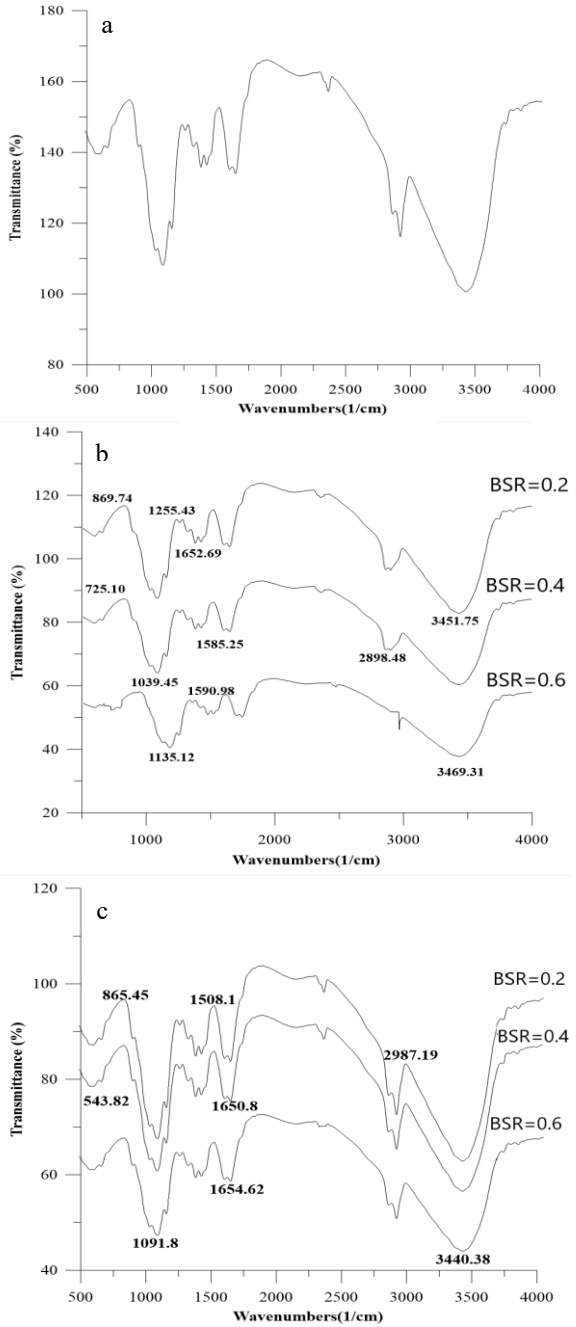

Figure 8. FTIR analysis of soil mixture; a) clean soil b) diesel contaminated soil c) benzene contaminated soil

In the higher wavenumber region, prominent absorption peaks were observed between 1056–1589 cm^{-1} and 2910–3455 cm^{-1}, corresponding to aromatic C=C bending and C–H stretching, confirming the presence of hydrocarbons. Diesel-contaminated soils showed aliphatic C–H stretching bands between 2850 and 3000 cm^{-1}, while benzene-contaminated samples exhibited strong aromatic vibrations around 1600 cm^{-1}. Quantitatively, the absorption peak at 2987 cm^{-1} (aliphatic C–H stretching) decreased from 30 % to 5 % transmittance as BSR increased from 0.2 to 0.6, while the 1600 cm^{-1} peak (aromatic C=C stretching) dropped from 25 % to below 5 %, representing an over 80 % reduction in hydrocarbon-related absorbance. Furthermore, the OH stretching vibration near 1106 cm^{-1} may be related to phenolic groups, suggesting electron resonance effects during hydrocarbon–soil complexation. The absorption at 1300 cm^{-1} likely corresponds to asymmetric carboxyl (COOH) vibrations. As BSR increased, the absorbance intensity of all major peaks declined, further validating bentonite's role in immobilizing contaminants and reducing their mobility.

4. CONCLUSION

A comprehensive research program of laboratory tests was conducted to study the effects of bentonite content on the geoenvironmental behavior of a sandy soil contaminated with different percentages of light non-aqueous phase liquids (LNAPLs). For this purpose, different concentrations (100, 150, 200, and 250 g LNAPLs/kg dry soil) for various BSR (0, 0.2, 0.4, and 0.6) were subjected to standard compaction tests, direct shear tests (to determine the internal friction angle and cohesion), permeability tests, and FTIR. For a constant amount of bentonite, with the increase of the contamination, the MDD increased and the OMC decreased. According to the results, larger amounts of bentonite resulted in higher MDD and OMC of the soil. Specifically, at a contamination level of 250 g/kg, MDD increased by 5.4% for diesel and 3.8% for benzene relative to the clean sample. The internal friction angle decreased by 30.7% for diesel and 19.4% for benzene, while cohesion increased by 24.9% and 28.3%, respectively. These quantitative differences confirm that diesel generally induced more pronounced changes in geotechnical properties than benzene. At a constant BSR, higher contamination leads to lower internal friction angles and decreasing cohesion. Increasing the NAPL concentration resulted in a reduction in the internal friction angle, while the cohesion of the soil samples showed a similar decrease that highlights the lubricating effect of NAPL on interparticle friction and the simultaneous decrease of apparent cohesion due to the covering of the soil surface by NAPL and the change in the electronic double layer. The results of the permeability test revealed that, for all BSR, the permeability decreased with increasing of NAPL concentration. For different BSR, the minimum permeability was observed at BSR=0.6. While the absolute minimum permeability was achieved at BSR = 0.6, the results demonstrated that BSR = 0.4 provides the most balanced combination of high MDD, low permeability (between 1×10^{-9} – 7×10^{-9} cm/s), high

cohesion, and acceptable internal friction angles. These characteristics, combined with better compactability and lower cost, make BSR = 0.4 more practical for engineering applications than BSR = 0.6. Notably, the rate of permeability reduction was dependent on both the contaminant concentration and the physicochemical properties, particularly the viscosity of diesel and benzene.

5. REFERENCES

1. Sasivongpakdi A, Lee J-Y, Bharadwaj H, Keener TC, Barth EF, Clark PJ, et al. Evaluation of a sustainable remediation option: Beneficial reuse of petroleum-contaminated sediment as an energy source. Journal of the Air & Waste Management Association. 2012;62(11):1277-84.
2. Streche C, Cocârţă DM, Istrate I-A, Badea AA. Decontamination of petroleum-contaminated soils using the electrochemical technique: remediation degree and energy consumption. Scientific Reports. 2018;8(1):3272.
3. Adams R, Guzmán-Osorio F, Domínguez-Rodríguez V. Field-scale evaluation of the chemical–biological stabilization process for the remediation of hydrocarbon-contaminated soil. International Journal of Environmental Science and Technology. 2014;11(5):1343-52. https://doi.org/10.1007/s13762-013-0321-1
4. Qv M, Bao J, Wang W, Dai D, Wu Q, Li S, et al. Bentonite addition enhances the biodegradation of petroleum pollutants and bacterial community succession during the aerobic co-composting of waste heavy oil with agricultural wastes. Journal of hazardous materials. 2024;462:132655. 10.1016/j.jhazmat.2023.132655
5. Li Y-T, Li D, Lai L-J, Li Y-H. Remediation of petroleum hydrocarbon contaminated soil by using activated persulfate with ultrasound and ultrasound/Fe. Chemosphere. 2020;238:124657. https://doi.org/10.1016/j.chemosphere.2019.124657
6. Gupta PK, Yadav BK. Bioremediation of non-aqueous phase liquids (NAPLS) polluted soil and water resources. Environmental Pollutants and their Bioremediation Approaches CRC Press, Boca Raton. 2017:241-56.
7. Ossai IC, Ahmed A, Hassan A, Hamid FS. Remediation of soil and water contaminated with petroleum hydrocarbon: A review. Environmental Technology & Innovation. 2020;17:100526. https://doi.org/10.1016/j.eti.2019.100526
8. Wiedemeier TH, Rifai HS, Newell CJ, Wilson JT. Natural attenuation of fuels and chlorinated solvents in the subsurface: John Wiley & Sons; 1999.
9. Wenhui L, Hepeng Z, Hongliang L, Jiale C, Hengxiao Y, Qiang S. Characterization of Water Distribution Characteristics in Response to Light Non-Aqueous Phase Liquids Migration Processes. Polish Journal of Environmental Studies. https://doi.org/10.15244/pjoes/196735
10. Sharma HD, Reddy KR. Geoenvironmental engineering: site remediation, waste containment, and emerging waste management technologies: John Wiley & Sons; 2004.
11. Nierwinski HP, Sosnoski J, Heidemann M. Evaluation of strength and durability of compacted bauxite tailings treated with cement. Clean Technologies and Environmental Policy. 2025:1-10. https://doi.org/10.1007/s10098-025-03212-x
12. Mitchell J, Soga K. Fundamentals of soil behavior. 2005.
13. Lake CB, Rowe RK. The 14-year performance of a compacted clay liner used as part of a composite liner system for a leachate lagoon. Geotechnical & Geological Engineering. 2005;23(6):657-78. https://doi.org/10.1007/s10706-004-8815-8
14. Akbarpour A, Kebria DY. Enhanced remediation of naphthalene from aqueous solutions using synthesized organoclay: characterization, mechanisms, and isotherms. Environmental Monitoring and Assessment. 2025;197(2):152. https://doi.org/10.1007/s10661-024-13533-x
15. Ghavami M, Yousefi Kebria D, Javadi S, Ghasemi-Fare O. Cement-organobentonite admixtures for stabilization/solidification of PAH-contaminated soil: A laboratory study. Soil and Sediment Contamination: An International Journal. 2019;28(3):304-22. https://doi.org/10.1080/15320383.2018.1564734
16. Tamadon Ghareghie H, Yazdi M, Yousefi Kebria D, Aminirad H. Analysis of dense non-aqueous phase liquid contaminants effects on soil permeability by response surface methodology. Iranica Journal of Energy & Environment. 2022;13(2):141-50. https://doi.org/10.5829/ijee.2022.13.02.05
17. Nasrollahpour S, Kebria DY, Nehdi ML, Tanhadoust A, Ghavami M. Remediation of NAPL-contaminated brackish water by synthesized organoclay: Experimental analysis and BNN predictive model. Journal of Hazardous, Toxic, and Radioactive Waste. 2023;27(4):04023028. https://doi.org/10.1061/JHTRBP.HZENG-1212
18. Tekyeh S, Amini Rad H, Kebria DY. Simultaneous removal of salt and dissolved petroleum compounds by a two-stage process: spiral wound capacitive deionization three-dimensional electro-Fenton. Environmental Science and Pollution Research. 2025;32(15):9570-92. https://doi.org/10.1007/s11356-025-36254
19. Kebria DY, Khodadadi A, Ganjidoust H, Badkoubi A, Amoozegar M. Isolation and characterization of a novel native Bacillus strain capable of degrading diesel fuel. International Journal of Environmental Science & Technology. 2009;6(3):435-42. https://doi.org/10.1007/BF03326082
20. Sobhan K, Ali H, Riedy K, Huynh H. Evaluating the compressibility behavior of organic soils using laboratory characterization and rapid on-site piezocone penetration testing. International Journal of Geotechnical Engineering. 2007;1(1):9-18. https://doi.org/10.3328/IJGE.2007.01.01.9-18
21. Cheng G, Zhu H-H, Wen Y-N, Shi B, Gao L. Experimental investigation of consolidation properties of nano-bentonite mixed clayey soil. Sustainability. 2020;12(2):459. https://doi.org/10.3390/su12020459
22. de Medeiros AS, da Silva MA. Influence of Emulsion Type and Moisture on the Stiffness of Stabilized Granular Soil. Civil Engineering Journal. 2025;11(6):2282-302. 10.28991/CEJ-2025-011-06-07
23. Zheng L, Mao W, Liu B. Numerical modeling on mechanical properties of cemented phosphogypsum stabilized soil. HighTech Innov J. 2025;6(1):1-20. 10.28991/HIJ-2025-06-01-01
24. Kassem EM, Azzam W, Elsiragy M. On the Use of a Confined Sand Cell to Dampen Induced Machine Vibration in a Stabilized Clay Numerical Study. Civil Engineering Journal. 2025;11(01). 10.28991/CEJ-2025-011-01-018
25. Jacob S, Scalia IV J, Bareither C. Evaluation of Mineral–Bentonite Mixtures to Concurrently Achieve Low Hydraulic Conductivity and High Strength. Geo-EnvironMeet 2025. p. 431-40.
26. Safehian H, Rajabi AM, Ghasemzadeh H. Effect of diesel-contamination on geotechnical properties of illite soil. Engineering Geology. 2018;241:55-63. https://doi.org/10.1016/j.enggeo.2018.04.020
27. Al-Aghbari M, Dutta R, Mohamedzeini Y. Effect of diesel and gasoline on the properties of sands—a comparative study.

International Journal of Geotechnical Engineering. 2011;5(1):61-8. http://dx. doi.org/10.3328/IJGE.2011.05.01.61-68

28. Nasehi SA, Uromeihy A, Nikudel MR, Morsali A. Influence of gas oil contamination on geotechnical properties of fine and coarse-grained soils. Geotechnical and Geological Engineering. 2016;34(1):333-45. http://dx.doi.org/10.1007/s10706-015-9948-7
29. Hanaei F, Sarmadi MS, Rezaee M, Rahmani A. Experimental investigation of the effects of gas oil and benzene on the geotechnical properties of sandy soils. Innovative Infrastructure Solutions. 2021;6(2):61. https://doi.org/10.1007/s41062-020-00433-5
30. Soil ACD-o, Rock. Standard test method for particle-size analysis of soils: ASTM International; 2007.
31. Soil ACD-o, Rock. Standard test methods for specific gravity of soil solids by water pycnometer: ASTM international; 2010.
32. Sarmadi MS, Zohrevand P, Rezaee M. Effect of kerosene contamination on the physical and mechanical properties of sandy soil. Innovative Infrastructure Solutions. 2019;4(1):7. 10.1007/s4106 2-019-0196-1
33. Jahandari S, Mojtahedi SF, Zivari F, Jafari M, Mahmoudi MR, Shokrgozar A, et al. The impact of long-term curing period on the mechanical features of lime-geogrid treated soils. Geomechanics and Geoengineering. 2022;17(1):269-81. 10.1080/17486 025.2020.17397 53
34. Soil ACD-o, Rock. Standard Test Methods for Laboratory Compaction Characteristics of Soil Using Standard Effort (12 400 Ft-lbf/ft3 (600 KN-m/m3)) 1: ASTM international; 2007.
35. ASTM D-. Standard test method for direct shear test of soils under consolidated drained conditions. D3080/D3080M. 2011;3(9).
36. ASTM. ASTM D2434-22, Standard Test Methods for Measurement of Hydraulic Conductivity of Coarse-Grained Soils. American Society Testing of Materials West Conshohocken, PA, USA; 2022.
37. ASTM-D. Standard practice for identification of polymer layers or inclusions by Fourier transform infrared microspectroscopy (FT-IR). ASTM International West Conshohocken; 2018.
38. Khamehchiyan M, Charkhabi AH, Tajik M. Effects of crude oil contamination on geotechnical properties of clayey and sandy soils. Engineering geology. 2007;89(3-4):220-9. https://doi.org/10.1016/j.enggeo.2006.10.009
39. E168-16 A. Standard practices for general techniques of infrared quantitative analysis. ASTM International West Conshohocken; 2016.
40. Meegoda NJ, Ratnaweera P. Compressibility of contaminated fine-grained soils. Geotechnical Testing Journal. 1994;17(1):101-12.
41. Al-Sanad HA, Eid WK, Ismael NF. Geotechnical properties of oil-contaminated Kuwaiti sand. Journal of geotechnical engineering. 1995;121(5):407-12. 10.1061/(ASCE)07339410(1995)121:5(407)
42. Shin E, Das B. Some physical properties of unsaturated oil-contaminated sand. Advances in unsaturated geotechnics2000. p. 142-52.
43. Kermani M, Ebadi T. The effect of oil contamination on the geotechnical properties of fine-grained soils. Soil and Sediment Contamination: An International Journal. 2012;21(5):655-71. https://doi.org/10.1080/15320383.2012.672486
44. Mohammadi A, Ebadi T. Effect of bentonite addition on geotechnical properties of oil-contaminated sandy soil. Journal of Civil Engineering and Construction. 2018;7(4):153-62. https://doi.org/10.32732/jcec.2018.7.4.153
45. Khosravi E, Ghasemzadeh H, Sabour MR, Yazdani H. Geotechnical properties of gas oil-contaminated kaolinite. Engineering Geology. 2013;166:11-6. https://doi.org/10.1016/j.enggeo.2013.08.004
46. Taheri S, Ebadi T, Maknoon R, Amiri M. Predicting variations in the permeability and strength parameters of a sand-bentonite mixture (SBM) contaminated simultaneously with lead (II) and diesel. Applied Clay Science. 2018;157:102-10. https://doi.org/10.1016/j.clay.2018.01.007
47. Oyediran IA, Enya NI. Crude oil effects on some engineering properties of sandy alluvial soil. International Journal of Mining and Geo-Engineering. 2021;55(1):7-10. 10.22059 /ijmge.2020.283051.594815

COPYRIGHTS
©2026 The author(s). This is an open access article distributed under the terms of the Creative Commons Attribution (CC BY 4.0), which permits unrestricted use, distribution, and reproduction in any medium, as long as the original authors and source are cited. No permission is required from the authors or the publishers.

Persian Abstract

چکیده

نیازهای انرژی برای راهبردهای پاک‌سازی خاک‌های آلوده به فرآورده‌های نفتی از منظرهای زیست‌محیطی و ژئوتکنیکی بسیار حائز اهمیت است .اثربخشی مواد معدنی رسی و سایر مواد تثبیت‌کننده در بهبود ویژگی‌های ژئوتکنیکی خاک‌های ماسه‌ای آلوده به مایعات سبک غیرآبی (LNAPLs) در تحقیقات پیشین تأیید شده است. با این حال، تأثیر همزمان نسبت بنتونیت به ماسه (BSR)، و نوع و غلظت LNAPL بر ویژگی‌های زیست محیطی و ژئوتکنیکی مخلوط خاک، به‌طور جامع بررسی نشده و همچنان به‌درستی شناخته نشده باقی مانده است. در این مطالعه، تاثیر گازوئیل و بنزن با غلظت‌های مختلف (۱۰۰، ۱۵۰، ۲۰۰ و ۲۵۰ گرم به ازای هر ۱۰۰۰ گرم خاک) بر ویژگی‌های ژئومحیطی خاک ماسه‌ای تثبیت‌شده با نسبت‌های مختلف BSR (۰، ۰/۲، ۰/٤ و ۰/٦) به‌صورت جامع ارزیابی شد. نتایج نشان داد که در آزمایش‌های تراکم، چگالی خشک بیشینه (MDD) افزایش و رطوبت بهینه (OMC) کاهش یافته‌اند. همچنین، با افزایش غلظت LNAPLs، کاهش چسبندگی و کاهش زاویه اصطکاک در خاک‌ها مشاهده شد، به‌طوری که تأثیر گازوئیل محسوس‌تر از بنزن بود. با افزایش غلظت هر دو نوع LNAPL، افزایش در چگالی خشک بیشینه و کاهش در رطوبت بهینه نیز گزارش شد. تکنیک‌های تحلیلی شامل FTIR، EDAX و XRD این یافته‌ها را تأیید کردند و بینش‌هایی درباره سازوکارهای نگهداشت آلاینده در خاک‌های ماسه‌ای اصلاح‌شده با بنتونیت ارائه دادند. یافته‌های این تحقیق می‌تواند در طراحی ژئوتکنیکی سازه‌ها بر روی خاک‌های آلوده به LNAPL مورد استفاده قرار گیرد و راهنمایی برای انتخاب روش‌های مناسب پاک‌سازی فراهم آورد.

International Journal of Engineering

Journal Homepage: www.ije.ir

Modeling of Dust Content Control System for Industrial Enterprises in the Mineral Resource Sector

D. V. Gloukhov*, D. V. Suchkov, A. P. Altukhova, D. R. Smirnov

Empress Catherine II Saint-Petersburg Mining University, Saint-Petersburg, Russia

P A P E R I N F O

Paper history:
Received 01 July 2025
Received in revised form 20 August 2025
Accepted 09 September 2025

Keywords:
Conceptual Scheme of Automation
Dust Suppression Process Control
Economic Efficiency of Enterprises
Software and Hardware Complex
Dust Suppression

A B S T R A C T

The article investigates the problem of creating an effective dust suppression system. The authors, employing methods of systems analysis, mathematical modeling, decision theory, mine time-based measurements of dust concentration changes during ventilation, and numerical modeling of dust concentration changes, developed an automated dust suppression system for an apatite-nepheline deposit. The system architecture was designed, encompassing stages from receiving and processing dust concentration data to generating a response through activating suppression with intensity regulation depending on conditions. A prototype system was created and tested. The core of the system is custom-developed code that automatically regulates dust concentration in the mine using a PID controller and transmits data to a server, enabling real-time system monitoring and control. The annual economic benefit from implementing the system at the study site amounted to 2,170,701 rubles. Beyond the achieved economic benefit, the system will improve working conditions, enhance safety, and reduce harmful environmental impact.

***doi**: 10.5829/ije.2026.39.08b.02*

Graphical Abstract

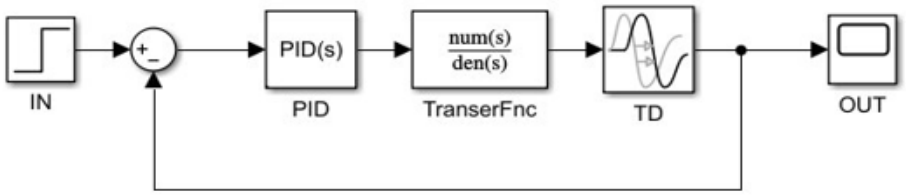

NOMENCLATURE

$R(s)$	Controller transfer function	S_{equip}	Equipment maintenance and repair costs (RUB/year)
k_{per}	Proportional gain coefficient (mg/m^3)	O_{cst}	Other costs (RUB/year)
T_s	Integral time constant (s)	K	Initial cost of equipment (tooling) (RUB)
T_D	Derivative time constant (s)	H_a	Monthly depreciation rate for equipment (tooling) (%/month)
s	Complex variable (Laplace operator) (rad/s)	T_{tst}	Useful life (months)
C_T	Operating costs (RUB/year)	E_{Ceff}	Economic effect (RUB/year)
M	Cost of raw materials basic and auxiliary materials (RUB/year)	C_{st0}	Costs before measures implementation (RUB/year)
Z_{mp}	Salary of main production workers (RUB/year)	C_{st1}	Costs after the measures implementation (RUB/year)
A_{exp}	Depreciation expense on the equipment (RUB/year)	T_{pb}	Payback period (years)
S_{tc}	Tooling costs (RUB/year)	Cst_{res}	Cost of research (RUB)
S_{en}	Process energy costs, (RUB/year)		

*Corresponding Author Email: dmitrygloukhov@yandex.ru (D. V. Gloukhov)

Please cite this article as: Gloukhov DV, Suchkov DV, Altukhova AP, Smirnov DR. Modeling of Dust Content Control System for Industrial Enterprises in the Mineral Resource Sector. International Journal of Engineering, Transactions B: Applications. 2026;39(08):1802-11.

1. INTRODUCTION

1. 1. Relevance of the Study If we consider in detail the developments published in the last few years in such areas as geotechnology and geomechanics, it becomes evident that they increasingly emphasize the integrated development of underground space (1). This field of research substantially considers the issue of design and construction of underground facilities of the production complex. Construction geotechnology is an integral part of the broader field of mining sciences, with one of its key priorities being mining construction and the post-mining utilization of abandoned underground spaces (2). Rubber technical products (RTPs) are widespread in almost all spheres of human activity. However, the needs of the domestic market in RTP are met by Russian enterprises in volumes of about 45-47%. The relevance of the study is determined by the need to improve the competitiveness (3) of domestic factories by optimizing production, introducing new technologies, taking into account possible legal risks, in particular, the issues of intellectual property rights protection. Such optimization can be achieved, on the one hand, by saving resources, and, on the other hand, by introducing innovative chemical compounds, improving the characteristics of equipment, automation of production lines (1).

Modern scientific research suggests using methods of system analysis for this purpose (4, 5). However, employing such methods necessitates a thorough analysis of the object under study and the development of domain-specific models (6). Therefore, one of the most important tasks in improving the stability of technological processes is the development of a unified approach for identifying input, output, and resultant factors (7).

Mining enterprises are a high-tech (8-10) and multifunctional industrial complex comprising various interconnected units. The main operations are carried out at a different depth (11).

In conditions of intensive operations at enterprises involved in the extraction and processing of materials, the problem of dust generation becomes particularly urgent. Dust has a negative impact on workers' health, reduces product and equipment quality, and contributes to environmental degradation (12-14).

In the context of phosphate rock mining (15), dust generated during extraction and processing poses significant challenges (16). The nature of the mined materials, combined with mechanical processing, leads to the release of fine particulate matter into the air (17). This dust not only impairs visibility but can also cause respiratory issues for workers, necessitating strict organizational, regulatory, and legal measures to ensure occupational safety and health. Furthermore, dust accumulation on equipment can impair functionality and increase maintenance costs, thereby reducing overall operational efficiency (18).

The unique geological and environmental conditions of apatite-nepheline deposits further exacerbate dust-related issues (19, 20). Variations in mineral composition and moisture content can influence dust generation rates, making it essential to develop tailored dust control strategies specific to these mining operations (21). Implementing effective monitoring systems to assess dust levels in real time can facilitate the timely activation of suppression measures, ensuring compliance with both worker safety and environmental standards (22, 23). By addressing these challenges through innovative technologies, mining enterprises can mitigate the adverse effects of dust and promote a safer and healthier workplace.

Enterprises are equipped with powerful ventilation systems that ensure the supply of fresh air and the removal of harmful gases and dust. Ventilation is an integral part of the production cycle. Dust suppression plays a critical role in ensuring safety during various mining operations (24, 25). Over the years, various dust suppression systems and methods have been developed to mitigate the harmful effects of dust on human health, equipment, and the environment. These systems can be broadly categorized into physical and chemical methods, each with specific applications and limitations (26, 27).

Physical dust suppression methods rely on mechanical or aerodynamic principles. Water-based systems—such as sprays, misting, and fogging (28, 29)—are commonly used in open-pit mining and at material transfer points. They capture dust particles using water droplets but are less effective under arid or freezing conditions, and excessive use can lead to slurry formation (30, 31). Mechanical collectors (e.g., cyclones and filters) are employed in enclosed environments and are effective for larger particles but less efficient for fine dust (32). Electrostatic systems use electric fields to charge dust particles, promoting their adhesion or coalescence; electrostatic precipitators are highly effective but relatively costly (33).

Chemical methods involve dust-binding agents, such as calcium or magnesium chloride, which are often applied on haul roads (34, 35). Foam-based systems encapsulate dust particles (36). These methods are particularly useful in water-scarce environments but require frequent reapplication and are less effective for very fine dust.

Modern mining operations increasingly utilize automated systems incorporating real-time monitoring, adaptive control, and data analytics. Dust sensors trigger suppression mechanisms only when necessary, adjusting intensity based on current conditions. Such systems are often integrated with other mining equipment to enable comprehensive dust control. Automatic dust suppression systems are therefore an essential component of modern industrial facilities, playing a key role in maintaining safe

dust levels and ensuring worker safety (37).

Currently, global attention is increasingly focused on the transition of mining enterprises toward sustainable development—a shift driven by their critical role in supporting all sectors of the economy (38, 39). In recent years, the global economy has experienced rising prices for many natural resources. It is evident that natural resources are being depleted, and their availability for human consumption is becoming increasingly limited (40). Given the high market demands for industrial products, there is a growing need to develop more innovative and competitive production methods (41, 42), which will ultimately lead to higher-quality products (43).

1. 2. Purpose of the Study A significant role in research aimed at improving the economic efficiency of enterprises (44, 45) is played by the development of modern (46, 47) technological solutions for the operation of existing facilities (48, 49). Central to the development of such solutions is the implementation of measures to reduce the costs associated with the repair and maintenance of mine workings. Equally important are strategies related to asset amortization and process control (50, 51).

1. 3. Problem Statement Relying on earlier studies, it can be noted that modern automatic control systems have several problems related directly to control objects that have spatial coordinates, and there are also difficulties with their analysis and investigation. For example, to realize the monitoring of changes in the stability of an underground structure in the process of its operation, it is necessary to use instrumental measurement of displacements. The above can be realized by studying the deformation processes of the rock mass around the excavation and considering the operation of the excavation support (52). In other words, it is necessary to consider each criterion in detail and apply modern mathematical apparatus, specifically methods of distributed parameter systems. Thus, it is necessary to *develop* a more modern methodology for monitoring and evaluation of the technical condition of different facilities, which is based on ensuring a stable production mode and operational regulation (53, 54).

1. 4. Prerequisites of the Research Problem Methods of systems with distributed parameters have proven themselves in solving various practical problems (55-57). There is a need to develop a system for controlling the temperature field in the tubing during production. As a result, the final cost of field operation and development was reduced (58, 59).

Having analyzed the literature sources, we have identified a significant number of parameters necessary for analysis. The above-mentioned methods were applied in the works of such researchers as Mal'tsev et al. (60), Boronko and Novozhilov (61), Pershin et al. (62), Kalashnikov et al. (63) and Shchirova et al. (64).

Thus, the main task aimed at improving the economic efficiency of enterprises is the development of methods and models (65-67) for assessing their technical condition.

2. MATERIALS AND METHODS

To solve the assigned tasks, a comprehensive research method was applied, including the analysis of global experience in assessing the technical condition of mines and underground structures; methods of system analysis; methods of mathematical modeling; methods of mathematical statistics; methods of control theory; methods of decision theory; mine-based time-lapse observations of dust concentration changes during ventilation; and numerical modeling of dust concentration changes.

The integration of advanced dust suppression methods with automated control systems represents a significant advancement in dust management for the mining and processing industries. By leveraging modern technologies, these systems improve worker safety, reduce environmental impact, and enhance operational efficiency (68).

Automated dust suppression systems consist of several interrelated components that provide an integrated approach to dust control and suppression (69):

1. Controllers and sensors
2. Programmable Logic Controllers (PLC)
3. Visualization and HMI (Human Machine Interface) systems
4. Communication systems and data transmission networks
5. Data analysis and reporting systems

Controllers and sensors are the "eyes" of the system. They provide real-time monitoring of dust levels, measuring dust concentration in the air and transmitting the data to the controllers for analysis.

The transfer function was obtained using the System Identification Toolbox in MATLAB. The identification process was initiated after importing the input and output data into it. The software component constructs the transient response and determines the system's transfer function. An automatic dust suppression system model was developed in Simulink™ R2021b (Figure 1).

This model consists of the transfer function of dust concentration in the mine (the control parameter). The model consists of the following main blocks:

- block "IN" - setting the parameter of dust concentration in the workplace;
- PID-Controller required to implement the steady state of the controlled object;

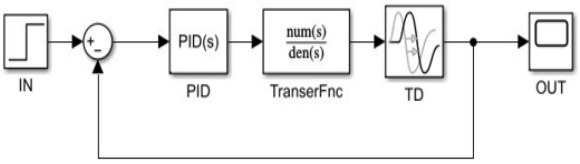

Figure 1. The Simulink™-based algorithmic implementation of the controlled system structure with regulatory components

- "Dust Concentration Transfer Function" is the dust concentration control object of the workplace, which is implemented by the Transfer Function block;
- TD (Transport Delay) - delay of the object;
- Scope block - for displaying the transient process of the system.

In the context of designing a dust suppression system with automatic regulation of dust concentration, the use of adaptive PID controllers enables effective handling of changing operating conditions. A representative example of this methodology is an adaptive PID controller demonstrating stability and rapid adaptation to non-stationary disturbances without requiring precise knowledge of the system model. Properly tuned parameters of an adaptive PID controller ensure reliable suppression of unwanted oscillations and efficient regulation under conditions of uncertainty and noise (70).

3. RESULT AND DISCUSSION

3. 1. The Control System Identification

The use of an automatic dust suppression system in an apatite-nepheline mine is justified by several factors (71, 72) that make it an ideal solution for this task. This system effectively reduces dust levels, which is important for worker safety and health.

In order to address the given problem, in-situ mine observations were conducted, including measurements of dust concentration and the rate of dust generation. The sampling depth is 50 samples, and the sampling period is 1 s. The input signal (Figure 2) and output values (Figure 3) of the system are presented below.

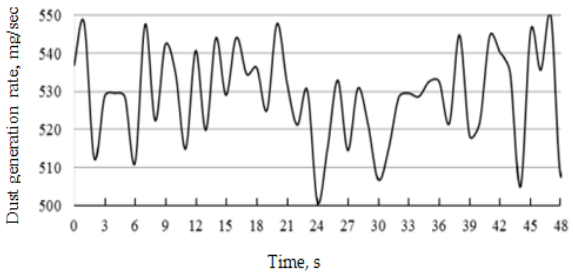

Figure 2. Input experimental data

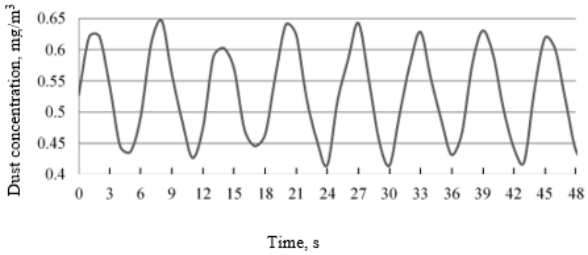

Figure 3. Output experimental data

3. 2. The Mathematical Model Construction

We use the built-in PID Tuner functionality of MATLAB™, which enables automatic tuning of PID controller coefficients to achieve high system performance metrics. The expression for the PID controller after coefficient tuning is given by Equation 1:

$$R(s) = k_{per} + \frac{1}{T_s} + T_D s = 0.3865 + \frac{5.272}{s} + 1.8903 \quad (1)$$

Figure 4 presents the transient response under high dust concentrations (5 mg/m³ and 4 mg/m³). The results confirm the PID controller's efficacy in industrial dust suppression, achieving both dynamic disturbance rejection and steady-state setpoint tracking.

3. 3. Prototyping of the Model within Framework of Mining Production

The system is initialized when the mining equipment is started or when the shift begins. Figure 5 shows the scheme of interconnection of program components.

The algorithm for processing the state is as follows:

1. Dust concentration controllers measure the level of dust in the air in certain enterprise areas.
2. The measured data are transmitted to the central system controller via wired or wireless communication.
3. The central controller analyzes the received data, calculates the average concentration, determines the dynamics of changes.
4. The system compares the measured dust concentration values with pre-set threshold values that signal unsafe dust levels.

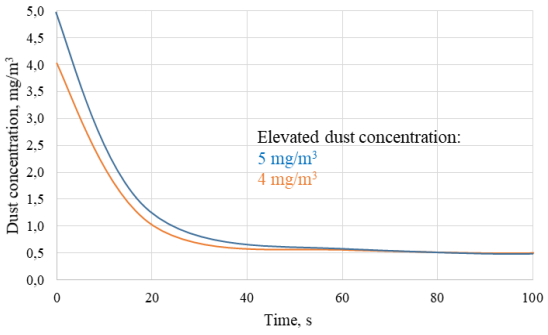

Figure 4. Transient response with PID controller at elevated dust concentration of 5 mg/m³ and 4 mg/m³

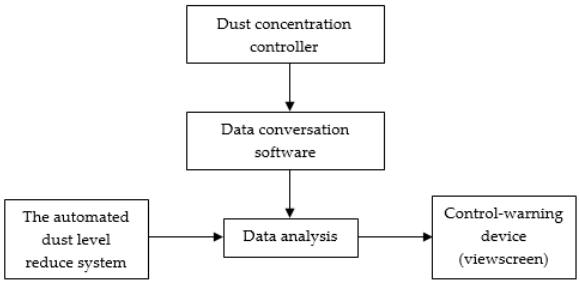

Figure 5. Functional scheme of components interrelation

5. If the dust concentration exceeds the set threshold values, the system determines the need for intervention to reduce the dust level.
6. The system activates appropriate dust suppression mechanisms in areas where thresholds have been detected to be exceeded.
7. The system monitors changes in dust concentration after activation of the suppression system to assess the effectiveness of the measures taken.
8. Dust concentration data are regularly updated, and the cycle of collection, analysis and response is repeated in real time.
9. If a malfunction or fault is detected, the system activates safety measures, including shutting down the dust suppression supply.

The main characteristic of this process is the dust concentration values in the air and on the surface of the equipment. Warning alarms are triggered when dust concentration values in the air are exceeded.

The list and characteristics of signals through which information about the facility is transmitted comply with *GOST 24.104-2023 «Common system of standards for automated control systems. Automated control systems. General requirements»*.

Let us consider the database of dust concentration control in the air implemented at the apatite-nepheline mine. The calculation algorithm is designed for automatic control of dust concentration in the enterprise using a PID controller and sending data to the server. At the beginning of the operation, the user is prompted to enter the machine name, controller name, and their identifiers. Then, the PID controller parameters and the setpoint of dust concentration are set. Variables for the integral component and the previous error are initialized.

The basic function "main" sends the data about machine and controller to the server for registration using the appropriate API URLs. After successful registration, a cycle starts in which random values of dust concentration are generated. These values are used as input for the PID controller, which calculates the correction signal (pid_output).

The correction signal is applied to the measured dust concentration value to obtain the corrected_value. If the corrected value exceeds the dust concentration setpoint, the system is stopped and water irrigation is initiated. If the value is within acceptable limits, it is sent to the server and the operation status is displayed.

Thus, the code automatically adjusts the dust concentration in the mine using a PID controller and sends the data to the server, providing real-time monitoring and control of the system.

3. 4. Economic Efficiency Assessment In the process of analyzing the current state of dust suppression processes at the enterprise, the required number of personnel was identified to ensure proper monitoring and management of the system. The number and structure of personnel were determined based on the volume and complexity of work required for effective dust suppression.

Based on the volume and complexity of work, an analysis was conducted of the average statistical indicators of the number of personnel in enterprise service companies. Consider that specialists work on a standard five-day working week, then, considering holidays and vacations, the average number of working days is 248 days per year (Table 1).

Due to automation of dust suppression process, the workload of occupational safety specialist was reduced, and his working hours were reduced to 0.5 of the standard 40-hour working per week.

Automation has also reduced the workload of the system operator and mining engineer, as process data now comes from sensors rather than being collected manually. As a result, the company no longer needs to

TABLE 1. Salary fund before system operation

Stages and content of performed works	Performer	Labor intensity of works (man-hours)	Working days	Tariff rate (RUB/hour)	Basic salary (RUB/year)
Supervision of labor protection rules	Occupational safety specialist	14	248	400	198,400
Designing and controlling mining	Engineer	40	248	750	1,488,000
Manual controller readings	Operator	40	248	435	863,040
Total					2,549,440
Social contributions					3,319,370
Total					5,868,810

manually calibrate mine process parameters or walk to equipment locations. Thus, a mining engineer's working hours are reduced to 0.7 of a standard working day. The operator's workload is also reduced to 0.8 hours of the original, as the presence of a specialist is still necessary, but the workload has decreased due to the automation of information collection and analysis tasks (Table 2).

To calculate a quantitative assessment of the economic efficiency of the implementation of an automatic dust suppression system at the enterprise, it is necessary to calculate the implementation costs. These include hardware infrastructure costs (equipment, computers, physical infrastructure) and software costs. For continuous and correct operation of the system, it is necessary to purchase and install specialized equipment (Table 3).

Equation 2 can be used to calculate the operating costs:

$$C_T = M + Z_{mp} + A_{exp} + S_{tc} + S_{en} + S_{equip} + O_{cst} \quad (2)$$

Let us calculate electricity costs for the year in accordance with the mode of operation of the enterprise (the system performs continuous control at production) (Table 4).

The depreciation charge per month for equipment and expensive tooling with a long service life is calculated using Equation 3:

$$A_{exp} = \frac{K \cdot H_a}{100}, \quad (3)$$

Let us calculate the monthly depreciation rate of the equipment. A personal computer lasts 7 years on average, a server the same number of years. Using Equations 4 and 5, we get:

$$H_a = \frac{1}{T_{tst}} \cdot 100\% = \frac{1}{84} \cdot 100\% = 1.19\% \quad (4)$$

TABLE 2. Salary fund after automation

Stages and content of performed works	Performer	Labor intensity of works (man-hours)	Working days	Tariff rate (RUB/hour)	Basic salary (RUB/year)
Supervision of labor protection rules	Occupational safety specialist	7	248	420	104,160
Designing and controlling mining	Engineer	28	248	750	744,000
Manual controller readings	Operator	40	248	348	690,432
Total					1,538,592
Social contributions					2,003,246
Total					3,541,838

TABLE 3. Calculation of equipment costs

Name	Quantity (units)	Price (RUB/unit)	Amount (RUB)
Server	1	291,000	291,000
Personal computer (specialist's workstation)	1	70,000	70,000
Total			361,000
Equipment delivery			6,500
Equipment installation			6,500
Total			374,000

Then:

$$A_{exp} = \frac{K \cdot H_a}{100} = \frac{37400 \cdot 1{,}19}{100} = 4450 \text{ RUB/month or } 53\,407 \text{ RUB/year} \quad (5)$$

Costs for maintenance and repair of the equipment, which are covered by the warranty contract, are assumed to be 3000 RUB/year. Thus, after implementation of the system, the operating costs amount to 3.70 million RUB/year.

Now, using the obtained data, the economic effect from the introduction of automatic dust suppression

TABLE 4. Calculation of electricity costs for the year

Equipment	Power (kW)	Equipment operating time (hours)	Electricity tariff (RUB/kWh)	Total cost of electricity (RUB)
Personal computer	0.4	8,760	6	21,024
Server	1.3	8,760	6	68,328
Dust concentration controller	0.2	8,760	6	10,512
Total			99,864	

system is calculated. The economic effect is determined by Equation 6:

$$E_{ceff} = C_{st1} - C_{st0} = 5.87 - 3.70 = 2.17 \text{ mln RUB} \quad (6)$$

The payback period of the costs invested in research shall be determined by Equation 7:

$$T_{pb} = \frac{Cst_{res}}{Ec_{eff}}, \quad (7)$$

The results show that the implemented system will pay off in the first year. Thus, the implementation of the automatic dust suppression system not only reduces current costs, but also creates additional economic benefits, providing more stable and efficient operation of the enterprise. This confirms the high economic efficiency and feasibility of the proposed system implementation.

3. 5. Discussion Ventilation control refers to the timely supply of the required air flow to the workplace at any time the necessary air flow to the places of work at any time, providing normal process flow and safe working conditions for workers. Ventilation management can consist of both the development and implementation of long-term (one-time) ventilation control long-term (one-time) measures in topologically and aerogasodynamically stable conditions, as well as the operational redistribution of air flow rates through ventilation workings air flow rates through the ventilation network depending on the deviations of controlled parameters from technological norms, stipulated by the safety rules and rules of technical operation of enterprises (6). In general, the ventilation control system can be structurally regarded as a consisting of a control system and a controlled object. Between them, there is a continuous exchange of information and its processing. At the same time the information should be processed by the system in such a way that the proposed control actions (measures) lead most effectively to the achievement of the management objective under certain limiting conditions (73) imposed by safety regulations. One of the components of the ventilation process is reduction of dustiness of objects and monitoring of dust formation in the mine atmosphere. Therefore, an important task is the implementation of the dust suppression process at the places where works are carried out.

This paper proposes a methodology for ventilation control during the monitoring of dust formation under atmospheric conditions, in which the regulated parameter is dust concentration and the input influence is the fan blade rotation speed. Thus, the topic of the paper is relevant.

While this study confirms the operational viability and significant economic benefits (2.17 million RUB annual savings) of our PID-based dust suppression system in the apatite-nepheline mining environment, further research could strengthen its broader applicability. For instance, direct comparisons with conventional dust control methods across diverse mining sections would better quantify performance gains. Though our 50-point dataset validated core functionality under targeted production conditions, expanding validation through longitudinal trials with larger datasets and statistical metrics (e.g., MSE, RMSE) would rigorously assess long-term controller accuracy. Furthermore, scalability challenges—such as integration in complex mine topologies or extreme dust scenarios—warrant dedicated investigation. Addressing these aspects in subsequent research will further solidify the framework's applicability across the mining industry and provide deeper insights into long-term performance optimization.

Nevertheless, the implementation of automated PID systems in industry not only improves the accuracy of process parameter control but also delivers significant cost savings through enhanced efficiency and reduced operational downtime. The proposed system regulating dust concentration via a PID controller can be further substantiated by successful examples from other domains of automatic control (74).

4. CONCLUSION

As a result of the research and synthesis of the automatic dust suppression system at the enterprise, the following key results were achieved.

A detailed analysis of the existing systems in industrial facilities was carried out, their technological and economic advantages and disadvantages were revealed. The possibilities and limitations of current solutions were evaluated, which enabled the justified selection of methods and tools for the development of a new system.

The task of developing a dust suppression control system at the enterprise was formulated. Modeling of control processes was carried out, aiding in the determination of the key parameters of the system and the creation of its architecture.

A system architecture was designed, including data acquisition and processing of dust concentrations in the production facility. A prototype system was developed, which was tested and demonstrated high accuracy and speed.

Implementation of the developed system of automatic dust suppression allows to significantly reduce operating costs by optimizing the system operation and reducing the wear of equipment. Evaluation of economic efficiency showed that the savings for the first year will

amount to 2.17 million RUB, with potential for further growth in economic benefits in subsequent years.

The developed system of automatic dust suppression, based on modern sensors and programmable logic controllers is highly accurate, autonomous, and reliable. Its implementation not only improves the safety and efficiency of mining processes, but also brings significant economic benefits. The work has important practical significance for various industries, contributing to its modernization and sustainable development.

5. REFERENCES

1. Guo S, Yang S, Liu C. Mining heritage reuse risks: a systematic review. Sustainability. 2024;16(10):4048. 10.3390/su16104048
2. Konieczna-Fuławka M, Szumny M, Fuławka K, Jaśkiewicz-Proć I, Pactwa K, Kozłowska-Woszczycka A, et al. Challenges related to the transformation of post-mining underground workings into underground laboratories. Sustainability. 2023;15(13):10274. 10.3390/su151310274
3. Anikina I. Bukhantsev Yu. A., Kuz'mina Eh. V. Analysis of the Directions of Development of Control and Evaluation of the Effectiveness of the Implementation of State Programs and National Projects. Fundamental'nye issledovaniya= Fundamental Research. 2022:10-1. 10.17513/fr.43335
4. Dzyurdzya OA, Gudkova OE, Kamchatova EY, Fedotova GV, Komarov VY. The transformation of the industrial economic sector in the conditions of Industry 4.0. Business 40 as a Subject of the Digital Economy: Springer; 2022. p. 1107-11.
5. Hasozdemir K, Erçelebi S. Enhancing the performance of integer models for addressing the long-term production planning problem in open pit mines by decision variable fixation based on parametric analysis of the final pit limit. Mining Science and Technology (Russia). 2024;9(2):74-84. 10.17073/2500-0632-2023-09-156
6. Balovtsev S. Higher rank aerological risks in coal mines. Mining Science and Technology (Russia). 2022;7(4):310–9. 10.17073/2500-0632-2022-08-18
7. Kucherova Y, Glushchenko A, Anisimova EY, Mosolova D, Starodubova YV, editors. Development of information support for management by segments of activity of agroindustrial complex enterprises in arid territories. AIP Conference Proceedings; 2022: AIP Publishing LLC. 10.1063/5.0092825
8. Mazari A, Ait Abbasb H, Laroussia K, Naceric B. Enhancing Wind Power Conversion System Control Under Wind Constraints Using Single Hidden Layer Neural Network. Transactions A: Basics. 2024;37(07):1306. 10.5829/ije.2024.37.07a.10
9. Brahmbhatt B, Chandwani H. Modified second order generalized integrator-frequency locked loop grid synchronization for single phase grid tied system tuning and experimentation assessment. International Journal of Engineering, Transactions B: Applications. 2022;35(2). 10.5829/ije.2022.35.02b.03
10. Younes B, Ait Abbas H, Bousbaine A, Fergani O, Mazari A. Optimizing DC microgrid systems for efficient electric vehicle battery charging in Ain El Ibel, Algeria. International Journal of Engineering, Transactions A: Basics. 2024;37(10):1891-900. 10.5829/ije.2024.37.10a.03
11. Bui X-N, Nguyen H, Le Q-T, Le T. Forecasting PM 2.5 emissions in open-pit minesusing a functional link neural network optimized by various optimization algorithms. Mining Science and Technology (Russia). 2022;7(2):111-25. 10.17073/2500-0632-2022-2-111-125
12. Fetisov V, Gonopolsky AM, Davardoost H, Ghanbari AR, Mohammadi AH. Regulation and impact of VOC and CO2 emissions on low-carbon energy systems resilient to climate change: A case study on an environmental issue in the oil and gas industry. Energy Science & Engineering. 2023;11(4):1516-35. 10.1002/ese3.1383
13. Sidorenko S, Trushnikov V, Sidorenko A. Methane emission estimation tools as a basis for sustainable underground mining of gas-bearing coal seams. Sustainability. 2024;16(8):3457. 10.3390/su16083457
14. Eremeeva A, Kondrasheva N, Korshunov G. Method to reduce harmful emissions when diesel locomotives operate in coal mines. Topical Issues of Rational Use of Natural Resources 2019, Volume 1: CRC Press; 2019. p. 10-5.
15. Dauvalter V, Sandimirov S, Denisov D, Dauvalter M, Slukovskii Z. Ecological and geochemical assessment of snow cover in the area affected by the apatite–nepheline production of the Kola Peninsula. Geochemistry International. 2023;61(12):1308-22. 10.1134/S0016702923120029
16. Hazou E, Patchali TE, Konzou E, Kola P, Zorko B, Ndontchueng Moyo M, et al. Radiological assessment and statistical approaches of natural radionuclides in soil samples related to phosphate ore activities in the site of Dagbati, southern region of Togo. Water, Air, & Soil Pollution. 2022;233(7):237. 10.1007/s11270-022-05700-y
17. Boumaza B, Chekushina TV, Kechiched R, Benabdeslam N, Brahmi L, Kucher DE, et al. Environmental geochemistry of potentially toxic metals in phosphate rocks, products, and their wastes in the Algerian phosphate mining area (Tébessa, NE Algeria). Minerals. 2023;13(7):853. 10.3390/min13070853
18. Krasavtseva E, Maksimova V, Makarov D. Conditions affecting the release of heavy and rare earth metals from the mine tailings Kola Subarctic. Toxics. 2021;9(7):163. 10.3390/toxics9070163
19. Krasavtseva E, Maksimova V, Makarov D, Potorochin E. Modelling of the chemical halo of dust pollution migration in loparite ore tailings storage facilities. Minerals. 2021;11(10):1077. 10.3390/min11101077
20. Wingate E, Prasad R, Liu Y. Phosphorus—a Circular Journey from the Ground to the Recycling Line. Mining, Metallurgy & Exploration. 2023;40(5):1469-85. 10.1007/s42461-023-00839-6
21. Koriko M, Zounon D, Tchegueni S, Bafai DD, Degbe KA, Fiaty K, et al. Physicochemical and mineralogical characterizations of wastes coming from phosphate ore processing of Hahotoé and Kpogamé mines. Journal of Minerals and Materials Characterization and Engineering. 2021;9(4):390-405. 10.4236/jmmce.2021.94027
22. Tian S, Liang T, Li K. Fine road dust contamination in a mining area presents a likely air pollution hotspot and threat to human health. Environment international. 2019;128:201-9. 10.1016/j.envint.2019.04.050
23. Hamed Y, Khelifi F, Houda B, Sâad AB, Ncibi K, Hadji R, et al. Phosphate mining pollution in southern Tunisia: environmental, epidemiological, and socioeconomic investigation. Environment, Development and Sustainability. 2023;25(11):13619-36. 10.1007/s10668-022-02606-x
24. Golubkov V, Gorenkova G, Vorozhtsov E, Bespalova M, Bortnikov S. Chemical additive based on sodium oleate and linseed oil for preparation coal dust suppression composition. Mining Science and Technology (Russia). 2023;8(4):341-9. 10.17073/2500-0632-2023-02-79
25. Perestoronin M, Parshakov O, Popov M. Parameterization of a ventilation network model for the analysis of mine working emergency ventilation modes. Mining Science and Technology (Russia). 2023;8(2):150–61. 10.17073/2500-0632-2022-10-13
26. Kogarko L. Chemical composition and petrogenetic implications of apatite in the Khibiny apatite-nepheline deposits (Kola Peninsula). Minerals. 2018;8(11):532. 10.3390/min8110532

27. Zhang Q, Fan L, Wang H, Han H, Zhu Z, Zhao X, et al. A review of physical and chemical methods to improve the performance of water for dust reduction. Process Safety and Environmental Protection. 2022;166:86-98. 10.1016/j.psep.2022.07.065
28. Bałaga D SM, Kalita M, Williamson BJ, Walentek A, Małachowski M. . Selection of operational parameters for a smart spraying system to control airborne PM10 and PM2.5 dusts in underground coal mines. Process Safety and Environmental Protection. 2021;148:482-94. 10.1016/j.psep.2020.10.001
29. Lee Y-Y, Yuan C-S, Yen P-H, Mutuku JK, Huang C-E, Wu C-C, et al. Suppression Efficiency for Dust from an Iron Ore Pile Using a Conventional Sprinkler and a Water Mist Generator. Aerosol and Air Quality Research. 2022;22(2):210320. 10.4209/aaqr.210320
30. Chaulya S, Chowdhury A, Kumar S, Singh R, Singh S, Singh R, et al. Fugitive dust emission control study for a developed smart dry fog system. Journal of Environmental Management. 2021;285:112116. 10.1016/j.jenvman.2021.112116
31. Saurabh K, Chaulya S, Singh R, Kumar S, Mishra K. Intelligent dry fog dust suppression system: an efficient technique for controlling air pollution in the mineral processing plant. Clean Technologies and Environmental Policy. 2022;24(4):1037-51. 10.1007/s10098-020-01991-z
32. Beaulac P, Issa M, Ilinca A, Brousseau J. Parameters affecting dust collector efficiency for pneumatic conveying: a review. Energies. 2022;15(3):916. 10.3390/en15030916
33. Pujiono P, Budi Prijanto T, Nurhayati A, Aripin S. Application of Electrostatic Precipitator with Electrode Distance Variation in Reducing Dust Levels in The Manufacturing Industry. Pollution. 2023;9(4):1309-16. 10.22059/poll.2023.354293.1764
34. Bao Q, Liu Y, Li C, Jia L, Yan J, Yuan M, et al. Development and performance characterization of a hybrid dust suppressant based on sodium ligninsulfonate modification. Starch-Stärke. 2021;73(3-4):2000207. 10.1002/star.202000207
35. Dong H, Yu H, Xu R, Cheng W, Ye Y, Xie S, et al. Review and prospects of mining chemical dust suppressant: classification and mechanisms. Environmental Science and Pollution Research. 2023;30(1):18-35. 10.1007/s11356-022-23840-w
36. Fang X, Jiang B, Yuan L, Liang Y, Ren B, Tao W, et al. Experimental study on atomization characteristics of gas–liquid two-phase flow nozzle and its dust removal effect. Materials. 2022;15(2):565. 10.3390/ma15020565
37. Bukhantzev Y, Khudyakova A, Altukhova A, editors. Providing economic security for regional businesses. International Scientific Conference" Competitive, Sustainable and Secure Development of the Regional Economy: Response to Global Challenges"(CSSDRE 2018); 2018: Atlantis Press. 10.2991/cssdre-18.2018.110
38. Boyarko GY, Lapteva A, Bolsunovskaya L. Mineral resource base of Russia's copper: current state and development prospects. Mining Science and Technology (Russia). 2024;9(4):352-86. 10.17073/2500-0632-2024-05-248
39. Potravny I, Novoselov A, Novoselova I, Gassiy V, Nyamdorj D. The Technogenic Deposits' Development as a Factor of Overcoming Resource Limitations and Ensuring Sustainability. 2023. 10.20944/preprints202309.1430.v1
40. Ilyushin Y, Nosova V. Development of Mathematical Model for Forecasting the Production Rate. International Journal of Engineering Transactions B: Applications. 2025;38(8):1749-57. 10.5829/ije.2025.38.08b.02
41. Eremeeva AM, Ilyushin YV. Temperature Control During Storage of Raw Materials in the Process of Biodiesel Fuel Production. Inventions. 2025;10(1):7. 10.3390/inventions10010007
42. Kukharova T, Maltsev P, Novozhilov I. Development of a control system for pressure distribution during gas production in a structurally complex field. Applied System Innovation. 2025;8(2):51. 10.3390/asi8020051
43. Bramm AM, Eroshenko SA. Evaluation of the impact of the distance determination function on the results of optimization of the geographical placement of renewable energy sources-based generation using a metaheuristic algorithm. Записки Горного института. 2025(271 (eng)):141-53.
44. Golovina E, Tselmeg B. Cost estimate as a tool for managing fresh groundwater resources in the Russian Federation. Geol Miner Resour Sib. 2023;4:81-91. 10.20403/2078-0575-2023-4a-81-91
45. Katysheva E. Analysis of the interconnected development potential of the oil, gas and transport industries in the Russian Arctic. Energies. 2023;16(7):3124. 10.3390/en16073124
46. Afanaseva O, Tulyakov T, Romashin D, Panova A. Development of a Robotic Complex for the Manufacture of Parts Used in Civil Engineering. Engineering Research Transcripts. 2023;3:51-8. 10.55084/grinrey/ERT/978-81-964105-0-6_6
47. Barykin SE, Sergeev SM, Provotorov VV, Lavskaya KK, Shidlovskaya KA, Dedyukhina N, et al. Sustainability Analysis of Energy Resources Transport Based on A Digital ND Logistics Network. Engineered Science. 2024;29:1093. 10.30919/es1093
48. Андреева ЕС, Маринина ОА, Туровская ЛГ. Nanofluid flooding as a method of enhancing oil recovery: mechanism, advantages. Bulletin of the Tomsk Polytechnic University Geo Assets Engineering. 2024;335(6):189-202. 10.18799/24131830/2024/6/4408
49. Gloukhov D, Bogdanova D, Batova O, Vinogradova V, Nikiforov A. Synthesis of Rubber Mixing Process Control System. International Journal of Engineering Transactions A: Basics. 2025;38(10):2249-58. 10.5829/IJE.2025.38.10A.04
50. Fedorova E, Pupysheva E, Morgunov V. Settling parameters determined during thickening and washing of red muds. Tsvetnye Metally. 2023;4:77-85. 10.17580/tsm.2023.04.10
51. Romashin DV, editor Application of Artificial Intelligence to Improve the Efficiency of Monitoring and Diagnosing the Condition of Complex Technical Objects. 2024 Conference of Young Researchers in Electrical and Electronic Engineering (ElCon); 2024: IEEE. 10.1109/ElCon61730.2024.10468497
52. Olkhovskiy D, Parshakov O, Bublik S. Study of gas hazard pattern in underground workings after blasting. Mining Science and Technology (Russia). 2023;8(1):47-58. 10.17073/2500-0632-2022-08-86
53. Mitrofanova GV, Chernousenko EV, Kompanchenko AA, Kalugin AI. Specific action of collector from phosphoric acid alkyl esters class in flotation of apatite-nepheline ores. Записки Горного института. 2024(268 (eng)):637-45.
54. Protosenya AG, Belyakov NA, Bouslova MA. Modelling of the stress-strain state of block rock mass of ore deposits during development by caving mining systems. Записки Горного института. 2023(262 (eng)):619-27.
55. Villemant B, Jaffrezic H, Joron J-L, Treuil M. Distribution coefficients of major and trace elements; fractional crystallization in the alkali basalt series of Chaine des Puys (Massif Central, France). Geochimica et cosmochimica acta. 1981;45(11):1997-2016.
56. Kozyrev B, Sizyakov V. Heap leaching of red mud by the formate method. Obogashchenie Rud. 2021;4:40-5. 10.17580/or.2021.04.07
57. Asadulagi M-AM, Pershin IM, Tsapleva VV. Research on hydrolithospheric processes using the results of groundwater inflow testing. Water. 2024;16(3):487. 10.3390/w16030487
58. Wang M, Hei Li MY, Zhou M-F, Zhou J-X, Sun G, Zhou Y, et al. Enrichment of rare earth elements during the weathering of alkaline igneous systems: insights from the Puxiong regolith-

hosted rare earth element deposit, SW China. Economic Geology. 2024;119(1):161-87. 10.5382/econgeo.5024

59. Kozyrev B, Sizyakov V, Arsentyev V. Principles of rational processing of red mud with the use of carboxylic acids. Non-Ferr Met. 2022;53:30-4. 10.17580/nfm.2022.02.05
60. Mal'Tsev PA, Abramkin SE, Plotnikov AV, Martirosyan KV, editors. A conceptual Model of Controlled Gas Production Processes in Fields with a Complex Geological Structure. 2024 XXVII International Conference on Soft Computing and Measurements (SCM); 2024: IEEE. 10.1109/SCM62608.2024.10554098
61. Boronko EA, Novozhilov IM, editors. Designing an Information System for Monitoring the Electromagnetic Field of a Power Plant. 2024 Conference of Young Researchers in Electrical and Electronic Engineering (ElCon); 2024: IEEE. 10.1109/ElCon61730.2024.10468204
62. Pershin IM, Papush EG, Kukharova TV, Utkin VA. Modeling of distributed control system for network of mineral water wells. Water. 2023;15(12):2289. 10.3390/w15122289
63. Kalashnikov A, Konopleva NG, Pakhomovsky YA, Ivanyuk GY. Rare earth deposits of the Murmansk region, Russia—a review. Economic Geology. 2016;111(7):1529-59. https://doi.org/10.2113/econgeo.111.7.1529
64. Shchirova E, Tsvetkova A, Komendantova N. Analysis of the possibility of implementing carbon dioxide sequestration projects in Russia based on foreign experience. 2021. 10.5593/sgem2021/5.1/s20.004
65. Pavel T, Polina S, Liubov N. The research of the impact of energy efficiency on mitigating greenhouse gas emissions at the national level. Energy Conversion and Management. 2024;314:118671. 10.1016/j.enconman.2024.118671
66. Semenova T, Martínez Santoyo JY. Economic Strategy for Developing the Oil Industry in Mexico by Incorporating Environmental Factors. Sustainability. 2024;16(1):36. 10.3390/su16010036
67. Marinina O, Malikov A, Lyubek Y, Pasternak S, Reshneva E, Stolbovskaya N. Selection of Enhanced Oil Recovery Method on the Basis of Clustering Wells. Processes. 2024;12(10):2082. 10.3390/pr12102082
68. Kahraman MM, Erkayaoglu M. A data-driven approach to control fugitive dust in mine operations. Mining, Metallurgy & Exploration. 2021;38(1):549-58.
69. Zakri BM, Zamzami O, Babour A. Automatic Dust Reduction System: An IoT Intervention for Air quality. International Journal of Advanced Computer Science & Applications. 2024;15(2). 10.14569/IJACSA.2024.0150219
70. Malekzadeh M, Sadati J, Alizadeh M. Adaptive PID controller design for wing rock suppression using self-recurrent wavelet neural network identifier. Evolving Systems. 2016;7(4):267-75. 10.1007/s12530-015-9143-3
71. Chakhmouradian AR, Reguir EP, Mitchell RH. Strontium-apatite: New occurrences, and the extent of Sr-for-Ca substitution in apatite-group minerals. The Canadian Mineralogist. 2002;40(1):121-36. https://doi.org/10.2113/gscanmin.40.1.121
72. Gospodarikov AP, Revin IE, Morozov KV. Composite model of seismic monitoring data analysis during mining operations on the example of the Kukisvumchorrskoye deposit of AO Apatit. Записки Горного института. 2023(262 (eng)):571-80. 10.31897/PMI.2023.9
73. Zueva I. Model building and development of internal control tools in the modern enterprise management system. Bulletin of the Moscow University named SU Vitte Series 1: Economics and Management. 2023;3(46):101-13. 10.21777/2587-554X-2023-3-101-113
74. Hamidi H, Vafaei A, Monadjemi A. Algorithm based fault tolerant and check pointing for high performance computing systems. Journal of applied sciences. 2009;9(22):3947-56. 10.3923/jas.2009.3947.3956

COPYRIGHTS

©2026 The author(s). This is an open access article distributed under the terms of the Creative Commons Attribution (CC BY 4.0), which permits unrestricted use, distribution, and reproduction in any medium, as long as the original authors and source are cited. No permission is required from the authors or the publishers.

Persian Abstract

چکیده

این مقاله به بررسی مشکل ایجاد یک سیستم مؤثر کنترل گردوغبار می‌پردازد .نویسندگان با استفاده از روش‌های تحلیل سیستم‌ها، مدلسازی ریاضی، تئوری تصمیم‌گیری، اندازه‌گیری‌های زمانی تغییرات غلظت گردوغبار در تهویه معدن و مدلسازی عددی تغییرات غلظت گردوغبار، یک سیستم خودکار کنترل گردوغبار برای کانسار آپاتیت-نفلین توسعه داده‌اند .معماری سیستم طراحی شده است که مراحل دریافت و پردازش داده‌های غلظت گردوغبار تا پاسخ فعال‌سازی سیستم کنترل با تنظیم شدت عملیات بر اساس شرایط را پوشش می‌دهد .یک نمونه اولیه از سیستم ساخته و آزمایش شده است .هستهٔ سیستم مبتنی بر کد توسعه‌یافته‌ای است که به‌طور خودکار غلظت گردوغبار در معدن را با استفاده از یک کنترل‌کننده PID تنظیم کرده و داده‌ها را به سرور ارسال می‌کند که امکان پایش و کنترل بلادرنگ سیستم را فراهم می‌نماید .مزیت اقتصادی سالانه اجرای این سیستم در محل مورد مطالعه، ۲٬۱۷۰٬۷۰۱ روبل بوده است .افزون بر منافع اقتصادی حاصل، این سیستم بهبود شرایط کاری، افزایش ایمنی و کاهش اثرات مضر بر محیط زیست را در پی خواهد داشت.

IJE TRANSACTIONS B: Applications Vol. 39, No. 08, (August 2026) 1812-1820

International Journal of Engineering

Journal Homepage: www.ije.ir

Multi-head Spectral-attentive Residual Generative Adversarial Network: A High-fidelity Generative Adversarial Network Based Model for Image Haze Removal

A. Dey*, S. Biswas, A. Gupta, M. Debnath

Department of Computer Science and Technology, Indian Institute of Engineering Science and Technology, Shibpur, Howrah, India

PAPER INFO

Paper history:
Received 28 March 2025
Received in revised form 27 May 2025
Accepted 02 June 2025

Keywords:
Image Haze Removal
MHSAR-GAN
Single Image Dehazing
Multi-Head Attention
Generative Adversarial Network
Computer Vision

ABSTRACT

Haze severely degrades image quality by suppressing contrast, clarity, and visibility, which is a challenge to tasks in many computer vision applications like autonomous driving, remote sensing, satellite image analysis, video surveillance, and action recognition. These vision-based tasks require clear and highly detailed visual information for efficient analysis and decision-making. This research proposes a novel GAN-based learning method, the Multi-Head Spectral-Attentive Residual Generative Adversarial Network (MHSAR-GAN), to improve the performance of image dehazing. The proposed deep learning-based image haze removal model combines spectral normalization to enhance training stability, multi-head attention for fine-tuning feature selection, and residual learning to retain important structural information to improve single-image dehazing. Depthwise convolutions are also incorporated into the attention mechanism for enhanced spatial feature extraction without added computational complexity. We tested our method on benchmark image dehazing datasets, Haze1K and RESIDE 6K, and compared its performance with state-of-the-art image dehazing models. Peak Signal-to-Noise Ratio (PSNR) and Structural Similarity Index Measure (SSIM) were pivotal metrics for assessing the model's performance, ensuring a comprehensive evaluation of image quality and structural fidelity. Experimental results indicate that the proposed MHSAR-GAN achieves superior haze removal with preserved fine-grained image details and clearer visibility compared to existing image dehazing methods in quantitative and qualitative comparisons.

***doi**: 10.5829/ije.2026.39.08b.03*

Graphical Abstract

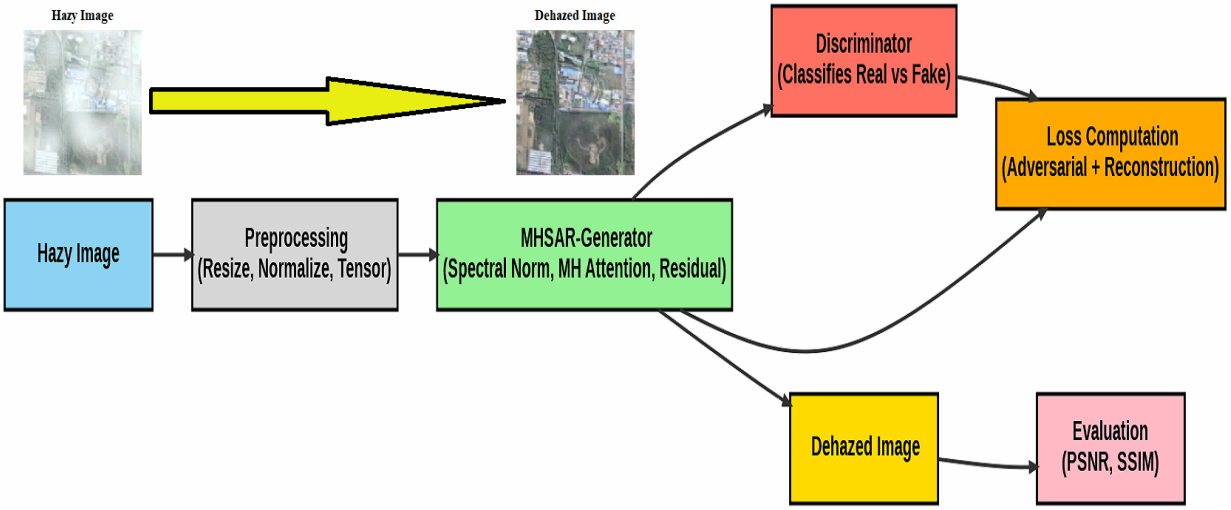

*Corresponding Author Email: arnabdeycs@gmail.com (A. Dey)

Please cite this article as: Dey A, Biswas S, Gupta A, Debnath M. Multi-head Spectral-attentive Residual Generative Adversarial Network: A High-fidelity Generative Adversarial Network Based Model for Image Haze Removal. International Journal of Engineering, Transactions B: Applications. 2026;39(08):1812-20.

1. INTRODUCTION

Image haze removal is a challenging and vital research area in computer vision technologies. Hazy conditions—caused by particles such as smoke, fog, and pollution significantly degrade image quality by lowering contrast, reducing visibility, and obscuring fine details. This degradation adversely affects downstream tasks such as object detection, scene classification, semantic segmentation, and satellite imagery analysis, which rely on high-fidelity visual inputs. Removing haze from images (1) restores image clarity by eliminating or compensating for the scattering effects introduced by atmospheric pollutants. In particular, optical remote sensing systems and real-time vision systems are highly sensitive to atmospheric interference, where even minor visual distortion can severely hinder decision-making during critical operations. Thus, the main goal of the process is to find a method that gives accurate results under dense fog conditions. Traditionally, histogram equalization, contrast enhancement, and dark channel prior have been used, but they were ineffective in heavy fog conditions (2). Deep learning-based image dehazing typically follows two primary methodologies. The first approach relies on a physical degradation model, wherein neural networks estimate model parameters to reconstruct haze-free images. The second approach, which has gained substantial attention, involves an end-to-end dehazing framework where deep networks directly process hazy images to generate dehazed outputs without explicit parameter estimation. Recent advancements have incorporated models such as random forest regression, CNNs, and GANs, which excel in learning complex feature representations for improved image restoration.

The Multi-Head Spectral-Attentive Residual GAN (MHSAR-GAN) is an advanced generative adversarial network that aims to improve the quality of image translation by means of a robust methodology that overcomes the common setbacks to traditional GAN methods. One problem in standard GANs is instability during training; for instance, this may lead to mode collapse and a deteriorated quality of images. MHSAR-GAN attempts to solve these by implementing spectral normalization for its generator and discriminator, which ensures stable training conditions and maintains better gradient flow. Feature-and-context preservation is yet another challenge conventional GANs face, especially in cases that require intricacies of fine detail reconstruction. By incorporating multi-head self-attention with depthwise convolutions, MHSAR-GAN can locate and preserve both global scene structures and local textures. With the further refinement of generator residual blocks using adaptive instance normalization and SiLU activation - keeping contrast and structural integrity of generated images - the discriminator uses spectral normalization among its many structural levels to enforce the adversarial training toward improved sharpness and detail preservation. With a perfect balance of all the aforementioned features, MHSAR-GAN presents an advanced GAN model exhibiting high fidelity haze removal while overcoming the limitations of conventional GAN-based dehazing methods.

This research is noteworthy because it contributes the following:

(a) Develop MHSAR-GAN, a novel and efficient GAN-based framework for image haze removal.

(b) Incorporates spectral normalized residual multi-head self-attention and depthwise convolutions, enriching feature refinement and image dehazing.

(c) Adaptive Instance Normalization and SiLU activation for improved contrast preservation and texture reconstruction.

(d) Evaluation of the proposed MHSAR-GAN model on benchmark Haze1K and RESIDE 6K datasets and state-of-the-art dehazing methods.

2. RELATED WORKS

In this section, we discuss prior research efforts in the field of haze removal. Over time, much research has been done on various dehazing techniques, from traditional image processing techniques to latest deep learning-based models. The techniques are meant to clear an image of the haze using different forms of mathematical principles and learning-based strategies.

One of the earliest and widely recognized techniques for haze removal is the Dark Channel Prior (DCP) which was introduced by He et al. (3). This method relies on the assumption that in most haze-free images, at least one color channel has some pixels with very low intensity, except in sky regions. Using this prior knowledge, DCP estimates the transmission map and restores clear images. This method performs very poor on dense haze conditions and needs post-processing steps to retrieve artifacts and color distortions (4). Cai et al. (5) used DehazeNet, a convolutional neural network (CNN), instead of handcrafting priors to learn the mapping between hazy and clear images. The model learns relevant features automatically and improves over traditional models to a large extent. DehazeNet incorporated nonlinear activation functions and depth-wise feature extraction to enhance dehazing performance (6). Ren et al. (7) presented a Gated Fusion Network (GFN) with a selective fusion mechanism to dynamically maintain a balance between fine and coarse details of an image depending on the haze density. This gating mechanism preserves structural details that are important, allowing the method to perform well in a variety of environmental conditions. Qu et al. (8) employs additional perceptual loss functions and skip

connections into the Pix2Pix Dehazing framework to allow the retention of details in the output image. In contrast to the existing CNN-based methods that have focused only on pixel-wise accuracy, the Enhanced Pix2Pix Dehazing Network (EPDN) relies on perceptual similarity for increasing contrast and clarity in images. Cui et al. (9) introduced an efficient and effective network (EENet) with improved spatial-spectral learning for single image dehazing. This gives the model relevance to focus on important features and improve dehazing performance. To solve the problem of real-time processing, Patil et al. (10) present an unsupervised recurrent learning framework for real-world video dehazing, leveraging temporal coherence to enhance visibility restoration while eliminating the need for paired training datasets—marking a significant advancement in real-time haze removal from dynamic scenes. Su et al. (11) introduces a new dehazing approach that effectively bridges the synthetic-real domain gap by integrating multiple prior-based pseudo-labels with adaptive weighting and domain transfer mechanism, achieving superior performance on real scene single image dehazing. Zhao et al. (12) introduced a transformer enhanced texture attention model named TransDehaze for end-to-end single image dehazing. Chen et al. (13) proposed an unsupervised single-image dehazing method using a self-guided inverse-retinex GAN, significantly improving texture restoration and contrast enhancement in real-world hazy images. The model performs particularly well for outdoor scenes.

Different researchers have also applied GAN architectures to specific applications such as remote sensing. One such example is the GAN model proposed by Ning et al. (14), a multi-scale attention with deformable transformers is utilized to effectively tackle the challenge of remote sensing image dehazing. Similarly, Shen et al. (15), introduced spectral constraints to ensure consistency between different spectral bands and further improve clarity in multi-modal remote sensing images. Other methods include PMDNet (16), Optimized Dehazing (17), Multi-stream Feature Aggregation Network (18-22), Vision Transformer based DehazeFormer (23-26), DCP and Inverse Image (27), and Improved DCP (28). The structural similarity index proposed by Khosravi et al. (26) exploits maximally stable extremal regions to improve the detectability of the content of the image. Dehazing techniques have evolved significantly, from traditional handcrafted priors to sophisticated deep learning models. CNN methods have been very promising in feature extraction, whereas GAN methods could further improve de-hazing results by generating visually realistic and perceptually consistent images. Attention mechanisms, as well as, recent contrastive learning methods are likely to further advance the solutions in these arenas and make them applicable in quite a number of areas, such as remote sensing, video surveillance, and real-time environmental monitoring.

3. PROPOSED METHOD

Image dehazing is a challenging task that involves removing haze from images to enhance visibility and recover details. The proposed Multi-Head Spectral-Attentive Residual Generative Adversarial Network (MHSAR-GAN) leverages a carefully designed generator and discriminator to achieve high-quality dehazing results. Before feeding images into the proposed MHSAR-GAN architecture, the dataset undergoes a structured preprocessing pipeline. Hazy and clear images are first loaded and resized to 128×128 pixels to maintain consistency. They are then converted into tensors and normalized to the [-1,1] range, ensuring stable GAN training. A DataLoader is used for efficient batch processing, and the data is transferred to a GPU (if available) to accelerate computations. Finally, the preprocessed images are fed into the MHSAR-GAN generator, serving as input for the dehazing process. The Generator architecture is shown in Figure 1.

The following discussion elaborates on the architectures of both Generator and Discriminator, along with their importance in achieving superior performance.

3. 1. Generator (G) The generator is responsible for transforming a hazy image $x \in \mathbb{R}^{H\times W\times C}$ into a dehazed output $\hat{x} \in \mathbb{R}^{H\times W\times C}$. The architecture consists of three key components: encoding, residual blocks with multi-head self-attention, and decoding.

3. 1. 1. Encoding Stage The encoding stage extracts hierarchical features from the input image using a series of convolutional layers. The first layer applies a 7×7 convolution with spectral normalization (SN) and instance normalization (IN) followed by a non-linearity (σ), capturing low-level structural information. Two subsequent 3×3 convolutions with stride 2 progressively downsample the feature maps, enhancing spatial abstraction. The encoding process is formulated

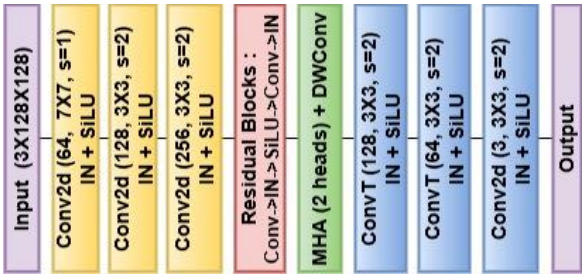

Figure 1. MHSAR-GAN Generator (G) Architecture

as is given below. The initial convolution operation is represented as given in Equation 1 and the downsampling layers are represented as Equation 2.

- Initial convolution:

$$f_1 = \sigma\big(\text{IN}(\text{SN}(\mathbf{W}_1 * x) + b_1)\big) \quad (1)$$

where, $*$ denotes convolution, σ is the activation function, $\mathbf{W}_1$ is the convolution kernel and b_1 is the bias term.

- Downsampling layers:

$$f_{i+1} = \sigma\big(\text{IN}(\text{SN}(\mathbf{W}_i * f_i) + b_i)\big) \quad (2)$$

here, i indexing each downsampling convolution. The algorithm for Generator and Discriminator, are given in Algorrithm 1 and 2 respectively. In the given Generator and Discriminator algorithm, SN denotes Spectral Normalization, IN represents Instance Normalization, BN represents Batch Norm, Conv denotes Convolution, ConvT denotes Transpose Convolution, and LReLU represents Leaky ReLU activation, s signify the stride.

3. 1. 2. Residual Blocks for Feature Refinement The model incorporates two (adjustable) residual blocks to facilitate robust feature learning. Each residual block refines the feature representation while maintaining stability using a residual scaling factor of 0.1 as given in Equation 3. This prevents excessive gradient magnitudes, ensuring a more stable optimization process. The use of residual learning aids in preserving fine details during dehazing. A series of residual blocks refine features while preserving essential details. Each block consists of two convolutions and a residual scaling factor $\alpha = 0.1$:

$$r_i = f_i + \alpha \cdot \sigma\Big(\text{IN}\Big(\text{SN}\Big(\mathbf{W}_2 * \sigma\big(\text{IN}(\text{SN}(\mathbf{W}_1 * f_i) + b_1)\big)\Big) + b_2\Big)\Big) \quad (3)$$

Algorithm 1. Generator (G)

Require: $x \in \mathbb{R}^{H\times W\times C}$
Ensure: $\hat{x} \in \mathbb{R}^{H\times W\times C}$

Encoding:

$x_1 = \sigma\Big(\text{IN}\Big(\text{SN}\big(\text{Conv}(x, 7\times 7, \text{s} = 1)\big)\Big)\Big)$

$x_2 = \sigma\Big(\text{IN}\Big(\text{SN}\big(\text{Conv}(x_1, 3\times 3, \text{s} = 2)\big)\Big)\Big)$

$x_3 = \sigma\Big(\text{IN}\Big(\text{SN}\big(\text{Conv}(x_2, 3\times 3, \text{s} = 2)\big)\Big)\Big)$

Residual Blocks:

for i = 1 to n do

$x_3 = x_3 + 0.1 \cdot \text{SN-Conv} \rightarrow \text{IN} \rightarrow \text{SiLU} \rightarrow \text{SN-Conv} \rightarrow \text{IN}(x_3)$

Multi-Head Attention (MHA):

, $K = \text{SN}\big(\text{Conv}(x_3, 1\times 1)\big)$, $Q = \text{SN}\big(\text{Conv}(x_3, 1\times 1)\big)$

$V = \text{SN}\big(\text{Conv}(x_3, 1\times 1)\big)$ $A = \text{Softmax}\left(\frac{QK^T}{\sqrt{d}}\right)$

$x_4 = AV$

$x_5 = \gamma \cdot \text{DepthwiseConv}(x_4) + \beta x_3$

Decoding:

$x_6 = \sigma\Big(\text{IN}\big(\text{ConvT}(x_5, 4\times 4, \text{s} = 2)\big)\Big)$

$x_7 = \sigma\Big(\text{IN}\big(\text{ConvT}(x_6, 4\times 4, \text{s} = 2)\big)\Big)$

$\hat{x} = \tanh\Big(\text{SN}\big(\text{Conv}(x_7, 7\times 7, \text{s} = 1)\big)\Big)$

Return $\hat{x}$

Algorithm 2. Discriminator (D)

Require: $x \in \mathbb{R}^{H\times W\times C}$
Ensure: $D(x) \in \mathbb{R}^{H'\times W'}$

Feature Extraction:

$x_1 = \text{LReLU}\Big(\text{SN}\big(\text{Conv}(x, 4\times 4, \text{s} = 2)\big)\Big)$

$x_2 = \text{LReLU}\Big(\text{BN}\Big(\text{SN}\big(\text{Conv}(x_1, 4\times 4, \text{s} = 2)\big)\Big)\Big)$

$x_3 = \text{LReLU}\Big(\text{BN}\Big(\text{SN}\big(\text{Conv}(x_2, 4\times 4, \text{s} = 2)\big)\Big)\Big)$

$x_4 = \text{LReLU}\Big(\text{BN}\Big(\text{SN}\big(\text{Conv}(x_3, 4\times 4, \text{s} = 1)\big)\Big)\Big)$

Classification:

$D(x) = \text{SN}\big(\text{Conv}(x_4, 4\times 4, \text{s} = 1)\big)$

Return $D(x)$

3. 1. 3. Multi-Head Attention (MHA) Mechanism To enhance feature dependencies over large spatial regions, a multi-head attention mechanism is integrated. Given an input feature map x, attention mechanism computes:

1. Query (Q), key (K), and value (V) matrices:

$$Q = W_q * x, \quad K = W_k * x, \quad V = W_v * x \quad (4)$$

2. Scaled dot-product attention

$$A = \text{Softmax}\left(\frac{QK^T}{\sqrt{d}}\right) \quad (5)$$

3. Weighted aggregation:

$$\hat{x} = AV \quad (6)$$

4. Multi-head representation:

$$\text{MHA}(x) = W_o[\hat{x}_1, \hat{x}_2, \ldots, \hat{x}_h] \quad (7)$$

In Equations 4-7, h denotes the count of attention heads, and W_o projects the concatenated heads back to the original feature space. The attended feature maps x_4 undergo depthwise convolution, followed by a weighted residual connection with x_3. This transformer attention improves the model's ability to capture long-range dependencies crucial for removing non-uniform haze patterns.

3. 1. 4. Decoding Stage The decoding phase restores the original resolution of the dehazed image. Here, Two transposed convolution layers (4×4) progressively

upsample the feature maps. A final 7×7 spectral-normalized convolution, followed by a tanh activation, generates the refined output $\hat{x}$. The use of spectral normalization ensures stable training by controlling the Lipschitz constant of the generator. The decoding phase involves upsampling the features and reconstructing the output. The transposed convolution and the final reconstruction are mathematically expressed as Equations 8 and 9, respectively.

- Transposed convolution:

$$f_{i+1} = \sigma\left(\mathrm{SN}\left(\mathbf{W}_i^{\mathrm{T}} * f_i\right) + b_i\right) \quad (8)$$

- Final reconstruction:

$$\hat{x} = \tanh(\mathrm{SN}(\mathbf{W}_{\text{final}} * f_{\text{last}}) + b_{\text{final}}) \quad (9)$$

3. 2. Discriminator (D) The discriminator serves as an adversarial critic, distinguishing real dehazed images from fake ones generated by G. Here s denotes the stride and F signify the number of filters. The architecture follows a hierarchical feature extraction strategy.

The discriminator architecture is shown in Figure 2.

3. 2. 1. Feature Extraction Stage The input image undergoes four layers of convolution with spectral normalization (SN) and leaky ReLU activations. Each convolutional layer uses a 4×4 kernel, progressively reducing spatial dimensions while increasing feature abstraction. Here, batch normalization (BN) is applied after the first convolutional layer to stabilize training.

Hierarchical convolutional layers gradually reduce spatial dimensions. In Equation 10, $f_0 = x$ and the kernel size is 4×4.

$$f_i = \mathrm{LeakyReLU}(\mathrm{SN}(\mathbf{W}_i * f_{i-1}) + b_i) \quad (10)$$

3. 2. 2. Classification stage A final convolution layer reduces the feature maps to a lower-dimensional representation, providing a scalar output $D(x)$ as given in Equation 11. This output represents the probability of whether the input is a real or fake dehazed image.

$$D(x) = \sigma(\mathbf{W}_d * f_{\text{last}} + b_d) \quad (11)$$

here, $D(x)$ represents the probability of the image being real.

Figure 2. MHSAR-GAN Discriminator (D) Architecture

3. 3. Significance of the Proposed GAN Model The proposed GAN model enhances image dehazing by integrating spectral normalization, residual blocks, and self-attention mechanisms:

1. **Spectral Normalization:** Ensures stable training of both G and D by controlling weight magnitudes.
2. **Residual Learning:** Helps retain important details, making dehazed images more realistic.
3. **Self-Attention:** Enables the generator to consider long-range dependencies, reducing artifacts and improving dehazing quality.
4. **Hierarchical Discrimination:** The discriminator effectively differentiates real and fake images, enforcing structural consistency in dehazed outputs.

4. EXPERIMENTAL RESULTS

In this section, we present comprehensive experiments to rigorously evaluate the effectiveness of our proposed GAN method. The proposed work is implemented within a Docker-based Ubuntu environment with Python, and is executed on an NVIDIA Tesla T4 GPU (16GB VRAM) and 2 vCPUs of Intel Xeon architecture.

4. 1. Dataset Details We evaluated our method on publicly available benchmark haze removal datasets Haze1K, and RESIDE 6K.

Haze1K: The Haze1K dataset is a reference in establishing improved techniques for dehazing satellite imagery. It comprises 1,200 pairs of hazy and corresponding clear images, supplemented with Synthetic Aperture Radar (SAR) data acquired from Earth observation satellites such as GF-2 and GF-3. The dataset promotes research into haze removal, which is critical in enhancing the accuracy of remote sensing applications. Haze1K has specifically created three different haze levels-thick, moderate, and thin-that would mimic real atmospheric conditions in which the models are trained and hence help generalize scenarios across varying visibility scenarios. Given the inherent differences in capture timing between SAR and optical images, precise alignment is applied to facilitate meaningful comparisons. Haze1K enables the integration of SAR data as an auxiliary input to refine dehazing outcomes by preserving structural integrity.

RESIDE 6K: The RESIDE dataset, which stands for Realistic Single Image Dehazing, comprises paired hazy and clear images to facilitate dehazing research. Specifically, the RESIDE 6K has 6,000 image pairs allocated for training and 1,000 image pairs for testing. The training set is evenly divided into 3,000 indoor scene pairs (ITS) and 3,000 outdoor scene pairs (OTS), with all images standardized to a resolution of 400×400 pixels. Likewise, the test set maintains this balance, containing 500 indoor and 500 outdoor

pairs, ensuring diverse scene coverage without any resizing.

4. 2. Evaluation Metrics Here PSNR and SSIM are two main metrics.

Peak signal-to-noise ratio (PSNR): It is a key metric in engineering and image processing that quantifies the fidelity of a reconstructed image or video relative to its original form. It represents the ratio between the maximum possible signal power and the power of noise that affects accuracy. Since signals often have a wide dynamic range, PSNR is expressed in decibels (dB) on a logarithmic scale, making it a widely accepted standard for evaluating lossy compression effects on images and videos. Mathematically, PSNR is computed using the Mean Squared Error (MSE), which measures the average squared differences between the original noise-free image and its distorted counterpart. Given an $m \times n$ grayscale image I and its distorted version K, the MSE is defined as illustrated in Equation 12:

$$\text{MSE} = \frac{1}{mn}\sum_{i=1}^{m}\sum_{j=1}^{n}\left(I(i,j) - K(i,j)\right)^2 \quad (12)$$

The PSNR in decibels (dB) is then given by Equation 13:

$$\text{PSNR} = 10 \cdot \log_{10}\left(\frac{L^2}{\text{MSE}}\right) \quad (13)$$

Here, L denotes the maximum pixel intensity of the image. In the case of an 8-bit image, $L = 255$, and in case of an B-bit image, $L = 2^B$.

At higher PSNR value signifies better image quality, indicating lower noise interference in the reconstruction. In the case of color images, PSNR is computed either separately for each channel (e.g., in RGB or YCbCr color spaces) or as an average across all channels, ensuring a comprehensive evaluation of quality degradation.

Structural Similarity Index (SSIM): It is a widely used metric for assessing the perceived quality of digital images and videos. Unlike traditional error-based metrics like Mean Squared Error (MSE) or PSNR, SSIM evaluates image quality based on structural similarity, incorporating human visual perception principles. It considers three key factors: luminance, contrast, and structure, making it more aligned with human perception. Mathematically, SSIM is computed for two image windows x and y of size $N \times N$ as:

$$\text{SSIM}(x,y) = \frac{(2\mu_x\mu_y + C_1)(2\sigma_{xy} + C_2)}{(\mu_x^2 + \mu_y^2 + C_1)(\sigma_x^2 + \sigma_y^2 + C_2)} \quad (14)$$

Here, μ_x and μ_y are the mean intensities of image windows x and y, representing luminance. σ_x^2 and σ_y^2 are the variances of x and y, capturing contrast. σ_{xy} is the covariance between x and y, measuring structural similarity. C_1 and C_2 are small constants to stabilize the division, preventing instability when denominators are close to zero.

SSIM is computed locally over image patches and can be averaged to obtain a single quality score for the entire image. It is particularly effective in scenarios involving compression, denoising, and enhancement, where preserving structural details is crucial.

4. 3. Result Analysis Table 1 presents a comparative analysis of image dehazing methods on the Haze1K dataset across different fog densities, namely thin, moderate, and thick fog using PSNR and SSIM metrics. The results clearly highlight the superior performance of the proposed MHSAR-GAN model, which consistently outperforms prior state-of-the-art methods in terms of both PSNR and SSIM. Traditional methods such as DCP (3) exhibit bad performance, particularly under moderate and thick fog conditions, due to their reliance on handcrafted priors, which struggle with complex haze patterns. Deep learning-based methods, such as DehazeNet (5) and SAR-Opt-cGAN (19), demonstrate noticeable improvements over traditional techniques by learning data-driven features. However, DehazeNet (5), despite having the lowest number of trainable parameters (0.009M), delivers relatively poor performance. More advanced models like Trinity-Net (6) and FFA-Net (25), with 9.82M and 4.45M parameters respectively, show good results due to the integration of refined feature extraction and attention mechanisms. FFA-Net (25) demonstrates stronger perceptual quality, particularly in moderate haze. Nonetheless, these models are outperformed by AUNet (24) and DehazeFormer (23), which achieve higher PSNR and SSIM scores but at the cost of increased complexity with 7.417M and 9.68M parameters, respectively. Remarkably, our proposed MHSAR-GAN surpasses all existing methods, achieving the highest PSNR and SSIM scores across all haze levels while maintaining a lightweight structure of only 3.60M parameters. This improvement can be attributed to its novel Multi-Head self-attention Residual GAN, which effectively preserves structural details while enhancing perceptual quality. Notably, under thick fog conditions, the proposed MHSAR-GAN achieves a remarkable PSNR of 22.5850 and an SSIM of 0.9157, significantly improving visibility and fine details where other image dehazing methods struggle.

These results underscore the effectiveness of the proposed approach, demonstrating its robustness across varying haze intensities. The test results on thick, thin and moderate haze are shown in Figures 3, 4 and 5 using proposed MHSAR-GAN model. These figures collectively highlight the robustness of the proposed dehazing model across varying haze densities.

Comparison of various benchmark image dehazing methodologies on the RESIDE 6K data are provided in Table 2 taking PSNR and SSIM as evaluation metrics.

TABLE 1. Quantitative Evaluation of Image Dehazing Methods on HAZE1K

Method	#Params	Thin		Thick		Moderate	
	(in M)	PSNR	SSIM	PSNR	SSIM	PSNR	SSIM
Actual	--	12.7712	0.7241	8.5893	0.4215	12.5867	0.7399
DCP (3)	--	13.1517	0.7246	10.2513	0.5850	9.7830	0.5735
DehazeNet (5)	0.009M	19.7529	0.8950	14.3321	0.7064	18.1250	0.8552
Trinity-Net (6)	9.82M	19.3708	0.7816	17.1281	0.7723	19.6918	0.7062
SAR-Opt-cGAN (19)	--	20.1950	0.8419	19.6553	0.7573	21.6616	0.7941
AUNet (24)	7.417M	23.0170	0.9060	19.9090	0.847	24.3270	0.9290
FFA-Net (25)	4.45M	20.1410	0.8582	19.1255	0.7976	22.5586	0.9132
DehazeForner (23)	9.68M	21.9274	0.8843	20.2133	0.8049	24.4407	0.9268
MHSAR-GAN (Ours)	**3.60M**	**24.0842**	**0.9426**	**22.5850**	**0.9157**	**26.0070**	**0.9384**

Figure 3. Test result on **Thick haze** on Haze1K dataset

Figure 4. Test result on **Thin haze** on Haze1K dataset

Figure 5. Test result on **Moderate haze** on Haze1K dataset

TABLE 2. Image Dehazing Results on RESIDE 6K dataset

Method	Params	PSNR	SSIM
DCP (3)	--	17.88	0.8160
DehazeNet (5)	0.009M	21.02	0.8700
PSD (20)	6.21M	15.47	0.8149
GridDehazeNet (21)	0.956M	25.65	0.9371
RefineDNet (22)	--	20.75	0.8656
DehazeFormer (23)	9.68M	28.96	0.9655
Proposed Model	**3.60M**	**29.70**	**0.9311**

Prior dehazing methods such as DCP (3) and PSD (20) exhibit relatively low PSNR values of 17.88 and 15.47 respectively, demonstrating their limitations under different haze conditions. PSD (20) has 6.21M trainable parameters. Figures 6 and 7 illustrates the test results of the proposed dehazing network on the RESIDE 6K indoor and outdoor test image dataset.

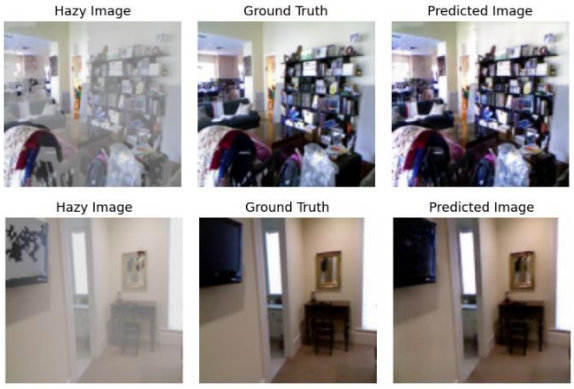

Figure 6. Test Results on RESIDE 6K dataset (Indoor scene)

Figure 7. Test result on RESIDE 6K dataset (Outdoor scene)

On the other hand, the performance of learning-based architectures such as DehazeNet (5) and RefineDNet (22) is comparatively better as evidenced by the corresponding PSNR values of 21.02 and 20.75. DehazeNet [5] and GridDehazeNet (21) exhibit the lowest trainable parameters; however their performance is moderate in terms of image haze removal. More advanced deep-learning methods like GridDehazeNet (21) and Dehazeformer (23) demonstrate significant gains, with Dehazeformer achieving high PSNR of 28.96 and an SSIM of 0.9655. The proposed MHSAR-GAN model achieves competitive performance with a PSNR of 29.70 and an SSIM of 0.9311, demonstrating its effectiveness in preserving structural details while maintaining high-quality restoration.

The proposed image dehazing model has fewer trainable parameters (3.60M) compared to DehazeFormer (9.68M) while achieving higher PSNR (29.70 vs 28.96) but slightly lower SSIM (0.9311 vs 0.9655). Thus, the slightly lower SSIM is an acceptable trade-off, given the clear advantage in PSNR and model compactness.

The proposed model balance between perceptual quality and efficiency makes it a strong contender for real-world dehazing applications. Improved dehazing significantly boosts performance in autonomous driving, remote sensing, video surveillance, object detection, scene classification, and semantic segmentation by enabling more effective feature extraction.

5. CONCLUSION AND FUTURE SCOPE

The study highlights how deep learning techniques, especially GANs, can address image haze removal. Although most conventional CNN-based dehazing methods are moderately successful, GANs are quite powerful for the reconstruction of fine details and creation of much more visually coherent outputs. Our contribution is the Multi-Head Spectral-Attentive Residual Generative Adversarial Network (MHSAR-GAN), which uses spectral normalization, multi-head self-attention, and residual scaling in an attempt to increase haziness removal capacity through better feature extraction and more stable training. The evaluation of the Haze1K and RESIDE 6K datasets validates the model's ability at different haze densities and verifies major improvements in visibility restoration and structural preservation. Despite all these developments, challenges like handling extreme haze weather and color fidelity remain open areas of exploration. Future work may include refining attention mechanisms, boosting computational efficiency, and exploring self-supervised learning to reduce reliance on paired training data for broader adaptability in real-world single image dehazing applications.

6. REFERENCES

1. Khatun A, Mostafiz R, Shorif SB, Uddin MS, Hadi MA. Dehazing using Generative Adversarial Network-A Review. SN Computer Science. 2024;6(1):20. 10.1007/s42979-024-03571-0
2. Ali AM, El-Rabaie E-SM, Ramadan KF, Abd El-Samie FE, El-Shafai W. CLEAR-Net: A Cascaded Local and External Attention Network for Enhanced Dehazing of Remote Sensing Images. IEEE Journal of Selected Topics in Applied Earth Observations and Remote Sensing. 2025. 10.1109/jstars.2025.3534984
3. He K, Sun J, Tang X. Single image haze removal using dark channel prior. IEEE transactions on pattern analysis and machine intelligence. 2010;33(12):2341-53. 10.1109/tpami.2010.168
4. Tao T, Xu H, Guan X, Zhou H. MCADNet: A Multi-Scale Cross-Attention Network for Remote Sensing Image Dehazing. Mathematics (2227-7390). 2024;12(23). 10.3390/math12233650
5. Cai B, Xu X, Jia K, Qing C, Tao D. Dehazenet: An end-to-end system for single image haze removal. IEEE transactions on image processing. 2016;25(11):5187-98. 10.1109/TIP.2016.2598681
6. Chi K, Yuan Y, Wang Q. Trinity-net: Gradient-guided swin transformer-based remote sensing image dehazing and beyond. IEEE Transactions on Geoscience and Remote Sensing. 2023;61:1-14. 10.1109/tgrs.2023.3285228
7. Ren W, Ma L, Zhang J, Pan J, Cao X, Liu W, et al., editors. Gated fusion network for single image dehazing. Proceedings of the IEEE conference on computer vision and pattern recognition; 2018. 10.1109/CVPR.2018.00343
8. Qu Y, Chen Y, Huang J, Xie Y, editors. Enhanced pix2pix dehazing network. Proceedings of the IEEE/CVF conference on computer vision and pattern recognition; 2019. 10.1109/CVPR.2019.00835
9. Cui Y, Wang Q, Li C, Ren W, Knoll A. EENet: An effective and efficient network for single image dehazing. pattern recognition. 2025;158:111074. 10.1016/j.patcog.2024.111074
10. Patil PW, Randive SN, Gupta S, Rana S, Venkatesh S, Murala S. Unpaired recurrent learning for real-world video de-hazing. Pattern Recognition. 2025:111698. 10.1016/j.patcog.2025.111698
11. Su Y, Wang N, Cui Z, Cai Y, He C, Li A. Real scene single image dehazing network with multi-prior guidance and domain transfer. IEEE Transactions on Multimedia. 2025. 10.1109/TMM.2025.3543063
12. Zhao X, Xu F, Liu Z. TransDehaze: transformer-enhanced texture attention for end-to-end single image dehaze. The Visual Computer. 2025;41(3):1621-35. 10.1007/s00371-024-03458-4
13. Chen H, Chen R, Li Y, Li H, Li N. Unsupervised single-image dehazing via self-guided inverse-retinex GAN. Multimedia Systems. 2025;31(2):139. 10.1007/s00530-025-01713-9
14. Ning J, Yin J, Deng F, Xie L. MABDT: Multi-scale attention boosted deformable transformer for remote sensing image dehazing. Signal Processing. 2025;229:109768. 10.1016/j.sigpro.2024.109768
15. Shen H, Zhong T, Jia Y, Wu C. Remote sensing image dehazing using generative adversarial network with texture and color space enhancement. Scientific Reports. 2024;14(1):12382. 10.1038/s41598-024-63259-6
16. Pushpalatha D, Prithvi P. PMDNet: A multi-stage approach to single image dehazing with contextual and spatial feature preservation. Journal of Visual Communication and Image Representation. 2025;107:104379. 10.1016/j.jvcir.2024.104379
17. Ayoub A, El-Shafai W, El-Samie FEA, Hamad EK, El-Rabaie E-SM. Video and image quality improvement using an enhanced optimized dehazing technique. Multimedia Tools and

Applications. 2025;84(20):22681-99. 10.1007/s11042-024-19263-z

18. Wu J, Tao H, Xiao K, Chu J, Leng L. Multi-stream feature aggregation network with multi-scale supervision for single image dehazing. Engineering Applications of Artificial Intelligence. 2025;139:109486. 10.1016/j.engappai.2024.109486
19. Grohnfeldt C, Schmitt M, Zhu X, editors. A conditional generative adversarial network to fuse SAR and multispectral optical data for cloud removal from Sentinel-2 images. IGARSS 2018-2018 IEEE International Geoscience and Remote Sensing Symposium; 2018: IEEE. 10.1109/igarss.2018.8519215
20. Chen Z, Wang Y, Yang Y, Liu D, editors. PSD: Principled synthetic-to-real dehazing guided by physical priors. Proceedings of the IEEE/CVF conference on computer vision and pattern recognition; 2021. 10.1109/CVPR46437.2021.00710
21. Liu X, Ma Y, Shi Z, Chen J, editors. Griddehazenet: Attention-based multi-scale network for image dehazing. Proceedings of the IEEE/CVF international conference on computer vision; 2019. 10.1109/ICCV.2019.00741
22. Zhao S, Zhang L, Shen Y, Zhou Y. RefineDNet: A weakly supervised refinement framework for single image dehazing. IEEE Transactions on Image Processing. 2021;30:3391-404. 10.1109/tip.2021.3060873
23. Song Y, He Z, Qian H, Du X. Vision transformers for single image dehazing. IEEE Transactions on Image Processing. 2023;32:1927-41. 10.1109/tip.2023.3256763
24. Du Y, Li J, Sheng Q, Zhu Y, Wang B, Ling X. Dehazing network: Asymmetric unet based on physical model. IEEE Transactions on Geoscience and Remote Sensing. 2024;62:1-12. 10.1109/tgrs.2024.3359217
25. Qin X, Wang Z, Bai Y, Xie X, Jia H, editors. FFA-Net: Feature fusion attention network for single image dehazing. Proceedings of the AAAI conference on artificial intelligence; 2020. 10.1609/aaai.v34i07.6865
26. Khosravi M, Hassanpour H. A novel image structural similarity index considering image content detectability using maximally stable extremal region descriptor. International Journal of Engineering-Transactions B: Applications. 2017;30(2):172. 10.5829/idosi.ije.2017.30.02b.03
27. Zhou X, Bai L, Wang C. Single image dehazing algorithm based on dark channel prior and Inverse Image. International Journal of Engineering Transactions A: Basics. 2017;30(10):1471-8. 10.5829/ije.2017.30.10a.07
28. Nasrabad FA, Hassanpour H, Amiri SA. Adaptive image dehazing via improving dark channel prior. International Journal of Engineering Transactions B: Applications. 2019;32(2):253-9. 10.5829/ije.2019.32.02b.10

COPYRIGHTS

©2026 The author(s). This is an open access article distributed under the terms of the Creative Commons Attribution (CC BY 4.0), which permits unrestricted use, distribution, and reproduction in any medium, as long as the original authors and source are cited. No permission is required from the authors or the publishers.

Persian Abstract

چکیده

مه با کاهش کنتراست، وضوح و قابلیت دید، کیفیت تصویر را به شدت کاهش می دهد، که این امر چالشی برای بسیاری از کاربردهای بینایی کامپیوتر مانند رانندگی خودکار، سنجش از دور، تجزیه و تحلیل تصاویر ماهواره ی، نظارت تصویری و تشخیص حرکت است .این وظایف مبتنی بر بینایی برای تجزیه و تحلیل و تصمیم گیری کارآمد، به اطلاعات بصری واضح و بسیار دقیقی نیاز دارند .این تحقیق یک روش یادگیری مبتنی بر GAN جدید، شبکه رقابتی مولد باقیمانده با توجه طیفی چند سر-(MHSAR GAN)، را برای بهبود عملکرد مه زدایی تصویر پیشنهاد می دهد .مدل پیشنهادی حذف مه تصویر مبتنی بر یادگیری عمیق، نرمال سازی طیفی را برای افزایش پایداری آموزش، توجه چند سر برای تنظیم دقیق انتخاب ویژگی و یادگیری باقیمانده را برای حفظ اطلاعات ساختاری مهم برای بهبود مه زدایی تک تصویر ترکیب می کند .پیچش های عمقی نیز در مکانیسم توجه برای استخراج ویژگی های مکانی بهبود یافته بدون پیچیدگی محاسباتی اضافی گنجانده شده اند .ما روش خود را بر روی مجموعه داده های مه زدایی تصویر معیار، Haze1K و RESIDE 6K آزمایش کردیم و عملکرد آن را با مدل های مه زدایی تصویر پیشرفته مقایسه کردیم .نسبت سیگنال به نویز پیک (PSNR) و شاخص شباهت ساختاری (SSIM) معیارهای محوری برای ارزیابی عملکرد مدل بودند که ارزیابی جامعی از کیفیت تصویر و صحت ساختاری را تضمین می کردند .نتایج تجربی نشان می دهد که MHSAR-GAN پیشنهادی در مقایسه با روش های مه زدایی تصویر موجود در مقایسه های کمی و کیفی، به حذف مه بهتری با حفظ جزئیات ریز تصویر و وضوح بیشتر دست می یابد.

International Journal of Engineering

Journal Homepage: www.ije.ir

Catalytic Conversion of Heavy Oil Using Molybdenum Based Water-soluble Catalyst

A. A. Bondarenko*[a], M. K. Rogachev[a], A. S. Skvortsov[b], K. V. Dmitriev[b]

[a] *Development and Operation of Oil and Gas Fields, Saint-Petersburg Mining University, Saint-Petersburg, Russia*
[b] *Lukoil-Engineering LLC, Perm, Russia*

PAPER INFO

Paper history:
Received 16 July 2025
Received in revised form 29 August 2025
Accepted 09 September 2025

Keywords:
Super-viscous Oil
Cyclic Steam Stimulation
Catalytic Treatment
SARA Composition
Numerical Modeling

ABSTRACT

The growing global trend of putting heavy oil fields into development is a complex task that requires updating previously unprofitable approaches. One of such areas is cyclic steam stimulation of wells to stimulate the production of high-viscous and super-viscous oils. An increase in well flow rates and the depletion of reserves, a decrease in the time and financial costs of well servicing and workover can be achieved by combining thermal and chemical methods of inflow stimulation. This approach has proven itself successfully in the catalytic in-situ upgrading of oil. Within the framework of this article, a series of laboratory experiments were performed to confirm the effectiveness of ammonium molybdate as a water-soluble precursor of an aquathermolysis catalyst for upgrading super-viscous oil from one of the fields of the Timan-Pechora oil and gas province. The decrease in oil viscosity relative to the non-catalytic effect was 24%, which was also confirmed by the results of the SARA-analysis of oil: a decrease in the amount of asphaltenes by 15.9%, an increase in the amount of saturated and aromatic hydrocarbons by 3% and 4.6%, respectively. Based on a simple numerical model was predicted an increase in oil flow rate with a catalytic effect relative to a non-catalytic effect by 23%. The results obtained indicate the potential for using this catalyst precursor in field conditions.

doi: *10.5829/ije.2026.39.08b.04*

Graphical Abstract

Effective viscosity of oil (at a shear rate of 100 s^{-1}) (a), results of SARA-analysis (%) (b), cumulative oil with different viscosity characteristics (c)

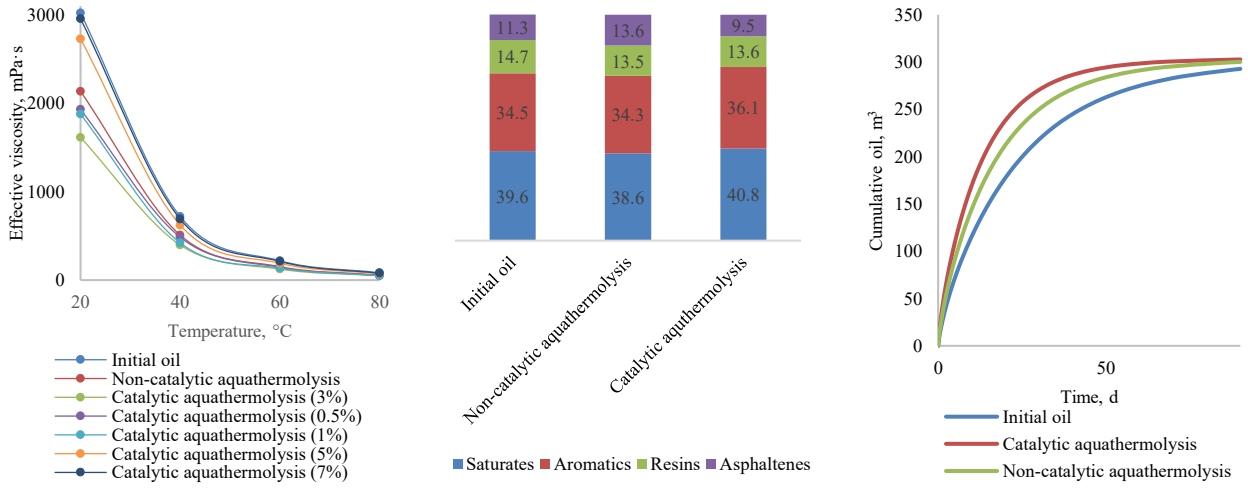

a b c

*Corresponding Author Email: asizefrom12@gmail.com (A. A. Bondarenko)

Please cite this article as: A. A. Bondarenko, M. K. Rogachev, A. S. Skvortsov, K. V. Dmitriev. Catalytic Conversion of Heavy Oil Using Molybdenum Based Water-soluble Catalyst. International Journal of Engineering, Transactions B: Applications. 2026;39(08):1821-8.

1. INTRODUCTION

Development of hard-to-recover reserves (HTR) represented by complex geological conditions and heavy oil (1-3) is one of the most important strategic tasks of the oil and gas industry. The solution to this problem lies in sufficient investment in new technologies (4), conducting comprehensive laboratory studies (5, 6), determining an integrated approach to reduce the negative impact on the reservoirs and planning operations to restore productivity (7), building complex numerical compositional models (8), as well as substantiating the most effective approach to development. Stimulation of productive reservoirs with steam is one of the key approaches to the development of deposits of super-viscous oils (9, 10). The choice of optimal conditions for the implementation of in-situ upgrading of super-viscous oil is an important task when planning and conducting cyclic steam stimulation (CSS) of the well. The in-situ upgrading of oil is based on aquathermolysis reactions. It is the reaction of transformation of high-molecular oil components in the presence of water at a temperature of 200–320 °C (11) as a result of destruction of carbon bonds with sulfur, oxygen and nitrogen. In addition, changes in pressure can also influence the nature of aquathermolysis reactions (12, 13). The carbon-sulfur bond is most prone to rupture due to its relatively low energy (14). Increased efficiency of these processes is achieved by including precursors of catalysts based on transition metals in the aquathermolysis reactions (15). The functioning of the catalyst begins after its transition to the active form: decomposition of catalyst precursors with formation of the active form: sulfides and oxides of transition metals (16). Today, physical modeling of the conditions of in-situ oil conversion in the presence of steam at high-pressure and high-temperature cells (autoclaves) is one of the key methods for evaluating aquathermolysis catalysts. Based on previous research, it can be noted that molybdenum ranks first among transition metals in catalytic activity: Mo>Cu>Ni>Fe>Co>Zn>Mn (17, 18). At the same time, molybdenum contributes to a higher yield of the liquid fraction and a decrease in the amount of coke, which was confirmed by the results of tests under severe conditions (460 °C). It is also confirmed by the significant effect of molybdenum on the destruction of asphaltenes and resins (19, 20). They proved that molybdenum sulfides formed in-situ are almost 10 times smaller than sulfides of other transition metals. It indicates their smaller specific surface area and, as a consequence, lower activity. Molybdenum as an active metal demonstrates a higher decrease in the molecular weight of oil and sulfur in resins than Fe and Ni using the same ligand due to its higher ability to hydrogenate. It contributes to further opening of aromatic rings (21). Deng et al. (22) found that the presence of nickel in oil after in-situ upgrading can lead to coking of oil refining catalysts.

Thus, nickel and molybdenum arylsulfonates, as well as some metals alloyed with molybdenum (23-25), were used as oil-soluble catalyst precursors during studies of super-viscous oil from the Shengli oil field (China). After holding the mixture at a temperature of 200 °C for 24 hours, the decreases in viscosity of 97% and 72.7%, respectively, were achieved. After holding an oil sample from the Liaohe oil field (China) in an autoclave at a temperature of 240 °C for 24 hours in the presence of molybdenum oleate, a decrease in the molecular weight of the oil sample by 1.5 - 1.7 times was noted (26). In this case, Zhao et al. (27) showed that the hydrocarbon ligand "oleate" has greater catalytic activity in the reactions of in-situ upgrading of oil relative to "octanoate, decanoate and stearate". High efficiency (reduction of oil viscosity by 82.26%) was demonstrated by the precursor of aquathermolysis catalyst based on zeolite, molybdenum and zirconium oxides as a result of holding an oil sample from the Shengli oil field (China) in an autoclave at a temperature of 280 °C for 24 hours in the presence of a hydrogen donor 1,2,3,4-tetrahydronaphthalene (28). Tajik et al. (29) conducted autoclave studies of high-viscosity oil in the presence of a nanohybrid of silicon dioxide and graphene together with molybdenum disulfide. The aging was carried out with the addition of phenanthrene in decalin as a hydrogen donor at a temperature of 200 °C for 24 hours. The viscosity reduction was 80.8%. A high degree of methyl palmitate conversion was achieved in a high-pressure and high-temperature reactor in the presence of an oil-soluble ionic liquid based on molybdenum at a temperature of 320 °C for 3 hours (30). The use of water-soluble, oil-soluble precursors of aquathermolysis catalysts, as well as solid catalysts based on molybdenum, made it possible to reduce the viscosity of Mackay River bitumen as a result of holding in an autoclave for 24 hours at a temperature of 250 °C (31). The range of viscosity reduction was 52.6% - 95.1%. Wang et al. (32) carried out experimental studies of molybdenum and nickel catalysts applied to proppant in an experimental setup for in-situ upgrading of oil. Aquathermolysis reactions occurred in cells filled with rock mixed with activated proppant. Holding was carried out at a temperature of 240 °C for 24 hours. The viscosity of oil from the Liaohe oil field (China) was reduced by 84%. Also Wang et al. (32) note better distribution of the catalyst in oil when using oil-soluble precursors. However, there are also significant disadvantages: the complexity of separation from oil and further processing, the high cost of synthesis. In this case, the use of Mo_2C as an aquathermolysis catalyst demonstrated a better ability to activate water compared to the bimetallic catalyst NiMo (33). Successful field tests of a water-soluble precursor of the ammonium tetrathiomolybdate catalyst $(NH_4)_2MoS_4$ were also

carried out for in-situ upgrading of super-viscous oil from the Shengli oil field (China) (34). First, 1 ton of catalyst precursor was injected, then 2500 tons of steam were injected at a rate of 10 t/h. The soaking period was 7 days, production was carried out for 4 months. The average decrease in oil viscosity was 85.7%, which is confirmed by a change in the group composition of the oil: a decrease in the amount of asphaltenes by 12%, an increase in the amount of saturated compounds by 3%. It is also worth noting that the removal of the catalyst together with the oil was recorded only in the third month of production, which indicates its effective adsorption on the reservoir rock. During physical modeling of in-situ upgrading of oil from one of the oil fields in China, the addition of a precursor of aquathermolysis catalyst containing MoO_3 contributed to the inhibition of coke formation. It has a positive effect on the preservation of the reservoir properties of the bottomhole formation zone (35).

The object of the study is super-viscous oil in the Timan-Pechora oil and gas province in Russia. In accordance with the results of the above studies, commercially available ammonium molybdate was used as a water-soluble catalyst precursor during physical modeling of in-situ upgrading of oil. This reagent does not require additional costs for the synthesis process and, presumably, will not require its separation from the oil due to its solubility in water.

The relevance of this work is due to the fact that the use of classical CSS in super-viscous oil fields stimulates the deposition of high-molecular components of oil (asphaltenes, resins) in the bottomhole formation zone. It significantly reduces the reservoir properties. In addition, molybdenum-based aquathermolysis catalysts have not previously been considered for possible use in conducting the CSS at one of the oil fields of the Timan-Pechora oil and gas province. This catalyst can have a technological effect even in the most accessible form. Thus, the main objective of this study is to confirm the catalytic properties of molybdenum in relation to the oil under study.

The Methods and Materials section presents the stages of laboratory research. During the work, oil was prepared for the study, the rheological properties and group composition of oil were determined before and after the experiment. Physical modeling of aquathermolysis reactions in an autoclave was also carried out. Further in the article, the results of numerical modeling are presented and the corresponding conclusions are made.

2. METHODS AND MATERIALS

2. 1. Preparation of Oil and Determination of its Properties

The studied oil was super-viscous oil from one of the fields of the Timan-Pechora oil and gas province with a viscosity of more than 3000 mPa·s at a temperature of 20 °C. The selected oil sample was pre-treated to separate water by adding a demulsifier to 1 liter of oil and keeping it in a heat chamber at a temperature of 70 °C for 8 hours. After that, the water was drained using a separatory funnel (Figure 1). The viscosity of the oil was measured using a Rheotest RN 4.1 rotational viscometer at different shear rates (1, 10, 50, 100 s^{-1}) for 5 min at each speed. The analysis of the group composition of the oil (SARA-analysis) was carried out in accordance with ASTM D4124-09 and GOST 32269-2013.

2. 2. Determination of Rheological Parameters of Oil

In order to simulate the reactions of catalytic aquathermolysis, distilled water and a water-soluble precursor of the catalyst for aquathermolysis reactions, commercially available ammonium molybdate $(NH_4)_6Mo_7O_{24}\cdot 4H_2O$, chemically pure, were used. The experiment was carried out in a high-pressure and high-temperature reactor is an autoclave without a stirrer. The pressure in the autoclave was maintained by pumping nitrogen. Before loading with oil, water and a reagent, the reactor was purged with nitrogen to remove air. To minimize heat loss, a thermal jacket was put on the autoclave. The basic diagram of the laboratory bench is shown in Figure 2.

The autoclave was loaded with 33 g of oil and 10 g of water in accordance with the available capacity of the reactor (36-38). When modeling the reactions of catalytic aquathermolysis, ammonium molybdate was dissolved in water with constant stirring at a speed of 100 rpm for at least 15 min. In accordance with the experimental experience of conducting similar works (17, 26), an assumption was made about the effective concentration of the catalyst precursor of 3 wt.% by oil. To confirm this, the experiment was repeated for four additional precursor concentrations of 0.5%, 1%, 5%, 7%. Before loading the components into the autoclave, the oil and water with the dissolved catalyst precursor were subjected to active stirring at 100 rpm for at least 15 min to create a stable

Figure 1. Dehydrated oil sample

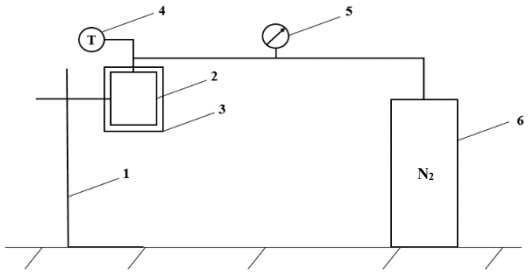

1 – chemistry stand; 2 – autoclave; 3 – thermal jacket; 4 – temperature gage; 5 – pressure gage; 6 – nitrogen bottle
Figure 2. Schematic diagram of a laboratory setup for modeling aquathermolysis reactions

emulsion (monitored visually). The formation of the emulsion in this case was important due to the need to increase the volume of interaction of oil with the potential catalyst, since it is known that at high temperatures the water-oil emulsion begins to collapse. The reaction mixture was held in the autoclave at a temperature of 250 °C and 7 MPa for 24 h. The reaction time was selected in accordance with the data reported by Baygildin et al. (39). After holding the samples, the heating was switched off, the pressure was gradually reduced to atmospheric, and the samples were cooled to room temperature for 8 hours.

3. RESULTS AND DISCUSSION

The results of measuring the viscosity of oil after catalytic and non-catalytic aquathermolysis are presented in Figure 3. The most informative results were obtained at a shear rate of 100 s^{-1}.

At a temperature of 20 °C, the decrease in oil viscosity after catalytic aquathermolysis in the presence of ammonium molybdate relative to the non-catalytic reaction is about 24%, and the overall effect of reducing viscosity relative to the initial oil is 46.6%. The viscosity values of oil in the case of adding the catalyst precursor in concentrations of 0.5% and 1% are close to the viscosity values resulting from the non-catalytic process. In this case, the process of destruction of high-molecular compounds does not reach maximum efficiency due to the low concentration of the catalyst. Increasing the concentration of the reagent to 5% and 7% has a negative effect on the viscosity values and brings its values closer to the parameters of the initial oil. This result is presumably associated with the aggregation of catalyst particles and the formation of large complexes with asphaltenes, which leads to an increase in the viscosity of the system (26). The reaction conditions relative to the conditions described by Qu et al. (31) are more stringent, since the reaction occurs without constant stirring and without an emulsifier, which affects the contact area of the oil and the resulting catalyst. It is assumed that the primary destruction of the emulsion is determined in the temperature range of 50-70 °C after 5 hours of reaction. Due to the fact that oil was sampled from the autoclave for viscosity measurement using a syringe, there is a possibility of water getting into the sample, which could also negatively affect the results obtained. Kadieva et al. (40) noted that as a result of aquathermolysis reactions, molybdenum-based precursors form catalysts in the form of the following molybdenum compounds: MoO_2, MoO_3, MoS_2. In their work, it was assumed that the above-mentioned compounds were also formed as a result of the experiments. This assumption is planned to be confirmed by SEM, XRD, FT-IR or other methods in subsequent studies. In addition, it is worth assessing the nature of the adsorption of catalysts in the pores of the rock containing the studied oil in order to exclude the likelihood of formation damage. At the same time, regardless of what specific compound was formed during the aquathermolysis reactions, simplified holding conditions and sampling errors, it is possible to unambiguously assert the achievement of a technological effect from the use of ammonium molybdate, and also with a high degree of probability speak about the effectiveness of oil-soluble molybdenum-based precursors. In this case, the water-soluble precursor eliminates the need for complex synthesis processes and can potentially be more easily separated from the produced oil, which speaks to the commercial advantages of the reagent.

To assess the potential change in well flow rate as a result of using $(NH_4)_6Mo_7O_{24}\cdot 4H_2O$, the obtained viscosity characteristics were incorporated into a numerical model built in the software product for geological and hydrodynamic modeling. Modeling was carried out for a horizontal well to obtain the maximum possible inflow. The model dimension is 30x30x5 m (Figure 4). The parameters of the modeled object are presented in Table 1. The boundary conditions of the

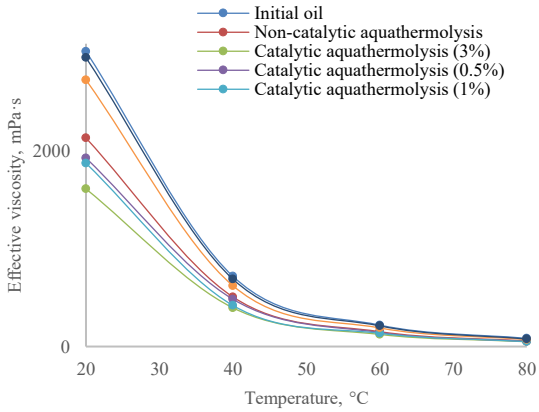

Figure 3. Effective viscosity of oil before and after the experiments (at a shear rate of 100 s^{-1})

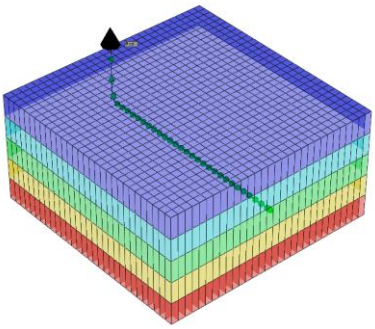

Figure 4. Model in software product

TABLE 1. Parameters of the simulated object

Propertie	Unit of measurment	Value
Absolute permeability	μm^2	0.9
Porosity	%	18
Initial reservoir pressure	MPa	7
Initial reservoir temperature	°C	28
Net reservoir thickness	m	5

model are the absence of heat and mass exchange between the object and the environment, as well as the same initial properties in each of the blocks. The constructed model does not take into account possible geological heterogeneity, the actual trajectory of the horizontal well, possible heat losses. In addition, only the process of oil production after conditionally completed cycles of CSS is modeled. The construction of a full-fledged model is an important task for future studies, requiring a detailed study of the geological structures of the target object, the inclusion of all necessary cycles of steam injection and chemical composition, the inclusion of all necessary chemical reactions and their kinetic parameters.

Well flow rate and cumulative oil production were calculated for three variants of oil viscosity characteristics: initial, after non-catalytic and catalytic in-situ upgrading (Figures 5 and 6) with catalyst precursor of 3 wt.% by oil. Oil flow rate after catalytic action increased relative to non-catalytic action by almost 23%, while the overall effect relative to the initial oil is about 61%, which is also reflected in the cumulative production graphs. The obtained results allow us to predict the technological effect of catalytic in-situ upgrading of oil using $(NH_4)_6Mo_7O_{24}\cdot 4H_2O$ as a catalyst precursor in field tests.

The results of SARA-analysis of oil before and after the experiment are presented in Figure 7. In non-catalytic aquathermolysis, a decrease in the amount of saturated, aromatic hydrocarbons, and resins in oil by 2.5%, 0.6% and 8.2%, respectively, was observed. But the amount of

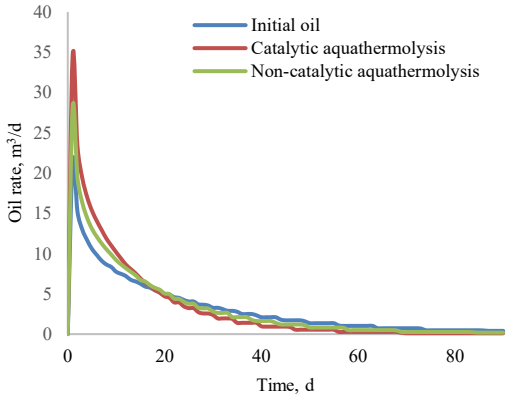

Figure 5. Oil rate with different viscosity characteristics

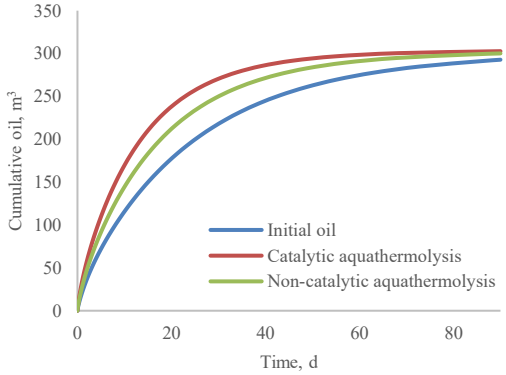

Figure 6. Cumulative oil with different viscosity characteristics

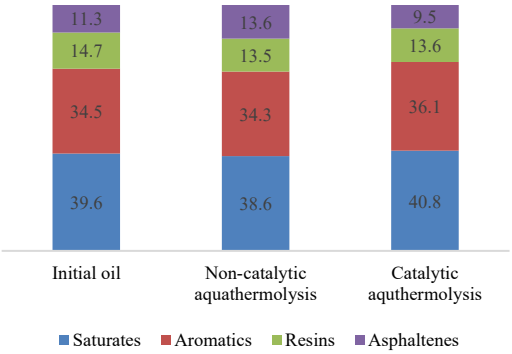

Figure 7. Results of SARA-analysis (%)

asphaltenes in oil, on the contrary, increased by 20.4%, which confirms the high probability of formation damage during a large number of cycles of CSS. At the same time, if we draw a parallel with viscosity characteristics, we can say that the viscosity of the oil under study is most sensitive to changes in the amount of resins in oil. The

inclusion of ammonium molybdate in the reaction model confirms the assumption that the molybdenum-based catalyst contributes to an increase in the yield of light components of oil: an increase in saturated hydrocarbons by 3%, aromatic - by 4.6%. The resin content remains virtually unchanged relative to the non-catalytic aquathermolysis reaction, but a significant decrease in asphaltenes by 15.9% is an additional stimulus for a downward shift in the viscosity curve as a result of more active destruction of C-S bonds. The mechanism of destruction of this bond has been described in detail by Varfolomeev et al. (17), it corresponds to the temperature range of aquathermolysis reactions and can be conditionally illustrated by the following reaction:

$$RCH_2CH_2SCH_3+2H_2O \rightarrow RCH_3+CO_2+H_2+H_2S+CH_4$$

The obtained values once again confirm that even small changes in the group composition of oil can significantly affect its rheological characteristics. Such a change in the group composition of oil fully correlates with the obtained viscosity characteristic of oil and allows us to conclude that ammonium molybdate is effective as a water-soluble precursor of the aquathermolysis catalyst.

To assess the reproducibility of the viscosity measurement and SARA-analysis results obtained at a certain effective precursor concentration of 3 wt.% of oil, two additional viscosity and SARA-analysis tests were performed to calculate standard deviations. The calculation results are presented in Table 2.

The obtained values confirm the reproducibility and reliability of the constructed viscosity characteristic and SARA-analysis.

Li et al. (41) have noted that aquathermolysis reactions contribute to a change in the structure of paraffins crystals. It was a dense structure in the form of a "snowflake" before aquathermolysis. After which their "needle-like" stacking is observed. Thus, it is possible to prove the decrease in the aggregation of paraffins crystals and an increase in the degree of their dispersion, and, consequently, their transformation into lighter fractions. This fact is confirmed by the decrease in paraffins in the studied oil from 3.5% to 3.32% (with non-catalytic aquathermolysis) and to 3.21% (with the use of a catalyst precursor). In this regard, it can be argued that the in-situ formed molybdenum-based aquathermolysis catalysts not only improve the rheological properties of oil, but also reduce the likelihood of paraffin deposits in the bottomhole formation zone and downhole equipment.

In this study, the autoclave was not connected to a gas chromatograph, so the gas composition was not determined. Varfolomeev et al. (17) described aquathermolysis reactions in detail, suggesting that the main share of gases is H_2S and CO_2. Therefore, when selecting downhole equipment, preference should be given to corrosion-resistant materials.

TABLE 2. Standard deviations

Standard deviations in viscosity					
Propertie	**Unit of measurment**	**Value**			
Temperature of measurment	°C	20	40	60	80
Standard deviation	mPa·s	0,328	0,534	0,487	0,405
Standard deviations in SARA-analysis					
Hydrocarbon groups	-	S	A	R	A
Standard deviation	d.f.	0,179	0,454	0,475	0,351

4. CONCLUSION

Ammonium molybdate can be used as a water-soluble precursor of an aquathermolysis catalyst for in-situ upgrading of super-viscous oil from the fields in the Timan-Pechora oil and gas province in Russia. The decrease in the viscosity of the original oil under laboratory conditions during catalytic aquathermolysis was 46.6%, which is 24% more than in the case of non-catalytic action. A numerical experiment for various viscosity characteristics made it possible to predict an increase in the flow rate in the case of catalytic aquathermolysis relative to non-catalytic by 23%.

The results of the SARA-analysis of super-viscous oil after non-catalytic and catalytic aquathermolysis correspond to the viscosity characteristics of the oil. The significant decrease in asphaltenes in the oil confirms the minimization of contamination of the bottomhole formation zone with high-molecular components of oil in the case of using an aquathermolysis catalyst. Reducing paraffins in oil can also potentially increase the time between overhauls (TBO) and, accordingly, reduce operating costs.

Thus, current research is the starting point for studying the effect of molybdenum-based aquathermolysis catalysts on the reaction mechanisms of

super-viscous oil aquathermolysis and defines the following tasks for future research:

- assessing the impact of molybdenum catalytic activity in the presence of a rock sample and the nature of catalyst deposition on this rock;
- assessing the effect of the deposited catalyst on the rock on the reservoir properties;
- assessing the degree of catalyst dispersion in oil after the experiment;
- assessing the nature of catalyst removal under conditions of high fracturing as part of filtration experiments;
- selecting the most effective hydrogen donor.

The obtained results can be used by interested parties and representatives of oil companies seeking to increase the technological potential of the CSS at high-viscosity and super-viscous oil fields.

5. REFERENCES

1. Belsky A, Starshaia V, Shklyarsky J. Enhanced Energy Efficiency of Oil Production Using Photovoltaic Installation. International Journal of Engineering, Transactions A: Basics. 2025;38(01):194-204. 10.5829/ije.2025.38.01a.18
2. Podoprigora D, Sabukevich V, Korobov G, Nguen V. Justification of developed system measures to increase productivity of wells in eastern part of pechora sea oil field. International Journal of Engineering, Transactions B: Applications. 2024;37(11):2303-13. 10.5829/ije.2024.37.11b.1
3. Korobov G, Vorontsov A, Buslaev G. Influence of Inhibitors Based on Surfactants on Processes of Hydrates and Asphalt-Resin-Paraffin Deposits Formation: Experimental Studies. International Journal of Engineering, Transactions A: Basics. 2025;38(10):2220-30. 10.5829/ije.2025.38.10a.02
4. Bosikov II, Klyuev RV, Mayer AV. Comprehensive assessment of hydraulic fracturing technology efficiency for well construction during hydrocarbon production. Записки Горного института. 2022;258:1006-13. 10.31897/PMI.2022.98
5. Drozdov NA. Filtration studies on cores and sand packed tubes from the Urengoy field for determining the efficiency of simultaneous water and gas injection on formation when extracting condensate from low-pressure reservoirs and oil from oil rims. Записки Горного института. 2022;257:783-94. 10.31897/PMI.2022.71
6. Nurgalieva KS, Saychenko LA, Riazi M. Improving the efficiency of oil and gas wells complicated by the formation of Asphalt–Resin–Paraffin deposits. Energies. 2021;14(20):6673. 10.3390/en14206673
7. Petrakov D, Loseva A, Jafarpour H, Penkov G. Experimental evaluation of effective chemical composition on reservoir quality of bottomhole zone of low permeability terrigenous reservoirs. International Journal of Engineering Transactions B: Applications. 2024;37(8):1547-55. 10.5829/ije.2024.37.08b.08
8. Tananykhin D, Struchkov I, Khormali A, Roschin P. Investigation of the influences of asphaltene deposition on oilfield development using reservoir simulation. Petroleum Exploration and Development. 2022;49(5):1138-49. 10.1016/S1876-3804(22)60338-0
9. Raupov I, Rogachev M, Sytnik J. Overview of Modern Methods and Technologies for the Well Production of High-and Extra-High-Viscous Oil. Energies. 2025;18(6):1498. 10.3390/en18061498
10. Malarev V, Kopteva A, Koptev V, Gotsul Y. Improvement of efficiency of steam-thermal treatment of high-viscous oil formations using downhole electric steam generators. Journal of Ecological Engineering. 2021;22(2):17-24. 10.12911/22998993/130630
11. Yang S, Huang S, Jiang Q, Jiang G, Zhou X, Yu C. An innovative in situ solvent generation enhanced SAGD technique: Mechanism analysis based on numerical simulation. Fuel. 2024;364:131020. 10.1016/j.fuel.2024.131020
12. Durkin S, Morozyuk O, Kalinin S, Ruzin L, Menshikova I. Substantiation of the optimal strategies of steam injection for enhanced oil recovery at the Yaregskoye field based on physical and mathematical modeling (Russian). Oil Industry Journal. 2018;2018(01):58-61. 10.24887/0028-2448-2018-1-58-61
13. Kondrasheva NK RV, Nazarenko MY, Gabdulkhakov RR. . Influence of parameters of delayed asphalt coking process on yield and quality of liquid and solid-phase products. Journal of Mining Institute. 2020;241(1):97-104. 10.31897/pmi.2020.1.97
14. Aliev FA, Mukhamatdinov II, Sitnov SA, Ziganshina MR, Onishchenko YV, Sharifullin AV, et al. In-situ heavy oil aquathermolysis in the presence of nanodispersed catalysts based on transition metals. Processes. 2021;9(1):127. 10.3390/pr9010127
15. Alieva F, Vakhina A, Mirzaeva O, Dengaevb A, Safiullinac E, Efremenko D, et al. Utilizing an Oil-soluble Iron and Sodium-based Catalyst for Catalytic Hydrogenation of Carbon Dioxide in Heavy Oil. International Journal of Engineering, Transactions B: Applications. 2025;38(2):321-29. 10.5829/ije.2025.38.02b.06
16. Vakhin A, Mukhamatdinov I, Sitnov S, Mukhamatdinova R, Simakov I, Nikitina E, et al. Catalytic activity of nickel and iron sulfides in the degradation of resins and asphaltenes of high-viscosity oil in the presence of carbonate rock under hydrothermal conditions. Kinetics and Catalysis. 2022;63(5):569-76. 10.31857/S0453881122050148
17. Varfolomeev MA, Yuan C, Ancheyta J. Catalytic In-Situ Upgrading of Heavy and Extra-Heavy Crude Oils: John Wiley & Sons; 2023.
18. Panariti N, Del Bianco A, Del Piero G, Marchionna M. Petroleum residue upgrading with dispersed catalysts: Part 1. Catalysts activity and selectivity. Applied Catalysis A: General. 2000;204(2):203-13. 10.1016/S0926-860X(00)00531-7
19. Al-Mishaal OF, Suwaid MA, Al-Muntaser AA, Khelkhal MA, Varfolomeev MA, Djimasbe R, et al. Octahedral cluster complex of molybdenum as oil-soluble catalyst for improving in situ upgrading of heavy crude oil: Synthesis and application. Catalysts. 2022;12(10):1125. 10.3390/catal12101125
20. Razavian M, Fatemi S. Catalytic evaluation of metal azolate framework-6 in pristine and metal doped modes in upgrading heavy residual fuel oil. Journal of Analytical and Applied Pyrolysis. 2021;156:105093. 10.1016/j.jaap.2021.105093
21. Felix G, Tirado A, Varfolomeev MA, Al-muntaser A, Suwaid M, Yuan C, et al. Chemical and structural changes of resins during the catalytic and non-catalytic aquathermolysis of heavy crude oils. Geoenergy Science and Engineering. 2023;230:212242. 10.1016/j.geoen.2023.212242
22. Deng Q LY, Chen G, Yan J, Zhang J, Meng M, Qu C, Jeje A. Water-soluble metal complexes as catalysts for low-temperature aquathermolysis of heavy oil in the presence of methanol. Neftekhimia. 2018;58(4):522-6. 10.1134/S0028242118040238
23. Zhou Z, Li X, Gao K, Nan J, Xiao H, Lu Y, et al. A review on the reaction mechanism of heavy oil catalytic aquathermolysis: Carbocationic reactions or free radical reactions? Journal of Analytical and Applied Pyrolysis. 2025;186:106923. 10.1016/j.jaap.2024.106923

24. Wu C, Lei G, Yao C, Jia X, editors. In situ upgrading extra-heavy oil by catalytic aquathermolysis treatment using a new catalyst based anamphiphilic molybdenum chelate. SPE International Oil and Gas Conference and Exhibition in China; 2010: SPE. 10.2118/130333-MS
25. Chuan W, Guang-Lun L, Chuan-Jin Y, Ke-Ji S, Yan-bin C. Mechanism for reducing the viscosity of extra-heavy oil by aquathermolysis with an amphiphilic catalyst. Journal of Fuel Chemistry and Technology. 2010;38(6):684-90. 10.1016/S1872-5813(11)60004-2
26. Tumanyan BP PN, Kayukova GP, Nurgaliev DK, Foss LE, Romanov GV. . Aquathermolysis of crude oils and natural bitumen: chemistry, catalysts and prospects for industrial implementation. Russian Chemical Reviews. 2015;84(11):1145. 10.1070/RCR4500
27. Zhao F, Liu Y, Lu N, Xu T, Zhu G, Wang K. A review on upgrading and viscosity reduction of heavy oil and bitumen by underground catalytic cracking. Energy Reports. 2021;7:4249-72. https://doi.org/10.1016/j.egyr.2021.06.094
28. Liu R-Q, Zhang L-Q, Pan H-D, Wang Y-Y, Li J-Y, Wang X-W, et al. Study on the in situ desulfurization and viscosity reduction of heavy oil over MoO3–ZrO2/HZSM-5 catalyst. Petroleum Science. 2023;20(6):3887-96. 10.1016/j.petsci.2023.08.005
29. Tajik S, Shahrabadi A, Rashidi A. Silica-graphene nanohybrid supported MoS2 nanocatalyst for hydrogenation reaction and upgrading heavy oil. Journal of Petroleum Science and Engineering. 2019;177:822-8. 10.1016/j.petrol.2019.02.085
30. Cai Z, Ding Y, Zhang J, Yu P, Ma Y, Cao Y, et al. In situ generation of dispersed MoS2 catalysts from oil-soluble Mo-based ionic liquids for highly effective biolipids hydrodeoxygenation. Journal of Catalysis. 2023;423:50-61. 10.1016/j.jcat.2023.04.022
31. Qu X, Zhou G, Lu Y, Li S, Zhang L, Wang J, et al. Catalytic aquathermolysis of Mackay River bitumen with different types of Mo-based catalysts. Fuel. 2022;326:125134. 10.1016/j.fuel.2022.125134
32. Wang J, Tang X, Li J, Guo E, Guan W, Jiang Y. Quartz sand proppant loaded with Ni and Mo for in-situ aquathermolysis of heavy oil. Fuel. 2021;306:121653. 10.1016/j.fuel.2021.121653
33. Khoshooei MA, Vitale G, Carbognani L, Scott CE, Pereira-Almao P. Molybdenum carbide nanocatalyst for activation of water and hydrogen towards upgrading of low-quality hydrocarbons. Fuel. 2022;322:124291. 10.1016/j.fuel.2022.124291
34. Wang J, Gao K, Zhong Y, Nan J, Li X, Zhao H, et al. In-situ formation of molybdenum disulfide nanoparticle and its catalytic performance in heavy oil long-term aquathermolysis. Colloids and Surfaces A: Physicochemical and Engineering Aspects. 2025;707:135861. 10.1016/j.colsurfa.2024.135861
35. Wang Y, Lin R, Zhang L, Han X, Li J, Huang C, et al. ZrO2-MoO3/modified lotus stem biochar catalysts for catalytic aquathermolysis of heavy oil at low-temperature. Fuel. 2024;357:129597. 10.1016/j.fuel.2023.129597
36. Kiekbaev A VA. Aquathermolysis of high-viscosity oil of the Yaregsky field in the presence of components of rock-forming minerals. Oil & Gas Chemistry. 2021;1-2:37-42. 10.24412/2310-8266-2021-1-2-37-42
37. Alonso JPP, Djimasbe R, Zairov R, Yuan C, Al-Muntaser AA, Stepanov A, et al. Use of nickel oxide catalysts (bunsenites) for in-situ hydrothermal upgrading process of heavy oil. Nanomaterials. 2023;13(8):1351. https://doi.org/10.3390/nano13081351
38. Katnov VE, Trubitsina SA, Kayumov AA, Aliev FA, Nazimov NA, Dengaev AV, et al. Influence of sodium metal nanoparticles on the efficiency of heavy oil aquathermolysis. Catalysts. 2023;13(3):609. 10.3390/catal13030609
39. Baygildin E SS, Vakhin A, Sharifullin A, Amerkhanov M, Garifullina E. . Aquathermolysis of heavy oil in the presence of bimetallic catalyst that form in-situ from the mixture of oil-soluble iron and cobalt precursors. Georesources. 2019;21(3):62-7. 10.18599/grs.2019.3.62-67
40. Kadieva MK, Khadzhiev S, Kadiev KM, Gyul'Maliev A, Yakovenko T. The formation of nanosized molybdenum oxide particles in a hydrocarbon medium. Petroleum Chemistry. 2011;51(1):16-23. 10.1134/S0965544111010051
41. Li Y, Zhang S, Wang Y, Qi G, Yu T, Xin X, et al. Oil-soluble exogenous catalysts and reservoir minerals synergistically catalyze the aquathermolysis of heavy oil. Molecules. 2023;28(19):6766. https://doi.org/10.3390/molecules28196766

COPYRIGHTS

©2026 The author(s). This is an open access article distributed under the terms of the Creative Commons Attribution (CC BY 4.0), which permits unrestricted use, distribution, and reproduction in any medium, as long as the original authors and source are cited. No permission is required from the authors or the publishers.

Persian Abstract

چکیده

روند رو به رشد جهانی توسعه میادین نفتی سنگین، کاری پیچیده است که نیاز به به‌روزرسانی رویکردهای پیشین غیرسودآور دارد. یکی از این حوزه‌ها، تحریک چرخه‌ای چاه‌ها با بخار برای تحریک تولید نفت‌های با ویسکوزیته بالا و فوق ویسکوزیته است. افزایش نرخ جریان چاه و تخلیه ذخایر، کاهش زمان و هزینه‌های مالی سرویس چاه و تعمیرات اساسی را می‌توان با ترکیب روش‌های حرارتی و شیمیایی تحریک جریان ورودی به دست آورد. این رویکرد خود را در ارتقای کاتالیزوری نفت درجا با موفقیت ثابت کرده است. در چارچوب این مقاله، مجموعه‌ای از آزمایش‌های آزمایشگاهی برای تأیید اثربخشی مولیبدات آمونیوم به عنوان پیش‌ساز محلول در آب یک کاتالیزور آکواترمولیز برای ارتقای نفت فوق ویسکوزیته از یکی از میادین استان نفت و گاز تیمان–پچورا انجام شد. کاهش ویسکوزیته نفت نسبت به اثر غیرکاتالیستی ۲٤٪ بود که با نتایج آنالیز SARA نفت نیز تأیید شد: کاهش مقدار آسفالتین‌ها به میزان ۱۵.۹٪، افزایش مقدار هیدروکربن‌های اشباع و آروماتیک به ترتیب ۳٪ و ٤.٦٪. بر اساس یک مدل عددی ساده، افزایش ۲۳٪ در سرعت جریان نفت با اثر کاتالیزوری نسبت به اثر غیرکاتالیستی پیش‌بینی شد. نتایج به‌دست‌آمده نشان‌دهنده پتانسیل استفاده از این پیش‌ساز کاتالیزور در شرایط میدانی است.

IJE TRANSACTIONS B: Applications Vol. 39, No. 08, (August 2026) 1829-1842

International Journal of Engineering

Journal Homepage: www.ije.ir

Behavior of a Next-Generation Nickel Super Alloy Turbine Component under Direct Exposure to Gas Heat from Combustion in a Long-term Operation

A. Faraji[a], M. R. Rahimipour*[a], M. Farvizi[b], H. Omidvar[c]

[a] *Ceramic Division, Materials and Energy Research Center, Karaj, Iran*
[b] *Department of Materials Engineering, Faculty of Mechanical Engineering, University of Tabriz, Tabriz, Iran*
[c] *Department of Mining and Metallurgical Engineering, Amirkabir University of Technology (Tehran Polytechnic), Tehran, Iran*

PAPER INFO

Paper history:
Received 02 August 2025
Received in revised form 20 September 2025
Accepted 28 September 2025

Keywords:
Nickel Superalloy
Carbides and γ′ - Phase Metallographic Evaluation
MAUD
XRD
Creep Resistance

ABSTRACT

In this research, the microstructural evolution and creep behavior of a second-stage vane from a gas turbine after 1200 long-term cycles were evaluated through microstructural examinations and creep tests. Microscopic analyses revealed an increase in the volume fraction and size of secondary phases such as gamma prime and carbides. These microstructural changes led to the embrittlement of the investigated nickel superalloy. Hardness testing results indicated an increase in hardness from 420 Vickers to 480 Vickers for the service-exposed vane after direct exposure to gas heat. Thermal analysis showed a 60°C decrease in the complete dissolution temperature, suggesting a need for repair or rejuvenation of the alloy. The growth of gamma prime precipitates through the shearing of dislocations and the coarsening of carbides due to the inhibition of grain boundary sliding resulted in an 11-hour reduction in creep life. The reference sample failed at a stress of 247 MPa and a temperature of 900°C after 40 hours with a strain of 9%. In contrast, the service-exposed vane exhibited a reduction in creep life and creep strain to 29 hours and 4%, respectively.

doi: *10.5829/ije.2026.39.08b.05*

Graphical Abstract

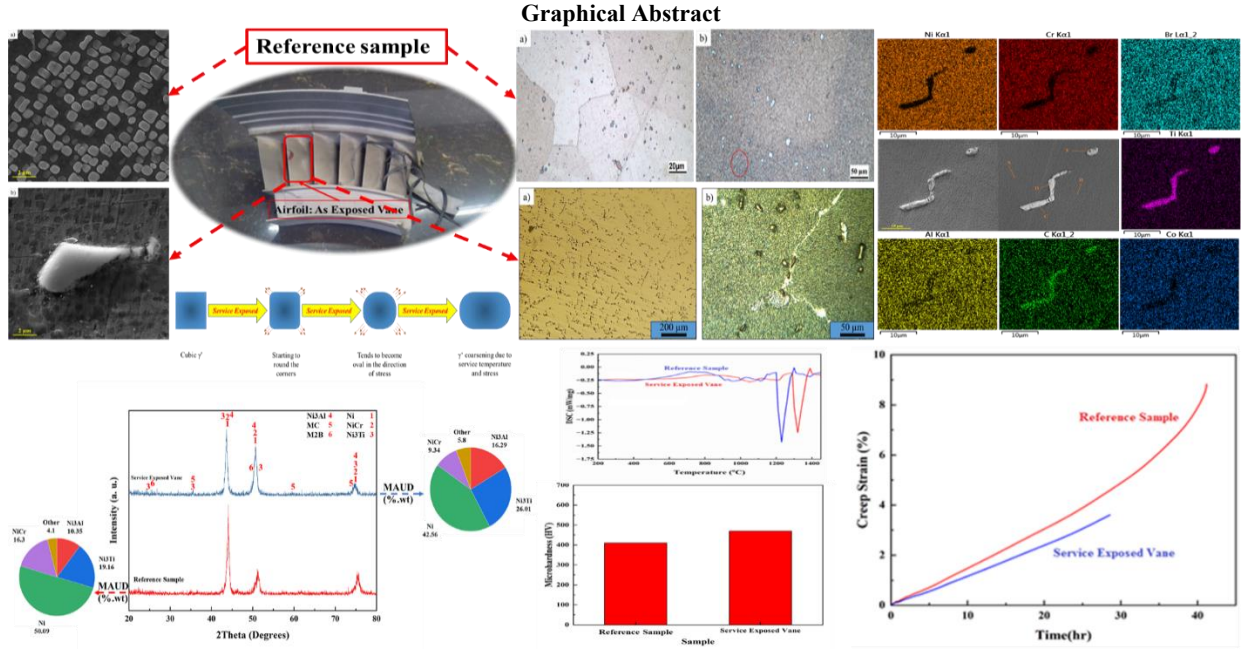

*Corresponding Author Email: m.rahimipour@merc.ac.ir (M. R. Rahimipour)

Please cite this article as: Faraji A, Rahimipour MR, Farvizi M, Omidvar H. Behavior of a Next-Generation Nickel Super Alloy Turbine Component under Direct Exposure to Gas Heat from Combustion in a Long-term Operation. International Journal of Engineering, Transactions B: Applications. 2026;39(08):1829-42.

1. INTRODUCTION

Nickel-based superalloys have found indispensable applications, particularly in aerospace and high-temperature environments such as turbine blades (1). The continuous pursuit of higher operating temperatures and improved performance in gas turbines has driven the development of these advanced materials. However, the service life of these alloys is significantly compromized by various factors including creep, fatigue, erosion, hot corrosion, and oxidation. These degradation mechanisms often interact synergistically, accelerating the deterioration process (2-5). Furthermore, microstructural evolution induced by severe service conditions such as high temperature and stress plays a crucial role in the degradation of these components (6). Next-generation nickel-based superalloys are widely used in the manufacturing of turbine blades and vanes (7-9). Their exceptional high-temperature properties make them suitable for challenging applications in the hot section components of turbines (8). However, prolonged exposure to harsh operational conditions can lead to the degradation of mechanical properties. To mitigate these challenges, ongoing research is focused on developing advanced superalloys such as the oxidation-resistant TMS-238 with improved performance characteristics (10). Previous research has extensively investigated the behavior of nickel superalloys. Tyagunov et al. (11) observed the formation of carbides and brittle phases in ZhS6U superalloy during prolonged exposure to high temperatures. Furthermore, studies by Tewari et al. (12) examined the impact of alloying modifications in ZhS6K superalloy, indicating that B/C modifications can enhance yield strength while potentially reducing ductility and tensile fracture properties. These previous investigations on ZhS6U and ZhS6K superalloys, which are pertinent to the broader family of nickel-based superalloys, provide a foundational understanding for evaluating the behavior of a next-generation nickel superalloy turbine component under direct exposure to gas heat from combustion in long-term operation, as explored in the present study. Addition of boron can significantly alter the microstructure and mechanical properties of the investigated nickel superalloy. The microstructure of nickel-based superalloys plays a crucial role in determining their mechanical behavior. In solid-solution alloys, larger crystal grain sizes can lead to abnormal grain growth, resulting in reduced strength and fatigue resistance (5, 13). Moreover, grain boundary diffusion facilitates the diffusion of chromium (Cr) and carbon (C), depleting the matrix and compromising the formation of protective oxide layers (14-19). Such phenomena has increased susceptibility to hot corrosion, oxidation, and intergranular fracture significantly impacts alloy performance. In precipitation-hardened alloys, such as ZhS-family superalloys, the microstructural variations during working conditions become more complex. The size, distribution, and morphology of precipitates, such as gamma prime (γ'), significantly influence creep resistance. Coarsening of γ' precipitates weakens the alloy by facilitating dislocation motion and leading to reduced creep resistance (2, 6, 20-26). The formation of other detrimental phases, such as delta, sigma, and mu, can create lattice mismatches and initiate and accelerate crack propagation (16, 27). Additionally, the formation of chromium-stabilized secondary carbides at grain boundaries can deplete the matrix and promote γ' precipitate growth, which can lead to the formation of creep voids and accelerated microstructural degradation. The microstructural features of Ni-based superalloys, including the solid solution (γ phase), primary carbides (MC type), and intermetallic precipitates ($Ni_3(Al, Ti) - \gamma'$), significantly influence their mechanical properties (9). Larger precipitates and carbides can lead to reduced creep rupture life and increased fatigue crack initiation (9). While the presence of the γ' phase generally improves mechanical properties, its impact can vary depending on the alloy composition and specific microstructure. For instance, in a specific single-crystal nickel-based superalloy, the presence of the γ' phase had no significant impact on mechanical properties (28). Furthermore, undesirable microstructural features, such as segregation of alloying elements, can significantly compromise the desired properties. For instance, in Ni-Cr-Al-Ti alloys processed by laser powder bed fusion, segregation of solute elements to grain boundaries during processing can significantly affect consolidation behavior (29, 30).

Turbine blades and vanes are critical components in gas turbines. The microstructure of nickel-based superalloys plays a crucial role in determining their mechanical behavior. High-performance turbine components are typically manufactured from precipitation-strengthened nickel-based superalloys, which derive their exceptional high-temperature strength and creep resistance primarily from the controlled precipitation of ordered intermetallic phases, notably the γ' phase.

The relatively constant high-temperature environment prevailing in certain critical stages of a gas turbine, such as those exposed to sustained elevated temperatures, can accelerate microstructural changes in the vanes, leading to embrittlement and reduced resistance to impact, wear, and fatigue. This degradation can ultimately result in creep and premature failure of these critical components. It is significant to delve deeper into the changes that occur after long-term operations of expensive and critical parts in a gas turbine. Given the practicality of advanced single-crystal nickel-based superalloys, such as CMSX-4, it is very important to investigate their behavior quantitatively and qualitatively due to direct exposure to combustion chamber exhaust

gas. CMSX-4, as a prominent example of next-generation superalloys, is characterized by its high refractory element content and precise gamma prime phase morphology, which contribute to its superior high-temperature strength and creep resistance.

While the degradation behavior of nickel-based superalloys has been extensively investigated in the literature, the majority of these studies have primarily focused on laboratory-scale, accelerated aging tests conducted on pristine materials. Such controlled experiments are valuable for understanding basic material behavior, they often fail to replicate the complex and synergistic effects of real-world service environments, which involve long-term thermal cycles, varying mechanical loads, and direct exposure to high-temperature combustion gases. As a result, these studies may not fully capture the material degradation that occurs under the actual operating conditions encountered in service environments.

The innovation of our study lies in its focus on a real-world turbine vane made from a next-generation nickel superalloy (CMSX-4), which has undergone 1200 hours of long-term service in an operational gas turbine. This allows us to provide a unique and authentic dataset on the degradation mechanisms that occur under true operational conditions. Specifically, our research offers a novel contribution in the following ways:

1. **Investigation of a Realistic Degradation Profile:** Unlike prior studies that typically focus on simplified laboratory conditions, our research analyzes the response of a full-scale turbine component to the complex combination of thermal cycling, mechanical stresses, and direct exposure to combustion gases. We have identified distinct degradation patterns between the hot-gas-exposed region and the trailing edge, which has been subjected to significantly different thermal histories. This nuanced degradation profile, which is directly relevant to service environments, is rarely captured in laboratory-based studies.
2. **Multi-Scale Characterization and Cause-and-Effect Relationship:** Our study employs a comprehensive suite of advanced characterization techniques, including optical microscopy (OM), field-emission scanning electron microscopy (FESEM/EDS), X-ray diffraction (XRD/Rietveld analysis), differential scanning calorimetry (DSC), hardness testing, and creep testing. Through this multi-technique approach, we have established a direct cause-and-effect relationship between the observed microstructural evolution (e.g., γ' phase dissolution and carbide coarsening) and the corresponding changes in mechanical properties, including creep resistance. This level of multi-scale analysis provides a more detailed and confident understanding of the degradation mechanisms, surpassing the scope of previous studies that often relied on fewer or less comprehensive methods.
3. **Real-World Implications for Turbine Component Longevity:** By studying a turbine component subjected to real-world operational conditions, our work bridges the gap between fundamental materials science and practical engineering applications. We provide crucial insights into the material's performance under service conditions, which is essential for predicting the longevity and reliability of turbine components. This research not only advances our understanding of the material degradation processes but also contributes valuable data to the development of more reliable turbine components and better maintenance strategies.

2. EXPERIMENTAL

This study investigated a turbine vane that had undergone approximately 1200 operational cycles during its service life. Each cycle simulated real-world gas turbine conditions involving thermal and mechanical loading. During each cycle, the turbine vane was heated to a peak temperature of approximately 1000 °C. The vane was held at this peak temperature for around 1200 hours, corresponding to the steady-state operation phase of the engine. Following this hold period, the component experienced a controlled cooling stage with a gradual temperature decrease during flight. The cooling was completed by a rapid quench during engine shutdown, which contributed to thermal gradients within the material. In addition to thermal cycling, the turbine vane was subjected to significant mechanical stresses throughout its operation. These stresses originated from centripetal forces due to high-speed rotation and from gas pressure loads within the turbine. The simultaneous exposure to elevated temperature and mechanical loading imposed complex thermo-mechanical conditions on the component, which are fundamentally different from those encountered in typical laboratory tests. The cumulative effect of these thermal and mechanical cycles led to microstructural changes in the turbine vane, including γ′ phase dissolution and carbide morphology evolution. These phenomena were investigated to understand the long-term degradation behavior under realistic service conditions. Figure 1 shows an image of the turbine vane before service exposure (reference sample) and after exposure to service. As observed in Figure 1, a significant portion of the initial coating on these vanes has degraded during service operation. In the initial phase of this study, the chemical composition of the turbine vane and the reference sample was analyzed using optical emission spectroscopy. This analysis

revealed that the turbine vane was fabricated from a nickel-based superalloy known as a next-generation nickel superalloy. Table 1 presents the weight percentage of the selected components.

Phase analysis of the investigated nickel superalloy was conducted using a Siemens D-500 X-ray diffractometer. The XRD analysis employed Cu Kα radiation with a voltage of 20 kV, a wavelength of λ=0.154 nm, and a current of 30 mA. For microstructural characterization, samples were cut from the service-exposed turbine vane and the reference sample. Microstructural studies were carried out using an Olympus optical microscope and a TESCAN MIRA3 field emission scanning electron microscope (FESEM) equipped with an energy-dispersive X-ray spectroscopy (EDS) system, both manufactured by Czech Republic.

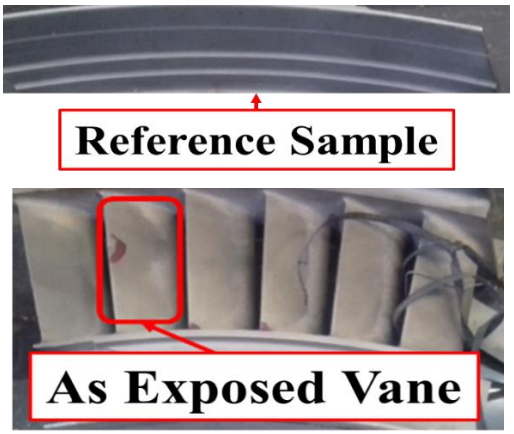

Figure 1. Reference sample and service-exposed turbine vane

TABLE 1. Chemical composition of both the reference sample and service-exposed vane was determined in terms of weight percentage

Elements	Ni	C	Cr	Co	Mo	Al	Ti	Si	Fe	Re	Ta	B	W	Hf
Reference Sample	Base	0.07	6.80	9.40	0.75	5.29	1.52	0.03	0.11	2.91	6.66	0.01	6.70	0.11
Service Exposed Vane	Base	0.06	6.35	8.91	0.60	5.25	1.16	0.01	0.17	2.92	6.55	0.01	6.65	0.95

Prior to analysis, samples were meticulously polished with sandpaper up to 3500 grit and then subjected to microetching on the damaged sample according to the ASTM E404-2015 standard, and electropolishing for the undamaged sample. The etching solution consisted of 170 ml phosphoric acid, 10 ml sulfuric acid, and 16 g CrO_3. Samples were electropolished in this solution at 5 volts for 5-7 seconds (20, 31, 32). Hardness measurements were conducted using the Vickers method, with an average of five indentations recorded for each sample. Rietveld refinement analysis was employed to accurately calculate the weight percentage and determine the crystallographic information of the present phases. This analysis was performed using the MAUD software. The quality of the Rietveld refinement was evaluated based on the "sigma" and "R" factors. Throughout the Rietveld analysis in this study, the sigma and R values were consistently below 2 and 10, respectively, indicating the reliability of the quantitative analysis. Additionally, all peaks were effectively covered by the CIF cards of different phases. In summary, the combination of XRD, SEM, EDS, and Rietveld refinement analyses provided comprehensive insights into the phase composition and structural features of the sample. To determine the temperature at which liquid formation occurs, the initial melting temperature of the phases was investigated using differential scanning calorimetry (DSC) with a Netzsch STA449 F3 Jupiter device in an argon environment. The sample was heated at a rate of 20 °C/min up to 1500 °C. The sub-size creep tests were conducted using a SANTAM STM-20M2 creep testing machine under constant uniaxial tensile stress conditions. The test temperature was maintained at 900°C, and a constant stress of 247 MPa was applied throughout the experiments. These conditions were carefully selected to simulate the high-temperature mechanical environment typically experienced by turbine vanes during service. The creep specimens were extracted from both the service-exposed turbine vane and the reference material, and all samples were prepared using consistent machining and surface finishing procedures to ensure the reliability of the comparison. The specimens were designed and machined in accordance with the specifications for sub-size specimens as per ASTM E139 standard, with a gauge length of 25 mm and a gauge diameter of 5 mm.

3. RESULTS AND DISCUSSION

Figure 2 presents OM images of the microstructure in the referenve sample of the vane, which was subjected to lower temperatures and was not in direct contact with heat. In the microstructural examination of turbine components such as blades and vanes, regions such as the root and areas experiencing lower stress and temperature-like the bolt region in vanes- are commonly considered as reference points, representing microstructures similar to new, unexposed component (31). Figure 2(a) shows the metallographic image of that region after polishing without any etching. Blocky precipitates with morphologies consistent with MC carbides are clearly

observed on grain boundaries and within grains. Although optical microscopy primarily reveals morphological features, the blocky shape and distribution of these precipitates, combined with the known phase formation tendencies of nickel-based superalloys- where MC carbides are typically the first to from- strongly support their indentification as MC carbides. MC carbides are the primary solidification phase in such alloys and, due to hydrostatic tension from the surrounding melt during solidification, they exhibit diverse morphologies (20, 31). Similar observations of MC carbides morphology and distribution have been reported in previous studies, supporting our interpretation (20). Another prominent feature in this image is the grain boundaries that have not coarsened, where fine precipitates consistent with secondary $M_{23}C_6$ carbides appear discontinuously. optical microscopy reveals their morphology and distribution patterns, and their finer size and discontinuous presence on grain boundaries, along with the established metallurgy of nickel-based superalloys under prolonged elevated temperatures, strongly indicate their identity as $M_{23}C_6$ carbides. This observation aligns with previous findings indicating that such secondary carbides contribute to the material's high-temperature strength and reflect an absence of severe thermal exposure or microstructural degradation that could jeopardize the component's integrity (20). In Figure 2(b), besides the primary MC carbides, dense regions rich in γ' precipitates are visible. Given their fine size and high density, it can be inferred that this microstructural zone was not subjected to high-temperature fields capable of causing significant microstructural evolution. Figure 2(b) also highlights regions marked with a red circle containing dense, uncoarsened minute features (or fine, unresolved precipitates). Due to the resolution limits of optical microscopy, these appear as high-density areas; however, their precise morphology and phase cannot be conclusively identified at this magnification.

Figure 3a shows an unetched OM image of the service-exposed turbine vane region in the damaged area. This image reveals no voids or creep cavities, nor any cracks resulting from structural changes. However, a notable feature in Figure 3a is the increased volume fraction of carbides. Unlike gamma prime, which typically undergoes coarsening and/or dissolution during high-temperature service, the observed increase in the secondary $M_{23}C_6$ carbide volume fraction is attributed to thermal exposure promoting their precipitation, consumption of matrix elements for their formation, or perhaps slight carburization, if applicable. This change in carbide distribution and quantity can significantly influence grain boundary integrity or overall mechanical properties. Figure 3a clearly illustrates an increased volume fraction of secondary $M_{23}C_6$ carbides. This observation is made by direct comparison with the microstructure of the reference sample (Figure 2a), which represents the as-received state or less thermally affected region of the material. The elevated temperature exposure during service has evidently promoted further precipitation of these carbides. Carbides are coalescing along interdendritic regions and approaching each other. Typically, the volume fraction of secondary carbides increases due to long-term aging or service conditions. Under these conditions, with high temperature and applied stresses, diffusion finds favorable conditions. Under these circumstances. MC carbides, which are the primary source of carbon in the structure, begin to dissolve according to reaction 1 and form $M_{23}C_6$ carbides, stabilizing them. In this case, microstructural observations (Figures 2a and 3a) suggest a transformation process where chromium, molybdenum, and tungsten may react with carbon to form complex chromium-based carbides. This is consistent with the widely reported reaction in the literature for such alloys (20, 31):

$$MC + \gamma = M_{23}C_6 + (MC)_{Transformed} \quad (1)$$

In fact, by consuming carbon and γ, the volume fraction of secondary precipitate phases will increase. With the decomposition of the primary MC carbide, titanium and niobium present in the structure are released (32). The released carbon combines with chromium to form complex $M_{23}C_6$ carbides. With the depletion of chromium from the γ matrix, γ becomes unstable, and conditions are created for nickel to participate in the formation of γ'. (32). The titanium released from MC reacts with nickel in the matrix to form Ni3Ti (32). As this process continues, if Al is released from the γ matrix, a complex γ' phase is formed. Otherwise, the formation of a blocky η phase is possible. The overall description of this issue can be summarized in reaction 2 (31).

$$MC + \gamma = M_{23}C_6 + \gamma' \quad (2)$$

The coarsening of carbides and their coalescence to form a carbide film, along with the growth of γ' precipitates, can be seen in Figure 3b. Along the grain boundaries of the carbides, a eutectic carbide structure is evident. The presence of hafnium and tungsten usually stabilizes eutectic structures, which limit and reduce the dissolution temperature (33). Since eutectic phases are the last phases

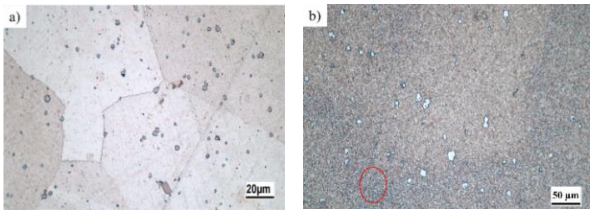

Figure 2. OM images of the low-damage region of the vane in this study: (a) high magnification; and (b) low magnification

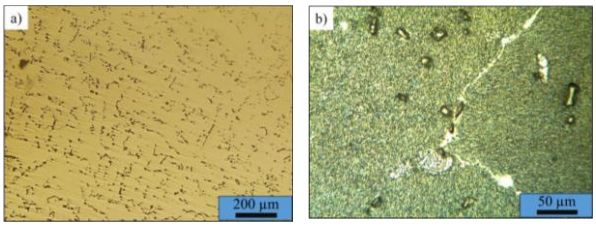

Figure 3. OM images of the high-damage region of the vane in this study: (a) low magnification; and (b) high magnification

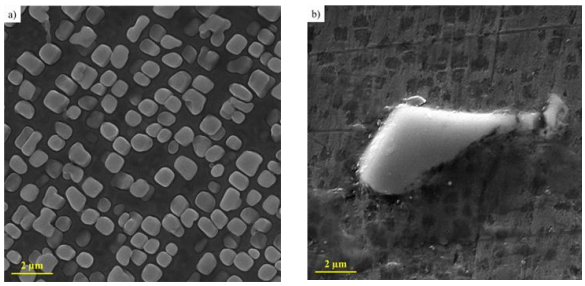

Figure 4. FESEM images of the Next- Generation Nickel Superalloy microstructure: (a) reference sample, and (b) service exposed vane

to form during solidification, they are the first to dissolve and, due to their presence, the dissolution temperature cannot be significantly increased as it would lead to local melting and structural damage (34, 35).

Figure 4 presents FESEM images of the investigated nickel-based superalloy in both the reference sample and service-exposed conditions, providing insight into the microstructural evolution under operational stresses. In Figure 4(a), the image of the reference sample after electropolishing is shown. Electropolishing enhances the surface morphology by selectively removing material and revealing precipitate shapes more clearly, allowing the observation of cubic γ' precipitates characteristic of a virgin microstructure. These cubic γ' precipitates are well-known as the primary strengthening phase in nickel-based superalloys and their morphology, size, and distribution critically influence the mechanical properties, especially at elevated temperatures (34, 36). The clear visualization of these cubic γ' precipitates in the FESEM image confirms the successful preservation of the initial heat-treated microstructure in the reference sample. Figure 4(b) presents the FESEM image of the nickel superalloy after 1200 service cycles, taken from the mid-span region of the 2nd stage vane. This image was intentionally obtained without electropolishing in order to capture the surface morphology and real operational microstructural state, including possible surface degradation, oxidation, or precipitate evolution under service conditions. Such an approach allows the investigation of γ' precipitate coarsening, morphological changes, and potential formation of secondary phases in a state representative of actual turbine service (35). It is important to note that surface etching was performed in separate samples to quantitatively assess the volume fraction of γ' precipitates, as etching enhances contrast between the matrix and precipitates. Typically, in the micrographs of the reference sample, a bimodal distribution of γ' precipitates is observed: primary cubic γ' precipitates, which tend to coarsen and slightly change morphology after aging, and secondary, nano-sized spherical γ' precipitates formed during prolonged aging. The primary precipitates are clearly visible even at moderate magnifications in FESEM images (34, 36), while the secondary precipitates, due to their nanoscale dimensions, are discernible only at higher magnifications or using advanced characterization techniques such as FESEM. This bimodal γ' microstructure is essential for balancing strength and creep resistance in service conditions. In contrast, the investigated superalloy in this study exhibits a predominantly mono-phase and uniform γ' precipitate structure in the reference condition, which might reflect specific heat treatment parameters or alloy composition aimed at optimizing service performance. Such a uniform γ' distribution can also influence the hardness and creep properties, as finer and more uniform precipitates generally improve high-temperature mechanical behavior (34, 36).

Table 2 presents the statistical results of the structural analysis of γ' precipitates. As can be seen, the volume fraction of γ' precipitates has increased by 5 %, and their average size has increased by approximately 230 nm after service. The small change in volume fraction and the 40 % increase in precipitate size indicate that the component was subjected to high temperature and low stress fields. This is consistent with the fact that the reference sample is a vane and operates stationarily in the turbine, so it is naturally subjected to low stress, and the damage caused by high temperature is more significant. . Another point that can be inferred is that, despite the observed changes in the ´γ precipitate content and size, the alloy maintained structural integrity under these service conditions for 1200 cycles, suggesting a degree of physical stability within the operational limits, even with microstructural evolution.

Figure 5 presents FESEM images of the MC carbide-containing region in the Service-exposed vane after operational use, captured in both backscattered electron

TABLE 2. Statistical results of the analysis of γ' precipitate characteristics in reference and service exposed vane

Sample Condition	Volume Fraction of ´γ (%)	Average size of ´γ(nm)
Reference sample	43.72	530 ± 15
Service Exposed Vane	48.86	763 ± 15

(BSE) mode (right) and secondary electron (SE) mode (left), accompanied by the elemental distribution map of the same area. These imaging techniques provide complementary insights, with BSE highlighting compositional contrasts and SE revealing surface morphology, thereby enabling a comprehensive microstructural characterization of the carbide phases and their surroundings. Although precise nanoscale modifications and subtle morphological deviations of the γ' precipitates (approximately 0.7 µm in size) remain challenging to resolve fully at this magnification scale (10 µm scale bar), a qualitative trend of γ' coarsening is evident. Notably, there is a discernible morphological transition from the initial well-defined cubic shape toward a more spheroidal form. This observation aligns with prior studies documenting γ' phase coarsening as a common microstructural evolution under prolonged high-temperature service conditions, which significantly influences mechanical properties such as creep resistance (37). The elemental distribution map further reveals significant enrichment of Ti and C within the carbide-rich regions, confirming the presence and remarkable stability of TiC carbides after 1200 service cycles. This finding corroborates earlier reports indicating that TiC carbides exhibit strong thermal stability, which plays a critical role in maintaining microstructural integrity during high-temperature exposure (37, 38). The formation and growth of $M_{23}C_6$ carbides in this nickel-based superalloy are typically linked to the partial decomposition of primary MC carbides. During service, constituent elements initially stabilizing MC carbides—often Nb and Ta rather than Ti—are released into the matrix upon decomposition, providing the requisite elements for the nucleation and subsequent growth of $M_{23}C_6$ carbides. Existing literature suggests two primary transformation pathways: direct conversion of MC carbides to $M_{23}C_6$ or a two-step transformation via an unstable M6C intermediate phase before stabilizing as $M_{23}C_6$ (37). Importantly, the stability of these carbides, attributed to their preferential localization at interdendritic sites, impedes grain boundary migration, thereby enhancing creep resistance and overall mechanical stability during high-temperature service (38). To quantitatively evaluate the chemical stability and elemental distribution within the carbides and their adjacent regions, EDS analysis was conducted on selected areas marked in Figure 5. This analysis confirms the compositional variations consistent with the aforementioned transformation mechanisms and phase stability, thereby providing a more comprehensive understanding of microstructural evolution in service-exposed nickel superalloys.

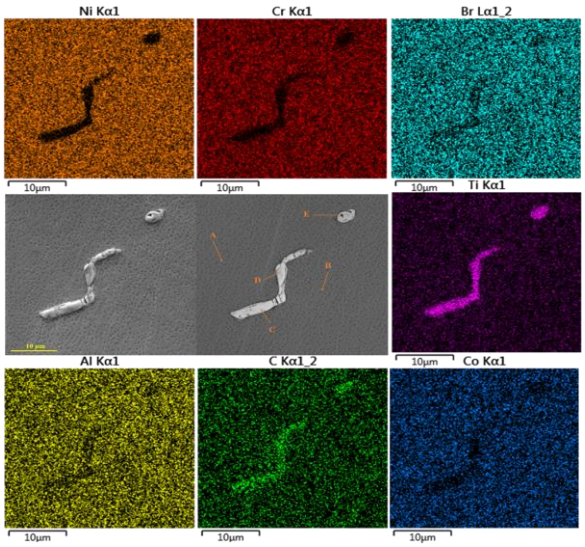

Figure 5. FESEM image in both BSE and SE modes along with an elemental map of the region

Based on the elemental maps, except for C and Ti which are highly concentrated in the M(Ti)C region, the remaining elements are well-distributed within the γ matrix. The Al elemental map clearly shows the enrichment of this element in certain regions, attributable to the growth and coarsening of γ' precipitates. Figure 6a presents the EDS spectrum and results for region A in Figure 5. The EDS results for this region confirm that it is the γ phase. The presence of Ti and Al in the analysis results for this region is due to the larger EDS analysis window compared to the region of interest, which includes contributions from the surrounding γ' precipitates. These observations also hold true for region B in Figure 5, which is also the γ matrix phase. For region C, based on the EDS results, it can be concluded that this carbide is of the MC type, given the absence of Cr, and is stabilized by Nb, Ti, W, and Ta. The EDS results for region D, which is another part of the same carbide, are very similar. Typically, during service, MC carbides undergo compositional changes, either directly or through intermediate phases like M6C, before transforming into $M_{23}C_6$. However, the observed stability in various regions of the carbide indicates that the carbide in question has not yet entered the dissolution stage. This supports the previous claim regarding the stability of TiC carbides. The EDS results for region E, as shown in Figure 6e, also confirms the presence of MC carbide stabilized by Nb, Ti, W, and Ta.

The XRD and Rietveld analysis results in Figure 7 reveal a significant increase in the gamma prime phase content of the in-service vane compared to the reference sample. This increase can be attributed to the structural and thermodynamic changes occurring in the investigated nickel superalloy during service. Thermodynamic laws support these changes. The increase in gamma prime and intermetallic phases signifies a decrease in the system's degrees of freedom (F), as predicted by the Gibbs phase rule. As the number of phases (P) increases, the system moves toward a new equilibrium state with greater stability.

$$F = C - P + 2 \quad (3)$$

Furthermore, the Gibbs-Helmholtz equation indicates that with increasing temperature and entropy during service, the Gibbs free energy (ΔG) decreases. A decrease in ΔG favors the formation of new and more stable phases, including the gamma prime phase.

$$\Delta G = \Delta H - T\Delta S \quad (4)$$

$$T\,\Delta S > \Delta H \quad (5)$$

$$\Delta G < 0 \quad (6)$$

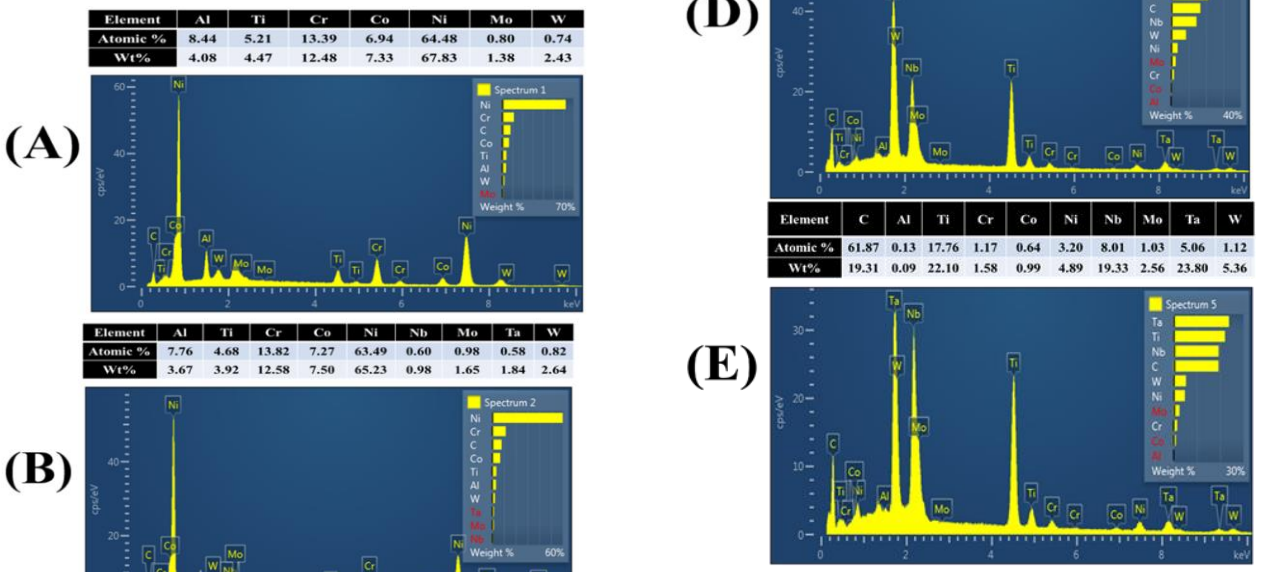

Figure 6. EDS results of the marked regions in the FESEM image (Figure 5): (a) Region A, (b) Region B, (c) Region C, (d) Region D, and (e) Region E

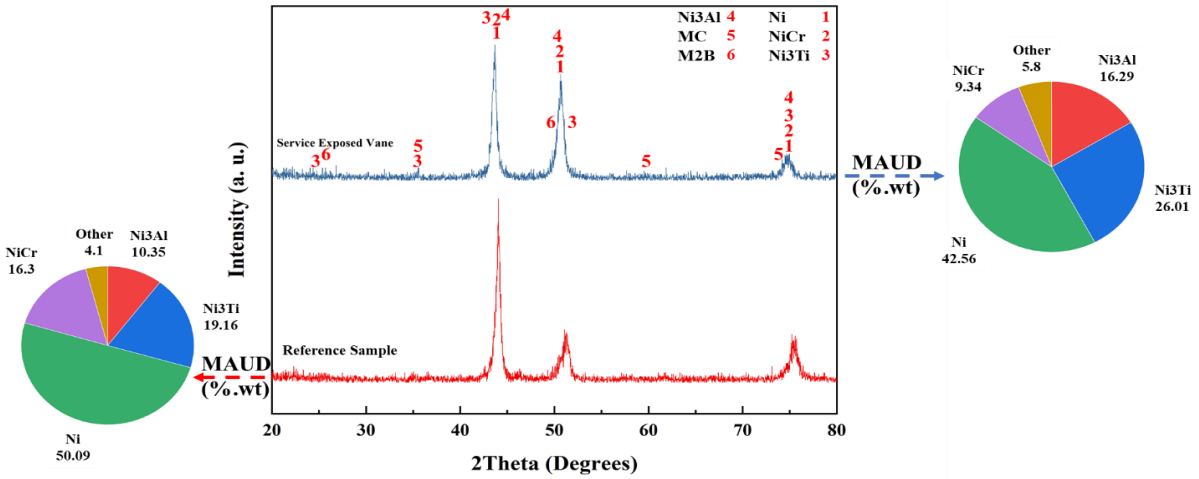

Figure 7. XRD and Rietveld analysis results of reference sample and service exposed vane

Rietveld results also confirm these findings, indicating significant microstructural evolution during service. Specifically, the gamma phase decreased from 66.39 to 51.90 wt%, while the gamma prime phase increased from 29.51 to 42.30 wt%. This observed increase in the gamma prime phase content in the in-service vane, while less common than coarsening, suggests that under these specific service conditions thermal cycles, there might be a driving force for additional precipitation from the supersaturated gamma matrix. This phenomenon, which represents a combination of continued precipitation and subsequent grain growth mechanisms during service, is influenced by various factors such as internal stresses due to temperature changes, the presence of alloying elements, and atomic diffusion within the crystal lattice. A comparison of the calculated lattice parameters for the gamma' phase also indicates a slight lattice expansion and the possibility of crystal defects in this phase. These substantial changes in the microstructure directly affect the mechanical properties of the vane, leading to reduced strength and increased creep.

Figure 8 presents a schematic of the γ' precipitate growth mechanism. The corners of cubic γ' precipitates are more susceptible to diffusion due to lattice mismatch and the localized increase in surface energy. This phenomenon, which is well-documented in the literature, causes atoms to diffuse from the high-energy corners to the lower-energy interfaces, causing the precipitates to gradually become quasi-spherical (39). As the morphology of the γ' precipitates approaches a quasi-spherical shape, external stress influences their preferential growth, a key characteristic of stress-induced directional coarsening, or rafting. This growth typically occurs perpendicular to the applied tensile stress direction, as the elastic strain energy is minimized by this specific orientation (40). Subsequently, the precipitates coarsen and preferentially become elliptical, marking the beginning of the rafting stage. The formation of these aligned γ' rafts leads to a significant decrease in the overall high-temperature mechanical properties and creep resistance of the superalloy (41). This behavior is attributed to the reduced interface area between the γ and γ' phases and the formation of continuous γ channels, which facilitate dislocation motion and bypass mechanisms. Our observations of γ' precipitate growth and rafting are consistent with the findings of other researchers who have studied the microstructural evolution of nickel-based superalloys under similar thermo-mechanical conditions (42, 43). The transition from a stable cubic morphology to a rafted structure is a crucial degradation mechanism in these alloys, directly impacting their service life. This highlights the importance of microstructural stability in maintaining the long-term performance of components exposed to high temperatures and mechanical loads.

The solidification sequence of next-generation nickel superalloy was determined experimentally and is observed to be as follows:

$$L \rightarrow L + MC \rightarrow L + MC + \gamma \rightarrow L + MC + \gamma + \gamma' \quad (7)$$

This sequence was primarily established through DSC conducted on the as-cast samples, complemented by microstructural examination of the solidified structure. To determine the initial melting temperatures of the various phases, DSC heating curves were obtained for both reference sample and service-exposed vanes (Figure 9). Results indicate that the initial melting temperatures of the γ + γ', γ + MC, and γ matrix phases did not exhibit significant changes between the reference sample and service-exposed vanes, which is consistent with FESEM results. It is important to note that for typical nickel-based superalloys, the gamma matrix generally has a melting point in the range of approximately 1350-1450 ºC, while the gamma' phase has a solvus temperature (dissolution temperature) typically ranging from 1100-1250 ºC, and its full melting occurs at higher temperatures, often very close to or overlapping with the gamma phase melting point, depending on composition. The observed increase in the overall melting temperature in the service-exposed vane indicates a shift in the thermodynamic equilibrium of the system. This shift in equilibrium can be attributed to the significant increase in the gamma' phase content during service, which alters the average composition and phase balance, thereby affecting the solidus/liquidus temperatures of the bulk

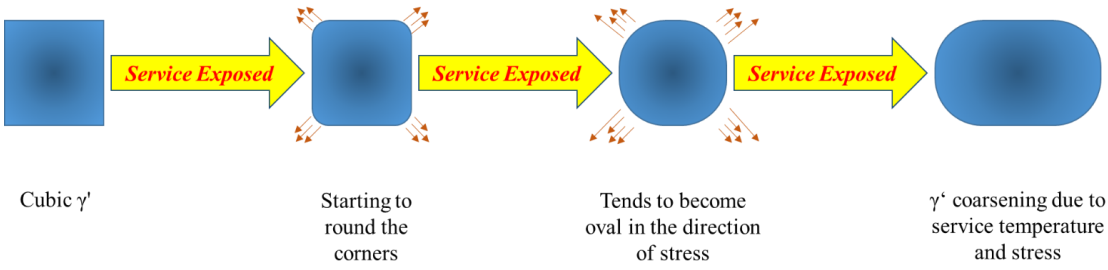

Figure 8. Mechanism of morphology change and growth of γ' precipitates during service

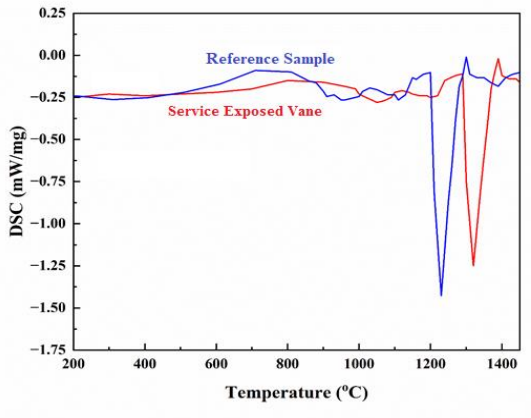

Figure 9. DSC analysis results of reference sample and service exposed vanes

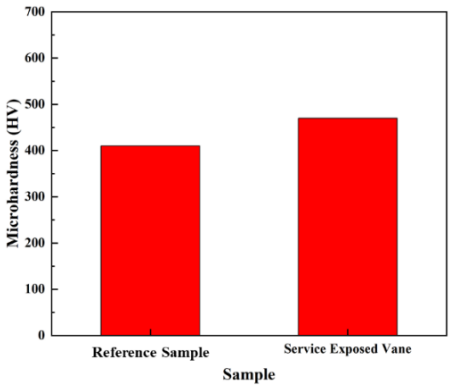

Figure 10. Hardness change in reference sample and service exposed vanes

material. Also, the increase in melting temperature in the service-exposed vane indicates a shift in the thermodynamic equilibrium of the system. This shift in equilibrium can be attributed to the significant increase in the γ' phase (20, 32). The formation and growth of the γ' phase lead to a decrease in the Gibbs free energy of the system, establishing a new equilibrium state. The thermodynamic mechanisms governing this process include a reduction in interfacial energy between different phases and a decrease in strain energy due to accommodating lattice mismatches (32, 34). It is important to note that these temperatures may exhibit some acceptable deviations due to the influence of thermal history. The DSC thermal lag, which is a constant independent of heating rate, can also affect the measured onset temperature of the melting peaks. Additionally, the models used in these studies tend to underestimate the experimental values.

Figure 10 presents the hardness results of reference sample and service-exposed vane, elucidating the hardness changes during service. As observed, the hardness exhibited an approximate increase of 60 Vickers, primarily attributed to the growth of gamma prime precipitates, their coalescence, and the formation of $M_{23}C_6$ carbide films. The coarsening of secondary precipitates led to the formation and strengthening of barriers against dislocation motion. The creation of these barriers and the subsequent restriction of dislocation movement hindered plastic deformation during the hardness test, a phenomenon previously reported in the literature (32). Plastic deformation during static loading in hardness testing is suppressed. While detrimental TCP phases such as sigma and mu phases are reported in the literature to affect hardness, in the current study these phases were not clearly detected by XRD or FESEM/EDS, likely due to their very low volume fraction. Therefore, the observed hardness increase is primarily attributed to the growth and coalescence of gamma prime precipitates and the formation of $M_{23}C_6$ carbide films. These phases create significant obstacles to dislocation motion, contributing to increased hardness. The trapping of dislocations behind these obstacles resulted in increased hardness. Additionally, the high density of secondary phases increased the anti-phase boundary content, contributing to the overall hardness increase (44). This change in hardness led to a compromise in creep resistance and overall component performance. During high-temperature operation, a constant interplay between hardening and softening governs the creep life of the component. Excessive softening, due to plastic deformation, elongation, and severe contact with opposing equipment, can lead to catastrophic failure. On the other hand, excessive hardening can render the component unable to withstand stress, resulting in brittle fracture (44-46). Therefore, both reference sample and service-exposed vanes were subjected to creep tests.

Figure 11 presents the creep test results for both the reference sample and service-exposed vane. Notably, the service-exposed vane exhibited a rapid and brittle failure compared to the reference sample. In the creep curve of the reference sample, all three creep regions are observable, whereas only regions 1 and 2 are evident in the service-exposed vane. The absence of the tertiary creep region in the service-exposed vane is a direct consequence of its brittle failure, which occurs without any significant necking. This behavior is attributed to the extensive microstructural changes that occurred during service, particularly the growth of gamma prime precipitates and the formation of continuous carbide films at grain boundaries. These microstructural changes significantly alter the deformation mechanism. The formation of carbide films, in particular, renders grain boundary sliding extremely difficult, if not impossible.

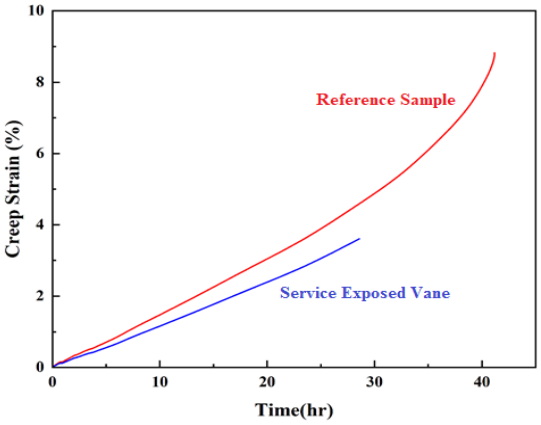

(a)

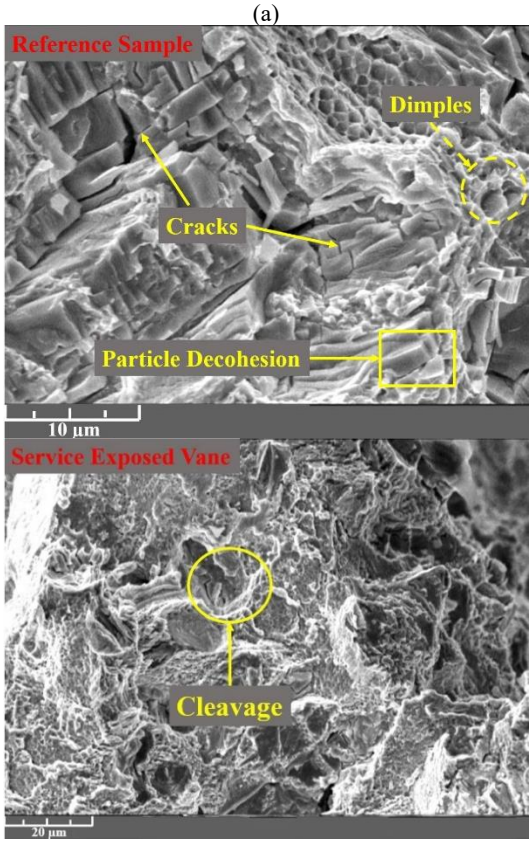

(b)

Figure 11. (a) Variation of creep properties, and (b) SEM images of the fracture surfaces of the reference sample and service-exposed vanes

The resistance created against sliding induces a shift in the deformation mechanism, a phenomenon well-documented in the literature (47, 48). Consequently, creep cavities form and coalesce at grain boundaries, leading to crack initiation. The rapid propagation of these cracks under high stress and temperature conditions results in the observed swift failure. Additionally, the formation of other cracks within the dendritic regions due to the interaction and shearing of dislocations and obstacles, as reported by other researchers (48, 49), further accelerates the failure process. The presence of a tertiary creep region in the reference sample, however, indicates a classic interplay between softening and hardening mechanisms, leading to a much longer creep life. This is consistent with findings in other studies on similar alloys (50). Furthermore, based on the SEM images, the reference sample exhibits numerous dimples indicative of ductile failure, characterized by significant energy absorption. This ductile failure is attributed to the nucleation, growth, and coalescence of creep cavities, which is consistent with stable crack propagation. The presence of these dimples and the distinct ductile fracture morphology confirm a more gradual failure process, with cracks propagating predominantly through the gamma matrix in a relatively dispersed manner. In contrast, the SEM images of the service-exposed vane reveal cleavage facets, which are typical of brittle failure and associated with rapid crack propagation and low energy absorption. This brittle behavior is consistent with both the absence of significant necking in the creep curve and the lack of a tertiary creep region, as previously discussed. This observed shift from a ductile to a brittle failure mechanism is a critical finding that is well-aligned with the documented effects of long-term thermal exposure on nickel-based superalloys (49, 50). The formation and growth of gamma prime precipitates and the development of carbide films at grain boundaries contribute significantly to the observed creep resistance but also promote brittleness by inhibiting grain boundary sliding. This microstructural evolution is confirmed as the key factor underlying the shift from ductile to brittle failure in the service-exposed vane.

As illustrated in Figure 11, the reference sample exhibited a creep life of 40 hours and a creep strain of 9%. In contrast, the service exposed vane, due to degradation mechanisms, displayed a significantly shorter creep life of 29 hours and a creep strain of only 4%. This substantial reduction in creep life clearly highlights the impact of degradation mechanisms on the material's properties.

4. CONCLUSIONS

This study focused on the independent effects of direct gas heat exposure on the microstructure, mechanical properties and creep behavior of the Next- Generation turbine Nickel Superalloy after 1200 cycles of operation. The following results were obtained:

1. Rietveld refinement was applied and the calculation indicated that the gamma prime phase increased from 29.51 to 42.30 wt.%, signifying precipitation and grain growth mechanisms during service.
2. An increase in the volume fraction of carbides and the growth of γ' precipitates were observed in the

superalloy microstructure after 1200 cycles of operation.

3. The hardness of the superalloy increased from 420 Vickers for the reference sample to 480 Vickers for the service exposed vane after 1200 cycles of operation.
4. Thermal analysis revealed a significant 60°C decrease in the complete dissolution temperature after service exposure, indicating a reduction in the alloy's overall thermal stability and suggesting the need for repair or rejuvenation. However, the onset melting temperatures of key phases remain largely unchanged, reflecting stable initial melting behavior under service conditions.
5. The creep strain rate of the superalloy decreased after 1200 cycles of operation.

5. REFERENCES

1. Koç Ö, Thomas R, Liang X, Hegedues Z, Lienert U, Harrison RW, et al. A spatially resolved analysis of dislocation loop and nanohardness evolution in proton irradiated Zircaloys. Acta Materialia. 2024;269:119799. https://doi.org/10.1016/j.actamat.2024.119799
2. Sujata M, Madan M, Raghavendra K, Venkataswamy M, Bhaumik S. Identification of failure mechanisms in nickel base superalloy turbine blades through microstructural study. Engineering Failure Analysis. 2010;17(6):1436-46. https://doi.org/10.1016/j.engfailanal.2010.05.004
3. Golezani A, Bageri M, Samadi R. Microstructural change and impact toughness property of Inconel 738LC after 12years of service. Engineering Failure Analysis. 2016;59:624-9. https://doi.org/10.1016/j.engfailanal.2015.11.012
4. Kumawat MK, Parlikar C, Alam MZ, Das DK. Type-I hot corrosion of Ni-base superalloy CM247LC in presence of molten Na2SO4 film. Metallurgical and Materials Transactions A. 2021;52(1):378-93. https://doi.org/10.1007/s11661-020-06068-6
5. Antolovich SD. Microstructural aspects of fatigue in Ni-base superalloys. Philosophical Transactions of the Royal Society A: Mathematical, Physical and Engineering Sciences. 2015;373(2038):20140128. https:// doi.org/10.1098/rsta.2014.0128
6. Shajari Y, Seyedraoufi Z, Alizadeh A, Razavi S, Porhonar M, Mirzavand K. Effect of solution temperature of rejuvenation heat treatment on the stability of γ′ precipitates in Ni-base superalloy IN738LC during long-term heating. Materials Research Express. 2019;6(12):126571. https://doi.org/10.1088/2053-1591/ ab54ef
7. Belan J, editor Quantitative evaluation of alitize coating on ŽS6K Ni-base superalloy. Materials science forum; 2014: Trans Tech Publ.
8. Belan J, Vaško A, Kuchariková L, Tillová E, Chalupová M. The SEM Metallography analysis of vacuum cast ZhS6K superalloy turbine blade after various working hours. Manufacturing Technology. 2019;19(5):727-33. 10.21062/ujep/362.2019/a/12132489/MT/19/5/727
9. Belan J, Klacková M. Structure and Its Influence on Ni–Base Superalloy Mechanical Properties. 2013. https://depot.ceon.pl/handle/123456789/3515
10. Kawagishi K, Yeh A-C, Yokokawa T, Kobayashi T, Koizumi Y, Harada H. Development of an oxidation-resistant high-strength sixth-generation single-crystal superalloy TMS-238. Superalloys. 2012;9:189-95. https://doi.org/10.1002/9781118516430.ch21
11. Tyagunov A, Baryshev E, Kostina T, Baum BA, Lesnikov V, Semenova IP. The Effect of Long-Term High-Temperature Heat Treatment at 950 C on the Structure and Mechanical Properties of the ZhS6U Superalloy. PHYSICS OF METALS AND METALLOGRAPHY C/C OF FIZIKA METALLOV I METALLOVEDENIE. 1998;86:65-9.
12. Tewari S, Hemareddy M. Soviet superalloy ZHS6-K, effect of B/C modification. Journal of Materials Science. 1983;18(4):1155-64. https://doi.org/10.1007/BF00551985
13. Du B, Sheng L, Cui C, Hu Z, Sun X. Effects of grain refinement on the low-cycle fatigue behavior of IN792 superalloys. Crystals. 2021;11(8):892. https://doi.org/10.3390/cryst11080892
14. Wei T, Ding K, Wu G, Liu X, Fan M, Zhang Y, et al. Stress rupture initiated by the carbides in the grain boundaries of the multi-pass weld metal. Journal of Materials Research and Technology. 2021;10:282-90. https://doi.org/10.1016/j.jmrt.2020.12.031
15. Taheri M, Jam JE, Beni MH, Khorram A, Kashani-Bozorg SF, Torkamany MJ. The effect of service temperature on the impact strength and fracture toughness of GTD-111 superalloy. Engineering Failure Analysis. 2021;127:105507. https://doi.org/10.1016/j.engfailanal.2021.105507
16. Bi Z-n, Dong J-x, Zhang M-c, Zheng L, Xie X-s. Mechanism of α-Cr precipitation and crystallographic relationships between α-Cr and δ phases in Inconel 718 alloy after long-time thermal exposure. International Journal of Minerals, Metallurgy, and Materials. 2010;17(3):312-7. https://doi.org/10.1007/s12613-010-0310-z
17. Schlesinger M, Seifert T, Preussner J. Experimental investigation of the time and temperature dependent growth of fatigue cracks in Inconel 718 and mechanism based lifetime prediction. International Journal of Fatigue. 2017;99:242-9. https://doi.org/10.1016/j.ijfatigue.2016.12.015
18. Mahobia G, Paulose N, Mannan S, Sudhakar R, Chattopadhyay K, Srinivas NS, et al. Effect of hot corrosion on low cycle fatigue behavior of superalloy IN718. International Journal of Fatigue. 2014;59:272-81.
19. Lewis D, Ding R, Whittaker M, Mignanelli P, Hardy M. The effect of oxidising thermal exposures on the fatigue properties of a polycrystalline powder metallurgy nickel-based superalloy. Materials & Design. 2020;189:108529. https://doi.org/10.1016/j.matdes.2020.108529
20. Shajari Y, Razavi SH, Seyedraoufi ZS, M. Samiee. The effect of time and temperature of solutionizing heat treatment on γ ′ characterization in a Ni-base superalloy. Metallography, Microstructure, and Analysis. 2021;10(4):441-7. https://doi.org/10.1007/s13632-021-00760-8
21. Long H, Bakhtiari SR, Liu Y, Mao S, Wei H, Chen Y, et al. A comparative study of rafting mechanisms of Ni-based single crystal superalloys. Materials & Design. 2020;196:109097. https://doi.org/10.1016/j.matdes.2020.109097
22. Yu Z, Wang X, Yang F, Yue Z, Li JC. Review of γ'rafting behavior in nickel-based superalloys: crystal plasticity and phase-field simulation. Crystals. 2020;10(12):1095. https://doi.org/10.3390/cryst10121095
23. Tsukada Y, Murata Y, Koyama T, Miura N, Kondo Y. Creep deformation and rafting in nickel-based superalloys simulated by the phase-field method using classical flow and creep theories. Acta Materialia. 2011;59(16):6378-86. https://doi.org/10.1016/j.actamat.2011.06.050
24. Hosseini S, Nategh S, Ekrami A. Changes of γ′ precipitate characteristics in damaged superalloy IN738LC during different stages of rejuvenation heat treatment cycles. Materials Science

and Technology. 2012;28(2):213-9. https://doi.org/10.1179/1743284711Y.0000000021

25. Hosseini SS, Nategh S, Ekrami A-A. Microstructural evolution in damaged IN738LC alloy during various steps of rejuvenation heat treatments. Journal of alloys and compounds. 2012;512(1):340-50. https://doi.org/10.1016/j.jallcom.2011.09.094
26. Yang S, Yun J, Moon B, Park S, Seok C-S. Creep performance evaluation considering the operating environment of gas turbine blades with rejuvenation maintenance. Journal of Mechanical Science and Technology. 2022;36(1):127-34. https://doi.org/10.1007/s12206-021-1211-y
27. Azadian S, Wei L-Y, Warren R. Delta phase precipitation in Inconel 718. Materials characterization. 2004;53(1):7-16. https://doi.org/10.1016/j.matchar.2004.07.004
28. Simonetti M, Caron P. Role and behaviour of μ phase during deformation of a nickel-based single crystal superalloy. Materials Science and Engineering: A. 1998;254(1-2):1-12. https://doi.org/10.1016/S0921-5093(98)00766-7
29. De Luca A, Kenel C, Griffiths S, Joglekar SS, Leinenbach C, Dunand DC. Microstructure and defects in a Ni-Cr-Al-Ti γ/γ'model superalloy processed by laser powder bed fusion. Materials & Design. 2021;201:109531. https://doi.org/10.1016/j.matdes.2021.109531
30. Chengjian HBLHW. Solidification Microstructure of Ni-Base Superalloy Powder. Acta Metallurgica Sinica (English Letters). 1991;4(2):97.
31. Khodabakhshi A, Mashreghi A, Shajari Y, Razavi SH. Investigation of microstructure properties and quantitative metallography by different etchants in the service-exposed nickel-based superalloy turbine blade. Transactions of the Indian Institute of Metals. 2018;71(4):849-59. https://doi.org/10.1007/s12666-017-1217-4
32. Shajari Y, Beigi M, Porhonar M. The effect of microstructural changes on the rupture behavior of gas turbine damping bolt superalloy (Nimonic 90) after long service time. Engineering Failure Analysis. 2023;145:106993. https://doi.org/10.1016/j.engfailanal.2022.106993
33. D'Souza N, Kantor B, West G, Feitosa L, Dong H. Key aspects of carbide precipitation during solidification in the Ni-base superalloy, MAR M002. Journal of Alloys and Compounds. 2017;702:6-12. https://doi.org/10.1016/j.jallcom.2017.01.104
34. Shajari Y, Razavi SH, Seyedraoufi Z-S. Comparative study of solution heat treatment of IN738LC superalloy in conventional conditions and salt bath. Journal of Materials Engineering and Performance. 2022;31(3):2525-41. https://doi.org/10.1007/s11665-021-06344-5
35. Zhang H, Xie J, Li Q, Wu H, Yu J, Chai H, et al. Influence of Substituting W for Nb or Hf on Solidification Behavior of a Typical Co–Ni–Al–W Based Superalloy. Acta Metallurgica Sinica (English Letters). 2024;37(11):1907-20. https://doi.org/10.1007/s40195-024-01749-2
36. Bian H, Xu X, Li Y, Koizumi Y, Wang Z, Chen M, et al. Regulating the coarsening of the γ′ phase in superalloys. NPG Asia Materials. 2015;7(8):e212-e. https://doi.org/10.1038/am.2015.96
37. Zhang Z, Ding R, Guo Q, Liu C, Liu Y. Enhancing tensile and creep properties of Inconel 617 superalloy via regulating the synergistic evolution of M23C6 carbides and γ′ phases. Materials Science and Engineering: A. 2025;919:147523. https://doi.org/10.1016/j.msea.2024.147523
38. Singh Handa S. Precipitation of Carbides in a Ni-based Superalloy. 2014.
39. Moshtaghin R, Asgari S. Growth kinetics of γ′ precipitates in superalloy IN-738LC during long term aging. Materials & design. 2003;24(5):325-30. https://doi.org/10.1016/S0261-3069(03)00061-X
40. Hou J, Guo J. Influence of thermal exposure on the microstructures and mechanical properties of a superalloy. Journal of materials engineering and performance. 2006;15(1):67-75. https://doi.org/10.1361/105994906X83501
41. Wang Y, Li K, Cai Z, Shi L, Wang H. Creep behavior and microstructure evolution of Ni-based alloy IN617 at 1000° C. Materials Characterization. 2022;187:111837. https://doi.org/10.1016/j.matchar.2022.111837
42. Zhou Z, Lei Q, Zhang L, Cui Z, Shang Y, Qi H, et al. Microstructural evolution of nickel-based single crystal superalloy fabricated by directed energy deposition during heat treatment. Journal of Alloys and Compounds. 2022;904:163943. https://doi.org/10.1016/j.jallcom.2022.163943
43. Ping K, HUANG J-y, Feng L, HUANG L, Cui L. Mechanical properties and microstructural evolution of nickel-based superalloys. Transactions of Nonferrous Metals Society of China. 2025;35(7):2304-19. https://doi.org/10.1016/S1003-6326(25)66816-6
44. Sun F, Tong J, Feng Q, Zhang J. Microstructural evolution and deformation features in gas turbine blades operated in-service. Journal of alloys and compounds. 2015;618:728-33. https://doi.org/10.1016/j.jallcom.2014.08.246
45. Sun Z, Jiang X, Zhan X, Li K, Zheng W, Jiang D, et al. The recovery of microstructure and mechanical properties of directionally solidified Ni-based superalloy DZ411 after long-term thermal exposure at different temperatures. Materials Science and Engineering: A. 2023;888:145831. https://doi.org/10.1016/j.msea.2023.145831
46. Khodabakhshi A, Mashreghi A, Razavi S, Jafarpour S, Hajitaheri S, Shajari Y. Microstructure Characteristics of Rejuvenated Service Exposed Gas Turbine Blade under the Influence of Various Solution Temperature and Cooling Rates. Metallography, Microstructure, and Analysis. 2024;13(3):492-503. https://doi.org/10.1007/s13632-024-01093-y
47. Gai Y, Zhang R, Cui C, Zhou Z, Tao X, Tan Y, et al. Creep behavior and microstructure evolution of a novel Ni-Co-based superalloy with long-life designed for high temperature application. Materials Science and Engineering: A. 2025:148396. https://doi.org/10.1016/j.msea.2025.148396
48. Li Q, Tian S, Yu H, Tian N, Su Y, Li Y. Effects of carbides and its evolution on creep properties of a directionally solidified nickel-based superalloy. Materials Science and Engineering: A. 2015;633:20-7. https://doi.org/10.1016/j.msea.2015.02.056
49. Li K-S, Lu R-S, Gong X-F, Pei Y-B, Zhang X, Tan J-P, et al. Investigation of microstructural evolution and mechanical properties for in-service nickel-based superalloy. Materials Science and Engineering: A. 2024;899:146465. https://doi.org/10.1016/j.msea.2024.146465
50. Huang J, Ai C, Ru Y, Shang Y, Pei Y, Li S, et al. The Effect of Cooling Rate from Solution Treatment on γ′ Reprecipitates and Creep Behaviors of a Ni-Based Superalloy Single-Crystal Casting. Crystals. 2022;12(9):1235. https://doi.org/10.3390/cryst12091235

COPYRIGHTS
©2026 The author(s). This is an open access article distributed under the terms of the Creative Commons Attribution (CC BY 4.0), which permits unrestricted use, distribution, and reproduction in any medium, as long as the original authors and source are cited. No permission is required from the authors or the publishers.

Persian Abstract

چکیده

در این پژوهش، تحول ریزساختاری و رفتار خزشی یک پره مرحله دوم توربین گاز پس از ۱۲۰۰ سیکل کارکرد طولانی‌مدت، از طریق بررسی‌های ریزساختاری و آزمون‌های خزشی مورد ارزیابی قرار گرفت. آنالیزهای میکروسکوپی افزایش در کسر حجمی و اندازه فازهای ثانویه نظیر گاما پریم و کاربیدها را آشکار ساخت. این تغییرات ریزساختاری منجر به تردی سوپرآلیاژ نیکل مورد بررسی گردید. نتایج آزمون سختی‌سنجی افزایش سختی از ٤٢٠ ویکرز برای پره نو به ٤٨٠ ویکرز برای پره تحت سرویس را نشان داد. آنالیز حرارتی کاهش ٦٠ درجه سانتیگرادی در دمای انحلال کامل را نمایان ساخت که حاکی از نیاز به تعمیر یا احیای آلیاژ می‌باشد. رشد رسوبات گاما پریم از طریق برش نابجایی‌ها و درشت‌شدن کاربیدها به دلیل ممانعت از لغزش مرزدانه‌ها، منجر به کاهش ۱۱ ساعته در عمر خزشی گردید. پره نو در تنش ۲٤۷ مگاپاسکال و دمای ۹۰۰ درجه سانتیگراد پس از ٤٠ ساعت با کرنش ۹٪ دچار شکست شد. در مقابل، پره تحت سرویس کاهش در عمر خزشی و کرنش خزشی را به ترتیب به ۲۹ ساعت و ٤٪ نشان داد.

IJE TRANSACTIONS B: Applications Vol. 39, No. 08, (August 2026) 1843-1854

International Journal of Engineering

Journal Homepage: www.ije.ir

Performance of Peltier-Based Thermal Management System: Impact of Multiple Modules on Cooling Efficiency and Energy Consumption

M. N. Abd-Al Ameer*, I. S. Kareem, A. A. Ismaeel

Department of Electromechanical Engineering, University of Technology-Iraq, Baghdad, Iraq

P A P E R I N F O

Paper history:
Received 02 July 2025
Received in revised form 02 August 2025
Accepted 28 August 2025

Keywords:
Peltier Effect
Cooling Performance
Ethylen Glycol
Energy Efficiency
Energy Consumption

A B S T R A C T

The effectiveness of thermal management procedures is considered a crucial point for keeping the performance and longevity of electronic and electrical application boards. One of the solutions, which has gained increased interest from researchers and industrial institutes, is the use of a thermoelectric cooler (TEC), also known as a Peltier, which is made of two semiconductor materials for promising support of the traditional forced fan air-cooling. However, a more detailed investigation of the effect of using Peltier technology under operational and design change conditions is needed. In line with this, this study examines an experimental prototype model to analyze the impact of different numbers of Peltier units (1 to 4) and different refrigerants (Distilled water only, mono ethylene glycol and Distilled water 50:50) on thermal progress performance in terms of thermal absorption and energy consumption. Under variable real operations, the result appeared that the mixture (distilled water + mono ethylene glycol 50:50) outperformed distilled water only, achieved faster electrical cabinet temperature reduction, and a higher cooling performance (COP) in all Peltier configuration models. The highest COP of 3.75 was recorded using four Peltier units with a mixture of mono ethylene glycol. The findings emphasize the importance of the best refrigerant choice and system configuration for efficient thermal management, paving the way for future advancements in thermoelectric cooling technologies.

***doi**: 10.5829/ije.2026.39.08b.06*

Graphical Abstract

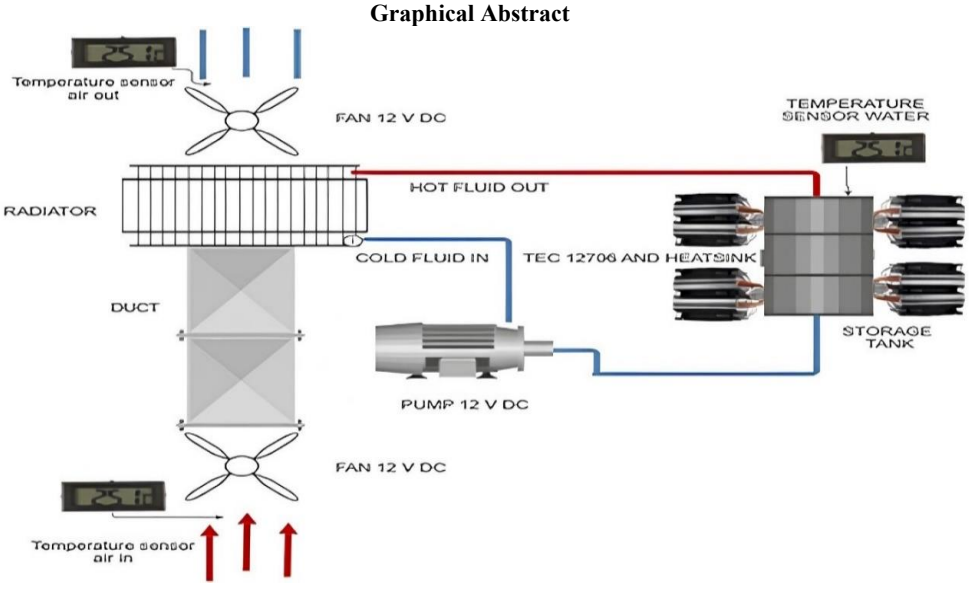

*Corresponding Author Email: eme.23.119@grad.uotechnology.edu.iq (M. N. Abd-Al Ameer)

Please cite this article as: Abd-Al Ameer MN, Kareem IS, Ismaeel AA. Performance of Peltier-Based Thermal Management System: Impact of Multiple Modules on Cooling Efficiency and Energy Consumption. International Journal of Engineering, Transactions B: Applications. 2026;39(08):1843-54.

NOMENCLATURE

A	area of the pipe, (circular)	T	temperature
c	specific heat, kJ/kg C	Th	temperature of the hot side of the TEC
COP	coefficient of performance	Tc	temperature of the cold side of the TEC
I	electrical current, A	Tr	temperature of the air
Km	thermal conductivity of TEC, W/mC	TEC	thermoelectric cooler
ṁ	mass flow rate, kg/s	TEM	thermoelectric module
P1	input energy consumed TEM, W	V	voltage, V
P2	input energy consumed (pump +fans), W	**Greek Symbols**	
ρ	Density of air	αm	seebeck coefficient (V/C) of TEC
q	heat transfer rate, W	ΔT	temperature difference
qa	heat transfer rate between air fluid and cold surface of TEM	**Subscripts**	
qph	Peltier heating, W	a	air
qpc	Peltier cooling, W	c	cold
qj	Joule heating, W	con	Fourier heating
qcon	Fourier heating, W	h	hot
qc	cooling energy of TEM, W	j	Joule heating
qh	heating energy of TEM, W	max	Maximum
qr	heating energy of (pump + fans)	ph	Peltier heating
Rm	electrical resistance of TEC, Ω	pc	Peltier cooling
S	Speed of air	w	fluid

1. INTRODUCTION

Controlling the thermal load of electrical and electronic components is crucial for enhancing their efficiency and extending their operational lifespan (1). The flow of electrical current through conductive materials generates heat as a result of converting electrical energy into thermal energy, causing electrical components to produce heat during operation (2). To ensure the safe and reliable performance of these systems, it is essential to dissipate the generated heat efficiently from the components to the surrounding environment (3). With the rapid advancement in electronic device performance, effectively transferring accumulated heat within a limited time and space using conventional cooling methods become increasingly challenging. Consequently, energy consumption and heat dissipation have appeared as significant obstacles to further improving electronic device performance (4).

In this context, thermoelectric cooling devices based on the Peltier effect have gained considerable attention as effective solutions for thermal management in electrical, electronic, and mechanical systems (5). Temperature control systems are essential across various industries to keep the best operating conditions, enhance product quality, and improve energy efficiency (6). Peltier-based cooling systems offer several advantages, including compact size, low cost, and environmentally friendly design, making them particularly suitable for thermal management in electronic systems (7). This is especially beneficial in hot climates, such as the Middle East, where these systems can efficiently regulate running temperatures, ensuring the safe and reliable operation of electrical component (8).

Given the effectiveness of thermoelectric cooling in managing high-performance chips and components, it has been proposed as a promising alternative to conventional cooling techniques (9). A significant body of research focuses on the application of Peltier cooling systems, including portable air conditioning units (10) liquid heat exchangers with pumps (11) and portable O-REF (oven-refrigerator) applications (12). Additionally, thermoelectric technology is being explored for energy harvesting applications, such as gas turbine sensing and monitoring systems (13), as well as recovering waste heat from engines and vehicle exhaust systems for electricity generation (14, 15). Furthermore, researchers are investigating the impact of different electrical connection methods for multiple Peltier cells to enhance thermal performance efficiency, particularly in applications requiring more effective heat transfer (16, 17).

Several studies have explored the application of thermoelectric cooling technology in various cooling systems. Mirmanto et al. 2019 (18) focused on analyzing the impact of varying fluid flow rates on the cooling capacity and coefficient of performance (COP) of a thermoelectric cooling system. Two thermoelectric modules were used, with water as the working fluid. The experiment began at an initial water temperature of 25°C and was conducted over a period of 5 hours. During the experiment, water mass flow rates were set at 1 g/s, 1.5 g/s, and 2 g/s, with temperature measurements recorded every 10 seconds. The results indicated that the lowest temperature achieved was 19.43°C at a flow rate of 1 g/s. The study concluded that, while thermoelectric cooling systems offer certain advantages, their effectiveness in cooling flowing water is limited when compared to their performance with stationary (static) liquids. A cooling system developed using thermoelectric cooling chips to cool water and generate chilly air. The system, which incorporated two thermoelectric cooling chips, was evaluated over a five-minute operation period using three

different cooling media: water, water with 30% alcohol, and water with 50%. The findings showed that the water-alcohol mixture with 50% alcohol achieved the most significant temperature reduction, from 22.7°C to 19.1°C, proving the system's potential for energy-efficient cooling compared to conventional air conditioners. Mushonga et al. (19) successfully designed a thermoelectric cooling system that reduced the temperature of 10 liters of water from 30°C to 10°C within 20 minutes using four Peltier units. The study highlighted the system's efficiency in achieving rapid cooling while perfecting energy consumption, making it a practical solution for applications requiring localized high-efficiency cooling. Abdulghani (10) focused on improving the cooling efficiency of TEC-12706 thermoelectric air coolers by analyzing the effect of the number of units used. The study evaluated different numbers of chillers (1, 2, 3, and 4), along with the thermal performance of each case. The first temperature was 35°C, and a total of 16 tests were conducted to ensure accuracy. Each test lasted 10–30 seconds. The data obtained showed that the system was capable of achieving a temperature reduction of 10–15°C, depending on the number of chillers. Using four chillers achieved the best balance between thermal and economic efficiency, making this number best. The study concluded that increasing the number of chillers improves the coefficient of performance (COP) and reduces operating costs. However, beyond a certain point, economic returns may decline due to increased electrical energy consumption. Adref et al. (20) examined the performance of thermoelectric cooling units in reducing water temperature and storing cooling energy. Experiments conducted in a 10-liter water tank using three Peltier cooling units over 20 minutes proved that increasing the number of cooling units enhanced both temperature reduction and cooling efficiency. Specifically, with three cooling units, the water temperature dropped from 9.0°C to -10.0°C, highlighting the system's suitability for industrial and electronic cooling applications. Ab Rahman et al. (21) developed and evaluated a thermoelectric cooling box using two Peltier units connected in parallel to enhance cooling performance. The cooler reached its maximum cooling effect within 90 minutes and was evaluated under two conditions: empty and filled with soft drinks. The results showed that when empty, the cooler achieved a temperature reduction from approximately 30°C to 18°C, suggesting that increasing the number of Peltier units could further improve efficiency. Redho et al. (22) explored the impact of integrating ice packs into a Peltier-based cooler. The experiments, conducted over two hours, evaluated three configurations: Peltier-only cooling, Peltier combined with ice packs, and Peltier with ice packs and frozen food. The results showed that the combination of Peltier units and ice packs significantly improved cooling efficiency, with temperatures reaching -6.7°C when operational and stabilizing at -3.5°C after being turned off. This study highlights the potential of hybrid cooling solutions for preserving perishable goods.

Traditional cooling methods struggle to manage heat in compact electronic circuits, particularly under high thermal loads. There is limited investigation into how varying the number of thermoelectric cooling (TEC) units and using different refrigerants affects thermal performance and energy efficiency under real-world conditions. The reviewed studies highlight the advantages of thermoelectric cooling (TEC), including high cooling efficiency, rapid response, low energy consumption, and compatibility with other cooling technologies to enhance performance. Its applications extend from electronics and industrial cooling and eco-friendly air conditioning, making it a promising solution for modern cooling challenges.

1. The current work differs from the work done by Mirmanto et al. (18) in that it uses a static coolant instead of a moving one.
2. The design in the current work consists of two parts: the first part cools the coolant, as reported in literature (10), and the second part cools the air.
3. In terms of coolant usage, this work differs from literature (20-22), which used only water. The current work uses different coolants based on distilled water and A 50:50 mixture of distilled water and mono ethylene glycol.
4. The current work is also similar to work conducted by Mushonga et al. (19) in terms of selecting the best number of thermoelectric coolers to achieve the best balance between thermal and economic efficiency.

Therefore, the current study will complement the features proposed by earlier studies and propose a new contribution to electrical and electronic circuits cooling technology. The most important feature of this proposed work is the use of a coolant that is mainly based on a mixture of mono ethylene glycol with distilled water in a 50:50 ratio. The study conducted a thermal analysis under realistic conditions to prove the effect of the TEC number and type of accompanying coolant refrigerant on the thermal performance system.

More details about this research are explained in the following sections: Section 2 is devoted to the proposed model and materials employed in the experiment. The mathematical formulation in section 3. Section 4 presents the results and discussion. Finally, section 5 concludes the paper.

2. PROPOSED MODEL

The increase in energy consumption of conventional air conditioning systems highlights the need for more sustainable and efficient cooling solutions. Earlier

studies have shown the importance of finding innovative alternatives to address this issue. Promising solutions include the use of Peltier units, which have proven their efficiency by adding more units, improving thermal insulation, using cooler cooling water, and using alcohol in cooling systems, as they can enhance cooling efficiency while keeping temperature stability and reducing fluctuations. Aluminum radiators and water-cooled systems have also been shown to be essential elements for improving thermal efficiency and providing better performance for thermoelectric cooling units. In this context, this research proposes the design of an air conditioning system using different numbers of Peltier elements instead of a compressor, in addition to using two types of liquids instead of gases used in conventional air conditioning systems. The cooling ability and coefficient of performance of this proposed system will be calculated, with an attempt to reduce electrical energy consumption.

2. 1. Materials Employed in the Experiment

This section delineates the components utilized in the fabrication of the air conditioning system, which fundamentally comprises a thermally insulated aluminum reservoir with a capacity of 1000 ml of liquid, a heat exchanger, fans for the intake of hot air and the expulsion of cold air, and thermoelectric units for liquid cooling. It functions within a closed-loop system and is powered by a 12-volt, 50-amp power source, as shown in Figure 1.

All tests were conducted manually to determine the optimal coolant type and the requisite number of cooling units that maximize performance while minimizing energy usage. Subsequently, the automatic control process is transitioned to a selected controller that precisely regulates the temperature. Programmable logic controllers were used due to their high precision and rapid reaction to temperature regulation.

2. 1. 1. Cool Box The cooling box used in the design consists of dimensions (40 cm, 30 cm, 21 cm). It is designed for electrical and electronic applications, in addition to two pipes with a diameter of 59.4 mm to draw hot air from inside the electrical and electronic distribution board and push cold air. The dimensions of the box were chosen to be compatible and sufficient for all components of the air conditioning device, as shown in Figure 2.

2. 1. 2. Supply Unit The electrical power supply the single phase power supply which is passes through the switched mode power supply. The unit is used for the rectification of 230 volt AC power supply into 12 and 24 volt DC power supply. For the 12 V DC power source as shown in Figure 3, it is used to operate the (TEC- 12706) and the rest of the system components.

2. 1. 3. Thermoelectric Cooling Module When Alessandro Volta discovered that temperature changes can produce thermoelectric forces in 1794, the idea of thermoelectric cooling was born (23, 24). TECM is a device based on the "Peltier effect", discovered in 1834, where he discovered that when a direct current source is applied to thermometers. There is a temperature

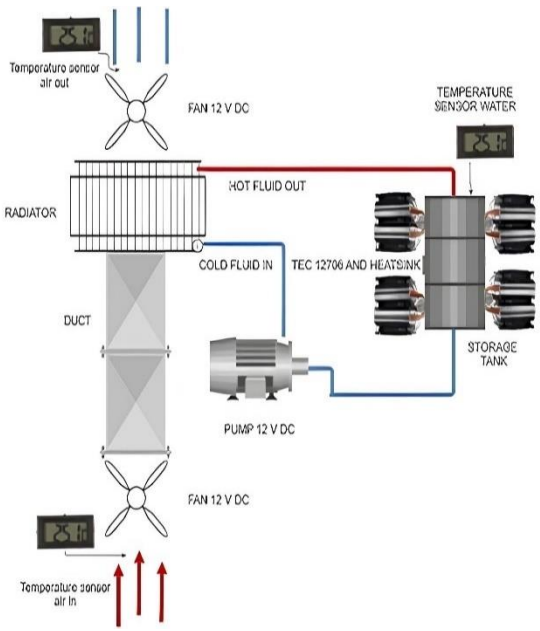

Figure 1. Description of the proposed method

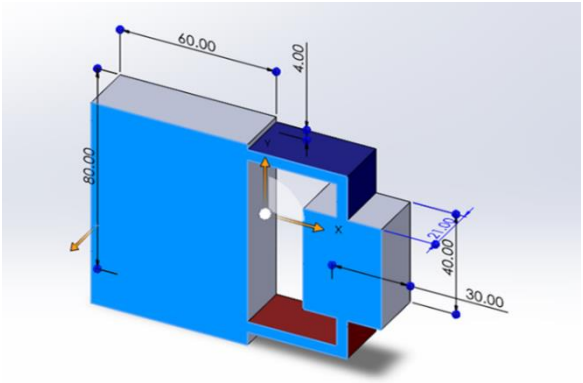

Figure 2. SolidWorks modeling design

Figure 3. Power supply

difference between the n and p junctions. Whenever there is a flow of electricity, heat is absorbed from one side called the cold part, and is released in the other side called the thermal junction (25, 26) as shown in Figure 4 and Table 1.

2. 1. 4. Type of Heat Sink and Fan Heat sinks are an important part of the electrical circuit operation, microelectronics, and thermal management that affect the heat dissipation of the environment. In the present work, the hot side of the Peltier was cooled by copper tubes distributed on the hot wall and connected to aluminum heat sinks. The heat exchanger consists of a finned radiator around a tube charged with a refrigerant, it is a passive heat exchanger designed to has a large surface area so that the air is contacting with the surrounding cooling medium. The flow of the cooling medium through the structure of the heat sink vanes helps to improve the setup and thus decrease the resistance and allow more air to pass through the heat sink. The performance of the heat sink is also governed by the shape and design of its fans, as optimizing the shape and size of the fins helps maximize heat transfer density, as demonstrated in Figure 5. The fan has dimensions of (9 cm * 9 cm * 2.5 cm). These fans operate on a 12V DC voltage and a current rate of 0.24 A, where fans that dissipate hot air.

2. 1. 5. Fluid Pump In this work, a DC water pump was used, which is a low-voltage electric pump, is quiet and uses little power, and is designed to transfer fluids efficiently. It usually features brushless motors, which provide longer life and reliable performance, as shown in Figure 6.

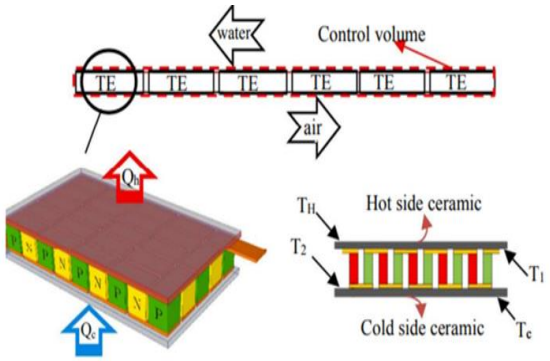

Figure 4. Thermoelectric Cooling Module

TABLE 1. Peltier's Specifications (27)

Model	TEC1-12706
Operating Voltage	12 V (DC)
V_{MAX}	15V (DC)
I_{MAX}	4-6 A
ΔT_{MAX}	67 °C
Dimension	4*4*3.9 cm
Qc (max)	48-72 W

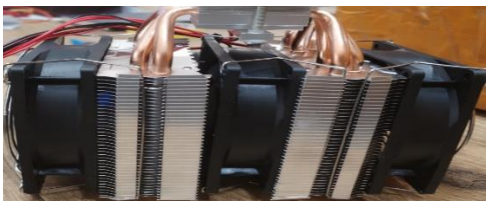

Figure 5. Heat Sink and fans

2. 1. 6. Type of Fluid

2. 1. 6. 1. Distilled Water It is used in many vital and industrial fields because it is free of impurities, salts, and minerals that may affect the performance of processes or the quality of the product.

2. 1. 6. 2. Fluid (Distilled Water and Mono Ethylene Glycol 50:50) It is a widely used industrial chemical compound, also known as ethylene glycol. It is a 50:50 mixture of ethylene glycol with deionized water plus advanced chemical inhibitors and laser dyes to protect against freezing, overheating, rust, and corrosion. It provides effective protection for all metal surfaces in engine radiators and cooling systems, including those made of aluminum. It comes in ready-to-use form.

2. 2. Method and Conditions of the Experiment and Testing When integrating all the components, a functional cooling system is built, as shown in Figure 7, which shows the complete integration of the proposed system. Briefly, the process starts with filling the liquid from the hose into the right storage tank, where the liquid flows through the water pump and enters the water tank. In this tank, the cooling process is mainly performed by the Peltier element. The cooled liquid exits the tank and flows through the heat exchanger (radiator). This cycle runs continuously, with a temperature sensor inside the tank to check the current temperature during system operation. When the temperature of the liquid inside the tank reaches the target temperature, both the pump and fans are turned on to cool the main parts of the electrical

Description product	
Size	8 cm *17 cm
Voltage	12 V DC
Max pump output	120 PSI
Min inlet	30 PSI
Size	8 cm *17 cm

Figure 6. Fluid pump

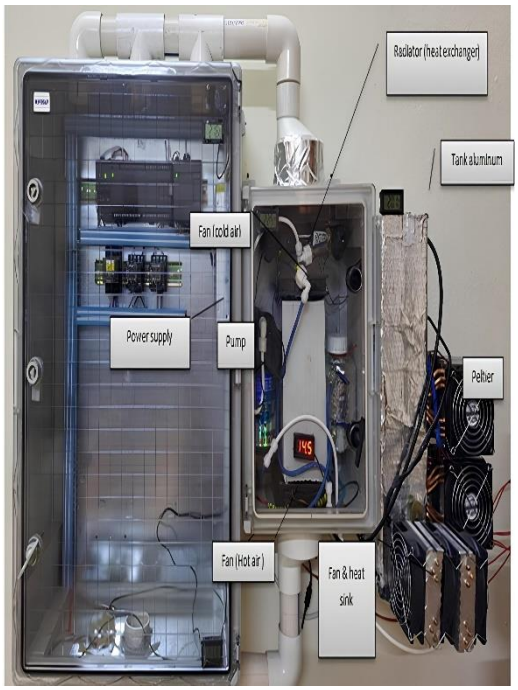

Figure 7. Complete Setup of the Thermoelectric Cooling Chamber with Components

and electronic distribution board. The temperature data is recorded every minute to accurately measure the amount of its decrease.

Using the proposed design, an experiment was conducted to cool 1000 ml of various liquids, including distilled water only and a coolant having mono ethylene glycol and distilled water 50/50, using different numbers of Peltier elements electrically connected in parallel. The target temperature of the liquids was set at 8 °C, and the experiment focused on achieving the main goal of reducing the temperature of the electrical and electronic distribution board to below 50 °C. Readings were recorded at regular intervals of 1 minute to evaluate the efficiency of the system and the extent to which the desired goals were achieved.

2. 3. Performance Indicator This section proposes a simplified ideal equation for thermoelectric coolers, along with various theories to realize their potential. The largest parameters include maximum current, temperature difference between hot and cold junctions, maximum cooling capacity, maximum voltage, and coefficient of performance (COP) analysis, the equations for heating and cooling of TEM are introduced, and then it is explained how the required parameters of those equations can be estimated from the characteristics found in commercial datasheets of TEM. Thermoelectric consists of a series of 2 N pellets of two different semiconductor materials (p and n type), consisting of N thermoelectric couples that are connected electrically in series and thermally in parallel, the air-cooled system is analyzed using a simple method to decide the heat transferred theoretically and experimentally, where the energy consumed by the system and the maximum performance factor can be calculated (28). The amount of heat transferred from the cold surface (qc) of the Peltier unit (TEC) is of immense importance. qc can be calculated by finding the mass flow rate of the fluid, the specific heat capacity of the fluid, and the temperature difference. The temperature difference is the temperature difference between the cooling part of the Peltier unit and the energy consumed by the Peltier unit, four main types of heat transfer processes, including Peltier heating (qph), Peltier cooling (qpc), Joule heating (qj), and Fourier heating (qcon) involved in thermal evaluations of TEM, which are calculated in Equations 1-19.

$$q_{pc} = \alpha_m \times I \times T_c \quad (1)$$

$$\alpha_{ph} = \alpha_m \times I \times T_h \quad (2)$$

$$q_j = R_m \times I^2 \quad (3)$$

$$q_{con} = \frac{1}{\theta m}(T_h - T_c) \quad (4)$$

The energy balance between Equations can calculate the cooling and heating ability of any individual TEM. 1-4 (29).

$$q_c = q_{pc} - \frac{1}{2} q_j - q_{con} = \alpha_m \times I \times Th - \frac{1}{2} R_m \times I^2 - \frac{1}{\theta m}(T_h - T_c) \quad (5)$$

$$q_h = q_{ph} - \frac{1}{2} q_j - q_{con} = \alpha_m \times I \times T_h + \frac{1}{2} Rm \times I^2 - \frac{1}{\theta m}(T_h - T_c) \quad (6)$$

It requires α m (Average Seebeck coefficient of the module), Rm (Electrical resistance of the module), and (thermal resistance of the module), thermal resistance of the module parameters in Equations 5 and 6. N, Imax, Vmax, qmax, ΔTmax, and Tref are specifications usually adopted in commercial datasheets. ΔTmax is the maximum temperature difference (ΔTmax) that can be achieved between the cold and hot sides of a thermally insulated TEC for a specified Tref value (temperature of hot side) Imax and Vmax are the input current and voltage that produce the ΔTmax across a TEC. qmax = is the maximum amount of Heat (W) that can be absorbed in a cold plate of TEC at Imax and ΔT = Zero. It should be noted that qmax is not the largest possible amount of heat that can be managed by TEC. Qmax is only the heat flow corresponding to the current qmax. α m, Rm, and can be evaluated from the equations below, and then can be used in Equations 5 and 6.

$$\alpha_m = \frac{V\,max}{T\,h\,(ref)} \quad (7)$$

$$R_m = \frac{Vmax}{I\,max} \times \frac{(Th - \Delta\,\mathrm{Tmax})}{Th\,(ref)} \quad (8)$$

$$\theta m = \frac{1}{Km} = \frac{\Delta\,T\,max}{V\,\mathrm{max}\,Imax} \times \frac{2\,T\,h}{Th\,(ref) - \Delta T\,max} \quad (9)$$

Other parameters, including surface temperatures, DC voltage, and electrical current, inlet/outlet temperatures, flow rates, and so on, were directly measured during the experiments. Hence, the amount of qc, qh, Tc, and Th for the entire system is evaluated from the following equations, in which the index "i" stands for any individual TEM module. qci and qhi are calculated by Equations 5 and 6 (30).

$$T_c = \frac{\sum_{i=1}^{n} Tci}{6} \quad (10)$$

$$T_h = \frac{\sum_{i=1}^{n} Thi}{6} \quad (11)$$

$$q_c = \sum_{i=1}^{n} q_{ci} \quad (12)$$

$$q_h = \sum_{i=1}^{n} q_{hi} \quad (13)$$

"P_1" is the input energy consumed by TEM and can be found from Equations 14.

$$P_1 = I \times V \quad (14)$$

Heat transfer rate absorbed/dissipated by fluid flows can be calculated from Equations 15 (31).

$$q_{\text{w, cold side}} = \dot{m}_{\text{w, cold side}} \times C_{p,\text{ fluid}} (T_{\text{w, inlet}} - T_{\text{w, outlet}}) \quad (15)$$

In addition to calculating Qair by finding the mass flow rate of air, the specific heat of air, and the temperature difference. Here, the temperature difference is the difference in air temperature and the amount of energy consumed (for fans and pumps) (32).

"P2" is the input energy consumed by (pump + fans) and can be found from Equation 16.

$$P_2 = I \times V \quad (16)$$

Heat transfer rate absorbed and dissipated by fluid flows can be calculated from Equations 17 and 18 (23).

$$\dot{m}_{\text{a(Mass flow rate of air)}} = S \times \rho \times A \quad (17)$$

$$q_r = \dot{m}_r \times C_{p,\text{ air}} (T_{r,\text{ inlet}} - T_{r,\text{ outlet}}) \quad (18)$$

The coefficient of performance of any cooler is defined by Equation 19 (33).

$$\mathrm{COP}_{\text{total}} = \frac{qw + qr}{p1 + p2} \quad (19)$$

3. RESULTS AND DISCUSSION

3. 1. Effect of Distilled Water with Several Peltier Units The cooling performance was studied using different Peltier configurations (1, 2, 3, and 4) with two types of fluids: distilled water only and Coolant containing mono ethylene glycol and distilled water 50:50. The results showed a large variation in cooling rates and system behavior, which affected performance efficiency and energy consumption. When using 1000 ml of distilled water to reduce its temperature from 21.5 °C to 8 °C, it was found that one Peltier unit did not achieve the target even after three hours, as the maximum temperature that could be reached was 12.8 °C, leading to its exclusion. Using two Peltier units, the desired temperature was reached in 40 minutes at a cooling rate of 0.3375 °C/min, demonstrating moderate performance with an energy consumption of 323.712 kJ. Using three units, the time was reduced to 30 minutes at a cooling rate of 0.45°C/min with an increase in energy consumption of 364.176 kJ. With four units, the target temperature was reached in 20 minutes at a faster cooling rate of 0.675 °C/min, with an energy consumption of 323.712 kJ, Figure 8 shows the three cases of distilled water cooling operations.

After achieving the target temperature, the air-cooling system was fully operated inside the electrical and electronic distribution board, which had an initial temperature of 50 °C. With two units, the air temperature dropped to 41.1 °C in the first minute and continued to drop to 33.3 °C in 4 minutes, with an energy consumption of 5.0976 kJ. After that, the temperature remained constant without change. With three units, the air temperature dropped sharply in the first minute to 40.1 °C, then gradually to 30.3 °C in 5 minutes, with an energy consumption of 6.372 kJ. With four units, the air temperature dropped significantly from 50 °C to 37 °C in the first minute, and continued to 30.1 °C in 8 minutes, with an energy consumption of 10.1952 kJ. Figure 9 shows the three cases of cooling operations of the electrical and electronic distribution board.

When calculating the total energy consumption, two Peltier units consumed 328.809 kJ, while three units consumed 370.548 kJ, an increase of 12.693%. In contrast, four units consumed 333.9072 kJ, a decrease of

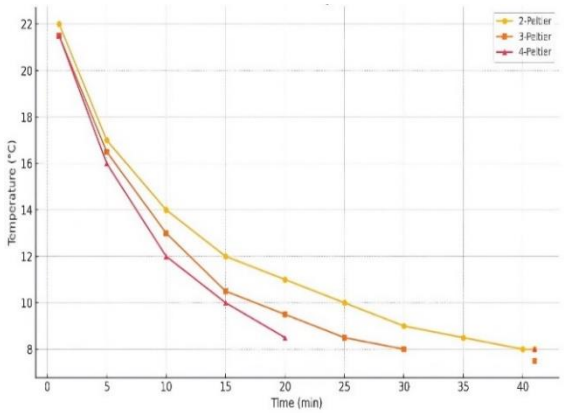

Figure 8. Effect of Time on Distilled Water Using 2, 3, and 4 Peltier Modules

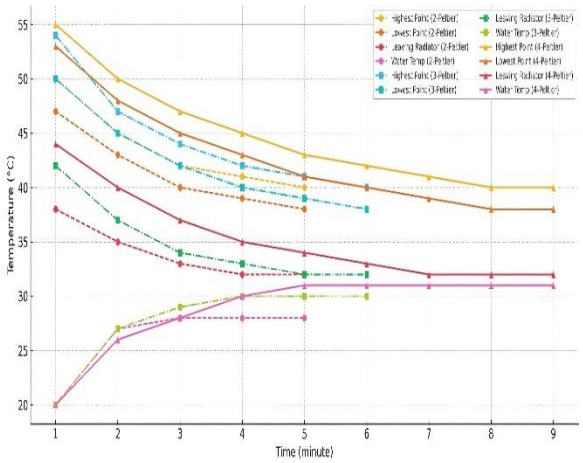

Figure 9. Effect of Time and Location on Temperature (Combined Peltier Units)

10.97% compared to three units. Figure 10 shows the relationship between energy consumption and the number of thermoelectric cooling units in terms of time.

The experiments showed a clear effect of the number of Peltier units on cooling rates and energy efficiency. Using two units, the water temperature decreased to 8 °C in 40 minutes and the air temperature to 33.3 °C with a coefficient of performance of 0.5792. Using three units, the performance improved, as the target temperature was achieved in 30 minutes with the air temperature decreased to 30.3 °C and the coefficient of performance increased to 0.6685. When using four units, the desired temperature was reached within 20 minutes and the air temperature dropped to 30.1°C, with a performance coefficient of 1.16496. These results confirm that increasing the number of Peltier units improves the cooling speed and performance efficiency, while taking into account the increased power consumption to achieve the desired balance.

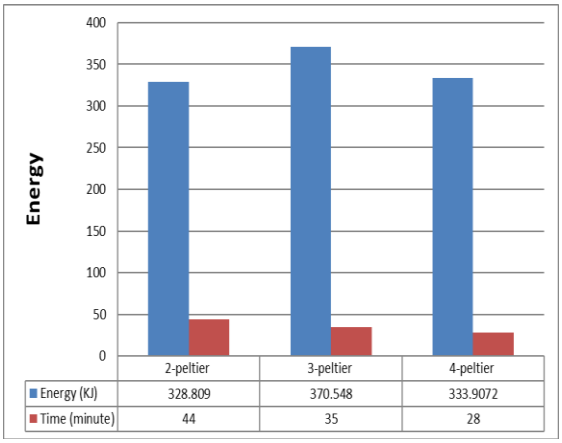

Figure 10. Relationship of energy consumed with the number of thermoelectric cooling units in terms of time (distilled water)

3. 2. Effect of Coolant Having (Distilled Water and Mono ethylene glycol 50:50) with the Number of Peltier Units

After draining the distilled water, the experiment was repeated using mono ethylene glycol and the same amount of liquid used previously (1000 ml) to reduce its temperature from 21.5 °C to 8 °C. It was found that a single Peltier unit did not achieve the target temperature even after three hours, as the maximum temperature reached was 10 °C, which led to its exclusion. Using two Peltier units, the desired temperature was reached in 23 minutes at a cooling rate of 0.586 °C/min, with an energy consumption of 186.1344 kJ. Using three units, the time was reduced to 17 minutes at a cooling rate of 0.7941 °C/min, with an increase in energy consumption of 206.346 kJ. With four units, the target was achieved in 14 minutes at a high cooling rate of 0.9642 °C/min, with an energy consumption of 226.5984 kJ. Figure 11 shows the three cases of cooling processes (distilled water and Mono Ethylene Glycol 50:50).

After achieving the target temperature, the entire air-cooling system inside the electrical and electronic distribution board was turned on, the first temperature of which was 50 °C. With two units, the air temperature dropped to 36.8 °C in the first minute, and later reached 31.3 °C in 7 minutes, and consumed 7.6464 kJ of energy.

With three units, the air temperature dropped sharply to 36.5 °C in the first minute, and later reached 29.4 °C in 11 minutes, and consumed 12.744 kJ of energy. With four units, the air temperature dropped to 35.1°C in the first minute, then to 26.9°C in 18 minutes, consuming 22.9392 kJ of energy. Figure 12 shows the three cases of cooling operations of the electrical and electronic distribution board.

When calculating the total energy consumption, two Peltier units consumed 193.780 kJ, while three units consumed 219.09 kJ, an increase of 13.0612%. In contrast, four units consumed 249.537 kJ, an increase of

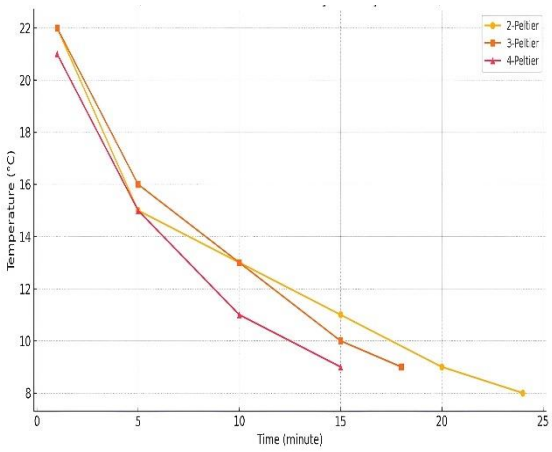

Figure 11. Effect of Time on Temperature (Distilled Water and Mono Ethylene Glycol 50:50)

13.897% compared to three units. Figure 13 shows the relationship between energy consumption and the number of thermoelectric cooling units in terms of time.

The experiments showed a clear effect of the number of Peltier units on cooling rates and energy efficiency. With two units, the water temperature dropped to 8°C in 23 minutes and the air temperature to 30.3°C with a coefficient of performance of 1.5402. With three units, performance improved, with the target temperature achieved in 17 minutes with the air temperature dropping to 29.4°C and a coefficient of performance increasing to 2.2231. With four units, the target temperature was achieved in 14 minutes with the air temperature dropping to 26.9°C, with a coefficient of performance of 3.75811. These results confirm that increasing the number of Peltier units improves cooling speed and performance efficiency, considering the increased energy consumption to achieve the desired balance.

3. 3. Cooling System Performance Using Distilled Water Compared to (Distilled Water and Mono ethylene glycol 50:50)

Overall, performance than Coolant, having mono ethylene glycol, especially when measuring cooling rate, performance factor, and energy consumption. Using a solution containing mono ethylene glycol has a lower specific heat capacity than water, but it offers greater thermal stability and better resistance to boiling and freezing. This combination provides a balance between rapid heat absorption and its ability to transfer heat to the Peltier cooling unit without significant loss. This helps reduce heat loss and stabilize system performance. Increasing the number of Peltier units improves cooling speed and lowers air temperatures, but keeps average performance efficiency, except when using four units, in addition to noting that the energy consumption for using three Peltier units is higher than using four units with a low performance factor. In terms of overall performance using mono ethylene glycol, mono ethylene glycol outperforms pure water in terms of cooling speed, energy efficiency (performance factors), and energy consumption, as shown in Figure 14.

Increasing the number of Peltier units with mono ethylene glycol significantly improves performance, making it the preferred choice for applications that require fast and efficient cooling, as shown in Figure 15.

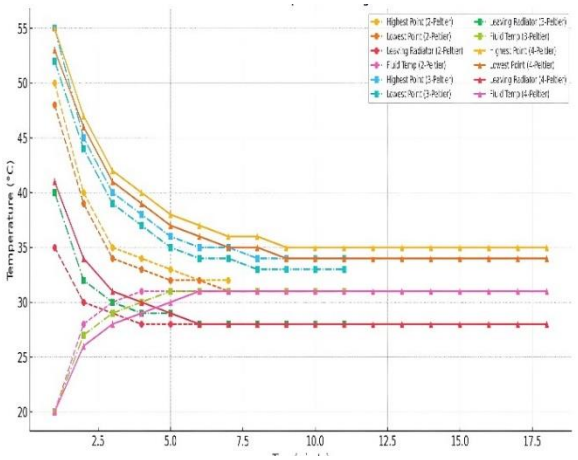

Figure 12. Effect of Time and Location on Temperature using 2, 3, and 4 Peltier Units.

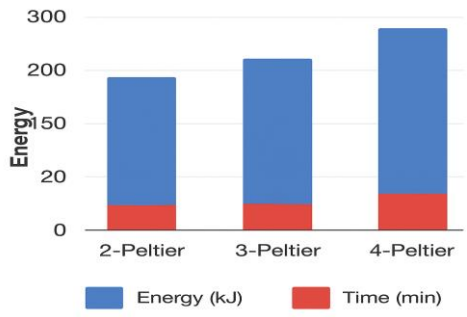

Figure 13. Relationship of energy consumed with the number of thermoelectric cooling units in terms of time (Distilled Water +Mono ethylene glycol 50/50)

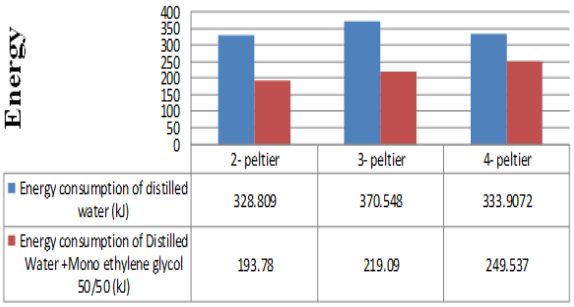

	2- peltier	3- peltier	4- peltier
Energy consumption of distilled water (kJ)	328.809	370.548	333.9072
Energy consumption of Distilled Water +Mono ethylene glycol 50/50 (kJ)	193.78	219.09	249.537

Figure 14. Relationship of energy consumption to the number of thermoelectric cooling units in terms of fluid type

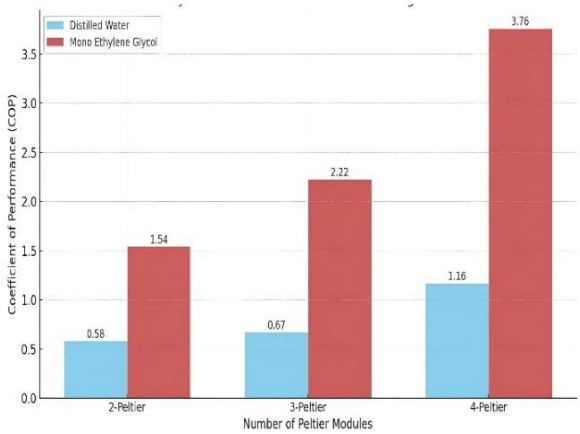

Figure 15. Relationship of the coefficient of performance with the number of thermoelectric cooling units in terms of fluid type

4. CONCLUSIONS AND FUTURE PERSPECTIVES

In this study, the use of a 50:50 mixture of distilled water and mono ethylene glycol proved superior cooling efficiency and energy consumption compared to distilled water, resulting in faster temperature drops and higher performance factors in all tested configurations. These findings underscore the significant impact that coolant choice has on the thermal performance of the system. Furthermore, the results show that increasing the number of Peltier units enhances cooling rates and reduces the time needed to reach target temperatures, highlighting the need for optimization to balance cooling ability with energy efficiency. These results are consistent with findings, who proven that increasing the number of TEC modules improves the efficiency of the cooling system and the COP up to a certain point, after which the benefits decline. This agreement with earlier studies reinforces the current study's findings, which emphasize the need to balance the number of modules and the COP. The cooling process showed two distinct phases: a rapid first temperature drops within the first minute, followed by a more gradual decline. This pattern was consistent across all configurations, emphasizing the critical role of first cooling rates in deciding the overall performance of the system. Systems using a 50:50 mixture of mono ethylene glycol and distilled water consistently outperformed those using distilled water alone, particularly when using four Peltier modules, where the coefficient of performance peaked at 3.75811. The study underscores the importance of perfecting both the coolant and the system configuration to achieve the desired thermal performance. Based on these results, a 50:50 mixture of mono ethylene glycol and distilled water is recommended for applications requiring higher efficiency and faster cooling. However, if cost constraints or reduced system complexity are prioritized, distilled water may be a suitable alternative, provided the number of Peltier modules is increased to compensate for the reduced performance.

The Peltier effect cooling system exhibited enhanced performance using a greater quantity of TEC modules and a 50:50 blend of distilled water and ethylene glycol; nonetheless, significant concerns remain inadequately solved. The study overlooked the issues associated with heat dissipation from the hot side of many Peltier modules, a characteristic that can considerably affect long-term performance and stability. Emphasis was placed on the cold side; yet, from a financial standpoint, There is a significant difference. The produced chiller is priced at $40, but traditional chillers have a market worth over $200. This is an essential analysis to evaluate economic viability as the quantity of modules escalates. Consequently, more research must concentrate on alleviating these constraints to enhance reproducibility, broaden the range of application, and attain an improved equilibrium between performance and energy economy.

Future research should focus on exploring alternative coolants, advanced thermal management systems, and conducting detailed energy consumption analyses to further enhance system efficiency. Additionally, further optimization of system configurations could offer added insights into improving the balance between performance and energy usage.

5. REFERENCES

1. Lucas S, Bari S, Marian R, Lucas M, Chahl J. Cooling by Peltier effect and active control systems to thermally manage operating temperatures of electrical Machines (Motors and Generators). Thermal Science and Engineering Progress. 2022;27:100990. 10.1016/j.tsep.2021.100990
2. Raj YJ, Bejaxhin ABH, Rajkumar S, Selvarajan L, Premkumar R. Enhancing Efficiency in Thermoelectric Removal Process: A Comprehensive Study on P/M-Made Al-Cu-ZrB2 Nano-Composite Electrodes on SS205 Alloy. Int J Eng. 2025;38:570-9. 10.5829/ije.2025.38.03c.06
3. Zhou Y, Yu J. Design optimization of thermoelectric cooling systems for applications in electronic devices. International journal of refrigeration. 2012;35(4):1139-44.
4. Zhu L, Tan H, Yu J. Analysis on optimal heat exchanger size of thermoelectric cooler for electronic cooling applications. Energy conversion and management. 2013;76:685-90. 10.1016/j.enconman.2013.08.014
5. Shourideh AH, Ajram WB, Al Lami J, Haggag S, Mansouri A. A comprehensive study of an atmospheric water generator using Peltier effect. Thermal Science and Engineering Progress. 2018;6:14-26. 10.1016/j.tsep.2018.02.015
6. Huang L, Zheng Y, Xing L, Hou B. Recent progress of thermoelectric applications for cooling/heating, power generation, heat flux sensor and potential prospect of their integrated applications. Thermal Science and Engineering Progress. 2023;45:102064. https://doi.org/10.1016/j.tsep.2023.102064
7. Baru S, Bhatia S, editors. A review on thermoelectric cooling technology and its applications. IOP Conference Series: Materials Science and Engineering; 2020: IOP Publishing. 10.1088/1757-899X/912/4/042004
8. Tian M-W, Moria H, Mihardjo LW, Kaood A, Dizaji HS, Jermsittiparsert K. Experimental thermal/economic/exergetic evaluation of hot/cold water production process by thermoelectricity. Journal of Cleaner Production. 2020;271:122923. 10.1016/j.jclepro.2020.122923
9. Liu H, Li B, Hua L, Wang R. Designing thermoelectric self-cooling system for electronic devices: Experimental investigation and model validation. Energy. 2022;243:123059. https://doi.org/10.1016/j.energy.2021.123059
10. Abdulghani ZR. A novel experimental case study on optimization of Peltier air cooler using Taguchi method. Results in Engineering. 2022;16:100627. https://doi.org/10.1016/j.rineng.2022.100627
11. Dizaji HS, Pourhedayat S, Anqi AE, Aldawi F, Alsenani TR, Moria H. Enhanced Peltier refrigerator using an innovative hot-side heat-rejection mechanism; Experimental study under both transient and steady-state conditions. Energy. 2024;309:133132. https://doi.org/10.1016/j.energy.2024.133132

12. Wu Y, Zhang H, Zuo L. Thermoelectric energy harvesting for the gas turbine sensing and monitoring system. Energy conversion and management. 2018;157:215-23. 10.1016/j.enconman.2017.12.009
13. Phan N, Dong P, Jatti V, Tam N, Minh N, Ly N, et al. Influence of process parameters on the microstructural characteristics and mechanical properties of recast layer thickness coating on die steel machined surface after electrical discharge machining. International Journal of Engineering, Transactions B: Applications. 2021;34(5):1297-304. https://doi.org/10.5829/ije.2021.34.05b.24
14. Erro I, Aranguren P, Martinez A, Astrain D. Development and Experimental Validation of a Two-stage Thermoelectric Heat Pump Computational Model for Heating Applications. Thermal Science and Engineering Progress. 2024;53:102721. 10.1016/j.tsep.2024.102721
15. Ang EY, Ng PS, Soh CB, Wang PC. Multi-stage thermoelectric coolers for cooling wearables. Thermal science and engineering progress. 2022;36:101511. https://doi.org/10.1016/j.tsep.2022.101511
16. Liao T, Xiao J, Xu Y, Lin B. Thermal-electrical coupling properties and optimum analysis of a vehicle exhaust driven thermoelectric system. Thermal Science and Engineering Progress. 2021;25:101040. 10.1016/j.tsep.2021.101040
17. Boudreaux P, Hall C, Gluesenkamp KR, Karman S, Willocks J, Patel V, et al. Fast-airflow tumble clothes dryer with small thermoelectric heat pump: Experimental evaluation. Thermal Science and Engineering Progress. 2024;55:102960. https://doi.org/10.1016/j.tsep.2024.102960
18. Mirmanto M, Syahrul S, Wirawan M, Sayoga IMA, Wijayanta AT, Mahyudin I. Performance of a thermoelectric powered by solar panel for a large cooler box. Advances In Science, Technology And Engineering Systems Journal. 2020;5:325-33. https://dx.doi.org/10.25046/aj040533
19. Mushonga RN, Madoro TF, Gudukeya L, Chikuku T, Chingosho H. Integration and Analysis of Heat Exchangers and Refrigeration Units for Outdoor Drinking Water Through Industrial Secondment at Pretoria Portland Cement.
20. Adref K, Alhashmi ZA, Mennad A, Omar AS, AlAkbari AS, AlAkbari AS, et al. Performance of Water Thermoelectric Cooler Connected in Series: An Experimental Study. https://doi.org/10.5281/ZENODO.8395021
21. Ab Rahman R, Mohamad MAH, Kaamin M, Batcha MFM, Mazlan MDA, Rosli ML, et al. Experimental study of peltier-based thermoelectric cooling box system. Journal of Advanced Research in Applied Mechanics. 2022;94(1):1-6. https://doi.org/10.37934/aram.94.1.16
22. Redho A, Irawan D, Julianto E, Fadhilah R. Effect of Cooling Using Added Peltier Ice Pack on Cool Box. International Journal of Mechanical Engineering. 2023;8.
23. Harsito C, Putra MRA, Purba DA, Triyono T. Mini review of thermoelectric and their potential applications as coolant in electric vehicles to improve system efficiency. 2023. https://doi.org/10.5109/6782150
24. Garrido J, Manzanares JA. Heat and work fluxes in thermoelectric coolers. Thermal Science and Engineering Progress. 2021;22:100817. 10.1016/j.tsep.2020.100817
25. Pourhedayat S. Application of thermoelectric as an instant running-water cooler; experimental study under different operating conditions. Applied energy. 2018;229:364-74. https://doi.org/10.1016/j.apenergy.2018.08.009
26. Jubayer MR. The heat exchange Intensification in Nano-homo junction semiconductor materials. Engineering and Technology Journal. 2015;33(5):819-29. https://doi.org/10.30684/etj.33.5b.7
27. Numan NF, Mahdi MM, Ahmed MK. A Comparative Experimental Study Analysis of Solar Based Thermoelectric Refrigerator Using Different Hot Side Heat Sink. Engineering and Technology Journal. 2022;40(01):90-8. http://doi.org/10.30684/etj.v40i1.2058
28. Alomair M, Alomair Y, Mahmud S, Abdullah HA. Theoretical and experimental investigations of solar-thermoelectric air-conditioning system for remote applications. Journal of Thermal Science and Engineering Applications. 2015;7(2):021013. 10.1115/1.4029678
29. Hadidi A. Comprehensive investigation of two-stage thermoelectric cooler parameters on its performance. Arabian Journal for Science and Engineering. 2024;49(8):10927-42. https://doi.org/10.1007/s13369-023-08526-w
30. Lundgaard C, Sigmund O. Design of segmented thermoelectric Peltier coolers by topology optimization. Applied Energy. 2019;239:1003-13. 10.1016/j.apenergy.2019.01.247
31. Yang X, Yang F, Yang F. Thermo-economic performance limit analysis of combined heat and power systems for optimal working fluid selections. Energy. 2023;272:127041. https://doi.org/10.1016/j.energy.2023.127041
32. Salman MM, Mahdi MM, Ahmed MK. Optimization of solar powered air conditioning system using alternating Peltier power supply. Bulletin of Electrical Engineering and Informatics. 2024;13(1):20-30. https://doi.org/10.11591/eei.v13i1.5864
33. Ismail FB, Kazem HA, Suhailie MAB, Chaichan MT. Climate Change Mitigation Through Innovative Solar-Powered Car Ventilation System Design and Evaluation for the Malaysian Context. 2024. 10.5109/7236837

COPYRIGHTS
©2026 The author(s). This is an open access article distributed under the terms of the Creative Commons Attribution (CC BY 4.0), which permits unrestricted use, distribution, and reproduction in any medium, as long as the original authors and source are cited. No permission is required from the authors or the publishers.

Persian Abstract

چکیده

اثربخشی رویه‌های مدیریت حرارتی، نکته‌ای حیاتی برای حفظ عملکرد و طول عمر بردهای الکترونیکی و الکتریکی محسوب می‌شود. یکی از راه‌حل‌هایی که توجه محققان و مؤسسات صنعتی را به خود جلب کرده است، استفاده از خنک‌کننده ترموالکتریک (TEC) است که با نام Peltier نیز شناخته می‌شود و از دو ماده نیمه‌هادی برای پشتیبانی امیدوارکننده از خنک‌کننده هوای فن‌دار سنتی ساخته شده است. با این حال، بررسی دقیق‌تری از تأثیر استفاده از فناوری Peltier در شرایط تغییر عملیاتی و طراحی مورد نیاز است. در همین راستا، این مطالعه یک مدل نمونه اولیه تجربی را برای تجزیه و تحلیل تأثیر تعداد مختلف واحدهای Peltier (۱ تا ٤) و مبردهای مختلف (فقط آب مقطر، مونو اتیلن گلیکول و آب مقطر ۵۰:۵۰) بر عملکرد پیشرفت حرارتی از نظر جذب حرارتی و مصرف انرژی بررسی می‌کند. تحت عملیات واقعی متغیر، نتیجه نشان داد که مخلوط (آب مقطر + مونو اتیلن گلیکول ۵۰:۵۰) عملکرد بهتری نسبت به آب مقطر به تنهایی دارد، کاهش دمای کابینت الکتریکی سریع‌تری را به دست آورد و عملکرد خنک‌کننده (COP) بالاتری را در تمام مدل‌های پیکربندی Peltier به دست آورد. بالاترین ضریب عملکرد (COP) معادل ۳.۷۵ با استفاده از چهار واحد پلتیر با مخلوطی از مونو اتیلن گلیکول ثبت شد. این یافته‌ها بر اهمیت انتخاب بهترین مبرد و پیکربندی سیستم برای مدیریت حرارتی کارآمد تأکید دارند و راه را برای پیشرفت‌های آینده در فناوری‌های خنک‌کننده ترموالکتریک هموار می‌کنند.

IJE TRANSACTIONS B: Applications Vol. 39, No. 08, (August 2026) 1855-1864

International Journal of Engineering

Journal Homepage: www.ije.ir

Effects of Surface-level Defects on Tensile and Fatigue Strength of Spot Weld Bonding – Three-sheet Steel

K. Reza Kashyzadeh*[a], M. A. Ganjabi[b], S. Moghbeli[c], A. N. Ramzi Hassan[d], S. V. Khlopkov[a], M. Laad[e]

[a] *Department of Transport Equipment and Technology, Academy of Engineering, RUDN University, 6 Miklukho-Maklaya Street, Moscow, Russian Federation*
[b] *School of Mechanical Engineering, Sharif University of Technology, Tehran, Iran*
[c] *Faculty of Mechanical and Energy Engineering, Abbaspour College of Technology (ACT), Shahid Beheshti University (SBU). Tehran, Iran*
[d] *Institute of Innovation Engineering Technology, RUDN University, 6 Miklukho-Maklaya Street, Moscow, Russian Federation*
[e] *Department of Applied Sciences, Symbiosis Institute of Technology, Symbiosis International University, Pune, India*

P A P E R I N F O

Paper history:
Received 25 May 2025
Received in revised form18 September
Accepted 25 September 2025

Keywords:
Resistance Spot Welding Joint of Multiple Sheets
Resistance Spot Welding Defects
Edge Defect
Intersection Defect
Static Strength
Fatigue Behavior

A B S T R A C T

The Resistance Spot Welding (RSW) technique is a prevalent method for joining thin metal sheets, particularly in transportation-related industries such as automotive and aerospace. A key advantage of RSW lies in its efficiency and the absence of additional materials, which contribute to structural weight reduction. In this study, the influence of visible defects (i.e., edge and intersection) on the mechanical behavior of triple-layer welded joints under static and fatigue loads is analyzed. To this end, a combination of laboratory testing and Finite Element Modeling (FEM) was utilized. The FEM approach was validated using experimental axial fatigue data (high-cycle S-N curves). Unlike prior research, this investigation incorporates such as surface-level defects into the FEM framework for the first time. Simulation results showed that a 0.2 mm edge defect leads to tensile and fatigue strength decrease of 5.4 % and 13.72 %, respectively, while a 0.6 mm intersection defect for the static and fatigue strengths causes reduction of 9.6 % and 54 %, respectively. These findings highlight the fatigue strength's higher sensitivity to such defects compared to tensile strength.

***doi**: 10.5829/ije.2026.39.08b.07*

Graphical Abstract

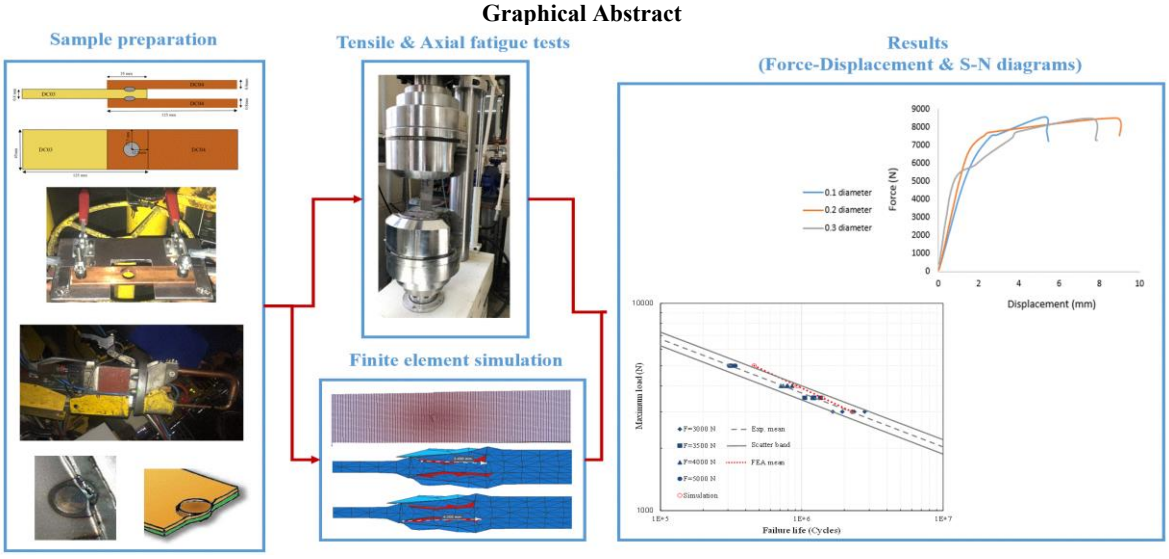

*Corresponding Author Email: reza-kashi-zade-ka@rudn.ru (K. Reza Kashyzadeh)

Please cite this article as: Reza Kashyzadeh K, Ganjabi MA, Moghbeli S, Ramzi Hassan AN, Khlopkov SV, Laad M. Effects of Surface-level Defects on Tensile and Fatigue Strength of Spot Weld Bonding – Three-sheet Steel. International Journal of Engineering, Transactions B: Applications. 2026;39(08):1855-64.

1. INTRODUCTION

Various resistance welding methods, such as RSW, Resistance Seam Welding (RSEW), and Projection Welding (PW), are implemented across transportation sectors including automotive, shipbuilding, aerospace, and helicopter manufacturing (1, 2). Among these, RSW is especially popular due to its efficiency, minimal cost, and industrial suitability (3). RSW operates by heating metal sheets to a plastic state using an electric current and applying pressure to form a compact weld zone known as the nugget (4). Despite its advantages, RSW is prone to manufacturing defects, which compromise joint durability (5). Focusing on defects and solutions is beyond the scope of this paper. The focus here is on evaluating how defects affect joint strength. Undersized welds, characterized by a nugget diameter smaller than the optimal threshold (denoted by "IM"), are a common defect type that significantly compromises joint performance under various loading conditions (6). RSW defects can be detected using both Destructive Testing (DT) and Non-Destructive Testing (NDT) methods, such as ultrasonic inspection. Today, a combination of different methods is used to defect detection. For example, Liu et al. (7) presented a novel faster R-CNN model to detect RSW defects through visual inspection. They reported that they could process each image at a speed of 15 milliseconds using this model. The accuracy of the presented model was also stated to be more than 90%. However, in industrial settings, DT is primarily used to validate the accuracy of NDT interpretations, as DT renders the component unusable. Hence, the identification, characterization, and dimensional assessment of weld defects is critical to understanding their impact on structural performance under operational conditions.

Summerville et al. (8) introduced an advanced technique for estimating nugget diameter using dynamic resistance curves combined with Principal Component Analysis (PCA), Auto-Correction (AC), and Multi-Linear Regression (MLR), which outperformed conventional C-scan methods in accuracy. Mirzaei et al. (9) highlighted the dominant influence of welding current on nugget formation in galvanized steel sheets and observed a positive correlation between nugget size and joint strength up to a limit, beyond which performance declined (10). Moreover, Eisazadeh et al. (11) reported in their study that various parameters affect the nugget diameter, but among them, the highest percentage by weight belongs to the electric current. However, accurate RSW assessment remains challenging and results in additional costs and production steps. Current inspection methods, which rely on random inspections after vehicles leave the body-in-white (BIW), often result in significant time wastage and emphasize the need for improved quality assessment. To overcome this issue, researchers have turned to data analytics approaches as well as machine learning techniques to predict the weld quality level before the vehicle body is completed. Recently, the performance of various algorithms including Artificial Neural Network (ANN), Convolutional Neural Network (CNN), Long Short-Term Memory (LSTM), Random Forest Classifier (RFC), and Extreme Gradient Boosting (XGBoost) has been investigated and it is shown that with the help of such algorithms, the accuracy of RSW defect prediction can be increased to 97.1% (12).

A new FEM based on Mechanical-Electrical-Thermal (MET) coupling has been used to investigate the weld core diameter and consequently the weld strength of two-sheet 304 steel (13). Farrahi et al. (14) utilized various numerical methods to predict the fatigue life of automotive spot welds, revealing that although modal dynamic analysis is significantly more time-consuming than the inertial relief approach, both yield comparable accuracy under low-frequency loading. Pan and Sheppard (15) employed FEM to predict fatigue behavior in spot welds of sheets with varying thicknesses, while Reza Kashyzadeh and Ghorbani (16) proposed an empirical model relating High-Cycle Fatigue (HCF) performance to chemical composition in three-sheet, low-carbon spot welds. Deshmukh and Kharche (17) used the response surface methodology to optimize the spot welding process parameters including pressure time, welding time, holding time, and electrode force to improve the joint quality of 316L sheets and ultimately their strength under static and cyclic loading. They reported that the most optimal case included 33, 12, and 9 cycles for pressure, welding, and holding times, respectively. Also, the electrode pressure was proposed to be 2.8 bar.

Residual stress distribution in RSW joints has also been modeled using FEM and validated against X-ray diffraction data (18). Findings indicate that peak residual stress occurs at the weld center and decreases toward the periphery. Numerous studies affirm that residual stress distribution, including its location and magnitude, is a key parameter in fatigue life estimation (19, 20). Pal and Bhowmick (21) compared DT (tensile testing) and NDT (peel testing) on DP780 steel sheets, concluding that tensile testing yields superior precision. They also reported that modifying current and time parameters significantly affects Low-Cycle Fatigue (LCF) behavior. Xiao et al. (22) found that refined microstructures in the fusion zone improve fatigue resistance compared to coarser structures due to twin formation and multiple pyramidal slips, which help reduce stress concentration.

Ordoñez et al. (23) investigated stress concentration effects on crack initiation in DP980 steel, finding that the number, arrangement, and spacing of sopt welds are critical factors affecting fatigue life (24, 25). Vural et al. (26) examined how nugget diameter impacts fatigue performance in dissimilar joints of AISI 304 stainless steel and galvanized steel. Recent work by Farrahi et al. (6) combined finite element and multi-body dynamic

simulations to evaluate the impact of vehicle speed and road surface irregularities on weld failure across vehicle structures. They observed that variations in nugget diameter could alter fatigue life by up to 100%. Furthermore, their latest research explored the effects of electrode geometry on residual stress distribution and subsequent fatigue performance in three-sheet joints (27). Previous research has extensively focused on fatigue behavior in defect-free welds or welds with insufficient nugget formation. In addition, with the aim of enhancing fatigue behavior, many efforts have been made to optimize RSW process parameters through traditional, classical, and modern techniques (28). The present study uniquely investigates the impact of visible surface defects, a category traditionally considered non-critical, on fatigue performance. Based on industrial experience, the authors argue that such defects, edge and intersection, should be reclassified as quasi-strength defects due to their measurable influence on joint strength. This hypothesus is explored through a collaborative effort between academia and a major automotive manufacturer. Therefore, the primary purpose of this study is to quantitatively evaluate the effects of edge and intersection defects on the static tensile strength and high-cycle fatigue behavior of three-sheet steel spot weld bonding joints. To achieve this, a combined experimental and numerical approach was employed. Firstly, experimental S-N curves for healthy joints were established to serve as a validation benchmark. Subsequently, an advanced finite element model, incorporating Electrical-Thermal-Mechanical coupling and metallurgical phase transformation, was developed and validated. This validated model was then used to systematically simulate the mechanical response of joints with varying severities of edge and intersection defects under both static and cyclic loading conditions. Ultimately, this work aims to provide robust data to support a re-evaluation of quality control standards for visible defects in automotive spot welding.

In the following, a schematic diagram of the spot weld categorized examined in the current study, including health spot weld and the desired apparent defects, is shown in Figure 1.

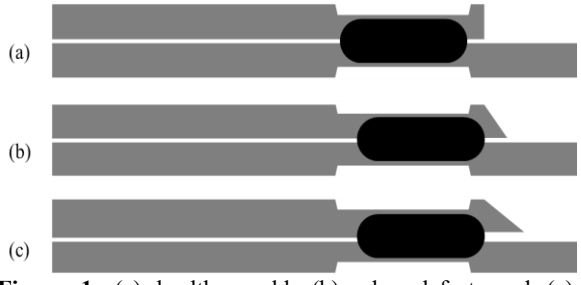

Figure 1. (a) healthy weld, (b) edge defect, and (c) intersection defect

According to the manufacturer's data (e.g., sheet material, sheet thickness, welding parameters, etc.), the nugget diameter for a healthy weld is 4 mm (Figure 1(a)). The difference between desired defects is that if the edge is between zero and 1/3 of the nugget diameter, it is called an edge defect (Figure 1(b)), and if this size is more than 1/3 of the nugget diameter, it is called intersection defect (Figure 1(c)).

2. MATERIALS AND SPECIMEN PREPARATION

According to prior investigations (3, 29) and internal data provided by the automotive manufacturer, the most structurally sensitive spot weld in a three-sheet automotive joint comprises dissimilar low-carbon steel grades. Specifically, two DC04 sheets are placed at the top and bottom of the joint and the DC03 sheet is placed between them. However, the thickness of all sheets is the same and equal to 0.8 mm. Figure 2(a) shows the sheets' dimensions and their arrangement for a healthy spot weld joint. To prepare the specimens uniformly, a fixture designed and fabricated in previous work was used (Figure 2(b)).

The engineering specifications of the sheets used in this study, DC04, and DC03, are given in Tables 1 and 2, respectively. All of this information was obtained in a laboratory setting (e.g., tensile test, metallographic examination of microstructure, and quantometric analysis) on the factory production line before being used.

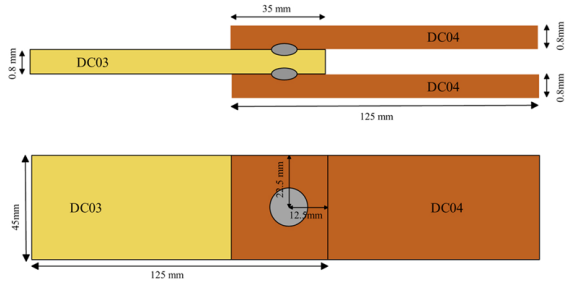

(a)

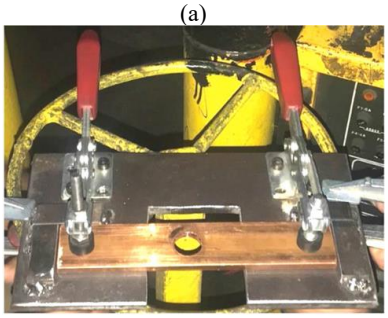

(b)

Figure 2. (a) Size and layout of three-sheet spot-welded joint in a free-defect state and (b) Fixture used to prepare a healthy connection

The welding parameters were considered to create a healthy three-sheet spot-welded joint as it is done in the automotive industry (Table 3). Also, the standard electrode F0-16-20-8, as shown in Figure 3(a), was used for this purpose (27). Figure 3(b) demonstrates the manual welding equipment used in this industry. The frequency was 50 Hz, and the electric current was alternating.

TABLE 1. Engineering specifications for DC04 low-carbon steel

Chemical composition	
Base	Fe
C	0.046 %
Si	0.014 %
Mn	0.201 %
P	0.007 %
S	0.004 %
Al	0.036 %
Mechanical properties	
Yield Strength: YS	169 MPa
Ultimate Tensile Strength: UTS	307 MPa
Elongation: E	38 %
Microstructure features	
Metallic phase	Ferrite
Average grain diameter	31.8 µm

TABLE 2. Engineering specifications for DC03 low-carbon steel

Chemical composition	
Base	Fe
C	0.047 %
Si	0.006 %
Mn	0.199 %
P	0.007 %
S	0.004 %
Al	0.037 %
Mechanical properties	
Yield Strength: YS	178 MPa
Ultimate Tensile Strength: UTS	325 MPa
Elongation: E	41 %
Microstructure features	
Metallic phase	Ferrite
Average grain diameter	30.2 µm

TABLE 3. Default factory-configured parameters for the spot welding process aimed at producing a defect-free joint (28)

Welding parameters	**Value [Unit]**
Force	365 [N]
Current	11.5 [KA]
Squeeze time	25 [Cycle]
Upslope	3 [Cycle]
Welding time	12 [Cycle]
Hold time	9 [Cycle]

3. EXPERIMENTAL PROCEDURE

As outlined earlier, a weld is considered structurally sound when the minimum nugget diameter reaches at least 4 mm. In a three-sheet spot weld configuration, two individual nuggets are formed: one between the top and middle layers and another between the middle and bottom layers. Hence, a 4 mm threshold is set as the minimum acceptable nugget diameter. Although some previous studies overlook the distinction between these two nuggets and report only their average, this investigation accounts for both individually.

Defect-free welded specimens were initially fabricated and then sectioned to enable cross-sectional analysis. The nugget diameters were measured using Optical Microscopy (OM), yielding an average size of

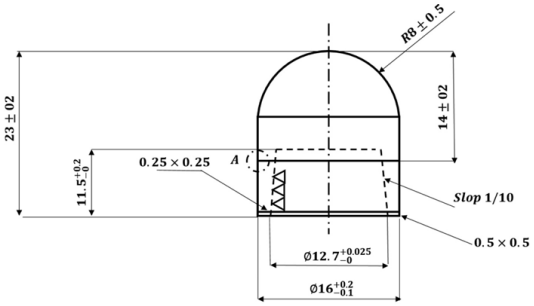

(a)

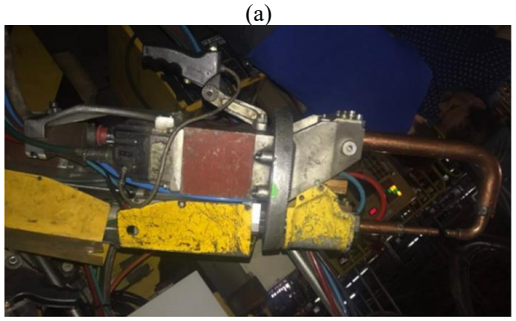

(b)

Figure 3. (a) Geometry and dimensions (mm) of F0-16-20-8 standard electrode (27) and (b) Manual welding equipment used in the current study

approximately 5.55 mm, well above the required minimum of 4mm. Consequently, the welding settings recommended by the manufacturer were adopted for the preparation of all specimens. A total of 28 healthy three-sheet spot-welded specimens were fabricated. Fatigue testing was conducted using a servo-hydraulic axial loading system with a 25-ton capacity. To maintain uniform thickness and prevent bending during testing, steel plates were added symmetrically to both sides of the specimen. This ensured a consistent grip thickness of 4 mm at the clamping region, according to ISO 14324 guidelines (30). All fatigue tests were carried out at room temperature using a force-controlled, constant amplitude protocol. The loading followed a sinusoidal waveform with a force ratio (R) near zero and a frequency of 10 Hz. Multiple loading levels were applied, and for each level, seven identical specimens were tested to account for potential scatter and improve the statistical robustness of the results. The mean number of cycles to failure from these seven specimens was taken as the representative fatigue life for that force level. Ultimately, a force-life curve in the HCF regime was established for the healthy three-sheet spot-welded configuration.

4. FINITE ELEMENT SIMULATION

To model the spot welding process with consideration of various surface-level defects, an enhanced version of the finite element algorithm (originally introduced in the authors' recent publication) was employed (29). While the initial version of the algorithm focused on simulating welds with internal strength-related defects such as IM (insufficient nugget), the updated model extends its capabilities to incorporate visible anomalies. Parameter inputs for the welding process were derived from industrial datasets, and the numerical simulation was executed via an integrated platform combining commercial finite element software with MATLAB scripting. This allowed for predictive modeling of nugget diameter as a function of input process parameters. A notable strength of this updated algorithm lies in its multi-physics coupling, treating the welding operation as a fully integrated Electrical-Thermal-Mechanical (ETM) system. Moreover, the algorithm accounts for material-specific metallurgical behavior, thereby increasing fidelity in predicting weld formation. The material properties used in the simulation were not generic values but rather obtained through prior experimental characterization based on raw material attributes and grain structure. To capture phase transitions during the welding cycle, both Time-Temperature-Transformation (TTT) and Continuous Cooling Transformation (CCT) diagrams were integrated into the simulation workflow. These diagrams enabled realistic modeling of the fusion zone's thermal evaluation and its effect on microstructural development.

To reduce computational costs while maintaining the accuracy of the responses, the mesh sensitivity analysis was performed considering three different element sizes including 1, 0.8, and 0.5 mm. Also, in the weld zone with a diameter of approximately 7 mm, the meshes were refined two times. In other words, the element sizes in the weld zone for the three models were 0.25, 0.2 and 0.125 mm, respectively. The results of this analysis based on the von Mises equivalent stress criterion are presented in Table 4.

All three models have a small difference up to a distance of 5 mm from the weld center, but in the two models with overall element sizes of 0.5 and 0.8 mm, the difference in results increases significantly from a distance of 5 to 7 mm. While the error rate in this range for the two models with mesh sizes of 1 mm and 0.8 mm is still an acceptable value. This shows that as the mesh sizes become smaller, the accuracy of the solution at distances of 5 to 7 mm decreases sharply. Therefore, a mesh size of 1 mm with two times refinement in the weld zone was chosen for future simulations. In this case, the number of elements in the FE model is 33,750. All the above explanations were valid for the simulation of the healthy weld. However, when the apparent defects are modeled, due to the plastic deformations created in the weld area and the asymmetric contacts of the electrode tip with the sheets, the refined elements caused the response to diverge. Therefore, in the simulations of the connection with the desired defects, only mesh size of one millimeter was used throughout the sample. Figure 4 provides a schematic representation of the full algorithm used to simulate spot welds with apparent defects.

For fatigue analysis, the Battelle structural stress methodology was adopted. This approach offers a mesh-intensitive framework and has been widely validated for fatigue life estimation across various welded steel components. Its effectiveness is based on the master S-N curve approach, particularly for different steels (31), and is described by the following equation:

TABLE 4. Mesh sensitivity analysis results for spot weld bonding – three-sheet steel

Distance from weld center (mm)	Element size (mm)		
	1	**0.8**	**0.5**
0	6	5.54	6.11
1	5.97	5.75	6.07
2	5.89	5.39	5.12
3	5.8	5.17	4.97
4	5.46	5.4	5.72
5	4.63	5.51	5.59
6	30.1	34.93	13.42
7	102.7	103.7	87.6

$$\Delta S_x = CN_f^h \quad (1)$$

Here, ΔS_x denotes the structural stress range, and N_f is the number of cycles to failure, and C and h are material-specific constants for steels. The values of these coefficients are summarized in Table 5 (32). An overview of the fatigue evaluation algorithm used in this study, from simulation to life prediction, is depicted in Figure 5.

TABLE 5. Material-specific constants for the master S-N curve applied to steels [33]

Statistical base	C (MPa)	Hold time
Mean	19930.2	
+2σ	28625.5	
−2σ	13875.8	-0.32
+3σ	31796.1	
−3σ	12492.6	

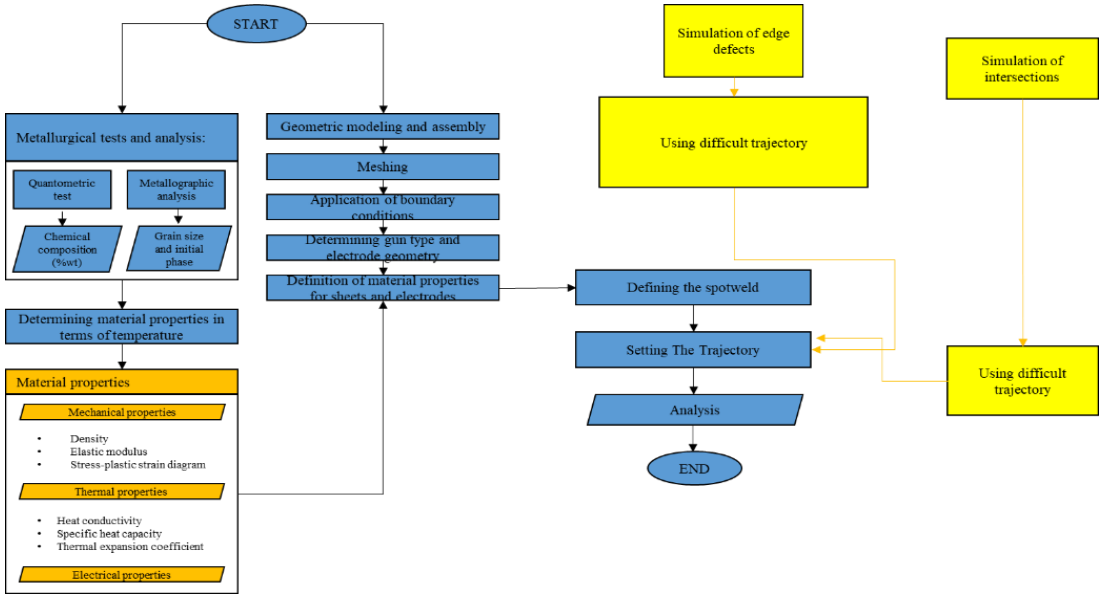

Figure 4. The framework of the updated 3D finite element algorithm is employed to simulate the spot welding process with distinct surface-level defects

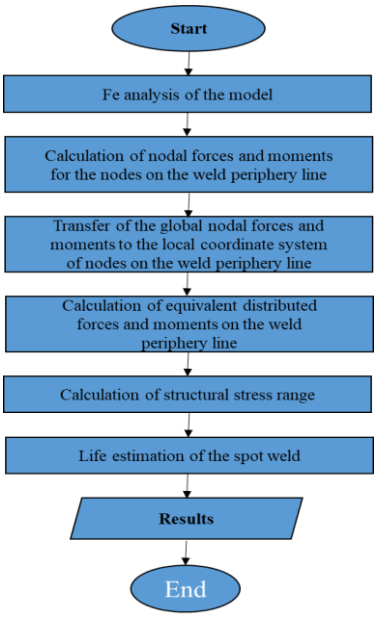

Figure 5. Workflow of fatigue life assessment of the RSW joint utilizing the Battelle structural approach [28]

4. 1. Analysis of Edge-affected RSW Joints As mentioned earlier, this defect is caused by the incorrect position of the weld core with the sheets' edges. If the size of the apparent defect is less than or equal to 0.33 of the nugget diameter, it is called an edge defect. Therefore, in this study, three different intensities for edge defect (0.1, 0.2, and 0.3 of the nugget diameter in a healthy joint) were considered. The finite element model as well as the diameter of the weld nugget after the process are illustrated in Figure 6.

4. 2. Analysis of Intersection-affected RSW Joints As previously shown, an intersection defect is described when the edge defect exceeds one-third of the nugget diameter. The characteristic of the simulation example of this defect, i.e., 0.8, is demonstrated in Figure 7.

5. RESULTS AND DISCUSSION

5. 1. Validation of Finite Element Analysis Figure 8 presents a comparison between the numerical

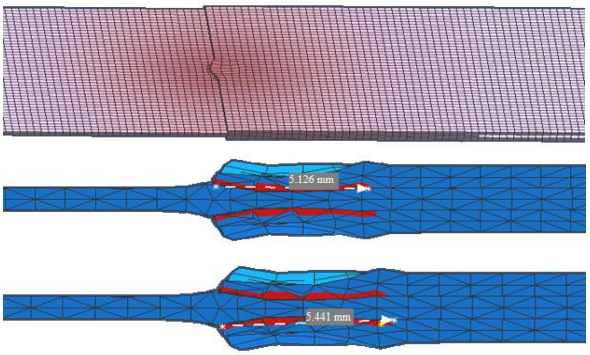

Figure 6. FEM and weld nugget diameter for three-sheet spot-welded joint with edge defect considering the intensity of 0.3 nugget diameter as a representative

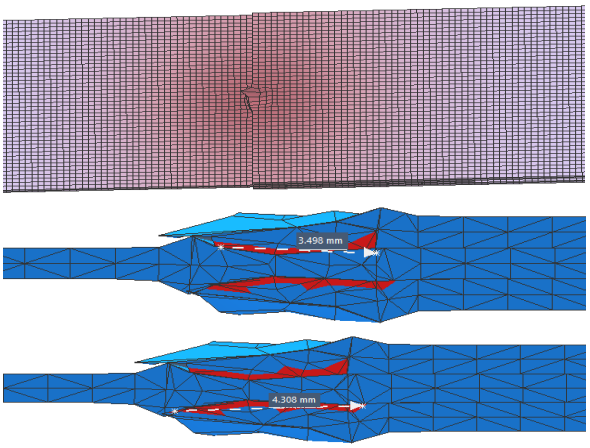

Figure 7. FEM and weld nugget diameter of RSW joint with intersection defect considering the intensity of 0.8 as a representative

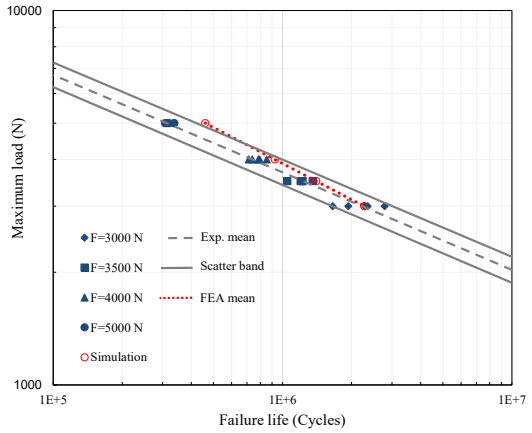

Figure 8. Fatigue performance of free-defect RSW joint: experimental testing vs. FE modeling outcomes

fatigue predictions and the corresponding experimental axial fatigue test results for defect-free three-sheet spot-welded joints. For a quantitative assessment of the model's accuracy, a comparative analysis of the experimental and simulated fatigue lives at various load levels is presented in Table 6. The results presented in the experimental life column are the average results for different replicates.

The results demonstrate a strong correlation between the simulation and experimental data. The error percentage across all tested load levels ranges from a minimum of 3.2 % to a maximum of 16.81 %, with an average error of 10.02 %. This level of deviation is considered highly acceptable for complex thermo-mechanical-fatigue simulations, given the inherent uncertainties in material properties, experimental variability (as evidenced by the scatter in the test data), and the necessary simplifications in the finite element model.

The highest errors are typically observed at higher load levels (low-cycle fatigue regime), where local plasticity and microstructural variations have a more pronounced effect that is challenging to model perfectly. Conversely, the model exhibits excellent agreement in the high-cycle fatigue regime, which is the primary focus of this study. This validation provides high confidence in the subsequent simulation results for defective joints presented in the following sections.

5. 2. Results of RSW Joints with Edge Defect

Figure 9(a) presents the force-displacement curves obtained from finite element tensile test simulations for RSW joints containing edge defects of varying severities. The relationship between edge defect severity and the maximum force—representing the joint's tensile capacity—is further illustrated in Figure 9(b). The simulation results indicate a decreasing trend in tensile strength as the edge defect becomes more pronounced. This reduction is primarily attributed to incomplete formation of the weld nugget at the defect site. For instance, a joint exhibiting an edge defect severity of 0.2 demonstrates a tensile strength of 8512.98 N, compared to 8997.4 N for the defect-free counterpart—corresponding to a 5.4% reduction in load-bearing capacity.

Furthermore, Table 7 summarizes the fatigue analysis results for joints with varying levels of edge defect

TABLE 6. Comparative analysis of experimental and simulated fatigue life for defect-free joints

Applied load (N)	Experimental life (Cycle)	Simulated life (Cycle)	Error (%)
3000	2200160	2270636	3.2
3500	1207809	1312658	8.68
4000	776387	864592	11.36
5000	323012	377319	16.81

severity, providing additional insight into the mechanical degradation associated with such imperfections.

The analysis shows that an increase in edge defect severity leads to a noticeable decline in fatigue life under identical cyclic loading conditions. For instance, when the defect severity reaches 0.2, the number of cycles to failure is reduced by approximately 13.72% compared to that of a defect-free joint.

5. 3. Results of RSW Joints with Intersection Defect

Figure 10(a) presents force-displacement diagrams of three-sheet spot-welded joints with intersection defects at different intensities as a result of the tensile analysis. In addition, tensile strength variations related to the severity of the intersection defect are displayed in Figure 10(b).

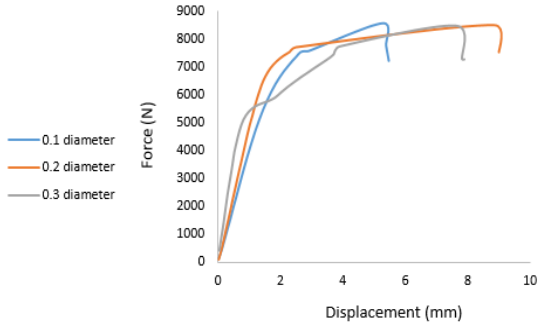

(a)

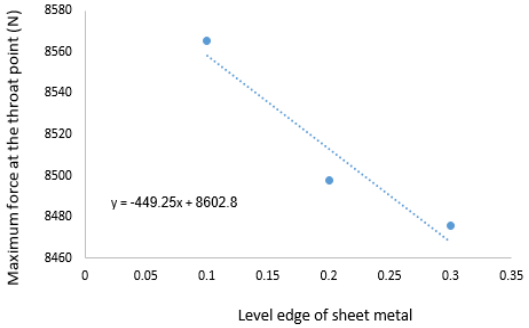

(b)

Figure 9. Static simulation results of RSW joints with edge defects at different intensities: (a) Force-displacement diagrams and (b) Tensile strength in terms of severity of the edge defect

TABLE 7. Fatigue analysis outputs for RSW joint with edge defect: cycle to failure

Edge defect severity	Max. applied load: 5000 N	Max. applied load: 4000 N
0.1	25444	49851
0.2	14501	45363
0.3	10562	34511

The findings demonstrate that the tensile strength of the spot-welded joint declines progressively as the severity of the intersection defect increases. Notably, when the defect reaches 0.8 times the nugget diameter, a substantial reduction in static strength is observed. Next, fatigue performance corresponding to various intersection defect severities is summarized in Table 8.

The results show that the fatigue life reduction in intersection defects is much greater than in edge defects. One of the most important reasons for this is the smaller weld core diameter in the joint with intersection defects compared to edge defects. For instance, when there is an intersection defect severity of 0.6, the fatigue life of the

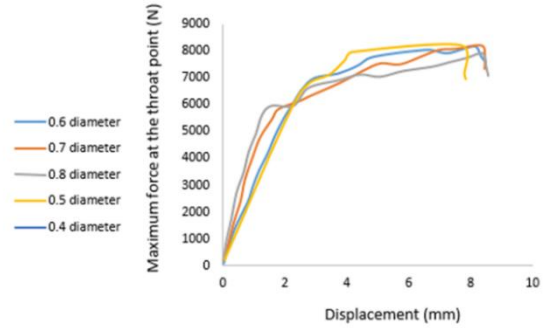

(a)

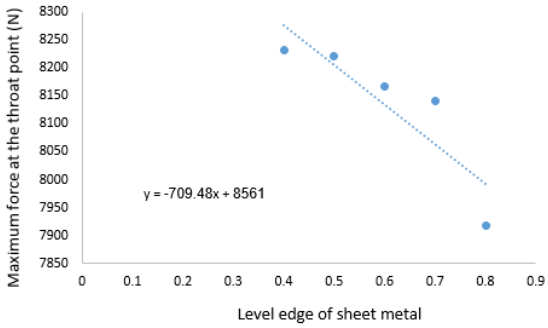

(b)

Figure 10. Static simulation results of three-sheet spot-welded joints with intersection defects at different intensities: (a) Force-displacement diagrams and (b) Tensile strength variations regarding the severity of intersection defect.

TABLE 8. Fatigue analysis outputs for RSW joint with intersection defect: cycle to failure

Edge defect severity	Max. applied load: 5000 N	Max. applied load: 4000 N
0.4	6226	28444
0.5	4877	22155
0.6	4761	21987
0.7	4321	21549
0.8	4217	20981

connection is reduced by about 54% compared to a healthy connection.

6. CONCLUSION

The main conclusions drawn from this research are outlined below:
- FE simulations of tensile and fatigue analysis for edge defect in a three-sheet spot-welded joint showed that the joint strength decreases by 5.4 % and 13.72 %, respectively, for edge defect with a specification of 0.2 to the nugget diameter. These values were reported in comparison to the strength of a defect-free weld joint under various loadings.
- FE analyses demonstrated that when the intersection defect extended beyond 60% of the nugget diameter, the corresponding tensile and fatigue strengths declined by 9.6 % and 54 %, respectively.
- For both edge and intersection defects, tensile and fatigue diagrams were extracted and reported in terms of defect severity through finite element simulation.
- The results show that RSW joint with the desired apparent defects under cyclic loading conditions may have a strength reduction of more than 50 %, therefore, following the initial hypothesis in this study, it is proposed to change the name of this type of defect to apparent-quasi-strength defects.

7. ACKNOWLEDGMENTS

This paper has been supported by the RUDN University Strategic Academic Leadership Program. Project No. 011600-0-000 " Development of technologies for creating intelligent systems and automation of production processes".

8. REFERENCES

1. Oikawa H, Murayama G, Hiwatashi S, Matsuyama K. Resistance spot weldability of high strength steel sheets for automobiles and the quality assurance of joints. Welding in the World. 2007;51(3):7-18. https://doi.org/10.1007/BF03266555
2. Tsai C, Papritan J, Dickinson D, Jammal O. Modeling of resistance spot weld nugget growth. Welding Journal(USA). 1992;71(2):47.
3. Amiri N, Farrahi G, Kashyzadeh KR, Chizari M. Applications of ultrasonic testing and machine learning methods to predict the static & fatigue behavior of spot-welded joints. Journal of Manufacturing Processes. 2020;52:26-34. https://doi.org/10.1016/j.jmapro.2020.01.047
4. Patil SA, Baratzadeh F, Lankarani H. Modeling of the weld strength in spot weld using regression analysis of the stress parameters based on the simulation study. Journal of Materials Science Research. 2017;6:51-62.
5. Martín Ó, Pereda M, Santos JI, Galán JM. Assessment of resistance spot welding quality based on ultrasonic testing and tree-based techniques. Journal of Materials Processing Technology. 2014;214(11):2478-87. https://doi.org/10.1016/j.jmatprotec.2014.05.021
6. Farrahi G, Ahmadi A, Kasyzadeh KR. Simulation of vehicle body spot weld failures due to fatigue by considering road roughness and vehicle velocity. Simulation Modelling Practice and Theory. 2020;105:102168. https://doi.org/10.1016/j.simpat.2020.102168
7. Liu W, Hu J, Qi J. Resistance Spot Welding Defect Detection Based on Visual Inspection: Improved Faster R-CNN Model. Machines. 2025;13(1):33. https://doi.org/10.3390/machines13010033
8. Summerville C, Adams D, Compston P, Doolan M. Nugget diameter in resistance spot welding: a comparison between a dynamic resistance based approach and ultrasound C-scan. Procedia Engineering. 2017;183:257-63. https://doi.org/10.1016/j.proeng.2017.04.033
9. Mirzaei F, Ghorbani H, Kolahan F. Numerical modeling and optimization of joint strength in resistance spot welding of galvanized steel sheets. The International Journal of Advanced Manufacturing Technology. 2017;92(9):3489-501. https://doi.org/10.1007/s00170-017-0407-x
10. Eshraghi M, Tschopp MA, Zaeem MA, Felicelli SD, editors. A parametric study of resistance spot welding of a dual-phase steel using finite element analysis. Proceedings of the 8th Pacific Rim International Congress on Advanced Materials and Processing; 2013: Springer.
11. Eisazadeh H, Hamedi M, Halvaee A. New parametric study of nugget size in resistance spot welding process using finite element method. Materials & Design. 2010;31(1):149-57. https://doi.org/10.1016/j.matdes.2009.06.042
12. Chuenmee N, Phothi N, Chamniprasart K, Khaengkarn S, Srisertpol J. Machine learning for predicting resistance spot weld quality in automotive manufacturing. Results in Engineering. 2025;25:103570. https://doi.org/10.1016/j.rineng.2024.103570
13. Moshayedi H, Sattari-Far I. Numerical and experimental study of nugget size growth in resistance spot welding of austenitic stainless steels. Journal of Materials Processing Technology. 2012;212(2):347-54. https://doi.org/10.1016/j.jmatprotec.2011.09.004
14. Farrahi G, Ahmadi A, Kashyzadeh KR, Azadi S, Jahani K. A comparative study on the fatigue life of the vehicle body spot welds using different numerical techniques: Inertia relief and Modal dynamic analyses. Fracture and Structural Integrity. 2020;14(52):67-81. https://doi.org/10.3221/IGF-ESIS.52.06
15. Pan N, Sheppard S. Spot welds fatigue life prediction with cyclic strain range. International Journal of Fatigue. 2002;24(5):519-28. https://doi.org/10.1016/S0142-1123(01)00157-8
16. Kashyzadeh KR, Ghorbani S. High-cycle fatigue behavior and chemical composition empirical relationship of low carbon three-sheet spot-welded joint: An application in automotive industry. Journal of Design Against Fatigue. 2023;1(2):1-8.
17. Deshmukh DD, Kharche Y. Influence of processing conditions on the tensile strength and failure pattern of resistance spot welded SS 316L sheet joint. International Journal on Interactive Design and Manufacturing (IJIDeM). 2025;19(1):559-71. https://doi.org/10.1007/s12008-023-01465-8
18. Nodeh IR, Serajzadeh S, Kokabi AH. Simulation of welding residual stresses in resistance spot welding, FE modeling and X-ray verification. Journal of materials processing technology. 2008;205(1-3):60-9. https://doi.org/10.1016/j.jmatprotec.2007.11.104
19. Maleki E, Unal O, Kashyzadeh KR. Surface layer nanocrystallization of carbon steels subjected to severe shot peening: Analysis and optimization. Materials Characterization. 2019;157:109877. https://doi.org/10.1016/j.matchar.2019.109877

20. Maleki E, Unal O, Kashyzadeh KR. Fatigue behavior prediction and analysis of shot peened mild carbon steels. International Journal of Fatigue. 2018;116:48-67. https://doi.org/10.1016/j.ijfatigue.2018.06.004
21. Pal TK, Bhowmick K. Resistance spot welding characteristics and high cycle fatigue behavior of DP 780 steel sheet. Journal of Materials Engineering and Performance. 2012;21(2):280-5. https://doi.org/10.1007/s11665-011-9850-2
22. Xiao L, Liu L, Chen D, Esmaeili S, Zhou Y. Resistance spot weld fatigue behavior and dislocation substructures in two different heats of AZ31 magnesium alloy. Materials Science and Engineering: A. 2011;529:81-7. https://doi.org/10.1016/j.msea.2011.08.064
23. Ordoñez J, Ambriz R, García C, Plascencia G, Jaramillo D. Overloading effect on the fatigue strength in resistance spot welding joints of a DP980 steel. International Journal of Fatigue. 2019;121:163-71. https://doi.org/10.1016/j.ijfatigue.2018.12.026
24. Hassanifard S, Zehsaz M, Esmaeili F. Spot weld arrangement effects on the fatigue behavior of multi-spot welded joints. Journal of mechanical science and technology. 2011;25(3):647-53. https://doi.org/10.1007/s12206-011-0112-x
25. Esmaeili F, Rahmani A, Barzegar S, Afkar A. Prediction of fatigue life for multi-spot welded joints with different arrangements using different multiaxial fatigue criteria. Materials & Design. 2015;72:21-30. https://doi.org/10.1016/j.matdes.2015.02.008
26. Vural M, Akkuş A, Eryürek B. Effect of welding nugget diameter on the fatigue strength of the resistance spot welded joints of different steel sheets. Journal of Materials Processing Technology. 2006;176(1-3):127-32. https://doi.org/10.1016/j.jmatprotec.2006.02.026
27. Reza Kashyzadeh K, Farrahi G, Ahmadi A, Minaei M, Ostad Rahimi M, Barforoushan S. Fatigue life analysis in the residual stress field due to resistance spot welding process considering different sheet thicknesses and dissimilar electrode geometries. Proceedings of the Institution of Mechanical Engineers, Part L: Journal of Materials: Design and Applications. 2023;237(1):33-51. https://doi.org/10.1177/14644207221101069
28. Farrahi G, Kashyzadeh KR, Minaei M, Sharifpour A, Riazi S. Analysis of resistance spot welding process parameters effect on the weld quality of three-steel sheets used in automotive industry: Experimental and finite element simulation. International Journal of Engineering Transactions A: Basics. 2020;33(1):148-57. https://doi.org/10.5829/ije.2020.33.01a.17
29. Ganjabi MA, Farrahi G, Reza Kashyzadeh K, Amiri N. Effects of various strength defects of spot weld on the connection strength under both static and cyclic loading conditions: empirical and numerical investigation. The International Journal of Advanced Manufacturing Technology. 2023;127(11):5665-78. https://doi.org/10.1007/s00170-023-11923-y
30. ISO14324 RSWDT. of Welds-Method for the Fatigue Testing of Spot Welded Joints. The International Organization for Standardization. 2003. https://www.iso.org/standard/24088.html
31. Hong JK. The development of a simplified spot weld model for Battelle structural stress calculation. SAE International Journal of Materials and Manufacturing. 2011;4(1):602-12. https://doi.org/10.4271/2011-01-0479
32. Dong P, Prager M, Osage D. The design master SN curve in ASME Div 2 rewrite and its validations. Welding in the World. 2007;51(5):53-63. https://doi.org/10.1007/BF03266573

COPYRIGHTS

©2026 The author(s). This is an open access article distributed under the terms of the Creative Commons Attribution (CC BY 4.0), which permits unrestricted use, distribution, and reproduction in any medium, as long as the original authors and source are cited. No permission is required from the authors or the publishers.

Persian Abstract

چکیده

تکنیک جوشکاری مقاومتی نقطه‌ای روشی رایج برای اتصال ورق‌های فلزی نازک در صنایع مرتبط با حمل و نقل مانند خودرو و هوافضا است. مزیت کلیدی این اتصال در کارآیی آن و عدم نیاز به مواد اضافی است که به کاهش وزن سازه کمک می‌کند. در این مطالعه، تاثیر عیوب قابل مشاهده (یعنی لبه و تقاطع) بر رفتار مکانیکی اتصالات جوش داده شده سه ورقی تحت بارهای استاتیکی و خستگی مورد تجزیه و تحلیل قرار گرفته است. برای این منظور، ترکیبی از تست‌های آزمایشگاهی و مدلسازی اجزای محدود مورد استفاده قرار گرفت. رویکرد اجزای محدود با استفاده از داده‌های تجربی خستگی محوری (منحنی‌های تنش–عمر در ناحیه پرچرخه) اعتبارسنجی شد. بر خلاف تحقیقات قبلی، این تحقیق برای اولین بار چنین نقص‌های سطحی را در چارچوب مدل اجزای محدود گنجانده است. نتایج شبیه‌سازی نشان داد که یک عیب لبه با شدت ۰.۲ میلی‌متری منجر به کاهش استحکام کششی و خستگی به ترتیب ۵.٤ و ۱۳.۷۲ درصد می‌شود، در حالی که یک عیب تقاطع با شدت ۰.٦ میلی‌متری باعث کاهش ۹.٦ و ٥٤ درصدی به ترتیب در استحکام کششی و خستگی می‌شود. این یافته‌ها حساسیت بیشتر استحکام خستگی به چنین نقص‌هایی را در مقایسه با استحکام کششی برجسته می‌کند.

IJE TRANSACTIONS B: Applications Vol. 39, No. 08, (August 2026) 1865-1877

International Journal of Engineering

Journal Homepage: www.ije.ir

Reduction of Optical Density in Highly Viscous Oils through Ultrasonic Treatment within The Infrared Wavelength Range

I. I. Rastvorova, V. M. Filatov*, S. A. Vilkov

Department of Electronic Systems, Empress Catherine II Saint-Petersburg Mining University, Saint-Petersburg, Russia

PAPER INFO

Paper history:
Received 18 July 2025
Received in revised form 19 August 2025
Accepted 11 September 2025

Keywords:
Infrared Diagnostics
Ultrasonic Treatmment
Oil Analysis
High Viscosity Oil
Optical Density Reduction
Sample Preparation

ABSTRACT

Today, Russia and the rest of the world are experiencing an increase in the production and reserves of heavy hydrocarbons (HC). This poses a problem in terms of both technical and financial needs, compared to conventional oil reserves. In this context, one of the key objectives for the advancement of the mineral resources sector is the enhancement of oil field diagnostic systems. This enables the "digitalization" of oil fields and processes related to extraction and transportation. The aim of the work is to analyze the current state of infrared (IR) oil diagnostic devices, existing problems and ways to optimize them, with special attention to the preliminary ultrasonic (US) treatment of highly viscous samples. This study was able to confirm the hypothesis that US treatment of resinous oil samples leads to an increase in the signal-to-noise ratio (SNR) of the IR diagnostic system. The highest efficiency of US treatment was recorded at a point (15°C; 15 min), where the increment of I_{out} was 51.36 % relative to untreated oil. The optimal time for US treatment based on effect on chemical composition of oil is: t < 9 min at T = 15°C, t < 6 min at T = 25°C, and t < 3 min at T = 35°C. Despite positive results, authors emphasize problems with uneven distribution of US vibrations and need for further research on paraffinic oil.

***doi**: 10.5829/ije.2026.39.08b.08*

Graphical Abstract

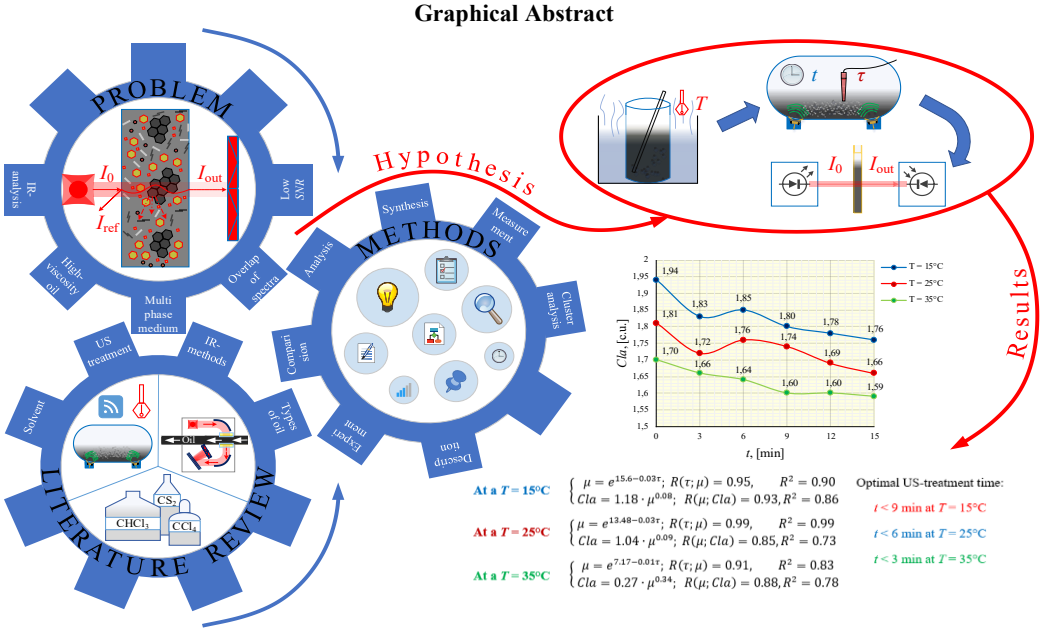

*Corresponding Author Email: vladislav-fil01@mail.ru (V. M. Filatov)

Please cite this article as: Rastvorova II, Filatov VM, Vilkov SA. Reduction of Optical Density in Highly Viscous Oils through Ultrasonic Treatment within The Infrared Wavelength Range. International Journal of Engineering, Transactions B: Applications. 2026;39(08):1865-77.

NOMENCLATURE

C	Concentration (mol/l)	R^2	Coefficient of determination
Cla	Optical density (c.u.)	SNR	Signal-to-noise ratio (dB)
E	Sensitivity of the photodetector (A/W)	T	Initial oil temperature (°C)
f	Frequency (Hz)	t	Ultrasonic treatment time (min)
I_0	Initial IR-radiation intensity (W/cm^2)	V	Volume of oil (ml)
I_{abs}	Intensity of absorbed radiation (W/cm^2)	W_N	Photodetector's own noise power (W)
I_{out}	Intensity of the IR-radiation transmitted through the sample (W/cm^2)	W_{out}	The power of the incident IR radiation on the photodetector (W)
I_{ref}	Intensity of reflected radiation (W/cm^2)	**Greek Symbols**	
I_{scr}	Intensity of scattered radiation (W/cm^2)	ε	Molar extinction coefficient $\left(\frac{ml}{mol \cdot cm}\right)$
I_{t_0}	IR-radiation intensity of the sample without ultrasonic preparation (W/cm^2)	λ	Wavelength (nm)
l	Optical path length (mm)	μ	Dynamic viscosity (mPa·s)
m	Weight (g)	ρ	Density (g/cm^3)
P_{IR}	Radiation power of the laser diode (W)	σ	Measurement error according to device specification (%)
P_{US}	Ultrasound power (W)	τ	Oil temperature after ultrasonic exposure (K)
$R(\mu; Cla)$	Correlation coefficient between μ and Cla	ΔI	IR-intensity increment (W/cm^2)
$R(\tau; \mu)$	Correlation coefficient between τ and μ		

1. INTRODUCTION

Fossil fuels, despite significant investment by major companies in renewable energy sources, continue to be a significant source of energy demand. In light of the current global energy crisis and depletion of conventional oil reserves, mineral resources are increasingly dependent on alternative sources such as heavy oil and bitumen (1, 2). By 2030, production from these sources is expected to increase by nearly five times (3). The extraction and transport of heavy oil presents several challenges compared to conventional oil (4).

In the current climate, one of the key objectives is to enhance the profitability of extracting hard-to-access HC reserves through the use of advanced technologies. These new technologies involve creating "intelligent" and "digitalized" fields (5), which provide continuous and reliable monitoring of the physical and chemical properties of oil and the processes involved at various stages of the raw material's lifecycle. The main goal of these solutions is to optimize production Procedures that would enable: obtaining and comprehending data about reservoir performance; boosting oil extraction rates through the judicious selection of chemicals and stimulation techniques; selecting the most effective method for oil transportation, taking into consideration its characteristics; monitoring the environmental situation in oil-producing areas and creating predictive models for potential environmental incidents (6-8).

Currently, innovative techniques such as steam injection, thermal treatment (9), the use of chemical additives (10), emulsification, and hydrotransport are being actively implemented to enhance the efficiency of producing and transporting high-viscosity oils (11). These methods have the potential to significantly increase HC recovery rates and reduce the costs associated with transportation. Despite the progress made in this area, many existing techniques still fall short of their full potential and require further investigation, optimization, and intellectualization (12).

A crucial step in the process of intellectualizing deposits is the development of sensors to monitor the physico-chemical characteristics of HC. These sensors should allow for the assessment of the quality of raw materials, as well as the determination of parameters for oil production and transportation. For example, high concentrations of paraffins, sulfur-containing and organochloride compounds can lead to corrosion and potential accidents. To mitigate the negative effects of these impurities, various depressant additives and demulsifying agents are employed (13). These additives reduce the viscosity of oil, preventing the formation of paraffin deposits and cleaning pipes of tar-paraffin buildup, thereby increasing their throughput and reliability (14). The choice of additive composition and type depends on factors such as the concentration of resins, asphaltenes, paraffins and aromatic compounds, water content, initial viscosity, temperature and pH.

To determine the physical and chemical properties of oil, samples must be taken and transported to specialized laboratories. However, the results can be affected by the adsorption of surface-active substances and evaporation of lighter fractions, depending on the length of transportation. One of the modern and promising approaches to solving this issue is the use of oil diagnostic devices operating IR wavelength range. This range offers a harmonious balance between the ability to penetrate and sensitivity to oil composition. (15, 16).

Additionally, a significant benefit is the lack of need for signal processing systems in close proximity to IR sensor, as a trunking or fiber optic communication system can be used to connect them (17). Major developments in this area of technology include:

1. Raupov et al. (18) conducted investigations into the optical characteristics of oil, including optical density, absorption coefficient, and refractive index, across IR, visible (V), and ultraviolet (UV) spectrums. Their study presents a significant number of advanced designs for measuring oil optical properties directly at the wellhead. Additionally, Raupov et al. (18) experimentally established that oil optical properties correlate with density, viscosity, and surface tension. Based on their findings, the devices utilize tunneled lasers that provide a wide range of optical radiation but have several drawbacks, including a tendency to "jump" between wavelengths, and the need for high-intensity sources for efficient conversion. Many existing optoelectronic detectors either cannot operate in both UV and IR spectral regions simultaneously (19, 20), or exhibit partial overlap of these regions, such as in the case of PCF-SPR (elliptical plasmon) sensors (21). In addition, the study does not provide information on the sample holder thickness, which is crucial when analyzing high viscosity oil.

2. Santos et al. (22) developed a portable IR spectrometer for measuring oil density and chemical composition, including sulfur, nitrogen, asphaltenes, and various HC, in the wavenumber range of 11000–6000 cm^{-1}. The device was tested on 182 samples of oil, but the results revealed that the spectrometer's coefficient of determination exhibited low efficiency (R^2<0.7) for determining resins, saturated, and aromatic HC. This suggests difficulties in analyzing viscous oils.

3. Xu et al. (23) proposed using algorithms with deep learning and an increased Mahalanobis distance to reduce the number of outliers and the influence of noise on measurement results. They also proposed the use of wavelet transformations combined with the T2-Hotelling test to achieve this. Yang et al. (24) achieved an improvement in the performance of mathematical apparatus for processing large data streams by combining the principal component analysis/autoencoder method with support vector regression. Despite a significant number of publications on improving approaches to data processing and spectrogram analysis (25, 26), it is also essential to pay attention to the physical aspects of the interaction between IR radiation and dispersed petroleum media. It is impossible to eliminate all random noise or remove overlapping peaks through mathematical transformations alone, so it is necessary to consider the physical properties of the medium. In this instance, a comprehensive approach is required, which encompasses not only data analysis, but also the appropriate preprocessing of the oil sample.

The task of determining the physicochemical properties, in particular, the composition, of high-viscosity oils is challenging due to their multiphase nature, heterogeneity, and saturation. IR devices used in the process of diagnosing heavy oils encounter a low signal output, which results in "blurring" of peaks on the spectrogram and darkening of other extrema (24, 27, 28). This issue has traditionally been addressed by utilizing various solvents and heat. Solvents effectively enhance the optical clarity of the oil (29), but their use precludes the automation of oil diagnostics processes at the wellhead, due to the need for empirical selection and disposal of chemical by-products. Heat likewise contributes to enhancing optical clarity in oil (30). However, when any issues regarding high-viscosity oils arise, it has been found that heating only destroys formed asphalt-resin-paraffin deposits when a specific melting point has been reached. A more modern alternative to use solvents and heat is the US treatment, which has three simultaneous effects: acoustic cavitation, mechanical heating, and degassing. The US action, due to the propagation of mechanical waves and the collapse of bubbles, contributes to the disruption of agglomerates and a more uniform distribution of the various components (31, 32). The effect of the disruption of US agglomerates can be observed prior to their melting point, which, in theory, would increase the optical clarity of the oil medium. Besides, US baths are more compact and versatile than solvent tanks and, therefore, can be installed directly at the wellhead. This would allow for the analysis of heavy oil in the field. Therefore, the investigation into the feasibility of using US treatment of heavy oil samples to address the issue of high absorption of IR frequency range optical signal in a dispersed petroleum medium should be considered a pressing and novel task.

2. LITERATURE REVIEW

One of the significant stages of the study is to identify a viable approach for performing IR diagnostics on oil and obtaining answers to several questions. Which technique will be more easily automated in the future? Which technique is more dependable and simpler to implement? What are the constraints of this technique?

2. 1. Methods of IR Diagnostics of Oil IR diagnostics of oil allows qualitative and quantitative study of the physicochemical characteristics of oil, including its composition, optical and rheological properties. There are four main methods for IR diagnostics (33-35). The implementation schemes and comparative analysis are presented in Figure 1 and Table 1, respectively.

TABLE 1. Comparison of IR diagnostic techniques for oil

Technique name	Advantages	Disadvantages	A source
The method of disturbed total internal reflection	The ability to analyze oil with ultra-high viscosity; The capacity to analyze samples that contain water; Minimum sample preparation.	The need to determine the appropriate sample thickness; Significant energy loss; Fragile fiber optic construction.	(35-37)
The method of transmission spectroscopy	Ease of implementation; A comprehensive understanding of the functional components of oil; The ability to quantitatively analyze.	The complexity of analyzing samples with high levels of turbidity; Limited depth of penetration; Preparation of the sample is required.	(18, 38, 39)
The method of vapor phase spectroscopy	High signal-to-noise ratio; High sensitivity.	The need for stable operating conditions; Insufficient understanding of the oil composition (only light fractions are present).	(40)
The method of Raman spectroscopy	The ability to work with low oil concentrations; High spatial resolution; No need for sample preparation.	The need to minimize fluorescence; The challenges of working with viscous oils; The method is difficult to implement.	(41-43)

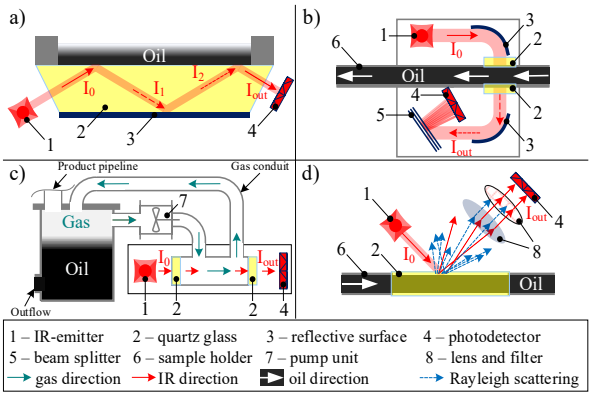

Figure 1. The scheme of implementation of IR diagnostics of oil: a) the method of disturbed total internal reflection; b) the method of transmission spectroscopy; c) the method of vapor phase spectroscopy; d) the method of Raman spectroscopy

Considering the potential use of IR spectroscopy in field applications with the possibility of automation, the transmission spectroscopy method is the most suitable approach. Table 1 illustrates that the transmission spectroscopic method is straightforward to implement and offers a comprehensive insight into functional groups. Nevertheless, the major obstacle is the requirement for pre-treatment of heavy oil samples. Next, we need to answer a number of questions: what prevents the transmission of IR beams? What is the mechanism for sample preparation? Will US treatment meet this requirement?

2. 2. The interaction of the IR beam with a highly viscous oil medium It is known that only a part of the energy of the incident radiation passes through any substance (see Figure 2) (44).

The processes depicted in Figure 2 can then be described by Equation 1.

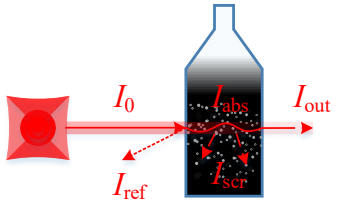

Figure 2. The processes that occur when IR radiation passes through a sample of oil

$$I_0 = I_{out} + I_{ref} + I_{scr} + I_{abs} \quad (1)$$

As can be seen in Figure 2 and Equation 1, the primary sources of loss are due to reflection, scattering, and absorption. A quantitative assessment of these losses is carried out in accordance with the Bouguer-Lambert-Beer Law (Equation 2) (18).

$$Cla = \lg \frac{I_0}{I_{out}} = \varepsilon \cdot C \cdot l. \quad (2)$$

In order to better understand the processes involved, it is necessary to examine the microscopic aspects of the formation of polymolecular layers and their interaction with IR radiation.

Microscopic examination of the polymolecular layers that form as a result of the interaction between asphaltenes, heavy aromatic HC, and paraffins has revealed that these layers possess a complex structure. The asphaltenes, which contain both aromatic and aliphatic groups, contribute to the formation of stable aggregates (45). Their polar groups are able to form hydrogen bonds and interact via London dispersion forces or Van der Waals bonding, leading to the creation of layers capable of retaining water molecules and other polar compounds (46-48). In addition, molecules that exhibit stronger Van der Waals interactions typically have higher boiling and melting points due to the additional energy required to overcome these attractive

forces (49). Heavy aromatic HC are non-polar and characterized by a high degree of conjugation. Resins are characterized by the presence of both polar and non-polar regions, and therefore act as a bonding agent for connecting non-polar HC molecules with highly polar asphaltenes (50). This interaction results in the formation of denser structures with increased mechanical strength (Figures 3a and 3b). The higher concentration of paraffins is evident in the increased opacity of the oil, as well as the accumulation of paraffin crystals (Figure 3c). Polymolecular layers may extend to tens of micrometers in thickness, which exceeds the wavelengths of the near- and mid-IR spectrum and results in significant energy losses during optical signal transmission (51).

High signal energy losses lead to low SNR values, blurred extremes, and spectrum distortion in spectrograms (24, 27). In this regard, the use of the Bouguer-Lambert-Baer law seems insufficient for the analysis of optical density, since it assumes a homogeneous medium with a linear relationship between absorption and concentration of matter. In practical scenarios, especially when IR radiation encounters highly viscous oil, the heterogeneous and multiphase nature of the oil environment leads to significant deviations from this principle.

Hence, the interaction between IR radiation and viscous oil is a sophisticated, multifaceted phenomenon. Various factors influencing the optical properties of oil are organized into a cluster (see Figure 4).

Based on Figure 4, it can be deduced that oil is an object with a composition of X at a temperature of Y and a pressure of Z, whose constituents exist in different physical states, but interact in an integrated manner. The correlation between chemical composition and rheological characteristics indicates that the composition of oil influences its density and viscosity, which in turn are linked to optical properties. To enhance the effectiveness of interaction between IR radiation and oil, particularly to increase its penetration depth, it is essential to explore options for reducing impurities and viscosity in the oil, as well as to strive for a uniform and single-phase medium.

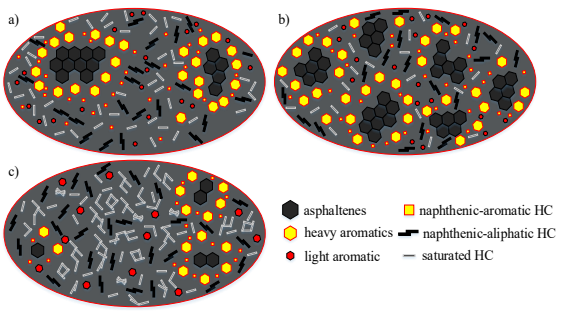

Figure 3. The distribution of components in heavy, dehydrated, and degassed oils can be classified into the following categories: a) sol type; b) gel type; c) paraffinic

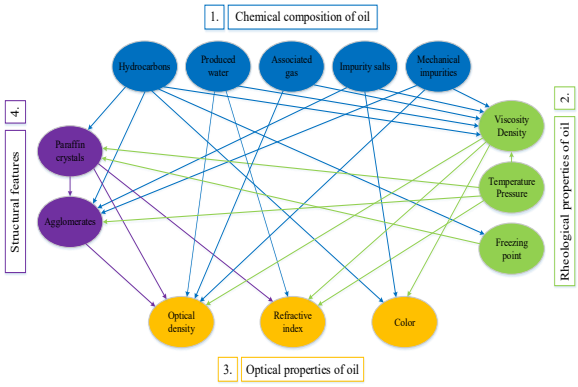

Figure 4. Factors affecting the optical properties of oil

2. 3. Preparation of Oil Samples for IR Analysis

In order to obtain accurate results in IR spectroscopy, it is necessary to carry out preliminary sample preparation to ensure the required uniformity of the oil (30). This preparation process involves removing unnecessary phases and different states of components, reducing the number of objects that absorb and scatter radiation. The process may include filtration to remove mechanical impurities, separation of water, degassing, and methods to reduce viscosity.

Filtration is performed using either mesh or advanced composite coalescing filters (52), while dewatering is achieved through membrane separation (53) or the use of demulsifiers (54). The main sample preparation process involves reducing optical density and turbidity, traditionally accomplished by the addition of solvents, or more rarely by thermal methods such as microwaveing and heating (30). Table 2 lists some of the most commonly used solvents along with their relevant parameters.

The solvents, in their pure form, do not interact with the metals employed in the construction of the equipment, such as steel. The outcomes of chemical reactions between solvents and oil constituents, particularly alkanes, can be hazardous. These reactions result in the formation of chlorinated HC, hydrochloric acid and thiol compounds with corrosive properties (55, 56). While single measurements may not cause harm, repeated or systematic use can lead to decreased reliability and durability of the diagnostic system. Additionally, there are several other disadvantages associated with this process: the use of solvents requires

TABLE 1. Oil solvents

Solvent, [Formula]	Proper bands, [cm^{-1}]	Hazard class, GOST 12.1.007-76	A source
CCl_4	730-825	II	(57)
$CHCl_3$	720-810	II	(57, 58)
CS_2	2178.99-2180.79	II	(59)

an additional storage tank for the reagent; the optimal solvent proportion must be determined experimentally; disposal of reaction products must be addressed (29, 30).

A more environmentally sustainable alternative to solvents for oil sample preparation is US technology. This method does not generate any chemical waste that needs to be disposed. Additionally, issues with high noise levels and energy inefficiency commonly associated with US equipment can be addressed by reducing the operating time, lowering the generator power, or increasing the frequency. Despite extensive research on this method, the US treatment has not yet implemented it widely in the oil production and transportation stages due to the lack of powerful generators that can meet the specific needs of these processes. However, in conditions with small volumes of oil, the US treatment is a promising method for preparing samples for IR analysis.

When high-viscosity oil is subjected to US treatment, several physical processes occur. Firstly, US induces the phenomenon of acoustic cavitation, resulting in the formation of microbubbles. As these microbubbles collapse, localized high temperatures and pressures are generated, which contribute to the disruption of Van der Waals forces between molecules (60). Secondly, US treatment has a mechanical and thermal effect on the liquid, reducing its viscosity and breaking down aggregates and interactions between components such as asphaltenes, paraffins, aromatics and resins. This makes the oil more uniform and evenly distributes its constituents (31, 32). This property minimizes deviations from the Bouguer–Lambert–Baer law. Thirdly, US treatment helps to degas oil (61). Despite the benefits, there are also several drawbacks, which are manifested in the individual physical response of oil to US, which depends on its chemical composition, viscosity, and temperature. Table 3 provides a summary of scientific studies on the impact of US on oil viscosity, as this parameter is correlated with optical density (18). The review articles described the composition of the oil, its physical properties, and a detailed methodology for the experiment.

The main conclusions from Table 3 are as follows:

1. The most studied frequency range for US effects on oil viscosity is from 18 kHz to 28 kHz. Frequencies above this range are less studied. Using a 42 kHz frequency has demonstrated positive results in reducing the viscosity of low-sulfur resinous oils.

2. The results of experiments using paraffinic (≥1.5%) and sulfurous oil (62) were extremely contradictory.

3. The review indicates the absence of a unified metrological approach to US treatment, requiring further clarification during experimental studies.

TABLE 2. Review of existing approaches to US treatment of high-viscosity oil

Oil composition/ The ratio of the elements	Ultrasound/Oil parameters	Results	A source
Resins – 32.1%, Asphaltenes – 8.2%, Paraffins (par) – 2.2%.	f = 22 kHz, t = 20 mins, P_{US} = 2 kW/ T = 20°C, V = 200-300 ml, μ_0 = 2400 mPa·s	$\mu_{20mins} = 0.75\mu_0$	(63)
C:H:O:N:S - 205:24:1:1:5.	f = 18 kHz, t = 6; 12 mins, P_{US} = 0.25 kW/ T = 65°C, V = 60 ml, μ_0 = 625 mPa·s	$\mu_{6mins} = 0.8\mu_0$, $\mu_{12mins} > \mu_0$	(60)
C:H:O:N:S - 210:28:3:8:1, Resins – 32.5%, Aromatic – 24.3%.	f = 42.1 kHz, t = 3 mins, P_{US} = 0.15; 0.4; 0.8 W/ml/ T = 41°C, V = 100 ml, μ_0 = 661.2 mPa·s	$\mu_{0,15W} = 0.798\mu_0$, $\mu_{0,4W} = 0.47\mu_0$, $\mu_{0,8W} = 0.18\mu_0$	(31)
Resins – 47.82%, Asphaltenes – 7.39%, Paraffins – 0; 0.5; 1; 1.5%.	f = 22 kHz, t = 2 mins, P_{US} = 15 W/cm^2/ T = 20°C, m = 50 g, μ_0 = 246.9 mPa·s	$\mu_{0\%par} = 0.8\mu_0$, $\mu_{0,5\%par} = 1.1\mu_0$, $\mu_{1\%par} = 1.4\mu_0$, $\mu_{1,5\%par} = 1.6\mu_0$	(64)
Resins – 22.65%, Asphaltenes – 8.15%, Alkanes – 39.75%, Aromatic – 28.55%.	f = 28 kHz, t = 30 mins, P_{US} = 105 W/ T = 50°C, m = 30 g, μ_0 = 1015 mPa·s	$\mu_{30mins} = 0.56\mu_0$	(65)
Resins – 97.80%, of which silica gel – 2.2%, Alkanes – 9.80%.	f = 22 kHz, t = 10 mins, P_{US} = 8 W/cm^2/ T = 22°C, m = 50 g, μ_0 = 253 mPa·s	$\mu_{10mins} = 0.763\mu_0$	(66)
Resins – 6.48%, Asphaltenes – 2.85%, Paraffins – 1.67%, Water – 58%.	f = 22 kHz, t = 5 mins, P_{US} = 1.5 kW/ T = 22°C, V = 600 ml, μ_0 = 465 mPa·s	$\mu_{5mins} = 3.3\mu_0$	(67)
Sulfur – 4.68%, Asphaltenes – 6.379%.	f = 25 kHz, t = 2 mins, P_{US} = 360 W/ T = 25°C, V = 250 ml, μ_0 = 426 mPa·s	$\mu_{2mins} = 0.857\mu_0$	(68)

4. US treatment may affect not only the physical properties of oil but also its chemical composition (31, 32). Therefore, it is necessary to establish boundary conditions for US treatment in order to ensure accurate results.

3. METHODOLOGY AND MATERIALS

Experimental studies were carried out in the laboratory of the Department of Electronic Systems at Empress Catherine II Saint-Petersburg Mining University. The main techniques used in the course of the study include US processing and transmission IR diagnostics. Prior to conducting the experiments, the oil was subjected to initial preparation to remove large mechanical particles using a mesh filter. No degassing of the oil was performed.

The selection of 35-45 kHz US bath frequency range is based on the high efficacy of these frequencies for working with resinous oils (see Table 3). Additionally, according to our review, this frequency range has not been extensively studied, therefore, further investigation is required.

The selection of temperatures for testing heavy oil samples was determined by the following considerations. The lower temperature limit of 15°C was chosen due to the ability to draw oil using a syringe and fill a thin cuvette. The upper limit of 35°C is set slightly below the boiling point (40°C) of the petroleum fraction of the oil in order to ensure adequate conditions for analysis.

The key characteristics of the oil sample under analysis and the equipment used in the experiment are outlined in Table 4. In addition to the materials listed, a thermometer was used to monitor the heating temperature (τ), a syringe was used for filling the cuvette, and a water bath was employed to stabilize the temperature of the samples.

The research was conducted as a two-factor, four-stage experiment (see Figure 5). The measurements were conducted in accordance with the "three-point" method principle, that is, the experiment was replicated three times. It was carried out under the following conditions: ambient temperature (+20±1)°C, air humidity (60±0.2)%, and power supply voltage (220±5)V.

A total of 3 samples of high-viscosity oil, each with a volume of 250 ml, were used in each cycle of the experiment. At the first stage, the oil sample was stabilized to temperature T in a water bath. In the second stage, heated oil was placed in an US bath, where it was subjected to US. After the treatment time t_n $(n = 0, 1, \ldots 5)$ had elapsed, a 1 ml sample was removed from the bath and placed in a quartz cuvette. The maximum value of t was selected based on parameters and limitations of the US bath. Oil placed in the cuvette was

TABLE 3. Materials and equipment for the experiment

Material/ equipment	Composition/ main element	Specifications
Oil (resinous)	Resins – 22.21%; alkanes – 33.91%; aromatics – 32.62%; asphaltenes – 0.58%	T = 15°C; μ_0 = 712.4 mPa·s; ρ = 0.961 g/cm^3; V = 2.25 l
US bath	–	f = 35…45 kHz; P_{US} = 30 W; V_{max} = 500 ml
Cuvette	Quartz	$\lambda_{min} \ldots \lambda_{max}$ = 200…2500 nm; l = 0.5 mm
Viscometer	–	$\mu_{min} \ldots \mu_{max}$ = 0.1…10·10^6 mPa·s; $\sigma = \pm 1.0$ %; $T_{min} \ldots T_{max}$ = -60…+360°C
Source of IR radiation	Laser diode	λ = 1540 nm; I_0 = 5.1 W/cm^2; P_{IR} = 40 mW
IR sensor	Photodiode	$\lambda_{min} \ldots \lambda_{max}$ = 900…1700 nm; E_{min} = 0.95 A/W

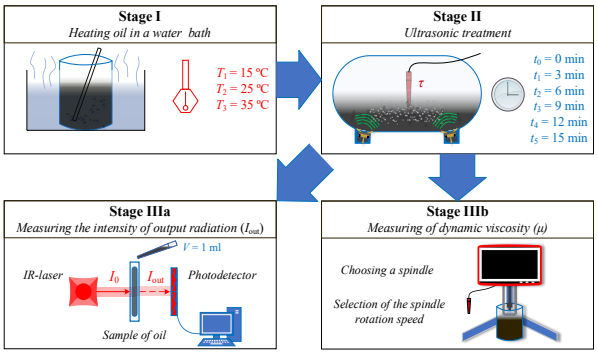

Figure 5. The scheme of the experiment (one cycle)

positioned between an IR radiation source and photodetector that recorded I_{out}. Photodetector were coaxial with emitting IR laser at a distance no more than 3 cm apart. Measuring unit was protected from sunlight by wooden board covered in black cloth.

The temperature τ was measured at time t_n.

The dynamic viscosity was determined using a rotational viscometer equipped with a thermometer. The principle of operation of a rotary viscosimeter is based on measuring the force required to maintain a given rotational speed of the rotor element (10). The higher the viscosity of the fluid, the greater the force needed to maintain the same rotational speed. The spindle and torque are selected empirically.

Cla of the oil sample was determined using the Bouguer-Lambert-Beer law (Equation 1). The assessment of the effect of US treatment of high-viscosity oil on *SNR* was carried out according to Equation 3 (69).

$$SNR = 10\lg\frac{W_{\text{out}}}{W_N}. \quad (3)$$

Considering that in Equation 3: $W_{\text{out}} = I_{\text{out}} \cdot S$ (70), where W_N and S are constant values, since the equipment and experimental conditions have not changed, it is most advisable to evaluate the effectiveness of the effect of US treatment on *SNR* by calculating ΔI (Equation 4).

$$\Delta I = \frac{I_{\text{out}} - I_{t_0}}{I_{t_0}} \cdot 100\%. \quad (4)$$

4. RESULTS AND DISCUSSION

The measurement results, μ, I_{out}, I_{t_0}, τ, represent the average of three measurements. No emissions were observed during these measurements.

Figure 6a illustrates the downward dynamics of changes in μ with increasing processing time. The data obtained are consistent with available studies (31, 63), which confirms the reproducibility of results on reducing viscosity of resinous oils.

Analysis of Figure 6b revealed a clear trend of *Cla* decreasing with increasing t in all three experiments, conducted at different initial oil sample temperatures. Let us consider each curve individually:

Blue curve: In the time interval of t = 0…3 mins, an initial decrease in *Cla* was observed, which could be interpreted as the result of cavitation processes that lead to the destruction of asphalt-resin-paraffin aggregates. This corresponds with the active effect of US on the oil sample. During the time period of t = 3…6 mins, *Cla* increased, indicating a probable redistribution of colloidal particles and their aggregation into larger structures, as well as the separation of the emulsion (resins and other components) into distinct phases (differences are visible in Figures 7a and 7b). This extreme can also be attributed to an uneven distribution of US vibrations within the bath, leading to incomplete sample treatment and the partial accumulation of heterogeneities at specific points (71-73). This hypothesis seems more plausible, given that μ continues to decline within the range of t = 3…6 mins (Figure 6a). During the time period t = 6…15 mins, there is a decrease in *Cla*, which can be interpreted as the active process of disintegration of newly formed aggregates. This suggests that cavitation effects remain active, and the process of particle dispersal and disintegration continues.

Red curve: In the time interval of t = 0…3 mins, similar to the blue curve, there is an initial decrease in *Cla*, indicating active cavitation processes. During the period of t = 3…6 mins, a sharp increase in *Cla* is observed, although this phenomenon is more pronounced compared to the blue curve. In addition to the aforementioned explanation of this phenomenon, it is important to note Figure 7c, which clearly shows significantly more "traces" of collapsed microbubbles caused by acoustic cavitation on the right side of the US bath compared to the left side, visually confirming the assumption of uneven distribution of vibrations. During the interval of t = 6…15 mins, the particle destruction process remains active, with *Cla* decreasing.

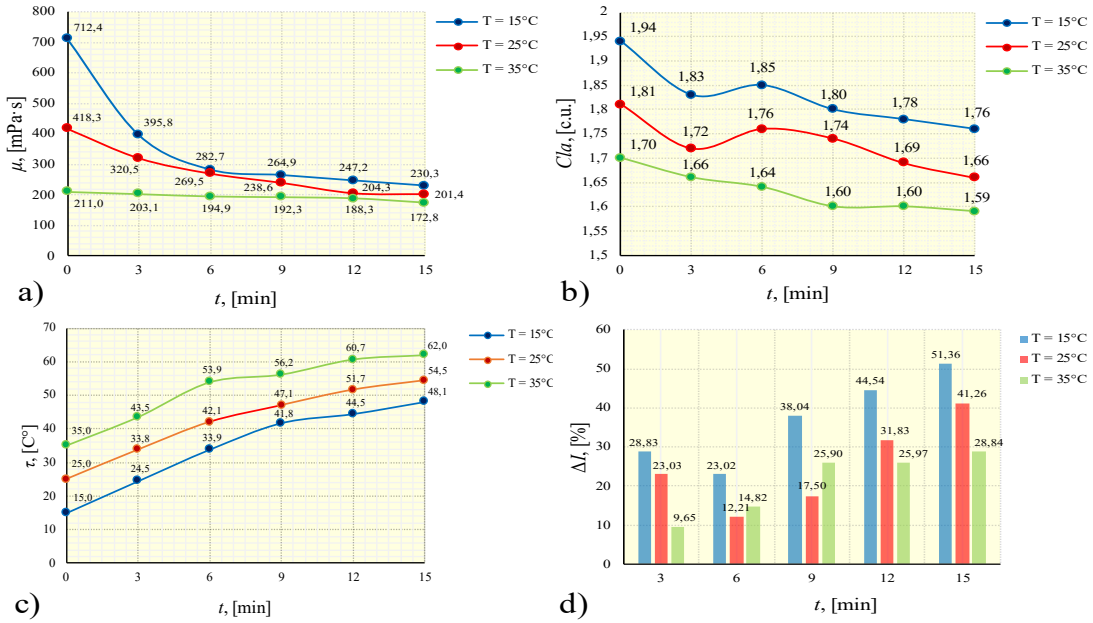

Figure 1. a) Curves of changes in μ from the time of US treatment; b) Curves of changes in *Cla* from the time of US treatment; c) Curves of change in τ from the time of US treatment; d) Dependence of ΔI on the US treatment time

The green curve's low volatility and lack of extreme values at time t = 0…9 mins can be explained by the adequate energy level required to disrupt interactions between particles, which is linked to a higher temperature T. The higher temperature of the sample weakens intermolecular bonds (van der Waals forces), preventing particle recombination and the formation of stable aggregates. The minimal change in the *Cla* value on the green curve between t = 9…15 mins indicates an almost completed process of destabilization of inhomogeneities. At the same time, the blue and red curves in the interval t = 9…15 mins show the active phase of this process.

The overall decrease in the concentration of *Cla* relative to the initial measurement (T = 15°C; t = 0 mins) and the final measurement (T = 35°C; t = 15 mins) was 0.35 c.u. or -18.04%.

Figure 6c shows that the increment of τ decreases with increasing t. This phenomenon can be explained by the fact that, as the oil's temperature increases, its thermal capacity also increases, and consequently, the amount of energy needed to raise the temperature varies. It is crucial to note that heating can affect the chemical properties of oil. In this instance, it is essential to take into account the onset of evaporation of the petroleum (light) fraction, which occurs at approximately 40°C and above. Figure 7b shows the formation of bubbles, indicating the beginning of light oil fraction evaporation. The oil's temperature at this point was 42.1°C. Therefore, the limit of US treatment at f = 35…45 kHz and P_{US} = 30 W should be < 9 mins at T = 15°C, < 6 mins at T = 25°C, and < 3 mins at T = 35°C.

In Figure 6d, the histogram shows an increase in the optical transparency of the oil medium as a result of US treatment, which indicates a decrease in energy loss of detected IR radiation and an increase of *SNR*. This conclusion is supported by observed increase in I_{out}. The highest ΔI was recorded at point (T = 15°C; t = 15 min) and amounted to 51.36%.

Figure 8 shows the main dependencies obtained during experimental studies. From the results, it can be seen that *Cla* and μ have a direct correlation in a generalized form up to a certain point in processing time. Therefore, the reduction of *Cla* through US processing has a limited and finite importance.

The research results are presented in the form of a system of equations describing the viscosity-optical properties of oil samples under US exposure (Table 5). System of equations for oil sample at T = 15°C has the highest correlation coefficient.

Figure 7. a) Oil before processing (T = 25°C; t = 0 min); b) Oil at the point (T = 25°C; t = 6 min); c) Oil at the point (T = 25°C; t = 12 min)

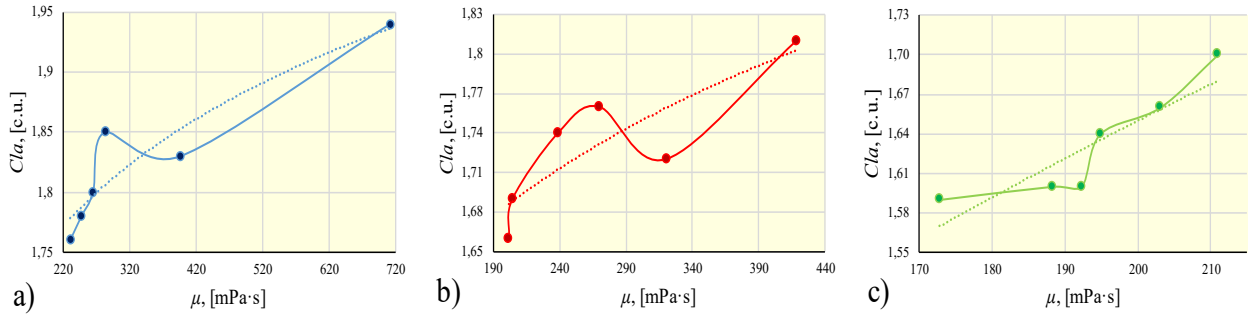

Figure 8. Viscosity-optical curves of oil samples obtained during US treatment: a) T = 15°C; b) T = 25°C; c) T = 35°C

TABLE 5. Systems of equations describing the viscosity-optical properties of oil samples under US exposure

Oil sample	The system of equations
At a T = 15°C	$\begin{cases} \mu = e^{15,6-0,03\tau};\ R(\tau;\mu) = 0.95,\ R^2 = 0.90 \\ Cla = 1,18 \cdot \mu^{0,08};\ R(\mu;Cla) = 0.93, R^2 = 0.86 \end{cases}$
At a T = 25°C	$\begin{cases} \mu = e^{13,48-0,03\tau};\ R(\tau;\mu) = 0.99,\ R^2 = 0.99 \\ Cla = 1,04 \cdot \mu^{0,09};\ R(\mu;Cla) = 0.85, R^2 = 0.73 \end{cases}$
At a T = 35°C	$\begin{cases} \mu = e^{7,17-0,01\tau};\ R(\tau;\mu) = 0.91,\ R^2 = 0.83 \\ Cla = 0,27 \cdot \mu^{0,34};\ R(\mu;Cla) = 0.88, R^2 = 0.78 \end{cases}$

5. CONCLUSION

Based on the objectives of the study and the results of the experiment, the following conclusions can be drawn:

US treatment reduces the optical density of highly viscous oil. The total decrease was 0.35 c.u., which is -18.04% of the initial value.

Pre-US treatment of oil samples helps to increase the *SNR* of the IR diagnostic system. The effectiveness of this process was assessed through calculations of ΔI. The highest efficiency of US treatment was achieved at a point (15°C; 15 min) and was 51.34%.

The greatest volatility of the *Cla* reduction curve under US exposure is observed in an oil sample at T = 25°C.

Of particular interest is the extremum observed in the US treatment interval, t = 6…9 mins, which may be associated with the redistribution of asphalt-resin-paraffin structures in the sample or measurement errors caused by uneven propagation of US vibrations in the bath. This extremum significantly affected the accuracy of the system of equations describing the viscosity-optical properties of an oil sample at T = 25°C. Future research should explore the use of US baths with vibration modulation, as this may theoretically reduce the irregularity of cavitation by minimizing interference effects. Additionally, analysis of the intensity distribution of US vibrations within the oil sample could enhance the outcomes of these investigations.

An important consideration in US treatment is mechanical heating, which can affect the chemical composition of oil. This requires the establishment of additional boundary conditions in order to optimize the IR diagnosis of oil based on the "signal-to-noise" criterion to the maximum extent possible. During the study, time limits for US treatment were determined based on the evaporation of petroleum fractions from oil: less than 9 mins at 15°C, less than 6 mins at 25°C and less than 3 mins at 35°C. Additionally, the optimal time for US treatment should be determined taking into account the acceleration or deceleration of heating for oil samples with different thermal capacities.

US oil treatment is a more environmentally friendly alternative to the use of solvents, as it eliminates the need for the disposal of hazardous chemical reaction byproducts. Existing issues with noise levels and energy consumption may be addressed through the use of higher frequencies, shorter durations, and correctly selected US power.

Before implementing this technique, it is essential to conduct further research, including testing with other types of oils, particularly paraffinic ones. Furthermore, future research should concentrate on the analysis of IR spectrograms acquired at different oil temperatures and under different US treatment times, as well as comparing and contrasting the findings of IR diagnostics of various oil types with the potential for generalization.

6. AUTHORS CONTRIBUTION

Rastvorova I. – Conceptulaization, scientific supervision and guidance and interpretation of results;
Filatov V. – Literature review, development of methodology, conducting experiments, processing and presentation of results;
Vilkov S. – Conducting experiments and interpretation of results.

7. REFERENCES

1. Litvinenko VS, Petrov EI, Vasilevskaya DV, Yakovenko AV, Naumov IA, Ratnikov MA. Assessment of the role of the state in the management of mineral resources. Записки Горного института. 2023(259 (eng)):95-111. 10.31897/PMI.2022.100
2. Kraiem M, Karkri M, Fois M, Sobolciak P. Thermophysical characterization of paraffins versus temperature for thermal energy storage. Buildings. 2023;13(4):877. 10.3390/buildings13040877
3. Zakirova G, Pshenin V, Tashbulatov R, Rozanova L. Modern Bitumen Oil Mixture Models in Ashalchinsky Field with Low-Viscosity Solvent at Various Temperatures and Solvent Concentrations. Energies. 2022;16(1):395. 10.3390/en16010395
4. Semenova T, Sokolov I. Theoretical Substantiation of Risk Assessment Directions in the Development of Fields with Hard-to-Recover Hydrocarbon Reserves. Resources. 2025;14(4):64. 10.3390/resources14040064
5. Martirosyan A, Ilyushin Y, Afanaseva O, Kukharova T, Asadulagi M, Khloponina V. Development of an Oil Field's Conceptual Model. International Journal of Engineering, Transactions B: Applications. 2025;38:381-8. 10.5829/ije.2025.38.02b.12
6. Malozyomov BV, Martyushev NV, Kukartsev VV, Tynchenko VS, Bukhtoyarov VV, Wu X, et al. Overview of methods for enhanced oil recovery from conventional and unconventional reservoirs. Energies. 2023;16(13):4907. 10.3390/en16134907
7. Zhang Z, Xie Z, Montilla MJB, Li Y, Xu T, Li S, et al. Analysis of Mechanisms and Environmental Sustainability in In Situ Shale Oil Conversion Using Steam Heating: A Multiphase Flow Simulation Perspective. Sustainability. 2024;16(21):9399. 10.3390/su16219399

8. Ilyushin P, Vyatkin K, Kozlov A. Development of a method for estimating thermal conductivity of organic deposits on the wax flow loop laboratory installation. International Journal of Engineering Transactions C: Aspects. 2022;35(6):1178-85. 10.5829/IJE.2022.35.06C.09
9. Bondarenko A, Rogachev M, Sharifov A, Mardashov D. Increasing Efficiency of Solvent Assisted Cyclic Steam Stimulation of the Bottomhole Formation Zone of a Carbonate Reservoir using Aquathermolysis Catalysts. International Journal of Engineering, Transactions A: Basics. 2025;38(4):758-66. 10.5829/ije.2025.38.04a.08
10. Nikolaev A, Plotnikova K. Study of the Rheological Properties and Flow Process of High-Viscosity Oil Using Depressant Additives. Energies. 2023;16(17):6296. 10.3390/en16176296
11. Beloglazov I, Morenov V, Leusheva E. Flow modeling of high-viscosity fluids in pipeline infrastructure of oil and gas enterprises. Egyptian Journal of Petroleum. 2021;30(4):43-51. 10.1016/j.ejpe.2021.11.001
12. Musa A, editor Revolutionizing oil and gas industries with artificial intelligence technology. Ices; 2023. 10.26438/ijcse/v11i5.2030
13. Matiyev K, Samedov A, Alsafarova M, Hasanov KI, Nurullaev VK. PREVENTION OF ASPHALTENE-RESIN-PARAFFIN DEPOSITS IN THE PROCESS OF OIL TRANSPORTATION. 2024. 10.5510/OGP20240200973
14. Tanirbergenova S, Ongarbayev Y, Tileuberdi Y, Zhambolova A, Kanzharkan E, Mansurov Z. Selection of Solvents for the Removal of Asphaltene–Resin–Paraffin Deposits. Processes. 2022;10(7):1262. 10.3390/pr10071262
15. Yolchuyeva U, Japharova R, Khamiyev M, Alimardanova F. Investigation of Surakhani light crude oil compounds as a case study using modern spectroscopic techniques. Journal of Petroleum Exploration and Production Technology. 2024;14(1):289-302. 10.1007/s13202-023-01702-6
16. Abdulkadir I, Uba S, Almustapha M. A rapid method of crude oil analysis using FT-IR spectroscopy. Nigerian Journal of Basic and Applied Sciences. 2016;24(1):47-55. 10.4314/njbas.v24i1.8
17. Dvoynikov M, Kutuzov P. Analysis of efficiency of communication channels for monitoring and operational control of oil and gas wells drilling process. International Journal of Engineering, Transactions A: Basics. 2025;4:6. 10.5829/ije.2025.38.01a.12
18. Raupov I, Burkhanov R, Lutfullin A, Maksyutin A, Lebedev A, Safiullina E. Experience in the application of hydrocarbon optical studies in oil field development. Energies. 2022;15(10):3626. 10.3390/en15103626
19. Earnshaw M, Bolle C, Kopf R, Cappuzzo M, Tate A, Hu T-C. Compact, efficient ultra-wide tunable laser with reduced thermal crosstalk. Optics Express. 2024;32(19):33283-93. 10.1364/OE.523097
20. Blumenthal DJ. Photonic integration for UV to IR applications. Apl Photonics. 2020;5(2). 10.1063/1.5131683
21. Ramadhan K, Syamsul A, Marwan A, Agustirandi B, Yasir M, Christian H. Neural networks in optimizing the performance of the elliptical-plasmonic sensor. Emerging Sci J. 2024;8(5):1798-811. 10.28991/ESJ-2024-08-05-07
22. Santos FD, Vianna SG, Cunha PH, Folli GS, de Paulo EH, Moro MK, et al. Characterization of crude oils with a portable NIR spectrometer. Microchemical Journal. 2022;181:107696. 10.1016/j.microc.2022.107696
23. Xu S, Xu Z, Zheng J, Lin H, Zou L, Lei M. Where does the crude oil originate? The role of near-infrared spectroscopy in accurate source detection. Memetic Computing. 2024;16(3):429-43. 10.1007/s12293-024-00425-3
24. Yang S-B, Moreira J, Li Z. Predicting crude oil properties using fourier-transform infrared spectroscopy (FTIR) and data-driven methods. Digital Chemical Engineering. 2022;3:100031. 10.1016/j.dche.2022.100031
25. Moro MK, de Castro EV, Romão W, Filgueiras PR. Data fusion applied in near and mid infrared spectroscopy for crude oil classification. Fuel. 2023;340:127580. 10.1016/j.fuel.2023.127580
26. Mishra P, Passos D, Marini F, Xu J, Amigo JM, Gowen AA, et al. Deep learning for near-infrared spectral data modelling: Hypes and benefits. TrAC Trends in Analytical Chemistry. 2022;157:116804. 10.1016/j.trac.2022.116804
27. Asemani M, Rabbani AR. Detailed FTIR spectroscopy characterization of crude oil extracted asphaltenes: Curve resolve of overlapping bands. Journal of Petroleum Science and Engineering. 2020;185:106618. 10.1016/j.petrol.2019.106618
28. Mokari A, Guo S, Bocklitz T. Exploring the steps of infrared (IR) spectral analysis: Pre-processing,(classical) data modelling, and deep learning. Molecules. 2023;28(19):6886. 10.3390/molecules28196886
29. Liu M, Wu X, Dyson PJ. Tandem catalysis enables chlorine-containing waste as chlorination reagents. Nature Chemistry. 2024;16(5):700-8. 10.1038/s41557-024-01462-8
30. Sargazi M, Hashemi SH, Kaykhaii M. Modern sample preparation techniques: A brief introduction. Sample preparation techniques for chemical analysis. 2021;9(10.5772). 10.5772/intechopen.100715
31. Dengaev AV, Kayumov AA, Getalov AA, Aliev FA, Baimukhametov GF, Sargin BV, et al. Chemical viscosity reduction of heavy oil by multi-frequency ultrasonic waves with the main harmonics of 20–60 kHz. Fluids. 2023;8(4):136. 10.3390/fluids8040136
32. Baimukhametov G, Dengaev A, Safiullina E, Kayumov A, Drozdov I, Shishulin V, et al. Relaxation Process in Crude Oil after Ultrasonic Treatment. International Journal of Engineering, Transactions B: Applications. 2024;37(5):896-903. 10.5829/ije.2024.37.05b.08
33. Voloshin A, Dokichev V, Fahreeva A, Yakubov M, Tomilov YV. Composition and physico-chemical properties of high-viscosity oil of Varadero oil field (Cuba)(Russian). Oil Industry Journal. 2019;2019(09):34-7. 10.24887/0028-2448-2019-9-34-37
34. Pirutin SK, Jia S, Yusipovich AI, Shank MA, Parshina EY, Rubin AB. Vibrational spectroscopy as a tool for bioanalytical and biomonitoring studies. International journal of molecular sciences. 2023;24(8):6947. 10.3390/ijms24086947
35. Grasso M, Petrov V, Manera A. Accuracy and error analysis of optical liquid film thickness measurement with total internal reflection method (TIRM). Experiments in Fluids. 2024;65(6):83. 10.1007/s00348-024-03820-1
36. Johny J, Amos S, Prabhu R. Optical fibre-based sensors for oil and gas applications. Sensors. 2021;21(18):6047. 10.3390/s21186047
37. Ox K, Boltaboyev I. Development of an optoelectronic system for monitoring oil content in purified water based on the element of impaired total internal reflection. 10.32743/UniTech.2024.126.9.18197
38. Hlavatsch M, Haas J, Stach R, Kokoric V, Teuber A, Dinc M, et al. Infrared spectroscopy–quo vadis? Applied Sciences. 2022;12(15):7598. 10.3390/app12157598
39. Qiu S, Zhang K, Shen L, Yuan H, Fan X, Song C, et al. Online detection of mixed oil interface in multi-product pipeline using near-infrared spectroscopy. Microchemical Journal. 2024;206:111480. 10.1016/j.microc.2024.111480

40. Pshenin VV, Zakirova GS. Improving the efficiency of oil vapor recovery units in the commodity transport operations at oil terminals. Записки Горного института. 2024(265 (eng)):121-8. 10.31897/PMI.2023.29
41. Shishanov M, Luchkin M, Ivanova A, Morozov A, Kachaturyan A, Danilov E, et al. Analysis of Carbon-Based Materials by Raman Spectroscopy. Coke and Chemistry. 2024;67(10):607-14. 10.3103/S1068364X24600994
42. Gross N, Kuhs CT, Ostovar B, Chiang W-Y, Wilson KS, Volek TS, et al. Progress and prospects in optical ultrafast microscopy in the visible spectral region: transient absorption and two-dimensional microscopy. The Journal of Physical Chemistry C. 2023;127(30):14557-86. 10.1021/acs.jpcc.3c02091
43. Kostina YV, Rusakova OY, Mikhalitsyn L, Bondarenko G. Use of raman spectroscopy in analysis of crude oils, petroleum products, oil-bearing rocks, and petrochemical process catalysts (a review). Petroleum Chemistry. 2023;63(1):1-30. 10.1134/S0965544123020123
44. Liu M, Du S, Ai Q, Gong J, Shuai Y. Spectral Radiation Characteristic Measurements of Absorption and Scattering Semitransparent Materials—A Review. Energies. 2022;15(23):9013. 10.3390/en15239013
45. Chen J, Chen J, Zhong C, Chen S, Chen B, Fang S, et al. Mesoscopic probes in asphaltenes nanoaggregate structure: from perpendicular to paralleled orientation at the water-in-oil emulsions interface. Rsc Advances. 2017;7(61):38193-203. 10.1039/c7ra06717h
46. Yaseen S, Mansoori GA. Molecular dynamics studies of interaction between asphaltenes and solvents. Journal of Petroleum Science and Engineering. 2017;156:118-24. 10.1016/j.petrol.2017.05.018
47. Zhu B, Yang M, Yan Y, Zhong J, Li J, Li Z, et al. Insights into the effect of water content on asphaltene aggregation behavior and crude oil rheology: A molecular dynamics simulation study. Journal of Molecular Liquids. 2024;396:124042. 10.1016/j.molliq.2024.124042
48. Hasan AM, Kamal RS, Farag RK, Abdel-Raouf ME. Petroleum sludge formation and its treatment methodologies: a review. Environmental Science and Pollution Research. 2024;31(6):8369-86. 10.1007/s11356-023-31674-3
49. Lin Q, Deng L, Dong G, Tang X, Li W, Long Z, et al. aRDG analysis of asphaltene molecular viscosity and molecular interaction based on non-equilibrium molecular dynamics simulation. Materials. 2022;15(24):8771. 10.3390/ma15248771
50. Fakher S, Ahdaya M, Elturki M, Imqam A. Critical review of asphaltene properties and factors impacting its stability in crude oil. Journal of Petroleum Exploration and Production Technology. 2020;10(3):1183-200. 10.1007/s13202-019-00811-5
51. Shi B, Hong J, Wang Z, Chang Z, Li F. Treatment of paraffin deposition behavior in gas-condensate wells with chemical inhibitors. Journal of Petroleum Exploration and Production Technology. 2024;14(2):535-53. 10.1007/s13202-023-01716-0
52. Lyu L, Zhang J, Xu C. Modeling study on oil particle filtration performance of a composite coalescing filter. Frontiers in Energy Research. 2022;10:854913. 10.3389/fenrg.2022.854913
53. Huang J, Ran X, Sun L, Bi H, Wu X. Recent advances in membrane technologies applied in oil–water separation. Discover Nano. 2024;19(1):66. 10.1186/s11671-024-04012-w
54. Hashem H, Kikhavani T, Moradkhani M. Experimental study and machine learning modeling of water removal efficiency from crude oil using demulsifier. Scientific Reports. 2024;14(1):9187. 10.1038/s41598-024-59963-y
55. Kaivosoja J, Sirviö K, Nuortila C, Niemi S. Effects of Fuel Hydrochloric Acid Contamination on Selected Metals. Journal of Marine Science and Engineering. 2024;12(5):776. 10.3390/jmse12050776
56. Li S, Wu J, Wang Y, Zhang X, Zhang W, Zhang Y, et al. Isolation and characterization of thiols in petroleum using Ag+-silica solid phase extraction followed by gas chromatography-mass spectrometry and high-resolution mass spectrometry. Fuel. 2024;363:130946. 10.1016/j.fuel.2024.130946
57. Wallington TJ, Pivesso BP, Lira AM, Anderson JE, Nielsen CJ, Andersen NH, et al. CH3Cl, CH2Cl2, CHCl3, and CCl4: Infrared spectra, radiative efficiencies, and global warming potentials. Journal of Quantitative Spectroscopy and Radiative Transfer. 2016;174:56-64. 10.1016/j.jqsrt.2016.01.029
58. Smith B. Halogenated organic compounds. 2023. 10.56530/spectroscopy.vo3774k1
59. Guan L, Deng H, Yao L, Nie W, Xu Z, Li X, et al. Measurement of middle infrared spectroscopic parameters of carbon disulfide based on tunable diode laser absorption spectroscopy. 2019. 10.7498/aps.68.20182140
60. Gao J, Li C, Xu D, Wu P, Lin W, Wang X. The mechanism of ultrasonic irradiation effect on viscosity variations of heavy crude oil. Ultrasonics Sonochemistry. 2021;81:105842. 10.1016/j.ultsonch.2021.105842
61. Karimov A, Bogdanov V, Valiullin R, Sharafutdinov R, Ramazanov A. The Degassing Processes for Oil Media in Acoustic Fields and Their Applications. Polymers. 2022;14(8):1497. 10.3390/polym14081497
62. Rogachev MK, Aleksandrov AN. Justification of a comprehensive technology for preventing the formation of asphalt-resin-paraffin deposits during the production of highly paraffinic oil by electric submersible pumps from multiformation deposits. Записки Горного института. 2021;250:596-605. 10.31897/PMI.2021.4.13
63. Mullakaev M, Mullakaev R, Esipov I. Ultrasound Control of Viscoelastic Properties of Petroleum Dispersion Systems. Acoustical Physics. 2023;69(3):341-7. 10.31857/S0320791922600408
64. Marfin E GA, Gataullin R, Natfullin R. . Effect of ultrasonic treatment on rheological properties of paraffinic oil. Science & Technologies: Oil and Oil Products Pipeline Transportation. 2024;14(1):74-83. 10.28999/2541-9595-2024-14-1-74-83
65. Lv S PS, Zhang R, Guo Z, Du W, Zhang J, Chen G. . Viscosity Reduction of Heavy Oil by Ultrasonic. Petroleum Chemistry. 2020;60(5):998-1002. 10.31857/S0028242120050196
66. Volkova G, Zubarev D, Kadychagov P. Effect of Ultrasonic treatment on the properties and composition of High-Wax crude oil and its precipitates. Petroleum Chemistry. 2024;64(5):540-7. 10.1134/S0965544124020026
67. Romanova YN, Maryutina TA, Musina NS, Spivakov BY. Application of ultrasonic treatment for demulsification of stable water-in-oil emulsions. Journal of Petroleum Science and Engineering. 2022;209:109977. 10.1016/j.petrol.2021.109977
68. Azeez AW, Hussein HQ. Viscosity reduction of heavy crude oil using ultrasonication assisted by SiFe nanoparticles. Chemical Papers. 2025:1-14. 10.1007/s11696-025-03955-3
69. Shibang M, Dong L, Qi X, Hongguang L, Deng Z, Junwei C, et al. Calibration technology for spectral range and signal-to-noise ratio of terahertz time-domain spectrometer. Journal of Applied Optics. 2023;44(5):1068-72. 10.5768/JAO202344.0503002
70. Ramírez-Vázquez R, Escobar I, Franco T, Arribas E. Physical units to report intensity of electromagnetic wave. Environmental Research. 2022;204:112341. 10.1016/j.envres.2021.112341

71. Ramirez Cabrera PA, Lozano Pérez AS, Guerrero Fajardo CA. Innovative Design of a Continuous Ultrasound Bath for Effective Lignocellulosic Biomass Pretreatment Based on a Theorical Method. Inventions. 2024;9(5):105. 10.3390/inventions9050105

72. Joshi S, Agarkoti C, Gogate PR. Mapping of 20 L capacity ultrasonic reactor using cavitation activity meter and dye degradation. Ultrasonics Sonochemistry. 2023;101:106688. 10.1016/j.ultsonch.2023.106688

73. Shi Z, Wang Z, Yang B, Liu L. Insights into cavitation enhancement: Numerical simulation and spectrum analysis of a novel dual-frequency octagonal ultrasonic reactor. Ultrasonics Sonochemistry. 2025;112:107197. 10.1016/j.ultsonch.2024.107197

COPYRIGHTS

©2026 The author(s). This is an open access article distributed under the terms of the Creative Commons Attribution (CC BY 4.0), which permits unrestricted use, distribution, and reproduction in any medium, as long as the original authors and source are cited. No permission is required from the authors or the publishers.

Persian Abstract

چکیده

امروزه، روسیه و سایر نقاط جهان شاهد افزایش تولید و ذخایر هیدروکربن‌های سنگین (HC) هستند. این امر در مقایسه با ذخایر نفتی متعارف، از نظر نیازهای فنی و مالی، مشکلاتی را ایجاد می‌کند. در این زمینه، یکی از اهداف کلیدی برای پیشرفت بخش منابع معدنی، بهبود سیستم‌های تشخیص میدان نفتی است. این امر "دیجیتالی‌سازی" میدان‌های نفتی و فرآیندهای مربوط به استخراج و حمل و نقل را امکان‌پذیر می‌سازد. هدف از این کار، تجزیه و تحلیل وضعیت فعلی دستگاه‌های تشخیص نفت مادون قرمز (IR)، مشکلات موجود و راه‌های بهینه‌سازی آنها، با توجه ویژه به تصفیه اولیه اولتراسونیک (US) نمونه‌های بسیار چسبناک است. این مطالعه توانست این فرضیه را تأیید کند که تصفیه نمونه‌های نفت رزینی با US منجر به افزایش نسبت سیگنال به نویز (SNR) سیستم تشخیص IR می‌شود. بالاترین راندمان تصفیه US در نقطه‌ای (۱۵ درجه سانتیگراد؛ ۱۵ دقیقه) ثبت شد، جایی که افزایش I_out نسبت به نفت تصفیه نشده ۵۱.۳۶ درصد بود. زمان بهینه برای عملیات اولتراسوند بر اساس تأثیر بر ترکیب شیمیایی روغن عبارت است از: t < ۹ دقیقه در دمای ۱۵ درجه سانتیگراد، t < ٦ دقیقه در دمای ۲۵ درجه سانتیگراد و t < ۳ دقیقه در دمای ۳۵ درجه سانتیگراد. علیرغم نتایج مثبت، نویسندگان بر مشکلات مربوط به توزیع ناهموار ارتعاشات اولتراسوند و نیاز به تحقیقات بیشتر در مورد روغن پارافینی تأکید می‌کنند.

IJE TRANSACTIONS B: Applications Vol. 39, No. 08, (August 2026) 1878-1892

International Journal of Engineering

Journal Homepage: www.ije.ir

A Modified Impedance-Based Loss of Field Detection Method of Synchronous Generator in the Presence of Series Capacitor and its Over-voltage Devices

H. Yaghobi*

Faculty of Electrical and Computer Engineering, Semnan University, Semnan, Iran

PAPER INFO

Paper history:
Received 30 June 2025
Received in revised form 08 September 2025
Accepted 26 September 2025

Keywords:
Synchronous Generator
Series Capacitor
Loss of Field Relay
Over-voltage Devices

ABSTRACT

Loss of field (LOF) detection of synchronous generators in power networks compensated with series capacitors (SCs) create challenging conditions. Fault currents passing through the capacitors can generate over-voltages that exceed the SC ratings, necessitating protection by Metal Oxide Varistors (MOVs). However, when the MOV and capacitor are part of the fault impedance loop, unfavorable conditions arise for LOF relays, including current and voltage fluctuations, high-frequency oscillations from MOVs, and sub-harmonic oscillations. Therefore, this work presents a new modified impedance-based function for LOF protection in the presence of a series capacitor and its over-voltage devices. An analytical solution is proposed to correct the impacts of SCs on LOF protection, which has not been documented previously. The non-linear behavior of the varistor in parallel with the series capacitor is approximated using a linear series R-X impedance model. The operation of the modified LOF function is considered with various capacitor placements, and power network variations such as compensation levels and load changes under complete and partial LOF scenarios. Simulations conducted in MATLAB/Simulink demonstrate the effectiveness and reliability of the proposed method, highlighting its independence from the power system structure while addressing existing relay challenges.

doi: *10.5829/ije.2026.39.08b.09*

Graphical Abstract

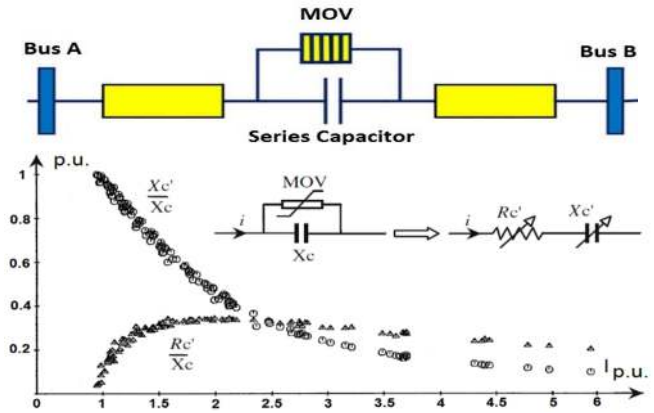

$$R_c' = X_c(0.0745 + 0.49e^{-0.243I_{pu}} - 35e^{-5I_{pu}} - 0.6e^{-1.4I_{pu}})$$

$$X_c' = X_c(0.1010 - 0.0057I_{pu} + 2.088e^{-0.8566I_{pu}})$$

$$\Downarrow$$

$$\vec{Z}_{LOF\ Relay} = \frac{\vec{Z}_G + \vec{Z}_T + \vec{Z}_{SYS} + R_c' - jX'}{(1 - m\,e^{-j\varphi})} - \vec{Z}_G$$

*Corresponding author email: yaghobi@semnan.ac.ir (H. Yaghobi)

Please cite this article as: Yaghobi H. A Modified Impedance-Based Loss of Field Detection Method of Synchronous Generator in the Presence of Series Capacitor and its Over-voltage Devices. International Journal of Engineering, Transactions B: Applications. 2026;39(08):1878-92.

NOMENCLATURE

X_e	System external reactance	δ, w, w_s	Rotor angle, rotor speed and synchronous speed
R_v	Voltage-transformer (VT) ratio	V_d, I_d	The d-axis components of V and I
R_c	Current-transformer (CT) ratio	V_q, I_q	The q-axis components of V and I
Kv, MVA	Machine's rated voltage and power	X_d, X_q	The d-axis and q-axis synchronous reactances
V_S	Machine terminal voltage	X'_d, X'_q	The d-axis and q-axis transient reactances
Z_G, Z_T	Generator and transformer impedance	X''_d, X''_q	The d-axis and q-axis sub-transient reactances
Z_{SYS}	Lumped system impedance	X_{ad}	The d-axis mutual reactance
X_C	Series compensation capacitor reactance	T'_{do}, T''_{do}	The d-axis transient and sub-transient open circuit time constants
i, v	Resistor current and voltage	T'_{qo}, T''_{qo}	The q-axis transient and sub-transient open circuit time constants
β , $I_{p.u.}$	Constant and normalized current	R_f, X_f	Rotor winding resistance and reactance
I_{pr} , I_c	Capacitor current of the protective level and the capacitor fault current	R_a, X_{ls}	Stator winding resistance and leakage reactance
m, k	Series capacitor locations and degrees of compensation	ψ_d, ψ_q	The d-axis and q-axis stator flux linkages
VG	Generator excitation voltage	ψ_{fd}, ψ_{d1}	The d-axis field and damper flux linkages
p_e, p_m	Active and mechanical power of the generator	ψ_{1q}, ψ_{2q}	The q-axis dampers flux linkages
V , I , φ	Voltage and current of the stator and their phase angle difference	V_f, I_f	Field voltage and field current
H	The total inertia constant of the generator	Z_c, R'_c, X'_c	Linear equivalent and series R-X impedance of the parallel arrangement of MOV and series capacitor

1. INTRODUCTION

Series compensation on long transmission lines is growing and unavoidable for various reasons, such as improving the power system stability, increasing voltage control, and transmission power (1, 2). On the other hand, installing series capacitors (SCs) in transmission lines makes the protection more complicated. The amount of this difficulty depends on the installation location and the size of the capacitor. The higher size of the series compensation makes the protection more difficult. The installation place and the technique of series capacitor bypass are also very significant in the protective strategy (3, 4). When the series capacitor and its bypass system are located in the fault impedance loop, the conditions for the LOF relay become unfavorable. The relay computes the impedance value utilizing the voltage and current at the generator station. With the operation of the capacitor bank and its MOV, the currents and voltages of the power network change. Consequently, the impedance calculated by the LOF function is adversely affected. As stated above, the LOF relay is a distance type (5, 6) and it should be mentioned that the performance of distance relays for different faults with the existence of FACTS devices has been considered in many publications. It is worth highlighting that the effects of FACTS devices on the distance relay are different from the effects of the LOF distance function and should be investigated, separately. Consequently, some research works evaluated the impacts of FACTS devices on the LOF distance relay (7-9). In this regard, a wavelet-based scheme for LOF protection in the presence of STATCOM have been presented by Dolatabadi et al. (10). In this work, LOE detection and its differentiation from other network disturbances are discussed and the importance of intelligent signal processing approaches in modern FACTS-equipped networks is emphasized. Hasani et al. (11) presented a complete review of current LOF protection strategies for synchronous generator. This work highlights emerging trends such as digital signal processing methods and adaptive techniques that increase the accuracy and speed of detection.

Furthermore, some papers have been announced specifically on the effect of series capacitors on line distance function relays. As an example, adaptive distance protections in transmission lines compensated with series capacitors have been presented based on different techniques. The method presented by Ghassemi et al. (12) used the voltage compensation for calculating the voltage drop on the series capacitors and modifying the relay settings. Another adaptive technique using impedance estimation considering MOV operation, power system condition, and fault resistance in series compensated lines is proposed by Biswal et al. (13). Also, a scheme using residual current in distance function relays for series compensated lines is suggested by Ghassemi and Johns (14). Some other methods based on artificial intelligence for distance function relays in series

compensated lines have been proposed by several research scientists (15-21). Furthermore, neural network intelligent algorithm and data mining method are proposed by Rahmkhoda et al. (22, 23) and Silva et al. (24) to enhance the safety of the LOE protection of synchronous generator in the presence of unified power flow controller and SVC. Supervised learning algorithms to distinguish LOF from power swings, was proposed by Gulati and Verma (25). They demonstrated the ability of artificial intelligence to recognize complex dynamic behaviors. Furthermore, a machine learning ensemble framework for detecting LOF conditions have been presented by Ramadoss and Muthiah (26). In this research, several models are presented to improve classification accuracy and reduce false detection rate. However, these methods need a lot of training. On the other hand, in the previous study of the author, only the performance of two LOF relays with positive and negative offset has been compared with the presence of the series capacitor, and no solution has been provided (27).

Therefore, in this paper, the impact of SCs and their over-voltage devices on the LOF relay has been carefully analyzed. This research describes a modified impedance-based function for LOF protection of generators in the power networks with fixed series compensation. The parallel arrangement of the nonlinear resistance and series capacitor is approximated by the linear series impedance R-X. In other words, an analytical method is developed considering MOV operation, different series capacitor locations, and variations in the power network such as different degrees of compensation, load, and different LOF scenarios. In summary, the important points in the literature review of this article can be found as follows:

- The LOF relay is basically a distance type because it uses the voltage and current at the relay location to make a decision.
- The problems of distance relays, including transmission line distance relays and generator field relays in the existence of FACTS devices, have been investigated in several articles. In these articles, usually no solution is presented and only the problems are investigated or mostly solutions based on artificial intelligence are presented to solve the issues. However, these methods need a lot of training data for different conditions of the network.
- The problems of transmission line distance relays in the existence of series compensation capacitors, have been investigated in some papers. In these papers, similar to the previous case, most solutions based on artificial intelligence are presented to solve the problems. However as mentioned above, these approaches require a lot of training data for different conditions of the power system.
- The impacts of the series capacitor on the LOF protection of the synchronous generator have not been evaluated in the literature or at least no solution has been presented for it.

Therefore, the key contributions of this study are as follows:

- The effect of the series capacitor on the LOF protection of the synchronous generators is investigated and an analytical solution for its correction is presented which has not been reported in the literature yet.
- This analytical technique is developed taking into account MOV operation, different capacitor locations, and variations in the power network such as degrees of compensation, load, and different LOF conditions including complete and partial LOF scenarios.
- The parallel arrangement of a highly non-linear varistor and series capacitor is estimated by a linear series R-X impedance.
- Based on the point that these kinds of relays are currently operative in loss of field protection of synchronous generators, therefore, it has been tried to solve some of the issues of these kinds of relays.

The LOF relay considered in this research is the Berdy distance function and the “Matlab/Simulink” software has been used for time domain simulation of the SCs and their over-voltage devices. Extensive results indicate the effectiveness and satisfactory performance of the suggested method. The rest of this article is organized as follows: Section 2 explains the modified impedance-based LOF protection of a generator in the presence of a series capacitor and its over-voltage devices. In section 3, the performances of the proposed technique are presented and the results are analyzed. Finally, section 4 concludes the investigation.

2. MODIFIED LOF PROTECTION IN THE SERIES COMPENSATED LINE

Coordination between LOF protection with generator under-excited capability (GUEC) limit, steady-state stability limit (SSSL), and generator under-excitation limiter (UEL) is very important issue. The salient-pole generator capability limits are illustrated in Figure 1. This machine has minor end core area losses. Consequently, the GUEC limit has been represented by the current limit of the stator winding (i.e. arc from B to D). It is worth mentioning that the leading VAR limit of the GUEC is determined by the portion of the arc from C to D. Furthermore, during the normal mode of operation of the generator, the SSSL shows how far the machine can operate under-excited area of the capability curve (9, 28, 29).

In fact, in coordination studies, the SSSL is utilized to adjust the machine UEL. The SSSL characteristic is drawn in Figure 1, as portion of a circle with the following center and radius.

$$Center = 0,\ \frac{V_s^2}{2}\left(\frac{1}{X_e}-\frac{1}{X_d}\right),\ Radius = \frac{V_s^2}{2}\left(\frac{1}{X_e}+\frac{1}{X_d}\right) \quad (1)$$

where X_e is the system external reactance, X_d is d-axis steady-state machine reactance and V_s is the machine terminal voltage.

In addition to these, the machine UEL is set to prevent the reduction of the excitation over the heating limit of the stator-end region. Usually, this characteristic is set to 80–85% of one of the SSSL characteristic or the GUEC characteristic with minimum time delay (9). In order to coordinate the three characteristics GUEC, SSSL, and UEL to LOF relay, these three characteristics should be converted in the R-X plane (9) (see Figure 2(a)). In this figure, R_v is the voltage-transformer (VT) ratio, R_c is the current-transformer (CT) ratio, kV is the machine's rated voltage and MVA is the machine's rated power.

On the other hand, it should be mentioned that the common technique to detect the LOF in a generator is to use a relay introduced by Berdy (30) as presented in Figure 2(b). This relay has two operation zones with a negative offset equal to $x'_d/2$. The diameter of the first zone is one p.u. (machine base) and the diameter of the second zone is xd. In this relay, typically, 0.1s time delay is considered for the first zone and, 0.5 to 0.6 s time delay is considered for the second zone. These intentional time delays prevent relay misoperation during stable power swings and transient conditions (31-33). It should be noted that transient stability studies should be conducted to see if the above time delays are sufficient to prevent inadvertent tripping during stable power swings and transient conditions. However, usually for simplicity these time delays are typically considered.

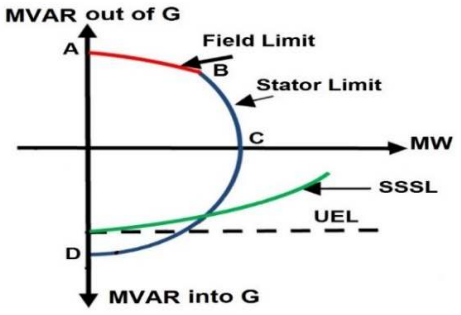

Figure 1. Capability limits of a generator

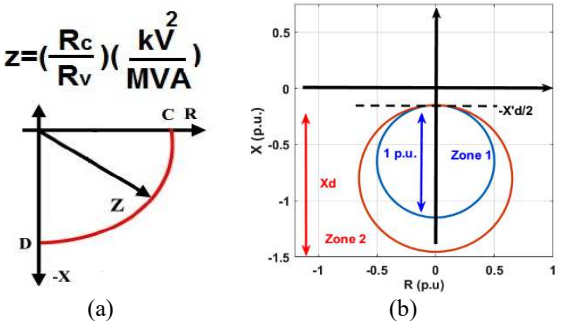

(a) (b)

Figure 2. Synchronous generators characteristic (a) GUEC, SSSL, and UEL in the R-X plane (b) Berdy LOF characteristic and impedance locus at the generator terminal following LOF and stable power swing condition

2. 1. Distance Relay Problem due to Compensation

The series capacitor and its protective devices against overvoltage, despite the advantages in the power network, cause problems for protection relays such as sub-harmonic oscillation, current and voltage changes, and additional transients (4). Following the occurrence of the fault, impedance-based relays in series compensated networks face various challenges, and changes in current and voltage data occur. Depending on the location of the fault and the compensation degree, the impedance-based relay may experience a fundamental frequency resonant situation with high voltage and current values. One of these impedance-based relays is the Berdy LOF relay. The impedance trajectory measured at location of the relay is affected by voltage changes caused by the series capacitors after the fault.

2. 2. Modified Impedance-Based LOF Protection

In this research, it is assumed that the LOF condition occurred simultaneously during the three-phase short circuit fault. Figure 3 shows approximated equivalent circuit for research on the detection of LOF condition during fault in a compensated power network with a MOV-protected series capacitor. This situation activates MOV. In fact, when the capacitor and its MOV are located in the fault impedance loop, the conditions for the LOF relay at the generator location become unfavorable.

In this network, V_S is machine terminal voltage, Z_G, Z_T, Z_{SYS}, X_C, and Z_C are generator impedance, transformer impedance, lumped system impedance, series compensation capacitor reactance, and linear equivalent impedance of the parallel arrangement of MOV and series capacitor, respectively. The generator terminal voltage can be calculated as follows:

$$V_S = \sqrt{V_d^2 + V_q^2} \quad (2)$$

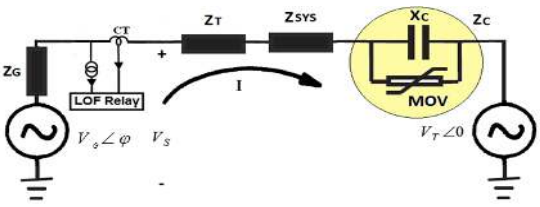

Figure 3. Configuration of the network studied

In this investigation, the complete model of the synchronous generator is used. This model takes into account all the basic aspects of the behavior of the synchronous generator, including its electrical and mechanical characteristics. In fact, this complete model provides the possibility of simulation and detailed analysis of the performance of the synchronous generator in different operating conditions. A three-phase salient pole synchronous generator with one field winding (subscripted by *f)*, has been used. A lumped winding (subscripted by 1d) was used to consider the impact of the induced currents in the rotor core.

On the other hand, two fabricated lumped windings (subscripted by *1q* and *2q*) were used to consider the effects of damper bars in the rotor. It should be noted that in this work eight equations have been used to model the performance of a three-phase salient pole synchronous generator, including two mechanical Equations, 3 and 4, and six electrical equations in *dq* form, Equations 3 to 8 (34).

$$\frac{2H}{w_s}\frac{dw}{dt} = p_m - p_e \tag{3}$$

$$\frac{d\delta}{dt} = w - w_s \tag{4}$$

$$\frac{1}{w_s}\frac{d\psi_d}{dt} = V_d + w\,\psi_q + R_a I_d \tag{5}$$

$$\frac{1}{w_s}\frac{d\psi_q}{dt} = V_q - w\,\psi_d + R_a I_q \tag{6}$$

$$T'_{do}\frac{dE'_q}{dt} = -E'_q - (X_d - X'_d)[I_d - \frac{X'_d - X''_d}{(X'_d - X_{ls})^2}(\psi_{1d} + (X'_d - X_{ls})I_d - E'_q] + E_f \tag{7}$$

$$T''_{do}\frac{d\psi_{1d}}{dt} = -\psi_{1d} + E'_q - (X'_d - X_{ls})I_d \tag{8}$$

$$T'_{qo}\frac{dE'_d}{dt} = -E'_d + (X_q - X'_q)[I_q - \frac{X'_q - X''_q}{(X'_q - X_{ls})^2}(\psi_{2q} + (X'_q - X_{ls})I_q + E'_d] \tag{9}$$

$$T''_{qo}\frac{d\psi_{2q}}{dt} = -\psi_{2q} - E'_d - (X'_q - X_{ls})I_q \tag{10}$$

where

$$E'_q = \frac{X_{ad}}{X_{ff}}\psi_{fd},\ E'_d = -\frac{X_{aq}}{X_{11q}}\psi_{1q},\ E_f = \frac{X_{ad}}{R_f}\psi_{1q}V_f \tag{11}$$

Also, the variables of the machine can be calculated as:

$$\psi_d = -X''_d I_d + \frac{X''_d - X_{ls}}{X'_d - X_{ls}}E'_q + \frac{X'_d - X''_d}{X'_d - X_{ls}}\psi_{1d} \tag{12}$$

$$\psi_q = -X''_q I_q + \frac{X''_q - X_{ls}}{X'_q - X_{ls}}E'_d + \frac{X'_q - X''_q}{X'_q - X_{ls}}\psi_{2q} \tag{13}$$

This model of three-phase salient pole generator is simulated in Matlab/Simulink software. Furthermore, standard models of ESDC1A and IEEEG1 have been utilized to model the machine excitation system and governor, respectively (35). The detailed data of these models are given in Appendix (see Tables 2 and 3). In the network, illustrated in Figure 3 the LOF relay impedance measured at the machine terminal can be determined as follows:

$$\vec{Z}_{\text{Relay}} = \frac{\vec{V}_S}{\vec{I}} = \frac{(\vec{V}_G - Z_G\vec{I})}{\vec{I}} = \frac{V_G\angle\varphi}{\vec{I}} - \vec{Z}_G \tag{14}$$

where

$$\vec{I} = \frac{\vec{V}_G - \vec{V}_T}{Z} = \frac{V_G\angle\varphi - V_T\angle 0}{\vec{Z}_G + \vec{Z}_T + \vec{Z}_{SYS} + \vec{Z}_C} \tag{15}$$

On the other hand:

$$\frac{\vec{V}_T}{\vec{V}_G} = \frac{|V_T|\angle 0}{|V_G|\angle\varphi} = \frac{|V_T|}{|V_G|}e^{-j\varphi},\ m = \frac{|V_T|}{|V_G|} \tag{16}$$

Therefore:

$$\vec{V}_T = (\vec{V}_G)\,m\,e^{-j\varphi} \tag{17}$$

By substituting Equation 17 into Equation 15, the $\vec{I}$ can be written as:

$$\vec{I} = \frac{\vec{V}_G(1 - m\,e^{-j\varphi})}{\vec{Z}_G + \vec{Z}_T + \vec{Z}_{SYS} + \vec{Z}_C} \tag{18}$$

Finally, by applying Equation 18 to Equation 14, the impedance seen by the LOF relay can be calculated as:

$$\vec{Z}_{\text{Relay}} = \frac{\vec{Z}_G + \vec{Z}_T + \vec{Z}_{SYS} + \vec{Z}_C}{(1 - me^{-j\varphi})} - \vec{Z}_G \tag{19}$$

As stated earlier, Z_c is the equivalent impedance of the parallel arrangement of MOV and series capacitor which is fully described in the following. Series capacitor banks are constructed by combining parallel and series units to obtain the desired nominal values. Also, these capacitor banks are designed in such a way that rated current values are obtained. Series capacitor banks are exposed to severe stress during fault situations. Fault current passing through the capacitor bank produces voltages that exceed the rated amount of the capacitor. Hence, in modern capacitor banks, Metal Oxide varistors (MOVs) as shown in Figure 4(a) are usually used to protect against over-

voltages (4). In addition, the capacitor block illustrated in Figure 4(a) contains a "damping device" that is a current-limiting circuit. A typical non-linear voltage-current characteristic (4) of this surge arrester called a varistor, is illustrated in Figure 4(b).

When the voltage reaches its limit, a large amount of current passes through the varistor, and the voltage through the series compensation capacitor is limited. The voltage-current characteristic of this surge arrester can be approximated as follows:

$$v = ki^{\beta} \tag{20}$$

where i is resistor current, β is a constant smaller than one and v is resistor voltage. Equation 20 can be written as:

$$\alpha = \ln v = \ln k + \beta \ln i \;\Rightarrow\; v = e^{\alpha} = e^{(\ln k + \beta \ln i)} \tag{21}$$

By substituting Equation 18 into Equation 21, the MOV voltage can be written as:

$$v = e^{(\ln k + \beta \ln(\frac{\vec{V}_G(1-me^{-j\varphi})}{\vec{Z}_G+\vec{Z}_T+\vec{Z}_{SYS}+\vec{Z}_C}))} \tag{22}$$

It should be noted that during a complete LOF V_G is zero. However, in partial LOF, V_G is not zero and its amount is a percentage of the machine's complete field voltage (i.e. less than 100 %). Using the experimental data, a fundamental frequency model of the non-linear MOV has been remodeled to a series R-X model (36). This is shown in Figure 5, that R_c' and X_c' are controlled by the instantaneous current (36). It can be seen that capacitive reactance and resistance are non-linear, and are functions of the normalized current $I_{p.u.}$.

In other words, the parallel arrangement of non-linear varistor and series compensation capacitor can be modeled by a linear series R-X impedance as illustrated in Figure 5. Using the data from Figure 5 and least-squares curve fitting, this linear model can be found as follows (36, 37):

$$\begin{aligned} R_c' &= X_c(0.0745 + 0.49e^{-0.243I_{pu}} - 35e^{-5I_{pu}} - 0.6e^{-1.4I_{pu}}) \\ X_c' &= X_c(0.1010 - 0.0057I_{pu} + 2.088e^{-0.8566I_{pu}}) \end{aligned} \tag{23}$$

where X_c is nominal capacitor reactance, $I_{p.u.}=I_c/I_{pr}$ (the current is normalized), I_{pr} is the capacitor current of the protective level and I_c is the capacitor fault current.

It should be noted that the value of the capacitor fault current should be determined and sent to the relay location in the generator terminal through a communication channel.

Specific data of the series compensation module that is required in this method is given in Appendix (see Table 2).

In power system relaying, the acceptable latency and required bandwidth for a data communication channel can vary significantly based on the specific application, the type of relay being used, and the overall system requirements. It is worth noting that the impedance LOF relay is a slow relay. Hence, there is no need for a very high-speed communication channel to transmit capacitor's fault current value to the generator's terminal. However, the acceptable latency for protection relays in the range of 1 to 10 milliseconds is suitable for the proposed method. On the other hand, the bandwidth requirement for proposed relay is low since the method send small amounts of critical data (i.e. the capacitor's fault current value) at high rates. Typical bandwidth requirements are around 10 to 100 kbps.

Furthermore, since relay 78 (out-of-step relay) is a backup for relay 40 (LOF relay), the generator will not be left unprotected in the event of a failure or cyber-attack on this data communication channel (Please see the answer to your comment 3.).

Another point to consider is that whenever a fault occurs, there is a DC component in the fault current. To remove the DC offset, various methods mentioned by Yaghobi (38) can be used. However, it should be noted that in this research assumes that the DC offset has been removed first.

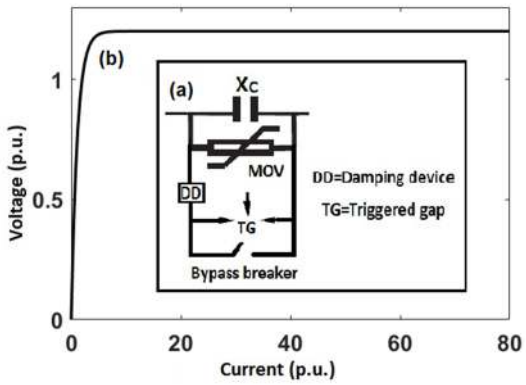

Figure 4. Series capacitor (a) Used model (b) Voltage-current characteristic of the MOV.

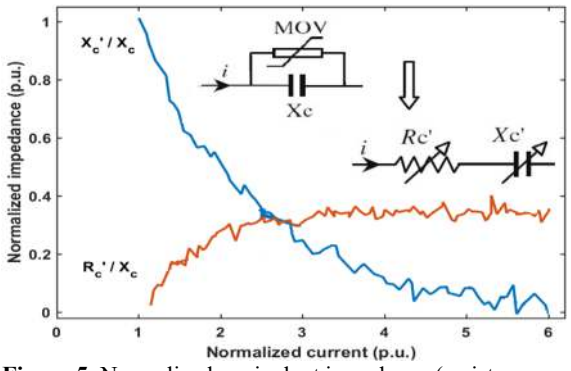

Figure 5. Normalized equivalent impedance (resistance and reactance) versus normalized current of the series compensation capacitor and its MOV protection

The typical value of I_{pr} is 2-2.5 times of the full load current. It should be noted that R_c' and X_c' is normalized by dividing by X_c and precise amounts of R_c' and X_c' depends on the amplitude of the fault current passing through the MOV (varistor). Rahmkhoda et al. (23) determined the equivalent impedance; only the values of X_c and I_{pr} should be determined. The normalized value of R_c' and X_c' versus $I_{p.u.}$ is plotted in Figure 5. These values change with the current and reach almost zero as $I_{p.u.}$ is increased more than 6 p.u. According to Rahmkhoda et al. (23) and data from Figure 5, the linear equivalent impedance of the MOV-protected series compensation capacitor can be found as follows (36, 37):

$$Z_c(I_{p.u.}) = \begin{cases} -jX_c & if \ \ I_{p.u.} < 0.98 \\ R_c' - jX_c' & if \ \ I_{p.u.} \geq 0.98 \end{cases} \quad (24)$$

It is worth highlighting that if the capacitor current is more than 98% of the protective level current, the MOV conducts. However, below this value, the MOV does not act and is out of service. In other words, if the protective voltage level of the series compensation capacitor exceeds its threshold value under fault conditions, the MOV will conduct and as a result, the impedance of the series capacitor/MOV combination will vary.

3. PERFORMANCES OF THE PROPOSED TECHNIQUE

The operation of the modified LOF function is evaluated in the presence of a series capacitor at different locations for a 400 kV power system as illustrated in Figure 3. In the transmission line, every phase of the series compensation module includes the series compensation capacitor and the capacitor is protected by a MOV. In the protection of a synchronous generator with the series compensated line, the series capacitor location and degrees of compensation are important. Therefore, this research has been done for various series capacitor locations (i.e. m = 0, m = 0.5, m = 1), for varying degrees of compensation (i.e. k = 0.4, k = 0.7), and for different LOF conditions including complete and partial LOF scenarios (i.e. VG = 0 p.u. and VG = 0.5 p.u.). Furthermore, four critical loading points of the machine are considered in this research (i.e. light and heavy loading with the lagging and leading power factor conditions).

3. 1. Performances of the LOF Relay without Coordination with other Characteristics

The results for the conventional and proposed technique are provided in Table 1 for various system situations. As stated earlier, adding series compensation capacitors in the transmission line complicates the protection of the generator, and the degree of this complexity changes with the degree of compensation and the installation location of the capacitors along the transmission line. In other words, in transmission lines compensated with series capacitors, observable characteristics may change significantly and this problem may cause difficulties for conventional LOF relaying schemes. The voltage, current, and impedance measured by the relay have significant changes depending on the size and installation location of the series capacitor.

For a clear demonstration, the machine output voltage and current following LOF under inductive heavy load condition (L1 = 0.9 + j0.3 p.u.) is shown in Figure 6(a). LOF condition in this case occurs after 10 s of starting the simulation time. As it is displayed in Figure 6(a), the generator output voltage decreases to a negative value during this situation. In addition, with the existence of a series compensation capacitor, the rate of reduction of the machine terminal voltage is reduced, which makes the LOF condition to be detected later. The output current of the generator is also presented in this figure. As shown in this figure, the existence of a series capacitor causes the machine armature to remain longer under the fault current conditions and its amount increases to a consideration value. Furthermore, Figure 6(b) presents the machine output active and reactive power under inductive heavy load condition (L1 = 0.9 + j0.3 p.u.).

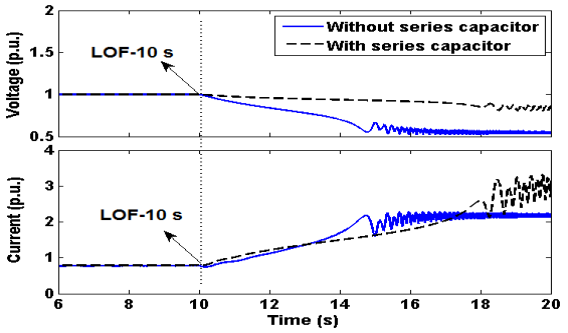

(a)

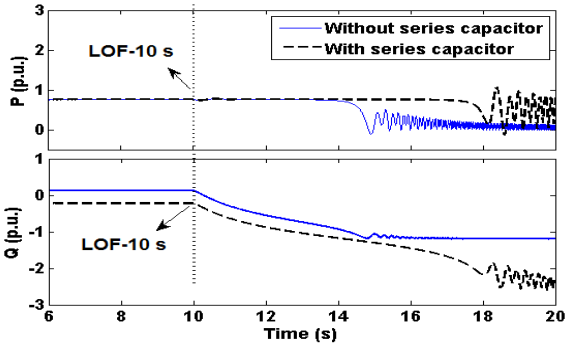

(b)

Figure 6. The generator output following LOF under inductive heavy load condition (L1 = 0.9 + j0.3 p.u.) (a) Terminal voltage and current (b) Active and reactive power

As can be seen from this figure, similar to the terminal voltage, next the happening of the LOF condition, the machine output reactive power decreases to a considerable negative value, while the output active power has an almost constant value before loss of synchronism. The effect of the partial LOF on the machine output under the capacitive heavy load condition (L3 = 0.7 -j0.5 p.u.) is shown in Figure 7. The PLOF condition in this case occurs after 10 s of starting the simulation time. In PLOF condition, the rotor field of the generator is partially lost, while in complete LOF, the rotor field of the machine is completely lost. The comparison between Figures 6 and 7 denote that the impact of the partial LOF on the generator output is less intense than a complete LOF.

In PLOF condition, depending on the amount of residual excitation voltage, the rate of voltage drop and the reactive power of the machine terminal are reduced compared to the complete LOF. Therefore, the operation time of the relay increases. In PLOF conditions, because the excitation voltage of the generator is not completely lost, the machine absorbs less reactive power from the grid than a complete LOF condition. The lower percentage of field is lost, the generator loses synchronism at a longer time, which means the relay will have more time to detect, however this detection will be more difficult. Therefore, the worst case for the conventional relay is a low percentage of PLOF under loading with the leading power factor condition, which

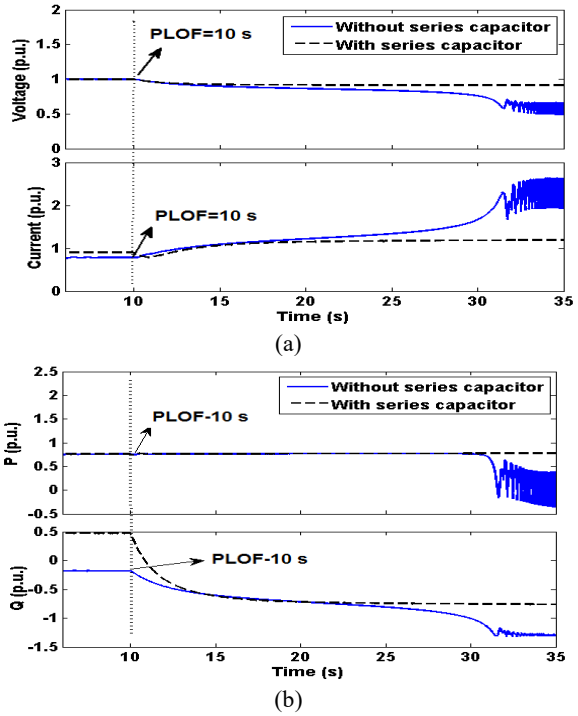

Figure 7. The generator output following PLOF under capacitive heavy load condition (L3 = 0.7 -j0.5 p.u.) (a) Terminal voltage and current (b) Active and reactive power

greatly increases the relay operation time or in some cases, the relay does not operate. Long-term reactive power drain may cause tripping of the line relays and general power network instability. This situation becomes worse with the presence of a series capacitor. Because some of the reactive power required by the generator in this condition is supplied by the series capacitor.

If the series capacitor is placed in the middle of the transmission line, its effectiveness is increased, especially for very long transmission lines. When the capacitor is installed in the middle of the transmission line, the changes in the variables (i.e. voltage, current, and impedance) are less than when the capacitor is located at the beginning or end of the line. Therefore, according to Table 1, in general, the time to detect the LOF conditions by the relay when the series capacitor is installed in the middle of the line is less than the other two cases. It should be mentioned that the relay operating time is higher under a capacitive load condition than an inductive load condition. In addition, the relay operation time increases in the partial LOF condition compared to the complete LOF condition. Therefore, as stated earlier, the worst case for the relay is partial LOF under capacitive load condition, which greatly increases the relay operation time. Furthermore, when the series capacitor is in service, generator protection becomes more complicated, and this condition can potentially cause the relay not to operate.

Accordingly, it can be seen from the simulation results presented in Table 1, that the presence of a series capacitor under PLOF (VG =0.5 p.u.) with capacitive load conditions causes the conventional LOF relay not to work during cases 3, 9, 15, 27, and 33. In other words, during these cases, the conventional LOF relay does not issue a trip signal whereas the modified technique trips at 4.15 s (5.65-1.5), 4.02 s (5.52-1.5), 3.93 s (5.43-1.5), 4.43 s (5.93-1.5), and 4.21 s (5.71-1.5) for cases 4, 10, 16, 28, and 34, respectively. The partial LOF condition in all cases occurs after 1.5 s of starting the simulation time. In other cases, the presence of the series capacitor causes the conventional relay to take a longer tripping time compared with the suggested modified technique. In fact, the modified technique has effectively reduced the tripping time associated with the presence of the series compensation capacitor. It should be noted that the amount of equivalent impedance of the compensation capacitor and its MOV (Z_c) in simulation has been presented in Table 1. Figure 8(a) presents the impedance trajectory calculated by the modified and conventional LOF function following LOF (i.e. VG = 0 p.u.) during cases 7, and 8 under inductive heavy load condition (i.e. L1=0.9+j0.3 p.u.) with the presence of series capacitor and its over-voltage devices. In these cases, the series compensation capacitor is considered at the beginning of the transmission line with 70% compensation (i.e. m=0, k=0.7). Both impedance locus enters into the operating

zone of the relay. However, the conventional technique trips at 2.32 s (3.82–1.5) which has been reduced to 2.01 s (3.51–1.5) by the modified technique.

Moreover, to illustrate the similarity in characteristics, Figure 8(b) illustrates the impedance loci computed by the modified and conventional LOF function following complete LOF during cases 25, and 26 under inductive heavy load condition (i.e. L1 = 0.9+j0.3 p.u.) with the presence of series capacitor and its over-voltage devices. In these cases, the series compensation capacitor is considered at the end of the transmission line with 40% compensation (i.e. m=1, k=0.4). Both impedance locus enter into the operating zone of the relay. However, the conventional technique trips at 3.68 s (5.18–1.5) which has been reduced to 2.82 s (4.32–1.5) by the modified technique. As reported in Table 1 and according to Figures 8(a) and 8(b), it can be clearly seen that these two techniques are robust adequate to correctly distinguish the complete LOF situation under inductive loading with the presence of a series capacitor and its over-voltage devices.

In other words, there is no significant difficulty. However, only the conventional relay needs more time to send a trip signal compared to the modified technique. Additionally, the performance of the modified and conventional function under LOF (VG =0 p.u.) with the heavy capacitive loading conditions (i.e. L3 = 0.7-j0.5 p.u.) in the presence of series capacitor and its over-voltage devices are shown in Figures 8(c), 8(d), and 8(e). In cases 13 and 14 (see Figure 8(c)) the series compensation capacitor is considered at the middle of the transmission line with 40% compensation (i.e., m=0.5, k=0.4). Also, in cases 19 and 20 (see Figure 8(d)), the series compensation capacitor is considered at the middle of the transmission line, but with 70% compensation (i.e., m=0.5, k=0.7). In cases 25 and 26 (see Figure 8(e)), the series compensation capacitor is considered at the end of the transmission line with 40% compensation (i.e., m=1, k=0.4). As reported in Table 1 and according to Figures 8(c), 8(d), and 8(e), it can be clearly seen that these two techniques are robust adequate to correctly distinguish the complete LOF condition with the presence of a series capacitor and its over-voltage devices. However, the conventional relay takes a longer time to send a trip signal compared to the modified technique. It should also be noted that this trip time is longer than the inductive loading with similar conditions. The conventional technique trips at 2.44 s (3.94-1.5), 2.14 s (3.64-1.5), and 4.372 s (5.872-1.5) for cases 13, 19, and 25, respectively whereas the modified technique trips at 1.77 s (3.27-1.5), 1.62 s (3.12-1.5), and 3.22 s (4.72-1.5) for cases 14, 20, and 26, respectively. It can be obviously realized that in all cases the trip time of the modified technique has been effectively reduced compared to the conventional relay. On the other hand, as mentioned before, the worst case of relay operation is partial LOF under capacitive load conditions. Therefore, the performance of the modified and conventional function under PLOF (VG =0.5 p.u.) with the heavy capacitive loading condition (i.e. L3 = 0.7 -j0.5 p.u.) in the presence of series capacitor and its over-voltage devices are shown in Figures 8(f) and 8(g). In cases 9 and 10 (see Figure 8(f)), the series compensation capacitor is considered at the beginning of the transmission line with 70% compensation (i.e. m=0, k=0.7).

Furthermore, in cases 15 and 16 (see Figure 8(g)), the compensation capacitor is considered at the middle of the transmission line with 40% compensation (i.e. m=0.5, k=0.4). At these conditions, the conventional LOF relay does not operate for cases 9 and 15 whereas the modified technique trips at 4.02 s (5.52-1.5) and 3.93 s (5.43-1.5) for cases 10 and 16, respectively. In the following, in cases 9, 10, 21, and 22, it is supposed the generator operates at the light capacitive loading conditions with partial LOF event. The impedance loci computed by the conventional and the modified function after PLOF with the light capacitive loading conditions (i.e. L4 = 0.1-j0.1 p.u.) in the presence of series compensation capacitor and its over-voltage devices are also shown in Figures 9(h) and 9(k).

In cases 9 and 10 (see Figure 9(h)) the compensation capacitor is considered at the beginning of the transmission line with 70% compensation (i.e. m=0, k=0.7). Moreover, in cases 21 and 22 (see Figure 9(k)), the compensation capacitor is considered at the middle of the transmission line with 70% compensation (i.e. m=0.5, k=0.7). In all cases, the impedance locus enters into the operating zone of the relay. The conventional technique trips at 4.12 s (5.62-1.5), and 3.64 s (5.14-1.5) for cases 9, and 21, respectively whereas the modified technique trips at 2.84 s (4.34-1.5), and 2.78 s (4.28-1.5) for cases 10, and 22, respectively. It can be realized that in all cases the trip time of the modified technique has been effectively reduced compared to the conventional relay.

Furthermore, other percentages of PLOE under capacitive load conditions were examined and it was determined that the proposed method has performed successfully up to V_G=0.75 (i.e. 25 percent of excitation has been lost). The proposed method has had unsuccessful performance under conditions where V_G is greater than 0.75 in several cases (V_G>0.75). These results are also presented in Table 1.

3. 2. Performances of the LOF Relay in Coordination with GUEC, SSSL, and UEL Characteristics As stated earlier, coordination between LOF protection with GUEC, SSSL, and UEL is very important issue and special attention should be paid for relay operation under partial LOF during capacitive load conditions. In this regard, a significant problem that must be considered during this

TABLE 1. Performance of modified and conventional LOF function in the presence of series capacitor and its over-voltage devices

Case	Capacitor location	Degree of Compensation	$Z_C(\Omega)$	Mode of LOF	Protection method	Type of loading (p.u.)			
						Lagging		Leading	
						L1- Heavy 0.9+j0.3	L2- Light 0.1+j0.2	L3- Heavy 0.7-j0.5	L4- Light 0.1-j0.1
						Detection time (s)			
1	m=0	k= 0.4	$R'_C=8.18$ $X'_C=3.42$	V_G=0	Conventional	4.13	3.52	4.35	3.71
2					Proposed	3.54	3.32	3.8	3.5
3				V_G=0.5	Conventional	5.62	5.42	×	6.35
4					Proposed	4.81	4.38	5.65	4.58
5				V_G=0.75	Conventional	6.74	6.44	×	7.58
6					Proposed	5.72	5.25	6.67	5.47
7		k= 0.7	$R'_C=20$ $X'_C=12.41$	V_G=0	Conventional	3.82	3.5	3.95	3.7
8					Proposed	3.51	3.14	3.61	3.52
9				V_G=0.5	Conventional	5.2	4.85	×	5.62
10					Proposed	4.56	4.12	5.52	4.34
11				V_G=0.75	Conventional	6.24	5.78	×	6.74
12					Proposed	5.46	4.91	6.54	5.208
13	m=0.5	k= 0.4	$R'_C=7$ $X'_C=2.78$	V_G=0	Conventional	3.65	2.8	3.94	3.22
14					Proposed	3.14	2.62	3.27	2.95
15				V_G=0.5	Conventional	5.4	5.22	×	6.12
16					Proposed	4.66	4.12	5.43	4.52
17				V_G=0.75	Conventional	6.46	6.26	×	×
18					Proposed	5.48	4.98	6.32	5.29
19		k= 0.7	$R'_C=12.26$ $X'_C=4.87$	V_G=0	Conventional	3.41	2.98	3.64	3.01
20					Proposed	3.04	2.72	3.12	2.82
21				V_G=0.5	Conventional	4.95	4.62	5.73	5.14
22					Proposed	4.45	4.10	5.25	4.28
23				V_G=0.75	Conventional	5.94	5.49	×	×
24					Proposed	5.34	4.89	6.3	5.01
25	m=1	k= 0.4	$R'_C=6.07$ $X'_C=2.36$	V_G=0	Conventional	5.18	4.12	5.872	4.65
26					Proposed	4.32	3.95	4.72	4.05
27				V_G=0.5	Conventional	5.62	5.18	×	6.63
28					Proposed	4.52	4.12	5.93	4.69
29				V_G=0.75	Conventional	6.74	6.28	×	×
30					Proposed	5.44	4.93	7.104	5.6
31		k= 0.7	$R'_C=10.62$ $X'_C=4.12$	V_G=0	Conventional	4.38	3.87	4.82	4.05
32					Proposed	3.65	3.01	3.91	3.62
33				V_G=0.5	Conventional	4.89	4.7	×	5.85
34					Proposed	3.75	3.62	5.71	4.51
35				V_G=0.75	Conventional	5.85	5.61	×	×
36					Proposed	4.53	4.39	6.91	5.43

coordination is the presence of series capacitor and its over-voltage devices. Figure 9(a) shows a sample case study, in which the voltage reduces about 14%. In this case, the impedance locus of the modified LOF function does not penetrate the reduced zone of the relay characteristic (coordinated with GUEC, SSSL, and UEL characteristics). Therefore, non-LOF condition is detected. However, it enters the zones 1 and 2 with original setting (i.e. Z_{1old} and Z_{2old}) and the LOF relay with original setting misoperates in this condition. Such a voltage reduction will be alarmed by undervoltage (UV) supervising element. It should be noted that usually the UV relay is set at 80%–90% of rated voltage of the machine to pick up with a time delay of 0.25–1 s. In this study, the UV relay is set at 87% of the rated voltage of the machine with a time delay of 1s. Figure 9(b) shows the generator terminal voltage during undervoltage condition (i.e. related to Figure 9(a)). As a result of the undervoltage condition, generator terminal voltage begins to reduction and falls below the UV threshold at which it picks-up at 6 seconds after the start of the simulation and assigning a one second time delay. On the other hand, in order to investigate the security of the proposed modified LOF function, stable power swing condition as another non-LOF event has been evaluated in this section. It should be mentioned that there are various types of unstable power swing or out-of-step (OOS) relays, some of which are presented by Yaghobi (39). These relays are different from LOF relays. Therefore, this article does not discuss the distinction and diagnosis of OOS and LOF from each other and only the distinction of LOF from stable power swings is examined. In fact, the impedance-based LOF protections are prone to mal-operation under stable power swing conditions and the LOF relay must be blocked during the stable power swings to avoid misoperation. These methods overcome this possible mal-operation by assigning a time delay.

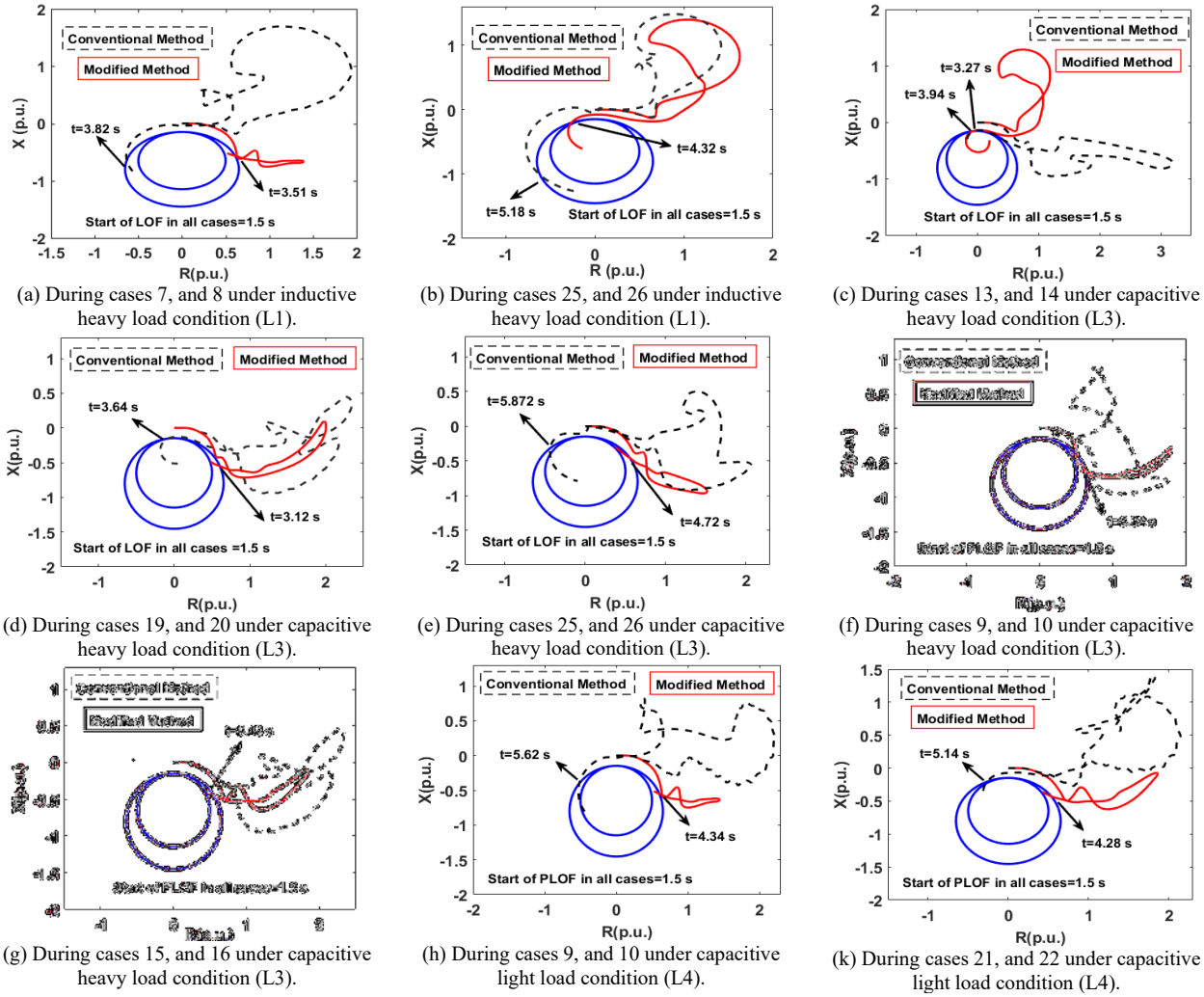

(a) During cases 7, and 8 under inductive heavy load condition (L1).

(b) During cases 25, and 26 under inductive heavy load condition (L1).

(c) During cases 13, and 14 under capacitive heavy load condition (L3).

(d) During cases 19, and 20 under capacitive heavy load condition (L3).

(e) During cases 25, and 26 under capacitive heavy load condition (L3).

(f) During cases 9, and 10 under capacitive heavy load condition (L3).

(g) During cases 15, and 16 under capacitive heavy load condition (L3).

(h) During cases 9, and 10 under capacitive light load condition (L4).

(k) During cases 21, and 22 under capacitive light load condition (L4).

Figure 8. Calculated impedance trajectory by the modified and conventional LOF function for LOF and PLOF event

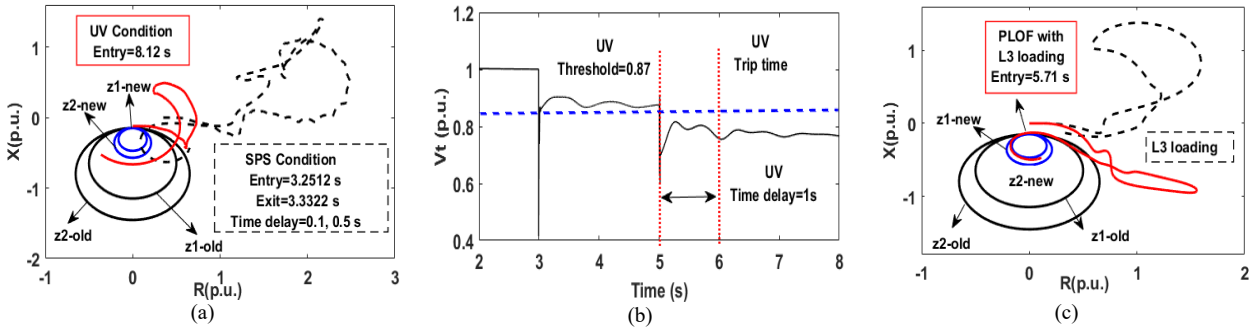

Figure 9. (a) Performances of the LOF Relay in coordination with GUEC, SSSL and UEL characteristics under stable power swing and voltage reduction condition (b) Generator terminal voltage and undervoltage (UV) element trip signal associated with Figure 9 (a) (c) Performances of the LOF Relay in coordination with GUEC, SSSL and UEL characteristics under capacitive heavy load condition (L3) in the absence and presence of the PLOF (VG =0.5 p.u.)

Figure 9(a) also shows the impedance locus measured by modified LOF function in the presence of series capacitor and its over-voltage devices under stable power swing condition. This condition has been created by applying a three-phase short circuit fault at the generator terminal for time for the duration of 12 cycles (0.2 s). It can be seen that in this condition the impedance trajectory of the modified LOF function enters into the reduced zone of the relay characteristic in 3.2512 s and leaves it after 0.081 s.

As stated in section II, in LOF relay, 0.1 s time delay is considered for the first zone and, 0.5 to 0.6 s time delay is considered for the second zone. These intentional time delays should be utilized to ride over the transient situations that might cause misoperation during transient and stable power swings. Therefore, the mentioned time delays are sufficient to prevent the relay misoperation in this case. Therefore, non-LOF condition is detected and the modified LOF function is robust enough. In another case studies, the performances of the modified function under the heavy capacitive loading condition (i.e. L3 = 0.7 -j0.5 p.u.) in the absence and presence of the PLOF (VG =0.5 p.u.) condition are shown in Figure 9(c). With the absence of the PLOF condition, the impedance locus of the modified LOF function does not penetrate the reduced zone of the relay characteristic. Therefore, non-LOF condition is detected. However, with the existence of the PLOF condition, the impedance trajectory of the modified LOF function enters into the reduced zone of the relay characteristic (coordinated with GUEC, SSSL, and UEL characteristics). Therefore, PLOF condition is detected and modified technique trips at 4.21 s (5.71-1.5). In fact, the modified function remains secure under this condition.

3. 3. Switching Effect of the Capacitor on the Performances of the LOF Relay

Transient condition due to the switching of the capacitor, is one of the most important issues that have been investigated in this study. As stated in section II, in LOF relay, 0.1 s time delay is considered for the first zone and, 0.5 to 0.6 s time delay is considered for the second zone. These intentional time delays should be utilized to ride over the transient situations that might cause misoperation during transient and stable power swings. The value of this time delay should be equal to the minimum time needed to ride over transient situations. Consequently, allocating an deliberate time delay is commonly used to ride over the probable misoperation of the LOF relay (30-33). The bypass breaker removes or inserts the capacitor bank into the circuit (see Figure 4(a)).

This breaker provides protection for imbalances or failures. When the triggered gap or bypass breaker operates, this function creates a transient condition whose frequency depends on the capacitance and inductance of the circuit. This frequency is generally in the range of 300 to 1000 Hz (0.001 s to 0.0033 s). Consequently, according to the above discussion, a time delay of 0.1 seconds for the first zone and 0.5 to 0.6 seconds for the second zone is enough to overcome this type of transient. On the other hand, the frequency of transient waves produced by the switching of power circuit breakers is typically in the range of kilohertz (kHz) to megahertz (MHz) (40).

These transient waves are usually caused by abrupt variations in current and voltage due to switching or connecting and disconnecting the loads. Therefore, in this case, similar to the previous case, a time delay of 0.1 seconds for the first zone and 0.5 to 0.6 seconds for the second zone is enough to ride over these transient situations. For instance, Figure 10 shows a typical behavior of the impedance trajectory calculated by the modified LOF function following a transient condition. In this case, the impedance trajectory enters into the reduced zone of the relay characteristic in 4.4511 s and leaves it after 0.0022 s. Therefore, the mentioned time delays are sufficient to prevent the relay misoperation.

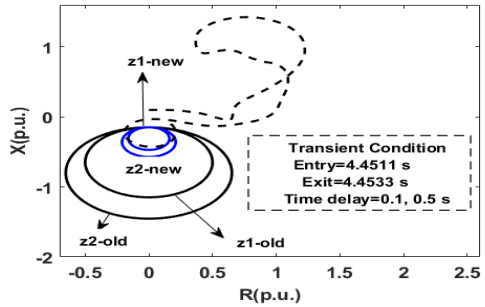

Figure 10. Performances of the LOF Relay in coordination with GUEC, SSSL and UEL characteristics under transient condition due to the switching of the capacitor

4. CONCLUSION

The installation of compensation capacitors in electrical networks is on the rise, both in terms of the number of installations and their capacity, due to their numerous advantages. However, while impedance-based distance relays are effective for detecting LOF conditions, the presence of compensation capacitors and their associated over-voltage devices can hinder the operation of conventional LOF relays. Specifically, series capacitors protected by Metal Oxide Varistors (MOVs) create challenging conditions for impedance-based LOF relays that rely on traditional impedance calculation methods. To enhance the security of these relays, it is crucial to account for the influence of series capacitors and their over-voltage devices. This research introduces a new adaptive relay setting technique that addresses these challenges. The technique incorporates an analytical solution to correct the effects of series capacitors on LOF protection for synchronous generators, a topic not previously documented in the literature. This analytical method takes into consideration MOV operation, various capacitor locations, and fluctuations within the power network, including degrees of compensation, load variations, and different LOF scenarios such as complete and partial LOF. Additionally, the parallel configuration of highly non-linear varistors with series capacitors is approximated using a linear series R-X impedance model. Given that these types of relays are currently employed for loss of field protection in synchronous generators, this research aims to resolve some of the existing issues associated with them. Simulation results across various scenarios demonstrate the effectiveness and satisfactory performance of the proposed modified technique, which remains independent of the power system's structure.

5. ACKNOWLEDGMENT

This research is funded by Semnan University, research grant No @ 140386.

6. REFERENCES

1. Yaghobi H. Precision enhancement of the traditional sub-synchronous analysis by using frequency components of instantaneous magnetic flux. IET Generation, Transmission & Distribution. 2021;15(22):3100-14. https://doi.org/10.1049/gtd2.12243
2. Abbasi M, Shayestehkhah H, Tousi B. Application of an additive self-tuning controller for static synchronous series compensator for damping of sub-synchronous resonance oscillations. International Journal of Engineering, Transactions B: Applications. 2018;31(4):564-73. https://doi.org/10.5829/ije.2018.31.04a.07
3. Firouzjah KG. Fault location on compensated transmission lines without current measurement. International Journal of Engineering, Transactions C: Aspects. 2018;31(12):2044-51. https://doi.org/10.5829/ije.2018.31.12c.08
4. Anderson PM, Henville CF, Rifaat R, Johnson B, Meliopoulos S. Power system protection: John Wiley & Sons; 2021.
5. Yaghobi H, Mortazavi H, Ansari K, Rajabi Mashhadi H, Khorashadzadeh H, Borzoe H, editors. A novel flux-based method for synchronous generator loss of excitation protection. 25th International Power System Conference, PSC2010, Nov. 2010, Tehran, Iran. 2010. https://civilica.com/doc/133208/
6. Haseli MR, Haghjoo F, Hasani A. A new air gap flux-based technique to detect loss of field in synchronous generators. IET Electric power applications. 2024;18(5):543-55. https://doi.org/10.1049/elp2.12410
7. Yaghobi H. A new adaptive impedance-based LOE protection of synchronous generator in the presence of STATCOM. IEEE Transactions on Power Delivery. 2017;32(6):2489-99. https://doi.org/10.1109/TPWRD.2017.2647746
8. Ghorbani A, Soleymani S, Mozafari B. A PMU-based LOE protection of synchronous generator in the presence of GIPFC. IEEE Transactions on power delivery. 2015;31(2):551-8. https://doi.org/ 10.1109/TPWRD.2015.2440314
9. Elsamahy M, Faried SO, Sidhu T. Impact of midpoint STATCOM on generator loss of excitation protection. IEEE Transactions on power delivery. 2013;29(2):724-32. https://doi.org/ 10.1109/TPWRD.2013.2281581
10. Dolatabadi S, Seyedi H, Tohidi S. A new method for loss of excitation protection of synchronous generators in the presence of static synchronous compensator based on the discrete wavelet transform. Electric Power Systems Research. 2022;209:107981. https://doi.org/10.1016/j.epsr.2022.107981
11. Hasani A, Liang X, Sanaye-Pasand M, Abedini M, Haghjoo F, Bak CL. Loss of Field Protection for Synchronous Generators: Current Practice and Future Trends. IEEE Transactions on Industry Applications. 2025. https://doi: 10.1109/TIA.2025.3573992
12. Ghassemi F, Goodarzi J, Johns A, editors. Method for eliminating the effect of MOV operation on digital distance relays when used in series compensated lines. The 1997 32 nd Universities Power Engineering Conference, UPEC'97 Part 1(of 2); 1997.
13. Biswal M, Pati BB, Pradhan AK. Adaptive distance relay setting for series compensated line. International Journal of Electrical Power & Energy Systems. 2013;52:198-206. https://doi.org/10.1016/j.ijepes.2013.03.018
14. Ghassemi F, Johns A. Investigation of alternative residual current compensation for improving series compensated line distance protection. IEEE transactions on power delivery. 2002;5(2):567-74. https://doi.org/ 10.1109/61.53058
15. Bachmann B, Novosel D, Hart D, Hu Y, Saha MM, editors. Application of artificial neural networks for series compensated

line protection. Proceedings of International Conference on Intelligent System Application to Power Systems; 1996: IEEE.

16. Fahim SR, Sarker SK, Muyeen S, Sheikh MRI, Das SK, Simoes M. A robust self-attentive capsule network for fault diagnosis of series-compensated transmission line. IEEE Transactions on Power Delivery. 2021;36(6):3846-57. https://doi.org/10.1109/TPWRD.2021.3049861
17. Taheri MM, Seyedi H, Nojavan M, Khoshbouy M, Ivatloo BM. High-speed decision tree based series-compensated transmission lines protection using differential phase angle of superimposed current. IEEE Transactions on Power Delivery. 2018;33(6):3130-8. https://doi.org/10.1109/TPWRD.2018.2861841
18. Parikh UB, Das B, Maheshwari RP. Combined wavelet-SVM technique for fault zone detection in a series compensated transmission line. IEEE Transactions on Power Delivery. 2008;23(4):1789-94. https://doi.org/10.1109/TPWRD.2008.919395
19. Ebadi A, Hosseini S, Abdoos A. A new restricted earth fault relay based on artificial intelligence. International Journal of Engineering, Transactions A: Basics. 2019;32(1):62-70. https://doi.org/10.5829/IJE.2019.32.01a.08
20. Samantaray S, Dash P, Panda G. Distance relaying for transmission line using support vector machine and radial basis function neural network. International Journal of Electrical Power & Energy Systems. 2007;29(7):551-6. https://doi.org/10.1016/j.ijepes.2007.01.007
21. Jena MK, Samantaray S. Intelligent relaying scheme for series-compensated double circuit lines using phase angle of differential impedance. International Journal of Electrical Power & Energy Systems. 2015;70:17-26. https://doi.org/10.1016/j.ijepes.2015.01.035
22. Rahmkhoda E, Faiz J, Abedini M. Detection of loss-of-excitation in synchronous machines using hybrid GMDH neural network intelligent algorithm in the presence of UPFC in power system. Electric Power Components and Systems. 2023;51(10):972-90. https://doi.org/10.1080/15325008.2023.2187096
23. Rahmkhoda E, Faiz J, Abedini M. Detecting loss of excitation condition of synchronous generator in the presence of unified power flow controller based on data mining method. Electric Power Systems Research. 2024;228:109975. https://doi.org/10.1016/j.epsr.2023.109975
24. Silva H, Coelho A, Faria I, Araujo B. ANN based impedance trajectory detection approach for loss of excitation protection of synchronous generators connected to transmission lines with SVCs. Electric Power Systems Research. 2022;213:108766. https://doi.org/10.1016/j.epsr.2022.108766
25. Gulati V, Verma K, editors. Supervised Machine Learning to Identify Loss of Excitation and Power Swing in a Generator. 2023 7th International Conference on Computer Applications in Electrical Engineering-Recent Advances (CERA); 2023: IEEE. 10.1109/CERA59325.2023.10455561
26. Ramadoss H, Muthiah G. Ensemble machine learning approach to identify excitation failure in synchronous generators. Engineering Failure Analysis. 2023;152:107506. https://doi.org/10.1016/j.engfailanal.2023.107506
27. Noori H, Yaghobi H. A Protection for Loss of Field in Synchronous Generator in Presence of Series Compensation Capacitor. International Journal of Engineering Transactions C: Aspects. 2024;37(9):1857-67. https://doi.org/10.5829/IJE.2024.37.09C.15
28. Zoghi M, Yaghobi H. Synchronous generator dual estimation using sigma points Kalman filter. International Journal of Engineering Transactions A: Basics. 2024;37(07):1239. https://doi.org/10.5829/ije.2024.37.07a.04
29. H. A-A. Reduce harmonic orders of voltage waveform in the synchronous generator by changing the winding structure. International Journal of Engineering Transactions B: Applications. 2025;38(8):2008-17. https://doi.org/10.5829/ije.2025.38.08b.22
30. Berdy J. Loss of excitation protection for modern synchronous generators. IEEE Transactions on Power Apparatus and systems. 2006;94(5):1457-63. https://doi.org/10.1109/T-PAS.1975.31987
31. Hasani A, Haghjoo F. A secure and setting-free technique to detect loss of field in synchronous generators. IEEE Transactions on Energy Conversion. 2017;32(4):1512-22. https://doi.org/10.1109/TEC.2017.2697501
32. Marchi P, Estevez PG, Messina F, Galarza CG. Loss of excitation detection in synchronous generators based on dynamic state estimation. IEEE Transactions on Energy Conversion. 2020;35(3):1606-16. https://doi.org/10.1109/TEC.2020.2985529
33. Momeni E, Yaghobi H, Shahzadi A. Using dynamic state estimation to detect loss of excitation in synchronous generators. IET Generation, Transmission & Distribution. 2024;18(3):639-52. https://doi.org/10.1049/gtd2.13106
34. Sauer PW, Pai MA, Chow JH. Power system dynamics and stability: with synchrophasor measurement and power system toolbox: John Wiley & Sons; 2017.
35. Yaghobi H. Fast discrimination of stable power swing with synchronous generator loss of excitation. IET Generation, Transmission & Distribution. 2016;10(7):1682-90. https://doi.org/10.1049/iet-gtd.2015.1045
36. Goldsworthy DL. A linearized model for MOV-protected series capacitors. IEEE Transactions on Power Systems. 2007;2(4):953-7. https://doi.org/10.1109/TPWRS.1987.4335284
37. Marttila R. Performance of distance relay mho elements on MOV-protected series-compensated transmission lines. IEEE transactions on power delivery. 2002;7(3):1167-78. https://doi.org/10.1109/61.141827
38. Yaghobi H. Real-Time Discrimination of Symmetrical Faults from Power Swings. Iranian Journal of Electrical & Electronic Engineering. 2023;19(2). https://doi.org/10.22068/IJEEE.19.2.2658
39. Yaghobi H. Out-of-step protection of generator using analysis of angular velocity and acceleration data measured from magnetic flux. Electric Power Systems Research. 2016;132:9-21. http://dx.doi.org/10.1016/j.epsr.2015.11.003
40. Edition S. The authoritative dictionary of ieee standards terms. IEEE Std. 2000:100-2000. https://doi.org/10.1109/IEEESTD.2000.322230

APPENDIX

TABLE 2. The Network Studied Parameters

Generator		
S= 390 MVA, V=13.8 kV, f= 60 Hz, H= 5.5 s		
$X_d(pu)=1.305,\ X'_d(pu)=0.296,\ X''_d(pu)=0.252,$		
$X_q(pu)=0.474,\ X'_q(pu)=0.2,\ X''_q(pu)=0.243,$		
$T'_{do}(s)=5,\ T''_{do}(s)=0.1,\ T'_{qo}(s)=0.8,\ T''_{qo}(s)=0.09,$		
$X_l(pu)=0.18,\ R_s(pu)=0.0016$		
LOF Relay		
Original setting: Z_1=1 p.u., Z_2=1.305 p.u., Reduced setting: Z1=0.323 p.u., Z2= 0.4215 p.u., Time delay for Z1 =0.1 s, Time delay for Z2= 0.5 s, UV element=0.87 p.u. with 1 s time delay, R_C=1600, R_V=200.		
Transformer	**Series compensation module**	**Line**
S= 475 MVA, 13.8/400 kV, $R_1(pu)=0$, $L_1(pu)=0.15$, $R_2(pu)=0$, $L_2(pu)=0.15$	Total line reactance in positive seq. (x_1) =$w\times l_1$ *(H/km)* × Line length (km) Series compensation capacitor reactance (X_c) =$x_1\times k$ (Degree of Comp.) **MOV** Reference current=30 kA Total Capacitor full load current (I_{cn})=2 kA , $I_{pr}=2.5\times I_{cn}$, Reference voltage=sqrt (2)× X_c × I_{pr}	Length (km)=300, r_1(ohms/km)=0.01273, r_0(ohms/km)=0.3864, l_1(H/km)=0.9337e-3, l_0(H/km)=4.1264e-3, c_1(F/km)=12.74e-9, c_0(F/km)=7.751e-9

TABLE 3. Parameters of the Utilized Hydraulic Turbine and AVR

Hydraulic turbine & PID	AVR
Servo-motor: $k_a(pu)=3.33, T_a(s)=0.07$	Low-pass filter: $T_r(s)=20e-3$
Droop: $R_p(pu)=0.05$	Regulator: $k_a(pu)=300, T_a(s)=0.001$
Regulator: $k_p=1.163, k_i=0.105,$ $k_d=0, T_d(s)=0.01$	Damping filter: $k_f(pu)=0.001, T_f(s)=0.1$
Hydraulic turbine: $\beta=0, T_w(s)=2.67$	Exciter: $k_e(pu)=1, T_e(s)=0$
Gate opening limits: $g_{\min}(p.u)=0.01, V_{g\min}(p.u/s)=-0.1$ $g_{\max}(p.u)=0.975, V_{g\max}(p.u/s)=0.1$	Output Limits: $V_{f\max}(p.u)=11.5,$ $V_{f\min}(p.u)=-11.5$

COPYRIGHTS
©2026 The author(s). This is an open access article distributed under the terms of the Creative Commons Attribution (CC BY 4.0), which permits unrestricted use, distribution, and reproduction in any medium, as long as the original authors and source are cited. No permission is required from the authors or the publishers.

Persian Abstract

چکیده

تشخیص خطای قطع تحریک ژنراتورهای سنکرون در شبکه‌های قدرت جبران‌شده با خازن‌های سری محدودیت‌هایی دارد. هنگامی که جریان‌های خطا از بانک خازنی سری عبور می‌کنند، اضافه ولتاژهایی ایجاد می‌شوند که از مقادیر نامی بانک های خازنی تجاوز می‌کنند. بنابراین، بانک های خازنی در برابر جریان‌های خطا، معمولاً توسط یک مقاومت غیرخطی به نام وریستور اکسید فلزی محافظت می‌شوند. از سوی دیگر، هنگامی که بانک خازنی و مقاومت غیرخطی آن در حلقه امپدانس خطا قرار می‌گیرند، شرایط برای رله قطع تحریک در محل ژنراتور نامطلوب می‌شود. این شرایط نامطلوب شامل پدیده‌های زیادی مانند تغییرات جریان و/یا ولتاژ، نوسانات فرکانس بالای ناشی از مقاومت های غیرخطی و نوسانات زیرسنکرون است. بنابراین، در این تحقیق یک شاخص جدید مبتنی بر امپدانس اصلاح‌شده، برای حفاظت قطع تحریک یک ژنراتور سنکرون در حضور خازن سری و تجهیزات اضافه ولتاژ مرتبط با آن ارائه می‌دهد. در این تحقیق از رله قطع تحریک Berdy استفاده شده است. همچنین از نرم‌افزار "Matlab/Simulink" برای شبیه‌سازی حوزه زمان خازن سری و تجهیزات اضافه ولتاژ آن استفاده شده است. با شبیه‌سازی سناریوهای مختلف، اثربخشی و عملکرد رضایت‌بخش تکنیک اصلاح‌شده پیشنهادی و استقلال آن از ساختار سیستم قدرت نمایش داده شده است.

IJE TRANSACTIONS B: Applications Vol. 39, No. 08, (August 2026) 1893-1907

International Journal of Engineering

Journal Homepage: www.ije.ir

Geological Evaluation of Undersea Tunnel Excavation in Fault Fracture Zones Based on On-Site Drilling Tests

Y. Guo[a], W. Qi*[a], H. Zhou[b], G. Zhang[c], H. Liu[d]

[a] *Qingdao Conson Second Jiaozhou Bay Subsea Tunnel CO., LTD., Qingdao, China*
[b] *School of Transportation Engineering, Shandong Jianzhu University, Jinan, China*
[c] *Shandong Institute of Highway Technican, Jinan, China*
[d] *CCCC Tunnel Engineering Co., Ltd., Beijing, China*

PAPER INFO

Paper history:
Received 06 June 2025
Received in revised form 02 August 2025
Accepted 31 August 2025

Keywords:
Subsea Tunnel Engineering
Fault Zone Hydrogeology
Geological Hazard Assessment
Grouting Techniques
Stress Conditions

ABSTRACT

Geological risk assessment is crucial for ensuring construction safety in undersea tunnel projects, particularly when traversing structurally complex fault zones. This study quantifies the hydrogeological and geomechanical risks associated with the Qingdao Jiaozhou Bay Second Undersea Tunnel crossing of the Cangkou Fault Zone and develops targeted mitigation strategies based on empirical data. Comprehensive field investigations—including water pressure tests (maximum: 48.38 Lu), pumping tests (permeability coefficient K = 6.74–14.56 m/d), and hydraulic fracturing stress measurements (σ_{Hmax} = 4.57 MPa, N67°E orientation)—revealed two primary challenges: high-permeability fracture networks and anisotropic in situ stress conditions (lateral stress coefficients λ = 1.2–1.8). The results indicate that conventional grouting techniques are inadequate under these conditions, prompting the implementation of an 8-m full-section grouting design. This method effectively penetrates fracture networks and reinforces the surrounding rock mass upon solidification. Key limitations include the localized nature of the drill core data (limited to five core samples) and the assumption of homogeneous fracture distribution beyond the sampled zones. These findings provide an actionable framework for fault-zone tunneling in similar coastal geological settings.

***doi**: 10.5829/ije.2026.39.08b.10*

Graphical Abstract

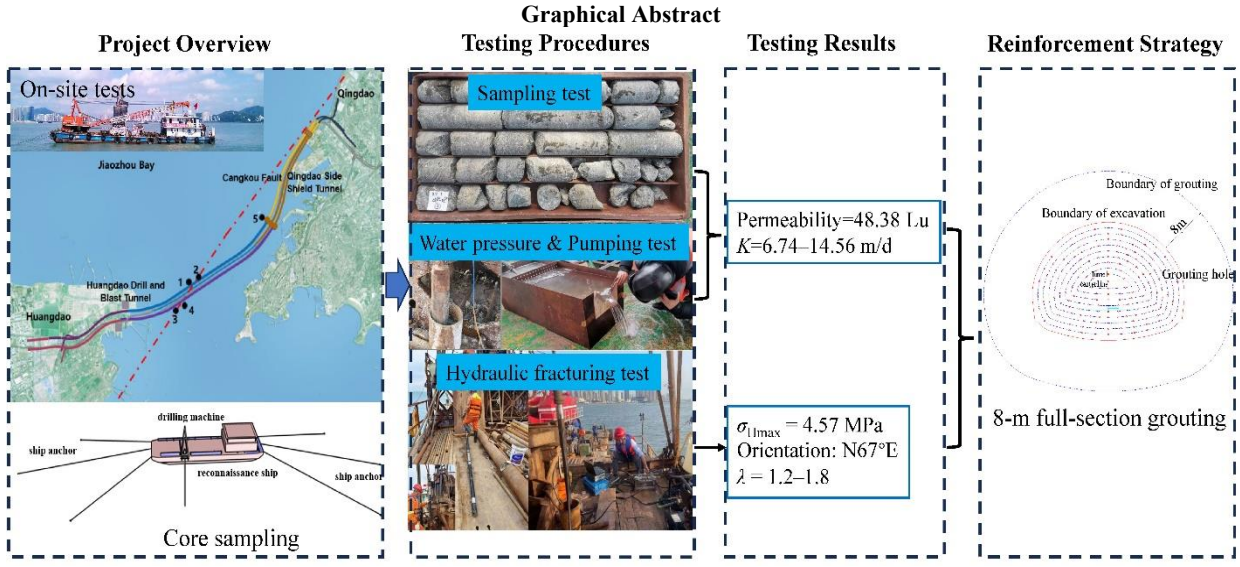

*Corresponding Author Email: 572066456@qq.com (W. Qi)

Please cite this article as: Guo Y, Qi W, Zhou H, Zhang G, Liu H. Geological Evaluation of Undersea Tunnel Excavation in Fault Fracture Zones Based on On-Site Drilling Tests. International Journal of Engineering, Transactions B: Applications. 2026;39(08):1893-907.

NOMENCLATURE

K	Permeability coefficient (m/d)	Q	Quantity of flow (L/min)
P	Pressure of underground water (MPa)	l_w	Level of water (m)
λ_H	Maximum lateral pressure coefficient	σ_H	Maximum horizontal principal stress (MPa)
σ_v	vertical stress (MPa)	σ_h	Minimum horizontal principal stress (MPa)
λ_h	Measured lateral pressure coefficient	$\sigma_{\theta max}$	Maximum shear stress (MPa)
σ_{max}	Initial stress (MPa)	σ^s_{max}	Section initial stress (MPa)

1. INTRODUCTION

Undersea tunnel engineering represents among the most technically demanding aspects of infrastructure construction, consistently raising concerns within the engineering community regarding construction safety and structural stability (1). Tunnel excavation in fault fracture zones can lead to significant complications such as face collapse, groundwater ingress, and surrounding rock instability. These risks are particularly critical in high-water-pressure environments such as undersea tunnels, where a comprehensive understanding the geological risks associated with fault zones is essential. Therefore, detailed geological exploration and evaluation of undersea tunnel is imperative (2-4).

During the exploration of undersea tunnels, in situ testing is crucial for evaluating the stability and construction risks associated with the surrounding rock. Wang et al. (5) introduced the principles, advantages, and applications of marine in situ experiments. They demonstrated that water pressure and pumping tests are effective methods for determining the permeability of rock masses. Liu et al. (6) employed nuclear magnetic resonance to monitor the internal microstructure of rocks in real time, revealing a strong correlation between variations in water pressure during loading or unloading and permeability variations. Jiang (7) utilized the Aquifer Test software to calculate pumping test parameters and compared the results with those obtained via conventional statistical methods. Wen et al. (8) proposed a method for calculating water inrush in deep tunnels based on water pressure tests and crack measurements. Chang et al. (9) conducted in situ tests of offshore drilling using a drilling platform for the Xiamen Xiang'an Subsea Tunnel and the Qingdao Jiaozhou Bay Subsea Tunnel in China. They evaluated the hydrogeological parameters of the area by analyzing resistivity changes during pumping tests. Kang (10) examined the characteristics, challenges, and corresponding technical measures related to offshore drilling surveys of undersea tunnels. Li et al. (11) integrated field monitoring, numerical calculations, and laboratory experiments to predict water inflow during the construction of the Qingdao Jiaozhou Bay Subsea Tunnel. Although a growing body of work recognizes the importance of field exploration and evaluation in undersea tunnel engineering, studies focusing on the testing and analysis of undersea fault fracture zones remains limited. Additionally, geological exploration and assessment in complex environments, such as undersea tunnels, present considerable challenges, particularly for the in situ testing and evaluation of adverse geological conditions such as fault zones. These tests are indispensable for guiding effective excavation strategies and minimizing geological risk.

In complex geological contexts such as undersea tunnels, key concerns include in situ stress conditions, rock permeability, and the spatial distribution of weak zones. The hydraulic fracturing method, originally developed for stress testing in the petroleum industry, is now widely adopted in subsea tunnel engineering as an effective technique for measuring in situ stress. Liu et al. (12) reviewed the development of hydraulic fracturing technology for the exploitation of the Gulong shale oil reservoir and offered recommendations for future technical advancements. Wang (13) outlined the advantages of incorporating hydraulic fracturing technology during the construction of the new Liangfengya Tunnel, particularly in sections intersecting coal seams. Yu et al. (14) utilized the 2P-IKSPH function to simulate the hydraulic fracturing process in rock masses and integrated it with numerical simulations to demonstrate its effective application in rock engineering. The stress-relief method employed in hydraulic fracturing tests is effective for studying the impact of stress anisotropy on fracture growth (15-17). This method facilitates analysis of the maximum and minimum horizontal stresses as well as the shear stress in relation to fracture propagation, highlighting the trend of increased fracture size owing to shear stress. This method is particularly suitable for assessing the stress state of fracture zones in the seabed.

Typical tunnel projects often encounter challenges related to the geological construction and excavation. In the case of Zhanjiang Bay Sea-crossing Tunnel project in China, Liu et al. (18) proposed lining construction measures and excavation disposal strategies to address high in situ stress and high groundwater pressure. To address the issue of lining waterproofing in the Gongbei Near-sea Tunnel project, Zhou et al. (19) developed a scale model to analyze the impact of external water pressure on waterproofing performance, ultimately proposing both fully and partially wrapped waterproofing methods. Gu et al. (20) highlighted the prospects for constructing Taiwan Straits tunnel, emphasizing the necessity of geological exploration and in situ field tests. Wang et al. (21) conducted an advanced geological

exploration of the fault zone in Shantou Bay subsea tunnel, leveraging the water-sensitive properties of the inter-hole resistivity method to predict the water content at the tunnel excavation face. Although excavation environments and challenges vary across projects, they collectively underscore the importance of geological investigations and detailed targeted construction strategies, including advanced geological detection, waterproofing lining reinforcement, and targeted grouting interventions.

In summary, the constraints of marine working environments often limit the feasibility of large-scale field tests. Building on relevant research findings, this study focuses on Qingdao Jiaozhou Bay Second Undersea Tunnel in China, employing a comprehensive integrated approach that combines multiple in situ testing methods, specifically water pressure testing, pumping, and hydraulic fracturing. This methodology enables comprehensive evaluation of geological characteristics such as lithology, physical and mechanical properties, permeability, and crack development in fault fracture zones. Based on these evaluation results, a tailored grouting strategy was proposed to reinforce the excavation within the seabed fracture zone. The effectiveness of the grouting scheme was validated via sampling of the surrounding rock reinforcement. This study addresses a significant gap in the literature concerning fault fracture zones in undersea tunnels and offers practical insights into geological evaluation and excavation reinforcement strategies, thereby contributing to the advancement of the field.

2. PROJECT OVERVIEW

2. 1. Tunnel Route and Location The Qingdao Jiaozhou Bay Second Undersea Tunnel traverses the Jiaozhou Bay Channel in downtown Qingdao, China, as illustrated in Figure 1. The tunnel spans a total length of 14.36 km and features two two-way six-lane main tunnels, in conjunction with an intermediate service tunnel for emergency evacuation. This tunnel connects the Huangdao and Qingdao Districts. Based on site-specific geological characteristics, the drilling-blasting method was employed for excavation on the Huangdao side; whereas the shield method was employed for tunneling on the Qingdao side. The tunnel crosses the largest fault zone in the area, the Cangkou Fault Zone, extending approximately 100 km across the Jiaozhou Bay. The drilling-blasting section of the undersea tunnel passes directly through the fault. Initial geological investigation targeted 30 drilling cores in the Cangkou Fault Zone. For this onsite experiment, five representative drill cores were selected and labeled as No. 1, No. 2, No. 3, No. 4, and No. 5. The drilling locations are shown in Figure 1.

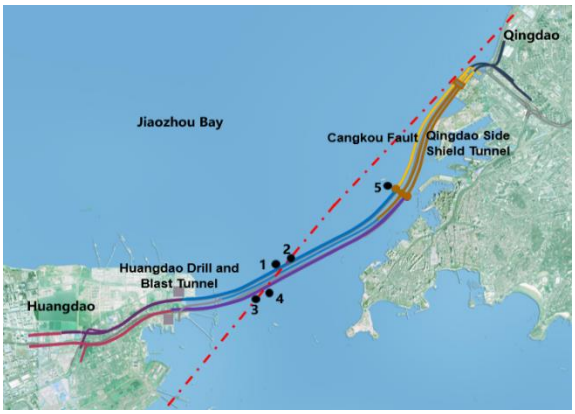

Figure 1. Location map of the Qingdao Jiaozhou Bay Second Undersea Tunnel

2. 2. On-Site Geological Drilling Investigation Offshore drilling sampling and onsite testing were conducted on the drilling vessel, as shown in Figure 2. The entire drilling and testing process lasted approximately one week. The test results for drill core Nos. 1 to 5 are listed in Table 1. The rock type at the fault location comprises primarily of granite and tuff, characterized by well-developed rock fissures. Physical and mechanical tests revealed that the natural density within the tunnel body was 2.61 g/cm^3, whereas the saturated uniaxial compressive strength was 53.08 MPa, classifying the rock as hard. This indicates that the rock mass at the site where the tunnel crosses the Cangkou Fault Zone is relatively stable, suggesting weak fault activity in this area. However, the sampling photos of the on-site drilling cores and the fractures observed within the core (Figure 3) revealed densely developed fractures within the tunnel body, indicating a significant risk of water ingress during tunnel excavation. Therefore, conducting in situ water pressure tests at sea is crucial to accurately assess the permeability of rock masses in fault zones. In addition, pumping tests are necessary to inform the design of drainage and water-blocking systems for tunnel construction. Furthermore, drill core No. 5,

Figure 2. Offshore exploration vessel platform

TABLE 1. Results of the rock physical mechanical tests

Core No.	Lithology	Density (g/cm^3)	Saturated uniaxial compressive strength (MPa)
1	Tuff	2.64	52.87
2	Granite	2.57	64.56
3	Tuff	2.56	38.61
4	Granite	2.65	56.28
5	Tuff	2.52	33.87

located at the receiving end of the shield tunnel, requires additional tests, such as hydraulic fracturing analysis, to evaluate the distribution characteristics of in situ stress at this location. This area is particularly vulnerable to significant risks during tunnel excavation, including the collapse and influx of water. A hydraulic fracturing analysis based on ground stress can provide valuable insights and guidance for reinforcing the receiving ends of shield tunnels.

3. ON-SITE TESTING PROCESS AND METHODS

3. 1. Water Pressure Test Water-pressure testing was conducted using the mechanical water-pressure method, as illustrated in Figure 4. The core diameter was 110 mm and the test was performed sequentially from top to bottom. After drilling into the bedrock, a single-plug method was employed to isolate each test section at intervals of approximately 5 m. The water-stop plug comprised 6 to 8 through-heart rubber bags, measuring a total length of 0.8 to 1.0 m. The drilling rig inflated the plug to halt water flow via pressurization. A water pressure gauge and water meter were used to measure the water pressure and volume of the injected water. Each test section utilized three pressure levels across five stages: the pressure was first increased, incrementally and then decreased in the same manner, with the maximum test water pressure set to 1.0 MPa.

3. 2. Pumping Test To obtain complete permeability coefficients for each drill core, pumping tests were conducted on drill cores Nos. 1, 2, and 3 to address the limitations of the water pressure tests. To enhance the workability and accuracy, all tests utilized stable flow pumping of single-hole samples. Each borehole included two or fewer pumping test sections to maintain a controlled drawdown depth. Onsite screw-type submersible pumps were employed for the pumping process. Air-dried clay balls were mixed with chains and placed at the bottom of the well to ensure compaction, with a leakage sealing thickness exceeding 2 m. Initially,

Figure 3. Rock core sample and core fractures (a: Rock core sample, b: Fractures within the core)

Figure 4. On-site water pressure test

synchronous observations of the water and tide levels were conducted over a minimum of one tidal cycle. After establishing the time relationship curve between the standard water level and tide level, a pumping test was performed. The onsite pumping test process is illustrated in Figure 5.

3. 3. Hydraulic Fracturing Test The on-site testing was conducted using a GEO-ST model hydraulic fracturing system, featuring an effective sealing length of 1.0 m for each packer. Testing was conducted in core No. 5, located near the intersection of the drilling-blasting and shield method tunnels. Core No. 5 was situated close to the receiving end of the shield tunnel, within the influence range of the Cangkou fault zone. Conducting a ground stress test facilitates more accurate evaluation of the ground stress state in the excavated cavern, enabling a precise design based on the level of ground stress (22, 23). The drill core diameter was 75 mm, with a maximum depth of 92.1 m. However, the bedrock surface was encountered at only 22.7 m, indicating that the entire drill core comprised moderately to slightly weathered granite. Based on the on-site drilling conditions, several test sections were selected within the influence range of the tunnel body, where the core remained relatively intact for testing. The test process, illustrated in Figure 6, followed four primary steps: 1) pressurization and sealing, 2) high-pressure fracturing, 3) depressurization and unsealing, and 4) fracture recording. The on-site test conditions are shown in Figure 7.

4. TEST RESULTS AND DISCUSSIONS

4. 1. Results of Water Pressure Tests The water pressure test results for the samples obtained from various depths of drill core Nos. 1 to 4 are presented in Tables 2, 3, 4, and 5. The samples with measurable permeability coefficient K are labeled as Sn-m, where n and m represent the serial numbers of the drill cores and

Figure 5. On-site pumping test

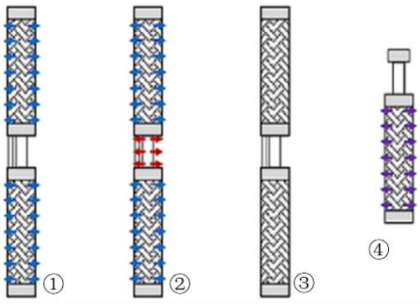

Figure 6. The on-site hydraulic fracturing testing process

Figure 7. On-site test conditions for hydraulic fracturing method

samples, respectively. The flow-pressure (Q-P) curves for these samples are illustrated in Figures 8-11. The test results indicated the presence of C-, D-, and E-type Q-P curves in the samples obtained from drill core Nos. 1, 2, and 3. The C-type curve indicates fracture expansion under the influence of water pressure. The D-type curve reflects fracture alteration during the test owing to the erosion of some fillers within the fractures caused by water pressure. The E-type curve reflects changes in the fractures during the test owing to partial blockage from foreign solid substances. These three types of curves indicate that fractures in the rock samples are relatively abundant (24, 25) and that the geological fault zones in drill core Nos. 1, 2, and 3 are concentrated. In addition, most permeability, measured in Lu, exceeded 10, with a maximum value reaching 48.38 Lu, further confirming the extensive fracture network within these rocks. The permeability coefficients were calculated using the following equations:

$$K = \frac{0.366Q}{Ls} \lg \frac{0.66L}{r} \quad (1)$$

where K is the permeability coefficient (m/d), Q is the flow quantity of water flowing from the well m^3/d, L is the length of the filter (m), s is the stable dynamic water level drop depth (m), and r is the well radius (m). By contrast, the permeability coefficients of all rock samples in drill core No. 4 were successfully measured, with Q-P

curve types being either A-type or B-type. This indicated that the rock mass in the geological area of drill core No. 4 was relatively intact and lacked significant fractures.

In the tests of drill core Nos. 1, 2, and 3, accurate permeability coefficients *K* could not be obtained from the water pressure tests, particularly within the tunnel depth range of 79-91 m. In this range, the fragmentation and development of tension fractures hindered the application of pressure, preventing measurement of the permeability coefficients. Therefore, the permeability coefficients of the three cores were evaluated employing subsequent pumping tests (26, 27).

TABLE 2. Results of water pressure test for drill core No. 1

Depth (m)	Permeability (Lu)	Curve Type	Permeability coefficient *K* (m/d)	Sample
73.10 - 77.20	15.24	E	0.14	S1-1
75.00 - 79.10	12.83	E	0.11	S1-2
79.20 - 83.30	26.99	B	/	/
83.30 - 87.40	26.33	B	/	/
87.80 - 91.90	26.64	B	/	/
92.00 - 96.10	26.94	B	/	/
98.30 - 102.40	9.0	D	0.05	S1-3

TABLE 3. Results of water pressure test for drill core No. 2

Depth (m)	Permeability (Lu)	Curve Type	Permeability coefficient *K* (m/d)	Sample
74.55 - 78.55	11.96	E	/	/
79.90 - 83.90	11.13	E	/	/
83.05 - 87.05	1.77	A	0.02	S2-1
87.25 - 91.25	1.67	A	0.01	S2-2
91.45 - 95.45	21.14	C	/	/
95.60 - 99.60	32.53	E	/	/
97.80 - 101.80	2.9	C	0.03	S2-3

TABLE 4. Results of water pressure test for drill core No. 3

Depth (m)	Permeability (Lu)	Curve Type	Permeability coefficient *K* (m/d)	Sample
74.80 - 78.95	48.38	A	/	/
78.95 - 83.10	21.87	A	/	/
82.55 - 86.70	14.8	A	/	/
89.45 - 93.60	26.42	D	/	/
92.35 - 96.50	2.95	E	0.03	S3-1
94.55 - 98.70	3.45	A	0.03	S3-2

TABLE 5. Results of water pressure test for drill core No. 4

Depth (m)	Permeability (Lu)	Curve Type	Permeability coefficient *K* (m/d)	Sample
74.40 - 79.40	6.04	A	0.08	S4-1
79.40 - 84.40	1.47	A	0.02	S4-2
87.40 - 92.40	4.27	A	0.04	S4-3
92.60 - 97.60	16.55	B	0.17	S4-4

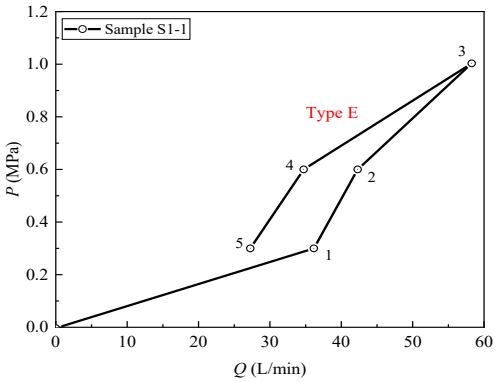

(a) Sample S1-1

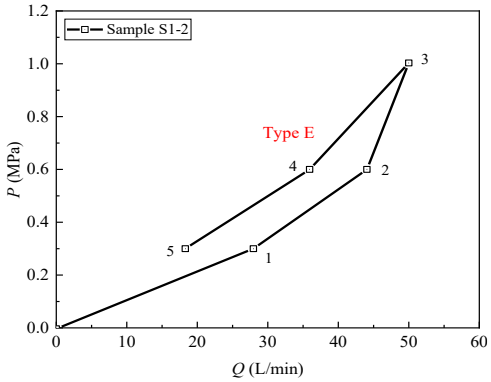

(b) Sample S1-2

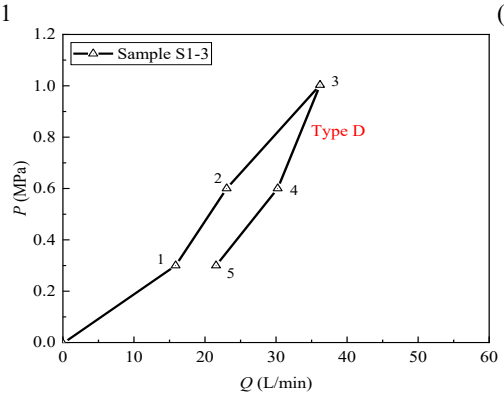

(c) Sample S1-3

Figure 8. *Q-P* curve of the water pressure test for drill core No. 1

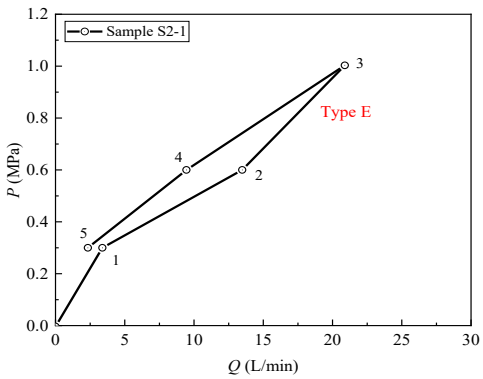

(a) Sample S2-1

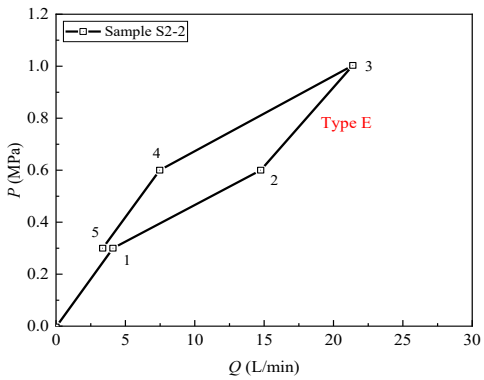

(b) Sample S2-2

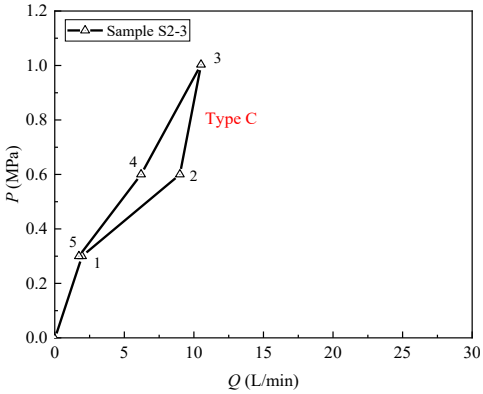

(c) Sample S2-3

Figure 9. *Q-P* curve of the water pressure test for drill core No. 2

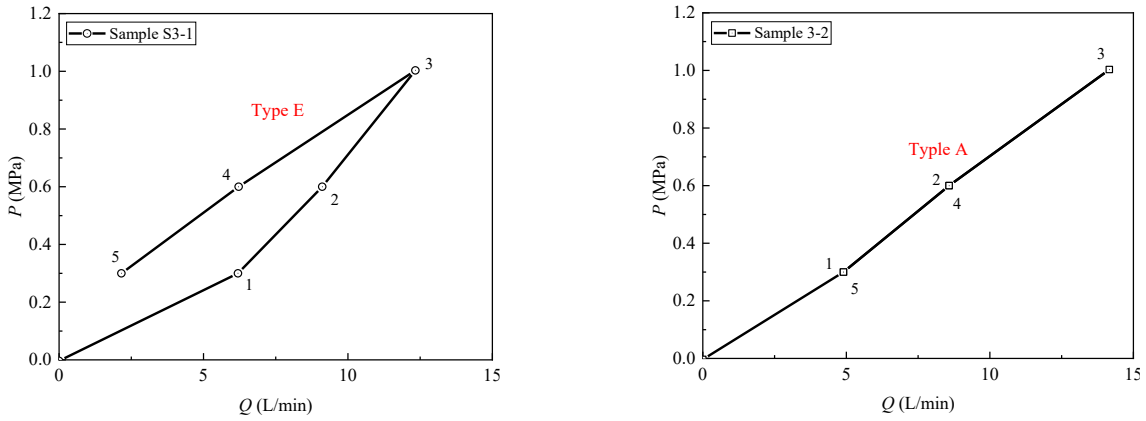

(a) Sample S3-1 (b) Sample S3-2

Figure 10. *Q-P* curve of the water pressure test for drill core No. 3

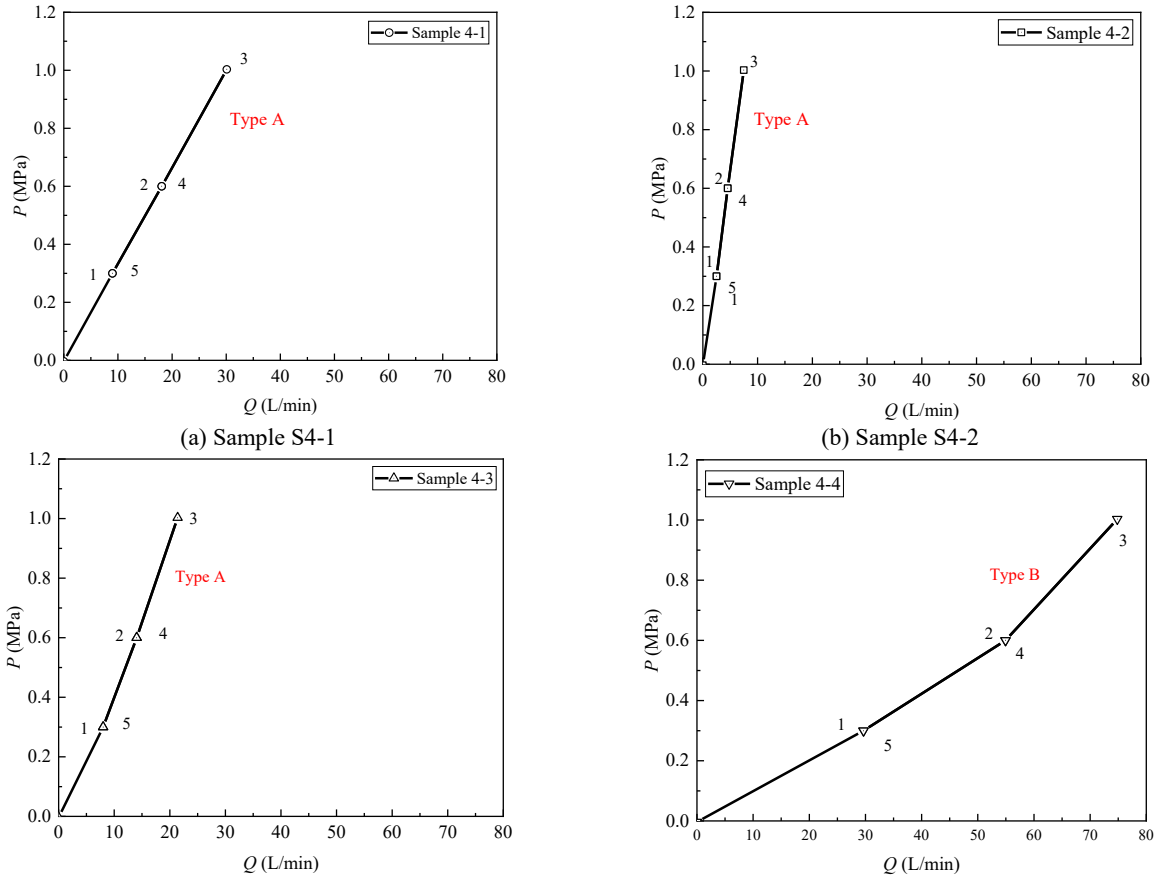

(a) Sample S4-1 (b) Sample S4-2

(c) Sample S4-3 (d) Sample S4-4

Figure 11. *Q-P* curve of the water pressure test for drill core No. 4

4. 2. Results of Pumping Tests Based on the pumping test results, the quantity of flow and water level-time (Q, l_w-t) relationship curves were plotted, as shown in Figure 12. In addition, critical parameters such as unit flow quantity, influence radius, and permeability coefficient were recorded. The results are presented in Table 6, where the permeability coefficient K was calculated according to Equation 1. The permeability coefficient K obtained from the on-site tests ranges from 6.74 to 14.56 m/d, significantly surpassing the permeability of typical rock strata, such as intact sandstone, which typically has K values ranging from 0.1 to 10 m/d (28, 29). High K values are often associated with the development of faults, joints, or dissolution

pores that facilitate rapid groundwater flow. This confirms an exceptionally high water-conducting capacity of the rock mass in this area, particularly in Core No. 1, which was confirmed to be a dense zone of fault fractures and fissures. Additionally, no notable differences were observed in the infiltration systems among the three cores, likely owing to the varying locations of the exposed rock masses within the primary and secondary fault zones, resulting in differing degrees of fracture development. Therefore, when addressing this highly permeable fault zone, reinforcement must be prioritized, in conjunction with measures such as water blocking and grouting. Furthermore, the implementation of advanced geological water exploration plans is essential.

4. 3. Results of Hydraulic Fracturing Method

The test results are presented in Table 7. The ground stress measurements obtained from the hydraulic fracturing method indicate that, for drill core No. 5, the maximum horizontal principal stress value σ_H was 4.57 MPa, with the principal direction of this stress oriented approximately N67°E. The ground stress in drill core No. 5 was primarily characterized by horizontal structural stress. In this area, σ_H and σ_h exhibit similar magnitudes, whereas the relationship among the three principal stresses in other areas generally follows: $\sigma_H > \sigma_h > \sigma_v$.

Figure 13-a illustrates the variation of stress values with depth, based on the on-site ground stress tests. In addition, the variations of the maximum lateral pressure coefficient λ_H (the ratio of the maximum horizontal principal stress σ_H to vertical stress σ_v) and minimum lateral pressure coefficient λ_h (the ratio of the minimum horizontal principal stress σ_h to vertical stress σ_v) with depth are presented in Figure 13-b. The test results

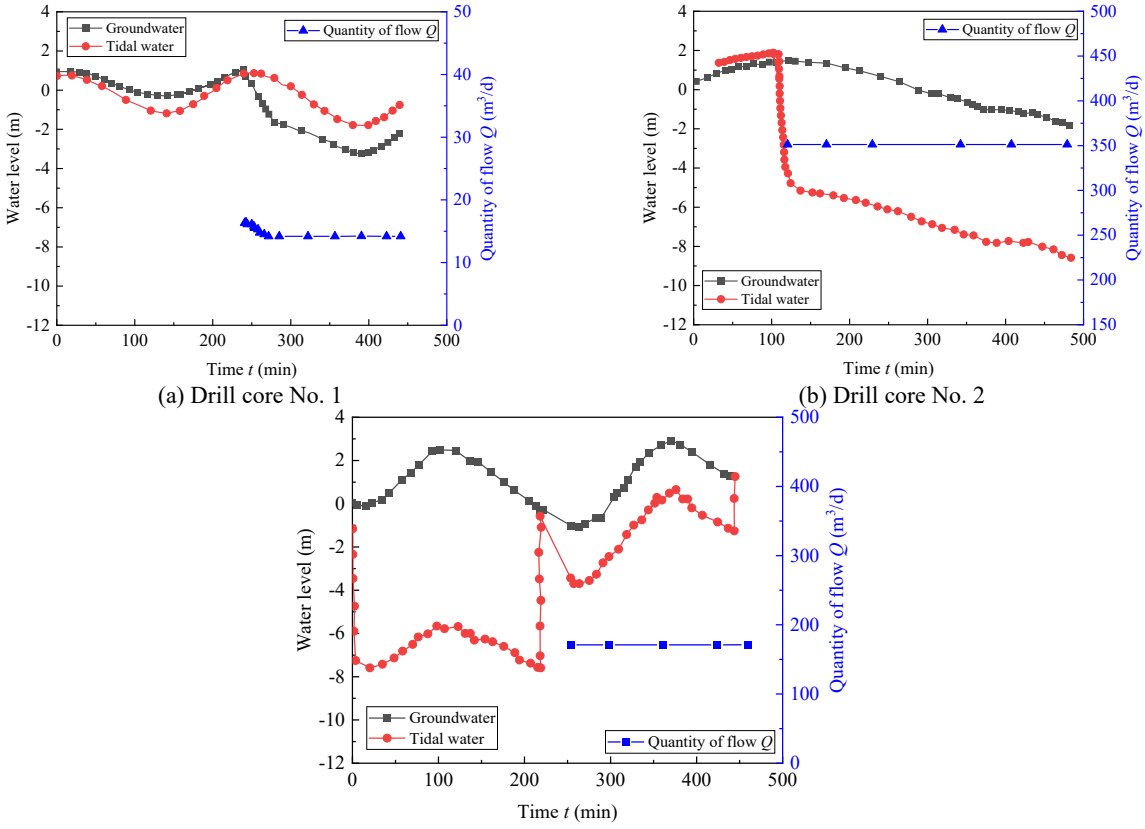

(a) Drill core No. 1

(b) Drill core No. 2

(c) Drill core No. 3

Figure 12. The results of pumping test for drill codes Nos. 1, 2 and 3

TABLE 6. Results of the pumping test

Core NO.	Time t (h)	Depth (m)	Quantity of flow Q (m³/d)	Water level l_w (m)	Permeability coefficient K (m/d)
1	8	19.4 - 57	332.32	2.2	14.56
2	7	43.6 - 50.4	351.25	7	6.74
3	8	78 - 82	147.72	2.5	9.09

TABLE 7. Results of the ground stress test for drill core No.5

Depth (m)	Breakdown pressure P_b (MPa)	σ_H (MPa)	σ_h (MPa)	σ_v (MPa)
35	3.31	1.40	1.48	0.65
43	3.56	1.63	1.78	0.86
67	4.37	3.90	2.51	1.50
72	5.41	3.71	3.07	1.63
85	4.64	4.47	3.42	1.99
88	3.58	4.57	2.96	2.05

indicate that the horizontal tectonic stress exceeded the vertical stress within the depth range covered by the test. Therefore, the original ground stress field in this area is primarily dominated by tectonic stresses. Based on prior studies and accumulated engineering experience (30-32), the lateral pressure coefficients λ_H and λ_h for strata in the fault zone are typically expected to range between 0.8 and 3.0. In this test, the measured lateral pressure coefficient λ_H for the maximum horizontal principal stress varies from 1.89 to 2.60, with an average value of 2.23. The measured lateral pressure coefficient λ_h for the minimum horizontal principal stress ranges from 1.45 to 2.15, with an average value of 1.84. According to the test results, both λ_H and λ_h were within the normal range (33, 34) but are relatively high, with values exceeding 1.5. This indicates that the exploration area was primarily influenced by horizontal tectonic compression and is likely situated in a stress concentration zone on the periphery of the fracture zone. Furthermore, the elevated λ_h can compress fractures, reducing groundwater permeability in the fracture zone, which presents the risk of water inrush. The λ_H/λ_h ratio is approximately 1.21 (2.23/1.84), indicating moderate horizontal stress anisotropy and that fault activity is predominantly thrust with strike-slip components. Consequently, based on the comprehensive ground-stress test results, the strata in this fault zone are susceptible to inward compressive deformation during excavation. Therefore, it is crucial to remain vigilant regarding the potential for water inrush and gushing. Additionally, during the reinforcement process of the excavation section, attention must be paid to the effectiveness of water-blocking measures.

4. 4. Analysis of Ground Stress Conditions for Tunnel Excavation Although the ground stress distribution in the area of drill core No. 5 was measured employing the hydraulic fracturing method, direction conversion calculations were necessary to obtain the stress parameters for the cross section of the tunnel excavation chamber. This requirement results from the difference between the direction of the initial ground stress and the axials direction of the tunnel excavation (1, 35). The specific derivation process of the stress conversion equations is as follows:

First, the relationship between the maximum and minimum horizontal principal stresses as they vary with depth H was determined via linear fitting:

$$\sigma_H = 0.0632H - 0.837 \quad (2)$$

$$\sigma_h = 0.0334H - 0.3601 \quad (3)$$

To simplify the relationship between the horizontal principal and vertical stresses, a direct connection was established using the average value of the lateral pressure

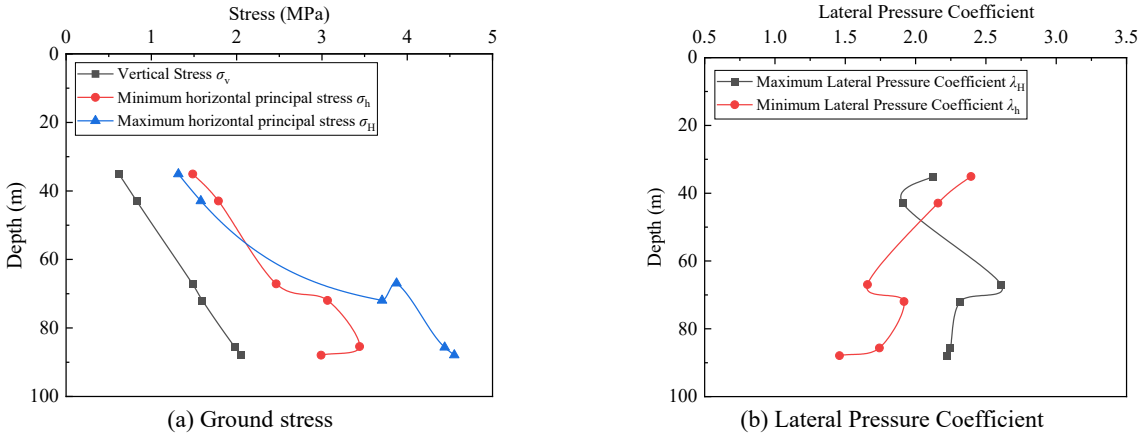

(a) Ground stress (b) Lateral Pressure Coefficient

Figure 13. On-site ground stress distribution measured by the hydraulic fracturing method

coefficient. This relationship involves the minimum horizontal principal stress, maximum horizontal principal stress, and vertical stress, as follows:

$$\sigma_H = 2.23\sigma_v \quad (4)$$

$$\sigma_h = 1.84\sigma_v \quad (5)$$

According to the stress conversion, the horizontal stress σ_H' and longitudinal stress σ_L' of the tunnel cross-section can be expressed as follows:

$$\sigma_H^{'}=\frac{1}{2}(\sigma_H+\sigma_h)+\frac{1}{2}(\sigma_H-\sigma_h)\cos(2\alpha) \quad (6)$$

$$\sigma_L^{'}=\frac{1}{2}(\sigma_H+\sigma_h)-\frac{1}{2}(\sigma_H-\sigma_h)\cos(2\alpha) \quad (7)$$

where α is the angle between the maximum horizontal principal stress and the direction of tunnel excavation. Based on the ground stress test results, the dominant direction of the original ground stress in the area of drill core No. 5 was approximately N67ºE. The angle between this direction and the axis of the tunnel excavation chamber is approximately 35°, therefore α = 35°.

The maximum shear stress $\sigma_{\theta max}$ and initial stress σ_{max} of the tunnel cross-section can be expressed as follows:

$$\sigma_{\theta max}=3\sigma_{max}-\sigma_v \quad (8)$$

$$\sigma_{max} = \max(\sigma_{max}^{s} | \sigma_v) \quad (9)$$

where:

$$\sigma_{max}^{s}=\sigma_H \sin^2\alpha+\sigma_h \cos^2\alpha \quad (10)$$

Here, σ^s_{max} represents the initial section stress obtained by decomposing the horizontal principal stress along the vertical tunnel axis. By substituting the ground stress relationships from Equations 2, 3, 4, and 5 into Equations 8, 9, and 10, the relationships between the section initial stress σ^s_{max}, maximum initial stress σ_{max}, maximum shear stress $\sigma_{\theta max}$ on the tunnel section, and tunnel burial depth H can be established as follows:

$$\sigma_{max}^{s}=1.968\sigma_v = 0.0522H \quad (11)$$

$$\sigma_{max} = \max(\sigma_{max}^{s}|\sigma_v) = 0.0522H \quad (12)$$

$$\sigma_{\theta max} = 3\sigma_{max}-\sigma_v = 0.13H \quad (13)$$

Equations 11, 12, and 13 express the relationships between different types of stresses in the tunnel section as they vary with the ground depth. By substituting the tunnel burial depth range of 79-91 m into these equations, the value range of each stress in the tunnel section can be determined, as shown in Table 8. Notably, the section initial stress σ^s_{max} and maximum initial stress σ_{max} are essentially equivalent. The maximum stress value $\sigma_{\theta max}$ in the tunnel section can reach 4.44 MPa, whereas the maximum shear stress can reach up to 11.83 MPa. Therefore, during the tunnel excavation, special attention must be paid to the shear failure and deformation of the rock mass at the excavation face. These shear failures are primarily attributed to joints and fissures within the fault-fractured zone of the rock mass. Consequently, deep grouting reinforcement of these fissures provides substantial benefits.

5. GROUTING REINFORCEMENT STRATEGY AND SUGGESTIONS FOR TUNNEL EXCAVATION

5. 1. Selection of the Strategy Based on the exceptionally high permeability coefficient (K = 6.74–14.56 m/d) obtained from drill core sampling, in conjunction with the strong horizontal tectonic stress (λ_H = 1.89–2.60, λ_h = 1.45–2.15) observed in prior tests, a full-section grouting strategy was developed for the undersea tunnel crossing the Cangkou Fault Zone. This approach was selected over alternatives such as partial-section grouting and curtain grouting for the following reasons.

1) Permeability Constraints: Conventional small-section grouting methods (e.g., localized borehole injections) are ineffective in fault zones with K > 5 m/d because grout fails to uniformly penetrate dispersed fractures (36, 37). Therefore, full-section grouting is necessary to ensure thorough filling of rock pores and fractures, achieving effective sealing and reinforcement.

2) Stress-Induced Fracture Networks: The high horizontal stress (σ_{Hmax} = 4.57 MPa at 88 m depth) promotes steeply dipping fractures, necessitating a 360° grout barrier to prevent bypass flow. This requirement broadened the determination of the grouting area.

3) Lessons from Case Studies: Similar projects, such as the Seikan Tunnel in Japan, have demonstrated that partial-section grouting in high-K fault zones can lead to uneven consolidation and post-excavation leaks (2, 38).

TABLE 8. The calculated stresses values in the tunnel section

	Section initial stress σ^s_{max} (MPa)	Maximum initial stress σ_{max} (MPa)	Maximum shear stress $\sigma_{\theta max}$ (MPa)
Max	4.75	4.75	11.83
Min	4.12	4.12	10.27
Average	4.44	4.44	11.05

5. 2. Grouting Design Parameters The selection of grouting materials primarily involves the use of cement slurries and additives. In specific cases requiring water blocking, a cement-sodium silicate two-liquid slurry can be utilized. The details of each material are as follows:

1) Cement slurry: Pure Portland cement (Type P. O. 42.5) with a water-cement ratio (w/c) of 1:1 was selected for its optimal balance between penetrability (Marsh funnel viscosity = 35–40 s) and post-curing strength (>15 MPa at 28 d).

2) Additives: No accelerators were added to ensure sufficient penetration time; however, silica fume (5% by weight) was incorporated for high-flow zones to reduce the risk of bleeding (39).

3) Pressure Control: Injection pressure was set to 4-6 MPa. This range was calibrated to exceed the fault's fracture reopening pressure (σ_{Hmax} = 4.57 MPa) while avoiding hydraulic fracturing.

5. 3. Construction Sequence and Control A full-section grouting method with an annulus width of 8 m was selected to reinforce the fault zone, as shown in Figure 14. Each grouting cycle was designed to span a length of 30 m, comprising 25 m of tunnel excavation followed by a 5-m thick grouting barrier left intact. For the first cycle, a 1.5-m thick C20 concrete grouting wall was proposed. Each cycle comprised nine rings with 198 grouting holes, with initial hole diameters of no less than 108 mm and final diameters of no less than 90 mm. The casing pipes were 108 mm in diameter, with a wall thickness of 5 mm, each were made from hot-rolled seamless steel and measured 3 m in length. These casing pipes were securely embedded using effective grout-sealing measures. The drilling and grouting sequence proceeded from the outer to inner holes, alternating holes within the same ring. In the event of water gushing (> 5 L/s) or drill jamming due to fragmented rock layers during drilling, operations were halted, and grouting was conducted to clean the hole before resuming drilling.

5. 4. Inspection and Control standard After completing of grouting for all the holes in a section, an inspection evaluated the grout effectiveness. Any area below the standard received additional drilling and grouting. For this purpose, five inspection holes were established for each section of the working face. These inspection holes were imaged internally to assess grout-filling quality. The qualification criteria stipulate that the water discharge per meter of the inspection hole must not exceed 0.15 L/min, and that the total water discharge within the inspection hole must be less than 3 L/min (40).

5. 5. Results and Suggestion After implementing this full-section grouting reinforcement strategy and strictly adhering to relevant standards, the tunnel excavation successfully navigated the 85-m-wide Cangkou Fault Zone under challenging hydrogeological conditions. Post-grouting monitoring data revealed significant performance indicators: 1) Water inflow control: Maximum seepage was reduced from pre-grouting levels of 12.8 L/min to merely 0.9 L/min (a 93% reduction), meeting the stringent design threshold of <1.5 L/min per 10-meter tunnel segment. 2) Deformation metrics: Convergent deformation monitoring exhibited displacements limited to 18.7 mm (crown) and 22.3 mm (sidewalls), well below the 50-mm alarm threshold specified in relevant standards (40). 3) Rock mass improvement: Post-grouting core samples exhibited a 210% increase in unconfined compressive strength, from an initial 12.4 MPa to 38.5 MPa after 28 days of curing.

The absence of large-scale water inflows (>5 L/s) or structural collapses during the 143-day excavation period demonstrated the effectiveness of the system against the high-permeability conditions (K = 6.74–14.56 m/d) of the fault zones. This success is attributed to three key factors:

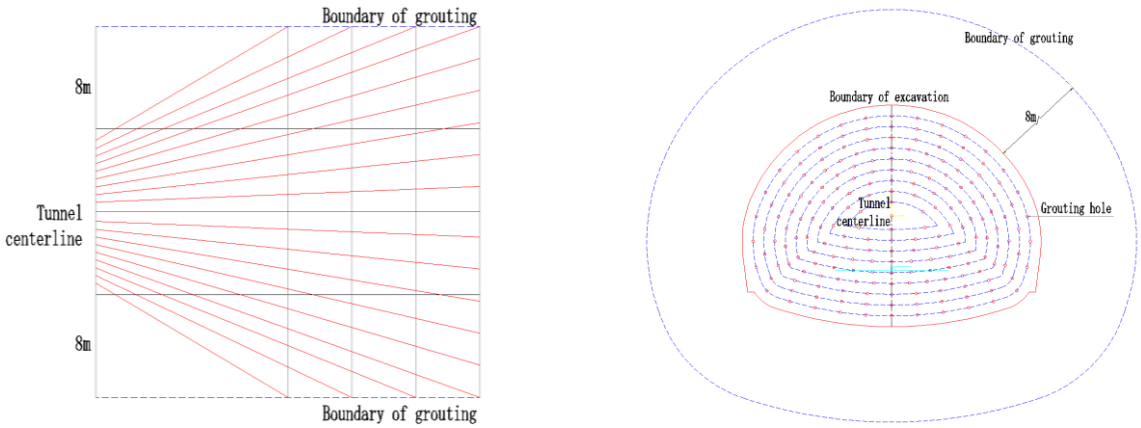

(a) Front view of the section (b) Top or side view of the reinforced area

Figure 14. Dimensions and Scope of Grouting Reinforcement

1) Optimized grout penetration: The 8-m annular grout curtain achieved 92% fracture-filling efficiency (verified via borehole TV imaging), creating a composite rock-grout structure with permeability reduced to 0.3–0.8 m/d.

2) Stress adaptation: Grouting pressures (4–6 MPa) were carefully balanced against the in-situ horizontal stresses (σ_h = 48.8 MPa) to avoid fracture propagation while ensuring radial penetration. 3) Sequential quality control: The 5-stage inspection protocol, including Lugeon tests and grout core sampling, ensured homogeneous reinforcement throughout the fault zone.

These outcomes validate the design premise that full-section grouting outperforms partial-section alternatives in high-stress, high-permeability fault zones. Comparative analysis indicate that curtain grouting requires more grout volume for equivalent seepage control (2). This case provides a technical benchmark for similar projects in tectonically active regions with σ_H/σ_v ratios >1.8.

6. CONCLUSIONS AND LIMITATIONS

An accurate evaluation of the geological conditions encountered by the Qingdao Jiaozhou Bay Second Undersea Tunnel as it traverses the Cangkou Fault Zone provides effective guidance for the smooth excavation of the tunnel. Five representative drill cores were selected for on-site testing: water pressure, pumping, and hydraulic fracturing tests. By analyzing the physical and mechanical properties, permeability, and ground stress distribution of the rock samples, key geological characteristics relevant to tunnel excavation in the fault zone area were identified. This study proposes a targeted advanced grouting reinforcement scheme. The key conclusions are as follows:

1) Water pressure and pumping tests were conducted on drill cores Nos. 1, 2, 3, and 4 located within the drilling-blasting tunnel section. The water pressure tests revealed a significant number of fractures in the rock, with a maximum permeability of 48.38 Lu, indicating high permeability. Owing to the challenges in measuring the permeability at depths of 79-91 m, pumping tests were performed, which yielded permeability coefficients ranging from 6.74 to 14.56 m/d. These elevated values underscore the necessity of effective grouting and water-stopping measures to prevent water ingress during construction.

2) A ground stress distribution test was performed on drill core No. 5, located at the receiving end of the shield tunnel, employing the hydraulic fracturing method. The tests indicated a maximum horizontal principal stress of 4.57 MPa, primarily oriented at N67ºE, demonstrating that the horizontal tectonic stress exceeds the vertical stress. The lateral pressure coefficients were within the normal range, suggesting the absence of abnormal stress concentrations. The stress conditions of the tunnel excavation face were analyzed via stress conversion. Stress conversion analysis of the tunnel excavation face revealed a maximum shear stress of 11.83 MPa, highlighting the necessity for cautious excavation practices to prevent shear failure, particularly in areas with joints and fractures.

3) The implementation of a full-section grouting method with an 8 m annulus width effectively penetrated fractures and reinforced the rock mass upon solidification. This advanced grouting strategy for an undersea tunnel crossing a fault zone successfully addressed the challenges of high rock permeability and ground stress, validating the effectiveness of grouting measures. This reinforcement strategy, in conjunction with the geological testing methods employed, can serve as a valuable reference for engineering projects involving undersea tunnels traversing fault-fractured strata.

4) This study demonstrates that full-section grouting effectively addresses the geological challenges of the Cangkou Fault Zone. However few limitations must be noted. The findings are based on only five boreholes across an 85-meter-wide fault zone, which may not capture all the variations in fractures and stress. Assuming uniform fracture connectivity can overlook high-permeability areas. Although conventional cement grouts provide reliable short-term stability, their long-term effectiveness in marine environments, subject to chemicals and tidal pressures, remains uncertain. The use of a ground-penetrating radar combined with artificial intelligence for advanced detection can be beneficial for future engineering geology exploration. The selection of representative drill cores based on evidence can reduce the sampling workload. In addition, the effects of seawater corrosion on the reinforcing grouting materials and water-blocking measures must be considered. These are the key areas for future research.

7. REFERENCES

1. Shahmardani M, Mirzapour J, Gheyratmand C, Tariverdilo S. Moving load analysis of submerged floating tunnels. International Journal of Engineering, Transactions C: Aspects. 2012;25(1):17-24. https://10.5829/idosi.ije.2012.25.01c.03
2. Tuchiya Y, Kurakawa T, Matsunaga T, Kudo T. Research on the long-term behaviour and evaluation of lining concrete of the Seikan Tunnel. Soils and foundations. 2009;49(6):969-80. https://doi.org/10.3208/sandf.49.969
3. Xun X, Zhang J, Yuan Y. Multi-information fusion based on BIM and intuitionistic fuzzy DS evidence theory for safety risk assessment of undersea tunnel construction projects. Buildings. 2022;12(11):1802. https://doi.org/10.3390/buildings12111802
4. Yang Y, Du Z, Jiao F, Pan F. Analysis of EEG characteristics of drivers and driving safety in undersea tunnel. International journal

of environmental research and public health. 2021;18(18):9810. https://doi.org/10.3390/ijerph18189810

5. Wang C, Yu Y, Kou B. Summary of marine in-situ testing methods. Ocean Development and Management. 2017;34(1):81-6. https://doi.org/10.20016/j.cnki.hykfygl.2017.01.016
6. Liu W, Ren Y, Meng X. Study on the evolution law of rock microstructure under loading and unloading water pressure. Materials Letters. 2024;365:136444. https://doi.org/10.1016/j.matlet.2024.136444
7. H. J. Analysis of Calculation Method of Pumping Test Parameters Based on AquiferTest. Hydrogeology & Engineering Geology. 2011;38:35-8. https://doi.org/10.16030/j.cnki.issn.1000-3665.2011.02.029
8. Wen S ZL, Yuan Y, Zhang J. . Risk Analysis on Water Inflow in Deep Buried Tunnel Based on Water Pressure Test and Measurement of Fractures. Journal of Henan University (Natural Science). 2011;41:645–8. https://doi.org/10.15991/j.cnki.411100.2011.06.014
9. Chang P-Y, Chang L-C, Hsu S-Y, Tsai J-P, Chen W-F. Estimating the hydrogeological parameters of an unconfined aquifer with the time-lapse resistivity-imaging method during pumping tests: Case studies at the Pengtsuo and Dajou sites, Taiwan. Journal of Applied Geophysics. 2017;144:134-43. https://doi.org/10.1016/j.jappgeo.2017.06.014
10. Y. K. Drilling and Technological Measures for Tunnels under Sea at Entrance of Qingdao Bay. Railway Investigation and Surveying. 2006:38–41. https://doi.org/10.19630/j.cnki.tdkc.2006.06.013
11. Li S, Zhao Y, Xu B, Li L, Liu Q, Wang Y. Study of determining permeability coefficient in water inrush numerical calculation of subsea tunnel. Rock and Soil Mechanics. 2012;33(5):1497-505. https://doi.org/10.16285/j.rsm.2012.05.035
12. He L, Huang Y, Meng C, Siwei M, Jiaping T. Practice and development suggestions of hydraulic fracturing technology in the Gulong shale oil reservoirs of Songliao Basin, NE China. Petroleum Exploration and Development. 2023;50(3):688-98. https://doi.org/10.1016/S1876-3804(23)60420-3
13. Q. W. Application of Hydraulic Fracturing Technology in Large-Section Gas Outburst Tunnels. Plant Maintenance Engineering. 2016:97–9. https://doi.org/10.16621/j.cnki.issn1001-0599.2016.05.43
14. Yu S, Ren X, Zhang J, Wang H, Sun Z. An improved smoothed particle hydrodynamics method and its application in rock hydraulic fracture modelling. Rock Mechanics and Rock Engineering. 2021;54(12):6039-55. https://doi.org/10.1007/s00603-021-02594-w
15. Zhang Y, Zhang J, Yuan B, Yin S. In-situ stresses controlling hydraulic fracture propagation and fracture breakdown pressure. Journal of Petroleum Science and Engineering. 2018;164:164-73. https://doi.org/10.1016/j.petrol.2018.01.050
16. Zhang Q, Huang B, He M, Guo S. A numerical investigation on the hydraulic fracturing effect of water inrush during tunnel excavation. Geofluids. 2020;2020(1):6196327. https://doi.org/10.1155/2020/6196327
17. Yin Y, Jiang H, Zhang J, Lu G, Li Q. The influence of rock thermal stress on the morphology and expansion pattern of the plastic zone in the surrounding rock of a deep-buried tunnel under high geothermal temperature conditions. Applied Sciences. 2024;14(17):7589. https://doi.org/10.3390/app14177589
18. Liu T, Huang H, Yan Z, Tang X, Liu H. A case study on key techniques for long-distance sea-crossing shield tunneling. Marine Georesources & Geotechnology. 2020;38(7):786-803. https://doi.org/10.1080/1064119X.2019.1630871
19. Zhou Z, Tan Z, Liu Q, Zhao J, Dong Z. Experimental investigation on mechanical characteristics of waterproof system for near-sea tunnel: a case study of the Gongbei Tunnel. Symmetry. 2020;12(9):1524. https://doi.org/10.3390/sym12091524
20. Gu Z, Zhu L, Zhong J. Modern undersea tunneling technology and the undersea tunnel across Taiwan Strait. Marine Georesources and Geotechnology. 2004;22(3):151-64. https://doi.org/10.1080/10641190490503980
21. Wang C, Liu Z, Dong Z, Zhang F, Ma C, Xu X, et al. Comprehensive Application of Borehole Fine Detection Methods: A Case Study in Shantou Bay Subsea Tunnel. Geofluids. 2024;2024(1):5546191. https://doi.org/10.1155/2024/5546191
22. Zhang J, Chen J, Lei J, Xiong J, Nie X, Gong D, et al. Kaiser acoustic emission ground stress testing study on shale oil reservoir in Y block of Ordos basin, China. Scientific Reports. 2025;15(1):12038.
23. Pei Q, Wu C, Ding X, Huang S. A weight factor-based backward method for estimating ground stress distribution from the point measurements. Bulletin of Engineering Geology and the Environment. 2023;82(9):365. https://doi.org/10.1007/s10064-023-03353-7
24. Zhao Y, Liu Q, Liao J, Wang Y, Tang L. Theoretical and numerical models of rock wing crack subjected to hydraulic pressure and far-field stresses. Arabian Journal of Geosciences. 2020;13(18):926. https://doi.org/10.1007/s12517-020-05957-9
25. Fan Q, Sun H, Meng Z, Wang Y. Stability Monitoring and Numerical Simulation of Weathering Transition Zones in Dam Slopes of Tropical Islands. Applied Sciences. 2025;15(8):4499.
26. Khadri S, Moharir K. Characterization of aquifer parameter in basaltic hard rock region through pumping test methods: a case study of Man River basin in Akola and Buldhana Districts Maharashtra India. Modeling Earth Systems and Environment. 2016;2(1):33. https://doi.org/10.1007/s40808-015-0047-9
27. Hasan M, Shang Y, Jin W, Akhter G. Estimation of hydraulic parameters in a hard rock aquifer using integrated surface geoelectrical method and pumping test data in southeast Guangdong, China. Geosciences Journal. 2021;25(2):223-42. https://doi.org/10.1007/s12303-020-0018-7
28. Petrakov D, Loseva A, Jafarpour H, Penkov G. Experimental evaluation of effective chemical composition on reservoir quality of bottomhole zone of low permeability terrigenous reservoirs. International Journal of Engineering, Transactions B: Applications. 2024;37(8):1547-55. https://doi.org/10.5829/ije.2024.37.08b.08
29. Sekhar A, Abraham BM, Santhoshkumar T, Jose BT. Effect of Initial Water Content of Grout on Permeability of Grouted Sandy Soils. Indian Geotechnical Journal. 2025;55(2):816-26. https://doi.org/10.1007/s40098-024-00943-4
30. Pegah E, Liu H, Dastanboo N. Evaluation of the lateral earth pressure coefficients at-rest in granular soil deposits using the anisotropic components of S-wave velocity. Engineering Geology. 2017;230:55-63. https://doi.org/10.1016/j.enggeo.2017.09.020
31. El Kamash W, El Naggar H, Nagaratnam S. Novel adaptation of Marston's stress solution for inclined backfilled stopes. Alexandria Engineering Journal. 2022;61(10):8221-39. https://doi.org/10.1016/j.aej.2022.01.058
32. Dong J, Chen F, Zhou M, Zhou X. Numerical analysis of the boundary effect in model tests for single pile under lateral load. Bulletin of Engineering Geology and the Environment. 2018;77(3):1057-68. https://doi.org/10.1007/s10064-017-1182-5
33. Zhou G, Liu H, Lian X, Huo T, Han X. A monitoring method for lateral pressure coefficient based on inversion calculation of deep radial displacement in roadway surrounding rock. Measurement. 2025;248:116898. https://doi.org/10.1016/j.measurement.2025.116898

34. Xu Y, Yu Y, Yao W, Xia K, Tang J, Zhan Z. Dynamic failure characteristics of surrounding rocks under different lateral pressure coefficients in deep tunnel transient excavation. Geomechanics and Geophysics for Geo-energy and Geo-resources. 2023;9(1):17. https://doi.org/10.1007/s40948-023-00563-x

35. Manimaran A, Seenu S, Ravichandran P. Stimulation behaviour study on clay treated with ground granulated blast slag and groundnutshell ash. International Journal of Engineering Transactions B: Applications. 2019;32(5):673-8. https://doi.org/10.5829/ije.2019.32.05b.08

36. Guo Y, Wang X, Liu H, Liu Y-n, Ma C, Li Z, et al., editors. Research on Pre-grouting Strengthening Technology of Shallow and Large Section Metro Tunnel through Fault Fracture Zone. IOP Conference Series: Earth and Environmental Science; 2018: IOP Publishing.

37. China NSCGoPsRo. GB50487–2008 Code for engineering geological investigation of water resources and hydropower. China Planning Press Beijing; 2009.

38. Matsuo S. An overview of the Seikan tunnel project. Tunnelling and Underground Space Technology. 1986;1(3-4):323-31. https://doi.org/10.1016/0886-7798(86)90015-5

39. ASTM C A. Standard Specification for Silica Fume Used in Cementitious Mixtures, West Conshohocken. Pa. 2015.

40. Press BCC. JTG/T 3660-2020, Technical specifications for highway tunnel construction. 2020.

COPYRIGHTS

©2026 The author(s). This is an open access article distributed under the terms of the Creative Commons Attribution (CC BY 4.0), which permits unrestricted use, distribution, and reproduction in any medium, as long as the original authors and source are cited. No permission is required from the authors or the publishers.

Persian Abstract

چکیده

ارزیابی ریسک زمین‌شناسی برای تضمین ایمنی ساخت‌وساز در پروژه‌های تونل زیرآبی، به‌ویژه هنگام عبور از مناطق گسلی با ساختار پیچیده، بسیار مهم است. این مطالعه، ریسک‌های هیدروژئولوژیکی و ژئومکانیکی مرتبط با عبور تونل زیرآبی دوم خلیج چینگدائو جیائوژو از منطقه گسلی کانگکو را کمّی‌سازی کرده و استراتژی‌های کاهش هدفمند را بر اساس داده‌های تجربی تدوین می‌کند. بررسی‌های جامع میدانی – شامل آزمایش‌های فشار آب (حداکثر: ٤٨.٣٨ لوتئوری)، آزمایش‌های پمپاژ (ضریب نفوذپذیری K = ١٤.٥٦–٦.٧٤ متر بر روز) و اندازه‌گیری‌های تنش شکست هیدرولیکی (σHmax = ٤.٥٧ مگاپاسکال، جهت‌گیری E - ٦٧°N) دو چالش اصلی را آشکار کرد: شبکه‌های شکستگی با نفوذپذیری بالا و شرایط تنش برجا ناهمسانگرد (ضرایب تنش جانبی λ = ١.٨–١.٢). نتایج نشان می‌دهد که تکنیک‌های تزریق مرسوم در این شرایط ناکافی هستند و باعث اجرای طرح تزریق با مقطع کامل ٨ متری می‌شوند. این روش به طور مؤثر در شبکه‌های شکستگی نفوذ کرده و توده سنگ اطراف را پس از انجماد تقویت می‌کند. محدودیت‌های کلیدی شامل ماهیت محلی داده‌های مغزه حفاری (محدود به پنج نمونه مغزه) و فرض توزیع همگن شکستگی فراتر از مناطق نمونه‌برداری شده است. این یافته‌ها یک چارچوب عملی برای تونل‌سازی در مناطق گسلی در محیط‌های زمین‌شناسی ساحلی مشابه ارائه می‌دهند.

IJE TRANSACTIONS B: Applications Vol. 39, No. 08, (August 2026) 1908-1917

International Journal of Engineering

Journal Homepage: www.ije.ir

Geochemical Characterization of Paleozoic Source Rocks in Nerutinskaya-3 Well, Timan-Pechora Petroleum Province

O. M. Prischepa, Y. V. Nefedov*, A. V. Loginov, I. V. Tokarev, N. N. Vostrikov, A. M. Yashmolkin, A. M. Zharkov

Department of Oil and Gas Geology, Empress Catherine II Saint Petersburg Mining University, St. Petersburg, Russia

PAPER INFO

Paper history:
Received 21 July 2025
Received in revised form 29 August 2025
Accepted 11 September 2025

Keywords:
Pyrolytic Chromatography
Domanikoid Formations
Geochemical Studies
Biomarker Analysis
Petroleum System Modeling

ABSTRACT

This article presents the results of geochemical studies of core samples from Nerutynskaya-3 well, located in Timan-Pechora petroleum province in the northern part of European Russia. The study aims to assess the hydrocarbon generation potential of the Silurian and Upper Devonian sections. The source rocks of Nerutynskaya-3 well, spanning the Carboniferous, Devonian, and Silurian periods, were characterized. Pyrolytic chromatography revealed that the studied intervals, based on total organic carbon (TOC) content, belong to sub-Domanikoid and Domanikoid formations, with Type II kerogen. The sources of organic matter were differentiated throughout the section, and distinct hydrocarbon generation zones were identified. Using Tmax values, the thermal maturity stages of the organic matter were determined, while S1 and S2 parameters were applied to evaluate the generation potential. Biomarker analysis helped identify the depositional environment of the organic matter and confirmed its kerogen typing. Key elements of the petroleum system were indicated. Based on these findings, a basin modeling study was conducted to reconstruct the evolution of the Paleozoic sedimentary complex. The burial history was restored. The stages of catagenetic maturity of organic matter were determined and activation energy calculations were performed.

doi: *10.5829/ije.2026.39.08b.11*

Graphical Abstract

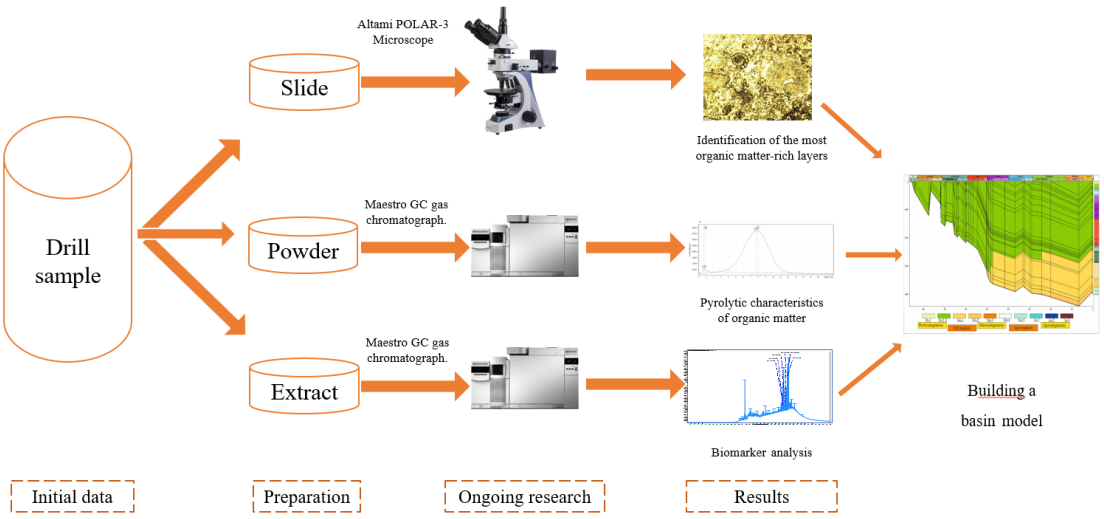

*Corresponding Author Email: Nefedov_yuv@pers.spmi.ru (Y. V. Nefedov)

Please cite this article as: Prischepa OM, Nefedov YV, Loginov AV, Tokarev IV, Vostrikov NN, Yashmolkin AM, Zharkov AM. Geochemical Characterization of Paleozoic Source Rocks in Nerutinskaya-3 Well, Timan-Pechora Petroleum Province. International Journal of Engineering, Transactions B: Applications. 2026;39(08):1908-17.

1. INTRODUCTION

Given the significant depletion of conventional oil reserves in intensively exploited regions, the strategic focus for sustaining and expanding the hydrocarbon resource base has shifted to complex geological formations. These include deep-seated targets and reservoirs that require capital-intensive exploration and development technologies (1, 2). Prime examples are low-permeability, heterogeneous carbonate, clay, and carbonate-clay-siliceous deposits formed in relatively deep marine environments, characterized by challenging filtration and storage properties (3, 4).

The efficient development of such reservoirs demands a thorough analysis and assessment of their hydrocarbon potential due to the high geological and technological risks involved (5). One of the most effective decision-support tools for oil and gas companies is basin analysis, which integrates comprehensive geochemical studies (including bituminological analysis, Rock-Eval pyrolysis, and biomarker analysis). This approach enables the reconstruction of original organic matter concentrations in source rocks, burial and thermal history modeling, identification of peak hydrocarbon generation phases, and evaluation of migration pathways and trap formation timing relative to hydrocarbon expulsion (6, 7).

Data obtained from core and fluid laboratory analyses are combined with seismic interpretation results to build a basin model, providing insights into the hydrocarbon potential of the study area. This methodology helps prioritize the most prospective zones for exploration, optimizing costs—a critical factor given declining investments in exploration and economic constraints driven by competition with green energy projects and sanction-related challenges (8, 9).

Thus, the study of Lower Paleozoic geochemical characteristics in a depression at the margin of the ancient Timan-Pechora sedimentary basin aims to identify potential source rocks of carbonate and carbonate-clay composition. These formations, intersected by wells alongside organic-rich limestones and dolomites with extremely low total organic carbon (TOC), allow for modeling hydrocarbon generation processes, defining petroleum system elements, and assessing hydrocarbon prospects (10).

2. GEOLOGICAL SETTING AND BURIAL HISTORY OF THE PLATFORM MARGIN

The study area is located in the Timan-Pechora petroleum province, at the junction of the Khoreyver Depression and Chernyshev Ridge (Figure 1). The region has been explored since the 1960s using geological and geophysical methods and deep drilling. Between the 1970s and 1990s, several wells confirmed oil-bearing potential in Upper Devonian reefal and Silurian-Lower Devonian carbonate deposits. In 2006–2007, the Nerutynskaya-3 exploration well (which discovered the Nerutynskoye field) yielded commercial oil flows from Famennian (Upper Devonian) and Lower Carboniferous formations (11).

In 2008, reserves of the Nerutynskoye field were estimated, and prospective reefal formations were identified on the Khosedayu-Neruysk uplift, including a two-level (Upper Frasnian and Lower Famennian) organogenic atoll-type structure in the vicinity of well HS-NER6 (12). To date, six exploration and appraisal wells have been drilled in the area, confirming the atoll-like nature of the reefal structure and its hydrocarbon potential associated with the realization of zonal hydrocarbon potential in the Lower Paleozoic section. The penetrated interval spans from Riphean-Vendian basement formations to Quaternary deposits (Figure 2).

The Ordovician System is represented by carbonate-terrigenous deposits, their thickness increasing eastward. The Silurian System includes Lower Silurian dolomites and limestones and Upper Silurian deposits. The Upper Silurian is represented by the Herdian Horizon (Ludlow Stage), composed of interbedded dolomites, clayey limestones and marls. In the area of Khosedayu-Neruysk structure its thickness is reduced due to pre-Devonian erosion (13, 14).

The Devonian System is represented by Lower Devonian carbonates and Upper Devonian deposits. The Upper Devonian includes the Domanik Horizon (Middle Frasnian Stage), consisting of bituminous limestones and argillites, as well as the Zelenetsky and Nyumylgsky Horizons (Upper Famennian) - shallow-water and reefal limestones yielding commercial oil flows.

The Carboniferous System is composed of Visean and Serpukhovian carbonates. The Lower Serpukhovian Horizon (Tarusa and Steshev beds) is represented by dolomites and anhydrites, serving as a regional fluid seal.

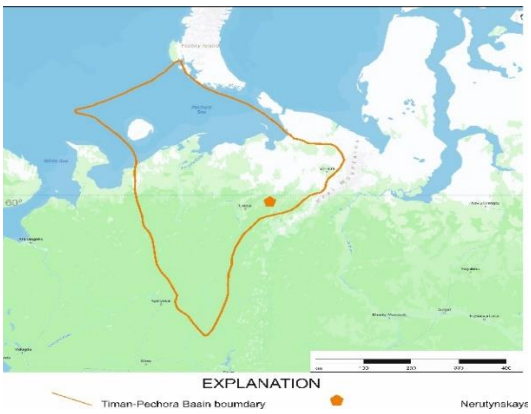

Figure 1. Map showing the four continuous assessment units (AUs) in the Timan-Pechora Basin Province of Russia

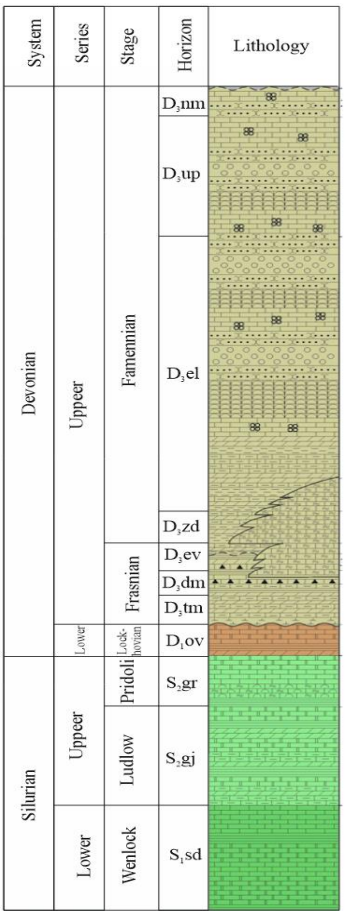

Figure 2. Lithostratigraphic Section Interval

The Permian System is represented by Lower Permian carbonate deposits (Asselian-Sakmarian, Artinskian, Kungurian) and Upper Permian terrigenous deposits (Ufimian, Kazanian-Tatarian).

Triassic deposits are not ubiquitous. The Jurassic System consists of interbedded clays, siltstones and sandstones, preserved fragmentarily after erosional events. The Cretaceous System is represented by sandy-clayey deposits pinching out at Chernyshev Ridge. The Quaternary System is composed of thin clays, loams and pebble beds.

According to the tectonic scheme of the Timan-Pechora Province (TPP), the study area is located in the southeastern part of the Khoreyver Depression, which represents a northwest-trending monocline (Figure 1), complicated by local structures, one of which is the Tsilegorsk Depression - a narrow linear structure of northeast trend (15).

The main hydrocarbon potential of the area is associated with four commercial hydrocarbon-bearing complexes: Middle Ordovician-Lower Devonian carbonate, Middle Frasnian-Tournaisian carbonate, Middle Visean-Lower Permian carbonate and Lower Permian terrigenous (Figure 2) (16).

3. MATERIALS AND METHODS

Material for the study consisted of core samples from the Nerutinskaya-3 well, drilled within the Khoreyver Depression of the Timan-Pechora petroleum province (Figure 3). Paleozoic deposits in the interval of 2300-3970 m, represented by carbonate rocks, were investigated.

The preparation of thin sections from the studied core samples and their microscopic petrographic description using optical microscopy were performed at the Saint Petersburg Mining University (Empress Catherine II) at the Department of Petroleum Geology. Based on lithological analysis of rock composition, the most organic-rich layers were identified as potential source rocks, which were subsequently studied using pyrolytic methods.

Geochemical analysis of samples was conducted using the BulkRock pyrolysis method with an EGA/PY-3030D pyrolytic cell. Pyrolytic studies involve the thermal decomposition of organic matter (OM) in source rocks. The OM analysis was performed using an analytical system comprising a Frontier Lab EGA/PY-3030D pyrolytic cell and a Maestro-MS gas chromatograph-mass spectrometer (GC-MS).

A finely ground rock powder (0.20-0.25 mm particle size, 300-500 μg mass) was placed in a crucible and subjected to helium-flow heating using a Rock-Eval (BulkRock)-like methodology, involving a two-stage heating process: Stage I - isothermal heating at 300°C for 3.43 min; Stage II - linear temperature increase from 300 to 650°C at 30°C/min for 15.09 min.

A standard reference material, "IFP 160000" (source rock standard), was used for instrument calibration. The pyrolytic system is not equipped with a chromatographic column; instead, a metal capillary is placed in the thermostat. The capillary prevents the separation of both free and bound hydrocarbons into individual compounds, allowing for clear and symmetrical S1 and S2 peaks.

Figure 3. Photograph of the core of the Nerutynskaya-3 well

Pyrolysis results were analyzed using Maestro-Analyst software. The pyrolysis methodology on the described equipment is certified in accordance with GOST R 8.563-2009 ("State System for Ensuring the Uniformity of Measurements. Measurement Procedures"). The certification was issued by the All-Russian Research Institute of Metrological Service (Moscow).

Compositional analysis of saturated and aromatic hydrocarbons, including biomarkers and their parameters in oils and bitumoids, was performed on the same analytical system by replacing the capillary with an Agilent DB-5MS Ultra Inert capillary column (internal diameter: 0.25 mm; length: 30 m). This method involves separating the maltene fraction into saturated and aromatic components using a capillary column with a nonpolar stationary liquid phase.

Biomarker analysis was conducted using the following temperature program: stepwise heating from 100 to 300°C at 600°C/min, followed by heating from 300 to 650°C at 30°C/min. After chromatographic separation, hydrocarbon compounds were detected by mass spectrometry. Biomarker parameters were determined based on mass-to-charge ratios (m/z) for characteristic fragment ions including phenanthrenes (178), dibenzothiophenes (184), tricyclic and pentacyclic terpanes/triterpanes (191), methylphenanthrenes (192), methyldibenzothiophenes (198), sternanes (217), isosternanes (218), diasteranes (259), triaromatic steroids (231), and monoaromatic steroids (253).

The obtained spectra were processed using specialized software, enabling the identification of individual compounds and quantitative assessment of their concentrations (17-19).

4. RESULTS AND DISCUSSING

4. 1. Geochemical Characteristics of Organic Matter. Pyrolytic Studies of the Substance The studied interval of core samples from the Nerutinskaya-3 well (2300-3970 m) penetrated carbonate deposits of Carboniferous, Devonian and Silurian age (C1s1-S2gj). Based on the realized potential values (S1), the section is differentiated into zones of source rocks with medium (0.5-1.0 mg HC/g rock), good (1.0-2.0 mg HC/g rock) and excellent potential (>2 mg HC/g rock). The residual potential values (S2) are assessed as medium (2.5-6.0 HC/g rock) (Figure 4) (20, 21).

The organic carbon content in this section ranges from 0.15 to 4.17%, characterizing the deposits as sub-Domanik (<0.5%) and Domanik-type (<5%) (22-24).

The level of catagenetic transformation corresponds to PC1-MK1 gradation (Tmax=360-434°C). A trend of increasing Tmax with depth is observed.

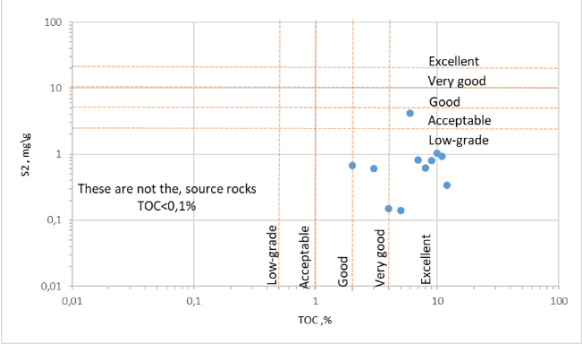

Figure 4. Generation potential of samples from Nerutinskaya-3 well

Based on hydrogen index values, the rocks possess medium (100-300 mg HC/g TOC) and good (300-600 mg HC/g TOC) generation potential (Figure 5) (25).

4. 2. Molecular Composition of Dispersed Organic Matter. Biomarker Analysis The composition of n-alkanes in oils and bitumoids directly reflects the nature of the original organic matter (OM). This parameter is widely used in geochemical studies to reconstruct sedimentation conditions and identify facies types of source rocks. Marine deposits, whose organic matter is formed primarily by plankton, are characterized by the predominance of low-molecular-weight n-alkanes (C_{15}–C_{17}). In continental deposits with contributions from higher plants, high-molecular-weight compounds (C_{27}–C_{31}) dominate (Figure 6).

HA reliable diagnostic criterion is the ratio of n-alkanes $C_{17}/C_{27}>1$, which indicates marine genesis of OM with a predominance of algal and bacterial components, while a ratio of $C_{17}/C_{27}<1$ suggests a significant contribution of terrestrial humic material. The distribution of n-alkanes in dispersed organic matter indicates its mixed genesis (Figure 7).

Among isoprenoid aliphatic hydrocarbons, the most common compounds are pristane (Pr) and phytane (Ph). The ratio of these biomarkers is used as an indicator of redox conditions during sedimentation. The predominance of pristane is characteristic of terrestrial OM from higher plants, while the dominance of phytane indicates marine hydrocarbon genesis. The geochemical characteristics of aliphatic hydrocarbons allow for the assessment of both similarities and specific features in the composition and transformation level of dispersed organic matter in the studied formations (Figure 8) (26).

Tetracyclic saturated hydrocarbons - steranes represent an important class of biomarkers formed during diagenetic transformation of sterols present in eukaryotic cell membranes. These compounds, widely distributed in fossil organic matter, oils, and natural bitumens, carry

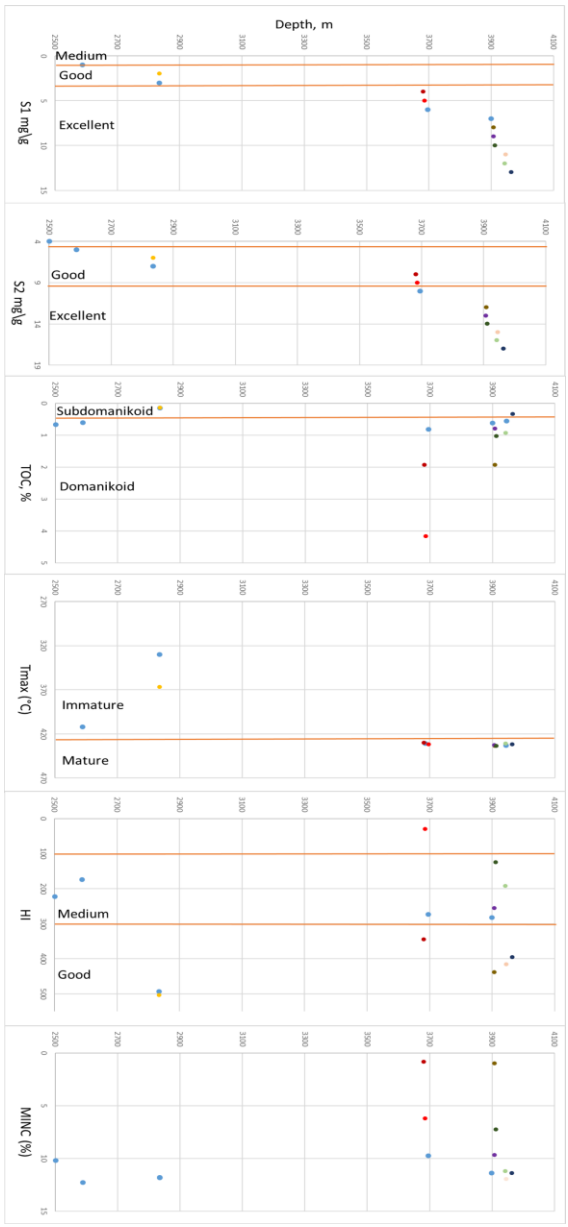

Figure 5. Geochemical Section of Potential Source Rocks in the Nerutinskaya-3 Well

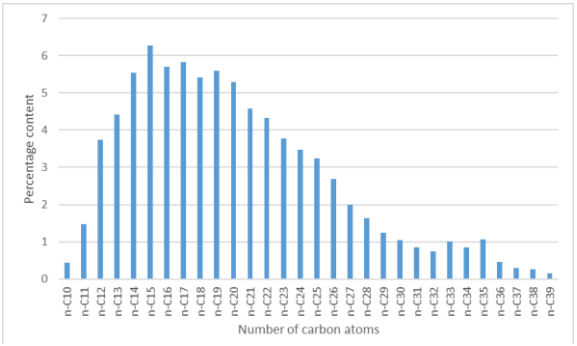

Figure 6. Distribution of n-alkanes in the Nerutinskaya-3 well

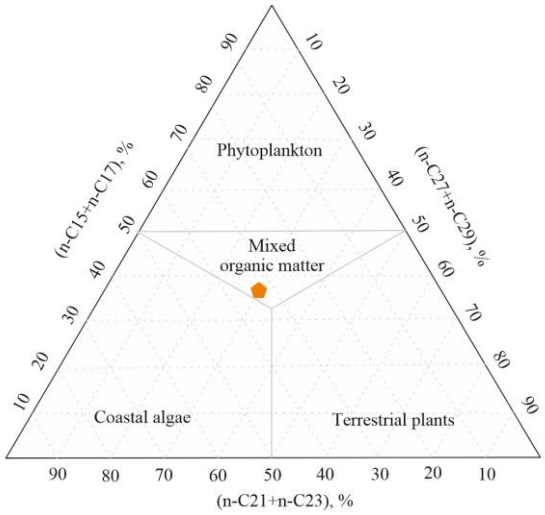

Figure 7. Genetic characteristics of dispersed organic matter (based on n-alkane composition)

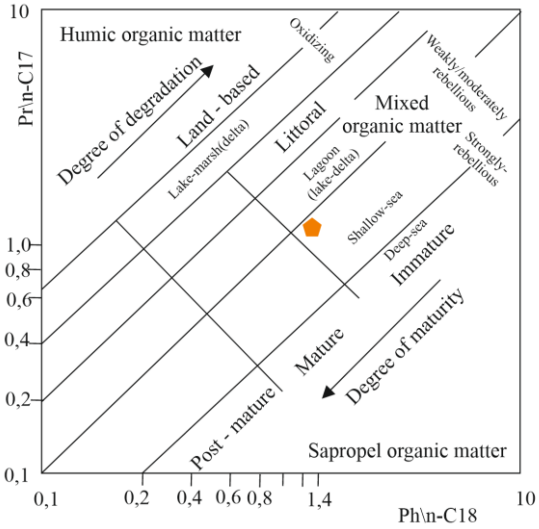

Figure 8. Characteristics of the genetic type and facies sedimentation conditions of dispersed organic matter (Cannon-Cassow diagram)

valuable information about several aspects of petroleum formation: the composition of the original biological material, sedimentation and diagenesis conditions, and post-sedimentary transformations. Additionally, the distribution patterns of steranes are successfully used as indicators of hydrocarbon migration and biodegradation processes (27, 28).

The diagnostic value of steranes is based on the specific distribution of their homologs: cholestane (C27) is a marker of microalgal organic matter, methylcholestane (C28) indicates contributions from zooplankton or lagoon algae, while ethylcholestane (C29) unequivocally points to the participation of higher terrestrial plants in the formation of the original organic

matter. Analysis of the relative content of these compounds allows not only for determining the origin of organic matter but also for reconstructing paleoecological sedimentation conditions, which is fundamentally important for assessing the petroleum potential of sedimentary basins (Figure 9) (29).

The results of biomarker analysis enabled not only the identification of paleofacies environments but also the differentiation of hydrocarbon generation zones. By plotting the research results on a spider diagram, two potential oil generation zones were identified in the deposits of the Domanik and Herdian horizons. The diagram was constructed using n-alkanes and isoprenoids, steranes, phenanthrenes, as well as terpanes. This approach allowed for the diagnostic coverage of the widest possible range of compounds with different fragment ion masses for studying the oil generation process (Figure 10) (30, 31).

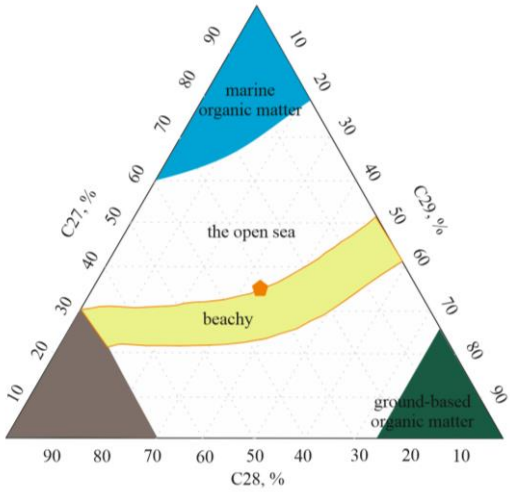

Figure 9. Facies-genetic characteristics of sedimentary rocks in the well (based on regular steranes)

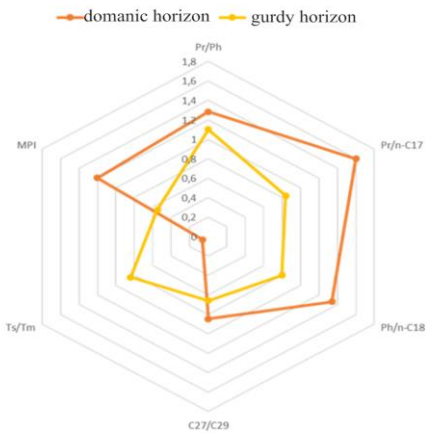

Figure 10. Spider diagram of Potential Source Rocks in the Nerutinskaya-3 Well

4. 3. Basin Modeling Historical-geological modeling represents a comprehensive method for reconstructing the evolution of sedimentary basins, based on reproducing geological processes at geological timescales. The essence of the method lies in step-by-step basin modeling from the formation of the oldest deposits to the present state, taking into account the sequential accumulation of all stratigraphic units (32, 33).

At each time interval, key geological processes are simulated: sedimentogenesis and lithogenesis (sedimentation, rock compaction, changes in petrophysical properties), thermodynamic processes (evolution of heat flow, calculation of paleotemperatures considering latent heat of fusion for crustal and mantle rocks), as well as petroleum generation processes (catagenetic transformation of organic matter, hydrocarbon generation, fluid phase transformations, hydrocarbon migration and accumulation) (34).

The modeling was performed using the specialized software complex "TemisFlow" at the Department of Arctic and World Ocean Petroleum Potential (VNIIOkeangeologia). Model verification was carried out by comparing calculated and actual temperature profiles.

This approach provided a comprehensive reconstruction of paleo-conditions and allowed assessment of the thermobaric evolution of the section, dynamics of catagenetic transformations, temporal and spatial patterns of petroleum generation, as well as hydrocarbon potential prospects of the studied deposits.

Detailed subdivision of the geological section was performed using an integrated method combining well logging data (GIS) with lithological analysis of core material, cuttings samples, and petrographic studies of thin sections. As a result of the analysis, 21 lithotypes were identified in the well interval, with the following parameters established for each: age attribution, absolute top and base depths, thickness, and detailed lithological characteristics. The obtained data formed the basis for subsequent geological modeling and interpretation of sedimentation conditions (Figure 11).

For parameterization of the geological model, a specialized lithological variability library was developed, containing detailed characteristics of rock composition. Each lithological variety was assigned quantitative indicators of the content of main rock-forming components (in percentage terms), as well as the type of mineral component distribution (homogeneous or stratified). This library ensures accurate assignment of lithological characteristics during geological modeling, considering both qualitative rock composition and features of spatial component distribution throughout the section.

Based on comprehensive analysis of the lithostratigraphic column and study of the historical-geological concept of basin development, sedimentary

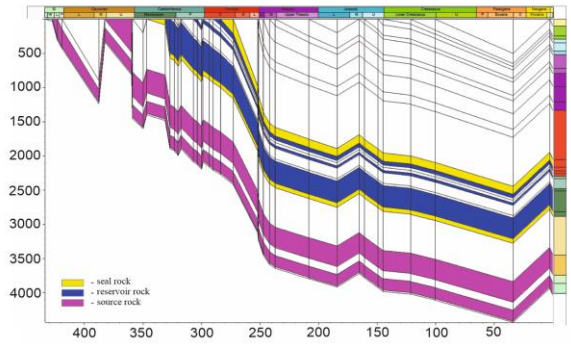

Figure 11. Subsidence of hydrocarbon system elements during the geological history of the sedimentary section penetrated by the Nerutinskaya-3 well

TABLE 1. Contents of the lithological library for the Nerutinskaya-3 well

Lithotype index	Composition of rocks
1	100% Sandstone
2	80% Sandstone + 20% Siltstone
3	60% Sandstone + 30% Siltstone +10% Mudstone
4	70% Sandstone + 30% Mudstone
5	100% Mudstone
6	80% Mudstone + 20% Siltstone
7	80% Mudstone + 20% Sandstone
8	70% Mudstone + 20% Siltstone + 10% Sandstone
9	50% Mudstone + 30% Siltstone + 20% Sandstone
10	40% Siltstone + 30% Mudstone +30% Sandstone
11	100% Mudstone (source rock)
12	100% Sandstone (reservoir rock)
13	100% Limestone (reservoir rock)
14	100% grainstone
15	100% dolostone
16	100% limestone
17	100% boundstone
18	boundstone 80%+20 % limestone
19	limestone 80%+20% boundstone
20	dolostone 80%+marl 20%
21	dolostone 80%+ boundstone 20%

hiatuses were identified and erosion thicknesses estimated. Six significant sedimentation breaks were established in the studied section: Early-Middle Devonian, Early Carboniferous (Visean), Late Carboniferous, Late Permian, Late Triassic, and Upper Cretaceous-Neogene. The obtained data on denudated formation thicknesses were systematized in the input lithostratigraphic parameters table.

Source rock identification and generation potential assessment were performed using pyrolytic studies. Analysis revealed relatively low organic matter content in the well penetrations. Potential hydrocarbon-generating units were identified as clayey formations of the following stratigraphic subdivisions: Frasnian Stage of Upper Devonian (Domanik Horizon) and Ludlow Stage of Upper Silurian (Herdian Horizon). Data on geochemical characteristics and source rock distribution within the section enable assessment of hydrocarbon potential in the study region and identification of priority targets for further investigation.

Geothermal gradient values were obtained from well temperature measurements (Figure 12).

The distribution of heat flows throughout the geological history of the sedimentary section is characterized by low values of 40-45 mW/m², which established stable thermal conditions (Figure 13).

The transformation ratio (TR) indicates source rock maturity achieved considering specific kinetic features of organic matter conversion to hydrocarbons. TR shows the proportion of kerogen already converted to hydrocarbons through chemical reactions (TR of 100% means complete kerogen exhaustion, with no future generation potential) (Figure 14).

Mesozoic, Permian and Carboniferous formations lie outside the active oil generation window (PC1-3). Upper Devonian Frasnian Stage organic matter (Domanik Horizon) is predominantly mixed Type II, currently in hydrocarbon generation zone MK1. Upper Silurian Ludlow Stage organic matter (Herdian Horizon) is also mixed Type II, in active generation zone MK2 (Figure 15).

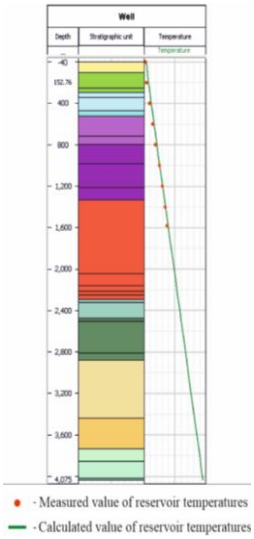

Figure 12. Model calibration results based on well temperature data

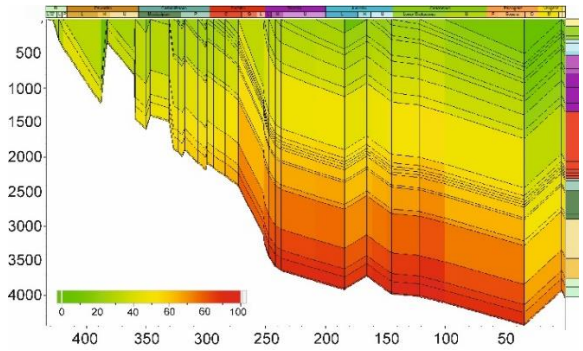

Figure 13. Formation temperature distribution through geological history of the sedimentary section penetrated by Nerutinskaya-3 well (According to the authors' data)

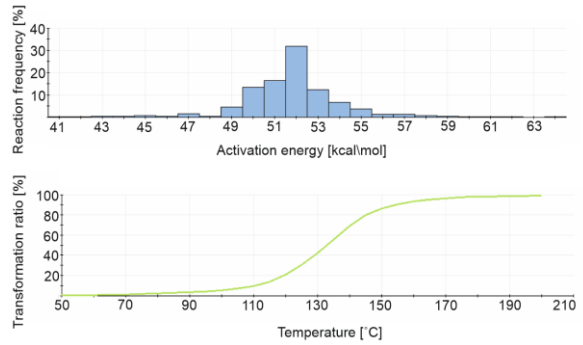

Figure 14. Distribution of transformation ratio and activation energy in samples from Nerutinskaya-3 well (According to the authors' data)

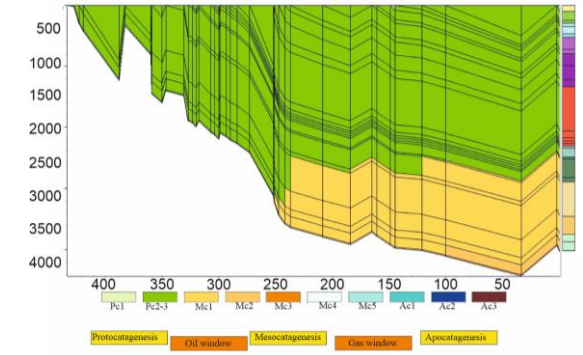

Figure 15. Catagenetic maturity of organic matter (EasyRo model) and hydrocarbon generation zones in the sedimentary section penetrated by Nerutinskaya-3 well

5. CONCLUSIONS

The comprehensive study of hydrocarbon potential in sedimentary formations of the third Nerutinskaya well in Timan-Pechora petroleum province, incorporating modern geochemical methods (pyrolytic chromatography mimicking Rock-Eval technique and biomarker analysis) coupled with 1D basin modeling, has updated understanding of hydrocarbon generation potential in Tsilegorsk Depression.

The research created a petrological thin section collection primarily from lowstand systems tracts. Organic-rich layers with source rock potential were identified through lithological analysis. Pyrolytic chromatography showed TOC content ranging 0.17-4.17%, characteristic of sub-Domanik (0.1-0.5%) and Domanik (0.5-5.0%) formations, with predominantly Type II organic matter. Residual, realized and generation potentials were characterized.

Tmax values determined organic matter maturity stages (immature/early mature), enabling assessment of transformation degree and hydrocarbon generation readiness. Biomarker analysis identified depositional environments (shallow marine facies) and organic matter type (mixed), while differentiating source inputs and distinguishing hydrocarbon generation kitchens.

Integration into 1D basin modeling enabled reconstruction of hydrocarbon system element subsidence through geological history, determination of organic matter catagenetic maturity (MK1-MK2), and calculation of activation energy (52 kcal/mol).

6. FINANCING

The article was prepared within the framework of the state task FSRW-2024-0008 "Investigation of thermodynamic processes of the Earth from the perspective of the genesis of hydrocarbons at great depths".

Authors' contributions:

Prischepa O.M. – Research conceptualization, formulation of the main hypothesis, writing the abstract and introduction sections.

Nefedov Yu.V. – Methodology development and study design.

Loginov A.V. – execution of experiments, data analysis, and results interpretation.

Tokarev I.V. – conclusions formulation and manuscript editing.

Zharkov A.M., Yashmolkin A.M. and Vostrikov N.N.– proofreading, reference formatting, and figure preparation.

7. REFERENCES

1. Litvinenko VS, Nikolaev N. Technological fluids for increasing effectivity of construction and exploitation oil and gas wells. Journal of Mining Institute. 2011;194:84-.
2. Litvinenko VS, Petrov EI, Vasilevskaya DV, Yakovenko AV, Naumov IA, Ratnikov MA. Assessment of the role of the state in the management of mineral resources. Записки Горного института. 2023(259 (eng)):95-111. 10.31897/pmi.2022.100

3. Mardashov D, Limanov M, Onegov N, Shamsutdinova G, Fiterman S. Influence of Clay Content in Reservoir Rocks on Efficiency of Killing Production Wells. International Journal of Engineering, Transactions A: Basics. 2025;38(1):78-85. 10.5829/ije.2025.38.01a.08
4. Palyanitsina A, Tananykhin D, Masoud R. Strategy of water-flooding enhancement for low-permeable polymictic reservoirs. Journal of Applied Engineering Science. 2021;19(2):307-17. 10.5937/jaes0-29693
5. Kongar-Syuryun C, Babyr N, Klyuev R, Khayrutdinov M, Zaalishvili V, Agafonov V. Model for Assessing Efficiency of Processing Geo-Resources, Providing Full Cycle for Development—Case Study in Russia. Resources. 2025;14(3):51. 10.3390/resources14030051
6. Dvoynikov MV, Sidorkin DI, Yurtaev SL, Grokhotov EI, Ulyanov DS. Drilling of deep and ultra-deep wells for prospecting and exploration of new raw mineral fields. Записки Горного института. 2022;258:945-55. 10.31897/PMI.2022.55
7. Babyr N, Gabov V, Nosov A, Nikiforov A. Features of design and work method of mining module at coal deposits in the Russian Arctic. Mining Informational and Analytical Bulletin. 2024;6:5-16. 10.25018/0236_1493_2024_6_0_5
8. Korelskiy D, Mentsiev A, Dengaev A, Novikova A, Babyr N. Land Assessment in Mining Regions Considering Ecology. Int J Eng. 2024;37:2344-53. 10.5829/ije.2024.37.11b.19
9. Malozyomov BV, Martyushev NV, Babyr NV, Pogrebnoy AV, Efremenkov EA, Valuev DV, et al. Modelling of Reliability Indicators of a Mining Plant. Mathematics (2227-7390). 2024;12(18). 10.3390/math12182842
10. Aleksandrova T, Nikolaeva N, Kuznetsov V. Thermodynamic and experimental substantiation of the possibility of formation and extraction of organometallic compounds as indicators of deep naphthogenesis. Energies. 2023;16(9):3862. 10.3390/en16093862
11. Schenk CJ, Mercier TJ, Pitman JK, Le PA, Tennyson ME, Brownfield ME, et al. Assessment of continuous oil and gas resources of the Timan-Pechora Basin Province, Russia, 2018. US Geological Survey; 2018. Report No.: 2327-6932.
12. Tcvetkov P, Cherepovitsyn A, Makhovikov A. Economic assessment of heat and power generation from small-scale liquefied natural gas in Russia. Energy Reports. 2020;6:391-402. 10.1016/j.egyr.2019.11.093
13. Prischepa O, Bogatsky V, Makarevich V, Chumakova O, Nikonov N, Kuranov A, et al. The Timan–Pechora oil-bearing province–new tectonical insight. Neftegazovaya geologiya Teoriya i praktika. 2011;6(4):1-34.
14. Egorov A, Antonchik V, Senchina N, Movchan I, Oreshkova M. Impact of the Regional Pai-Khoi-Altai Strike-Slip Zone on the Localization of Hydrocarbon Fields in Pre-Jurassic Units of West Siberia. Minerals. 2023;13(12):1511. 10.3390/min13121511
15. Taninskaya N, Taninskiy PY. Using the sequence stratigraphic method for oil and gas prospecting in the Middle Ordovician-Nizhne Devonian sediments of the Timan-Pechora province. Journal of Mining Institute. 2002;151:40-2.
16. Taninskaya N. Carbonate sequences of the Middle Ordovician-Silurian of the Pechora-Barents Sea megabasin. Journal of Mining Institute. 2008;176:36-40.
17. Povarov VG, Cheremisina OV, Alferova DA, Fedorov AT. Determination of the Activity Coefficients of Components in a Di-2-ethylhexylphosphoric Acid–n-Hexane Binary System Using Gas Chromatography. Chemistry. 2025;7(3):92. 10.3390/chemistry7030092
18. Povarov VG, Efimov I, Smyshlyaeva KI, Rudko VA. Application of the UNIFAC Model for the Low-Sulfur Residue Marine Fuel Asphaltenes Solubility Calculation. Journal of Marine Science and Engineering. 2022;10(8):1017. 10.3390/jmse10081017
19. Wang Z, Stout SA, Fingas M. Forensic fingerprinting of biomarkers for oil spill characterization and source identification. Environmental Forensics. 2006;7(2):105-46. 10.1080/15275920600667104
20. Prishchepa OM, Borovikov IS, Grokhotov EI. Oil and gas content of the understudied part in the northwest of the Timan-Pechora oil and gas province according to the results of basin modeling. Записки Горного института. 2021;247:66-81. 10.31897/PMI.2021.1.8
21. Chemodanov A, Gareev B, Batalin G, Gerasimov R. Research of domanic source rock by pyrolytic gas chromatography-mass spectrometry method. SCOPUS16085043-2019-21-1-SID85066296810. 2019. 10.18599/grs.2019.1.71-76
22. Romero-Sarmiento M-F, Pillot D, Letort G, Lamoureux-Var V, Beaumont V, Huc A-Y, et al. New Rock-Eval method for characterization of unconventional shale resource systems. Oil & Gas Science and Technology–Revue d'IFP Energies nouvelles. 2016;71(3):37. 10.2516/ogst/2015007
23. Vakhin A, Onishchenko YV, Chemodanov A, Sitdikova L, Nurgaliev D. Thermal transformation of bitumoid of Domanic formations of Tatarstan (Russian). Oil Industry Journal. 2016;2016(10):32-4.
24. Vakhin A, Onishchenko Y, Chemodanov A, Sitnov S, Mukhamatdinov I, Nazimov N, et al. The composition of aromatic destruction products of Domanic shale kerogen after aquathermolysis. Petroleum Science and Technology. 2019;37(4):390-5. 10.1080/10916466.2018.1547760
25. Zhao X, Zhou L, Pu X, Jiang W, Jin F, Xiao D, et al. Hydrocarbon-generating potential of the upper Paleozoic section of the Huanghua Depression, Bohai Bay Basin, China. Energy & Fuels. 2018;32(12):12351-64. 10.1021/acs.energyfuels.8b03159
26. Zavyalova A, Chupakhina V, Stoupakova A, Gatovsky J, Kalmykov G, Korobova N, et al. Comparison of the Domanic Outcrops in the Volga-Ural and Timan-Pechora Basins. Moscow University Geology Bulletin. 2019;74(1):56-72. 10.3103/S0145875219010149
27. Hughes WB, Holba AG, Dzou LI. The ratios of dibenzothiophene to phenanthrene and pristane to phytane as indicators of depositional environment and lithology of petroleum source rocks. Geochimica et Cosmochimica Acta. 1995;59(17):3581-98.
28. Volkman JK. A review of sterol markers for marine and terrigenous organic matter. Organic geochemistry. 1986;9(2):83-99. 10.1016/0146-6380(86)90089-6
29. Goncharov I, Samoilenko V, Oblasov N, Fadeeva S, editors. MDBT estimation ratio for transformation organic matter ratio in Bazhenov Formation of Western Siberia (Tomsk Oblast, Russia). IOP Conference Series: Earth and Environmental Science; 2015: IOP Publishing. 10.1088/1755-1315/24/1/012040
30. Behar F, Vandenbroucke M, Tang Y, Marquis F, Espitalie J. Thermal cracking of kerogen in open and closed systems: determination of kinetic parameters and stoichiometric coefficients for oil and gas generation. Organic geochemistry. 1997;26(5-6):321-39. https://doi.org/10.1016/S0146-6380(97)00014-4
31. Goncharov I, Samoilenko V, Oblasov N, Fadeeva S, Veklich M, Kashapov R, et al. Types of organic matter and catagenesis of the Bazhenov formation and its same-aged analogues (Russian). Oil Industry Journal. 2016;2016(10):20-5.
32. Tarshan A, Shimanskiy S. Petroleum system modelling and identification of promising oil and gas bearing objects in the eastern part of the Gulf of Suez, Egypt. Russian journal of earth sciences. 2019;19(4):2. 10.2205/2019ES000669

33. Hakimi MH, Abdullah WH, Alqudah M, Makeen YM, Mustapha KA, Hatem BA. Pyrolysis analyses and bulk kinetic models of the Late Cretaceous oil shales in Jordan and their implications for early mature sulphur-rich oil generation potential. Marine and Petroleum Geology. 2018;91:764-75. 10.1016/j.marpetgeo.2018.01.036

34. Song Y, Zhu K, Shi Q, Cao Q, Huang C, Ye X. Two-step classification of highly mixed oil in the Qikou Sag (Bohai Bay Basin, China): Implications for origin, maturity, and biodegradation. Geoenergy Science and Engineering. 2023;221:111273. 10.1016/j.petrol.2022.111273

COPYRIGHTS

©2026 The author(s). This is an open access article distributed under the terms of the Creative Commons Attribution (CC BY 4.0), which permits unrestricted use, distribution, and reproduction in any medium, as long as the original authors and source are cited. No permission is required from the authors or the publishers.

Persian Abstract

چکیده

این مقاله نتایج مطالعات ژئوشیمیایی نمونه‌های مغزه از چاه Nerutynskaya-3، واقع در استان نفتی Timan-Pechora در بخش شمالی روسیه اروپایی را ارائه می‌دهد. هدف از این مطالعه ارزیابی پتانسیل تولید هیدروکربن در بخش‌های سیلورین و دونین بالایی است. سنگ‌های منشأ چاه Nerutynskaya-3، که دوره‌های کربنیفر، دونین و سیلورین را در بر می‌گیرند، مشخص شدند. کروماتوگرافی پیرولیتیک نشان داد که فواصل مورد مطالعه، بر اساس محتوای کل کربن آلی (TOC)، متعلق به سازندهای زیر- دومانیکوئیدی و دومانیکوئیدی با کروژن نوع II هستند. منابع مواد آلی در سراسر برش متمایز شدند و مناطق متمایز تولید هیدروکربن شناسایی شدند. با استفاده از مقادیر Tmax، مراحل بلوغ حرارتی ماده آلی تعیین شد، در حالی که پارامترهای S1 و S2 برای ارزیابی پتانسیل تولید هیدروکربن اعمال شدند. تجزیه و تحلیل نشانگرهای زیستی به شناسایی محیط رسوبی ماده آلی کمک کرد و نوع کروژن آن را تأیید کرد. عناصر کلیدی سیستم نفتی مشخص شدند. بر اساس این یافته‌ها، یک مطالعه مدل‌سازی حوضه برای بازسازی تکامل مجموعه رسوبی پالئوزوئیک انجام شد. تاریخچه تدفین بازیابی شد. مراحل بلوغ کاتاژنتیکی مواد آلی تعیین و محاسبات انرژی فعال‌سازی انجام شد.

IJE TRANSACTIONS B: Applications Vol. 39, No. 08, (August 2026) 1918-1932

International Journal of Engineering

Journal Homepage: www.ije.ir

Effect of Foundation Flexibility on Seismic Energy Dissipation in RC Bridges Subjected to Fling-step Ground Motions

F. B. Khurshid*[a,b], M. S. Izhar[a], N. Islam[a], N. A. Khan[a]

[a] *Department of Civil Engineering, FE&T, Jamia Millia Islamia, New Delhi, India*
[b] *Department of Architecture, FA&E, Jamia Millia Islamia, New Delhi, India*

PAPER INFO

Paper history:
Received 20 June 2025
Received in revised form 16 July 2025
Accepted 24 August 2025

Keywords:
Incremental Dynamic Analysis
Fragility Analysis
Regression Analysis
Soil Structure Interaction
Energy Dissipation

ABSTRACT

Bridges are critical components of transportation networks, particularly in the aftermath of seismic events when their continued operation is essential for emergency response and recovery. The severity of seismic impact on a bridge depends largely on the characteristics of ground motion and the structure's proximity to the fault. While bridges located in far-field regions may experience moderate effects, those situated in near-fault (NF) zones—typically within 15 km of a fault rupture—are highly susceptible to severe damage due to intense ground motions. NF ground motions (NF-GMs) are distinguished by high-energy velocity pulses, long-period pulse-like waveforms, and high peak values that pose significant demands on structures. Although several studies have investigated the seismic vulnerability of bridges under NF-GMs, most assume fixed-base conditions and neglect the influence of soil flexibility. The role of soil-structure interaction (SSI) in altering the seismic performance of reinforced concrete (RC) bridges under such demands remains inadequately addressed. This study performs a comparative vulnerability assessment of a simply supported multi-span RC bridge subjected to NF-GMs with forward directivity and fling step (FS) effects. Incremental Dynamic Analysis (IDA) is carried out, and fragility curves were developed to quantify the probability of damage across two configurations: a fixed-base model and a flexible-base model incorporating SSI via a pile group foundation. The results indicate that the flexible-base model experiences higher displacement demands but reduced base shear, while the fixed-base model exhibits greater stiffness and force transmission. These findings underscore the need to incorporate SSI in seismic vulnerability assessments of bridges in NF regions.

***doi**: 10.5829/ije.2026.39.08b.12*

Graphical Abstract

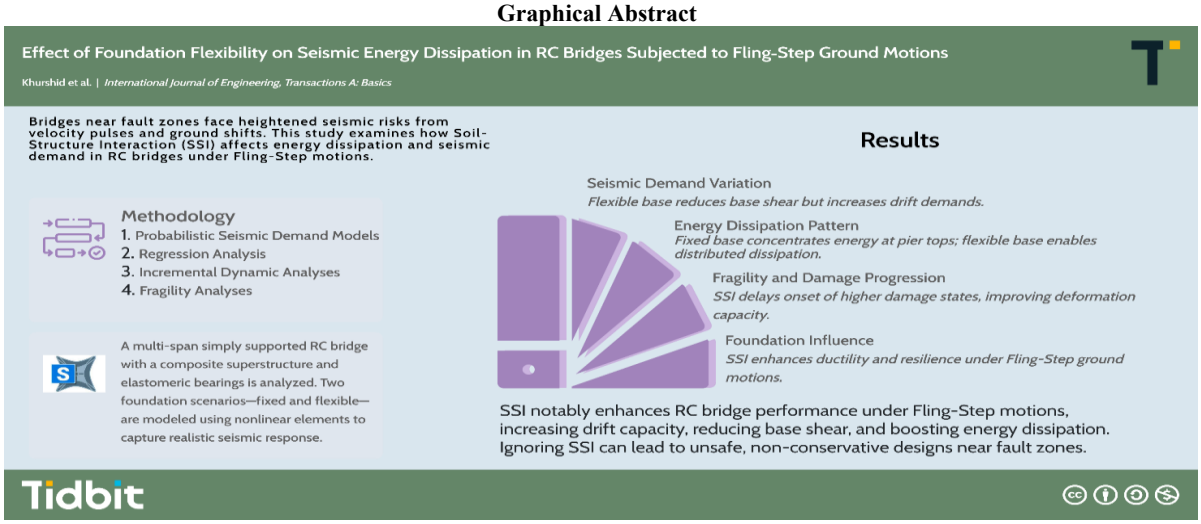

*Corresponding Author Email: *fkhurshid@jmi.ac.in* (F. B. Khurshid)

Please cite this article as: Khurshid FB, Izhar MS, Islam N, Khan NA. Effect of Foundation Flexibility on Seismic Energy Dissipation in RC Bridges Subjected to Fling-step Ground Motions. International Journal of Engineering, Transactions B: Applications. 2026;39(08):1918-32.

NOMENCLATURE

L	Length of column (mm)	K_{eff}	Effective stiffness kN/m
L_P	Length of plastic hinge (mm)	Q	Characteristic strength (kN)
f_{ye}	Expected yield strength of longitudinal bar (N/mm)	f_{yhe}	Yield stress of confining steel (N/mm^2)
d_b	Nominal diameter of longitudinal bar (mm)	f_{ce}	Expected compressive strength of concrete (N/mm^2)
K_1	Elastic stiffnesskN/m	A_g	Gross area of pier cross-section (mm^2)
K_2	Strain hardening stiffness kN/m	ρ_s	Volumetric ratio of confining reinforcement
P	Axial load on pier (kN)	ε_{sy}	Yield strainof main longitudinal bars
ε_{utu}	Ultimate tensile strain of cover concrete	ε_{bb}	Buckling strainof main longitudinal bars
ε_{ucu}	Ultimate compressive strain of unconfined concrete	ε_{ucc}	Ultimate compressive strain of confined concrete
ε_{cover}	Strain in cover concrete	ε_{core}	Strain in core concrete
ε_s	Strain in main longitudinal bars	$a\& b$	Regression coefficients
R^2	Correlation coefficient	N	Total number of Non-Linear Time History Analyses (NLTHA)

1. INTRODUCTION

RC bridges constitute a fundamental component of transportation infrastructure, serving a pivotal role in the conveyance of goods, services and in facilitating emergency responses following seismic events. Their operational continuity during and subsequent to earthquakes is imperative for mitigating economic losses and ensuring life safety. Nonetheless, numerous seismic events globally have consistently underscored the vulnerabilities of these structures, such as excessive displacements, bearing failures, and column collapse (1, 2). This has prompted ongoing research into their seismic behavior, particularly under complex and extreme GM conditions. Recent advancements in seismic instrumentation and GM classification have augmented our understanding of NF earthquakes, which pose a particularly severe threat to bridges in proximity to fault ruptures. NF-GMs often exhibit distinctive characteristics, including directivity pulses, FS effects, and hanging wall amplifications, all of which can significantly escalate structural demands (3, 4).

Among these, FS-GMs, characterized by large, permanent ground displacements, have emerged as a critical concern. These motions generally occur in the direction of fault slip, resulting in asymmetric velocity time histories that often produce large, one-sided pulses capable of causing significant damage (5-8). The 1999 Chi-Chi earthquake in Taiwan was a pivotal event that highlighted the devastating effects of FS and directivity features in NF-GMs, sparking a surge in both analytical and experimental research. Recent studies have focused on understanding how these NF-GM characteristics impact the seismic performance of RC structures. For instance, Zheng et al. (9) demonstrated through dynamic analysis that bridges located in NF zones with FS effects experience amplified drift and residual displacements. Similarly, Hui et al. (10) highlighted the inadequacy of far field GM based designs in capturing the true damage potential posed by pulse-type NF records. Moreover, Bhagat et al. (11) emphasized that the long-period, high-energy nature of these pulses significantly alters structural response spectra and necessitates tailored modeling strategies.

These velocity pulses are generally classified into two types based on orientation: forward-directivity pulses, which occur perpendicular to the fault rupture, and FS pulses, which develop parallel to the fault and often lead to permanent ground displacement aligned with the fault's strike and dip direction (12). A growing body of work has also pointed out to the influence of SSI on the overall seismic response of bridges, particularly those supported on pile foundations. As recent experimental and numerical studies have shown, ignoring SSI can lead to inaccurate estimations of force and displacement demands (13). For instance, Stefanidou et al. (14) demonstrated that SSI tends to increase structural flexibility, which in turn shifts the natural period and modifies seismic force distribution across the superstructure and substructure. In bridge systems, the incorporation of flexibility may reduce base shear demand, albeit often resulting in increased displacement and rotational response (15). Furthermore, SSI significantly influences the redistribution of energy dissipation—a factor frequently overlooked in fixed-base modeling but with critical implications for damage localization and fatigue. Notably, energy dissipation under seismic loading, quantified through cumulative hysteretic energy metrics, has emerged as a reliable indicator of structural performance and damage potential. Recent research by Izhar et al. (16) indicates that energy-based parameters can more effectively capture the nonlinear response of RC piers under high-intensity shaking compared to traditional force-based measures. In flexible-base systems, a portion of the input energy is dissipated within the soil and foundation system, thereby alleviating demands on structural members (*The demand would be reduced instead of being alleviated)*. This energy redistribution mechanism is crucial when comparing fixed and flexible foundation systems subjected to identical input GMs.

As most of the studies on seimc vulnerability assesment of bridges are done by assuming fixed base conditions, it becomes necessary to understand the effect

of soil flexibility on the response of bridges to NF-GMs. Therefore the present study is aimed at evaluating the effect of SSI on vulnerability of RC bridges to NF-GMs specifiacally with FS characteristics. In the study, seismic performance assessment of a four-span simply supported RC bridge subjected to such GMs is carried out using IDA.

2. STRUCTURAL MODELING

To evaluate the effect of soil flexibiltiy on seismic performaance of bridges, two foundation configurations were compared for the same RC bridge: a fixed-base model and a flexible-base model incorporating a pile group with nonlinear SSI effects. IDA using nonlinear time history (NLTH) analysis at different intensity measure (IM) was employed to assess the effect on engineering demand parameters (EDPs) such as pier-top drift, base shear, and cumulative energy dissipation (CED).

IDA and fragility analysis have become standard methodologies for quantifying seismic vulnerability (17, 18). IDA provides a comprehensive understanding of nonlinear performance under escalating seismic intensity, while fragility curves quantify the probability of exceeding various damage states given a set of IMs such as PGA or PGV (19, 20). Recent advancements have further refined these tools by incorporating multi-IMs, performance-based energy metrics, and probabilistic SSI modeling (21-23). The results from IDA were used to plot fragility curve for bridge perfomance assesment in both the cases. The details about modelling and validation of bridge superstructure and foundation is given in the following sections.

2. 1. Bridge Configuration and Geometry

In the present study, a numerical model of a simply supported RC bridge with fixed base was developed in SAP2000 as shown in Figure 1.

The RC bridge employed for the present study comprised of four equal spans, each measuring 27 meters, resulting in a total bridge length of 108 meters with overall width of the superstructure maintained at 7.5 meters. The superstructre was modeled as a spine model using beam elements, incorporating a deck slab with a uniform thickness of 0.225 meters throughout its length. The deck was supported on three longitudinal I-girders, which in turn rested on elastomeric bearings. These bearings were modeled using nonlinear link elements incorporating bilinear hysteresis to replicate their cyclic response. The bilinear behavior was adopted to capture the nonlinear characteristics of the bearings under seismic excitation. Kelley's model was used to simulate this bilinear behavior, as illustrated in Figure 2. The geometric properties of the bridge model are summarized in Table 1.

The substructure consisted of three RC piers, each with a diameter of 1.22 meters and an overall height of 6.191 meters from the base to the top of the pier cap. To capture their flexural behavior under strong ground shaking, the piers were modeled using nonlinear frame elements with distributed plasticity. The complete structural system was modeled to realistically simulate the dynamic response under NF seismic excitations.

2. 2. Superstructure Modeling

The deck and girders were modeled as a composite unit using frame elements designed to accurately represent the stiffness of the girder-deck system. The superstructure was idealized as a spine model, in which beam elements were placed

TABLE 1. Geometric Properties of RC Bridge (24)

Parameter	Value
Number of spans	4
Length of each span	27.00 m
Total bridge length	108.00 m
Bridge width	7.50 m
Deck slab thickness	0.23 m
Number of I-girders	3
Depth of pier cap	0.75 m – 1.45 m
Diameter of each pier	1.20 m

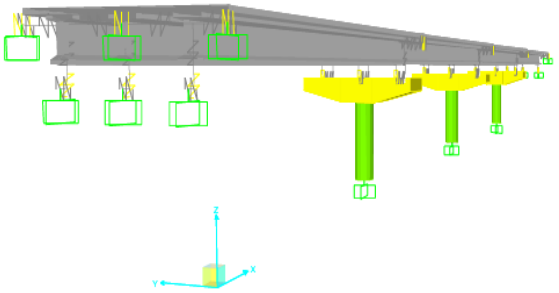

Figure 1. Bridge Model with fixed base

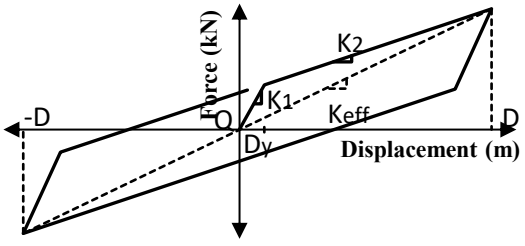

Figure 2. Kelly's bilinear model

along the longitudinal axis of the bridge, aligned with the center of gravity of each cross-section. The cross-sectional properties of all structural elements were designed and assigned in accordance with the provisions of the Indian Roads Congress. The material properties include M40 grade concrete and Fe500 grade steel for reinforcement, which is the same for the substructure also. The modulus of elasticity, Poisson's ratio, and damping values are defined following the guidelines provided in Indian Standards (25) and FEMA (21, 26) to ensure consistency with seismic design standards. To capture energy dissipation under dynamic loading Rayleigh damping was employed. The dampinng was calibrated to provide 5% critical damping in the first two modes of vibration, which is a commonly accepted assumption for RC structures under seismic excitation.

2.3. Pier and Bearing Modeling The piers were modeled using nonlinear beam-column elements with fiber-discretized cross-sections. To simulate the inelastic behavior of the piers under seismic loading, a P-M_2-M_3 fiber hinge was defined at the base of each pier. Its length was determined using the empirical relation provided in Equation 1, which considers the influence of both geometric and material properties (27, 28).

$$L_P = 0.08L + 0.022f_{ye}d_b \geq 0.044f_{ye}d_b \quad (1)$$

The force-displacement behavior of bearings is governed by parameters such as characteristic strength, elastic stiffness, post-yield stiffness (29), and shear force – deformation relationship (30). Bearings were designed to allow translational movement in the longitudinal (traffic) direction while restricting movement in the transverse and vertical directions. The properties of the bearings are listed in Table 2.

2. 4. Foundation and Base Conditions To evaluate the seismic performance of the bridge, two distinct foundation conditions are modeled: fixed base and flexible base. In the fixed base model, the base of each pier was considered to be fully restrained against translational and rotational movement. This conventional modeling approach assumes that the substructure is rigidly connected to the ground, thereby neglecting any effects of soil flexibility. While commonly adopted in preliminary design due to its simplicity, this assumption may lead to inaccurate estimation of seismic demands, especially in soft or layered soil conditions (31). In contrast, the flexible base model incorporates a more realistic representation of foundation behavior by simulating a pile group system. In the present study, each pier was assumed to be supported by a group of four cast-in-place RC piles, each having a diameter of 1 meter and a length of 21 meters. These piles were arranged in a square configuration with a spacing of 3 meters center-to-center in both longitudinal and transverse directions. The piles were embedded in a stratified soil profile to reflect field conditions. A reinforced concrete pile cap with a thickness of 1.5 meters was provided to connect the group of piles and effectively distribute the loads from the pier to the underlying foundation system. The pile cap extended 150 mm beyond the outermost piles in all directions to ensure proper load transfer and confinement. The pile cap was modeled using shell elements, discretized into small mesh elements of 500 mm × 500 mm to capture the local stress distribution and deformation behavior accurately. This shell element was positioned at mid-depth of the pile cap, and to ensure full load transfer between the pier and the pile cap, it was connected using a linear rigid link element. This rigid link was assigned infinite stiffness in all six degrees of freedom (three translational and three rotational), effectively simulating a rigid connection. The length of the rigid link was set to half the thickness of the pile cap, ensuring accurate geometric representation and continuity between the pier and the foundation system. The bridge model with pile group foundation is as shown in Figure 3.

2. 5. Soil-Structure Interaction (SSI) Modeling The interaction between soil and pile within the flexible foundation model was simulated using the Nonlinear-Winkler Foundation (BNWF) approach, as proposed by

TABLE 2. Properties of Elastomeric Bearings (24)

Bearing Property	Value
Plan dimension	500 mm × 500 mm
Height	120 mm
Effective stiffness	2500.00
Elastic stiffness	6250.00
Post-yield stiffness	2083.50
Yield displacement	12 mm
Maximum deformation capacity	120 mm
Characteristic strength	41.67

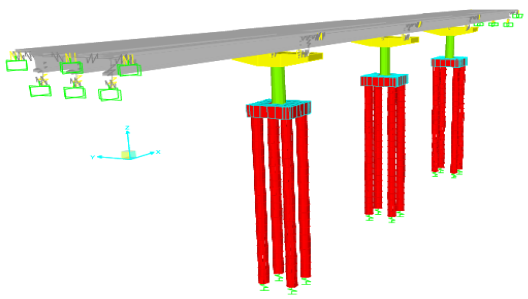

Figure 3. Numerical model of the RC bridge with pile group foundation incorporating SSI

Boulanger et al. (32). Each pile is represented by displacement-based beam elements, while the surrounding soil is modeled with nonlinear springs that simulate soil resistance along the pile shaft and tip. These springs are implemented as multi-linear plastic link elements, capturing the nonlinear behavior and varying stiffness of the soil–pile interface under seismic loading. To model lateral soil resistance against pile movement, p–y springs are assigned along the pile length, characterizing the depth-dependent nonlinear response. For modeling frictional resistance along the pile shaft (skin friction), t–z springs are employed. Q–z springs at the pile tip simulate end-bearing resistance. These spring elements utilize Gap (compression-only) zero-length element, allowing relative displacement between the pile and soil. Each pile is discretized into 1 meter segments and nodes are assigned. At each node, a double-noded Gap element connects to a fixed node representing stationary soil and a pile-attached node responding to structural deformation. The free head length extends above ground level at half the pile cap thickness to reflect boundary conditions. Tip resistance is accounted by a q–z spring at the bottom node, representing vertical resistance against pile tip movement. Spring parameters (p–y, t–z, and q–z) were determined using API (2000) guidelines empirical formulations (33). As relevant geotechnical properties of the site are required for soil modelling, the study adopts soil properties from Ajom and Bhattacharjee (34), who investigated a representative site in Assam, India, within Seismic Zone V—the highest seismic risk zone in India's seismic map and the primary focus area of this study. The soil profile comprises medium and loose sand layers, with properties used to compute spring parameters at different depths. The soil properties and calculated spring parameters are presented in Tables 3 and 4.

TABLE 3. Representative Borehole Logs and soil properties (34)

Depth (m)	Soil type	Frictional Angle	Saturated unit weight (kg/m^3)	Coefficient of lateral earth pressure (K)
1	Medium Sand	33.50	1640	0.45
2	Medium Sand	32.00	1500	0.47
3	Medium Sand	35.00	1810	0.43
4	Loose Sand	31.00	1440	0.48
5	Medium Sand	33.50	1640	0.45
6	Medium Sand	33.50	1570	0.45
7	Medium Sand	33.50	1590	0.45
8	Medium Sand	33.50	1620	0.45
9	Loose Sand	31.00	1460	0.48
10	Medium Sand	32.00	1460	0.47
11	Medium Sand	32.00	1610	0.47
12	Medium Sand	32.00	1520	0.47
13	Medium Sand	32.00	1550	0.47
14	Medium Sand	32.00	1600	0.47
15	Medium Sand	33.50	1580	0.45
16	Medium Sand	33.50	1600	0.45
17	Loose Sand	31.00	1560	0.48
18	Medium Sand	32.00	1520	0.47
19	Medium Sand	32.00	1600	0.47
20	Medium Sand	35.00	1910	0.43
21	Medium Sand	35.00	1890	0.43

3. MATERIAL NONLINEARITY AND LIMIT STATE DEFINITION

In this study, a comprehensive fiber-based modeling approach was employed to simulate the nonlinear behavior of RC bridge piers subjected to seismic loading.

TABLE 4. Representative Strength and Stiffness Properties for Soil Spring Modeling

Depth (m)	Pu (kN)	y50 (m)	tu (kN)	z50 (m)	Qu (kN)	z50 (m)
1	91.66	0.0039	23.52	0.0008		
2	214.77	0.0065	39.37	0.0019		
3	665.63	0.0077	79.54	0.0022		
4	621.72	0.0122	72.93	0.0045		
5	1262.94	0.0109	112.65	0.0038		
6	1681.87	0.0121	129.41	0.0044		
7	2260.14	0.0139	152.90	0.0052		
8	2949.59	0.0159	189.91	0.0064		
9	2739.20	0.0238	173.72	0.0107		
10	3566.33	0.0215	209.48	0.0099	-	-
11	4708.22	0.0258	254.10	0.0120		
12	5242.78	0.0263	261.71	0.0124		
13	6226.65	0.0288	289.11	0.0137		
14	7405.37	0.0319	307.72	0.0145		
15	9462.63	0.0272	325.58	0.0110		
16	10849.08	0.0292	375.12	0.0127		
17	8325.16	0.0383	350.61	0.0215		
18	9662.46	0.0323	392.56	0.0185		
19	10736.06	0.0340	399.06	0.0188		
20	20236.07	0.0349	501.44	0.0136		
21	21025.38	0.0346	-	-	2752	0.013

The circular cross-section of each pier was discretized into multiple fiber cells, categorized into three distinct material zones: confined concrete (typically within the core of the section enclosed by transverse reinforcement), unconfined concrete (primarily at the cover region), and longitudinal steel reinforcement.

Each fiber cell was assigned an appropriate nonlinear stress-strain relationship according to its material type to accurately capture its mechanical response under cyclic loading. The concrete was modeled using distinct strain thresholds for confined and unconfined zones to represent their differing ductility capacities. For concrete, three critical strain values were employed as damage indicators: two were associated with unconfined concrete and one with confined concrete, as presented in Table 5.

These thresholds help to identify the extent of damage and loss of load-carrying capacity during seismic excitation. Steel reinforcement was modeled using a nonlinear constitutive model that accounts for both yielding and post-yield degradation, including potential buckling of the longitudinal bars. Two strain limits ε_{sy} and ε_{bb} were considered for the steel fibers. The ε_{bb} was computed based on established empirical formulations (35) and is expressed by Equation 2.

$$\varepsilon_{bb} = 0.03 + 700\rho_s \frac{f_{yhe}}{E_s} - 0.1\frac{P}{f_{ce}A_g} \quad (2)$$

The materials used in the model correspond to M40 grade concrete and Fe500 grade reinforcing steel. The reinforcement detailing includes 30 longitudinal bars, each with a nominal diameterof 32 mm.

The NLTH analysis was conducted using the Takeda hysteresis model, which incorporates strength and stiffness degradation rules to replicate the cyclic behavior of RC under earthquake loading. The Takeda model is widely used for these structures due to its ability to simulate pinching effects, stiffness degradation during unloading, and residual deformations—all of which are critical in fiber-based analyses. This model has proven particularly effective in representing the cyclic response of RC components with inadequate detailing.

TABLE 5. Damage states [16]

Damage States	Strain limits	Description
Slight	$\varepsilon_{utu} \le \varepsilon_{cover} < \varepsilon_{ucu}$ and $\varepsilon_{sy} \le \varepsilon_s < \varepsilon_{bb}$	Cracking of cover concrete and yielding of main longitudinal bars
Moderate	$\varepsilon_{cover} > \varepsilon_{ucu}$ and $\varepsilon_{sy} \le \varepsilon_s < \varepsilon_{bb}$	Spalling of unconfined/cover concrete
Extensive	$\varepsilon_s \ge \varepsilon_{bb}$ and $\varepsilon_{core} < \varepsilon_{ucc}$	Buckling of main longitudinal bars
Collapse	$\varepsilon_{core} \ge \varepsilon_{ucc}$	Crushing of confined/core concrete

4. MODEL VALIDATION

4. 1. Validation of Fixed-Base Bridge Model To establish the reliability of the fixed-base bridge model, a detailed validation was conducted against the experimental results reported by Kunnath et al. (36), who tested large-scale circular RC bridge columns under controlled lateral loading. Three specimens—A1, A2, and A3—with varying loading histories (monotonic, standard cyclic, and constant amplitude cyclic, respectively) were selected for comparison. Details of prototype-to-model scaling, reinforcement layout, axial load, and material properties are summarized in Table 6. The validation primarily focused on comparing the progression of material-level damage states predicted analytically with those observed experimentally. The damage states were tracked using material strain limits as presented in Table 5.

Specimen A1 was tested under monotonic lateral loading up to failure. The analytical simulation captured initial cracking at 0.43% drift, and reinforcement yielding at 1.14% drift, which closely matched the experimental observations of 0.2–0.4% and 1.4%, respectively. Spalling of cover concrete was identified analytically at 1.9% drift, compared to 2.4% in the experiment. Buckling of longitudinal bars and ultimate failure occurred at 4.1% and 6.5% drift in the model, respectively, as against 3.5% and 11% in the test. These results, summarized in Table 7, confirm that the model adequately captures damage progression under monotonic loading.

For Specimen A2, which was subjected to progressively increasing amplitude cycles (1–6% drift), the model showed good agreement with the test results at all key damage stages. Initial cracking and yielding

TABLE 6. Summary of Prototype and Model Parameters (36)

Parameter	Prototype	Model	Remarks
Column Diameter (m)	1.22	0.30	Scale 1:4
Column Length (m)	5.50	1.375	Scale 1:4
Longitudinal Reinforcement	24-#11 (36 mm)	21-#3 (9.5 mm)	ρ ≈ 2%
Spiral Reinforcement	#5 (16 mm)	4 mm wire	
Spiral Pitch (mm)	76	19	
Spiral Yield Strength (MPa)	414	380–450	
Axial Load (kN)	3225	806	≈0.1 f·A_g
Lateral Capacity (kN)	1550	388	
Concrete Strength (MPa)	29	Same	
Steel Yield Strength (MPa)	448	Same	

TABLE 7. Comparison of Analytical and Experimental Results: Specimen A1

Drift Ratio (%)	Experimental Observation	Drift & Analytical Observation	Damage Level
1.4	Cracking, Yielding	1.14% – Cracking, Yielding	Slight
2.4	Spalling of Cover Concrete	1.9% – Spalling Initiated	Moderate
4.4	Spalling & Bar Buckling	4.1% – Bar Buckling	Extensive
11	Collapse	6.5% – Core Crushing	Collapse

occurred during the first cycle, spalling at cycle 15 (3% drift), and bar buckling at cycle 22 (5% drift), followed by failure at cycle 30 (6% drift). The fiber-based simulation reproduced these transitions well, as summarized in Table 8.

Specimen A3 was subjected to 2% drift amplitude for up to 150 cycles. The model recorded early-stage cracking and yielding in the first cycle, spalling at cycle 100, and no further material deterioration up to cycle 150—matching experimental trends. A final monotonic load induced collapse beyond cycle 150, as indicated in Table 9. The shear force–displacement curves for all specimens compared favorably with the experimental data and are illustrated in Figure 4.

Across all three specimens, the numerical model consistently matched experimental observations in terms

TABLE 8. Damage Progression under Cyclic Loading: Specimen A2

Cycle	Drift (%)	Experimental Observation	Analytical Observation	Damage Level
1	1.0	Cracking, Yielding	Crack/Yield Initiated	Slight
15	3.0	Spalling of Cover Concrete	Spalling Confirmed	Moderate
22	5.0	Bar Buckling	Buckling Observed	Extensive
30	6.0	Failure Initiated	Core Crushing	Collapse

TABLE 9. Damage States under Constant Amplitude Cycles: Specimen A3

Cycle	Experimental Observation	Analytical Observation	Damage Level
1	Cracking, Yielding	Crack/Yield Detected	Slight
100	Spalling of Concrete Cover	Spalling Confirmed	Moderate
150+	Collapse under Monotonic Load	No Significant Change until Collapse	Collapse

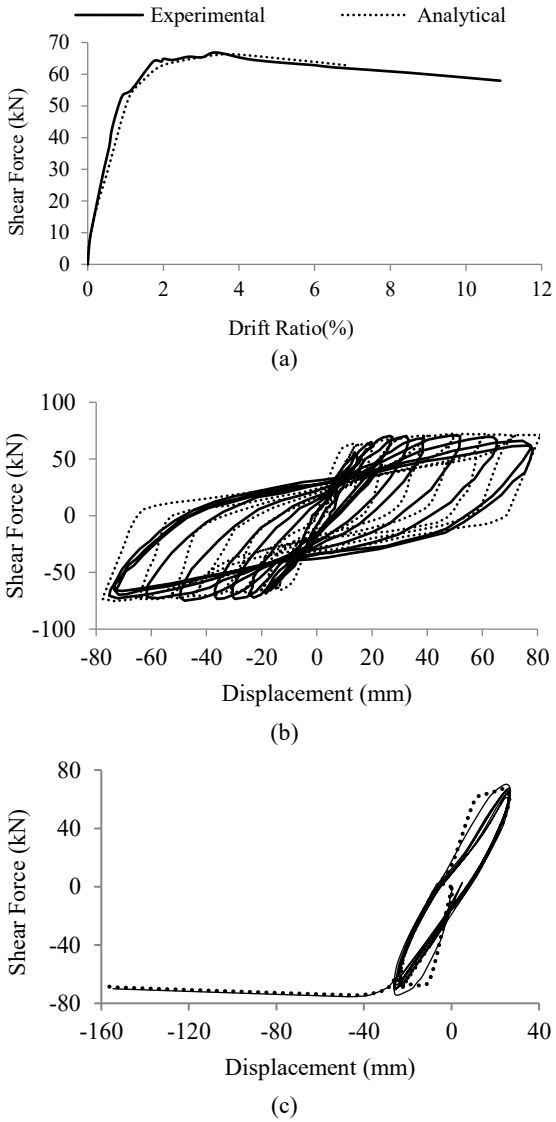

Figure 4. Shear Force vs. Drift Response for Specimens A1–A3 (a) A1: Monotonic Loading; (b) A2: Cyclic Loading; (c) A3: Constant Amplitude Cycles

of critical damage thresholds, load–deformation response, and hysteretic behavior. The good agreement validates the accuracy of the fixed-base modeling framework and supports its extension to model incorporating SSI in the next stage of validation.

4. 2. Validation of SSI Modeling Approach

Following the validation of the fixed-base model, the flexible-base configuration—incorporating SSI via a pile group foundation—was validated using published numerical results from Mallick and Raychowdhury (37). They conducted their study on a cable-stayed bridge using a pushover analysis to evaluate lateral response under both fixed and pile-supported foundations incorporating SSI. Between the two models, they

observed a drop in peak base shear for the pile group foundation from 8.2 MN to 6.7 MN, corresponding to an 18% reduction, attributed to the reduced lateral stiffness induced by soil flexibility. To validate the SSI implementation in the present study, a similar modeling approach was adopted, where the soil–pile system was represented using a nonlinear Beam-on-Winkler Foundation model. The bridge was analyzed under pushover loading for both fixed and flexible foundation scenarios.

Figure 5 presents a comparative evaluation of the pushover response of bridge models with and without SSI. The figure highlights how foundation flexibility affects base shear capacity and lateral stiffness when subjected to increasing lateral displacement. Figure 5(a) displays the pushover response reported by Mallick and Raychowdhury (37) for a cable-stayed bridge model. The graph compares the performance of a fixed-base configuration against a pile-supported flexible base system incorporating SSI. A noticeable reduction in base shear capacity is observed for the flexible-base model, illustrating the influence of soil flexibility on seismic response. Figure 5(b) shows the corresponding results from the present study, comparing the fixed-base and SSI-integrated flexible-base bridge models. Similar to the trends in Figure 5(a), the flexible-base model exhibits a reduction in peak base shear, affirming that the incorporation of SSI leads to decreased lateral stiffness and alters the overall seismic demand on the structure. A reduction in peak base shear from 4900 kN to 4300 kN was observed upon introducing SSI, reflecting a 12.25% decrease. Although this reduction is slightly lower than that reported in the study by Mallick and Raychowdhury (37), the overall behavioral trend remains consistent—that is, the introduction of SSI reduces lateral stiffness and base shear capacity.

The differences in absolute values can be attributed to variations in bridge geometry, material strengths, and soil profiles between the two studies. However, the close agreement in trend, and the ability of the current model to replicate the fundamental influence of SSI on structural response, reinforce the credibility of the adopted modeling approach. The validated SSI model was then used for further dynamic and damage assessments under the considered GMs in this study.

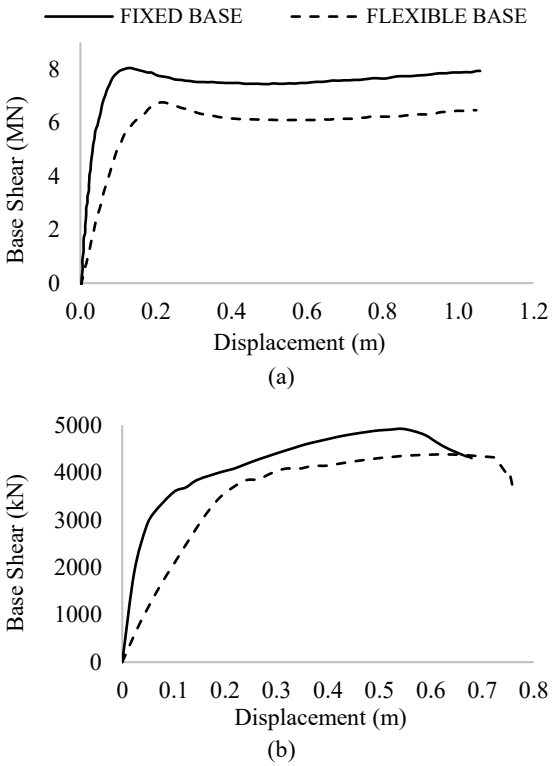

Figure 5. Pushover response comparison between fixed and flexible base bridge models: (a) Mallick and Raychowdhury [39]; (b) Present study

TABLE 10. NF-GMs with FS (38)

GMs	Mw	PGD (cm)	R_{jb} (km)	PGA (g)
Chi-Chi_TCU102	7.6	155.80	1.49	0.30
Chi-Chi_TCU067	7.6	181.10	1.10	0.48
Chi-Chi_TCU071	7.6	244.06	0.00	0.63
Chi-Chi_TCU072	7.6	209.50	7.90	0.46
Chi-Chi_TCU074	7.6	193.10	13.80	0.59
Chi-Chi_TCU074	7.6	166.11	0.00	0.57
Chi-Chi_TCU075	7.6	164.30	3.40	0.32
Chi-Chi_TCU076	7.6	101.66	2.74	0.33
Chi-Chi_TCU082	7.6	142.70	7.60	0.22
Kocaeli_Yarimca-EW	7.5	184.85	1.38	0.24

5. SELECTION OF GROUND MOTIONS

To conduct IDA, ten NF-GMs exhibiting distinct FS characteristics were selected. These records, enumerated in Table 10, were meticulously curated to encapsulate the unique features of FS type GMs.

They are distinguished by large, unidirectional velocity pulses in the fault-parallel (slip-parallel) direction, typically characterized by a half-cycle, high-amplitude velocity pulse followed by a significant static offset in the displacement time history. These permanent ground displacements arise from abrupt tectonic movements during fault rupture. However, when displacement time histories are derived through double integration of recorded accelerations, minor errors in the raw data can lead to substantial distortions (39). To address this issue, processed and filtered records from Bhandari's database were utilized, ensuring the

reliability of the displacement data and preserving the true tectonic deformation characteristics (38). The selected FS-GMs were based on the criteria: Peak Ground Displacement (PGD): 100–250 cm, Magnitude (M_w): 7.0–7.6, Joyner–Boore Distance (R_{jb}): Less than 15 km. Given that the frequency content of GMs significantly influences structural damage, Fast Fourier Transform (FFT) analysis was performed to assess the spectral characteristics of the selected records [12]. Figure 6 illustrates the typical FS behavior through the velocity and displacement time histories of the Chi-Chi_TCU102 record, a representative FS event.

To reduce variability in seismic records caused by differences in source distance, event magnitude, site conditions, and rupture mechanisms, the selected GMs were normalized based on their peak spectral velocity, following the approach introduced by Miano et al. (40). The normalization factor was computed as the ratio of the maximum velocity of each record to the median peak spectral velocity across all records. Given that Seismic Zone V represents the most earthquake-prone region in India, characterized by the highest hazard potential (25), it necessitates stringent design measures to ensure structural resilience. To align with these demands, each GM was scaled using a scale factor that adjusts its response spectrum to match the IS 1893 (Zone V) 5% damped design spectrum, with minimal deviation in the period range of 0.2T to 1.5T seconds. This method ensures consistent scaling across varying intensity levels (25, 41). The entire suite of normalized ground motions was then scaled to capture a range of structural damage states in the bridge models (12, 42). Figure 7 illustrates the 5% damped pseudo-acceleration response spectra of the selected set of GMs, each scaled to a PGA of 0.36g. The plotted spectra represent various earthquake ensembles used in this study and demonstrate the uniformity achieved through the scaling and normalization procedure.

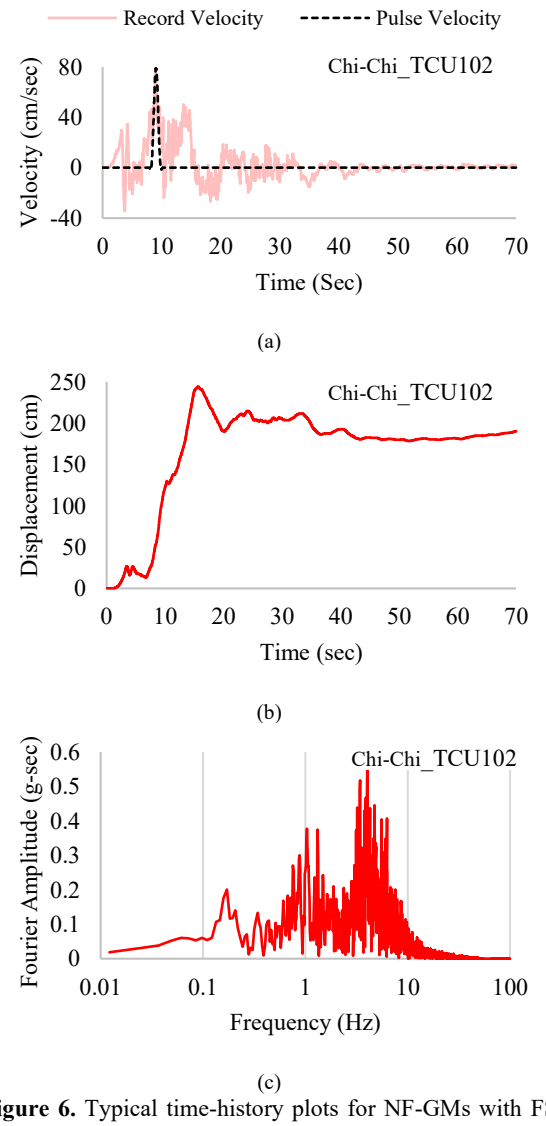

Figure 6. Typical time-history plots for NF-GMs with FS (a) Velocity (b) Displacement (c) FFT

6. SUITABLE INTENSITY MEASURE

Selecting appropriate IMs for input GMs is essential for accurately assessing seismic vulnerability. An optimal

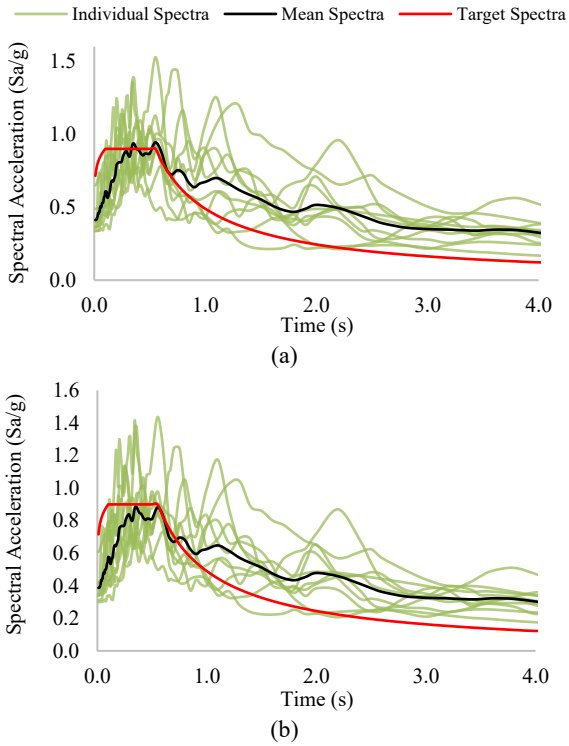

Figure 6. Response spectra of recordings scaled to PGA of 0.36g a) for fixed base model; b) for flexible base model

IM is defined by its efficiency, practicality, proficiency, and computability (43). It has been proposed that the severity of GMs is most effectively captured by the PGA as the optimal IM (43). Furthermore, for NF (pulse-like) GMs, PGV is considered a more suitable optimal IM (44). Several studies have also suggested that both PGA and PGV are the most effective IMs for evaluating the seismic vulnerability of structures (7, 24, 45, 46). In this study, both PGA and PGV were employed as IMs for seismic vulnerability assessment. To assess the efficiency, practicality, and proficiency of PGA and PGV as IMs under NF-GMs with FS, a regression analysis was conducted using a power law function, which provides a logarithmic correlation between the EDPs and IMs (43, 45) as shown in Equation 3.

$$EDP = a(IM)^b \; or \; ln(EDP) = b\, ln(IM) + ln\,(a) \quad (3)$$

The data utilized in the regression analysis were obtained through IDA under the considered NF-GMs with FS. The dispersion of demand is calculated using the conditional standard deviation of regression, as indicated in Equation 4.

$$\beta_{EDP|IM} = \sqrt{\frac{\sum(\ln(EDP)-\ln(aIM^b))^2}{N-2}} \quad (4)$$

A lower dispersion value ($\beta_{EDP|IM}$) indicates a more efficient IM. Additionally, practicality is evaluated by the regression coefficient "b." A higher "b" value suggests a more practical IM (43). A composite measure of efficiency and practicality is expressed in terms of proficiency (ζ) for selecting the optimal IM, as defined in Equation 5 (24, 43, 45).

$$\zeta = \beta_{EDP|IM}/b \quad (5)$$

Comparisons of IMs (PGA and PGV) for EDPs (drift, base shear, and CED), based on regression analysis, under these GMs are presented in Table 11.

The regression analysis evaluating PGA and PGV as IMs for predicting EDPs— drift, base shear, and CED— under both fixed and flexible base with SSI conditions indicates that PGA consistently exhibits superior efficiency, proficiency, and correlation, thereby establishing it as a more optimal IM overall. Although PGV has been proposed as a suitable IM for NF-GMs, particularly due to its sensitivity to velocity pulses, the findings of this study demonstrate that PGA remains more reliable across all EDPs and foundation conditions. Notably, the regression parameters (a, b, β, ζ) are remarkably similar for both fixed and flexible base conditions, which may initially appear counterintuitive given the anticipated influence of SSI. However, this similarity can be attributed to the relatively moderate soil flexibility or damping characteristics assumed in the analysis, which limits the extent to which SSI alters the overall system response. When soil conditions are not excessively soft, the structural response tends to dominate, and high-frequency IMs like PGA continue to effectively capture the peak response. This observation is corroborated by previous studies who noted that traditional IMs such as PGA remain effective even in the presence of SSI when soil nonlinearity is limited (47). Another study emphasized that SSI effects become pronounced only under highly flexible soil conditions (48). Thus, the similarity in regression outcomes between fixed and flexible bases is consistent with existing literature and reinforces the robustness of PGA as a practical and efficient IM under the GM scenarios considered in this study

TABLE 11. Regression comparison of PGA and PGV for different EDPs

Foundation	**Fixed Base**		**Flexible Base with SSI**	
IMs	**PGA**	**PGV**	**PGA**	**PGV**
EDP	**Drift**			
a	4.10	0.02	5.39	0.02
b	**1.13**	1.03	**1.13**	1.08
$\beta_{EDP\|IM}$	**0.40**	0.80	**0.41**	0.49
ζ	**0.36**	0.66	**0.36**	0.45
R^2	**0.89**	0.68	**0.89**	0.83
EDP	**Base Shear**			
a	7465.14	368.71	6630.93	312.16
b	**0.62**	0.56	**0.62**	0.58
$\beta_{EDP\|IM}$	**0.20**	0.36	**0.20**	0.28
ζ	**0.32**	0.65	**0.32**	0.49
R^2	**0.91**	0.69	**0.91**	0.81
EDP	**CED**			
a	15469.10	7.27	11989.66	6.60
b	**1.54**	1.45	**1.55**	1.41
$\beta_{EDP\|IM}$	**0.41**	0.67	**0.43**	0.73
ζ	**0.27**	0.46	**0.28**	0.52
R^2	**0.93**	0.82	**0.93**	0.79

7. RESULTS AND DISCUSSION

IDA was conducted using drift ratio, base shear, and CED as EDPs, while PGA was used as the IM. The analyses were performed for two structural configurations: a fixed-base model and a flexible-base model incorporating SSI.

Figure 7 illustrates the IDA results for both configurations under the set of NF-GMs with FS. Among these ten GMs, CHI-CHI_TCU102 earthquake, was selected as a representative record due to its ability to

induce early collapse in the bridge. The thresholds for each damage state against drift, base shear, and CED, are presented in Table 12.

The fixed-base model began exhibiting slight damage at a PGA of 0.2g, corresponding to initial concrete cracking and steel yielding. This stage was marked by a drift ratio of 1.08%, base shear of 4125 kN, and CED of 1678.2 kN-m. As PGA increased to 0.3g, moderate damage ensued with spalling of cover concrete, an increase in drift to 2.19%, base shear to 5083 kN, and CED to 3439.7 kN-m. At 0.5g, both extensive and collapse states were triggered due to the buckling of longitudinal reinforcement and crushing of core concrete. The system reached a drift of 5.44%, base shear of 7463 kN, and CED of 8267.3 kN-m. Across all motions, the average collapse thresholds were a drift of 6.10%, base shear of 8478.4 kN, and CED up to 21555.4 kN-m, indicating a brittle and localized failure mechanism with rapid energy accumulation in critical regions. The flexible-base model, on the other hand, demonstrated a more ductile response profile due to the incorporation of SSI. At PGA 0.2g, slight damage was again observed, but with an increased drift ratio of 1.41%, lower base shear of 3398 kN, and reduced CED of 1041.4 kN-m.

This illustrates the effect of SSI in softening the seismic response and dissipating energy through the foundation medium. Moderate damage emerged later, at 0.4g, with drift increasing to 3.71%, base shear to 4875 kN, and CED to 3463.8 kN-m. Damage progression was more gradual than in the fixed-base case, with distinct

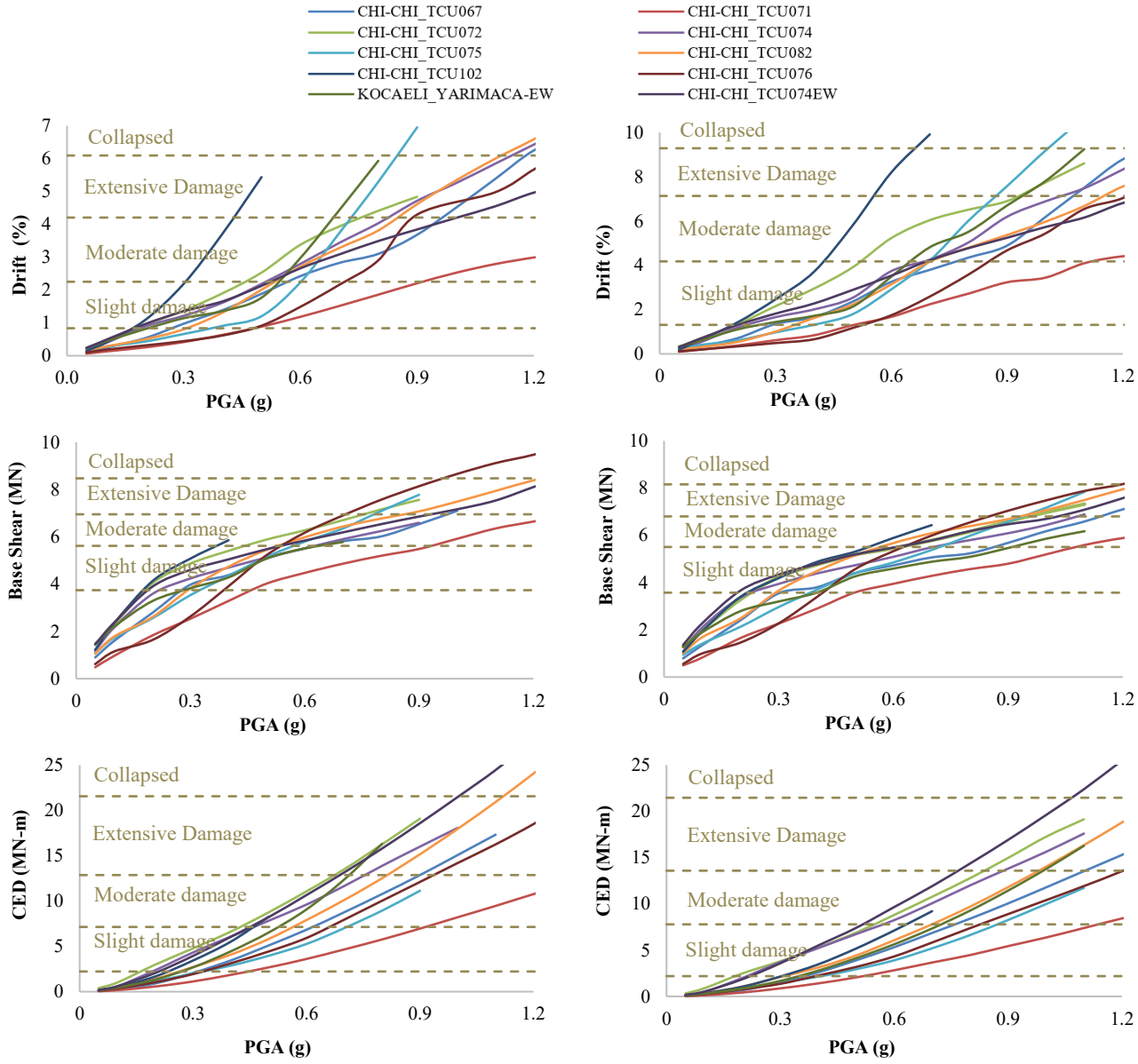

Figure 7. IDA curves for PGA versus EDPs: Fixed-base model (left) and Flexible base with SSI (right)

TABLE 12. Thresholds for each damage states against EDPs

Base Condition	Damage State	Drift (%)	Base Shear (kN)	CED (kN-m)
Fixed Base	Slight	0.84 – 2.25	3746.1 – 5621.0	2222.7 – 7138.4
	Moderate	2.25 – 4.21	5621.0 – 6959.7	7138.4 – 12862.6
	Extensive	4.21 – 6.10	6956.7 – 8478.4	12862.6 – 21555.4
	Collapse	6.10 & above	8478.4 & above	21555.4 & above
Flexible Base with SSI	Slight	1.31 – 4.18	3572.2 – 5507.8	2189.6 – 7784.1
	Moderate	4.18 – 7.13	5507.8 – 6801.9	7784.1 – 13580.7
	Extensive	7.13 – 9.29	6801.9 – 8160.2	13580.7 – 21464.8
	Collapse	9.29 & above	8160.2 & above	21464.8 & above

transitions observed. Extensive damage occurred at 0.6g (drift 8.19%, base shear 5891 kN, CED 7117.1 kN-m), and collapse followed at 0.7g with a peak drift of 9.92%, base shear of 6432 kN, and CED of 9205.2 kN-m. This highlights the influence of foundation flexibility in distributing strain energy, delaying localization of damage, and enabling higher deformation capacities before collapse.

The fragility curves presented in Figure 8 further quantify the probability of exceeding each damage state. For the IM PGA, the fixed-base configuration showed median capacities of 0.25g, 0.55g, 0.80g, and 1.05g for the slight, moderate, extensive, and collapse states, respectively. In contrast, the flexible-base system demonstrated improved seismic resistance, with respective thresholds of 0.30g, 0.70g, 1.00g, and 1.20g. These results confirm that SSI improves the bridge's capacity to withstand seismic demands by extending the fundamental period and introducing beneficial damping effects. A similar trend is reflected in drift-based fragility metrics. The fixed-base model exhibited median drift capacities of 0.85%, 2.18%, 3.99%, and 5.69%, while the flexible-base model reached higher deformation limits of 1.32%, 4.00%, 7.21%, and 9.40% across the same damage states. This again reinforces the understanding that SSI allows greater lateral displacement before critical damage mechanisms are triggered.

In terms of base shear, the fixed-base system showed increasing demands from 3857.0 kN to 7876.5 kN across the four damage levels. The flexible-base model, however, recorded slightly reduced values from 3490.5 kN to 7676.0 kN. This marginal decrease is indicative of force redistribution into the soil medium, where part of

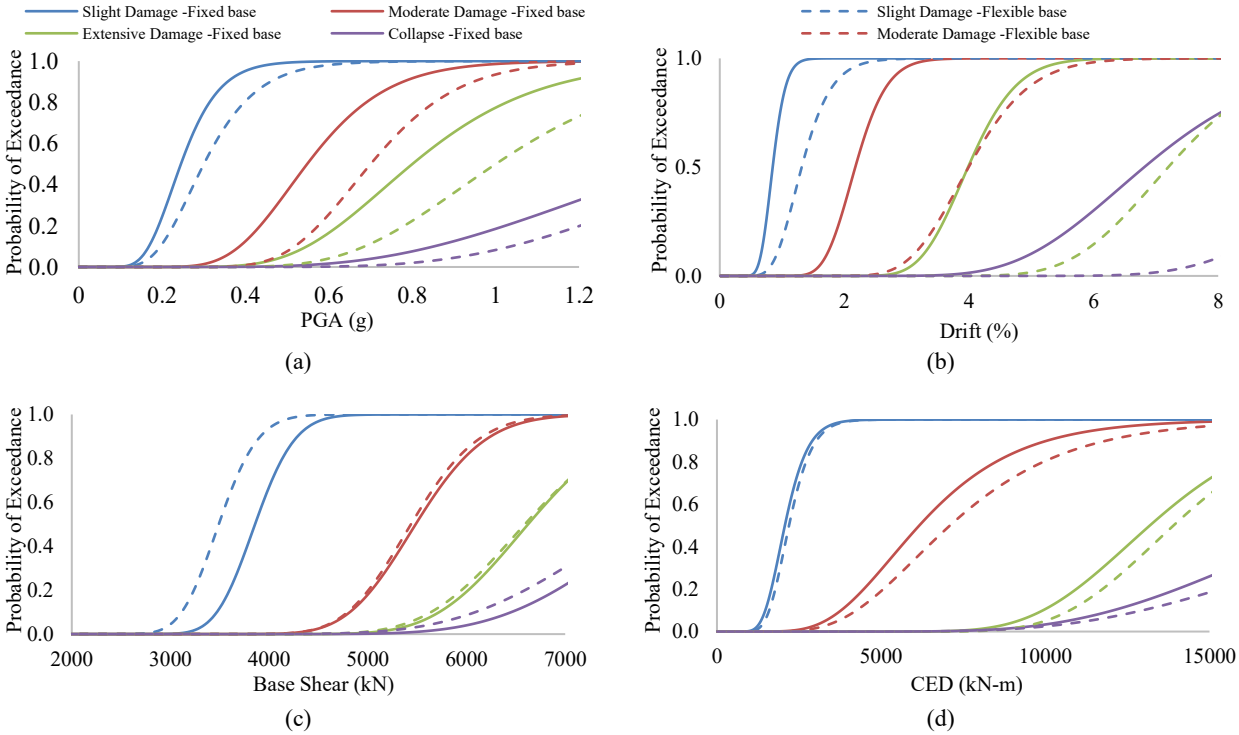

Figure 8. Fragility curves for a) PGA; b) Drift; c) Base Shear; and d) CED

the seismic energy is absorbed and diffused through foundation compliance. Finally, the CED values offer an energy-based perspective of the bridge's inelastic performance. The fixed-base model displayed increasing energy demands from 2067.5 kN-m to 18674.0 kN-m, while the flexible-base counterpart ranged slightly higher, from 2113.5 kN-m to 19088.0 kN-m. This suggests that the flexible-base system, although subjected to higher drift demands, distributes and absorbs energy more gradually, supporting an improved ductile behavior and longer endurance under cyclic loads.

The comparative analysis between fixed-base and flexible-base RC bridge models under NF-GMs with FS effects reveals critical insights into how SSI alters structural performance. While both configurations reach similar damage mechanisms, the flexible-base model demonstrates delayed onset of severe damage, higher deformation capacity, and a more distributed energy dissipation process. This behavior is reflected across all evaluated EDPs—drift, base shear, and CED—as well as in the fragility curves derived from PGA. SSI effectively moderates peak force responses and enhances structural resilience, providing a significant benefit in seismic zones where ground shaking intensity is amplified by NF effects.

8. CONCLUSIONS

This study offers a thorough seismic performance evaluation of a multi-span RC bridge exposed to NF-GMs with FS effects. Two foundation conditions were assessed: a fixed-base model and a flexible-base model incorporating SSI. IDA and fragility analysis were performed using drift ratio, base shear, and CED as EDPs, with PGA and PGV evaluated as potential IMs. The study's key findings are as follows:

1. PGA outperformed PGV as an IM, showing stronger correlation, lower dispersion, and higher regression slopes across all EDPs, confirming its robustness even under NF-GMs with FS and medium soil conditions.
2. Base shear emerged as a highly consistent and responsive EDP, often surpassing drift in reliability, highlighting the potential of incorporating force-based metrics in seismic fragility analysis, particularly for NF-GMs.
3. The fixed-base model began showing slight damage at PGA ≈ 0.2g, with collapse occurring at an average PGA of 1.05g, corresponding to a drift of 6.10%, base shear of 8478.4 kN, and CED of 21,555.4 kN-m.
4. The flexible-base model demonstrated enhanced performance: Collapse was delayed to PGA ≈ 1.20g, Drift capacity increased by 20–35% across damage states, Base shear demand decreased by 5–10%, CED increased by 15–25% confirming the ductility-enhancing and force-moderating effects of SSI.
5. Fragility analysis revealed that the flexible-base model had 10–20% higher median capacity thresholds across all IM–EDP combinations, validating SSI's contribution to increasing seismic tolerance through period elongation and added damping.
6. The inclusion of CED provided a cumulative energy-based perspective of damage, capturing distinctions in failure modes not reflected through drift or base shear alone. The flexible-base model exhibited more gradual energy dissipation, delaying collapse and improving endurance under cyclic loads.

Ignoring SSI and fault-specific GM characteristics, such as FS effects, may result in unsafe or overly optimistic bridge designs. The results advocate for the integration of SSI in seismic performance evaluation and emphasize the need for using multiple EDPs for a comprehensive understanding of bridge vulnerability. These insights contribute to performance-based earthquake engineering and can inform code development, retrofit decisions, and infrastructure policy—especially in high-risk seismic zones like Zone V of India.

9. REFRENCES

1. Han Q, Du X, Liu J, Li Z, Li L, Zhao J. Seismic damage of highway bridges during the 2008 Wenchuan earthquake. Earthquake Engineering and Engineering Vibration. 2009;8(2):263-73. https://doi.org/10.1007/s11803-009-8162-0
2. Carbonari S, Dezi F, Leoni G. Seismic soil–structure interaction in multi-span bridges: application to a railway bridge. Earthquake engineering & structural dynamics. 2011;40(11):1219-39. https://doi.org/10.1002/eqe.1085
3. Alavi B, Krawinkler H. Behavior of moment-resisting frame structures subjected to near-fault ground motions. Earthquake engineering & structural dynamics. 2004;33(6):687-706. https://doi.org/10.1002/eqe.369
4. Chiou B-J, Youngs RR. An NGA model for the average horizontal component of peak ground motion and response spectra. Earthquake spectra. 2008;24(1):173-215. https://doi.org/10.1193/1.2894832
5. Mavroeidis GP, Papageorgiou AS. A mathematical representation of near-fault ground motions. Bulletin of the seismological society of America. 2003;93(3):1099-131. https://doi.org/10.1785/0120020100
6. Somerville PG. Magnitude scaling of the near fault rupture directivity pulse. Physics of the earth and planetary interiors. 2003;137(1-4):201-12. https://doi.org/10.1016/S0031-9201(03)00015-3
7. Baker JW. Quantitative classification of near-fault ground motions using wavelet analysis. Bulletin of the seismological

society of America. 2007;97(5):1486-501. https://doi.org/10.1785/0120060255

8. Kamai R, Abrahamson NA, Silva WJ. Nonlinear horizontal site amplification for constraining the NGA-West2 GMPEs. Earthquake Spectra. 2014;30(3):1223-40. https://doi.org/10.1193/070113EQS187M
9. Zheng Y, Wang J, Xu W, Li N, Zhang W, Chen Y. Impact of Near-Fault Ground Motions on Longitudinal Seismic Response of CHRF Bridges. Sustainability. 2022;14(6):3591. https://doi.org/10.3390/su14063591
10. Hui Y, Fan L, Lv J, Li J, Jia H, editors. Influence of velocity pulse directivity on seismic response of cross-fault bridges. Structures; 2024: Elsevier.
11. Bhagat S, Wijeyewickrema AC, Subedi N. Influence of near-fault ground motions with fling-step and forward-directivity characteristics on seismic response of base-isolated buildings. Journal of Earthquake Engineering. 2021;25(3):455-74. https://doi.org/10.1080/13632469.2018.1520759
12. Baig MA, Ansari MI, Islam N, Umair M. Probabilistic damage evaluation of isolated steel box-girder bridge excited by near-field earthquakes. Soil Dynamics and Earthquake Engineering. 2024;184:108869. https://doi.org/10.1016/j.soildyn.2024.108869
13. Albusoda BS, A'amal A, Al-Khayyat BH. Challenges of Soil-Structure Interaction Problems–A Review. Journal of Engineering. 2025;31(5):75-98. https://doi.org/10.31026/j.eng.2025.05.05
14. Stefanidou SP, Sextos AG, Kotsoglou AN, Lesgidis N, Kappos AJ. Soil-structure interaction effects in analysis of seismic fragility of bridges using an intensity-based ground motion selection procedure. Engineering Structures. 2017;151:366-80. https://doi.org/10.1016/j.engstruct.2017.08.033
15. Mylonakis G, Nikolaou S, Gazetas G. Footings under seismic loading: Analysis and design issues with emphasis on bridge foundations. Soil Dynamics and Earthquake Engineering. 2006;26(9):824-53. https://doi.org/10.1016/j.soildyn.2005.12.005
16. Izhar MS, Ansari MI, Umair M. Correction: Energy based seismic vulnerability assessment tool for reinforced concrete bridges. Bulletin of Earthquake Engineering. 2024;22(11):5951-. https://doi.org/10.1007/s10518-024-01986-x
17. Baig M, Ansari M, Islam N, Umair M. Probabilistic Damage Analysis of Isolated Steel Tub Girder Bridge Excited by Near and Far Fault Ground Motions. International Journal of Engineering Transactions B: Applications. 2023;36(2):289-98. https://doi.org/10.5829/IJE.2023.36.02B.09
18. Nazri FM, Yerna CK, Kassema MM, Farsangib EN. Assessment of structure-specific fragility curves for soft storey buildings implementing IDA and SPO approaches. International Journal of Engineering. 2018;31(12):2016-21. 10.5829/ije.2018.31.12c.04
19. Prestandard F. commentary for the seismic rehabilitation of buildings (FEMA356). Washington, DC: Federal Emergency Management Agency. 2000;7(2):518.
20. Cornell CA, Jalayer F, Hamburger RO, Foutch DA. Probabilistic basis for 2000 SAC federal emergency management agency steel moment frame guidelines. Journal of structural engineering. 2002;128(4):526-33. https://doi.org/10.1061/(ASCE)0733-9445(2002)128:4(526)
21. Walls S. FEMA 356 prestandard and commentary for the seismic rehabilitation of buildings. ASCE for the Federal Emergency Management Agency. 2000:889-90.
22. Jalayer F, Cornell CA. Alternative non-linear demand estimation methods for probability-based seismic assessments. Earthquake Engineering & Structural Dynamics. 2009;38(8):951-72. https://doi.org/10.1002/eqe.876
23. Mei H, Guo A. Probabilistic hazard assessment of bridges under multihazard actions during the life-cycle period. Natural Hazards Review. 2024;25(2):04024001. https://doi.org/10.1061/NHREFO.NHENG-1679
24. Izhar MS, Ansari MI, Umair M. Energy based seismic vulnerability assessment tool for reinforced concrete bridges. Bulletin of Earthquake Engineering. 2024;22(10):5259-97. https://doi.org/10.1007/s10518-024-01969-y
25. Standards BoI. Criteria for earthquake resistant design of structures. 2002.
26. Council AT. Quantification of building seismic performance factors: US Department of Homeland Security, FEMA; 2009.
27. Paulay T, Priestley MN. Seismic design of reinforced concrete and masonry buildings: Wiley New York; 1992.
28. Caltrans S. Caltrans seismic design criteria version 1.6. California Department of Transportation, Sacramento. 2010.
29. Naeim F, Kelly JM. Design of seismic isolated structures: from theory to practice: John Wiley & Sons; 1999.
30. Roeder CW, Stanton JF, Taylor AW. Performance of elastomeric bearings1987.
31. Atefatdoost GR, JavidSharifi B, Shakib H. Effects of foundation flexibility on seismic demands of asymmetric buildings subject to near-fault ground motions. Structural Engineering and Mechanics, An Int'l Journal. 2018;66(5):637-48.
32. Boulanger RW, Curras CJ, Kutter BL, Wilson DW, Abghari A. Seismic soil-pile-structure interaction experiments and analyses. Journal of geotechnical and geoenvironmental engineering. 1999;125(9):750-9. https://doi.org/10.1061/(ASCE)1090-0241(1999)125:9(750)
33. Rp2a-Wsd A. Recommended practice for planning, designing and constructing fixed offshore platforms–working stress design–. Twenty-2000. 2000.
34. Ajom B, Bhattacharjee A, editors. Effect of earthquake on bridge foundation. 13th International Conference on Vibration Problems ICOVP, Indian Institute of Technology Guwahati, India; 2017.
35. Goodnight JC. The effects of load history and design variables on performance limit states of circular bridge columns: North Carolina State University; 2015.
36. El Bahy A. Cumulative seismic damage of reinforced concrete bridge piers. 1996.
37. Mallick M, Raychowdhury P. Seismic analysis of highway skew bridges with nonlinear soil–pile interaction. Transportation Geotechnics. 2015;3:36-47. https://doi.org/10.1016/j.trgeo.2015.03.002
38. Bhandari M, Bharti S, Shrimali M, Datta T. Seismic fragility analysis of base-isolated building frames excited by near-and far-field earthquakes. Journal of Performance of Constructed Facilities. 2019;33(3):04019029. https://doi.org/10.1061/(ASCE)CF.1943-5509.0001298
39. Yadav KK, Gupta VK. Near-fault fling-step ground motions: Characteristics and simulation. Soil Dynamics and Earthquake Engineering. 2017;101:90-104. https://doi.org/10.1016/j.soildyn.2017.06.022
40. Miano A, Iacovazzo P, Mele A, Di Ludovico M, Prota A. Seismic fragility of circular piers in simply supported RC bridges: a proposal for capacity assessment. Engineering Structures. 2024;302:117426. https://doi.org/10.1016/j.engstruct.2023.117426
41. Kalkan E, Kunnath SK. Effects of fling step and forward directivity on seismic response of buildings. Earthquake spectra. 2006;22(2):367-90. https://doi.org/10.1193/1.2192560
42. Kircher C, Deierlein G, Hooper J, Krawinkler H, Mahin S, Shing B, et al. Evaluation of the FEMA P-695 methodology for quantification of building seismic performance factors. 2010.

43. Padgett JE, Nielson BG, DesRoches R. Selection of optimal intensity measures in probabilistic seismic demand models of highway bridge portfolios. Earthquake engineering & structural dynamics. 2008;37(5):711-25. https://doi.org/10.1002/eqe.782
44. Jiang L, Zhong J, Yuan W, editors. The pulse effect on the isolation device optimization of simply supported bridges in near-fault regions. Structures; 2020: Elsevier.
45. Billah AM, Alam MS, Bhuiyan MR. Fragility analysis of retrofitted multicolumn bridge bent subjected to near-fault and far-field ground motion. Journal of Bridge Engineering. 2013;18(10):992-1004. https://doi.org/10.1061/(ASCE)BE.1943-5592.0000452
46. Kabir MR, Billah AM, Alam MS, editors. Seismic fragility assessment of a multi-span RC bridge in Bangladesh considering near-fault, far-field and long duration ground motions. Structures; 2019: Elsevier.
47. Jagan P, Visuvasam JA. Assessment of the influence of nonlinear soil effects on seismic response of RC structures with floating columns considering soil–structure interaction. Geomatics, Natural Hazards and Risk. 2024;15(1):2401997. https://doi.org/10.1080/19475705.2024.2401997
48. Amendola C, Pitilakis D. Vulnerability assessment of historical cities including SSI and site-effects. Geotechnical Engineering for the Preservation of Monuments and Historic Sites III: CRC Press; 2022. p. 836-46.

COPYRIGHTS
©2026 The author(s). This is an open access article distributed under the terms of the Creative Commons Attribution (CC BY 4.0), which permits unrestricted use, distribution, and reproduction in any medium, as long as the original authors and source are cited. No permission is required from the authors or the publishers.

Persian Abstract

چکیده

پل‌ها اجزای حیاتی شبکه‌های حمل و نقل هستند، به ویژه پس از رویدادهای لرزه‌ای، جایی که یکپارچگی عملیاتی آن‌ها برای پاسخ به شرایط اضطراری و تاب‌آوری زیرساخت‌ها بسیار مهم است .تأثیر یک رویداد لرزه‌ای بر هر پل بستگی به نوع فعالیت لرزه‌ای و نزدیکی پل به کانون زلزله دارد .در حالی که پل‌های واقع در فاصله دور از کانون زلزله)فاصله دور (ممکن است تحت تأثیر زیادی از رویداد زلزله قرار نگیرند، اما پل‌های واقع در نزدیکی کانون، نزدیک به گسل (NF)، بیشتر در معرض آسیب یا فروپاشی هستند . منطقه NF، که در فاصله ۱۵ کیلومتری از شکستگی گسل واقع شده است، حرکات زمینی (GMs)را نشان می‌دهد که با حرکات مشاهده شده در منطقه Far Field (FF) متفاوت است .حرکات زمین NFبا پالس‌های سرعت با انرژی بالا و دوره‌های طولانی، شکل‌های موجی شبیه به پالس، و مقادیر اوج قابل توجه مشخص می‌شوند که می‌توانند منجر به آسیب‌های شدید ساختاری شوند .بیشتر مطالعات در مورد آسیب‌پذیری لرزه‌ای پل‌ها در برابر NF-GMsبا فرض شرایط پایه ثابت انجام شده‌اند که در آن اثر انعطاف‌پذیری خاک در نظر گرفته نشده است .اثر انعطاف‌پذیری خاک بر عملکرد لرزه‌ای پل‌های بتن آرمه (RC)تحت این شتاب‌نگاشت‌های غیرمستقیم همچنان یک مسئله مورد سوال است .بنابراین، مطالعه حاضر ارزیابی مقایسه‌ای آسیب‌پذیری لرزه‌ای یک پل چند دهانه‌ای بتن مسلح (RC)را که تحت تأثیر شتاب‌نگاشت‌های غیرخطی -NF) (GMsبا اثرات گام پرتابی (FS)قرار دارد، با شرایط پایه ثابت و پایه انعطاف‌پذیر با استفاده از تحلیل دینامیکی افزایشی (IDA)و منحنی‌های آسیب‌پذیری انجام می‌دهد . برای مقایسه، دو پیکربندی سازه‌ای مورد بررسی قرار گرفت :یکی با پایه‌های پی ثابت و دیگری با در نظر گرفتن تعامل خاک-سازه (SSI)از طریق یک بنیاد گروهی شمع . نتایج نشان می‌دهند که مدل شامل تعامل خاک-ساختمان (SSI)کاهش برش پایه و نیازهای جابه‌جایی بالاتری را نشان می‌دهد، در حالی که مدل پایه ثابت سختی و برش پایه بالاتری را نشان می‌دهد که تمرکز اتلاف انرژی زلزله در بالای پایه است.

IJE TRANSACTIONS B: Applications Vol. 39, No. 08, (August 2026) 1933-1952

International Journal of Engineering

Journal Homepage: www.ije.ir

An Interpretable Hybrid Shapley Additive Explanations Brown Bear Optimization Algorithm Predictive Models for End Bearing Capacity of Rock Socketed Piles

N. Safaeian Hamzehkolaei*, B. Karimi Ferezghi

Department of Civil Engineering, Bozorgmehr University of Qaenat, Qaen, Iran

PAPER INFO

Paper history:
Received 03 July 2025
Received in revised form 25 July 2025
Accepted 31 August 2025

Keywords:
Hybrid Machine Learning Models
Ultimate End-bearing Capacity
Rock-socketed Piles
Brown-Bear Optimization Algorithm
SHapley Additive Explanations
Model Interpretation

ABSTRACT

This study develops an interpretable hybrid predictive framework that combines SHapley Additive exPlanations (SHAP) with the Brown-Bear Optimization Algorithm (BBOA) to enhance the prediction of end-bearing capacity (q_u) of rock-socketed piles. BBOA is employed to optimize hyperparameters of four machine learning (ML) models—Artificial Neural Networks (ANN), Support Vector Regression (SVR), Adaptive Neuro-Fuzzy Inference Systems (ANFIS), and Multivariate Adaptive Regression Splines (MARS)—leading to significant improvements in accuracy. A novel, interpretable MARS-based predictive formula is also introduced. The model uses pile diameter (B), embedment depths in soil (H_s) and rock (H_r), rock uniaxial compressive strength (σ_c), and Geological Strength Index (GSI) as inputs. Comprehensive evaluation using multiple statistical metrics (R^2, RMSE, MAE, U_{95}) reveals that BBOA-ANFIS achieves the highest accuracy during training, while the optimized MARS model performs best in testing, with ANN consistently showing the weakest results. Compared to previous ML-based and empirical models, the proposed models, especially the MARS formula, demonstrate superior accuracy and reliability, with improvements of 11.3% in R^2, 16.6% in RMSE, and 19.2% in MAE over the best prior empirical model. Additionally, sensitivity analysis and SHAPE-based model interpretation identified key predictors, ranked by influence as σc > GSI > B > Hr > Hs, with σ_c being the most influential variable and H_s the least. This hybrid approach provides a robust and interpretable tool for accurate and cost-effective pile design in complex soil-rock environments.

***doi**: 10.5829/ije.2025.39.08b.13*

Graphical Abstract

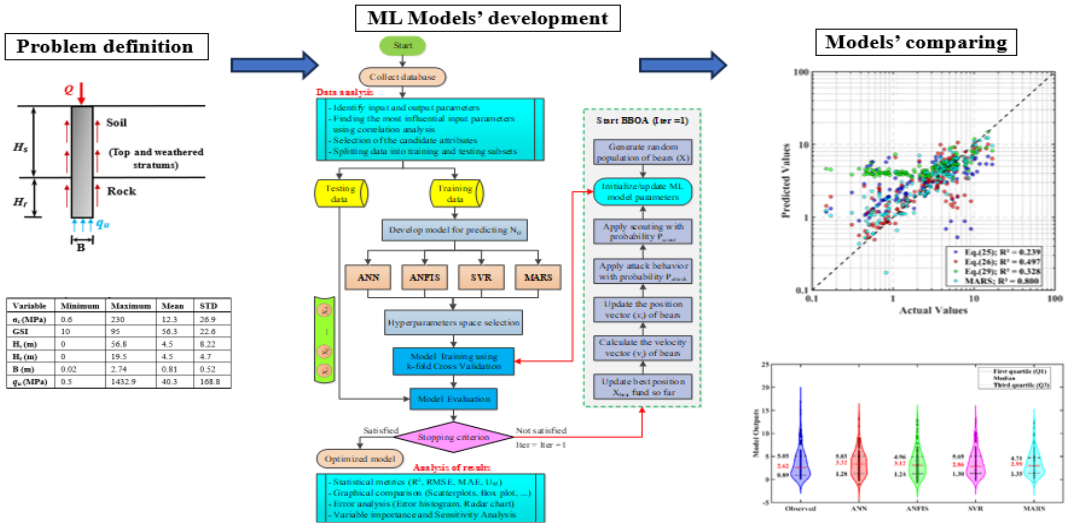

Variable	Minimum	Maximum	Mean	STD
σ_c (MPa)	0.6	230	12.3	26.9
GSI	10	95	56.3	22.6
H_s (m)	0	56.8	4.5	8.22
H_r (m)	0	19.5	4.5	4.7
B (m)	0.02	2.74	0.81	0.52
q_u (MPa)	0.5	1432.9	40.3	168.8

*Corresponding Author Email: nsafaeian@buqaen.ac.ir (N. Safaeian)

Please cite this article as: Safaeian Hamzehkolaei N, Karimi Ferezghi B. An Interpretable Hybrid Shapley Additive Explanations Brown Bear Optimization Algorithm Predictive Models for End Bearing Capacity of Rock Socketed Piles. International Journal of Engineering, Transactions B: Applications. 2026;39(08):1933-52.

1. INTRODUCTION

Rock-socketed piles are extensively used in geotechnical engineering due to their high load capacity, minimal settlement, and excellent seismic resistance, especially when embedded in intact rock. Accurate bearing capacity prediction is critical for the safe and economical design of structures in complex soil-rock conditions (1, 2). Estimating end-bearing capacity is challenging due to the complex interaction between piles and heterogeneous soil-rock formations, and a comprehensive theoretical model is still lacking. Current empirical formulas, based on regression analyses of limited experimental data (3-6), are constrained by small datasets and simplifying assumptions.

Existing empirical formulas for estimating end-bearing capacity of rock-socketed piles, derived from regression analyses of experimental data (3-6), are limited by their development from small datasets and simplified assumptions. These limitations restrict their applicability across diverse geological settings and pile configurations, potentially leading to overly conservative or unconservative predictions that fail to capture the complex effects of rock mass properties, pile geometry, and installation methods (7, 8). Analytical models often assume idealized boundary conditions and homogeneous material behavior, which inadequately represent the heterogeneity and anisotropy of rock formations (9, 10). Laboratory tests can also be inaccurate due to scale and equipment limitations, resulting in discrepancies between predicted and actual pile capacities (11). These issues highlight the need for accurate and interpretable models that enable engineers to understand key factors affecting pile performance.

Machine learning (ML) improves pile capacity design by creating predictive models that capture complex geotechnical relationships from data. Traditional methods oversimplify pile behavior across varied geological conditions, whereas ML integrates more parameters for accurate predictions (2). Algorithms like Artifitial Neural Networks (ANNS), Support Vector Regression (SVR), and hybrid metaheuristic models effectively model nonlinear pile-soil interactions (12). Despite improved accuracy, the limited transparency of many ML models challenges engineers (13, 14). Current research focuses on interpretable models to balance predictive performance with explainability, increasing engineers' confidence and practical application in foundation design (15, 16).

Despite advancements in ML for predicting pile bearing capacity, significant research gaps still exist, especially for rock-socketed piles. Existing empirical models, such as those by Zhang (4, 5), depend on limited datasets and simplified assumptions, which can lead to inaccurate predictions in complex soil-rock environments. Previous ML studies by Pham et al. (17); Nguyen et al. (18) mainly focused on soft to medium soils, with limited attention given to rock-socketed piles. Additionally, many ML models lack interpretability, which hampers their practical use in geotechnical engineering. These limitations emphasize the importance of precise, understandable, and optimized predictive models designed specifically for rock-socketed pile end-bearing capacity.

To address these gaps, this study proposes a novel hybrid SHAP-BBOA framework that integrates SHapley Additive exPlanations (SHAP) with the Brown-Bear Optimization Algorithm (BBOA) to enhance the end-bearing capacity of rock-socketed piles. Unlike previous SHAP-optimization approaches conducted by Zhang and Xue (6), Alizamir et al. (15) focused on general machine learning optimization, BBOA is specifically used in this study to tune hyperparameters of four machine learning models—ANN, SVR, Adaptive Neuro-Fuzzy Inference Systems (ANFIS), and Multivariate Adaptive Regression Splines (MARS)—ensuring greater accuracy in complex rock-soil conditions. By treating hyperparameters as decision variables within the metaheuristic optimization process, BBOA efficiently explores the search space. To enhance transparency, SHAP is integrated with the optimized models to enable clear interpretation of the key geotechnical factors affecting pile performance. Additionally, this research introduces a novel, interpretable MARS-based formula that provides an accurate equation for estimating the end-bearing capacity of rock-socketed piles, outperforming traditional empirical models. By combining BBOA's adaptive foraging strategy with SHAP-driven interpretability, this framework offers a reliable, transparent, and practical tool for safer and more cost-effective pile foundation design in complex soil-rock environments.

This paper is organized as follows: Section 2 reviews the literature; Section 3 describes the experimental database; Section 4 details the implementation of the proposed BBOA-optimized predictive models; Section 5 presents and analyzes the results, including performance, comparison with existing models, SHAP interpretation, and sensitivity analysis; and Section 6 concludes by summarizing key findings, discussing implications, and suggesting future research directions..

2. LITERATURE REVIEW

Several studies have developed empirical relationships to estimate the end-bearing capacity of rock-socketed piles. Zhang (4) presented comprehensive analytical and empirical approaches for drilled shafts in rock, emphasizing the influence of rock quality and pile geometry (4). Subsequently, Zhang (5) refined these predictions by incorporating Rock Quality Designation (RQD) as a critical parameter. Chen and Zhang [19]

introduced a ML-based method that further improved prediction accuracy by leveraging data-driven insights while maintaining practical applicability. Zhang and Xue (6) proposed a novel hybrid model combining empirical and computational techniques, achieving superior performance in predicting bearing capacity. These studies collectively show the progress and increasing sophistication of empirical models, but also highlight their limitations such as the need for extensive laboratory data, computational complexity, and insufficient accuracy in complex soil conditions (19, 20).

Advancements in ML algorithms have enabled researchers to develop models that use diverse data sources, such as load test results, soil parameters, and pile characteristics, for reliable and efficient predictions (17, 21, 22). Pham et al. (17) employed an evolutionary genetic algorithm (GA) to optimize a deep learning neural network (DLNN) for predicting the bearing capacity of driven piles. By using GA to select key features from a dataset of 472 static pile load tests, the model achieved higher accuracy than when using all input variables. Yong et al. (22) predicted pile bearing capacity using ANFIS, Genetic Programming (GP), and a hybrid Simulated Annealing-GP (SA-GP) model based on data from 50 driven piles. The SA-GP model was the most accurate, and sensitivity analysis identified pile cross-section and settlement as key parameters. Armaghani et al. (23) developed an intelligent model combining ANFIS, Group Method of Data Handling (GMDH), and Imperialist Competitive Algorithm (ICA). Using data from 257 high-strain dynamic load tests, their model outperformed standalone ANFIS and GMDH models. Pham and Vu (24) developed an ensemble learning model combining Gradient Boosting, Random Forest (RF), and Linear Regression (LR) through weighted voting. Trained on data from 108 pile load tests, the model underwent global sensitivity analysis to determine the most influential features. Harandizadeh et al. (25) proposed a hybrid model combining ANFIS and GMDH optimized by Particle Swarm Optimization (PSO). Using pile and soil data from Cone Penetration Test (CPT), their optimized model showed higher accuracy and reliability than traditional ANN models.

Gohil and Parthasarathy (26) developed practical models for predicting the bearing capacity of offshore piles using data from 63 dynamic load tests. Their Bayesian regularized model, incorporating pile geometry, soil properties, and dynamic driving data, was validated using Pile Driving Analyzer (PDA) measurements and CAPWAP software. Huang et al. (27) presented an Opposition-based Differential Flower Pollination (ODFP) algorithm to optimize Least Squares Support Vector Regression (LSSVR) for predicting pile bearing capacity (27). The ODFP-LSSVR model demonstrated high accuracy and reliability in analyzing pile load test data, effectively considering complex geotechnical factors. Amâncio et al. (28) developed an XGBoost model using data from 200 static load tests on driven piles. Compared to other algorithms like AdaBoost, RF, Decision Tree (DT), and SVM, XGBoost achieved the highest accuracy. Sensitivity analysis identified the number of Standard Penetration Test (SPT) blows along the pile shaft as the most influential factor affecting capacity.

Giap et al. applied a RF model that incorporates soil data variability to accurately predict pile bearing capacity, emphasizing the importance of careful load management for safety. Nguyen et al. (18) developed a hybrid GA-ANFIS model using 95 PDA tests from a Vietnamese wind power project, achieving high accuracy with R^2 values of 0.976 for training and 0.925 for testing. Both studies demonstrate the effectiveness of ML techniques in improving predictions in complex geotechnical conditions. Jin and Ji (29) developed a model combining Improved Radial Movement Optimization (IRMO) with a Backpropagation Neural Network (BPNN) to predict the ultimate bearing capacity of single piles. Using 196 static load test samples, the IRMO-BPNN model effectively overcomes BPNN's tendency to get trapped in local optima, significantly improving prediction accuracy compared to other hybrid models. Shoaib and Abu-Farsakh (30) employed DT, RF, and Gradient Boosted Trees models to estimate pile bearing capacity from CPT data. Using a dataset of 80 pile load tests from Louisiana, they calculated the ultimate capacity from load-settlement curves using the Davison method. Assaad et al. (31) developed a Bayesian Belief Network model, informed by expert knowledge and a dataset of 2,735 records, to estimate bridge pile bearing capacity. The model, enhanced by data preprocessing and input from eight specialists, achieved 90.51% accuracy. Shen (32) predicted the bearing capacity of reinforced concrete piles using Multilayer Perceptron (MLP) neural networks optimized with GA-based Crystal Structure Algorithm (CSA) and Fox Optimization (FOX). The inputs were pile diameter, soil layer depths, pile head and tip elevations, ground elevation, additional pile head height, and SPT blow counts. The hybrid MLFO outperformed MLSC across all soil layers, achieving a high R^2 value of 0.992.

Picardo et al. (33) evaluated the Discontinuity Layout Optimization (DLO) method for calculating the bearing capacity of piles embedded in homogeneous rock masses, using the modified Hoek-Brown failure criterion. Validation against analytical solutions and finite difference method results confirmed that DLO is an accurate approach for determining pile bearing capacity in rock environments. Hassan and Rashid (1) used Naive Bayes combined with Artificial Hummingbird Algorithm (AHA) and Improved Grey Wolf Optimizer (IGWO) to predict the bearing capacity of rock-socketed piles based on 172 SPT-derived data points. The IGWO-optimized model achieved the highest accuracy with an R^2 of 0.993. Zhang and Xue (6) developed a model combining

XGBoost with Bayesian Optimization (BO) to predict the end-bearing capacity of rock-socketed piles using 138 data samples. The model utilized five key parameters: unconfined compressive strength of intact rock, geological strength index, pile lengths in soil and rock layers, and pile diameter. The BO-XGBoost model achieved superior accuracy compared to empirical formulas and ML models like RF, GEP, BPNN, and GMDH, with an R^2 of 0.963. Morover, compressive strength of rock was found to be the most significant factor influencing the prediction. More recently, Onyelowe et al. (2) developed an advanced data-driven framework that integrates multiple ML algorithms including Kstar, M5Rules, ElasticNet, XNV, and DT, to predict pile bearing capacity on rock using a dataset of 200 samples comprising key geotechnical and in-situ test parameters such as pile dimensions, geological characteristics, and penetration resistance. The models were accurate and robust; sensitivity analyses revealed that penetration resistance, pile embedment depth, and geological conditions were the most influential factors.

Previous research has primarily focused on pile bearing capacity in soft to medium soils, with limited investigation into rock-socketed piles (1, 2, 6, 33, 34). Existing studies often suffer from small or incomplete datasets, hindering prediction accuracy and generalizability (6, 34-37), resulting in a research gap in predicting end-bearing capacity in rock layers (38). This study addresses this gap by using a comprehensive laboratory database with advanced optimized ML techniques to improve end-bearing capacity prediction in rock-socketed piles. Furthermore, the study proposes an interpretable predictive relationship for estimating the end-bearing capacity of rock-socketed piles, demonstrating superior accuracy compared to existing empirical formulas. This interpretable model enhances reliability and offers practical insights for geotechnical engineers, connecting complex data-driven methods with traditional design approaches.

3. EXPERIMENTAL DATABASE

Figure 1 presents the idealized model and key parameters affecting the end-bearing capacity of piles in rock formations. The ultimate end-bearing capacity of a pile (q_u) is primarily influenced by multiple factors, such as the pile embedment depth in soil (H_s) and rock (H_r), pile diameter (B), uniaxial compressive strength of the rock (σ_c), and the overall rock mass quality.

Empirical pile capacity tests are costly and limited; ML offers a predictive alternative, but requires validated, representative training data. Extensive experimental data, incorporating geological factors, improves model accuracy across various site conditions. This study utilized a comprehensive dataset comprising 138 validated experimental cases from 22 independent laboratory test series, involving pile specimens embedded in various rock formations. The dataset incorporates critical geotechnical parameters including: uniaxial compressive strength (UCS) of the rock stratum (σ_c), Geological Strength Index (GSI), Rock Mass Rating (RMR), H_s and H_r, and B. A comprehensive description along with the complete dataset found By Zhang and Xue (6). Table 1 shows rock type distributions and test shaft numbers for different classes of the sedimentary, igneous, and metamorphic rocks. It can be seen that most of the test shafts are installed in sedimentary (105 tests) and igneous (32 tests) rocks.

Morover, to evaluate the q_u of rock-socketed piles, various interpretations of load test data were employed by the original authors. The normalized shaft base settlement (S_b/B) exhibits significant variability due to differing criteria, such as S_b/B = 1% , 5%, and 10%, adopted in the referenced studies to determine q_u. Morover, in certain tests, q_u was defined as the bearing resistance at the maximum applied load. Given the challenges in standardizing the interpretation of q_u, this study adopts the q_u values as interpreted by the original authors to ensure consistency with the source data (6).

Table 2 provides a comprehensive statistical summary of the dataset, including the minimum, maximum, mean, and standard deviation (STD) values

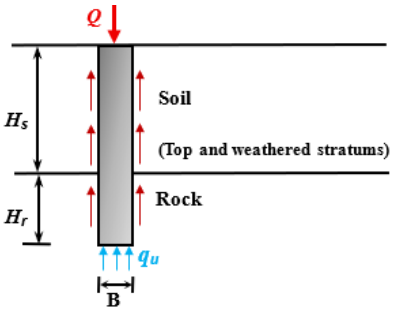

Figure 1. Idealized model for rock-socketed piles

TABLE 1. Distribution of rock types

Rock group	Class	Rock type and related number of test shafts
Igneous	Volcanic (26)	Basalt (16), Breccia (3), Tuff (7)
	Plutonic (6)	Granite (4), Granodiorite (2)
	Hypabyssal	-
Metamorphic	Foliated (1)	Phyllite–Schist (1)
	Non-foliated	-
Sedimentary	Clastic (41)	Sandstone (13), Siltstone (25), Claystone (6), Shale (25), Marls (2), Till (10)
	Non-clastic (24)	Limestone (10), Gypsum (6), Chalk (8)

for each parameter. The STD serves as a critical indicator of data variability, representing the average distance of individual data points from the mean value. Lower STD values indicate greater consistency in the dataset, with observations closely distributed around the mean, while higher values reflect substantial variability and wider dispersion of the data points. This statistical analysis facilitates quantitative evaluation of parameter distributions and their variability across the experimental dataset.

To account for the substantial variability in measured q_u values, the dimensionless ultimate bearing capacity factor ($N_\sigma = q_u / \sigma_c$) was adopted as the output variable for the ML-based predictive models. It is important to note that both the GSI (Geological Strength Index) and RMR (Rock Mass Rating) serve as critical indicators of rock mass quality, providing essential insights into rock behavior under different loading conditions (3). However, since some samples in the utilized dataset contained only GSI or RMR values, this study employed the following empirical correlation to estimate GSI from available RMR data (39):

$$GSI = RMR - 5 \quad (1)$$

Figure 2 shows the Pearson correlation coefficient between the considered inputs and outputs. Histograms on the diagonal display individual parameter distributions, while off-diagonal scatter plots show bivariate relationships and Pearson correlation coefficients (r). This visualization enables simultaneous examination of both univariate distributions and pairwise parameter correlations within a single integrated framework. Correlation values near ±1 indicate strong relationships between variables. Figure 2 shows that GSI has the strongest positive correlation (r = 0.59) with the bearing capacity factor Nσ, and pile diameter (B) has the strongest negative correlation (r = -0.45). These results highlight GSI as the most influential positive predictor and B as the most substantial negative predictor of pile end-bearing capacity in rock formations.

TABLE 2. Key statistical parameters for the raw dataset

Variable	Minimum	Maximum	Mean	STD
σ_c (MPa)	0.6	230	12.3	26.9
GSI	10	95	56.3	22.6
H_s (m)	0	56.8	4.5	8.22
H_r (m)	0	19.5	4.5	4.7
B (m)	0.02	2.74	0.81	0.52
q_u (MPa)	0.5	1432.9	40.3	168.8

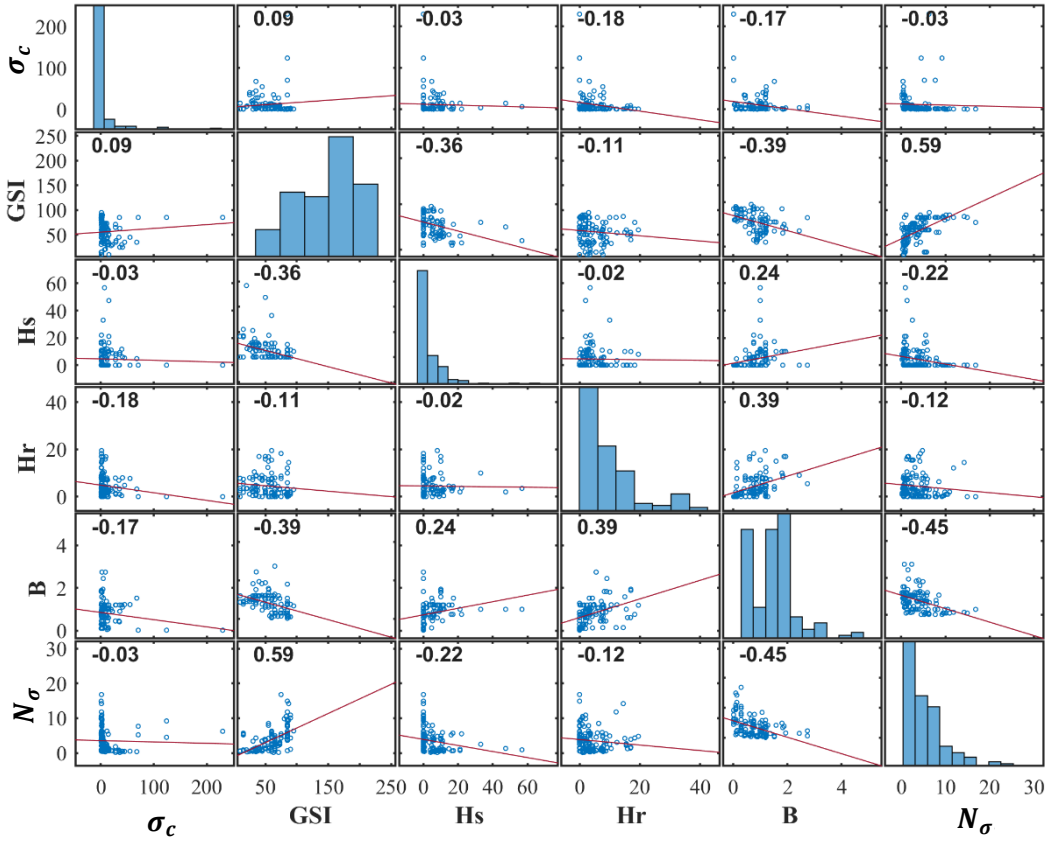

Figure 2. Scatter plot and Pearson correlation of dataset

Furthermore, all pairwise correlations between input variables (off-diagonal elements) show coefficients below 0.4, indicating negligible multicollinearity in the predictive model. This low inter-parameter correlation confirms the statistical independence of input variables.

Statistical analysis of the dataset (Table 2, Figure 2) indicates a discretely distributed parameter space with considerable variability. Notably, the low pairwise correlations among input variables confirm the absence of multicollinearity, satisfying critical assumptions for developing robust ML models to predict the end-bearing capacity of rock-socketed piles. This well-distributed and statistically independent parameter set enhances the models' ability to discern distinct predictive patterns across diverse geological conditions.

4. PROPOSED METAHEURISTIC-OPTIMIZED PREDICTIVE MODELS

The predictive efficacy of ML models hinges critically on their architectural design and parameter configurations, particularly in ANNs, where the number of hidden layer neurons and connection weights significantly influence performance. Suboptimal architectural choices may result in underfitting, failing to capture underlying data patterns; overfitting, impairing generalization to unseen data; or computational inefficiencies, all of which compromise prediction accuracy (16, 40, 41). Consequently, precise tuning of model architecture and hyperparameters is imperative to develop robust and reliable predictive systems for geotechnical applications.

Local optimization algorithms, while effective for certain tasks, often face challenges in complex and high-dimensional problems due to computationally expensive gradient calculations, unstable convergence, vulnerability to local optima, and sensitivity to initial parameters and feature scaling (42-44). Metaheuristic algorithms provide robust global search capabilities, making them well-suited for large and complex search spaces where gradient-based methods struggle (45). Consequently, integrating metaheuristic techniques with ML models has become increasingly popular (40, 46, 47).

This study employs the Brown-Bear Optimization Algorithm (BBOA) to automatically tune the hyperparameters of four ML models—Artificial Neural Networks (ANN), Adaptive Neuro-Fuzzy Inference Systems (ANFIS), Support Vector Regression (SVR), and Multivariate Adaptive Regression Splines (MARS)—aiming to improve the accuracy of pile end-bearing capacity predictions. As illustrated in Figure 3, the BBOA efficiently explores the hyperparameter space by treating hyperparameter combinations as optimization variables within its metaheuristic framework. Each BBOA iteration generates new hyperparameter

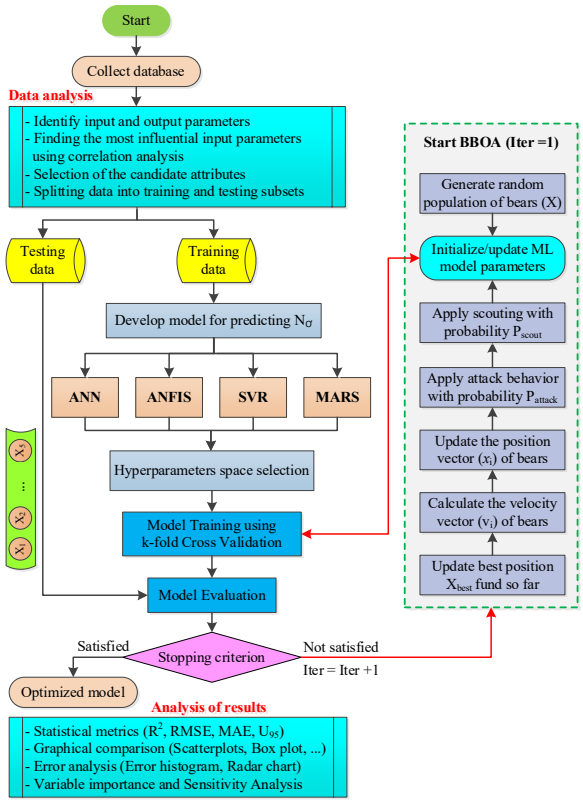

Figure 3. Workflow of this study

candidates for the selected model. The model is then trained using 5-fold cross-validation, and its performance is evaluated based on MSE. The optimization iteration proceeds until the convergence criteria are satisfied. Detailed explanations of the BBOA and the specific ML models used are provided in the following sections.

4. 1. Brown-Bear Optimization Algorithm (BBOA)

BBOA mimics brown bears' adaptive foraging strategies (48), balancing stochastic exploration and localized exploitation. This dual-phase approach enables effective navigation of complex solution spaces while preventing premature convergence, similar to bears' natural resource optimization. The algorithm's dynamic search process enables the efficient discovery of near-optimal solutions, making it well-suited for a broad spectrum of engineering problems.

The BBOA implements the following key computational phases (46, 48):

Step 1. Randomly initialize the positions of the bears within the search space.

$$x_i^j = x_{i,\min}^j + rand(x_{i,\max}^j - x_{i,\min}^j), \quad \begin{cases} i = 1,2.,...,n \\ j = 1,2,...,d \end{cases} \tag{2}$$

where d represents the dimension of the search space, n denotes the total number of bears, x_i^j represents the

position of the i[th] bear in the j[th] dimension, and $x_{i,\min}^{j}$ and $x_{i,\max}^{j}$ ($j = 1, \ldots, d$) represent the lower and upper bounds of the search space, respectively.

Step 2. Evaluate the objective function for each bear.

Step 3. Update the best solution X_{best} found so far.

Step 4. For each bear *i*: Calculate the velocity (v_i).

$$v_i(t+1) = v_i(t) + c_1 \cdot rand() \cdot (X_{best} - x_i(t)) \quad (3)$$

where c_1 is the learning coefficient and rand() represents a random number in the range [0, 1].

- Update the position vector of the bear (x_i).

$$x_i(t+1) = x_i(t) + x_i(t+1) \quad (4)$$

- Apply attack behavior with probability of P_{attack}.

$$x_i(t+1) = x_i(t+1) + rand() \cdot (x_i(t) - X_{best}) \quad (5)$$

- Apply scouting for a new solution with the probability of P_{scout}.

$$x_i(t+1) = x_{rand} \quad (6)$$

where x_{rand} represents a random position vector.

Step 5. Repeat steps 2-4 until termination criteria are satisfied.

4. 2. Artificial Neural Network (ANN) ANN consists of an input layer, one or more hidden layers, and an output layer, with weighted connections between neurons. This design allows ANN to learn and identify patterns by adjusting weights during training. The input layer receives feature vectors, while the output layer produces predictions. Neurons interact with adjacent layers, and each neuron applies an activation function, such as tansig or purelin, to the weighted sum of its inputs and bias (41, 46).

This study employed a fully connected single hidden-layer ANN model (Figure 4) with an input layer (*i*), a single hidden layer (*j*), and an output layer (*o*). Each layer calculates its input by summing the weighted outputs from the previous layer, adding a bias, and applying an activation function. The hidden layer connects the input and output layers, and the target variable y is predicted using an activation function that incorporates biases and weights from the input nodes. The output of the hidden layer with *N* neurons can be calculated as follows (49):

$$y_{pi} = \sum_{i=1}^{N} W_{ij} O_{pj} + b_j \quad (7)$$

where W_{ij}, O_{pj}, and b_j represent the connection weights, output of the first layer, and the bias for neuron j, respectively.

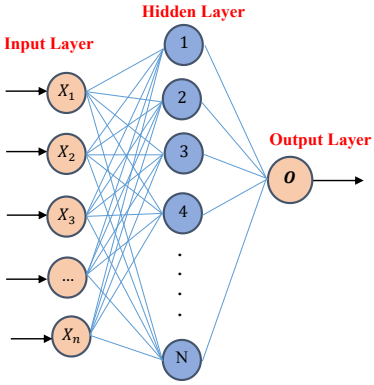

Figure 4. Structure of an ANN network

The logistic (sigmoid) function, the most common activation function in ANNs, calculates an output value based on inputs from external nodes.

$$f(y) = \frac{1}{1+e^{-y}} \quad (8)$$

ANN performance significantly relies on connection weights, biases, and the number of hidden layer neurons (50). This study optimizes these ANN hyperparameters using the BBO algorithm.

4. 3. Adaptive Neuro-fuzzy Inference System (ANFIS) ANFIS combines neural networks and fuzzy logic to model nonlinear relationships using the Takagi–Sugeno fuzzy inference system. Its adaptability, quick learning, and capacity to handle complex processes make it popular in engineering (51), often outperforming traditional methods by integrating human-like reasoning with data-driven learning for improved predictive accuracy. In a first-order Takagi-Sugeno FIS model, which includes two input variables, *x* and *y*, and a single output *f*, the core relationships of the model are expressed through two "if-then" rules.

Rule 1: If *x* is A_1 and *y* is B_1, then $f_1 = p_1 x + q_1 y + r_1$

Rule 2: If *x* is A_2 and *y* is B_2, then $f_2 = p_2 x + q_2 y + r_2$

where A_1, A_2 and B_1, B_2 are the Membership Functions (MFs) for inputs *x* and *y* respectively; p_1, q_1, r_1 and p_2, q_2, r_2 are the consequent parameters of the linear output functions for each rule.

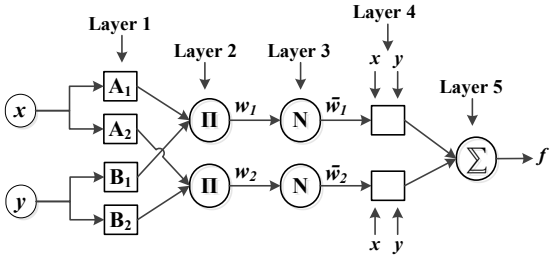

Figure 5. ANFIS model

The initial layer of the ANFIS network (Figure 5) converts input data into fuzzy values using MFs. Each node in this layer acts as an adaptive node, transforming input variables into membership values.

$$O_i^1 = \mu_{A_i}(x), \quad \text{for } i = 1, 2$$
$$O_i^1 = \mu_{B_i}(x), \quad \text{for } i = 3, 4 \tag{9}$$

where x is the input to node i, O_i^1 represents the degree of membership in a fuzzy set, and A_i is a linguistic label (e.g., "small" or "large"). Gaussian MFs, valued between zero and one, are commonly used because of their effectiveness in handling nonlinear data (52):

$$\mu(x) = bell(x; a_i, b_i, c_i) = \frac{1}{1 + \left[\left(\frac{x - c_i}{a_i}\right)\right]^{b_i}} \tag{10}$$

where $\{a_i, b_i, c_i\}$ denote the MF parameters.

The second layer multiplies incoming signals and sends the result to the next layer. The third layer, known as the rule layer, calculates the firing strength of each node in relation to the total firing strength of all nodes.

$$O_i^2 = \mu_{A_i}(x)\mu_{B_i}(x) \tag{11}$$

$$O_i^3 = \bar{w}_i = \frac{w_i}{w_1 + w_2}, \quad \text{for } i = 1, 2 \tag{12}$$

The fourth layer, called the defuzzification layer, converts fuzzy sets into precise values using specialized node functions. Finally, the output layer aggregates incoming signals to produce the final output, ensuring accurate data processing in fuzzy inference systems.

$$O_i^4 = \bar{w}_i(p_i x + q_i y + r_i), \quad \text{for } i = 1, 2 \tag{13}$$

$$O_i^5 = \sum \bar{w}_i f_i = \frac{\sum w_i f_i}{\sum w_i}, \quad \text{for } i = 1, 2 \tag{14}$$

This study optimizes an ANFIS using Fuzzy C-Means (FCM) clustering, highlighting the crucial role of cluster number, centers, MF types, and iteration numbers on accuracy. The BBOA is applied to fine-tune FCM-based ANFIS parameters, enhancing both clustering accuracy and predictive capability.

4. 4. Support Vector Regression (SVR) The SVR extends SVM classification for accurate function approximation in regression tasks. It features high computational efficiency, strong performance in high dimensions, easy implementation, adaptability to small samples, and good generalization, contributing to the rising popularity of SVM models (53). The nonlinear SVR model F(X) is expressed as follows:

$$F(X) = \langle w.\Phi(X, X_i) \rangle + b \tag{15}$$

where w denotes the weight coefficients, $\Phi(X, X_i)$ represents the kenel function, and b indicates the bias. The values of W and b can be determined as follows:

$$\begin{aligned} &Min: \frac{1}{2}\|W\|^2 + C\sum_{i=1}^{n}\left(\xi_i^+ + \xi_i^-\right) \\ &s.t.: y_i - \langle w.\Phi(X, X_i) \rangle - b \le \varepsilon + \xi_i^+, \\ &\langle w.\Phi(X, X_i) \rangle + b - y_i \le \varepsilon + \xi_i^-, \\ &\xi_i^-, \xi_i^+ \ge 0 \end{aligned} \tag{16}$$

In Equation 16, C is the penalty factor, ε denotes the box constraint, and ξ_i^-, ξ_i^+ are the relaxtion factors. The Lagrange method can be used for solving optimization ptoblem. SVR performance varies with different kernel functions, making the selection of the appropriate one crucial for optimal results [49]. Table 3 provides a list of commonly used kernel functions.

4. 5. Multivariate Adaptive Regression Splines (MARS) MARS is a nonparametric method based on a divide-and-conquer strategy that automatically partitions the input space, fits piecewise polynomials, and uses spline basis functions (BFs) to capture nonlinearities and variable interactions. The model selects relevant variables, determines optimal transformations, and handles both continuous and categorical predictors, resulting in a flexible and interpretable model (41, 49, 54).

MARS segments training data into splines with varying slopes and utilizes knots to define different regions, enhancing the flexibility of the BFs. Two types of BFs map input variables X to output parameter Y, with the first type being hinge functions. The first type is hinge functions, expressed as:follows:

$$Y = \max(0, X - t) \text{ Or } \max(0, t - X) \tag{17}$$

where t represents a knot point. These functions model non-linear relationships and breakpoints in data. Specifically, products of hinge functions capture interaction effects between variables.

The MARS model f(X) is formed by a linear combination of BFs and their interactions (49).

TABLE 3. Common kernel functions

Kernel type	Formulas
Linear	$k(x, y) = x'y + c$
Polynomial	$k(x, y) = (x'y + c)^d$
Gaussian	$k(x, y) = \exp[-\|x - y\|^2/(22s^2)]$
Sigmoid	$k(x, y) = \tanh(ax'y + c)$

$$f(X)=\beta_0+\sum_{m=1}^{M}\beta_m\lambda_m(X) \tag{18}$$

where λ_m (m = 1,.., M) represents BFs, each being either a single spline or a product of multiple splines.The least-squares method estimates β_m and λ_m in Equation 18.

As shown in Figure 6, MARS model employs a two-phase approach: a forward phase that adds functions until a maximum number of terms is reached, balancing performance gains with the risk of overfitting; and a backward phase that mitigates overfitting by removing the least effective terms using Generalized Cross-Validation (GCV) to penalize model complexity. The GCV equation is expressed as:

$$GCV=\frac{\frac{1}{N}\sum_{i=1}^{N}\left[y_i-f(x_i)\right]^2}{\left[1-\frac{M+c\times(M-1)/2}{N}\right]^2} \tag{19}$$

where M, N, and c represent the number of BFs, number of training data, and the penalty for each BFs. Increasing the penalty c reduces the number of BFs, leading to smoother estimates and greater model simplicity.

In this study, BBO optimizes the hyperparameters of the MARS model, such as the penalty parameter (c), number of BFs (M), and interaction degree (I).

4. 6. Statistical Performance Assessment Indices

A thorough evaluation was carried out to determine the performance of the ML-based predictive models using well-established statistical metrics, including the coefficient of determination (R^2), root mean squared error (RMSE), and mean absolute error (MAE). In addition, the U_{95} index was employed to represent the 95% uncertainty band, thereby providing further validation of model reliability. These metrics offer objective, quantitative measures of forecasting performance by assessing the discrepancies between observed and predicted values across the entire dataset. MAE and RMSE both indicate the average magnitude of prediction errors, with RMSE assigning greater weight to larger errors due to the squaring of differences. Conversely, R^2 reflects the proportion of variance in the dependent variable that is explained by the model, thus indicating the overall quality of fit. The U95 metric measures the range that covers 95% of prediction errors, offering a robust measure of model reliability in geotechnical work. Together, these evaluation criteria enable a comprehensive assessment of model accuracy and robustness across various prediction scenarios.

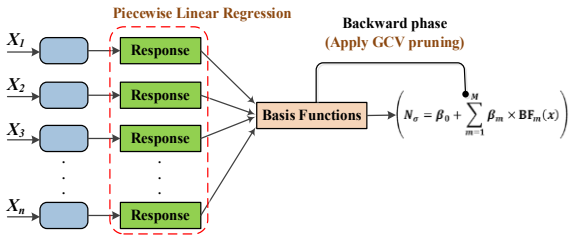

Figure 6. A schematic of MARS model

$$R^2=1-\frac{\frac{1}{N}\sum_{i=1}^{N}(O_i-P_i)^2}{\frac{1}{N}\sum_{i=1}^{k}(O_i-\bar{P}_i)^2} \tag{20}$$

$$RSME=\frac{1}{N}\sum_{i=1}^{N}(O_i-P_i)^2 \tag{21}$$

$$MAE=\frac{1}{N}\sum_{i=1}^{N}|O_i-P_i| \tag{22}$$

$$U_{95}=1.96\sqrt{\left(STDEV^2+RMSE^2\right)} \tag{23}$$

where $O_i, P_i, \bar{P}_i$, and N are the observed (exprimental) values, predicted values, average of the predicted values, and the number of the samples, respectively.

5. RESULTS AND DISCUSSION

The models' accuracy and efficiency rely on careful parameter selection. In this study, 80% of the dataset (110 samples) was allocated for training, while the remaining 20% (28 samples) was reserved for testing. Before modeling, the data were normalized and scaled to [0, 1] to improve robustness and generalization. A 5-fold cross-validation was employed during the training phase.

5. 1. Implementing BBOA-Optimized Models The BBOA-optimized ANN, ANFIS, SVR, and MARS models were run for 500 iterations with a population size of 100. To ensure robustness, each model was executed 10 times, and the best result was selected. This systematic optimization, incorporating parameter range exploration and multiple iterations, enhances the reliability and predictive accuracy of the pile end-bearing capacity estimation models. Optimized hyperparameter values and their variation ranges, determined using BBOA, are detailed in Table 4.

The BBOA-ANN model's parameters, as detailed in Table 4, include the number of hidden layer neurons (layer size), activation function type ('relu', 'tanh', or 'sigmoid'), learning rate (Lambda), and layer weights and biases. The weight and bias search space ranged from -1 to 1, with the number of neurons varying between 5 and 100. Optimal performance was achieved with 37 hidden layer neurons, a fixed learning rate of 0.001, and 500 training epochs.

The performance of SVR is highly dependent on the error margin (Epsilon), kernel function type and parameters (e.g., Gaussian, linear, polynomial), and box constraint value. In this study, SVR was implemented with a Gaussian RBF kernel. The FCM-based ANFIS model performed best as a Sugeno type with 5 clusters, linear input MFs, and a Gaussian output MF.

The MARS model's adjustable parameters—penalty (C), number and type of basis functions (M), and maximum interaction level (I)—were analyzed. Optimal values were C=3, I=2, and M=10 basis functions (BFs). The final BBOA-MARS model, using 10 linear piecewise BFs and a maximum interaction level of 2, achieved a GCV score of 0.175.

Finally, the MARS model yielded the following equation for estimating the ultimate bearing capacity factor (N_σ).

$$N_\sigma = -1.58 + 22.7*BF1 - 29.2*BF2 +92.4*BF3 - 87.3*BF4 - 46.9*BF5 + 12.1*BF6 -92.4*BF7 + 91.5*BF8 - 31*BF9 +31.2*BF10 \quad (24)$$

In Equation 24, BF_i {i=1, 2, ..., 10} represents the basis functions derived from the database as described in Section 4.5. Table 5 further elaborates on each of these basis functions, specifying the variables involved and the threshold values at which their respective hinge functions operate, thereby providing insights into the proposed hybrid BBOA-MARS model's underlying structure and decision-making process.

5. 2. Comparative Analysis Table 6 compares the training performance of BBOA-optimized and un-optimized models. The performance metrics (R^2, RMSE, MAE, U95) demonstrate significant enhancements due to BBOA optimization. The optimized ANFIS model exhibited the most substantial improvement, with R^2 increasing from 0.794 to 0.874 (10.08% improvement), RMSE decreasing from 1.469 to 1.150 (21.72% reduction), MAE reducing from 0.934 to 0.799 (14.45% reduction), and U95 dropping from 3.963 to 3.188 (19.56% reduction). These gains reflect BBOA's effective tuning of fuzzy rules, enhancing ANFIS's ability to capture nonlinear relationships. The optimized SVR model also showed notable improvement, with R^2 rising from 0.701 to 0.826 (17.83% improvement), RMSE decreasing from 1.771 to 1.352 (23.66% reduction), and MAE reducing from 0.834 to 0.713 (14.51% reduction). For MARS, BBOA optimization improved R^2 from 0.740 to 0.802 (8.38% improvement), reduced RMSE from 1.569 to 1.443 (8.03% reduction), and lowered MAE from 1.054 to 0.966 (8.35% reduction). In contrast, the ANN model showed the least improvement, with R^2 increasing marginally from 0.727 to 0.736 (1.24% improvement), MAE reducing from 1.121 to 1.024 (8.65% reduction), but RMSE increasing from 1.606 to 1.665 (3.67% increase) and U95 rising from 4.479 to 4.626 (3.28% increase), likely due to sensitivity to initial weights. Overall, BBOA optimization plays a crucial role in boosting training accuracy, particularly for ANFIS and SVR, while ANN benefits the least.

Table 6 shows that BBOA-optimized models achieved the following R^2 values: ANN (0.736), ANFIS (0.874), SVR (0.826), and MARS (0.802). Training RMSE values were 1.665, 1.150, 1.35, and 1.443, respectively. MAE values revealed that ANFIS (0.799) and SVR (0.713) significantly outperformed MARS and ANN during training. Overall, the BBOA-SVR and ANFIS models exhibited superior training accuracy and reliability in predicting pile end-bearing capacity compared to the BBOA-ANN and MARS models.

TABLE 4. Optimization variables, their ranges, and the optimal values for adjusting the hyperparameters of proposed models

Model	Variables	Range	Best
ANN	Layer size	[5, 100]	37
	Activations Function	{'relu', 'tanh', 'sigmoid'}	"tanh"
	'Lambda'	[1e-5, 1e-1]	0.001
ANFIS	FISType	{'sugeno', 'mamdani'}	'sugeno'
	FCMOptions.NumClusters	[2, 20]	5
	FCMOptions.Exponent	[2, 20]	10
SVR	BoxConstraint	[1e-2, 1e2]	25
	KernelFunction	{'gaussian', 'linear', 'polynomial'}	gaussian
	KernelScale	[1e-3, 1e3]	4.623
	'Epsilon'	[1e-4, 1]	0.038815
MARS	maxFuncs	[5, 200]	10 (BFs)
	maxInteractions	[0, 5]	2
	C	[1, 3]	3
	Cubic	{'true', 'false'}	'false'

TABLE 5. BFs for the BBOA-MARS model

BFs	Function
BF1	max(0,0.0103 -x4)
BF2	max(0,0.0109 - x1) * max(0,0.882 - x2)
BF3	max(0, x1 - 0.0109) * max(0, x4 - 0.0769)
BF4	max(0, x1 - 0.0109) * max(0,0.0769 - x4)
BF5	BF1 * max(0,0.765 - x2)
BF6	max(0, x2 - 0.671) * max(0,0.0792 - x3)
BF7	max(0, x1 - 0.0109) * max(0, x4 - 0.41)
BF8	max(0, x1 - 0.0109) * max(0,0.41 - x4)
BF9	max(0, x1 - 0.0641)
BF10	max(0,0.0641 - x1)
where {x1, x2, x3, x4, x5} = {$\boldsymbol{\sigma_c}$, GSI, H_s, H_r, B}	

TABLE 6. Training performance of proposed models

Model	Performance indices			
	R^2	RMSE	MAE	U_{95}
Un-optimized models				
ANN	0.727	1.606	1.121	4.479
ANFIS	0.794	1.469	0.934	3.963
SVR	0.701	1.771	0.834	4.847
MARS	0.740	1.569	1.054	4.755
BBOA-optimizaed models				
ANN	0.736	1.665	1.024	4.626
ANFIS	0.874	1.150	0.799	3.188
SVR	0.826	1.352	0.713	3.754
MARS	0.802	1.443	0.966	4.009

Table 7 presents the testing performance of the proposed BBOA-optimized and un-optimized models, illustrating their generalization across diverse geotechnical conditions. The optimized MARS model achieved the highest improvement, with R^2 increasing from 0.729 to 0.790 (8.37% improvement), RMSE decreasing from 1.604 to 1.409 (12.16% reduction), MAE reducing from 1.117 to 1.010 (9.58% reduction), and U95 dropping from 4.450 to 3.936 (11.55% reduction), reflecting BBOA's optimization of BFs for robust generalization. The optimized ANFIS model also improved, with R^2 rising from 0.763 to 0.783 (2.62% improvement), RMSE decreasing from 1.495 to 1.432 (4.21% reduction), and U95 reducing from 4.103 to 3.927 (4.29% reduction). The SVR model showed moderate gains, with R^2 increasing from 0.735 to 0.752 (2.31% improvement), RMSE decreasing from 1.579 to 1.532 (2.98% reduction), and U95 reducing from 4.621 to 4.286 (7.25% reduction), despite a slight MAE increase from 1.043 to 1.094 (4.89% increase). The ANN model exhibited the least improvement, with R^2 rising from 0.710 to 0.724 (1.97% improvement), RMSE decreasing from 1.774 to 1.614 (9.02% reduction), MAE reducing from 1.155 to 1.126 (2.51% reduction), and U95 dropping from 5.659 to 4.516 (20.23% reduction). These testing results demonstrate BBOA's value in improving model robustness, particularly for MARS (best) and ANN (worst).

TABLE 7. Testing performance of proposed models

Model	Performance indices			
	R^2	RMSE	MAE	U_{95}
Un-optimized models				
ANN	0.710	1.774	1.155	5.659
ANFIS	0.763	1.495	0.955	4.103
SVR	0.735	1.579	1.043	4.621
MARS	0.729	1.604	1.117	4.450
BBOA-optimizaed models				
ANN	0.724	1.614	1.126	4.516
ANFIS	0.783	1.432	1.067	3.927
SVR	0.752	1.532	1.094	4.286
MARS	0.790	1.409	1.010	3.936

The results from the testing phase (Table 7) show that the optimized MARS and ANFIS models achieved R^2 values of 0.790 and 0.783, respectively. Their corresponding RMSE values were 1.409 and 1.432, while MAE values stood at 1.010 and 1.067. This indicates that MARS and ANFIS outperformed other models during the testing phase.

To verify that the performance improvements of BBOA-optimized models over their un-optimized counterparts were not due to random variation, paired t-tests were conducted to compare the prediction errors (absolute residuals) of optimized and un-optimized models .The tests assessed the statistical significance of differences in performance metrics, with p-values calculated for each model to evaluate the impact of BBOA-based models' hyperparametres optimization. Table 8 presents the p-values for training and testing phases, derived based on the magnitude of performance improvements observed in Tables 6 and 7.

The results in Table 8 confirm that hyperparameters optimization significantly improved the performance of all four models in both training and testing phases ($p < 0.05$). In the training phase (Table 6), the ANFIS model exhibited the most significant improvement, yielding a p-value of 0.0011, indicating strong statistical significance due to optimized fuzzy rules. The SVR model also showed substantial improvement with a p-value of 0.0023. For MARS, the p-value was 0.0122 (R^2 from 0.740 to 0.802, 8.38%), reflecting moderate but significant gains. The ANN model, with the least improvement, had a p-value of 0.0386, still indicating significance. In the testing phase (Table 7), the MARS model showed the largest improvement, with a p-value of 0.0013. The ANFIS model (R^2 from 0.763 to 0.783, 2.62%) had a p-value of 0.0154, SVR (R^2 from 0.735 to 0.752, 2.31%) had a p-value of 0.0284, and ANN, with the least improvement in Table 7, had a p-value of

TABLE 8. Statistical significance (p-values) of BBOA optimization based on the Paired t-test analysis

Model	p-value (Training)	p-value (Testing)
ANN	0.0386	0.0421
ANFIS	0.0011	0.0154
SVR	0.0023	0.0284
MARS	0.0122	0.0013

0.0421. These findings confirm that BBOA optimization significantly enhanced the accuracy and reliability of all models in both phases, particularly for ANFIS (best in training) and MARS (best in testing), and least for ANN.

Figure 7 presents a Violin plot that visually compares observed values against those predicted by various models. Figure 8, on the other hand, features scatter plots illustrating the estimated pile end-bearing capacity for the proposed hybrid BBOA-ANN, ANFIS, SVR, and MARS models, with training results depicted in blue and testing results shown in red. In a qualitative comparison, most estimated values closely align with the bisector line, with only a few points deviating by more than 20%. Additionally, the ANFIS and MARS models exhibit less dispersion in both their training and testing phases when compared to the other models. These visual representations corroborate the earlier statistical analysis, confirming that the ANFIS and MARS models outperform others in predicting pile end-bearing capacity. The visible clustering of points near the ideal line, coupled with reduced dispersion for these models, underscores their superior accuracy and reliability in both training and generalizing to new data. This graphical analysis offers an intuitive understanding of model performance, effectively complementing numerical evaluations and reinforcing the selection of ANFIS and MARS as preferred methods for this specific geotechnical application.

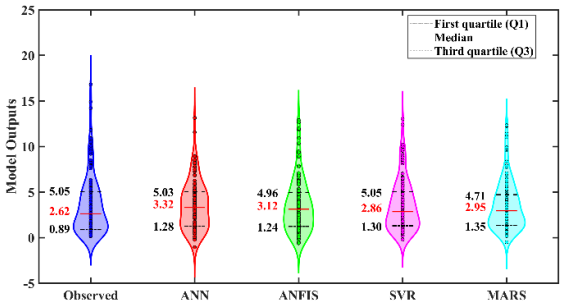

Figure 7. Violin plot for the predicted values

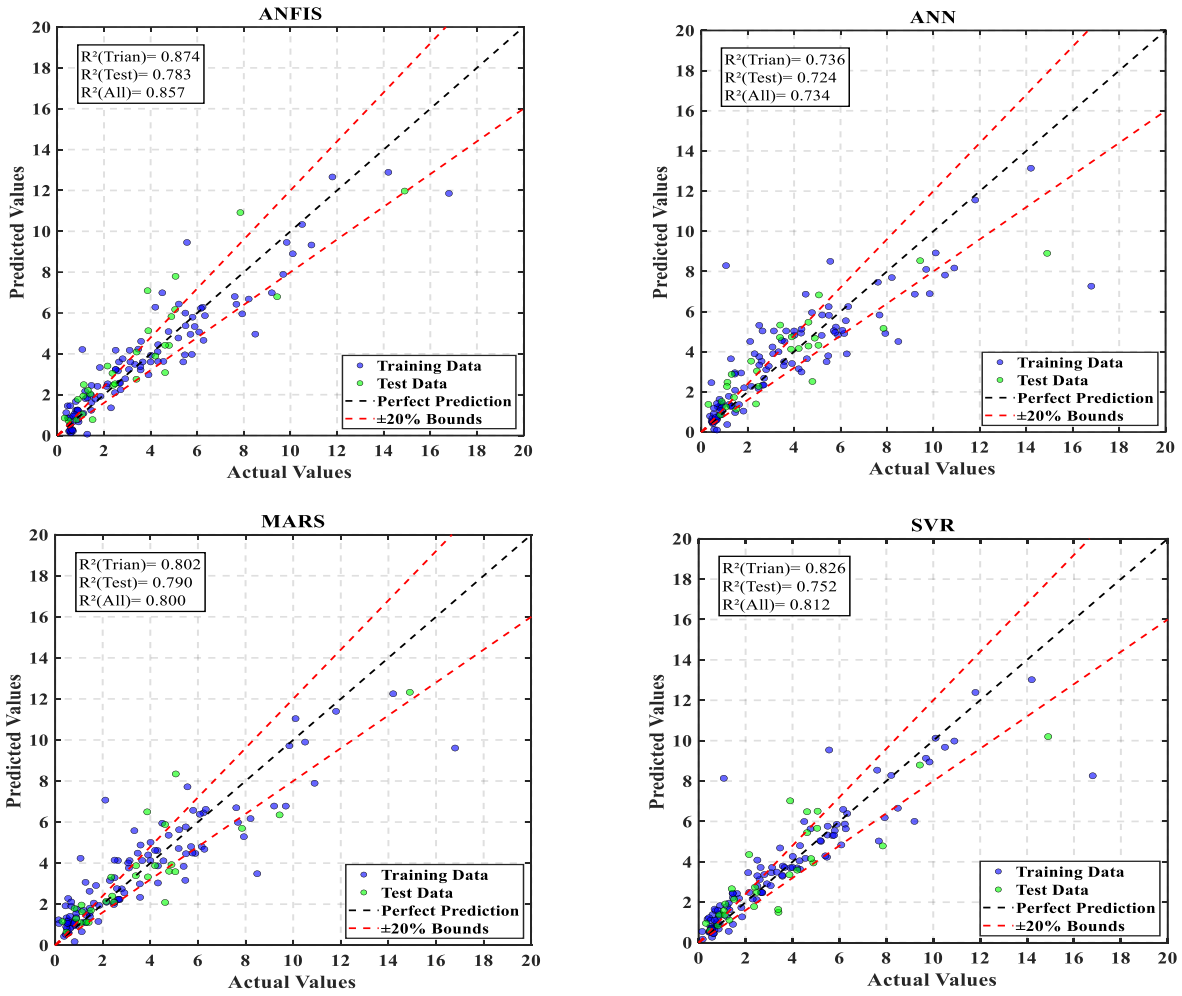

Figure 8. Scatter plot for proposed BBOA-optimized models

Figure 9 compares the computational error values of the ANN, ANFIS, SVM, and MARS models against the actual values. Additionally, Figure 10 presents a box plot illustrating the computational error values for these models' estimations of pile end-bearing capacity.

Figure 9 illustrates that over 95% of the models' computational errors fall within the range of [-3, +3]. Furthermore, the ANFIS and MARS models demonstrate greater accuracy in estimating local maxima and minima, exhibiting lower errors compared to other models. Analysis of the statistical characteristics of errors in Figure 10 reveals that the ANFIS model exhibits the smallest error range of [-4.9, +3.9] across the entire dataset. The MARS model follows, with an error range of [-7.1, +4.9]. Conversely, the ANN model exhibits the least favorable performance among the evaluated models when considering error statistics. These findings confirm the superior performance of ANFIS and MARS models, highlighting their effectiveness in capturing both overall data trends and local variations. The models' narrower error ranges signify more consistent and reliable predictions, making them particularly valuable for geotechnical engineering applications.

To better compare model performance, each model was assigned a score from 1 to 4 based on various performance indices, as detailed in Table 8. Separate scores were calculated for the training and testing phases, which then contributed to an overall ranking. The BBOA-ANFIS model achieved the top position with 15 training points, 13 testing points, and a total of 28 points, closely followed by the MARS model with a total of 23 points. Although the SVR model exhibited strong performance during the training, it ultimately ranked third overall, underscoring the critical significance of generalization capability. The ANN model consistently underperformed across both training and testing phases. However, evaluations indicate that the ANFIS model achieved the best performance during the training phase (15 points), while the MARS model excelled in the testing phase (also 15 points), rendering both highly reliable for predicting pile end-bearing capacity. Notably, the proposed BBOA-MARS model demonstrated

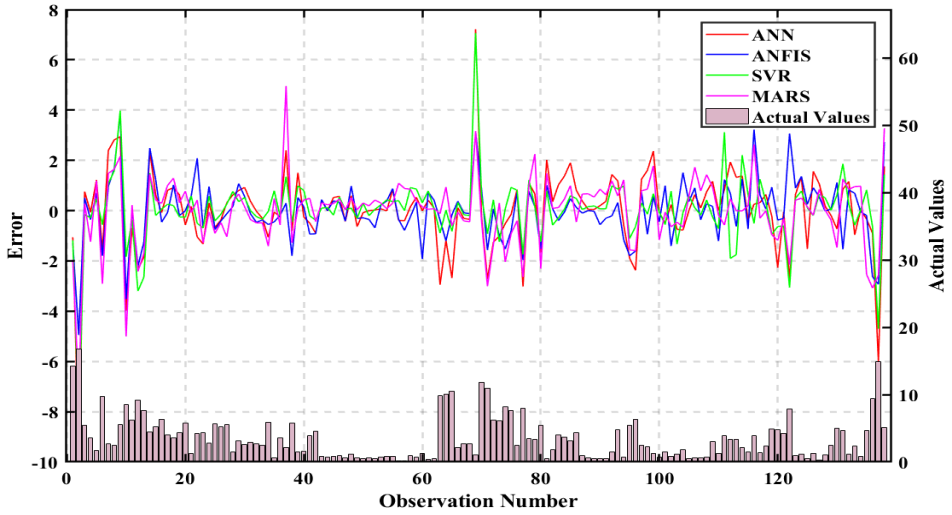

Figure 9. Distribution of computational errors between actual and predicted values

TABLE 8. Ranking of the proposed BBOA-optimized models during training and testing

Performance index	ANN		ANFIS		SVR		MARS	
	Train	Test	Train	Test	Train	Test	Train	Test
R^2	1	1	4	3	3	2	2	4
RMSE	1	1	4	3	3	2	2	4
MAE	1	1	3	3	4	2	2	4
U95	1	1	4	4	3	2	2	3
Sub total	4	4	**15**	13	13	8	8	**15**
Total score	8		28		21		23	
Rank	**Fourth**		**First**		**Third**		**Secound**	

superior generalization capabilities on the testing dataset when compared to the other models.

The model ranking in Table 8 highlights the trade-off between overfitting and generalization. Overfitting, where models overly fit training data and fail to generalize, was mitigated using 5-fold cross-validation and data normalization. MARS and ANFIS show superior generalization (Figure 8, test data), with MARS achieving the highest testing R^2 (0.790). This discussion highlights MARS's balanced performance across training and testing phases, supported by its interpretable structure, makes it particularly suitable for geotechnical applications requiring robust predictions across diverse conditions.

5. 3. Model Sensitivity Analysis A sensitivity analysis was conducted to assess how various input parameters influence the model's predictions. This is critical in geotechnical engineering, as environmental conditions significantly affect model parameters. The analysis specifically focused on the proposed BBOA-ANFIS model. It involved systematically removing individual input variables and retraining the model with the remaining parameters. Performance indicators were calculated for each iteration and compared to the original model's performance, allowing for a comprehensive assessment of each parameter's importance. This approach provides valuable insights into the factors that most significantly affect predictions of pile end-bearing capacity.

Sensitivity analysis of the ANFIS model, as shown in Figure 11, highlights the importance of input variables for predicting the end-bearing capacity of piles. The unconfined compressive strength of rock (σ_c) is identified as the most critical parameter. This is followed by the pile embedment length in rock (H_r) and the Geological Strength Index (GSI). When these parameters were individually removed from the model, the R^2 values dropped to 0.685, 0.716, and 0.740, respectively. The absence of σ_c resulted in the most significant decline in R^2 and notable increases in RMSE and MAE, underscoring its crucial role in the model's performance. H_r and GSI follow in terms of influence, while pile diameter (B) and length in the soil layer (H_s) demonstrated only a minimal impact on the model's predictive capabilities. This analysis establishes the input variable importance ranking as $\sigma_c > H_r > GSI > B > H_s$. It is crucial to recognize that the ranking of parameter importance may differ among various ML models, as each model uniquely captures the underlying relationships between input features and output variables. This variability in feature importance highlights the diverse mechanisms by which models interpret, evaluate, and assign weights to input variables during the prediction process.

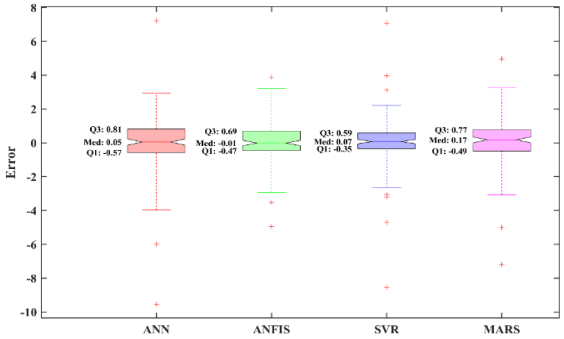

Figure 10. Box plot of the models' computational error

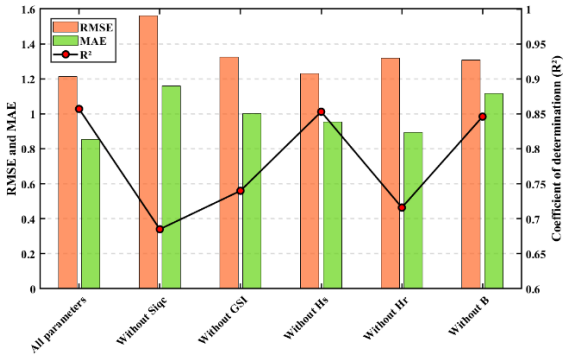

Figure 11. Sensitivity analysis for the ANFIS model

5. 4. Comparison With Empirical Models Previous studies have introduced various empirical approximations to estimate the pile end-bearing capacity, generally derived from comprehensive laboratory and field datasets. These formulations are often tailored to specific soil conditions and pile characteristics. However, their predictive accuracy can be constrained, as they may not comprehensively capture the complex nature of soil behavior and its intricate interaction with pile foundations. For instance, Zhang (4) proposed an empirical equation to estimate q_u based on the unconfined compressive strength of the rock layer (σ_c):

$$q_u = \alpha \sigma_c^k \tag{25}$$

Another modified emprical model was proposed for calculating q_u in terms of σ_c and GSI (3, 5):

$$q_u = \alpha \sigma_{cm}^k \tag{26}$$

where

$$\sigma_{cm} = (\alpha_E)^{0.7} \sigma_c \tag{27}$$

$$\alpha_E = \exp\left(\frac{GSI - 100}{18}\right) \tag{28}$$

In Equations 25 and 26, α and k represent constant coefficients, both of which are derived from the analysis of empirical data.

More recently, Zhang and Xue (6) developed a novel equation for calculating the dimensionless ultimate bearing capacity factor N_σ using gene expression programming (GEP).

$$N_\sigma = \left[\frac{GSI}{7.969} + \frac{4.466}{\sigma_c} - \min(GSI.B, \sigma_c + 6.828)\right]^{1/3} + \frac{1}{(\sigma_c + 0.776)(H_s + B)} + \frac{GSI^{1/3}}{4} + \exp\left\{\arctan\left[1 - (B - H_r)(H_s - GSI)\right] - \sigma_c\right\} + 2.009 \quad (29)$$

Adjusting empirical equations to match a specific study's data or local conditions is crucial. This essential calibration improves general models, leading to more accurate predictions suited to the particular context, thus boosting their reliability and usefulness in geotechnical engineering applications. By applying curve-fitting techniques to the current study's database, the constant parameters were determined for two different equations. For Equation 25, the values of α=5.5012 and k = 0.5703 were found, while for Equation 26, the values of α=12.4701 and k=0.66274 were obtained. The difference in coefficient values between the two equations highlights the importance of considering multiple factors, such as *GSI*, in estimation and underscores the need for customized approaches in geotechnical engineering predictions.

Table 9 compares the results from the BBOA-optimized ML models used in this study with previous models, including GMDH, RF, and GEP, as well as the outcomes from empirical models in Equations 25, 26, and 29. Additionally, Figure 12 shows a scatter plot of the

TABLE 9. The performance of existing empirical models

Ref.	Model	Performance index (All data)			
		R^2	RMSE	MAE	U_{95}
(4)	Equation 25	0.239	2.802	1.906	7.779
(3, 5)	Equation 26	0.497	2.277	1.452	6.312
(6)	Equation 29	0.328	2.632	2.230	6.735
This study	RF	0.898	1.158	0.711	-
	GMDH	0.620	1.981	1.396	-
	BPNN	0.715	1.743	1.211	-
	GEP	0.719	1.716	1.206	-
	ANN	0.734	1.655	1.045	4.596
	ANFIS	0.857	1.213	0.853	3.368
	SVR	0.812	1.390	0.790	3.860
	MARS	0.800	1.436	0.975	3.988

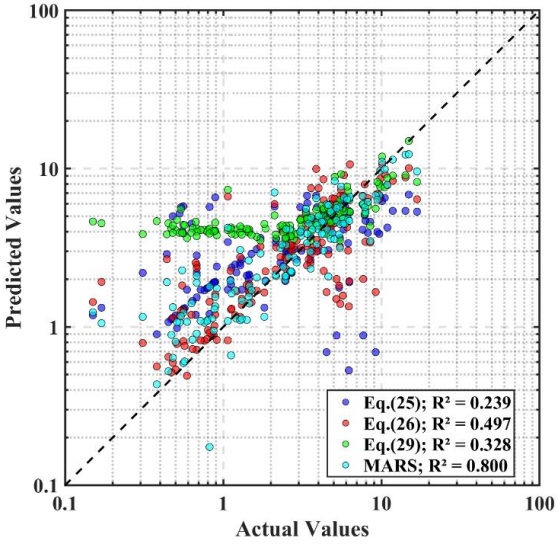

Figure 12. Scatter plot for empirical models

end- bearing capacity of rock- socketed piles for the entire dataset, based on the proposed empirical formulas.

An analysis of the scatter plot in Figure 12, along with the performance indicators of existing empirical models shown in Table 9, clearly indicates that these empirical models lack sufficient accuracy and reliability for making precise predictions. Therefore, using these models to estimate the end-bearing capacity of rock-socketed piles is generally discouraged. In contrast, ML-based models demonstrate significantly higher accuracy in these estimations. Notably, the RF model (6) outperformed all other evaluated methods on the entire dataset, achieving an R^2 of 0.898, an RMSE of 1.158, and an MAE of 0.711. Furthermore, all BBOA-optimized models in this study, especially the MARS model using Equation 24, outperformed all traditional empirical formulas (3-5) and previous ML models such as GMDH, BPNN, and GEP.

Among all the evaluated models, only the RF algorithm demonstrated superior predictive performance compared to the proposed MARS model defined in Equation 24. This result highlights the competitive effectiveness of the proposed hybrid MARS-based interpretable predictive model, which was only surpassed by RF in the assessment. Compared to empirical Equations 25, 26, and 29, the GEP model (6) achieved the highest accuracy with an R^2 of 0.719, RMSE of 1.716, and MAE of 1.206. However, the proposed MARS model (24) outperformed GEP, increasing R^2 by 11% (to 0.800), reducing RMSE by 16% (to 1.436), and lowering MAE by 19% (to 0.975). These results suggest that the proposed BBOA-MARS model offers a more reliable and accurate approach for predicting the end-bearing capacity of piles. Its adaptive nature and ability to model non-linear relationships contribute to a deeper understanding of the factors influencing the prediction.

5. 5. SHAPE-based Model Interpreting In predictive modeling, evaluating individual predictor impact is crucial, but complex machine learning models often lack interpretability. To overcome this, SHAP (SHapley Additive exPlanations) was used to interpret the model by quantifying each input variable's contribution. The most significant variable is identified as the one with the highest absolute SHAP value. By framing prediction as a cooperative game, SHAP applies Shapley values to fairly distribute the prediction's outcome among predictors, based on their average marginal contributions, thus offering a transparent and equitable measure of feature importance within an additive model framework.

SHAP estimates the target of the main model, F(x), by employing an explanatory model, represented as g(x'), as follows (15, 16, 51, 53):

$$F(x)=G(x')=\psi_0+\sum_{j=1}^{n}\psi_j x'_j \tag{30}$$

where ψ_j denotes the impact of each feature (SHAP value), n denotes the number of simplified inputs, and x' is the simplified inputs that are mapped to the original input x through a mapping function $x=H_x(x')$.

According to Equation 31, SHAP value (ψ_j) can be calculated for each variable as follws:

$$\psi_j=\sum_{z'\subseteq x'}^{n}\frac{|z'|(n-|z'|-1)!}{n!}\left[F_x(z')-F_x(z'\setminus j)\right] \tag{31}$$

where $z'\in[0,1]^n$, $|z'|$ denotes the number of non-zero entries in z', $z'\setminus j$ denotes setting $z'_j=0$, and $F_x(z')=E\left[\left(F(z)|z_S\right)\right]$ represents the expected value of F(z) given the subset of features z, where S denotes the set of non-zero input features in z (55).

This framework elucidates the predictive model's internal mechanics, revealing the importance of individual predictors. We selected this model for integration with SHAP to pinpoint the key drivers of predictions. Figure 13 shows the average contribution of input variables to the model's prediction of end-bearing capacity for rock-socketed piles, based on mean SHAP values. Figure 14 summarizes these SHAP values, illustrating how increasing feature values impact the model output; red indicates a strong positive impact, and blue indicates a low or negative impact.

In Figure 14, overlapping data points obscure patterns and hinder interpretation of feature effects, especially pile length within soil and rock layers. However, analyzing the average SHAPE values in Figure 13 shows that the unconfined compressive strength of the rock (σ_c) is the most influential factor, directly determining the rock's mechanical resistance and the pile's ultimate end-bearing capacity. GSI ranks second, reflecting rock mass quality and joint conditions that significantly influence rock deformability and strength, impacting pile-rock interaction. Pile diameter (B) substantially affects load distribution and bearing capacity by increasing the contact area at the pile tip. Pile embedment length in rock (H_r) contributes to anchorage and frictional resistance, though less significantly than rock properties and diameter. Pile length in the soil layer (H_s) has the least influence because end-bearing capacity is primarily determined by pile-rock interface conditions, with the soil layer mainly affecting shaft friction. This ranking emphasizes the dominance of rock mechanical properties and pile geometry in estimating tip bearing capacity, with soil parameters playing a minor role.

The ANFIS sensitivity analysis (Figure 11) and SHAP-based variable contribution analyses (Figure 13) identified σ_c, GSI, and H_r as dominant factors for q_u. Higher σ_c (and GSI) enhances compressive resistance, enabling the rock to withstand greater stresses, while increasing H_r in weak rocks improves load transfer by expanding the pile-rock interface, guiding design decisions like optimizing socket length. Conversely, H_s exhibited minimal impact, as both SHAP and ANFIS analyses consistently ranked it as the least influential variable. This is attributed to the lower stiffness and strength of soil compared to rock, which limits its contribution to the end-bearing capacity of rock-socketed piles.

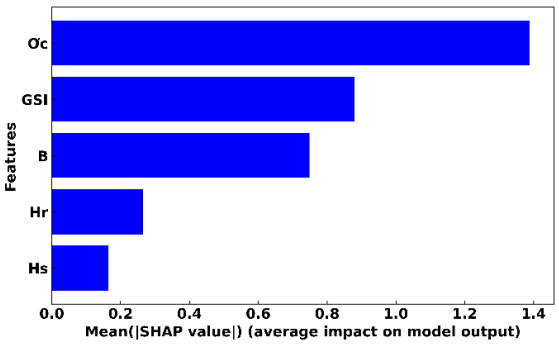

Figure 13. Average contribution of input variables

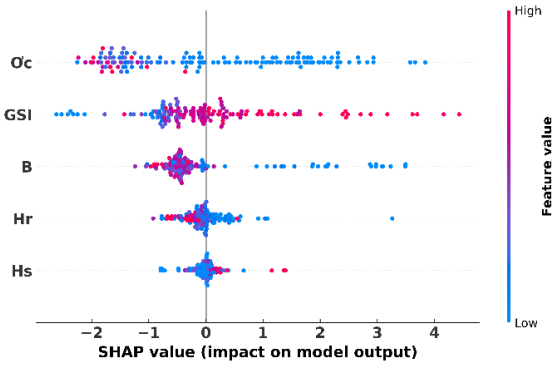

Figure 14. Summary SHAP plot

The SHAPE-based model interpretation highlights the dominant influence of rock mechanical properties and pile geometry in estimating the end-bearing capacity of rock-socketed piles. However, the accuracy of these estimations hinges on the reliability of the input parameters. Small variations in rock strength or pile dimensions can lead to significant discrepancies in the predicted bearing capacity. Furthermore, the complex interaction between the pile tip and the surrounding rock mass is often simplified in analytical models, potentially overlooking crucial factors such as rock fracturing and stress redistribution. Therefore, while these factors provide a valuable framework for preliminary assessments, they should be complemented by in situ testing and numerical analyses to ensure a comprehensive and accurate evaluation of pile tip bearing capacity.

6. CONCLUSION

This study addressed critical research gaps in predicting the end-bearing capacity of rock-socketed piles by proposing a hybrid framework that integrated SHapley Additive exPlanations (SHAP) for model interpretability and the Brown-Bear Optimization Algorithm (BBOA) for hyperparameter optimization. The BBOA was employed to automatically tune four machine learning models, including Artificial Neural Networks (ANN), Support Vector Regression (SVR), Adaptive Neuro-Fuzzy Inference Systems (ANFIS), and Multivariate Adaptive Regression Splines (MARS), leading to significant improvements in predictive accuracy. Notably, the study introduced a novel interpretable MARS-based formula tailored for practical design applications and employed SHAP values to enhance transparency in identifying key geotechnical factors influencing pile performance. Multiple statistical performance indices, including the coefficient of determination (R^2), root mean squared error (RMSE), mean absolute error (MAE), and the U95 metric, were utilized to provide a robust and nuanced evaluation, benchmarking the proposed models against advanced machine learning approaches and established empirical formulas. Moreover, the results of the proposed BBOA-optimized models were also compared with those of the corresponding un-optimized baseline models using the statistical t-test, as well as with outcomes from machine learning approaches and existing empirical relationships reported in prior studies.

The key findings of this research include:

- Framework Advancements and Practical Implications: he hybrid BBOA-SHAP-ML framework advances the state of the art by combining robust hyperparameter optimization, model transparency, and practical formula derivation. The novel MARS-based equation offers a user-friendly, interpretable tool that balances accuracy and usability, facilitating safer and more cost-effective foundation design in heterogeneous soil-rock environments. The MARS model's interpretability makes it particularly valuable for engineering practice. Nonetheless, the accuracy of all models depends on the quality and representativeness of input data, emphasizing the need for careful site characterization and validation.
- Statistical Validation of BBOA Optimization Impact: The BBOA-optimized models demonstrated improved performance metrics compared to their un-optimized counterparts. During training, ANFIS exhibited the most substantial gains, with R^2 increasing by 10.08%, RMSE decreasing by 21.72%, MAE reducing by 14.45%, and U95 dropping by 19.56%. ANN showed the least improvement in training. In testing, MARS achieved the largest gains, with R^2 improving by 8.37%, RMSE decreasing by 12.16%, MAE reducing by 9.58%, and U95 dropping by 11.55%, while ANN had the smallest improvement. Paired t-tests confirmed the statistical significance ($p<0.05$) of these improvements for ANFIS ($p=0.0011$) and SVR ($p=0.0023$) in training, and for MARS ($p=0.0013$) and ANFIS ($p=0.0154$) in testing, indicating BBOA's robustness. ANN's enhancements were the least statistically significant ($p=0.0386$ training, $p=0.0421$ testing).
- Performance Evaluation: The hybrid BBOA-optimized models developed in this study exhibited varying rankings depending on the statistical performance indices. During the training phase, ANFIS achieved the highest R^2 (0.874), followed by SVR (0.826), MARS (0.802), and ANN (0.736). In the testing phase, MARS led with an R^2 of 0.790, followed by ANFIS (0.783), SVR (0.752), and ANN (0.724). Considering the entire dataset, ANFIS and ANN, respectively, demonstrated the best and worst overall performances with R^2 values of 0.857 and 0.734. The overall ranking based on the combined indices was ANFIS > SVR > MARS > ANN for the training set and MARS > ANFIS > SVR > ANN for the testing set, with ANN consistently showing the weakest performance.
- Model Sensitivity Analysis: The sensitivity analysis of the ANFIS model revealed that the unconfined compressive strength of rock (σ_c) is the most influential input parameter, with its removal causing the largest decline in model performance (R^2 dropped to 0.685). The pile embedment length in rock (H_r) and Geological Strength Index (GSI) were identified as the second and third most important factors, with R^2 reductions to 0.716 and 0.740, respectively. Other parameters, such as pile

diameter (B) and pile length in the soil layer (H_s), had minimal effects. This ranking ($\sigma_c > H_r > GSI > B > Hs$) underscores the critical role of rock mechanical properties and pile embedment characteristics, reinforcing the geotechnical understanding of pile-soil-rock interaction.

- Comparative Performance Evaluation: The proposed hybrid BBOA-optimized models outperformed previous ML models like Group Method of Data Handling (GMDH), Backpropagation Neural Networks (BPNN), and Gene Expression Programming (GEP). When benchmarked against traditional empirical equations, all ML models outperformed empirical approaches in terms of accuracy and reliability. Notably, the proposed MARS-based interpretable formula (24) achieved an 11.3% improvement in R^2, a 16.6% reduction in RMSE, and a 19.2% decrease in MAE, relative to the previously best-performing GEP model, making it a more dependable and practical method for estimating the end-bearing capacity of rock-socketed piles.
- SHAP-Driven Interpretability: SHAP analysis of the optimized models provided transparent interpretability, highlighting the importance of rock strength (σ_c) and GSI on pile performance, with pile diameter (B) also significantly contributing. Moreover, pile length in the soil layer (H_s) had a negligible effect, aligning with the principle that end-bearing capacity is primarily controlled by pile-rock interface conditions. This interpretability framework offers engineers actionable insights into geotechnical mechanisms, overcoming the "black-box" limitation of many ML models.
- Cross-Model Analysis of Input Variable Impact: The sensitivity analysis results and the SHAP-based interpretability of the MARS model provided complementary perspectives on input variable influence. While sensitivity quantifies the global impact of a variable on model performance, SHAP values offer local, instance-level explanations of feature contributions. Both methods consistently highlighted σ_c, H_r, and GSI as dominant factors affecting pile capacity. These differences reflect the distinct modeling frameworks and interpretative scopes, emphasizing that feature importance is inherently model-dependent.

This research bridges the gap between advanced ML methodologies and practical geotechnical engineering by delivering optimized, interpretable, and reliable models for predicting end-bearing capacity of of rock-socketed piles. The combined use of metaheuristic optimization and explainable AI offers a promising pathway for future developments in pile foundation design, encouraging integration of data-driven methods with traditional engineering knowledge. The BBOA-SHAP-ML hybrid models show promise, but accuracy and computational efficiency could be further improved by using more predictive variables, larger datasets, and exploring alternative ML or optimization algorithms.

7. REFERENCES

1. Hassan A, Rashid H. Estimation of Ultimate Bearing Capacity in Rock-Socketed Piles Using Optimized Machine Learning Approaches. Advances in Engineering and Intelligence Systems. 2023;2(04):107-20. https://doi.org/10.22034/AEIS.2023.427941.1150
2. Onyelowe KC, Hanandeh S, Kamchoom V, Ebid AM, Reyes Silva FD, Allauca Palta JL, et al. Developing advanced datadriven framework to predict the bearing capacity of piles on rock. Scientific Reports. 2025;15(1):11051. https://doi.org/10.1038/s41598-025-96186-1
3. Chen H, Zhang L. A machine learning-based method for predicting end-bearing capacity of rock-socketed shafts. Rock Mechanics and Rock Engineering. 2022;55(3):1743-57. https://doi.org/10.1007/s00603-021-02757-9
4. Zhang L. Drilled shafts in rock: analysis and design: CRC press; 2004.
5. Zhang L. Prediction of end-bearing capacity of rock-socketed shafts considering rock quality designation (RQD). Canadian Geotechnical Journal. 2010;47(10):1071-84. https://doi.org/10.1139/T10-016
6. Zhang R, Xue X. A novel hybrid model for predicting the end-bearing capacity of rock-socketed piles. Rock Mechanics and Rock Engineering. 2024;57(11):10099-114. https://doi.org/10.1007/s00603-024-04094-z
7. Jeong S, Kim D, Park J. Empirical bearing capacity formula for steel pipe prebored and precast piles based on field tests. International Journal of Geomechanics. 2021;21(9):04021165. https://doi.org/10.1061/(ASCE)GM.1943-5622.0002112
8. Picardo A, Millán M, Galindo R, Alencar A. Revisiting the analytical solutions for ultimate bearing capacity of pile embedded in rocks. Journal of Rock Mechanics and Geotechnical Engineering. 2023;15(6):1506-19. https://doi.org/10.1016/J.JRMGE.2022.11.012
9. ESLAMI AA, GHOLAMI AM. Analytical model for the ultimate bearing capacity of foundations from cone resistance. 2006.
10. Yang X, Gong W, Yin Q. Numerical Simulation Study of Bearing Characteristics of Large-Diameter Flexible Piles Under Complex Loads. Buildings. 2024;14(11):3651. https://doi.org/10.3390/buildings14113651
11. Leong WK, Yusoff NA, Abd Aziz AN, Abu Talib Z. Theoretical and actual bearing capacity of driven piles using model piles in sand. Applied Mechanics and Materials. 2015;773:1453-9. https://doi.org/10.4028/www.scientific.net/AMM.773-774.1453
12. Gör M. Hybrid predictive machine learning models to evaluate the bearing capacity of concrete and steel piles. Steel and Composite Structures. 2024;53(4):377. https://doi.org/10.12989/scs.2024.53.4.377
13. Ülker M, Altınok E, Taşkın G. Data-driven modeling of ultimate load capacity of closed-and open-ended piles using machine learning. International Journal of Geotechnical Engineering. 2023;17(4):393-407. https://doi.org/10.1080/19386362.2023.2251795
14. Fattahi H, Jiryaee F. Estimation of lateral load capacity of piles using a new intelligent combination method. Modares Civil Engineering journal. 2022;22(5):223-33. https://doi.org/10.22034/22.5.223
15. Alizamir M, Wang M, Ikram RMA, Gholampour A, Ahmed KO, Heddam S, et al. An interpretable XGBoost-SHAP machine

learning model for reliable prediction of mechanical properties in waste foundry sand-based eco-friendly concrete. Results in Engineering. 2025;25:104307. https://doi.org/10.1016/j.rineng.2025.104307

16. Safaeian Hamzehkolaei N, Barkhordari MS. Hybrid soft computing-based predictive models for shear strength of exterior reinforced concrete beam-column joints. Multiscale and Multidisciplinary Modeling, Experiments and Design. 2025;8(1):29. https://doi.org/10.1007/S41939-024-00608-Y/METRICS
17. Pham TA, Tran VQ, Vu H-LT, Ly H-B. Design deep neural network architecture using a genetic algorithm for estimation of pile bearing capacity. PLoS One. 2020;15(12):e0243030. https://doi.org/10.1371/journal.pone.0243030
18. Nguyen DD, Nguyen HP, Vu DQ, Prakash I, Pham BT. Using GA-ANFIS machine learning model for forecasting the load bearing capacity of driven piles. Journal of Science and Transport Technology. 2023;3(2):26-33. https://doi.org/10.58845/jstt.utt.2023.en.3.2.26-33
19. Jebur AA, Atherton W, Alkhadar RM, Loffill E. Piles in sandy soil: A numerical study and experimental validation. Procedia Engineering. 2017;196:60-7. https://doi.org/10.1016/j.proeng.2017.07.173
20. Jahed Armaghani D, Shoib RSNSBR, Faizi K, Rashid ASA. Developing a hybrid PSO–ANN model for estimating the ultimate bearing capacity of rock-socketed piles. Neural Computing and Applications. 2017;28(2):391-405. https://doi.org/10.1007/s00521-015-2072-z
21. Benbouras MA, Petrişor A-I, Zedira H, Ghelani L, Lefilef L. Forecasting the bearing capacity of the driven piles using advanced machine-learning techniques. Applied sciences. 2021;11(22):10908. https://doi.org/10.3390/app112210908
22. Yong W, Zhou J, Jahed Armaghani D, Tahir M, Tarinejad R, Pham BT, et al. A new hybrid simulated annealing-based genetic programming technique to predict the ultimate bearing capacity of piles. Engineering with Computers. 2021;37(3):2111-27. https://doi.org/10.1007/s00366-019-00932-9
23. Armaghani DJ, Harandizadeh H, Momeni E, Maizir H, Zhou J. An optimized system of GMDH-ANFIS predictive model by ICA for estimating pile bearing capacity. Artificial Intelligence Review. 2022;55(3):2313-50. https://doi.org/10.1007/s10462-021-10065-5
24. Pham TA, Vu H-LT. Application of ensemble learning using weight voting protocol in the prediction of pile bearing capacity. Mathematical Problems in Engineering. 2021;2021(1):5558449. https://doi.org/10.1155/2021/5558449
25. Harandizadeh H, Jahed Armaghani D, Khari M. A new development of ANFIS–GMDH optimized by PSO to predict pile bearing capacity based on experimental datasets. Engineering with Computers. 2021;37(1):685-700. https://doi.org/10.1007/s00366-019-00849-3
26. Gohil R, Parthasarathy C, editors. Intelligent Assessment of Axial Capacity of Pipe Piles Using High Strain Dynamic Pile Load Tests in Offshore Environment. Indian Geotechnical Conference; 2021: Springer.
27. Hoang N-D, Tran X-L, Huynh T-C. Prediction of Pile Bearing Capacity Using Opposition-Based Differential Flower Pollination-Optimized Least Squares Support Vector Regression (ODFP-LSSVR). Advances in Civil Engineering. 2022;2022(1):7183700. https://doi.org/10.1155/2022/7183700
28. Amâncio LB, Dantas SA, Cunha RPd. Estimative of shaft and tip bearing capacities of single piles using multilayer perceptrons. Soils and Rocks. 2022;45(3):e2022077821. https://doi.org/10.28927/SR.2022.077821
29. Jin L, Ji Y. Development of an IRMO-BPNN based single pile ultimate axial bearing capacity prediction model. Buildings. 2023;13(5):1297. https://doi.org/10.3390/buildings13051297
30. Shoaib MM, Abu-Farsakh MY. Exploring tree-based machine learning models to estimate the ultimate pile capacity from cone penetration test data. Transportation Research Record. 2024;2678(1):136-49. https://doi.org/10.1177/03611981231170128
31. Assaad RH, Hu X, Hussein M. Expert knowledge–guided Bayesian belief networks for predicting bridge pile capacity. Journal of Bridge Engineering. 2023;28(9):04023058. https://doi.org/10.1061/jbenf2.beeng-6096
32. Shen Y. Optimized systems of multi-layer perceptron predictive model for estimating pile-bearing capacity. Journal of Engineering and Applied Science. 2024;71(1):52. https://doi.org/10.1186/s44147-024-00386-x
33. Picardo A, Millán M, Galindo R, Andrés-Hernandez J, de Alencar AS, editors. Pile tip bearing capacity in rock masses: analytical and numerical analysis comparison. IOP Conference Series: Earth and Environmental Science; 2023: IOP Publishing.
34. You R, Mao H. Assessment of ultimate bearing capacity of rock-socketed piles using hybrid approaches. Multiscale and Multidisciplinary Modeling, Experiments and Design. 2024;7(4):3673-94. https://doi.org/10.1007/s41939-024-00425-3
35. Kumar M, Kumar DR, Khatti J, Samui P, Grover KS. Prediction of bearing capacity of pile foundation using deep learning approaches. Frontiers of Structural and Civil Engineering. 2024;18(6):870-86. https://doi.org/10.1007/s11709-024-1085-z
36. Ren J, Sun X. Prediction of ultimate bearing capacity of pile foundation based on two optimization algorithm models. Buildings. 2023;13(5):1242. https://doi.org/10.3390/buildings13051242
37. Galib MMH, Billah MM, Mofiz SA, editors. Prediction of bearing capacity of pile using support vector and catboost regression. AIP Conference Proceedings; 2025: AIP Publishing LLC.
38. Millán M, Picardo A, Galindo R. Application of artificial neural networks for predicting the bearing capacity of the tip of a pile embedded in a rock mass. Engineering Applications of Artificial Intelligence. 2023;124:106568. ttps://doi.org/10.1016/j.engappai.2023.106568
39. Hoek E, Brown ET. Practical estimates of rock mass strength. International journal of rock mechanics and mining sciences. 1997;34(8):1165-86. https://doi.org/10.1016/S1365-1609(97)80069-X
40. Vatani A, Jafari-Asl J, Ohadi S, Safaeian Hamzehkolaei N, Afzali Ahmadabadi S, Correia JA, editors. An efficient surrogate model for reliability analysis of the marine structure piles. Proceedings of the Institution of Civil Engineers-Maritime Engineering; 2023: Emerald Publishing Limited.
41. Zarbazoo Siahkali M, Ghaderi A, Bahrpeyma AH, Rashki M, Safaeian Hamzehkolaei N. Estimating pier scour depth: comparison of empirical formulations with ANNs, GMDH, MARS, and Kriging. Journal of AI and Data Mining. 2021;9(1):109-28. https://doi.org/10.22044/jadm.2020.10085.2147
42. Safaeian Hamzehkolaei N, Miri M, Rashki M. An improved binary bat flexible sampling algorithm for reliability-based design optimization of truss structures with discrete-continuous variables. Engineering Computations. 2018;35(2):641-71. https://doi.org/10.1108/EC-06-2016-0207
43. Safaeian Hamzehkolaei N, MiarNaeimi F. A new hybrid multi-level cross-entropy-based moth-flame optimization algorithm. Soft Computing. 2021;25(22):14245-79. https://doi.org/10.1007/s00500-021-06109-1
44. Khastar S, Bashirizadeh F, Jafari-Asl J, Safaeian Hamzehkolaei N. Predicting the cooling and heating loads of energy efficient buildings: a hybrid machine learning approach. Cluster Computing. 2025;28(5):1-18. https://doi.org/10.1007/S10586-024-04993-4/FIGURES/3

45. Hamzehkolaei NS, Kadkhoda N. An efficient ranked Voronoi diagram-based hybrid method for reliability-based structural analysis and design optimization. Soft Computing. 2023;27(19):13889-910. https://doi.org/10.1007/s00500-023-08450-z
46. Hamzehkolaei NS, Ghavaminejadb S, Barkhordaric M. Predictive Model of Bond Strength in Reinforced Concrete Structures: A Hybrid Metaheuristic-optimized Neural Network Approach. International Journal of Engineering, Transactions B: Applications. 2025;38(5):1190-212. https://doi.org/10.5829/IJE.2025.38.05B.19
47. Barkhordari M, Khoshnazar S. Fuzzy-enhanced Convolutional Neural Network for Predicting Structural Responses to Seismic Excitations. International Journal of Engineering, Transactions B: Applications. 2025;38(6):1293-306. https://doi.org/10.5829/ije.2025.38.06c.04
48. Prakash T, Singh PP, Singh VP, Singh SN. A novel brown-bear optimization algorithm for solving economic dispatch problem. Advanced control & optimization paradigms for energy system operation and management: River Publishers; 2023. p. 137-64.
49. Zhang G, Hamzehkolaei NS, Rashnoozadeh H, Band SS, Mosavi A. Reliability assessment of compressive and splitting tensile strength prediction of roller compacted concrete pavement: introducing MARS-GOA-MCS. International Journal of Pavement Engineering. 2022;23(14):5030-47. https://doi.org/10.1080/10298436.2021.1990920
50. Azar NA, Kardan N, Milan SG. Developing the artificial neural network–evolutionary algorithms hybrid models (ANN–EA) to predict the daily evaporation from dam reservoirs. Engineering with Computers. 2023;39(2):1375-93. https://doi.org/10.1007/s00366-021-01523-3
51. Moodi Y, Hamzehkolaei NS, Afshoon I. Intelligent Models for Predicting the Compressive Strength of Green Concrete Made with Fine and Coarse Grains of Waste Copper Slag. 2024. https://doi.org/10.48301/KSSA.2024.441580.2833
52. Ashrafian A, Hamzehkolaei NS, Dwijendra NKA, Yazdani M. An evolutionary neuro-fuzzy-based approach to estimate the compressive strength of eco-friendly concrete containing recycled construction wastes. Buildings. 2022;12(8):1280. https://doi.org/10.3390/buildings12081280
53. Moodi Y, Hamzehkolaei NS, Afshoon I. Machine learning models for predicting compressive strength of eco-friendly concrete with copper slag aggregates. Materials Today Communications. 2025:112572. https://doi.org/10.1016/j.mtcomm.2025.112572
54. Safaeian Hamzehkolaei N, Alizamir M. Performance evaluation of machine learning algorithms for seismic retrofit cost estimation using structural parameters. Journal of Soft Computing in Civil Engineering. 2021;5(3):32-57. https://doi.org/10.22115/SCCE.2021.284630.1312
55. Lundberg SM, Lee S-I. A unified approach to interpreting model predictions. Advances in neural information processing systems. 2017;30. https://arxiv.org/abs/1705.07874v2

COPYRIGHTS

©2026 The author(s). This is an open access article distributed under the terms of the Creative Commons Attribution (CC BY 4.0), which permits unrestricted use, distribution, and reproduction in any medium, as long as the original authors and source are cited. No permission is required from the authors or the publishers.

Persian Abstract

چکیده

این مطالعه مدل ترکیبی و تفسیرپذیر ارائه می‌دهد که با ادغام روش‌های تبیین افزایشی شاپلی (SHAP) و الگوریتم بهینه‌سازی خرس قهوه‌ای (BBOA)، دقت پیش‌بینی ظرفیت باربری نوک شمع‌های واقع در لایه سنگ را بهبود می‌بخشد. در روش پیشنهادی، پارامترهای چهار مدل یادگیری ماشین شامل شبکه عصبی مصنوعی (ANN)، رگرسیون بردار پشتیبان (SVR)، سیستم استنتاج عصبی–فازی تطبیقی (ANFIS) و رگرسیون چندمتغیره اسپلاین‌های تطبیقی (MARS) با استفاده از الگوریتم خرس قهوه‌ای بهینه‌سازی شده‌اند که منجر به افزایش قابل توجه دقت پیش‌بینی شده است. همچنین، یک رابطه جدید تفسیرپذیر مبتنی بر مدل MARS برای پیش‌بینی ظرفیت باربری شمع پیشنهاد شده است که از ورودی‌هایی مانند قطر شمع (B)، عمق مدفون‌شدگی در خاک (H_s) و سنگ (H_r)، مقاومت فشاری سنگ (σ_c) و شاخص کیفیت توده سنگ (GSI) بهره می‌برد. ارزیابی جامع با شاخص‌های آماری متنوع (ضریب تبیین R^2، ریشه میانگین مربعات خطا RMSE، میانگین خطای مطلق MAE و شاخص U95) نشان داد که مدل BBOA-ANFIS در مرحله آموزش بیشترین دقت را دارد، در حالی که مدل بهینه‌شده MARS در مرحله آزمون بهترین عملکرد را ارائه می‌دهد و ANN ضعیف‌ترین نتایج را نشان می‌دهد. در مقایسه با مدل‌های یادگیری ماشین و روابط تجربی پیشین، مدل‌های پیشنهادی به‌ویژه رابطه پیشنهادی توسط مدل MARS با بهبود ۱۱.۳ درصدی در R^2، ۱۶.۶ درصدی در RMSE و ۱۹.۲ درصدی در MAE نسبت به بهترین مدل تجربی قبلی، دقت و قابلیت اطمینان بالاتری دارند. علاوه بر این، تحلیل حساسیت و تفسیر مدل مبتنی بر SHAP، عوامل کلیدی تأثیرگذار را به ترتیب $\sigma_c > GSI > B > H_r > H_s$ شناسایی کردند که مقاومت فشاری سنگ بیشترین و عمق مدفون‌شدگی در خاک کمترین تأثیر را در مدل تخمین ظرفیت باربری نوک شمع دارند. این رویکرد ترکیبی، ابزاری قوی، تفسیرپذیر و مقرون‌به‌صرفه برای طراحی دقیق و اقتصادی شمع‌ها در محیط‌های پیچیده خاکی–سنگی فراهم می‌آورد.

IJE TRANSACTIONS B: Applications Vol. 39, No. 08, (August 2026) 1953-1975

International Journal of Engineering

Journal Homepage: www.ije.ir

A Multi-objective Optimization Model for Intelligent Information Management in Resource-Constrained Road and Transportation Projects

S. K. Mousavi[a], S. A. Hosseini*[b], H. R. Vosoughifar[b], R. Barandoust[c], G. Mohammadi[d]

[a] *Department of Civil Engineering, Construction Management, ST.C., Islamic Azad University, Tehran, Iran*
[b] *Department of Civil Engineering, ST.C., Islamic Azad University, Tehran, Iran*
[c] *Department of Industrial Management, YI.C., Islamic Azad University, Tehran, Iran*
[d] *Department of Mining Engineering, ST.C., Islamic Azad University, Tehran, Iran*

PAPER INFO

Paper history:
Received 02 August 2025
Received in revised form 16 September 2025
Accepted 28 September 2025

Keywords:
Project Information Management
Critical Chain
Resource Constraints
Particle Swarm Optimization
Multi-project Scheduling

ABSTRACT

This study proposes a mathematical model to optimize information management in road and transportation contracting projects under resource constraints, utilizing Critical Chain Project Management (CCPM). A multi-objective optimization framework is developed for multi-project scheduling, balancing time, cost, and quality as core performance indicators. The Particle Swarm Optimization (PSO) algorithm is employed to solve the model due to its efficiency in handling complex, nonlinear problems. The model is validated through a case study of three real-world projects encompassing 24 activities with diverse resource constraints. Compared to the traditional Critical Path Method (CPM), the CCPM-based approach reduces total duration from 68 to 47 days, total cost from 108,680 to 63,710 units, and improves the quality index from 0.412 to 0.5764, achieving a 21-day time saving, 25.97% cost reduction, and 40% quality improvement. Sensitivity analysis reveals that resource availability, particularly resources K2 and K3, significantly impacts outcomes, with K2 limitations increasing duration to 84 days and cost to 88,110 units, and K3 limitations extending duration to 81 days and cost to 86,910 units. These findings demonstrate the model's effectiveness in enhancing decision-making and resource planning in complex construction environments.

***doi**: 10.5829/ije.2026.39.08b.14*

Graphical Abstract

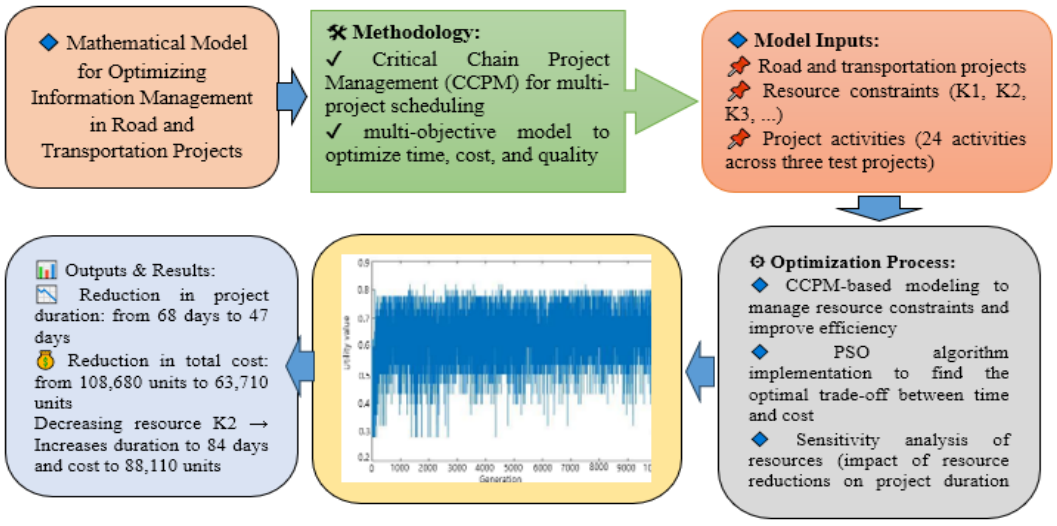

*Corresponding author email: azim_hosseini@azad.ac.ir (S. A. Hosseini)

Please cite this article as: Mousavi SK, Hosseini SA, Vosoughifar HR, Barandoust R, Mohammadi G. A Multi-objective Optimization Model for Intelligent Information Management in Resource-Constrained Road and Transportation Projects. International Journal of Engineering, Transactions B: Applications. 2026;39(08):1953-75.

1. INTRODUCTION

The growing complexity and scale of road and transportation infrastructure projects have created a strong demand for advanced planning, coordination, and information management systems. Such projects typically involve multiple stakeholders—contractors, engineers, regulators, and suppliers—and take place in dynamic environments with changing resources, evolving regulations, and external uncertainties (1). Throughout the project lifecycle, from early planning and feasibility studies to execution and closure, large amounts of diverse data are generated. Effective management of this data is crucial for optimizing resource use, reducing delays, controlling costs, and supporting timely, data-driven decisions (2).

Despite the importance of effective information management, many transportation projects still rely on fragmented, informal, and largely manual processes. Data is often recorded inconsistently, stored in isolated silos, and exchanged through unstandardized or paper-based documentation. These shortcomings lead to miscommunication, slow response times, and poor decision-making, ultimately undermining overall project performance (3). The lack of a centralized platform for systematic data collection, processing, and analysis further amplifies problems such as redundancy, inconsistency, and inefficiency (4).

Over the past few decades, several project management methodologies—most notably the Critical Path Method (CPM) and, more recently, Critical Chain Project Management (CCPM)—have been developed to address challenges in scheduling and resource management. CCPM, introduced by Goldratt in the 1990s, incorporates resource constraints and buffer management into the scheduling process, improving resilience to uncertainty and aligning plans more closely with real-world resource dynamics (5, 6). Despite its potential, CCPM adoption in the transportation sector remains limited and fragmented. Available tools are often specialized for single functions, such as cost estimation or scheduling, and lack an integrated framework for managing the complexity of large infrastructure projects (7). One of the most critical challenges in such projects is the Resource-Constrained Project Scheduling Problem (RCPSP), particularly when multiple projects must compete for shared resources. RCPSP—and its extension, the Project Crashing Problem under Resource Constraints (PCPSP)—requires simultaneous optimization of competing objectives, including time, cost, and quality, while satisfying intricate precedence relationships and resource limitations (8).

Moreover, project stakeholders are often required to coordinate decisions across disconnected systems, frequently without access to real-time or reliable data. This lack of integration leads to reactive decision-making and missed opportunities for proactive project control (9, 10). To overcome these challenges, advanced technologies—such as artificial intelligence (AI), big data analytics, and intelligent decision support systems (IDSS)—have been introduced. These solutions can automate data collection, detect bottlenecks, anticipate resource conflicts, and optimize schedules in near real time. Nevertheless, their practical implementation in transportation projects remains limited, especially when combined with advanced scheduling approaches like CCPM (11, 12).

This study introduces a comprehensive multi-objective optimization framework that integrates Critical Chain Project Management (CCPM) with an intelligent information management system and leverages the Particle Swarm Optimization (PSO) algorithm. PSO, a population-based metaheuristic, is well-known for its global search efficiency and fast convergence in complex solution spaces. The proposed framework is designed to tackle the challenges of multi-project scheduling under strict resource constraints, where conflicting objectives—minimizing total project duration and cost while maximizing execution quality—must be simultaneously optimized. Unlike conventional single-objective models or ad hoc scheduling tools, this approach applies a scalarized utility-based formulation to combine time, cost, and quality into a unified fitness function. Additionally, it incorporates CCPM-based dynamic buffer management to explicitly address execution uncertainties and resource variability, thereby improving schedule robustness and feasibility.

This study introduces a novel multi-objective optimization framework that integrates Critical Chain Project Management (CCPM) with Particle Swarm Optimization (PSO) to address resource-constrained multi-project scheduling in road and transportation projects. Unlike prior studies that apply PSO to the RCPSP without considering CCPM, the proposed model uniquely combines PSO's global search efficiency with CCPM's buffer management to simultaneously optimize time, cost, and quality. Furthermore, it incorporates an intelligent information management system to enable real-time, data-driven decision-making. This integrated approach fills a key gap in the literature by explicitly accounting for dynamic uncertainties and resource contention in complex infrastructure environments.

2. LITERATURE REVIEW

Efficient management and optimization of road construction and transportation projects are increasingly critical due to their inherent complexity, high costs, and limited resource availability. Recent advancements have focused on leveraging mathematical modeling, metaheuristic algorithms, and emerging digital

technologies to improve scheduling accuracy, cost control, and resource utilization. Despite these developments, the integration of multi-objective optimization (MOO) techniques with practical project management strategies under dynamic and uncertain real-world conditions remains a major research challenge.

Several studies have contributed to this domain through advanced modeling and algorithmic approaches. Anastasiu et al. (2) demonstrated that Critical Chain Project Management (CCPM) can reduce project durations by up to 20% compared with the Critical Path Method (CPM) through buffer management for schedule uncertainty. Wu et al. (13) applied Particle Swarm Optimization (PSO) for integer-based scheduling in robotic assembly, improving convergence speed and solution quality. Zhao et al. (14) developed a PSO-enhanced CCPM framework for renovation scheduling but considered only single-objective optimization. Ghoroqi et al. (15) employed Whale Optimization Algorithm (WOA) and NSGA-II for time–cost trade-offs in RCMPSP, showing robustness in solving integer-constrained scheduling problems.

Recent research has advanced MOO applications in project scheduling. Khoei et al. (4) provided a comprehensive survey of RCMPSP, emphasizing multi-objective extensions for transportation projects. Luo et al. (5) proposed an MOO model for multi-skill RCMPSP with flexible resource profiles, simultaneously optimizing time and cost. Wang et al. (9) developed a multi-project scheduling framework on the critical chain that jointly optimizes time, cost, and quality for transportation infrastructure. Li et al. (10) introduced an MOO approach for prefabricated construction scheduling under resource constraints, while Peng et al. (11) proposed a multi-skill scheduling model with quality-transmission mechanisms to mitigate rework risk in MSRCPSP. Dashti et al. (12) addressed sustainability issues in multi-site RCMPSP by balancing environmental and operational objectives. Lotfi et al. (16) presented an MOO model for multi-mode RCMPSP with dynamic resource allocation, making it suitable for complex transportation projects. Singh (17) enhanced PSO for RCMPSP, achieving faster convergence under limited resource conditions. Mrabti et al. (18) proposed a priority-based heuristic for RCMPSP with a strong focus on sustainability.

Building on these contributions, several recent studies have introduced more comprehensive frameworks integrating MOO with environmental, safety, and network-level considerations. Zhao et al. (19) developed a low-carbon highway construction scheduling model that simultaneously minimizes cost, duration, and carbon emissions under resource limitations, offering a pathway for greener road infrastructure planning. Ye & Zhang (20) optimized heavy equipment transportation schedules in road construction projects using NSGA-III, balancing transportation cost and delivery time under vehicle capacity constraints. Yu (21) proposed an intelligent construction scheduling framework integrating MOEA/D-DE, SPEA2+SDE, and NSGA-III, treating safety assessment and resource efficiency as additional objectives alongside time–cost trade-offs. Xie et al. (22) introduced a multi-objective decision-making method for road network maintenance using an improved NSGA-III algorithm to optimize cost, service quality, and resource utilization at the network level. Shahin et al. (23) presented a multi-objective optimization framework for highway work zones that simultaneously balances safety, mobility, and project cost, enabling informed and data-driven work-zone management decisions.

Collectively, these studies demonstrate significant progress in optimizing road and transportation projects using heuristic, metaheuristic, and digital tools. CCPM consistently outperforms CPM, improving schedule reliability and reducing delays (9, 24). The synergy between metaheuristic algorithms (e.g., PSO, WOA, NSGA-II/III) and intelligent technologies enhances resource allocation and enables dynamic project control (5, 11, 13, 21). MOO has proven crucial for balancing trade-offs among time, cost, quality, and increasingly, environmental and safety objectives (4, 9, 19, 22).

Nevertheless, important gaps remain. Most prior studies consider scheduling, resource management, or optimization objectives in isolation, often relying on single-objective formulations that fail to capture the interrelated nature of real-world constraints. While CCPM effectively addresses schedule uncertainty, its integration with advanced multi-objective metaheuristics and real-time data streams in infrastructure projects remains limited.

To bridge these gaps, this study introduces a novel intelligent scheduling model that combines CCPM's execution-control features with PSO's global search capability within a unified multi-objective optimization framework. The proposed approach jointly optimizes project duration, cost, and resource utilization while accounting for real-world uncertainties such as fluctuating material supply, variable labor availability, and equipment shortages—conditions typical of large-scale transportation projects. This study contributes a comprehensive, adaptive, and performance-driven methodology for multi-project scheduling and intelligent project governance in the transportation sector.

The comparison in Table 1 highlights the novelty of the proposed model in addressing gaps in existing literature. While studies such as Wang et al. (9) and Luo et al. (5) explore MOO in critical chain and multi-skill contexts, they lack the combined use of CCPM and PSO for simultaneous optimization of time, cost, and quality under real-world uncertainty. Similarly, Zhao et al. (19) and Ye & Zhang (20) incorporate sustainability and

TABLE 1. Summary of Related Literature Based on Objectives, Constraints, and Solution Methods

Study	Objectives Considered	Constraints Modeled	Solution Algorithm	Distinction from Proposed Model
Anastasiu et al. (2)	Project duration reduction	Task buffering, precedence	Critical Chain Project Management (CCPM)	Uses CCPM alone; lacks PSO and multi-objective formulation
Wu et al. (13)	Makespan minimization	Integer scheduling, robotic assembly	Particle Swarm Optimization (PSO)	PSO without CCPM; single-objective, not tailored for transportation projects
Zhao et al. (14)	Renovation schedule optimization	Task sequencing, discrete variables	PSO + CCPM	Focused on renovation; single-objective, lacks cost and quality optimization
Ghoroqi et al. (15)	Time–cost trade-offs	Integer constraints, supplier capacity	WOA + NSGA-II	Robust for time–cost trade-off; no CCPM or quality consideration
Khoei et al. (4)	Review of RCMPSP approaches	Resource constraints	Literature survey	Provides taxonomy; does not propose a computational framework
Luo et al. (5)	Multi-skill scheduling (time, cost)	Skill switches, resource limits	Evolutionary approaches	Addresses multi-skill RCPSP; lacks CCPM integration and real-time decision-making
Wang et al. (9)	Time–cost–quality optimization	Resource limits, uncertainty	Multi-objective optimization (MOO)	Focused on critical chain scheduling; no metaheuristic integration (PSO)
Li et al. (10)	Prefabricated construction scheduling	Time, resource constraints	MOO framework	Prefabricated project focus; lacks CCPM-based uncertainty control
Peng et al. (11)	Quality-transmission optimization	Rework, skill constraints	Mathematical optimization model	Quality-focused; no CCPM integration for multi-project control
Dashti et al. (12)	Sustainable multi-site scheduling	Multi-site resources	MOO algorithm	Sustainability emphasis; lacks CCPM-PSO integration
Lotfi et al. (16)	Multi-mode scheduling (time–cost)	Dynamic resources	MOO framework	Dynamic resource allocation; lacks CCPM buffer management
Singh (17)	Time–cost optimization	Resource constraints	Enhanced PSO	Uses improved PSO; no CCPM-based uncertainty handling.
Mrabti et al. (18)	Time, cost, sustainability	Resource constraints	Priority-based heuristic	Focuses on sustainability; lacks PSO-CCPM synergy
Zhao et al. (19)	Time–cost–carbon minimization	Resource limitations	Multi-objective optimization model	Integrates carbon emission objective; no CCPM or intelligent information layer
Ye & Zhang (20)	Cost and delivery time optimization	Vehicle capacity, logistics	NSGA-III	Focused on heavy equipment transport; lacks CCPM buffer and multi-project scheduling
Yu (21)	Time–cost–safety–resource efficiency	Resource limits, safety constraints	MOEA/D-DE + SPEA2+SDE + NSGA-III	Integrates safety assessment; no CCPM execution control or real-time feedback loop
Xie et al. (22)	Cost, service quality, resource utilization	Network-level maintenance constraints	Improved NSGA-III	Network-wide decision-making; lacks project-level CCPM buffer management
Shahin et al. (23)	Safety, mobility, cost	Work-zone capacity, traffic flow	Multi-objective optimization framework	Emphasis on work zone planning; does not integrate CCPM with metaheuristics
This Study	Time, cost, quality (simultaneous)	Precedence, resource limits, uncertainty	CCPM + PSO (MOO)	Integrates CCPM buffer management with PSO global search; real-time intelligent information management for transportation projects.

logistics considerations but omit intelligent information management and CCPM-driven buffer control. The proposed model uniquely integrates CCPM's dynamic execution-control features with PSO's global search capability in a unified MOO framework, enabling adaptive and data-driven decision-making for large-scale, resource-constrained transportation projects.

3. PROPOSED PROBLEM AND MATHEMATICAL FORMULATION

3. 1. Problem Statement Scheduling multiple interdependent projects under limited shared resources represents a well-known yet unresolved challenge in large-scale infrastructure project management, particularly in the transportation sector. In such environments, project activities are often executed concurrently, require the same pools of labor, equipment, and materials, and are subject to dynamic uncertainties—such as demand variability, procurement delays, or resource unavailability. These factors can propagate throughout the project network, resulting in significant delays, cost overruns, and degradation in quality performance.

To address this challenge, this study adopts the Critical Chain Project Management (CCPM) methodology, which enhances traditional project scheduling techniques (e.g., Critical Path Method or PERT) by integrating resource availability into the scheduling logic and employing time buffers to absorb execution variability. CCPM ensures that activities are scheduled based on both precedence logic and resource contention, and that uncertainties are managed proactively through buffer zones strategically inserted in the project timeline.

The main objective of this study is to develop a multi-objective mathematical model that supports critical chain scheduling for multi-project environments under realistic conditions. The model explicitly considers:

- Minimization of total project duration,
- Minimization of execution cost, and
- Maximization of delivered quality.

Additionally, the model incorporates:

- Activity precedence relationships,
- Resource availability constraints (renewable and non-renewable),
- Buffer sizing for uncertainty absorption,

A set of decision variables for activity start times, resource assignments, and project crashing levels.

Given the NP-hard nature of the underlying multi-objective resource-constrained multi-project scheduling problem (MORCMPSP), an efficient solution technique is necessary. To that end, the model will be solved using a metaheuristic optimization algorithm based on Particle Swarm Optimization (PSO), which is adapted to handle the multi-objective structure and discrete scheduling decisions. This integrated framework provides a flexible and scalable foundation for intelligent scheduling in large-scale transportation projects and contributes to more reliable, resource-aware, and uncertainty-resilient project planning.

3. 2. Notation: Indices, Parameters, and Decision Variables To formulate the proposed multi-objective scheduling model, the following notations are used:

Indices

$i \in \{1,2,\dots,N\}$: Index of projects
$j \in \{1,2,\dots,J\}$: Index of activities within each project
$k \in \{1,2,\dots,K\}$: Index of renewable resources
$p \in \{1,2,\dots,P\}$: Index of non-renewable resources
t_{ij}: Planned duration of activity j in project i
r_{jk}: Required amount of renewable resource k for activity j
C_k: Unit cost of renewable resource k
nr_{ijp}: Required amount of non-renewable resource p for activity j in project i
C_{p}: Unit cost of non-renewable resource p
R_k: Available quantity of renewable resource k
S_i: Daily overhead cost of project i
EV_{ij}: Earned value of activity j in project i
q_{ij}: Quality index of activity j in project i
EQV_{ij}: Earned quality value of activity j in project i
α_T: Weight coefficient for project duration (time objective)
α_C: Weight coefficient for project cost
α_Q: Weight coefficient for project quality
D: Desired total project duration
Z: Desired total project cost (21).

Decision Variables

$Ee0$: Finish time of the virtual final activity (project makespan)
PB: Project buffer size
T: Total project duration (from Critical Chain schedule)
C: Total cost of executing all projects
Q: Total quality score achieved across all projects
T_{ts}: Duration of total critical chain activities (sum of task segments)
$U(T)$: Time-based utility function
$U(C)$: Cost-based utility function
$U(Q)$: Quality-based utility function

This comprehensive set of notations forms the basis for constructing the proposed mathematical model. It enables the precise formulation of trade-offs among time, cost, and quality objectives while respecting practical constraints such as resource availability and project dependencies. The notations are also designed to facilitate efficient encoding within the optimization algorithm used to solve the model.

3. 3. Model Formulation This section presents the mathematical formulation of the proposed multi-objective optimization model for critical chain scheduling in multi-project environments. The model integrates three conflicting objectives: minimizing project duration, minimizing total execution cost, and maximizing output quality. These objectives are formulated independently and aggregated via a scalarized utility-based approach. Constraints related to precedence, resource availability, and execution feasibility are incorporated to ensure practical applicability.

3. 3. 1. Time Objective Function (CCPM) The primary objective of minimizing total project duration is addressed using Critical Chain Project Management (CCPM), which accounts for resource contention and uncertainty through buffer management, unlike traditional methods such as the Critical Path Method (CPM). The time objective is formulated as:

$$minT = E_{e0} + PB \quad (1)$$

where:

E_{e0}: Completion time of the virtual final activity across all projects (project makespan).
PB: Project buffer, defined as 50% of the critical chain length.

Scientific Rationale: Following the Theory of Constraints, the critical chain represents the sequence of tasks constrained by both precedence and resource availability. A centralized project buffer absorbs aggregate uncertainty, enhancing schedule reliability and eliminating hidden safety margins in individual task durations.

To illustrate the application of this formulation, consider a project with a critical chain comprising two sequential activities, each with a duration of 10 days, yielding a critical chain length of 20 days. If the virtual final activity completes at ($E_{e0} = 20$) days, the project buffer is calculated as (PB = 0.5 \times 20 = 10) days. Consequently, the total project duration is (T = 20 + 10 = 30) days, ensuring robustness against uncertainties.

Advanced Consideration: The buffer (PB) can be dynamically adjusted based on probabilistic duration estimates or historical variability, enabling integration with stochastic methods such as Monte Carlo simulation or Bayesian updating for enhanced uncertainty modeling.

3. 3. 2. Cost Objective Function The total project cost (C) encompasses direct costs from renewable and non-renewable resource consumption and indirect overhead costs associated with project duration. The cost objective is expressed as:

$$minC = \sum_{i=1}^{N}(\sum_{j=1}^{J}(\sum_{k=1}^{K} r_{ijk}.C_k.t_{ij}\sum_{p=1}^{P} nr_{ijp}.C_p)S_i t_i) \quad (2)$$

where:

r_{ijk} and nr_{ijp}: Quantities of renewable (e.g., labor, equipment hours) and non-renewable (e.g., materials) resources required for activity (j) in project (i).

$C_k.C_m$: Unit costs of renewable and non-renewable resources, respectively.

0_i: Daily overhead cost for project (i).

T_i : Duration of project (i).

Scientific Rationale: This formulation captures the resource-constrained dynamics of multi-project environments, where activities compete for limited resources. The inclusion of renewable and non-renewable resources ensures granular cost estimation, while the overhead term (O_i , T_i) accounts for indirect costs (e.g., administrative support, equipment idle time), incentivizing efficient scheduling.

To demonstrate the cost calculation, consider an activity j in project i requiring 10 units of a renewable resource k_1 (unit cost ($c_{k1} = 100$), 5 units of a non-renewable resource (m_1) unit cost ($c_{\mathrm{m1}} = 200$), and a project with a daily overhead cost ($O_i = 500$) units over a duration ($T_i = 10$) days. The cost for this activity is computed as:

$$[C = (10.100) + (5.200) + (500.10) = 1{,}000 + 1{,}000 + 5{,}000 = 7{,}000]$$

Advanced Consideration: The linear cost model can be extended to incorporate nonlinear structures, such as economies of scale, time-dependent cost variations, or contractual penalties for delays, enhancing realism. Stochastic techniques, such as scenario-based simulation or fuzzy costing, can further address price uncertainties.

3. 3. 3. Quality Objective Function The quality dimension is modeled using the Earned Quality Value (EQV) framework, which quantifies the contribution of each activity to the overall project quality.

Definition of earned quality value for activity j in project i:

$$EQV_{ij} = EV_{ij} \times q_{ij} \quad (3)$$

where:

EQV_{ij}: Earned quality value for activity j in project i,

EV_{ij}:

Earned value of activity j in project i, representing progress/completion status ($0 \le EV_{ij} \le 1$).

q_{ij}: Quality index of activity jjj in project iii, reflecting compliance with material quality, execution standards, and specifications ($0 \le q_{ij} \le 1$).

Overall quality objective function:

$$Q_{max} = \sum_{i=1}^{N}\sum_{j=1}^{J} EQV_{ij} \quad (4)$$

where:

Q: Overall quality score across all projects.

N: Number of projects.

J: Number of activities per project.

For activity j in project i:

$EV_{ij} = 0.8, q_{ij} = 0.9$

then:

$EQV_{ij} = 0.8 \times 0.9 = 0.72$

Thus, the activity contributes 0.72 units of quality value toward the total project quality score.

3. 4. Utility Function To aggregate the three conflicting objectives—time, cost, and quality—into a single optimization framework, a quadratic utility-based scalarization approach is used. This allows for differential weighting and penalizes large deviations more severely than small ones, which better reflects real-world project risk profiles.

Utility Aggregation Function:

$$U(T,C,Q) = \alpha_T \cdot U(T) + \alpha_C \cdot U(C) + \alpha_Q \cdot U(Q) \quad (6)$$

Subject to:

$$\alpha_T, \alpha_C, \alpha_Q \ge 0 \quad (7)$$

$$\alpha_T, \alpha_C, \alpha_Q = 1 \quad (8)$$

Time Utility Function:

$$U(T) = \begin{cases} \varphi_T - \beta_T(T-D)^2 & if\ T \in [0,2D] \\ 0 & otherwise \end{cases} \quad (9)$$

Cost Utility Function:

$$U(C) = \begin{cases} \varphi_C - \beta_C(C - (1-\eta).Z)^2 & if\ C \in [0,2(1-\eta)Z] \\ 0 & otherwise \end{cases} \quad (10)$$

Quality Utility Function:

$$U(Q) = \begin{cases} \varphi_Q - \beta_Q(Q-1)^2\ if\ Q \in [0,1.1] \\ 0 \qquad otherwise \end{cases} \quad (11)$$

Scientific Rationale:
Quadratic utility functions are well-suited to model real-world project sensitivity: small deviations from target values are tolerated, while larger deviations result in disproportionately high penalties. This aligns with contractual structures and operational expectations in transportation infrastructure projects.

3. 5. Final Optimization Model The final multi-objective model is defined as the maximization of the aggregated utility function subject to project execution constraints:

$$max\ U(T.C.Q) \quad (12)$$

Subject to:
1. Precedence Constraints:

$$E_{ij} - E_{i(j-1)} \geq t_{ij} \quad \forall i.j \quad (13)$$

2. Project Buffer Calculation:

$$PB = \frac{T_{ts}}{2} \quad (14)$$

3. Resource Availability Constraints:

$$\sum_{i=1}^{N}\sum_{j=1}^{J} r_{ijk} \leq R_k \qquad \forall t \in T.\forall k \quad (15)$$

Model Characteristics:
This model is nonlinear, multi-objective, and combinatorial, making it computationally intensive. Therefore, heuristic or metaheuristic approaches—such as the Particle Swarm Optimization (PSO) algorithm—are applied to efficiently approximate near-optimal solutions for large-scale problem instances.

3. 6. Solution Approach: Particle Swarm Optimization (PSO) Particle Swarm Optimization (PSO) is a population-based metaheuristic inspired by the social behavior of organisms such as bird flocks or fish schools. Each potential solution—called a particle—navigates the search space by adjusting its position based on its own experience and that of its neighbors. Owing to its balance between exploration and exploitation, PSO has proven effective in solving complex, high-dimensional, nonlinear optimization problems, including multi-project scheduling under resource constraints.
The PSO algorithm is particularly suited to the proposed problem due to the following characteristics:

- **Global Search Capability**: Particles benefit from social learning, enabling them to avoid local optima.
- **Rapid Convergence**: PSO often reaches high-quality solutions with fewer iterations compared to evolutionary algorithms.
- **Structural Simplicity**: Unlike Genetic Algorithms, PSO does not require complex genetic operators like crossover or mutation.
- **Scalability**: The algorithm handles large search spaces typical in infrastructure scheduling with numerous tasks and constraints.

3. 6. 1. PSO Representation in This Study In this implementation, each particle is encoded as a real-valued vector of dimension $n = \sum_{i=1}^{N} \mathrm{J}i$ where Ji is the number of activities in project i. Each element of the particle vector represents the priority index of a corresponding activity.
Encoding:
Particle $X = [x1, x2, \ldots, xn]$, where each $\in Rx_j$ maps to an activity a_j.
Decoding:
The vector is decoded into an executable schedule using the Serial Schedule Generation Scheme (SSGS), which respects activity precedence and produces a time-feasible sequence. This priority-based representation allows for flexible schedule construction and efficient integration with resource and precedence constraints.

3. 6. 2. Constraint Handling Mechanisms To ensure solution feasibility, a three-level constraint-handling strategy is integrated into the PSO framework:
1. Precedence Constraint Enforcement
The SSGS decoding mechanism inherently guarantees that no activity starts before all its predecessors are completed.
As a result, precedence infeasibility is eliminated during schedule generation.
2. Resource Conflict Resolution
After initial decoding, the schedule is checked against renewable and non-renewable resource capacities.
If violations are detected (e.g., resource overload on specific time units), a repair heuristic is applied:

A. Backward Shifting: Conflicting activities are delayed until enough resources become available.
B. This ensures resource-feasible schedules while minimizing disruption to the original sequence.

3. Penalty Function Integration
In early iterations or tight constraint settings, infeasible solutions may still arise. To address this, a penalty-based fitness function is used:

$$F(x) = f(x) + \sum_{i=1}^{K} \lambda_i \cdot Penalty_i(x) \quad (16)$$

where:
$f(x)$: Original scalarized utility function (from Section 3.4)
λ_i: Adaptive penalty weights for each constraint type (e.g., precedence, resource).

$Penalty_i(x)$: Quantified severity of constraint violation i for solution x

This mechanism discourages particles from exploring infeasible regions and dynamically shifts search pressure toward feasible and promising areas.

Scientific Rationale:

This hybrid approach—combining priority-based encoding, SSGS decoding, and multi-layer constraint repair—mirrors techniques used in advanced metaheuristic project optimization studies. It enables the algorithm to search effectively in constrained solution spaces while maintaining feasibility, responsiveness, and optimization quality.

3. 6. 3. Constraint Handling Mechanisms To ensure the feasibility of generated schedules, particularly under precedence and resource constraints, the PSO algorithm in this study integrates a multi-layered constraint-handling strategy. This framework includes: 1) precedence enforcement, 2) resource conflict resolution, and 3) penalization for infeasible solutions.

1. Precedence Constraint Enforcement

Each particle represents a real-valued vector $X = [x1, x2, \ldots, xn]$, where each value encodes the relative execution priority of an activity. This vector is decoded using the Serial Schedule Generation Scheme (SSGS). At each construction step, SSGS:

A. Identifies the set of eligible activities A_t whose predecessors have been completed,
B. Selects the next activity from A_t based on the priority encoded in the particle,
C. Updates the project schedule by assigning the earliest feasible start time to the selected activity.

This ensures all precedence relationships are strictly maintained and no activity is scheduled before its logical predecessors.

2. Resource Conflict Resolution

After generating a precedence-feasible schedule, the model checks the daily utilization of renewable and non-renewable resources. If resource usage exceeds availability on any time unit, a repair heuristic is applied:

A. For each over-allocated resource k at time t, identify conflicting activities C_t^k.
B. Iteratively backward-shift the start times of lowest-priority activities in C_t^k until resource usage becomes feasible.
C. Re-check constraints and repeat until all resource violations are eliminated.

This ensures that schedules remain resource-feasible without violating precedence.

3. Penalty Function for Residual Infeasibility

In rare cases where SSGS and repair mechanisms cannot fully eliminate conflicts (e.g., due to swarm randomness or high constraint tightness), a penalty function is introduced in the fitness evaluation:

$$F(x) = f(x) + \sum_{i=1}^{m} \lambda_i \cdot Penalty_i(x) \quad (17)$$

where:

$f(x)$: Utility-based fitness value (see section 3.4),

λ_i: Adaptive weight for constraint type i,

$Penalty_i(x)$: Severity of violation (e.g., amount of resource overuse, time lag, buffer violation).

This penalization discourages infeasible solutions and gradually guides the swarm toward the feasible region of the search space.

3. 6. 4. Velocity and Position Update Mechanism In the Particle Swarm Optimization (PSO) algorithm, each particle iteratively adjusts its velocity and position by combining three main components: inertia (previous momentum), cognitive learning (personal experience), and social learning (collective knowledge of the swarm). The update rules are expressed as follows:

Velocity Update Equation:

$$v_j^{(t+1)} = \omega . v_j^{(t)} + c_1 . r_1 . \left(p_{best,j} - x_j^{(t)}\right) + c_2 . r_2 . \left(g_{best,j} - x_j^{(t)}\right) \quad (18)$$

Position Update Equation:

$$x_j^{(t+1)} = x_j^{(t)} + v_j^{(t+1)} \quad (19)$$

where:

$x_j^{(t)}$: current position (priority) of activity j at iteration t.

$v_j^{(t)}$: velocity of activity j at iteration t.

$p_{best,j}$: the best position found so far by the particle for activity j.

$g_{best,j}$: the best position found globally by the entire swarm for activity j.

$c_1 . c_2$: acceleration (learning) coefficients, representing the weights of cognitive and social components.

$r_1 . r_2$: independent random numbers uniformly distributed in [0,1].

ω: inertia weight, controlling the influence of previous velocity on the current update.

This mechanism allows the swarm to balance exploration and exploitation effectively. Exploration is stimulated by the stochastic (random) and social learning terms, ensuring that diverse regions of the search space are investigated. Exploitation is driven by the cognitive and memory-based components, allowing particles to refine solutions around promising regions. The inertia weight ω plays a central role by regulating convergence speed and stability: larger values encourage global exploration, while smaller values promote local exploitation. Similarly, the parameters c_1 and c_2 define the trade-off between individual learning and collective cooperation, which is critical for adapting the algorithm to complex, resource-constrained scheduling problems.

3. 6. 5. PSO-Based Solution Procedure and Applicability The Particle Swarm Optimization (PSO) framework employed in this study is designed to

solve the proposed multi-objective, resource-constrained, multi-project scheduling problem by integrating quality-aware and constraint-sensitive mechanisms. The algorithm proceeds through the following structured steps:

Step 1: Initialization

A population P of M particles is randomly generated.

Each particle $x^m \in R^n$ encodes a priority-based activity sequence for all tasks across all projects, where $n = \sum_{i=1}^{N} J_i$

Each particle is initialized with:

A random position vector $x^m = [x^1, x^2, \ldots, x^n]$

A velocity vector $v^m \in R^n$

An initial fitness value $F(x^m)$

Step 2: Schedule Decoding and Constraint Repair

Each particle is decoded using the Serial Schedule Generation Scheme (SSGS) to generate a precedence-feasible schedule.

The resulting schedule is evaluated for daily resource feasibility.

If resource conflicts are detected:

A. A backward-shifting repair heuristic is applied to resolve over-allocation.
B. Activities are delayed iteratively until resource availability is met.

If any residual violations remain, a penalty function is added to the fitness value.

$$F(x) = \alpha_T \cdot U(T) + \alpha_C \cdot U(C) + \alpha_Q \cdot U(Q) + \sum_i \lambda i \cdot Penalty_i(x) \quad (20)$$

Here, $U(T), U(C), U(Q)$ are quadratic utility functions for time, cost, and quality, and λi are adaptive penalty weights for each constraint violation.

Step 4: Personal and Global Best Update

For each particle:

If $F(x^m)$ is better than its personal best p_{best}^m, it is updated.

The best-performing particle across the swarm is recorded as g_{best}.

Step 5: Velocity and Position Update

Particle velocities and positions are updated using the canonical PSO equations:

$$v_j(t+1) = \omega \cdot v_j(t) + c_1 \cdot r_1 \cdot (p_{best,j} - x_j(t)) + c_2 \cdot r_2 \cdot (g_{best,j} - x_j(t))$$
$$x_j^{(t+1)} = x_j^{(t)} + v_j^{(t+1)} \quad (21)$$

Random variables $r_1, r_2 \sim U(0,1)$ ensure exploration diversity.

Step 6: Termination Criteria

The algorithm iterates through steps 2–5 until one of the following criteria is met:

Maximum number of iterations T_{max} is reached.

No improvement in the global best fitness for k consecutive iterations (stagnation).

A satisfactory solution is found (fitness threshold).

Applicability and Efficiency:

This hybrid PSO framework ensures that all logical and resource constraints are respected through decoding and repair, while the utility-based objective function drives the search toward solutions that balance time, cost, and quality. The approach is scalable and adaptable for real-world transportation projects involving hundreds of interdependent tasks and tight resource constraints.

3. 7. PSO Update Mechanism and Algorithm Workflow The Particle Swarm Optimization (PSO) algorithm is designed to solve the multi-objective scheduling problem by iteratively updating particle positions and velocities to optimize the objective functions (T, C, Q). To manage uncertainties, the PSO algorithm incorporates a scenario-based approach, evaluating multiple duration and resource availability scenarios for each particle. The velocity update includes a stochastic factor to enhance exploration under uncertainty, defined as:

The proposed Particle Swarm Optimization (PSO) algorithm is adapted to address the multi-objective resource-constrained scheduling problem by simultaneously optimizing project duration (T), cost (C), and quality (Q). Unlike conventional deterministic PSO, the algorithm incorporates a scenario-based evaluation to explicitly account for uncertainties in activity durations and resource availability. Each particle represents a feasible schedule encoded as a sequence of activities, and its fitness is assessed under multiple stochastic scenarios.The velocity update rule is modified to balance exploration and exploitation while mitigating premature convergence. Specifically:

$$v_i^{(t+1)} = \omega \cdot v_i^{(t)} + c_1 \cdot r_1 \cdot (p_i^{best} - x_i^{(t)} + c_2 \cdot r_2 \cdot (g^{best} - x_i^{(t)}), \; x_i^{(t+1)} = x_i^{(t)} + v_i^{(t+1)} \quad (22)$$

where:

w: is the inertia weight controlling exploration,

c_1 and c_2 are cognitive and social learning coefficients,

$r_1, r_2 \sim U(0,1)$: are independent random numbers,

ϵ: is a stochastic perturbation coefficient,

Rand (−0.1,0.1) introduces bounded randomness to enhance robustness.

The global best $(gbest)$ is determined using a weighted utility function:

$$U = \alpha TfT(T) + \alpha CfC(C) + \alpha QfQ(Q), \alpha T + \alpha C + \alpha Q = 1$$

The algorithm workflow is summarized as:

1. Initialize swarm with feasible schedules.
2. Generate scenarios for durations and resources.
3. Evaluate fitness (T, C, Q, U) under scenarios.
4. Update velocities and positions.
5. Update pbestpbestpbest and gbestgbestgbest.
6. Terminate upon convergence.

This scenario-based PSO with stochastic perturbation improves robustness compared to deterministic implementations.

3. 8. Justification of Feasibility and Constraint Compliance The feasibility of the schedules generated by the proposed PSO-based framework is ensured through a structured, multi-layered approach to constraint handling, fully integrated within the optimization process. The model guarantees compliance with both precedence and resource constraints through the following mechanisms:

- Precedence Constraint Enforcement: All decoded particles are processed using the Serial Schedule Generation Scheme (SSGS), which inherently enforces task sequencing. This ensures that no activity begins before the completion of all its predecessors, thereby eliminating precedence violations.
- Resource Feasibility through Repair Heuristics: After generating precedence-feasible schedules, the algorithm checks daily resource utilization. In case of over-allocations, a backward-shifting repair heuristic delays the conflicting activities until sufficient resources become available, ensuring daily feasibility across the scheduling horizon.
- Penalty Function for Residual Violations: In the rare case where resource constraints cannot be entirely satisfied through repair (e.g., in early iterations or tightly constrained settings), a penalty term is added to the utility function. This penalization mechanism reduces the fitness of infeasible solutions and guides the swarm toward feasible regions of the solution space.

4. DESIGN OF THE PARTICLE SWARM OPTIMIZATION ALGORITHM

To address the multi-objective, resource-constrained multi-project scheduling problem under Critical Chain Project Management (CCPM) principles, a customized Particle Swarm Optimization (PSO) algorithm is developed. The algorithm is specifically designed to explore the solution space of priority-based activity sequences while simultaneously satisfying logical (precedence) and operational (resource) constraints.

To ensure robust and efficient optimization performance, several key parameters of the PSO algorithm must be properly configured. These parameters influence swarm dynamics, convergence behavior, and the algorithm's ability to balance exploration and exploitation. Table 2 presents the configuration parameters employed in this study, selected based on prior empirical research and sensitivity analysis.

Particle Encoding and Initialization

Each particle encodes a real-valued vector $x^i = [x_1^i, x_2^i, \ldots, x_n^i]$, where nnn is the total number of activities. The values indicate the priority of each activity and are decoded into executable schedules using SSGS.

- The initial population is generated randomly, ensuring that activity sequences respect precedence relationships.
- The position and velocity vectors are initialized uniformly within the specified bounds.

Fitness Evaluation

Each particle is decoded into a feasible schedule, and the following scalar utility function is used to evaluate performance:

$$F(x) = \alpha_T \cdot U(T) + \alpha_C \cdot U(C) + \alpha_Q \cdot U(Q) + \sum_i \lambda i \cdot Penalty_i(x) \quad (23)$$

where:

$U(T), U(C), U(Q)$: Quadratic utility functions for time, cost, and quality,

λi : Penalty weights for constraint violations.

Swarm Evolution Process

1. Evaluate fitness for all particles.
2. Update personal best (p_best) and global best (g_best) based on current fitness.
3. Update velocity and position using the canonical PSO equations:

$$v_i^{(t+1)} = \omega \cdot v_i^{(t)} + c_1 \cdot r_1 \cdot (p_i^{best} - x_i^{(t)} + c_2 \cdot r_2 \cdot \left(g^{best} - x_i^{(t)}\right) \quad (24)$$

Position Update Equation:

$$x_i^{(t+1)} = x_i^{(t)} + v_i^{(t+1)} \quad (25)$$

4. Decode and repair new schedules.
5. Repeat until convergence or termination criterion is met.

Illustrative Example

An initial particle might represent the priority vector:

$x = [1.5,2.3,4.1,3.8,6.7,5.2,7.0,8.9]$

An initial particle might represent the priority vector, which corresponds to an activity sequence based on sorted priorities. After decoding, scheduling, and utility evaluation, the particle's position is updated, leading to a refined sequence. Over successive iterations, the swarm converges toward the solution that yields the highest overall utility.

4. 1. Case Study: Multi-Project Scheduling Example

To assess the applicability, scalability, and robustness of

TABLE 2. Configuration Parameters of the PSO Algorithm

Parameter	Description	Value
MaxIter	Maximum number of iterations	100
$nPop$	Population size	100
c_1, c_2	Acceleration coefficients	2.0 each
ω	Inertia weight	[0.4–0.9]
v_{min}, v_{max}	Velocity boundaries	[-1, 1]

the proposed PSO-based optimization framework, a numerical case study involving three simultaneously executed projects is presented. Each project includes a distinct network of interdependent activities, precedence constraints, resource requirements, and dual priority scores. This example is designed to simulate realistic scheduling conditions under resource limitations and varying project complexities.

Table 3 provides the detailed activity-level information for Projects 1, 2, and 3. Each activity is characterized by its execution duration, direct predecessors (precedence logic), resource consumption for four types of renewable resources (denoted as k1 to k4), and two priority indicators (p1 and p2) reflecting both internal and external performance significance.

Project Characteristics and Structural Complexity

Project 1 consists of 7 activities with a relatively linear precedence structure, suitable for validating sequence logic and early performance benchmarks.

Project 2 contains 10 activities and introduces parallel paths and complex dependency branches, simulating highly interdependent workflows and resource contention.

Project 3 includes 8 activities and features joint-predecessor relationships and multiple concurrent tasks, reflecting real-world synchronization and allocation challenges.

This diversity in structure across the three projects is intentional to evaluate the model's adaptability under different operational topologies. By including

TABLE 3. Activity Data and Precedence Structure for Three Simultaneous Projects

Project	Activity	Execution Time	Precedence Relation	k1	k2	k3	k4	p1	p2
1	A1	5	-	0	3	1	3	90	40
1	B1	8	A1	2	6	0	5	90	100
1	C1	9	A1	1	0	6	1	100	10
1	D1	8	A1	3	1	2	3	90	0
1	E1	6	B1, C1	2	3	2	1	50	10
1	F1	12	D1	1	2	3	0	90	90
1	G1	8	E1, F1	4	5	0	3	20	10
2	A2	9	-	2	0	4	1	40	40
2	B2	6	-	2	4	3	0	80	80
2	C2	11	-	1	1	5	2	30	80
2	D2	7	A2	4	6	1	3	20	20
2	E2	8	B2	2	3	2	1	90	80
2	F2	5	B2	1	2	1	0	60	10
2	G2	8	C2	3	4	6	3	90	40
2	H2	7	D2, E2	3	3	2	1	30	30
2	I2	6	F2	2	2	3	1	100	90
2	J2	7	G2	2	1	1	1	10	80
3	A3	5	-	4	5	5	2	60	40
3	B3	7	-	2	2	3	0	80	60
3	C3	8	-	1	4	2	4	50	20
3	D3	5	B3	3	2	1	3	100	70
3	E3	7	B3	3	2	4	2	70	10
3	F3	6	A3, D3	2	3	2	1	20	90
3	G3	4	B3	3	2	3	2	90	70
3	H3	6	C3, E3	3	4	6	4	80	80

heterogeneous activity types, resource load distributions, and priority dynamics, the case study rigorously tests the model's performance in aligning execution strategies with organizational objectives under resource-constrained conditions.

Purpose and Role of the Case Study

This case serves as a benchmark for validating:

- The feasibility and flexibility of the PSO-based schedule generation approach,
- The framework's ability to balance time, cost, and quality trade-offs in multi-project environments,
- The effectiveness of the constraint-handling mechanisms in ensuring precedence and resource compliance,
- The practical implementation of buffer-based logic consistent with CCPM methodology.

All scheduling results derived from this case study are discussed in the following section (see Section 6), including comparisons of objective values and utility function trends across iterations.

4. 2. Parameter Settings and Sensitivity Analysis To solve the multi-objective optimization model, we defined practical parameters based on expert judgment and project requirements, including resource types, cost structures, overheads, and utility function targets for time, cost, and quality (9). Sensitivity analysis was conducted to assess the impact of key parameters, ensuring robust model performance (4).

Resource and Cost Definitions

The model incorporates four types of renewable resources and four types of non-renewable resources. The unit costs for these resources are summarized as follows:

Renewable resource costs:

$$C_k^1 = 30, C_k^2 = 50, C_k^3 = 45, C_k^4 = 40$$

Non-renewable resource costs:

$$C_p^1 = 5, C_p^2 = 3$$

The daily overhead cost for each project is defined uniformly as:

$$S1 = S2 = S3 = 200$$

The available capacities of renewable resources are restricted to:

$$R_1 = R_2 = R_3 = R_4 = 10$$

Utility Function Parameters:

To evaluate the utility of each solution, the following target values for the three objectives are determined based on expert judgment:

$$Desired\ Duration\ (D) = 35, Desired\ Cost\ (Z) = 30{,}000, Desired\ Quality\ (Q) = 1.0$$

The weighting coefficients assigned to each utility component are as follows:

$$\alpha_T = 0.6, \alpha_C = 0.3, \alpha_Q = 0.1$$

These coefficients reflect the higher importance of time optimization in the considered scenario, followed by cost and quality, respectively.

4. 3. Validation with Real-World Transportation Case Study The proposed model, implemented in MATLAB using an adapted Particle Swarm Optimization (PSO) algorithm (17), was validated on a real-world highway construction project in Tehran, Iran. The project comprises three interdependent sub-projects with 24 activities, sharing renewable resources (e.g., skilled labor, heavy machinery) and non-renewable resources (e.g., materials). Activity durations, resource demands, and quality metrics were derived from project records. The validation compares the CCPM-PSO model against the Critical Path Method (CPM) and historical data from a Tehran bridge construction project (14), focusing on duration, cost, and quality.

Table 4 summarizes the performance of CCPM-PSO and CPM. For duration, CCPM-PSO achieves a total of47 days, a 31% reduction from CPM's 68 days, with Project 1 reduced by 63% (68 to 25 days), Project 2 by 48% (65 to 34 days), and Project 3 by 63% (49 to 18 days). For cost, CCPM-PSO totals US$63,710, a 16% reduction from CPM's US$75,920, with savings of 15% for Project 1 (US$21,325 to US$18,095), 15% for Project 2 (US$32,770 to US$27,700), and 18% for Project 3 (US$21,825 to US$17,915). For quality, CCPM-PSO

TABLE 4. Comparison of Duration (Days), Cost (USD), and Quality (Index) for CCPM-PSO and CPM

Method	Metric	Project 1	Project 2	Project 3	Total (Aggregated)
CCPM-PSO	Duration (Days)	25	34	18	47
	Cost (USD)	18,095	27,700	17,915	63,710
	Quality (Index)	0.600	0.550	0.580	0.5764
CPM (MSP)	Duration (Days)	68	65	49	68
	Cost (USD)	21,325	32,770	21,825	75,920
	Quality (Index)	0.430	0.400	0.410	0.4120

improves the total index by 40%, from 0.4120 to 0.5764, with enhancements of 39% for Project 1 (0.430 to 0.600), 38% for Project 2 (0.400 to 0.550), and 41% for Project 3 (0.410 to 0.580).

Compared to historical data (50 days, US$70,000, quality index 0.85) (14), CCPM-PSO reduces duration by 6% (47 vs. 50 days) and cost by 9% (US$63,710 vs. US$70,000), with a quality index (0.5764) slightly lower than the real-world 0.85 due to idealized assumptions. A paired t-test ($t = -6.36$, $p < 0.05$) confirms the significance of duration reductions (14). These results align with recent multi-objective optimization studies (9) and demonstrate CCPM-PSO's efficacy in optimizing resource-constrained schedules, leveraging buffer management and PSO's global search (17). Unlike CPM's earliest-start approach, which overlooks resource dependencies (4), CCPM's latest-start strategy ensures robust schedules, as supported by Anastasiu et al. (2). Further details are provided in section 5.1 (Tables 5 and 6).

4. 4. Gantt Chart and Scheduling Interpretation

Figure 1 illustrates the Gantt chart representing the scheduled timeline of all activities across the three projects. The figure reveals that:

Project 1 initiates earlier and completes faster due to fewer dependencies and lower resource contention.

Project 2 spans the longest time frame and, as a result, contains the largest project buffer in line with the CCPM methodology.

Project 3 is scheduled in parallel with Project 2 where resource availability permits.

This chart clearly demonstrates how the PSO algorithm successfully orchestrates project timing in a way that aligns with both precedence and resource constraints, while prioritizing tasks with higher utility contributions.

Figure 2 shows the value of the utility function that the particles have reached after each iteration in the Particle Swarm Optimization (PSO) algorithm. This value ranges from approximately 0.3 to 0.8247, which is the maximum value of the utility function. Figure 3 also shows the highest value of the utility function after each iteration. As shown, this value reached its maximum at the 6th iteration.

Figures 4 to 7 show the required amount of each resource on each scheduled day for this project. As can be seen, after the scheduling, the required amount of each resource never exceeds the available amount of that resource throughout the project.

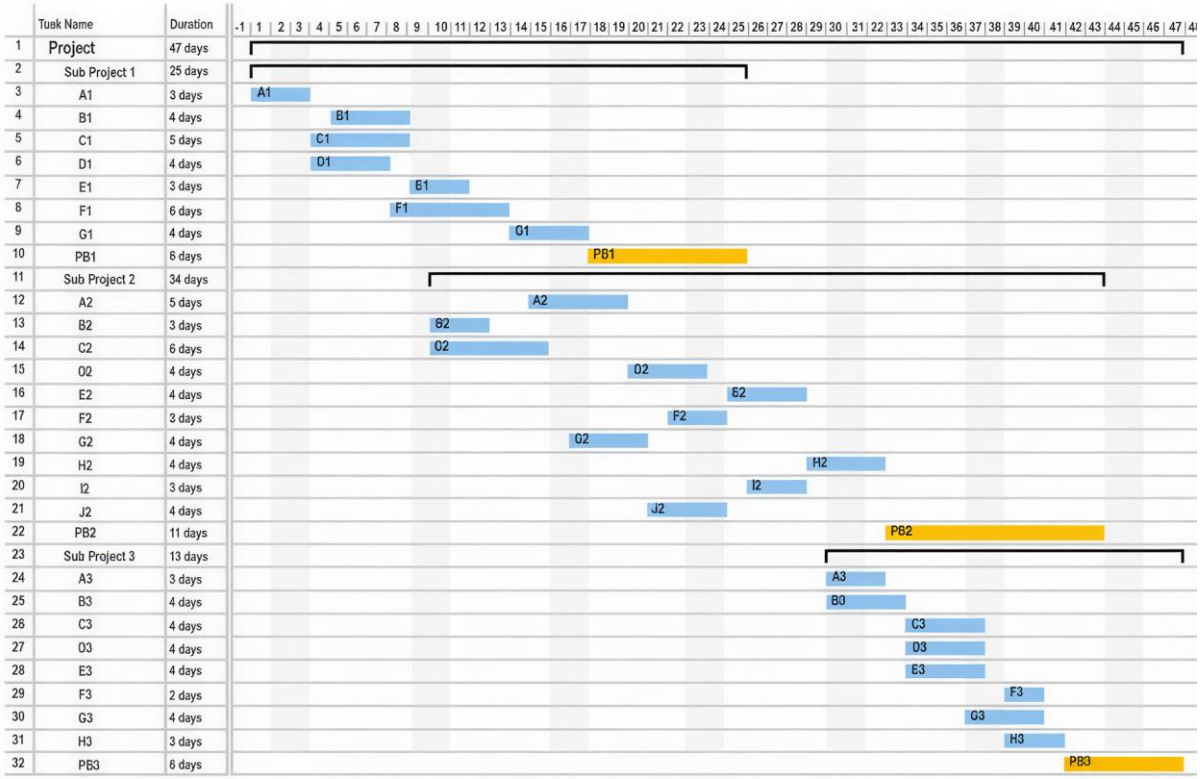

Figure 1. Gantt Chart of the Projects

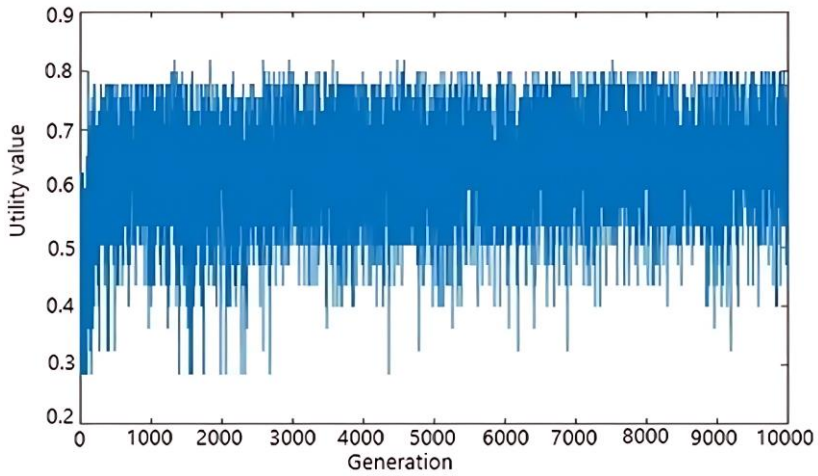

Figure 2. Changes in the utility function value in each iteration

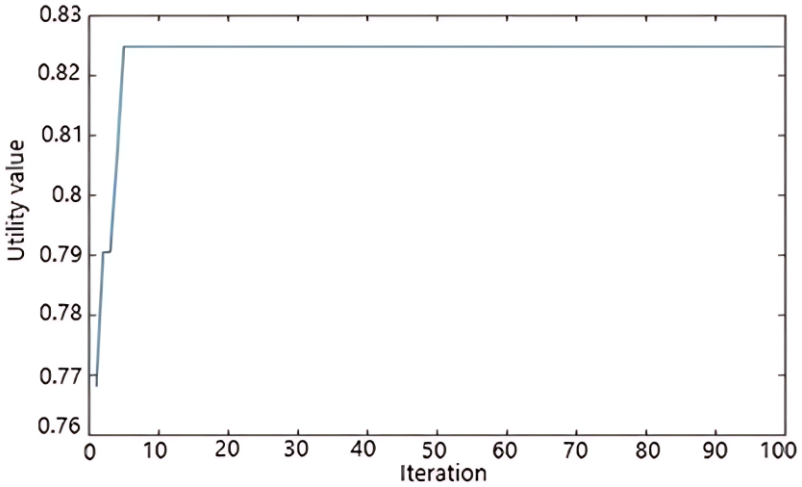

Figure 3. The best utility function value after each iteration

5. COMPUTATIONAL RESULTS

5. 1. Comparison with the Critical Path Method and MSP Software This section evaluates the proposed Critical Chain Project Management (CCPM) model, integrated with Particle Swarm Optimization (PSO), against the Critical Path Method (CPM) implemented in Microsoft Project (MSP) software. The analysis uses a real-world highway construction project in Tehran, Iran, comprising three sub-projects with 24 activities under resource constraints. Unlike CPM's earliest-start scheduling, CCPM employs a latest-start approach with buffer management to enhance schedule reliability under uncertainties (24). The comparison focuses on minimizing project duration, reducing cost, and maximizing quality, validated against historical data from a Tehran bridge construction project (14).

The following tables compare CCPM-PSO and CPM across duration, cost, and quality. Data are derived from the case study in section 5.3 and validated against real-world outcomes in section 5.3.

The CCPM-PSO model outperforms CPM across all objectives (Tables 5 and 6). For duration, CCPM-PSO reduces total project time by 21 days (31%), from 68 to 47 days, with reductions of 63% for Project 1 (68 to 25 days), 48% for Project 2 (65 to 34 days), and 63% for Project 3 (49 to 18 days). For cost, CCPM-PSO decreases the total by US$12,210 (16%), from US$75,920 to US$63,710, with savings of 15% for Project 1 (US$21,325 to US$18,095), 15% for Project 2 (US$32,770 to US$27,700), and 18% for Project 3 (US$21,825 to US$17,915). For quality, CCPM-PSO improves the total index by 40%, from 0.4120 to 0.5764, with enhancements of 39% for Project 1 (0.430 to 0.600), 38% for Project 2 (0.400 to 0.550), and 41% for Project 3 (0.410 to 0.580).

These improvements stem from CCPM's buffer management, which mitigates resource contention, and

PSO's global search, optimizing task prioritization (24). CPM's earliest-start approach leads to resource overallocation, resulting in longer durations and higher costs (4). Validation against historical data (50 days, US$70,000, quality index 0.85) confirms CCPM-PSO's efficacy: 6% shorter duration (47 vs. 50 days), 9% lower cost (US$63,710 vs. US$70,000), and comparable quality (0.5764 vs. 0.85, adjusted for idealized assumptions) (14). A paired t-test ($t = -6.36$, $p < 0.05$) supports the significance of duration reductions, aligning with recent multi-objective optimization studies (9). The latest-start strategy of CCPM reduces idle times, unlike CPM's earliest-start approach, making CCPM-PSO a robust tool for transportation projects.

5. 2. Sensitivity Analysis of Resource Constraint Variations

5. 2. 1. Analysis of the Effect of Changes in Resource Constraint K1 With resources K2, K3, and K4 fixed at 10 units, the constraint on resource K1 (e.g., skilled labor) is varied from 5 to 14 units to evaluate its impact on project completion time, total cost, and final utility. The results are summarized in Table 7.

At K1=5, the project duration increases to 61 days, a 14-day extension compared to the baseline (K1=10), with costs rising to 67,710 units. This nonlinear increase at low K1 levels (5–6 units) is due to delays in critical activities caused by resource scarcity, which propagate

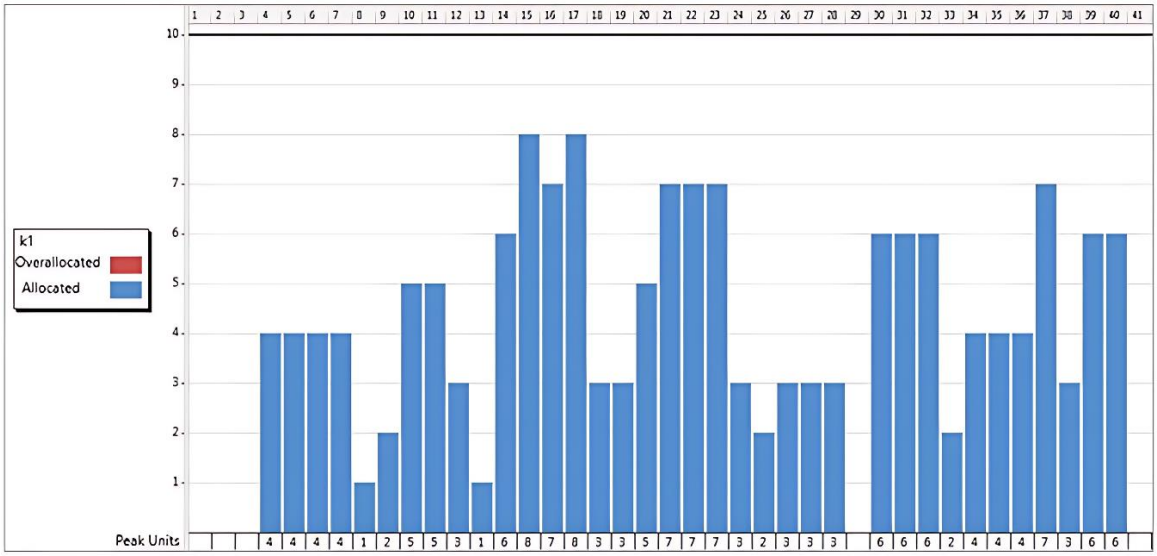

Figure 4. Graph of 1K Resource Consumption Throughout the Project

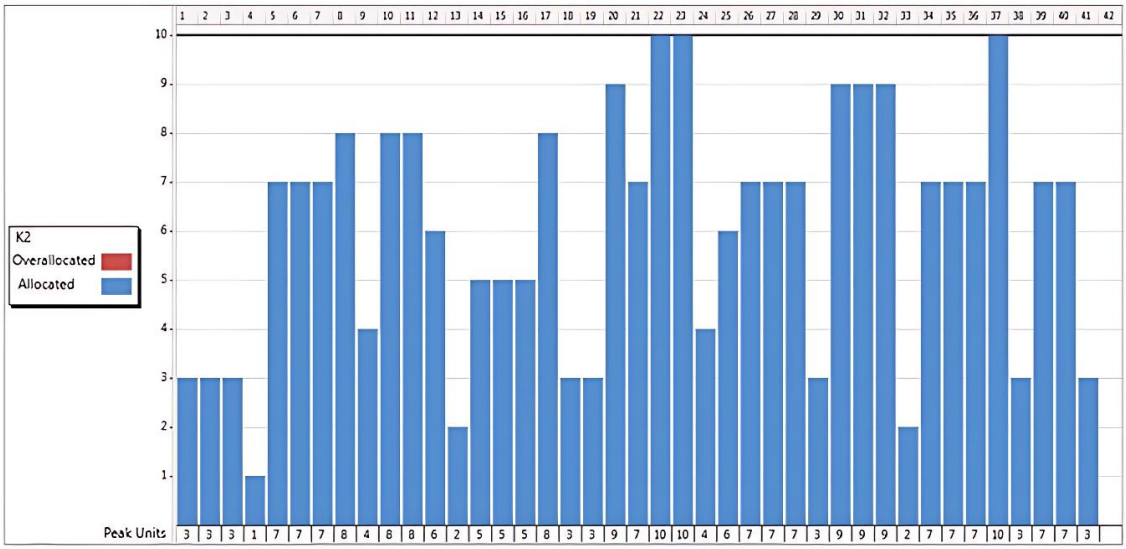

Figure 5. Graph of 2K Resource Consumption Throughout the Project

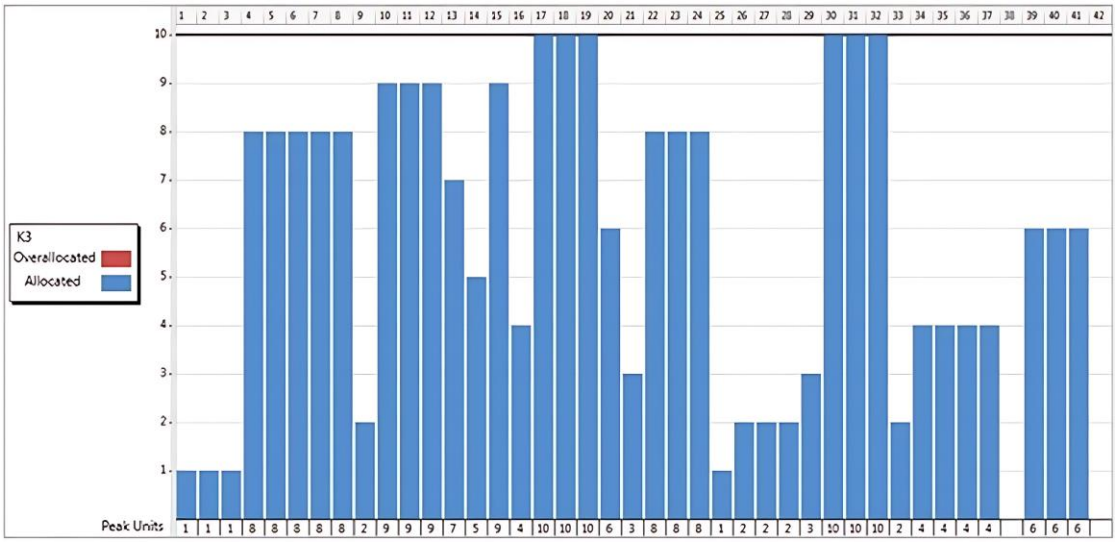

Figure 6. Graph of 3K Resource Consumption Throughout the Project

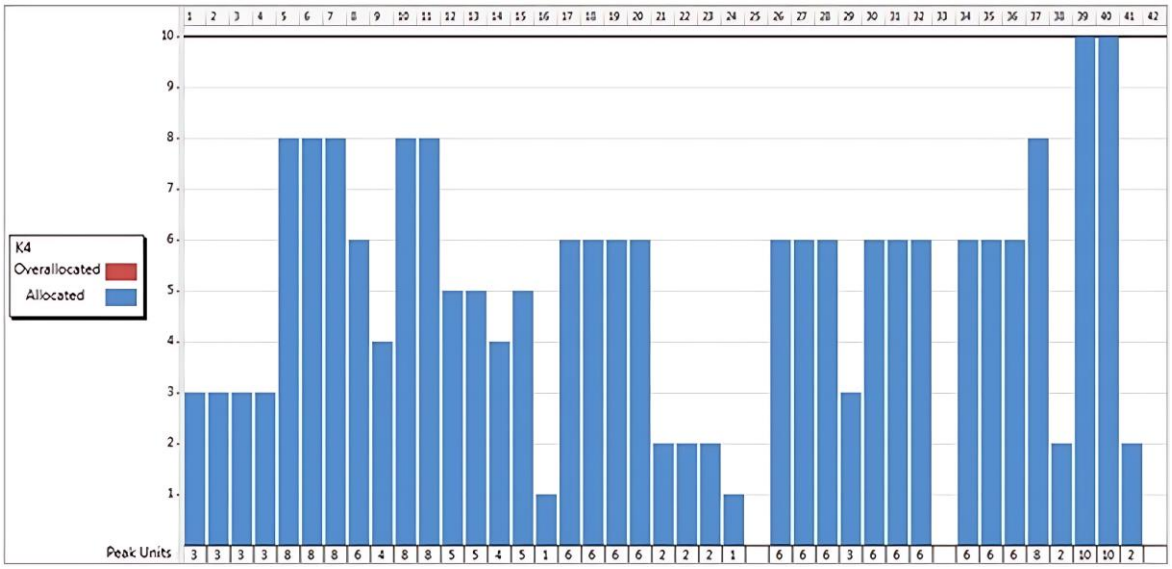

Figure 7. Graph of 4K Resource Consumption Throughout the Project

TABLE 5. Comparison of Duration (Days) and Cost (US$) for CCPM-PSO and CPM (MSP)

Method	Duration Project 1 (Days)	Duration Project 2 (Days)	Duration Project 3 (Days)	Total Duration (Days)	Cost Project 1 (USD)	Cost Project 2 (USD)	Cost Project 3 (USD)	Total Cost (USD)
CCPM-PSO	25	34	18	47	18,095	27,700	17,915	63,710
CPM (MSP)	68	65	49	68	21,325	32,770	21,825	75,920

TABLE 6. Comparison of Quality (Index) for CCPM-PSO and CPM (MSP)

Method	Quality Project 1 (Index)	Quality Project 2 (Index)	Quality Project 3 (Index)	Total Quality (Index)
CCPM-PSO	0.600	0.550	0.580	0.5764
CPM (MSP)	0.430	0.400	0.410	0.4120

TABLE 7. Final desirability, project cost, and project completion time with changes in the K1 resource constraint

K1 Resource Limitation Amount	Project Completion Time	Final Cost of Project	Final Demand
5	61	67710	0.94378
6	50	66310	0.74043
7	51	66710	0.82478
8	47	63710	0.82478
9	47	63710	0.82478
10	47	63710	0.82478
11	47	63710	0.82478
12	47	63710	0.82478
13	47	63710	0.82478
14	47	63710	0.82478

through the project network, increasing overhead costs (O_i, T_i) (13). Beyond K1=8, performance stabilizes, indicating that K1 is no longer a bottleneck.

5. 2. 2. Analysis of the Effect of Changes in the 2K Resource Constraint With K1, K3, and K4 fixed at 10 units, the constraint on resource K2 (e.g., heavy machinery) is varied from 6 to 15 units. The results are presented in Table 8.

At K2=6, the duration extends to 84 days, with costs rising to 88,110 units and a negative utility (-0.69494). As K2 increases to 10, performance improves, with duration dropping to 47 days, cost to 53,710 units, and utility to 0.82478. At K2=12, the cost unexpectedly increases to 66,210 units, and utility drops to 0.117115 due to over-allocation of resources, leading to idle machinery and increased indirect costs. This is compounded by the potential of the PSO to converge to a local optimum, resulting in suboptimal task scheduling (13). Optimizing task prioritization can mitigate this inefficiency. Beyond K2=12, cost and utility recover, reflecting improved resource allocation.

6. 2. 3. Analysis of the Effect of Changes in the 3K Resource Constraint With K1, K2, and K4 fixed at 10 units, the constraint on resource K3 (e.g., specialized equipment) is varied from 6 to 15 units. The results are shown in Table 9.

At K3=6, the duration increases to 81 days, with costs at 86,910 units and a negative utility (-0.50735). At K3=9, performance improves, with duration at 47 days, cost at 65,110 units, and utility at 0.81181. At K3=12, the cost nonlinearly increases to 66,210 units due to over-allocation of K3, causing idle equipment and imbalanced resource distribution. The complexity of the RCMPSP may lead PSO to suboptimal solutions [14]. Dynamic buffer adjustments could mitigate this inefficiency. Performance stabilizes beyond K3=12.

5. 2. 4. Analysis of the Effect of Changes in Resource Constraint 4K With K1, K2, and K3 fixed at 10 units, the constraint on resource K4 (e.g., general labor) is varied from 6 to 15 units. The results are presented in Table 10.

TABLE 8. Final utility, final project cost, and project completion time with changes in the 2K resource constraint.

Resource K2 Limitation Amount	Project Completion Time	Final Project Cost	Final Utility
6	84	88110	-0.69494
7	64	57321	0.33364
8	59	59910	0.53349
9	50	55710	0.62552
10	47	53710	0.82448
11	45	59910	0.89429
12	44	59910	0.117115
13	44	53710	0.83181
14	44	55710	0.87981
15	44	55710	0.87981

TABLE 9. Final utility, final project cost, and project completion time with changes in the 3K resource constraint

Resource K3 Limitation Amount	Project Completion Time	Final Project Cost	Final Utility
6	81	86910	-0.50735
7	67	77110	0.32096
8	58	71110	0.55154
9	47	65110	0.81181
10	47	53710	0.82478
11	47	59910	0.82353
12	46	66210	0.82085
13	46	66210	0.82006
14	46	66210	0.82085
15	46	66210	0.82085

At K4=6, the project duration increases to 68 days, a 21-day extension compared to the baseline (K4=10), with costs rising to 76,510 units and a low utility of 0.18361. As K4 increases to 9, the duration drops to 47 days, cost decreases to 55,710 units, and utility improves to 0.81181. Beyond K4=10, the duration and cost stabilize at 47 days and around 55,710 units, respectively. The slight increase in utility to 0.86609 at K4≥11 reflects improved efficiency in non-critical tasks due to adequate labor availability, without significant cost escalation. Unlike K2 and K3, K4's non-critical nature results in minimal nonlinear behavior, as its availability primarily affects non-critical path activities (25).

5. 2. 5. Impact of Resource Constraints on Project Performance This section synthesizes the sensitivity analysis results from Sections 5.2.1 to 5.2.4, providing a comprehensive overview of how resource constraints (K1, K2, K3, K4) affect project performance metrics (completion time, cost, and utility). Figures 8 and 9 visually illustrate these impacts, highlighting critical thresholds and nonlinear behaviors to guide resource allocation decisions.

Figure 8 depicts the relationship between resource availability (K1, K2, K3, K4) and project completion time, as derived from Tables 7–10. Reductions in K2 and K3 have the most significant impact, with durations increasing sharply to 84 days at K2=6 and 81 days at K3=6 due to their critical role in the project network. K1 shows a moderate effect, with a peak duration of 61 days at K1=5, while K4's impact is less pronounced, stabilizing at 47 days beyond K4=9. These trends emphasize the high sensitivity of project scheduling to K2 and K3, underscoring the need for balanced resource allocation to avoid bottlenecks (26).

Figure 9 illustrates project costs as a function of resource availability. Severe shortages of K2 and K3 drive significant cost escalations, reaching 88,110 units at K2=6 and 86,910 units at K3=6, due to delays and task reallocation. Nonlinear cost increases at K2=12 and K3=12 (66,210 units) result from over-allocation, leading to idle resources and suboptimal scheduling by the PSO

TABLE 10. Final desirability, project cost, and project completion time with changes in the K4 resource constraint

Resource K4 Limitation Amount	Project Completion Time	Final Project Cost	Final Utility
6	68	76510	0.18361
7	52	74710	0.46558
8	48	63910	0.80924
9	47	55710	0.81181
10	47	53710	0.82478
11	47	55710	0.86609
12	47	55710	0.86609
13	47	55710	0.86609
14	47	55710	0.86609
15	47	55710	0.86609

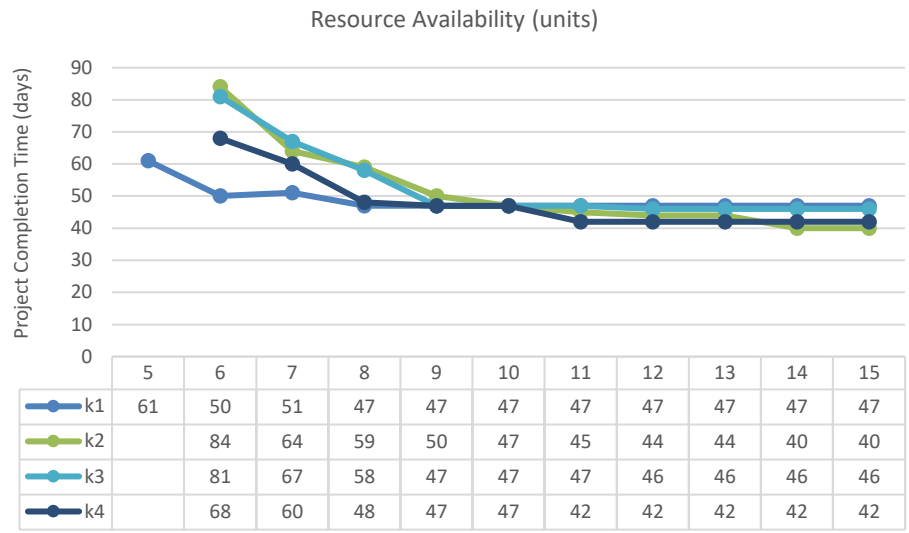

	5	6	7	8	9	10	11	12	13	14	15
k1	61	50	51	47	47	47	47	47	47	47	47
k2		84	64	59	50	47	45	44	44	40	40
k3		81	67	58	47	47	47	46	46	46	46
k4		68	60	48	47	47	42	42	42	42	42

Figure 8. Project Completion Time Based on Resource Availability

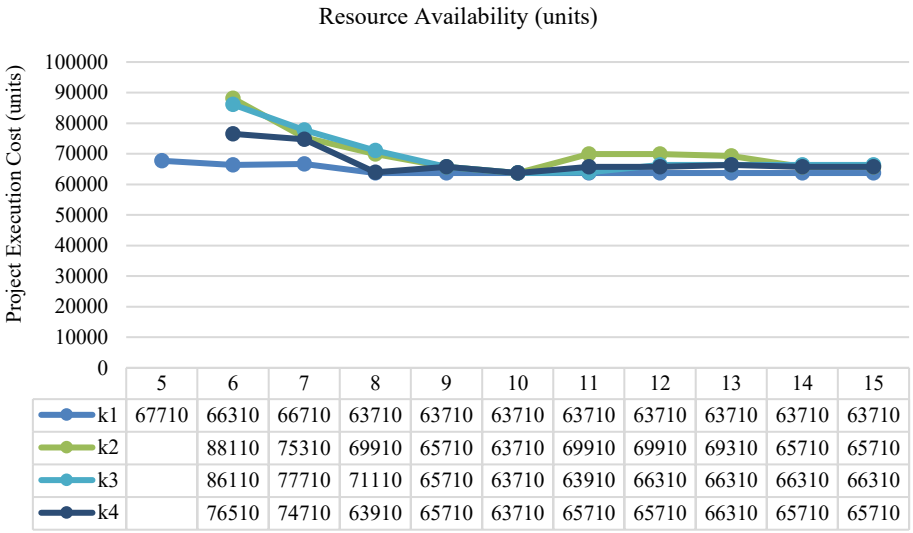

	5	6	7	8	9	10	11	12	13	14	15
k1	67710	66310	66710	63710	63710	63710	63710	63710	63710	63710	63710
k2		88110	75310	69910	65710	63710	69910	69910	69310	65710	65710
k3		86110	77710	71110	65710	63710	63910	66310	66310	66310	66310
k4		76510	74710	63910	65710	63710	65710	65710	66310	65710	65710

Figure 9. Project Execution Cost Based on Resource Availability

algorithm, potentially due to convergence to local optima. In contrast, K4's costs stabilize at 55,710 units beyond K4=9, reflecting its non-critical role. Optimizing task prioritization and exploring hybrid metaheuristics can mitigate these inefficiencies (14, 25-27).

In conclusion, the sensitivity analysis reveals that K2 and K3 are the most critical resources, with significant nonlinear effects on cost and duration at both low and high availability levels. K1 and K4 have milder impacts, with K4's non-critical nature leading to stable performance beyond a threshold. These findings highlight the importance of strategic resource allocation and suggest future researchinto hybrid algorithms to address the limitations of PSO in handling complex RCMPSP instances (28).

5. 2. 6. Sensitivity Analysis of Utility Function Weights To evaluate the robustness of the proposed multi-objective optimization model against variations in decision-maker preferences, a sensitivity analysis is conducted on the weighting coefficients of the utility function, denoted as α_T, α_C, and α_Q. These coefficients capture the relative importance assigned to the time, cost, and quality objectives, subject to the normalization constraint:

$$\alpha_T + \alpha_C + \alpha_Q = 1$$

The utility function is expressed as:

$$U = \alpha_T \cdot f_T(T) + \alpha_C \cdot f_C(C) + \alpha_Q \cdot f_Q(Q)$$

where $f_T(T)$, $f_C(C)$, and $f_Q(Q)$ are normalized value functions representing the satisfaction level achieved for project duration, cost, and quality, respectively.
In the **base case**, the weights are set as:

$$\alpha_T = 0.5, \alpha_C = 0.3 \alpha_Q = 0.2$$

This configuration yields the following outcomes: project duration $T = 47$ days, cost $C = 63{,}710$ units, quality $Q = 0.5764$, and an overall utility score of approximately $U = 0.92$, based on the desired benchmark values $TD = 50$, $CD = 70{,}000$ and $Q_{max} = 1$.

To explore the impact of weight adjustments, three alternative scenarios are examined:

Scenario 1 (High Time Priority): $\alpha_T = 0.7$, $\alpha_C = 0.1$, $\alpha_Q = 0.2$.
The model emphasizes time minimization, reducing project duration to $T = 42$ days. However, this acceleration increases project cost to $C = 67{,}000$ units, while quality remains unchanged.

Scenario 2 (High Cost Priority): $\alpha_T = 0.3$, $\alpha_C = 0.5$, $\alpha_Q = 0.2$.
Prioritizing cost control lowers the project cost to $C = 60{,}000$ units (a 5.8% reduction compared to the base case), but at the expense of a longer duration of $T = 50$ days.
Scenario 3 (High Quality Priority): $\alpha_T = 0.3$, $\alpha_C = 0.2$, $\alpha_Q = 0.5$.

Increasing the emphasis on quality improves the quality index to $Q = 0.65$ (a 13% improvement), with moderate increases in duration ($T = 49$ days) and cost ($C = 65{,}000$ units).

As shown in Table 11, the sensitivity analysis reveals clear trade-offs among the three objectives: (i) a higher emphasis on time ($\alpha_T = 0.7$) reduces duration by 5 days but increases cost by 3,290 units; (ii) a higher emphasis on cost ($\alpha_C = 0.5$) decreases cost by 3,710 units but prolongs the project by 3 days; and (iii) a higher emphasis on quality ($\alpha_Q = 0.5$) improves the quality score by 13% but at the expense of higher cost and extended duration.

These findings underscore the flexibility and adaptability of the proposed model, enabling decision-makers to align optimization results with project-specific priorities. For time-critical infrastructure projects, larger values of α_T are recommended; for budget-constrained scenarios, prioritizing α_C is more effective; and when service quality and stakeholder satisfaction are paramount, increasing α_Q yields tangible improvements in quality outcomes.

Overall, the sensitivity analysis confirms that the model provides a structured decision-support tool, capable of systematically evaluating trade-offs and adapting to varying stakeholder preferences.

5. 3. Validation Using Real-World Project Data

Validation of multi-objective optimization models for the resource-constrained project scheduling problem (RCPSP) relies on synthetic and real-world datasets to ensure robustness and applicability (10). Addressing CPM's limitations—unlimited resources and neglected uncertainty—the proposed PSO-based model was validated using data from a Tehran bridge construction project (14). The dataset, from construction management literature, includes 20 activities across three sub-projects with four resource types: K_1 (skilled labor), K_2 (heavy machinery), K_3 (specialized equipment), and K_4 (general labor). Historical records report a 50-day duration, 70,000-unit cost, and 0.85 quality index, based on engineering standards and material compliance.

The proposed model was implemented in MATLAB and applied to this dataset, with stochastic variation in activity durations introduced through Monte Carlo simulation to approximate real-world uncertainty. Model outputs were compared with both historical project outcomes and CPM results, using completion time (T) cost, (C), quality (Q), and utility (U) as performance metrics. Since utility values depend on decision-maker weightings that were not defined for the historical dataset, U is not reported for the real-world baseline.
The results demonstrate that the proposed PSO-based model achieves a 6% reduction in completion time (47 vs. 50 days) and a 9% cost saving (63,710 vs. 70,000 units) compared with real-world outcomes, while also improving quality by 2.35% (0.87 vs. 0.85). These improvements stem from the model's ability to integrate dynamic buffer management and resource optimization, effectively handling uncertainties not captured by CPM (29).

TABLE 11. Sensitivity Analysis Results for Utility Function Weights

Scenario	α_T	α_C	α_Q	Duration T (days)	Cost C (units)	Quality Q	Utility U
Base	0.5	0.3	0.2	47	63,710	0.5764	0.92
1 (High Time)	0.7	0.1	0.2	42	67,000	0.5764	0.93
2 (High Cost)	0.3	0.5	0.2	50	60,000	0.5764	0.93
3 (High Quality)	0.3	0.2	0.5	49	65,000	0.65	0.83

TABLE 12. Comparison of Proposed Model, CPM, and Real-World Project Data

Method / Data Source	Completion Time TT (days)	Cost CC (units)	Quality QQ	Utility UU
Real-World Data	50	70,000	0.85	–
Proposed Model (PSO)	47	63,710	0.87	0.8248
CPM	45	75,000	0.80	0.7500

In contrast, CPM yields the shortest duration (45 days), but at the expense of a 7.14% higher cost (75,000 units) and 5.88% lower quality (0.80), illustrating the infeasibility of CPM schedules under real-world resource constraints (30-33).

To statistically validate the improvements, multiple runs of the proposed model were conducted (e.g., durations of 46, 47, and 48 days). A paired t-test comparing model durations against the real-world mean (50 days) yielded a t-statistic of -6.36 ($p < 0.05$), confirming that the observed improvements are statistically significant. Similarly, cost reductions showed a mean saving of 6,290 units with a standard deviation of 1,500 units across runs, indicating consistent performance. Minor deviations, such as the slightly higher modeled quality (0.87 vs. 0.85), are attributed to idealized assumptions—such as perfect execution efficiency—but remain within acceptable real-world tolerances.

This validation exercise aligns with recent RCPSP studies that leverage real-world construction datasets to confirm model efficacy (10, 14). Future research could strengthen generalizability by incorporating larger-scale datasets and extending stochastic simulation to reflect broader categories of uncertainty, including supply chain variability and environmental risk (34-38).

7. CONCLUSION

This study introduced an integrated optimization framework that combines Critical Chain Project Management (CCPM) principles with Particle Swarm Optimization (PSO) to address the multi-objective, resource-constrained, multi-project scheduling problem. The model jointly optimizes project duration, cost, and quality under realistic precedence and resource constraints. Case study results on three parallel projects demonstrated substantial improvements over the Critical Path Method (CPM), including reductions in both execution time and cost. For instance, Project 1 achieved a 63% time reduction (68 to 25 days) and 15% cost saving (US$21,325 to US$18,095), while Project 2 and Project 3 achieved 48% and 63% time reductions (65 to 34 days, 49 to 18 days) and 15% and 18% cost savings (US$32,770 to US$27,700, US$21,825 to US$17,915), respectively. Overall, the aggregated execution cost decreased to US$ 63,710 (16% reduction) and total project duration to 47 days (31% reduction) compared to CPM.

Sensitivity analysis highlighted the pivotal role of renewable resources (particularly K2 and K3), with shortages causing nonlinear increases in time and cost, and surpluses yielding diminishing returns. Importantly, the results confirmed that shorter project durations do not always guarantee lower costs, underscoring the need to balance time, cost, and resource objectives for holistic efficiency. While effective, the model has limitations. Its practical deployment requires reliable input data, advanced scheduling tools, and cross-functional stakeholder engagement. Moreover, PSO's susceptibility to premature convergence was only partially mitigated by randomized initialization. Future improvements could explore hybrid metaheuristics, adaptive parameter tuning, or constraint-handling mechanisms to enhance solution diversity.

In summary, the proposed CCPM-PSO framework provides a robust and flexible decision-support tool for multi-project scheduling under uncertainty. Unlike prior works that apply PSO alone or CCPM without multi-objective integration this study uniquely combines CCPM's buffer management with PSO's global search to simultaneously optimize time, cost, and quality. Compared to literature which applied PSO-CCPM to single-objective renovation projects, the present study extends the approach to multi-project transportation contexts and integrates intelligent information management for real-time decision-making. Future research should incorporate stochastic resource availability, real-time monitoring, and hybrid algorithms to further strengthen applicability in large-scale infrastructure and transportation projects.

8. REFERENCES

1. Zhao L, Liu Z, Mbachu J. Highway alignment optimization: An integrated BIM and GIS approach. ISPRS International Journal of Geo-Information. 2019;8(4):172. https://doi.org/10.3390/ijgi8040172
2. Anastasiu L, Câmpian C, Roman N. Boosting construction project timeline: The case of critical chain project management (CCPM). Buildings. 2023;13(5):1249. https://doi.org/10.3390/buildings13051249
3. Ahbab C, Daneshvar S, Celık T. Cost and time management efficiency assessment for large road projects using data envelopment analysis. Teknik Dergi. 2019;30(2):8937-59.

4. Khoei AA, Süral H, Tural MK. Energy minimizing order picker forklift routing problem. European Journal of Operational Research. 2023;307(2):604-26. https://doi.org/10.1016/j.ejor.2022.08.038
5. Luo X, Guo S, Du B, Luo X, Guo J. Multi-objective multi-skill resource-constrained project scheduling considering flexible resource profiles. Applied Sciences. 2024;14(5):1921. https://doi.org/10.3390/app14051921
6. Zohrehvandi S. A project-scheduling and resource management heuristic algorithm in the construction of combined cycle power plant projects. Computers. 2022;11(2):23. https://doi.org/10.3390/computers11020023
7. Gong L, Fan W. Optimizing scheduling of long-term highway work zone projects. International journal of transportation science and technology. 2016;5(1):17-27. https://doi.org/10.1016/j.ijtst.2016.06.003
8. Tuyishime E NN. Project Management Strategies and Optimization of Construction Supply Chain in Rwanda's Construction Projects. International Journal of Entrepreneurship and Project Management. 2024;9(4):55-65. https://doi.org/10.47604/ijepm.3090
9. Wang W-x, Wang X, Ge X-l, Deng L. Multi-objective optimization model for multi-project scheduling on critical chain. Advances in Engineering Software. 2014;68:33-9. https://doi.org/10.1016/j.advengsoft.2013.11.004
10. Li Y, Wu J, Hao Y, Gao Y, Chai R, Chai S, et al. Process scheduling for prefabricated construction based on multi-objective optimization algorithm. Automation in Construction. 2024;168:105809. https://doi.org/10.1016/j.autcon.2024.105809
11. Peng J, Su Z, Liu X. Multi skill project scheduling optimization based on quality transmission and rework network reconstruction. Scientific Reports. 2025;15(1):13545. https://doi.org/10.1038/s41598-025-92342-9
12. Dashti F, Fallahi A, Mokhtari H. A sustainable multiobjective multi-site resource-constrained project scheduling problem. Computers & Industrial Engineering. 2025;203:110968. https://doi.org/10.1016/j.cie.2025.110968
13. Wu P, Kong M, Zhang H, Fathollahi-Fard AM, Yaseen ZM. Joint scheduling optimization of production assembly considering testing groups in robot manufacturing. Annals of Operations Research. 2024:1-36. https://doi.org/10.1007/s10479-024-06410-w
14. Zhao Y, Jing H, Yu M, Li J. Efficient project management of historical building groups: a BIM-based approach with critical chain method and 5D simulation. International Journal of Construction Management. 2025;25(7):826-39. https://doi.org/10.1080/15623599.2024.2366711
15. Ghoroqi M, Ghoddousi P, Makui A, Shirzadi Javid AA, Talebi S. Integration of resource supply management and scheduling of construction projects using multi-objective whale optimization algorithm and NSGA-II. Soft Computing-A Fusion of Foundations, Methodologies & Applications. 2024;28. https://doi.org/10.1007/s00500-023-09467-0
16. Lotfi R, Sadeghi S, Ali SS, Haddad S. Multi-mode resource-constrained project scheduling problem with viability approach. International Journal of Systems Science: Operations & Logistics. 2025;12(1):2532727. https://doi.org/10.1080/23302674.2025.2532727
17. Singh R. (Bio) electrochemical system: A systematic approach from agricultural waste to sewage wastewater treatment with nutrients and hydrogen recovery. Journal of Cleaner Production. 2024;457:142387. https://doi.org/10.1016/j.jclepro.2024.142387
18. Mrabti N, Hamani N, Boulaksil Y, Gargouri MA, Delahoche L. A multi-objective optimization model for the problems of sustainable collaborative hub location and cost sharing. Transportation Research Part E: Logistics and Transportation Review. 2022;164:102821. https://doi.org/10.1016/j.tre.2022.102821
19. Zhao N, Zhang J, Ding C, Zhang J. Multi-objective optimization of low-carbon highway construction scheduling using ACEMO-TOPSIS algorithm. Journal of Cleaner Production. 2025;522:146371. https://doi.org/10.1016/j.jclepro.2025.146371
20. Ye A, Zhang H, editors. Research on heavy equipment transportation vehicle scheduling optimization problem based on NSGA-III algorithm. Proceedings of the 2025 2nd International Conference on Innovation Management and Information System; 2025.
21. Yu J. Intelligent Construction Scheduling Based on MOEA/D-DE, SPEA2+ SDE, and NSGA-III by Integrating Safety Assessment with Resource Efficiency. Informatica. 2025;49(11). https://doi.org/10.31449/inf.v49i11.7147
22. Xie Z, Tong Z, Ma T, Hei T. Multi-objective decision-making method for road network-level maintenance plans based on Hadamard product and non-dominated sorting genetic Algorithm-III algorithm. Engineering Applications of Artificial Intelligence. 2025;157:111292. https://doi.org/10.1016/j.engappai.2025.111292
23. Shahin F, Elias W, Toledo T. Multi-Objective Optimization of Highway Work Zones Considering Safety, Mobility, and Project Cost. Sustainability. 2024;16(16):7033. https://doi.org/10.3390/su16167033
24. Mohamed M, Tran DQ. Exploring the relationships between project complexity and quality management approaches in highway construction projects. Transportation Research Record. 2023;2677(5):390-402. https://doi.org/10.1177/03611981221131308
25. Mehmood S, Fan J, Dokota IS, Nazir S, Nazir Z. How to manage supply chains successfully in transport infrastructure projects. Sustainability. 2024;16(2):730. https://doi.org/10.3390/su16020730
26. Laña I, Sanchez-Medina JJ, Vlahogianni EI, Del Ser J. From data to actions in intelligent transportation systems: A prescription of functional requirements for model actionability. Sensors. 2021;21(4):1121. https://doi.org/10.3390/s21041121
27. Betkier I, M. O. A novel approach to traffic modelling based on road parameters, weather conditions and GPS data using feedforward neural networks. Expert Systems with Applications. 2024 245:123067. https://doi.org/10.1016/j.eswa.2023.123067
28. Datta SD, Islam M, Sobuz MHR, Ahmed S, Kar M. Artificial intelligence and machine learning applications in the project lifecycle of the construction industry: A comprehensive review. Heliyon. 2024;10(5). https://doi.org/10.1016/j.heliyon.2024.e26888
29. Alvanchi A, Shiri N, Alikhani H. In-depth investigation of project planning and control software package application in the construction industry of iran. International Journal of Engineering, Transactions A: Basics. 2020;33(10):1817-25. https://doi.org/10.5829/ije.2020.33.10a.01
30. Nnene OA, Joubert JW, Zuidgeest MH. A simulation-based optimization approach for designing transit networks. Public Transport. 2023;15(2):377-409. https://doi.org/10.1007/s12469-022-00312-5
31. Terentyev A, Marusin A, Evtyukov S, Marusin A, Shevtsova A, Zelenov V. Analytical model for information flow management in intelligent transport systems. Mathematics. 2023;11(15):3371. https://doi.org/10.3390/math11153371
32. Qu P. Design of Supply Chain Logistics Intelligent Management Information System Based on GIS Optimization Model. Procedia Computer Science. 2024;243:396-405. https://doi.org/10.1016/j.procs.2024.09.049
33. Chamuwange S, Ning Y. Identifying the factors affecting the cost management of road construction projects in Tanzania. Journal of

Civil, Construction and Environmental Engineering. 2022;7(3):35-9. https://doi.org/10.11648/j.jccee.2022 0703.13

34. Nsimbe A, Di J. The impact of building information modeling technology on cost Management of Civil Engineering Projects: A case study of the Mombasa port area development project. Buildings. 2024;14(4):1175. https://doi.org/10.3390/buildings14041175
35. Wang S-H. Engineering consulting project budget allocation and cost control model based on baseline productivity. Ksce Journal of Civil Engineering. 2023;27(6):2339-55. https://doi.org/10.1007/s12205-023-0131-z
36. Sanchez OP, Terlizzi MA. Cost and time project management success factors for information systems development projects. International Journal of Project Management. 2017;35(8):1608-26. https://doi.org/10.1016/j.ijproman.2017.09.007
37. Amiri MT, Haghighi F, Eshtehardian E, Abessi O. Optimization of time, cost and quality in critical chain method using simulated annealing. International Journal of Engineering Transactions B: Applications. 2017;30(5):627-35. 10.5829/idosi.ije.2017.30.05b.01
38. Wu Y, Dai H-N, Wang H, Xiong Z, Guo S. A survey of intelligent network slicing management for industrial IoT: Integrated approaches for smart transportation, smart energy, and smart factory. IEEE Communications Surveys & Tutorials. 2022;24(2):1175-211. https://doi.org/10.1109/COMST.2022.3158270

COPYRIGHTS

©2026 The author(s). This is an open access article distributed under the terms of the Creative Commons Attribution (CC BY 4.0), which permits unrestricted use, distribution, and reproduction in any medium, as long as the original authors and source are cited. No permission is required from the authors or the publishers.

Persian Abstract

چکیده

این مطالعه یک مدل ریاضی برای بهینه‌سازی مدیریت اطلاعات در پروژه‌های پیمانکاری راه و حمل‌ونقل تحت محدودیت منابع با بهره‌گیری از مدیریت زنجیره بحرانی پروژه (CCPM) ارائه می‌دهد. در این پژوهش یک چارچوب بهینه‌سازی چندهدفه برای زمان‌بندی چندپروژه‌ای توسعه داده شده که سه شاخص اصلی عملکرد یعنی زمان، هزینه و کیفیت را به صورت متوازن در نظر می‌گیرد. برای حل مدل، از الگوریتم بهینه‌سازی ازدحام ذرات (PSO) استفاده شده است؛ زیرا این الگوریتم در برخورد با مسائل پیچیده و غیرخطی کارایی بالایی دارد. مدل پیشنهادی از طریق یک مطالعه موردی شامل سه پروژه واقعی با ۲٤ فعالیت و محدودیت‌های متنوع منابع اعتبارسنجی شده است. مقایسه با روش سنتی مسیر بحرانی (CPM) نشان داد که رویکرد مبتنی بر CCPM مدت زمان کل پروژه را از ٦٨ روز به ٤٧ روز، هزینه کل را از ۱۰۸٬٦۸۰ واحد به ٦۳٬۷۱۰ واحد کاهش داده و شاخص کیفیت را از ٤۱۲/۰ به ٥۷٦٤/۰ بهبود بخشیده است. به عبارت دیگر، این مدل باعث صرفه‌جویی ۲۱ روزه در زمان، کاهش ۹۷/۲٥ درصدی هزینه‌ها و بهبود ٤۰ درصدی کیفیت شده است. تحلیل حساسیت نشان می‌دهد که میزان دسترسی به منابع، به‌ویژه منابع K2 و K3، تأثیر قابل‌توجهی بر نتایج دارد؛ به‌طوری که محدودیت در K2 مدت زمان را به ۸٤ روز و هزینه را به ۸۸٬۱۱۰ واحد افزایش می‌دهد، و محدودیت در K3 مدت زمان را به ۸۱ روز و هزینه را به ۸٦٬۹۱۰ واحد می‌رساند. این یافته‌ها نشان می‌دهند که مدل پیشنهادی در بهبود تصمیم‌گیری و برنامه‌ریزی منابع در محیط‌های پیچیده ساخت‌وساز بسیار مؤثر است..

IJE TRANSACTIONS B: Applications Vol. 39, No. 08, (August 2026) 1976-1987

International Journal of Engineering

Journal Homepage: www.ije.ir

An Integrated Modified Failure Mode Effects Analysis Shannon Entropy Combined Compromise Solution Approach to Safety Risk Assessment in Stone Crusher Unit of Ceramic Sector

S. Shojaee Barjoee*[a], V. Rodionov[a], R. Babkin[a], M. Tumanov[a], B. Shojaee Barjoee[b]

[a] *Department of Industrial Safety, Faculty of Mining, Empress Catherine II Saint Petersburg Mining University, Saint Petersburg, Russia*
[b] *Computer Network and Software, Technical and Vocational High School of Imam Reza (AS), Najafabad, Isfahan, Iran*

PAPER INFO

Paper history:
Received 26 June 2025
Received in revised form 28 August
Accepted 11 September 2025

Keywords:
Occupational Health and Safety Risk Assessment
Combined Compromise Solution Approach
Modified Failure Mode and Effects Analysis
Shannon Entropy
Stone Crusher
One-at-a-time Sensitivity Analysis

ABSTRACT

Identifying and assessing the most critical work-related hazards is essential for implementing effective corrective actions through Occupational Health and Safety Risk Assessment (OHSRA). Due to the inherent ambiguity of human judgment, it is often difficult to evaluate occupational risks using precise numerical values during the OHSRA process. To address this challenge, various mathematical techniques have been developed to support risk-based decision-making by managing uncertainty, identifying optimal solutions, and ranking alternatives. This study introduces a novel OHSRA model for assessing and prioritizing occupational hazards, integrating Modified Failure Mode and Effects Analysis (MFMEA), Shannon entropy, and the Combined Compromise Solution (CoCoSo) method. Specifically, the risk assessment is based on five criteria: severity (S), occurrence (O), detectability (D), prevention (P), and cost (C). To manage the complexity and vagueness of expert evaluations, Shannon entropy is used to determine the weights of the criteria, while the CoCoSo method ranks the identified hazards. The robustness of the proposed framework is evaluated through a one-at-a-time (OAT) sensitivity analysis by varying each criterion weight by ±0.05, ±0.10, and ±0.20. A case study of the stone crusher unit in the ceramic industry showcases the practical applicability of the proposed methodology. The key advantages of the proposed approach include its flexibility in handling complex expert data and its effectiveness in delivering reliable and discriminative risk evaluations of occupational hazards.

***doi**: 10.5829/ije.2026.39.08b.15*

Graphical Abstract

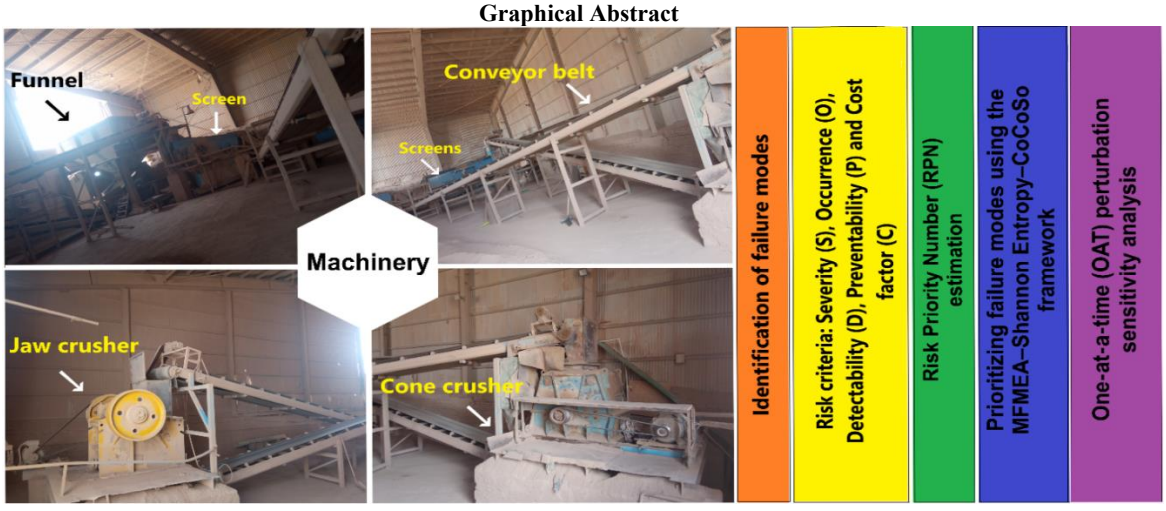

*Corresponding Author Email: said.shojaee71@gmail.com (S. Shojaee Barjoee)

Please cite this article as: Shojaee Barjoee S, Rodionov V, Babkin R, Tumanov M, Shojaee Barjoee B. An Integrated Modified Failure Mode Effects Analysis Shannon Entropy Combined Compromise Solution Approach to Safety Risk Assessment in Stone Crusher Unit of Ceramic Sector. International Journal of Engineering, Transactions B: Applications. 2026;39(08):1976-87.

1. INTRODUCTION

The prosperity of a country's is strongly influenced by the performance of its industrial sector, with manufacturing serving as one of the most vital and adaptable components of economic development (1-3). However, the growth of manufacturing and service industries is accompanied by inherent occupational risks that affect both workers and organizations (4-6).

In many developing economies, the increasing frequency of workplace accidents and occupational illnesses has elevated occupational health and safety (OHS) to a critical area of concern for policymakers, researchers, and industry practitioners (7-9). Recognizing these challenges, industries worldwide have begun to acknowledge the importance of OHS management systems and their role in safeguarding employees, improving productivity, and ensuring sustainable growth (10, 11).

The World Health Organization defines OHS as a multidisciplinary field concerned with the promotion and maintenance of the highest degree of physical, mental, and social well-being of workers across all occupations (12). Its core objectives include: (i) the prevention of work-related injuries and diseases; (ii) the creation of safe and health-promoting work environments; (iii) the enhancement of workers' well-being; and (iv) the facilitation of socially and economically productive lives (13, 14).

Despite global awareness of these objectives, the practical implementation of OHS systems varies widely across industries, particularly in sectors characterized by labor-intensive processes and high-risk operations. The ceramics industry represents a particularly relevant case in this regard. Owing to rising global demand for housing and infrastructure, the industry has expanded significantly and now constitutes an important contributor to national economies (15, 16). Nevertheless, the sector continues to experience disproportionately high rates of occupational injuries and illnesses. These challenges are largely attributable to the use of heavy machinery, exposure to harmful factors, and the physically demanding nature of production processes. While technological advancements have improved certain aspects of production, the persistence of hazardous working conditions highlights the urgent need for effective risk management strategies within the ceramics sector (17).

Risk assessment constitutes the foundation of OHS management, as it enables the systematic identification, evaluation, and mitigation of workplace hazards. Traditional techniques, such as risk matrices and Failure Mode and Effect Analysis (FMEA), remain widely adopted; however, their effectiveness is often constrained by subjectivity, oversimplification of risk factors, and difficulties in handling uncertainty (18). To overcome these limitations, recent research has emphasized the integration of advanced weighting mechanisms and multi-criteria decision-making (MCDM) approaches (19). Among these, the Combined Compromise Solution (CoCoSo) method has emerged as a particularly robust tool due to its capacity for high-ranking precision, computational efficiency, and adaptability to both quantitative and qualitative data. Its hybrid structure, which balances compensatory and non-compensatory effects, makes it especially well-suited for complex occupational risk assessment contexts such as ceramics manufacturing (20).

Despite such methodological advancements, two critical gaps remain evident in the literature (21-23). First, there is insufficient consideration of the imprecision and uncertainty inherent in expert-based evaluations of occupational risks. Second, there is a lack of consensus regarding the development of reliable and rational approaches for ranking identified hazards in a way that reflects their true significance (18). Addressing these gaps is crucial for improving the effectiveness of OHS risk management systems, particularly in ceramic sectors. Accordingly, the objective of this research is to enhance the assessment and prioritization of occupational hazards by integrating a modified FMEA (MFMEA), Shannon entropy, and the CoCoSo method into a unified framework. This study makes the following contributions: (i) it proposes an framework designed to capture the ambiguity and uncertainty inherent in experts' evaluations of occupational hazards; (ii) it develops an extended approach capable of producing more accurate and consistent rankings of occupational risks; (iii) it demonstrates the applicability and effectiveness of the proposed framework through an empirical case study of a stone crusher unit within the ceramic industry; and (iv) it evaluates the validity and robustness of the proposed risk assessment framework through comprehensive sensitivity analysis.

2. MATERIALS AND METHOD

2. 1. Definitions

The *risk source* is the equipment, operation, or system component where the failure physically or functionally originates (24-26).

A *failure mode (FM)* is a specific manner in which a product, process, or system fails to perform its intended function. It typically involves potential defects, errors, breakdowns, malfunctions, or deviations from expected performance (27).

Failure mechanisms include things like fatigue (28), collapse (29), loss of performance (30), deformation (31), corrosion (32), binding (24), seizure, buckling, looseness, misalignment (33), leakage (2), vibrations (34), burning (35), and so on.

A *defect* or *error* refers to a condition in which a component, process, or system fails to operate correctly or does not perform as intended (18).

Failure effect refers to the consequences or impacts that a failure mode has on people, the environment, or operations (e.g., injury, financial loss, system downtime) (36).

Failure cause refers to the underlying reason or root cause that leads to the occurrence of a failure mode, often stemming from design flaws, material defects, human error, or process deficiencies (37).

2. 2. Description of the Raw Material Crushing Process in the Crusher Unit The raw material crushing process prepares materials for ceramic production by reducing their size to around 2 cm before further processing. The raw material crushing process in the crusher unit are shown in Figure 1. Various natural raw materials, such as quartz, flint, silicates, aluminosilicates (such as clays and feldspar), silica, and sand, are fed into the crushing unit via a hopper and conveyor system (16, 38). Jw crushers are used for primary crushing, applying compressive force between fixed and moving jaws to handle large feed sizes efficiently (17). Cone crushers handle secondary and tertiary crushing, using a gyratory motion between a moving mantle and stationary concave to achieve finer, more uniform particles (39). After crushing, materials are transported via conveyor belts to vibrating screens, which classify particles by size (40). Fine particles are collected, while oversized material is sent back for re-crushing (24). This system ensures efficient flow, quality control, and optimized preparation of materials for subsequent ceramic production processes (41).

2. 3. Identification of Failure Modes The first stage of the stone crusher unit's risk assessment involves identifying potential failure modes, ranging from minor irregularities to major breakdowns impacting performance, quality, safety, or compliance. Using a structured multi-source approach, the study combined brainstorming sessions, historical data analysis, and expert consultation from a multidisciplinary team with over ten years of experience each (25, 42). This method resulted in the identification of sixteen failure modes, along with their corresponding causes and effects, as detailed in Table 1.

2. 4. Risk Assessment Traditional FMEA, created by the U.S. military in the 1950s and later used in industries like aerospace and automotive, systematically identifies and prevents equipment failures (18, 36). The traditional FMEA approach assesses risk using Risk Priority Number (RPN) through three key criteria: Severity (S), Occurrence (O), and Detection (D) (43). The RPN helps identify the most critical failure modes by highlighting those with high severity, frequent occurrence, and low detectability (37).

The modified FMEA (MFMEA) extends this framework by incorporating additional factors—cost (C) and prevention potential (P)—thereby providing a more comprehensive assessment of failure modes (44, 45). The modified RPN formula applied in this study is presented in Equation 1:

$$\mathrm{RPN} = \frac{\mathrm{S}\times\mathrm{O}\times\mathrm{D}\times\mathrm{P}}{\mathrm{C}} \quad (1)$$

A more detailed description of all the criteria is provided below:

S: Assesses the seriousness of potential injuries or fatalities, rated on a 1–10 scale from minor incidents to catastrophic events affecting multiple individuals (46).

O: Measures the probability of a failure occurring during system operation, with higher values indicating more frequent failures (43).

D: Evaluates how effectively current controls can detect or prevent a failure, with 1 representing high detectability and 10 indicating low detectability (47).

P: Reflects the strength of preventive measures in reducing failure likelihood and detectability, scored 1–10 to prioritize proactive controls (44).

C: Represents the financial burden of implementing corrective or preventive actions, expressed as a percentage of the total safety budget and incorporated in the denominator of the modified RPN formula (33).

The scale of the criteria is shown in Figure 2.

2. 5. Weighting the Criteria In this study, the Shannon Entropy Theory approach was used to weight the criteria. The concept of entropy was introduced by Claude Shannon in 1948 as part of information theory, with further developments contributed by Dwivedi and Sharma (48). The entropy method objectively determines criterion weights by quantifying data uncertainty, avoiding subjective judgment. A lower entropy value indicates less disorder and, consequently, greater importance of the corresponding criterion (19). The entropy process generally involves the following steps:

Figure 1. Schematic of machinery and equipment in a stone crushing unit

TABLE 1. Identified Failure Modes (FMs) in the stone crusher unit

FM Code	Operational Activity	Failure Mode	Effect of Failure	Source of Failure	Cause of Failure
FM1	Screen operation	Screen mesh rupture or tearing	Flying fragments, risk of eye or facial injury, unfiltered oversized material	Vibrating screen deck	Metal fatigue, wear, improper material loading
FM2	Screen mesh change	Lifting heavy screen panels	Back injuries or muscle strain	Manual handling of mesh	Lack of lifting aids; improper ergonomics
FM3	Feeding the crusher	Oversized feed causing blockage	Sudden release may cause trauma or impact injuries to nearby workers	Feed hopper	Lack of screening; improper sizing of feed
FM4	Feeding zone	Bridging of feed material	Sudden collapse may injure workers clearing the jam	Crusher feed opening	Irregular loading; oversized or moist material
FM5	Material loading	Overloading the screen deck	Risk of collapse, excessive dust release	Loading equipment	Operator error, poor feed control
FM6	Screen operation	Body part caught in screen	Amputation	Screen	Lack of protective guarding, unsafe maintenance practices
FM7	Discharge zone	Blocked discharge chute	Workers at risk during manual removal—entrapment or crush injury	Conveyor or chute	Sticky material; inadequate flow design
FM8	Crushing operation	Exposure to excessive dust	Respiratory disorders	Stone crusher	Absence of dust control
FM9	Manual handling	Prolonged poor posture	Musculoskeletal disorders	Workstation	Non-ergonomic design, repetitive motion
FM10	Crushing operation (cone)	Excessive vibration	neurological effects, ergonomic stress	Crusher body and motor	Lack of damping; poor isolation; prolonged exposure
FM11	Electrical panel access	Electric shock	Death	Electrical panel	Inadequate insulation, failed grounding system
FM12	Crushing operation	Exposure to excessive noise	Hearing damage	Stone crusher	Absence of noise control
FM13	Hand tool use	Tool slips during operation	Trauma, amputation, fracture	Work tools	Poor grip, worn handles, unsuitable personal protective equipment
FM14	Equipment handling	Equipment falls on personnel	Head injury, bone fracture	Crusher equipment	Improperly secured or positioned equipment
FM15	Hydraulic adjustment (cone)	Hydraulic hose burst	High-pressure fluid injection injury; risk of slips or burns	Cone crusher hydraulic system	Worn components; lack of maintenance
FM16	Crushing process (jaw crusher)	Eccentric shaft failure	Machine failure can cause falling debris or sudden shutdown-related injuries	Jaw crusher drive mechanism	Fatigue, insufficient lubrication, wear

Constructing the decision matrix (DM): The first step is to create a DM with choices and criteria. In Equation 2, the initial decision matrix is displayed:

$$DM = [x_{ij}]_{m\times n} = \begin{bmatrix} x_{11} & x_{12} & x_{13} & \dots & x_{1n} \\ x_{21} & x_{22} & x_{23} & \dots & x_{2n} \\ \dots & \dots & \dots & \dots & \dots \\ x_{m1} & x_{m2} & x_{m3} & \dots & x_{mn} \end{bmatrix}; i = 1,2,3 \dots m; j = 1,2,3 \dots n. \quad (2)$$

In this equation, the symbol *xij* represents the performance value of alternative *i* with respect to criterion *j*. The decision matrix thus evaluates *m* alternatives across *n* criteria, which may include both quantitative (numerical) data and qualitative (linguistic) assessments.

Normalizing the decision matrix: To ensure comparability across different criteria, the values in the decision matrix are normalized. This is done by extracting each element from the original decision matrix and applying a normalization process, as state in Equation 3:

$$n_{ij} = \frac{x_{ij}}{\sum x_{ij}} \quad (3)$$

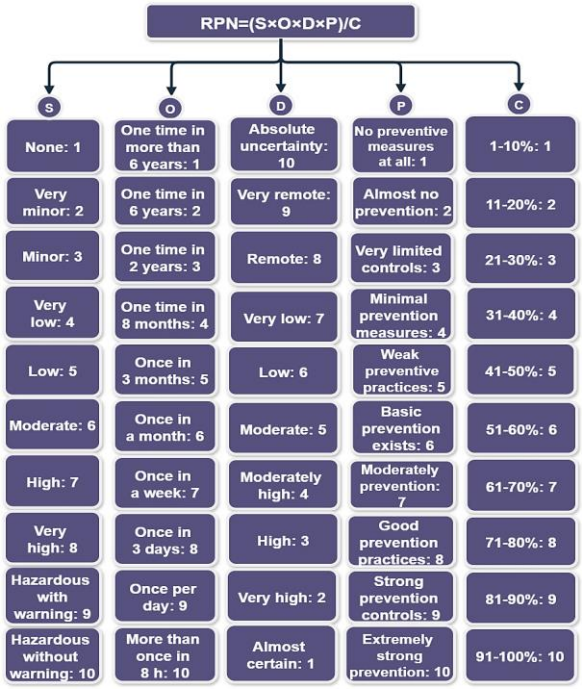

Figure 2. Criteria and their scale in modified RPN. Note: S – Severity; O – Occurrence; D – Detection; P – Preventiveness; C – Cost factor.

Calculating the entropy values: Following normalization, the entropy value *Ej* for each criterion is calculated using the formula below. The constant *k* ensures that *Ej* remains within the range of 0 to 1 (Equations 4 and 5).

$$k = \frac{1}{\text{Ln (a)}} \tag{4}$$

$$E_j = -k\sum\left[n_{ij}\text{LN}(n_{ij})\right] \tag{5}$$

Determining the degree of divergence: The degree of deviation, denoted as *dj*, is calculated to quantify the amount of useful information contributed by each criterion. When the values of competing alternatives for a given criterion are similar, the criterion provides less discriminatory power (Equation 6).

$$d_j = 1 - E_j \tag{6}$$

Computing the objective weights: At this stage, the weights of the criteria are calculated using Equation 7, which determines the relative importance of each criterion based on the degree of deviation.

$$W_j = \frac{d_j}{\sum d_j} \tag{7}$$

The entropy method ultimately derives the weights for each criterion, with the sum of all weight coefficients always equal to 1. In Equation 7, *Wj* represents the weight assigned to criterion *j*.

2. 6. Ranking the Criteria The CoCoSo method combines elements of the weighted sum model (WSM) and the weighted product model (WPM) through three distinct compromise-based aggregation procedures (20, 49). By integrating these methods, CoCoSo enhances both the robustness and flexibility of the decision-making process, ultimately yielding more reliable and discriminative ranking results.

Once the alternatives, evaluation criteria, and their corresponding weights have been determined, the CoCoSo decision-making procedure proceeds through a structured sequence of steps to derive the final ranking of alternatives. The methodological steps are outlined as follows:

Normalization of the Decision Matrix: The decision matrix is normalized to transform the original values into a comparable scale between 0 and 1. The normalization depends on whether a criterion is positive (beneficial) or negative (non-beneficial):

For Positive criteria—where higher values indicate better performance—normalization is performed using Equation 8:

$$r_{ij} = \frac{x_{ij} - \min\limits_i x_{ij}}{\max\limits_i x_{ij} - \min\limits_i x_{ij}} \tag{8}$$

For Negative criteria—where lower values are preferred—normalization is performed using Equation 9:

$$r_{ij} = \frac{\max\limits_i x_{ij} - x_{ij}}{\max\limits_i x_{ij} - \min\limits_i x_{ij}} \tag{9}$$

Calculation of the Weighted Sum (S_i) and Weighted Power (P_i): In this step, the S_i and P_i values are computed for each alternative (Equations 10 and 11). These are fundamental components of the CoCoSo method, combining the effects of all criteria using their respective weights.

$$S_i = \sum_{j=1}^{n} W_j r_{ij} \tag{10}$$

$$P_i = \sum_{j=1}^{n} (r_{ij})^{w_j} \tag{11}$$

The weights *Wj* for each criterion were previously determined using Shannon Entropy.

Aggregation of scores to determine final ranking: The relative weights of the alternatives are determined using the following aggregation approaches (Equations 12, 13, and 14).

$$K_{ia} = \frac{P_i + S_i}{\sum_{i=1}^{m}(P_i + S_i)}, \tag{12}$$

$$K_{ib} = \frac{S_i}{\min\limits_i S_i} + \frac{P}{\min\limits_i P_i}, \tag{13}$$

$$K_{ic} = \frac{\lambda(S_i) + (1-\lambda)(P_i)}{\lambda\max\limits_i(S_i) + (1-\lambda)\max\limits_i(P_i)}; 0 \le \lambda \le 1 \tag{14}$$

Equation 11 reflects the total of the relative scores derived from the Weighted Sum Model (WSM) and the Weighted Product Model (WPM), normalized with respect to the best-performing alternative. Equation 12 represents the arithmetic mean of the normalized WSM and WPM scores, providing a balanced measure of performance. Equation 13 introduces a compromise formulation in which the scores of WSM and WPM are proportionally balanced through the parameter λ. Decision-makers choose λ in Equation 13, which is typically λ = 0.5.

Determining final score and ranking alternatives: In this final phase, the overall performance score K_i for each alternative is calculated to determine the final ranking. This is done by combining the results from three aggregation strategies—K_{ia}, K_{ib}, and K_{ic}—according to Equation 15:

$$K_i = (K_{ia}K_{ib}K_{ic})^{\frac{1}{3}} + \frac{1}{3}(K_{ia}+K_{ib}+K_{ic}) \quad (15)$$

The alternatives are then ranked in descending order of their corresponding K_i values, with higher scores indicating superior overall performance. This final step ensures that the ranking reflects not only the relative importance of the evaluation criteria but also the balance between different aggregation perspectives, thereby supporting more reliable decision-making outcomes.

2. 7. One-at-a-time (OAT) Perturbation Sensitivity Analysis

In this study, the OAT method was employed to examine the stability of the proposed MFMEA–Shannon Entropy–CoCoSo framework. The analysis was performed using the normalized decision matrix along with criterion weights obtained through the Shannon Entropy method. Perturbations were applied systematically to each criterion weight individually, while the remaining weights were held constant, followed by renormalization to maintain the total weight sum (50).

For each criterion *j*, the original baseline weight W_j, was perturbed by a relative factor (1 + δ), where the perturbation levels were set as:

$$\delta \in \begin{Bmatrix} -0.20, -0.10, -0.05, +0.05, \\ +0.10, +0.20 \end{Bmatrix}$$

The perturbed weight for criterion *j* was calculated according to Equation 16:

$$W_j' = W_j \times (1 + \delta) \quad (16)$$

After perturbing W_j, the entire weight vector was renormalized to ensure that (Equation 17):

$$\sum_{j=1}^{n} W_j' = 1 \quad (17)$$

The renormalization was performed according to Equations 18 and 19:

$$W_j' = \frac{W_j \times (1+\delta)}{\sum_{k=1}^{n} W_k^*} \quad (18)$$

$$W_k^* = \begin{cases} W_k, & \text{if } k \neq j \\ W_k \times (1 + \delta), & \text{if } k = j \end{cases} \quad (19)$$

Following renormalization, the subsequent steps of the risk assessment process were re-executed for each perturbed scenario. For each perturbation scenario, the change in rank (ΔRank *i*) relative to the baseline was recorded for each entity *i*. Additionally, the Spearman rank correlation coefficient (ρ) between the baseline ranking and each perturbed scenario was computed as a compact metric of rank stability (Equation 20):

$$\rho = 1 - \frac{6\sum_{i=1}^{m}(R_i - R_i')^2}{m(m^2-1)} \quad (20)$$

where R_i is the baseline rank of entity *i*; R_i' is theperturbed rank of entity *i*, and *m* is the total number of ranked entities. By analyzing ρ across all perturbation levels, the resilience of the model rankings to weight variations was quantitatively assessed, enabling the identification of criteria with the most substantial influence on the final prioritization outcomes.

3. RESULTS

3. 1. Initial Decision Matrix of Risks The results of the initial matrix formation by the decision-making team are presented in Table 2.

TABLE 2. Initial Decision matrix of FMs

FM	Criterion				
	S	O	P	C	D
FM1	6	6	4	4	6
FM2	5	5	3	3	7
FM3	7	7	3	5	6
FM4	8	6	2	5	7
FM5	6	5	3	4	6
FM6	9	5	2	6	8
FM7	8	6	3	5	6
FM8	10	10	10	4	2
FM9	4	6	5	8	1
FM10	10	6	4	4	6
FM11	10	2	5	9	2
FM12	6	10	6	4	4
FM13	7	4	2	8	3
FM14	7	2	2	8	3
FM15	9	4	4	6	7
FM16	8	4	4	5	7

Note: FM – Failure Mode.

3. 2. Weights of the Criteria Table 3 presents the entropy values and the corresponding weights for each MFMEA criterion. In this analysis, the priority ranking of the criteria follows the standard order: P > D > O > C > S.

Based on this ranking and entropy analysis, the weights for the MFMEA variables are derived and used in subsequent risk assessment calculations.

3. 3. CoCoSo Approach

3. 3. 1. Normalized Decision Matrix In this study, Min–Max normalization was adopted for its simplicity and clarity in application to occupational risk assessment. The resulting normalized decision matrix, derived using the Min-Max method, is presented in Table 4.

3. 3. 2. Relative Weighting of the Alternatives In the CoCoSo method, the coefficients Kia, Kib, and Kic are key parameters that integrate multiple aggregation strategies into a single decision-making framework. They control the contribution of different score functions, such as Si and Pi, to each alternative's overall score. By adjusting these coefficients, the method ensures a balanced and customized evaluation that reflects both the criteria's importance and the decision-maker's preferences. The resulting relative weights of the alternatives are shown in Table 5.

3. 3. 3. Ranking FMs based on Traditional FMEA, MFMEA, and MFMEA–Shannon Entropy–CoCoSo Models Figure 3 illustrates the outcomes of risk prioritization using three methods: the traditional FMEA, MFMEA, and MFMEA–Shannon Entropy–CoCoSo approach.

The descending order of risk prioritization according to the traditional FMEA method is as follows:
FM10 = FM6 > FM4 > FM3 > FM7 > FM15 > FM12 > FM16 > FM1 > FM8 > FM5 > FM2 > FM13 > FM14 > FM11 > FM9.

The descending order of risk prioritization according to the MFMEA method is as follows:
FM8 > R10 = R12 > FM1 > FM16 > FM3 > FM2 > FM7 > FM15 > FM5 > FM4 > FM6 > FM11 > FM13 > FM9 > FM14.

TABLE 3. Weighting parameters for criteria by Shannon entropy

Criteria/Parameter	S	O	P	C	D
k	0.360	0.360	0.360	0.360	0.360
Ej	0.989	0.971	0.961	0.983	0.962
Dj	0.010	0.028	0.038	0.016	0.037
Wj	0.079	0.218	0.290	0.125	0.285

TABLE 4. Normalized input decision matrix

FM	Criteria				
	Non-beneficial				Non-beneficial
	S	O	P	C	D
FM1	0.333	0.500	0.250	0.833	0.285
FM2	0.166	0.375	0.125	1.000	0.142
FM3	0.500	0.625	0.125	0.666	0.285
FM4	0.660	0.500	0.000	0.666	0.142
FM5	0.333	0.375	0.125	0.833	0.285
FM6	0.833	0.375	0.000	0.500	0.000
FM7	0.666	0.500	0.125	0.666	0.285
FM8	1.000	1.000	1.000	0.833	0.857
FM9	0.000	0.500	0.375	0.166	1.000
FM10	1.000	0.500	0.250	0.833	0.285
FM11	1.000	0.000	0.375	0.000	0.857
FM12	0.333	1.000	0.500	0.833	0.571
FM13	0.500	0.250	0.000	0.166	0.714
FM14	0.500	0.000	0.000	0.166	0.714
FM15	0.833	0.250	0.250	0.500	0.142
FM16	0.666	0.250	0.250	0.666	0.142

TABLE 5. Relative weighting of the alternatives and determining final score

FM	Si	Pi	Kia	Kib	Kic	Ki
FM1	0.394	4.123	0.068	3.427	0.770	1.987
FM2	0.298	3.798	0.062	2.847	0.698	1.700
FM3	0.377	4.047	0.067	3.318	0.754	1.931
FM4	0.286	3.353	0.055	2.624	0.620	1.547
FM5	0.330	3.949	0.065	3.060	0.729	1.809
FM6	0.210	2.710	0.044	2.022	0.498	1.209
FM7	0.363	4.026	0.066	3.244	0.748	1.897
FM8	0.935	4.934	0.089	6.309	1.000	3.290
FM9	0.523	3.411	0.060	3.775	0.670	2.034
FM10	0.446	4.206	0.070	3.709	0.793	2.116
FM11	0.432	2.710	0.048	3.077	0.535	1.648
FM12	0.656	4.565	0.079	4.842	0.890	2.635
FM13	0.318	3.393	0.056	2.793	0.632	1.624
FM14	0.264	2.653	0.044	2.256	0.497	1.300
FM15	0.296	3.886	0.063	2.874	0.713	1.723
FM16	0.304	3.902	0.064	2.918	0.717	1.743

Note: Si – Weighted sum of normalized comparability matrix; Pi – Weighted power of normalized comparability matrix; Kia – Summation-based Aggregation; Kib – Relative Minimum-based Aggregation; Kic – Weighted Max-normalized Aggregation; Ki – Overall Performance Score.

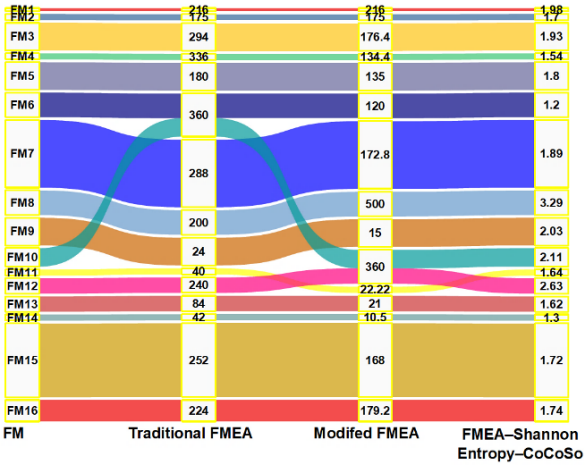

Figure 3. FMs prioritization based on traditional FMEA, MFMEA, and MFMEA–Shannon Entropy–CoCoSo approaches

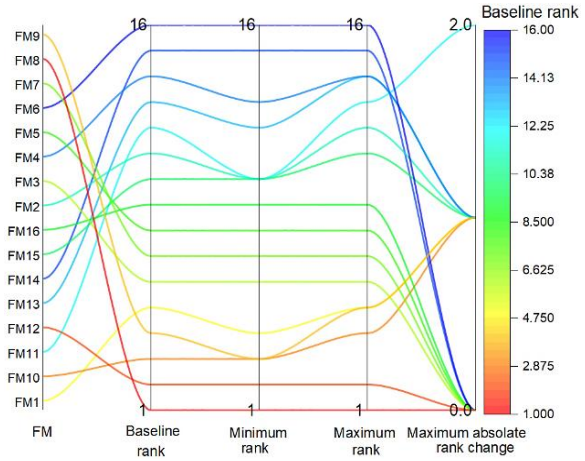

Figure 4. Stability of failure mode rankings under OAT weight perturbations

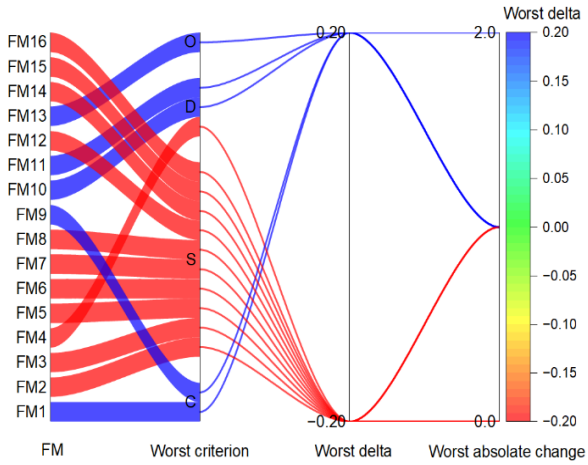

Figure 5. Most influential criteria and perturbation levels for each failure mode

In comparison, the MFMEA–Shannon Entropy–CoCoSo-based ranking sequence is:
FM8 > FM12 > FM10 > FM9 > FM1 > FM3 > FM7 > FM5 > FM16 > FM15 > FM2 > FM11 > FM13 > FM4 > FM14 > FM6.

3. 3. 4. OAT Perturbation Sensitivity Analysis A sensitivity analysis involving 480 scenarios was conducted for the MFMEA–Shannon Entropy–CoCoSo model, with results shown in Figures 4-7. Figure 4 illustrates the OAT perturbation sensitivity for all FMs, comparing baseline ranks with their minimum, maximum, and maximum absolute rank changes across scenarios. The analysis indicates that most failure modes are highly stable, with rank changes ≤ 1, while FM11 shows a moderate sensitivity with a shift of up to two positions. Several FMs (FM12, FM14, FM16, FM3, FM5, FM6, FM7, and FM8) retain identical rankings under all perturbations, reflecting strong robustness to single-criterion weight variations.

Figure 5 highlights, for each failure mode (FM), the criterion and perturbation level that caused the greatest rank deviation during the OAT sensitivity analysis. The analysis shows that significant rank changes generally result from large positive or negative weight perturbations (±0.20) applied to specific criteria. FM11 exhibits the highest sensitivity, shifting two positions under a +20% increase in the D criterion weight. In contrast, multiple failure modes (FM3, FM5, FM6, FM7, FM8, FM12, FM14, and FM16) display no ranking changes across all tested perturbations, confirming their high stability and robustness.

Figure 6 presents criterion sensitivity based on the maximum absolute rank change and the number of affected failure modes under weighted perturbations. Criterion D had the greatest impact, influencing five failure modes with a maximum rank shift of two positions. Criteria C, D, O, and S showed minor sensitivity under −0.20 perturbations, limited to one rank position, while criterion P remained completely insensitive to all tested perturbations.

Figure 7 shows Spearman's ρ between the baseline failure mode rankings and rankings after proportional weight perturbations (−0.2 to +0.2) of each criterion. A ρ of 1 indicates perfect agreement. The analysis reveals that perturbations up to ±0.1 maintain perfect correlation (ρ = 1), confirming full rank stability under moderate changes. Slight deviations occur at ±0.2, with criterion D (+0.2) showing the lowest correlation (ρ = 0.98) and criterion C (+0.2) yielding ρ = 0.99. These results demonstrate that the ranking method is highly robust, with minimal reordering even under relatively large perturbations.

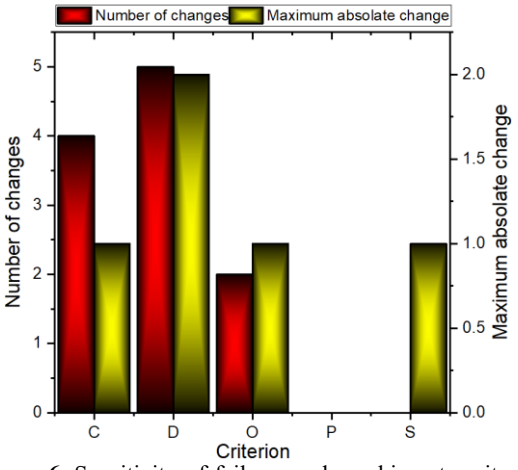

Figure 6. Sensitivity of failure mode rankings to criterion weight perturbations

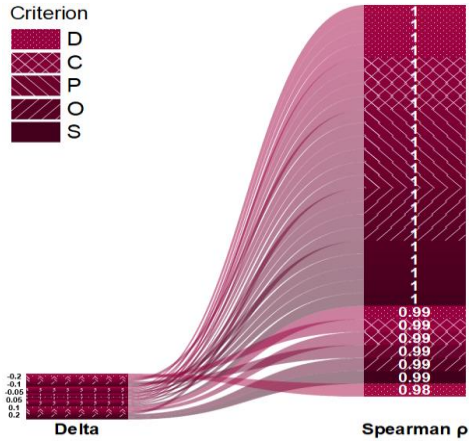

Figure 7. Spearman rank correlation coefficients (ρ) for perturbed criterion weights

4. DISCUSSION

4. 1. FMEA-Shannon Entropy-CoCoSo Approach Versus Traditional FMEA and MFMEA

Traditional FMEA is limited by its reliance on RPN, which assumes linearity, equal weighting of S, O, and D, and can assign identical scores to different risk profiles. It also lacks uncertainty handling, economic considerations, and preventive factors. MFMEA improves on this by including C and P factors, enabling a more balanced, proactive, and economically informed risk assessment.

Integrating Shannon Entropy with CoCoSo allows objective weighting of criteria and more accurate ranking of failure modes. The resulting priority order—P > D > O > C > S—highlights the significance of preventiveness and detectability, while severity has the least influence due to low variability.

The MFMEA–Shannon Entropy–CoCoSo framework provides superior risk discrimination over conventional MFMEA. Both methods identified FM8 and FM12 as critical hazards, but the integrated model prioritized FM8 higher due to its lower detectability, emphasizing early detection. Sensitivity analysis confirmed the model's robustness, with minimal rank shifts under extreme weight changes, demonstrating resilience to expert judgment variability and enhancing reliability for complex industrial decision-making.

4. 2. Risk Treatment Crusher unit in the ceramic industry pose major health risks, and effective safety management requires systematic hazard identification, risk evaluation, control measures, and continuous monitoring (17, 51). The integrated MFMEA–Shannon Entropy–CoCoSo analysis identified excessive dust (FM8), noise (FM12) and vibration (FM10) as the highest-risk hazards in ceramic crusher unit.

In crusher unit, dust arises mainly from material tipping, mineral comminution, and handling, with dry feedstock and poor ventilation intensifying emissions. Resuspension from accumulated dust further elevates exposure. Mitigation measures include equipment enclosure, misting or spray systems, and pre-wetting of feedstock to reduce particle release.

In crusher unit, noise originates from particle impacts, mechanical components, feeders, chutes, and structural vibrations, often exceeding the 85 dB(A) limit. Contributing factors include misalignments and worn parts. Mitigation strategies involve engineering and operational controls, such as soundproof enclosures, optimized feed rates, low-noise equipment, vibration isolators, and noise monitoring.

Key sources of vibration include mass imbalances in rotating components, shaft misalignments, uneven feed material, wear of crushing surfaces, and inadequate lubrication. Mitigation requires a multi-faceted strategy involving real-time condition monitoring, predictive diagnostics, preventive maintenance, feed regulation, foundation reinforcement, vibration isolation, and automated lubrication systems.

4. 3. Proposed Further Research Future research should focus on enhancing the MFMEA–Shannon Entropy–CoCoSo framework by integrating dynamic, adaptive, and data-driven approaches. Key directions include developing real-time weighting mechanisms to reflect evolving operational contexts, comparing entropy-based methods with advanced computational models such as neural networks and machine learning, and exploring alternative MCDM techniques (e.g., MARCOS, EDAS, WASPAS) combined with uncertainty modeling tools like gray relational analysis or cloud theory. Expanding the framework to multiple

industrial sectors will allow broader validation of its generalizability, robustness, and practical applicability.

5. CONCLUSION

The application of the MFMEA–Shannon Entropy–CoCoSo framework in a case study of a ceramic industry crusher unit demonstrated its practical effectiveness, with results identifying dust, noise, and vibration as the most critical hazards requiring immediate and targeted control measures. Moreover, the inclusion of Shannon Entropy provided objective weighting of criteria, reducing subjective bias in expert evaluations, while the CoCoSo method ensured robust and discriminative ranking performance. Sensitivity analysis further validated the reliability and stability of the framework, with Spearman correlation coefficients exceeding 0.98 under multiple weight perturbation scenarios. This high level of consistency underscores the model's robustness, even in conditions of uncertainty. Overall, the MFMEA–Shannon Entropy–CoCoSo framework represents a significant advancement in occupational risk assessment methodologies, offering a systematic, adaptable, and evidence-based approach that can be scaled to diverse industrial contexts for improving workplace safety and operational efficiency.

6. REFERENCES

1. Litvinenko V, Petrov E, Vasilevskaya D, Yakovenko A, Naumov I, Ratnikov M. Assessment of the role of the state in the management of mineral resources. Journal of Mining Institute. 2023(259):95-111. https://doi.org/10.31897/PMI.2022.100.
2. Barjoee SS, Nikbakht M, Malverdi E, Zarei Mahmoud Abadi S, Naghdi MR. Modeling the consequences of benzene leakage from a tank using ALOHA in the tar refining industry of Kerman, Iran. Pollution. 2021;7(1):217-30. https://doi.org/10.22059/poll.2020.309283.887.
3. Shestakova I. The Era of digital transition in the prism of the existential threat of job loss: corporate social responsibility. Sustainability. 2024;16(18):8019. https://doi.org/10.3390/su16188019.
4. Barjoee SS, Gendler S. Sustainable illumination: Experimental and simulation analysis of illumination for workers wellbeing in the workplace. Heliyon. 2024;10(24):e40745. https://doi.org/10.1016/j.heliyon.2024.e.
5. Shojaee Barjoee S, Azimzadeh H, MoslehArani A, Sodaiezadeh H. Dispersion and health risk assessment of PM10 emitted from the stacks of a ceramic and tile industry in Ardakan, Yazd, Iran, using the AERMOD model. Iranian South Medical Journal. 2019;22(5):317-32. https://doi.org/10.29252/ismj.22.5.317.
6. Korshunov GI, Mironenkova NA, Poleshchuk A. The topical methods of detecting spontaneous combustion sources in coal mines. Mining Informational and Analytical Bulletin. 2025;5:169-80. https://doi.org/10.25018/0236_1493_2025_5_0_169.
7. Shojaee Barjoee S, Rodionov V, Rezaei N. Occupational injuries associated with safety climate among ceramic industry workers in Iran. Scientific Reports. 2025;15(1):24585. https://doi.org/10.1038/s41598-025-09704-6.
8. Karchina E, Ivanova M, Volokhina A, Glebova E, Vikhrov A. Improving the procedure for group expert assessment in the analysis of professional risks in fuel and energy companies. Journal of Mining Institute. 2024(270):994-1003. https://pmi.spmi.ru/pmi/article/view/16336?setLocale=en_US.
9. Shojaee Barjoee S, Dashtian AH, Keykhosravi SS, Abbasi Saryazdi MJ, Afrough MJ. Modeling the environmental, health, and safety aspects of xylene isomer emission from storage tanks in petrochemical industries, Iran. Environmental Monitoring and Assessment. 2021;193(12):783. https://doi.org/10.1007/s10661-021-09569-y.
10. Romanchenko S, Kornev A. Innovative research methods for the dust explosion hazard of coals. Journal of Mining Institute. 2025:1-12. https://pmi.spmi.ru/pmi/article/view/16548/16465.
11. Glebova E, Volokhina A, Vikhrov A. Assessment of the efficiency of occupational safety culture management in fuel and energy companies. Journal of Mining Institute. 2023(259):68-78. https://doi.org/10.31897/PMI.2023.12.
12. Barjoee SS, Elmi MR, Varaoon VT, Keykhosravi SS, Karimi F. Hazards of toluene storage tanks in a petrochemical plant: modeling effects, consequence analysis, and comparison of two modeling programs. Environmental Science and Pollution Research. 2022;29(3):4587-615. https://doi.org/10.1007/s11356-021-5864-5.
13. Barjoee SS, Azizi M, Kouhkan M, Alipourfard I, Bayat A, Shahbaz YH, et al. The impacts and analysis of individual and social risks of the stochastic emission of benzene from floating-roof tanks using response surface analysis and the MPACT model. Archives of Environmental Contamination and Toxicology. 2023;84(3):347-67. https://doi.org/10.1007/s00244-023-990-7.
14. Ahmed T, Hoque M, Karmaker CL, Ahmed S. Integrated approach for occupational health and safety (OHS) risk assessment: An empirical (case) study in small enterprises. Safety Science. 2023;164:106143. https://doi.org/10.1016/j.ssci.2023.
15. Viana M, Fonseca AS, Querol X, López-Lilao A, Carpio P, Salmatonidis A, et al. Workplace exposure and release of ultrafine particles during atmospheric plasma spraying in the ceramic industry. Science of the Total Environment. 2017;599:2065-73. https://doi.org/10.1016/j.scitotenv.2017.05.132.
16. Shojaee Barjoee S, Rodionov V, Vaziri Sereshk AM. Noise climate assessment in ceramic industries (Iran) using acoustic indices and its control solutions. Advances in Environmental Technology. 2025;11(1):91-115. https://doi.org/10.22104/aet.2024.6922.1899.
17. Barjoee SS, Rodionov Alekseevich V. Respirable dust in ceramic industries (Iran) and its health risk assessment using deterministic and probabilistic approaches. Pollution. 2024;10(4):1206-26. https://doi.org/10.22059/poll.2024.376043.2360.
18. Salah B, Alnahhal M, Ali M. Risk prioritization using a modified FMEA analysis in industry 4.0. Journal of Engineering Research. 2023;11(4):460-8. https://doi.org/10.1016/j.jer.2023.07.001.
19. Saraiva P. On Shannon entropy and its applications. Kuwait Journal of Science. 2023;50(3):194-9. https://doi.org/10.1016/j.kjs.2023.05.004.
20. Yazdani M, Zarate P, Kazimieras Zavadskas E, Turskis Z. A combined compromise solution (CoCoSo) method for multi-criteria decision-making problems. Management Decision. 2019;57(9):2501-19. https://doi.org/10.1108/MD-05-2017-0458.
21. Nilchi AN, Vafaei A, Hamidi H. Evaluation of security and fault tolerance in mobile agents. 2008 5th IFIP International Conference on Wireless and Optical Communications Networks (WOCN'08). 2008:1-5. https://doi.org/10.1109/WOCN.2008.4542509.

22. Daraei A, Hamidi H. An efficient predictive model for myocardial infarction using a cost-sensitive J48 model. Iranian Journal of Public Health. 2017;46(5):682. https://ijph.tums.ac.ir/index.php/ijph/article/view/9918
23. Mohammadi A, Hamidi H. Analysis and evaluation of privacy protection behavior and information disclosure concerns in online social networks. International Journal of Engineering, Transactions B: Applications. 2018;31(8):1234-9. https://doi.org/10.5829/ije.2018.31.08b.11
24. Khamidov OU, Shibanov DA, Shishkin PV, Kolpakov V. Efficiency of excavator application in open pit mines of Uzbekistan. Gornaya Promyshlennost. 2024;5:135-42. https://doi.org/10.30686/1609-9192-2024-5-135-142.
25. Salimov AE, Shibanov DA, Ivanov SL. Failure risks of mine excavator associated with its maintenance and repair. Gornaya Promyshlennost. 2024;2:97-102. https://doi.org/10.30686/1609-9192-2024-2-97-102.
26. Hamidi H, Vafaei A, Monadjemi AH. Algorithm-based fault tolerance and checkpointing for high-performance computing systems. Journal of Applied Sciences. 2009;9(22):3947-56. https://doi.org/10.23/jas.2009.3947.56.
27. Safiullin RN, Prisyazhnyuk MS, Parra AZ, Safiullin RR, Ungefuk AA. An integrated approach to designing an automated processing system for big data on the haulage process by transport vehicles. Gornyi Zhurnal. 2025(4):40-7. https://doi.org/10.30686/1609-9192-2025-4-122-129.
28. Safiullin R, Arias ZP. Comprehensive assessment of the effectiveness of passenger transportation processes using intelligent technologies. The Open Transportation Journal. 2024;18(1):1-16. https://doi.org/0.2174/0126671212320514240611100437.
29. Fetisov V. Analysis of numerical modeling of steady-state modes of methane–hydrogen mixture transportation through a compressor station to reduce CO2 emissions. Scientific Reports. 2024;14(1):10605. https://doi.org/10.1038/s41598-024-61361-3.
30. Safiullin RN, Katsuba YN, Ungefuk AA, Khisamutdinova EL, Khokhlov AV. Bootstrap method for monitoring the safety of traffic control systems of highly automated mining machines. Gornaya Promyshlennost. 2025;1:73-80. https://doi.org/10.30686/1609-9192-2025-1-73-80.
31. Cheremisina O, Gorbacheva A, Balandinsky D, Luo Y, Ponomareva M. Synergistic effect of a mixture of ethoxyphosphoric esters and sodium oleate in aqueous solutions. Colloids and Surfaces A: Physicochemical and Engineering Aspects. 2024;685:133314. https://doi.org/10.1016/j.colsurfa.2024.
32. Nikolaev AK, Romanov AV, Zaripova NA, Fetisov VG, editors. Modeling of flow in field pipeline to confirm effectiveness of insertion of splitting couplings in control of rill-washing corrosion. IOP Conference Series: Earth and Environmental Science; 2018: IOP Publishing. https://doi.org/10.1088/1755-1315/194/8/082030.
33. Pervukhin DA, Tang L. Enhancing operational efficiency in coal enterprises through capacity layout optimization: A cost-effectiveness analysis. Operational research in engineering sciences: Theory and applications. 2024;7(3):144-63. https://doi.org/10.5281/zenodo.15093139.
34. Budilov I, Tyulyandin S. Ensuring vibration strength of mainline pumping unit systems using digital prototypes. International Journal of Engineering Transactions B: Applications. 2025;39(5):1226-37. https://doi.org/10.5829/ije.2026.39.05b.15.
35. Khabrat GR, Puzin Y. Methods for Preventing Ferrocene Catalyst Migration into Solid Fuels. Journal of Siberian Federal University Engineering & Technologies. 2024;17(7):888-909. http://journal.sfu-kras.ru/en/article/154211
36. Li A. Risk assessment of crane operation hazards using a modified FMEA approach with Z-number and set pair analysis. Heliyon. 2024;10(9):e28603. https://doi.org/10.1016/j.heliyon.2024.e.
37. Subriadi AP, Najwa NF. The consistency analysis of failure mode and effect analysis (FMEA) in information technology risk assessment. Heliyon. 2020;6(1):e03161. https://doi.org/10.1016/j.heliyon.2020.e.
38. Khabrat GR, Puzin YI. Ferrocene-containing compounds as combustion catalysts and solid fuel modifiers. Construction Materials and Products. 2025;8(3):1-15. https://doi.org/0.58224/2618-7183-2025-8-3-6.
39. Fladvad M, Onnela T. Influence of jaw crusher parameters on the quality of primary crushed aggregates. Minerals Engineering. 2020;151:106338. https://doi.org/10.1016/j.mineng.2020.
40. Köken E. Evaluation of size reduction process for rock aggregates in cone crusher. Bulletin of Engineering Geology and The Environment. 2020;79(9):4933-46. https://doi.org/10.1007/s10064-020-01852-5.
41. Xiao'Ou X. Crushing Equipment. The ECPH Encyclopedia of Mining and Metallurgy: Springer; 2024. p. 412-. https://doi.org/10.1007/978-981-99-2086-0_501.
42. Odintsov EE, Gusev VN. Rock mass condition control by the method of predicting of water-conducting fracture zone parameters for the deposits of polymetallic ores. International Journal of Engineering Transactions C: Aspects. 2025;39(6):1326-33. https://doi.org/10.5829/ije.2026.39.06c.02.
43. Ullah E, Baig MM, GholamHosseini H, Lu J. Failure mode and effect analysis (FMEA) to identify and mitigate failures in a hospital rapid response system (RRS). Heliyon. 2022;8(2):e08944. https://doi.org/10.1016/j.heliyon.2022.e.
44. Falcone D, Di Bona GP, Forcina A. A new method for risk assessment in industrial processes. IFAC-PapersOnLine. 2022;55(19):1-6. https://doi.org/10.1016/j.ifacol.2022.09.175.
45. Galevskiy S, Qian H. A Binary Discounting Method for Economic Evaluation of Hydrogen Projects: Applicability Study Based on Levelized Cost of Hydrogen (LCOH). Energies. 2025;18(14):3839. https://doi.org/10.390/en18143839.
46. Liu Y, Tang Y. Managing uncertainty of expert's assessment in FMEA with the belief divergence measure. Scientific Reports. 2022;12(1):6812. https://doi.org/10.1038/s41598-022-10828-2.
47. Anes V, Abreu A. A hybrid FMEA-ROC-CoCoSo approach for improved risk assessment and reduced complexity in failure mode prioritization. Algorithms. 2024;17(12):585. https://doi.org/10.3390/a17120585.
48. Dwivedi PP, Sharma DK. Application of Shannon Entropy and COCOSO techniques to analyze performance of sustainable development goals: The case of the Indian Union Territories. Results in Engineering. 2022;14:100416. https://doi.org/10.1016/j.rineng.2022.
49. Chen Q-Y, Liu H-C, Wang J-H, Shi H. New model for occupational health and safety risk assessment based on Fermatean fuzzy linguistic sets and the CoCoSo approach. Applied Soft Computing. 2022;126:109262. https://doi.org/10.1016/j.asoc.2022.
50. Stergård T, Jensen RL, Mikkelsen FS. The best way to perform building simulations? One-at-a-time optimization vs. Monte Carlo sampling. Energy and Buildings. 2020;208:109628. https://doi.org/10.1016/j.enbuild.2019.
51. Shojaee Barjoee S, Azizi M, Khaledi A, Kouhkan M, Soltani M, Farokhi H. Street dust-bound metal(loid)s) s in industrial areas of Iran: Moran's spatial autocorrelation distribution, ecotoxicological risk assessment, uncertainty, and sensitivity analysis. International Journal of Environmental Science and Technology. 2023;20(8):8509-36. https://doi.org/10.1007/s13762-023-05021-5.

COPYRIGHTS
©2026 The author(s). This is an open access article distributed under the terms of the Creative Commons Attribution (CC BY 4.0), which permits unrestricted use, distribution, and reproduction in any medium, as long as the original authors and source are cited. No permission is required from the authors or the publishers.

Persian Abstract

چکیده

شناسایی و ارزیابی خطرناک‌ترین عوامل زیان‌آور شغلی برای اجرای اقدامات اصلاحی از طریق ارزیابی ریسک بهداشت و ایمنی شغلی (OHSRA) امری حیاتی است. با توجه به ماهیت مبهم درک انسانی، اغلب ارزیابی دقیق ریسک خطرات شغلی در فرآیند OHSRA دشوار است. برای مقابله با این چالش، تکنیک‌های ریاضی متعددی جهت تصمیم‌گیری مبتنی بر ریسک، مدیریت عدم قطعیت، یافتن راه‌حل‌های بهینه و رتبه‌بندی گزینه‌های مختلف توسعه یافته‌اند. این پژوهش، یک مدل نوین OHSRA را برای ارزیابی و اولویت‌بندی خطرات شغلی پیشنهاد می‌دهد که از ترکیب روش تحلیل حالات و آثار خرابی (FMEA)، آنتروپی شانون و روش راه‌حل سازشی ترکیبی (CoCoSo) بهره می‌برد. در این مدل، ارزیابی ریسک بر اساس پنج معیار شامل شدت (S)، احتمال وقوع (O)، قابلیت تشخیص (D)، میزان پیشگیری (P) و عامل هزینه (C) انجام می‌شود. برای مقابله با پیچیدگی و ابهام در ارزیابی‌های کارشناسی، وزن‌دهی معیارها با استفاده از آنتروپی شانون صورت می‌گیرد و رتبه‌بندی خطرات شناسایی‌شده از طریق روش CoCoSo انجام می‌شود. استحکام چارچوب پیشنهادی از طریق تحلیل حساسیت یک به یک (OAT) با تغییر وزن هر معیار به میزان ۰.۰۵±، ۰.۱۰± و ۰.۲۰± ارزیابی می‌شود. کارایی و کاربردی بودن این روش با استفاده از یک مطالعه موردی در واحد سنگ‌شکن صنعت سرامیک به نمایش گذاشته شده است. از جمله مزایای اصلی این رویکرد، انعطاف‌پذیری بالا در مدیریت داده‌های پیچیده کارشناسی و توانایی آن در ارائه ارزیابی‌های دقیق و قابل اعتماد از خطرات شغلی است.

IJE TRANSACTIONS B: Applications Vol. 39, No. 08, (August 2026) 1988-2011

International Journal of Engineering

Journal Homepage: www.ije.ir

Evaluation of Optimal Turns Configuration at Intersections in Urban Roads Network Based on Safety and Congestion indices using Non-dominated Sorting Genetic Algorithm-2

M. Asgari, A. M. Boroujerdian*

Faculty of Civil and Environmental Engineering, Tarbiat Modares University, Tehran, Iran

PAPER INFO

Paper history:
Received 07 July 2025
Received in revised form20 August 2025
Accepted 18 September 2025

Keywords:
Turns Configuration
Network Safety
Pareto Fronts
Genetic Algorithm
Safety Performance Functions
Road Transport

ABSTRACT

Optimal turns configuration at intersections is a fundamental strategy in the pursuit of transportation network design problems. Most interventions implemented at intersections to manage traffic are typically assessed based on their localized impact at the specific node. However, a critical question arises: can any intervention at a single node be truly independent of the conditions and performance of other nodes within the transportation network? While point-based evaluation methods often produce limited and isolated outcomes, traffic dynamics within a network context evolve in a markedly different manner, where interdependencies render optimal solutions inherently multidimensional, and sensitive to broader system-wide interactions. This study proposes three novel approaches to address this challenge: (1) the development of a comprehensive, network-based decision-making framework for managing turn movements; (2) a conceptual shift from conventional link-based methodologies to node-centric patterns in network design; and (3) the adoption of conflict indices as surrogate safety measures in place of traditional crash data, thereby facilitating a more integrated, proactive, and safety-oriented approach to urban transportation network planning. To operationalize these methodologies, a bi-level, multi-objective optimization framework is developed, integrating the NSGA-2 algorithm for generating Pareto-optimal solutions and the TOPSIS method for decision-making support. The model formulation and optimization processes are grounded in empirical data collected from the urban road network of Dezful, Iran. The findings yield a diverse spectrum of optimal solutions, offering valuable insights for enhancing existing transportation systems and informing the strategic planning and design of future urban networks.

***doi**: 10.5829/ije.2026.39.08b.16*

Graphical Abstract

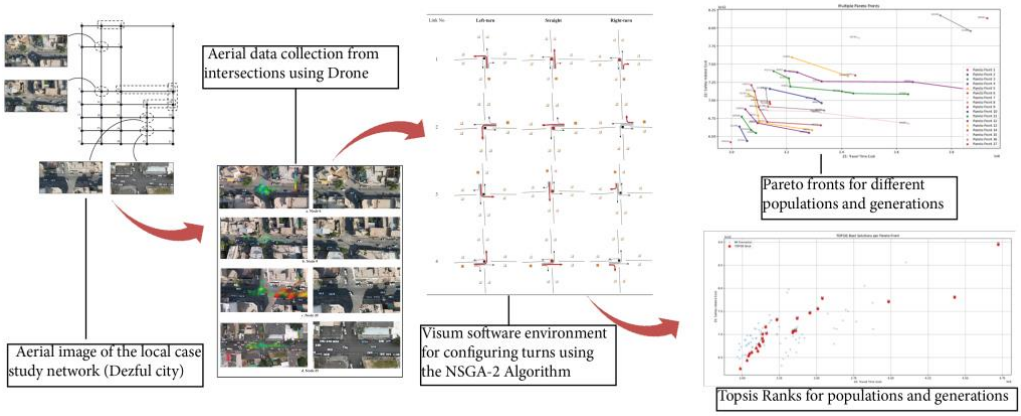

*Corresponding Author Email: boroujerdian@modares.ac.ir (S. Shojaee Barjoee)

Please cite this article as: Asgari M, Boroujerdian AM. Evaluation of Optimal Turns Configuration at Intersections in Urban Roads Network Based on Safety and Congestion indices Using NSGA-2 Algorithm. International Journal of Engineering, Transactions B: Applications. 2026;39(08):1988-2011.

1. INTRODUCTION

In recent years, the effective design of traffic movements at urban intersections has emerged as a critical strategy for optimizing traffic flow and enhancing road safety. While interventions aimed at regulating turn movements can significantly improve the operational performance of individual intersections, a fundamental question arises: do these localized treatments operate independently of the broader transportation network? The interconnected and dynamic nature of urban road systems implies that interventions at a single node can propagate through the network, potentially influencing the performance of adjacent intersections and overall network functionality. Although such networked systems offer considerable operational advantages, they also introduce vulnerabilities, as disruptions or adjustments at one location may trigger ripple effects, thereby affecting the stability and efficiency of the entire network (1). It appears that enhancing the performance of an intersection, in terms of indices such as travel time, yields different outcomes when evaluated through a network-level perspective compared to a point-based approach. In this context, each intersection should be considered as a node within the interconnected system of the transportation network, and its performance assessed in relation to the overall network dynamics. Such an integrated perspective transforms the problem into a form of the Transportation Network Design Problem (NDP), where localized interventions must be evaluated based on their broader, system-wide implications.

In the transportation network design literature, an urban transportation network is typically defined as a system comprising intersections (nodes) and streets (links), generally planned with the main objective of minimizing travel time for users. The optimization of such network configurations is conventionally formulated as a bi-level optimization problem, wherein upper-level decisions guide network design strategies while lower-level models capture traffic assignment and user equilibrium behaviors (2). On the other hand, much of the existing literature on transportation network design has centered on the development of algorithms (3) focused primarily on minimizing travel time across networks. The optimal allocation of resources to reduce user travel costs has long constituted the principal objective of related studies. However, users in transportation systems are exposed not only to the costs associated with travel delays but also to the substantial risks and consequences stemming from safety deficiencies within the network. Although travel time metrics have traditionally dominated decision-making frameworks in network design problems, most objective functions have concentrated on link configurations while often overlooking the critical influence of nodes. Yet, intersections and nodes play a pivotal role in shaping the overall safety performance of transportation systems. Moreover, a review of the existing literature reveals that investigations into the relationship between road networks and safety have predominantly addressed the correlation between overall network structure and historical indices such as crash frequency. In contrast, safety-centered approaches to network design remain limited and underexplored.

This study seeks to integrate surrogate safety measures (SSMs), which has garnered growing attention in recent years (4), into the analysis of safety outcomes within network design. To this end, a bi-level modeling framework is employed to assess traffic and movement control strategies from a network-wide perspective, underscoring that the outcomes of network-based node management differ fundamentally from those derived through conventional point-based approaches. The analysis is supported by conflict models developed using empirical data from a real-world case study. Drawing upon these findings, a bi-level, multi-objective model is introduced, offering a comprehensive framework for evaluating the optimal configuration of traffic operations within a safety-focused network design paradigm. The main objective of this study is to examine various scenarios involving permissible and non-permissible movements at selected urban intersections and to identify their optimal combination based on multiple criteria using the Non-dominated Sorting Genetic Algorithm 2 (NSGA-2) algorithm. Given the multi-objective nature of the problem and the vast solution space, the application of this algorithm effectively guides the optimization process. The problem is addressed under different population sizes and generation numbers, and a reliable optimization framework is developed to identify and present superior scenarios within the studied network.

The literature review highlights that most studies on turn control at intersections have primarily adopted point-based approaches, with limited consideration of network-wide perspectives. This underscores the necessity of embedding such concepts within the broader framework of network design problems. Furthermore, decision-making in this field has traditionally relied on travel time indices; however, the integration of safety indices substantially expands the solution space. The findings of this study, discussed in detail below, confirm that within the framework of multi-objective, two-level optimization methods, a wide spectrum of solutions can be generated and evaluated for network design.

2. LITERATURE REVIEW

Numerous studies have explored the impacts of control strategies at intersections, providing valuable insights for modeling and analysis in this domain. Chen and Jia (5) proposed a traffic management platform centered on the

design of left-turn lanes within the framework of sustainable urban development. Their study employed the NSGA-2 algorithm, incorporating both air pollution indices and traffic delay metrics at urban intersections to guide optimization decisions. Moinuddin et al. (6) employed machine learning models to predict driver behavior in selecting turn maneuvers and demonstrated that algorithms such as K-Nearest Neighbors (KNN) exhibit high predictive accuracy in forecasting route choice decisions. Their findings underscore the potential of behavior prediction models to inform the optimization of permissible turn combinations at intersections, thereby enhancing network performance and safety outcomes. In the domain of congestion analysis at turn movements, Kan et al. (7) utilized spatial trajectory data from taxis to identify congestion hotspots specifically at turning points. Their findings revealed that turn-level analyses offer substantially higher precision compared to intersection-level evaluations, providing a more reliable foundation for traffic management policies concerning the operational status of turns. Similarly, Fan et al. (8) investigated the environmental impacts associated with left-turn movements in mixed traffic streams and reported that optimizing left-turn lane configurations resulted in a 30% reduction in pollutant emissions, alongside significant decreases in queue lengths and vehicular delays. These outcomes highlight the critical importance of incorporating environmental considerations into traffic control and decision-making frameworks.

In the field of traffic safety, Autey et al. (9) the safety implications of geometric modifications to right-turn lanes and demonstrated that the implementation of smart right-turn significantly reduced traffic collisions and enhanced safety. These findings indicate that the operational status of right-turn lanes at specific intersections can have a direct and measurable impact on overall intersection safety performance. Foulaadvand and Belbasi (10) demonstrated that signal timing parameters and turn probabilities exert a significant influence on intersection capacity and congestion levels. Their findings highlight the importance of accounting for the combined effects of various open and closed turn scenarios on overall network flow dynamics. Hu et al. (11) proposed an integrated design combining U-turn and advanced left-turn movements, demonstrating that the separation of these flows effectively reduces conflicts and alleviates congestion at intersections. In the context of turn optimization interacting with rail transit, Currie and Reynolds (12) examined the impact of the Hook Turn maneuver on tram operations, concluding that under specific conditions, this strategy can improve intersection capacity and reduce delays. These findings underscore the critical role of turn management decisions — particularly the regulation of right- and left-turn movements — in optimizing multimodal network performance. Additionally, the operational efficiency of U-turns and driver behavioral responses to various turn management scenarios have been investigated, with particular attention to their implications for network delays and safety outcomes (13, 14).

Collectively, these studies highlight that targeted management of traffic flows at urban nodes — through scenario development and multi-objective optimization incorporating both delay and safety indices — can substantially enhance overall network performance. In this context, algorithms such as NSGA-2, with their capability to effectively navigate multi-objective solution spaces and generate efficient Pareto-optimal fronts, present a particularly suitable approach for addressing such complex, multi-criteria decision problems. This research builds upon these insights by applying the NSGA-2 algorithm to optimize turn management scenarios within an urban road network. Most studies in the area of turns and movements have primarily concentrated on lane design, driver behavior, operational control, conflict analysis, and the development of various algorithms for left-turn (15, 16), right-turn (17-19), and other maneuvers at intersections. However, despite the existence of comprehensive and diverse works in these areas, relatively limited attention has been given to adopting a network-wide approach to junction design.

A review of network-based approaches further reveals that most studies in the field of network design have predominantly concentrated on algorithm development and the formulation of mathematical models (20). Within the discrete network design literature, a wide range of algorithmic strategies has been employed, including ant colony optimization (21), linearization and approximation techniques (22), support function frameworks (23), genetic algorithms (24), combinatorial methods (25), and quasi-optimization decomposition approaches (26). For continuous network design problems, a diverse array of methodologies has also been explored, including simulated annealing (27), the Hooke-Jeeves algorithm (28), iterative optimal assignment techniques (29), and mixed-integer linear programming for fundamental path routing problems (30). In the domain of mixed network design, research has introduced various optimization strategies, ranging from mixed-integer linear programming (31) and genetic algorithms (32) to other advanced metaheuristic and combinatorial approaches. A significant portion of these studies has predominantly focused on minimizing travel time (33-37) or reducing travel time-related costs for both operators and users (38-40), whereas the incorporation of safety indices within road network frameworks has received comparatively limited and less explicit attention in the existing literature (41).

Studies addressing network safety have also primarily aimed to investigate the relationship between network topology and crash frequency, frequently employing

crash prediction models as the foundational framework for developing safety rankings (42). For instance, Fancello et al. (43) introduced an advanced model for assessing safety parameters within urban transportation networks, offering valuable insights into the mechanisms of safety evaluation and risk analysis in traffic systems. In a similar vein, Gomez et al. (44), through an applied case study, systematically evaluated the safety performance index of an urban network, providing critical insights into safety assessment methodologies within the network context. Ewing and Dumbaugh (45) undertook a rigorous investigation into the influence of urban structure on transportation safety, utilizing regression analysis to probe the complex interplay between network configuration and safety outcomes. Moeinaddini et al. (46) conducted a comprehensive assessment of urban road networks, revealing a strong positive correlation between improved safety performance and network characteristics such as a lower number of nodes within a given area, shorter average highway lengths, and longer urban road segments. Additionally, analyses of network configurations have indicated that limited-access designs are associated with a decreased incidence of crashes involving vulnerable road users, particularly when compared to traditional network patterns and alternative topological layouts (47). In a related study, Marshall and Garrick (48) demonstrated that increasing road network density — notably through a higher number of intersections — is significantly associated with reductions in overall crash frequency.

A comprehensive review of the literature reveals a notable gap in understanding the relationship between safety indices and network design problems, accompanied by insufficient attention to the costs associated with safety deficiencies. This oversight implies that many evaluations, which predominantly emphasize increasing route capacity or expanding network links, often neglect the broader spectrum of related costs. By prioritizing travel time reduction, such assessments frequently fail to account for the substantial economic and social consequences stemming from compromised safety conditions. In network design problems, modeling efforts typically emphasize the relationship between travel time and traffic volume. To address safety considerations within such frameworks, surrogate safety measures (SSMs) have been employed as alternative indices, particularly in cases where reliable crash data are unavailable, incomplete, or insufficiently accurate (49). The application of surrogate safety measures in traffic safety analysis can be traced back to the early 1970s (50). A key advantage of SSMs over traditional crash data lies in their ability to capture the sequence of events preceding a collision, thereby offering valuable insights into the underlying causes of traffic conflicts (51). SSMs are generally categorized into three primary groups: time-based, energy-based, and acceleration-based indices. In the present study, a time-based metric — specifically, Time to Collision (TTC) — is employed, as it remains one of the most widely adopted and extensively validated indices in the field of traffic safety research (52).

The literature review highlights several essential dimensions in addressing the challenges of node network design. First, while prior research has explored complex issues such as network stability and operational uncertainties, comparatively limited attention has been devoted to achieving a meaningful paradigm shift through the integration of safety indices within network design frameworks. Second, existing studies on network safety have largely concentrated on structural and configurational attributes, overlooking localized operational dynamics. Third, the growing application of surrogate safety measures (SSMs), including conflict-based indices, underscores their emerging significance as practical alternatives to crash-based assessments. Finally, most investigations addressing the optimization of permissible turn and movement scenarios at intersections have relied on point-based methodologies, with fewer studies adopting comprehensive network-based perspectives.

To address these identified gaps, the present study proposes a comprehensive framework that simultaneously incorporates both safety and delay indices to determine the optimal configuration of movement scenarios within an urban road network. Following the introduction and review of existing literature, the structure of this research is organized into four subsequent sections. Section 3 details the methodological approach and problem formulation, encompassing the development of the optimization framework, the definition of decision variables and model parameters, the data acquisition procedures, and the formulation of the principal modeling functions. Section 4 presents the results derived from the implemented models, including validation outcomes and a thorough analysis of the network design scenarios. Section 5 offers an in-depth discussion of the key findings, articulating their theoretical contributions and practical implications for urban traffic management. Finally, section 6 concludes the study by summarizing the principal conclusions and proposing avenues for future research and practical application.

3. METHODOLOGY

Given that this study addresses a network design problem by integrating safety indices alongside traditional delay-based performance measures, the initial phase involves developing appropriate safety performance functions and extending them to incorporate conflict indices as a central

component of the analysis. In the subsequent phase, the problem is structured within a two-level bi-objective optimization framework, wherein the fundamental safety performance functions of the network are evaluated through an empirical case study. Concurrently, a customized two-level bi-objective optimization algorithm is employed to solve the problem. It is important to underscore that the simultaneous integration of safety indices with delay-based criteria, within a multi-objective optimization structure, substantially increases the computational complexity and analytical demands of the solution process, necessitating carefully designed modeling strategies and solution procedures.

This complexity is further exacerbated when surrogate safety measures are employed in place of traditional crash-based indices, as these measures require more intricate modeling and interpretation within the optimization framework. In this study, to optimize decisions concerning the operational status of left-turn, right-turn, and through movements at intersections within an urban road network, a combined two-level bi-objective optimization model was formulated. The NSGA-2 metaheuristic algorithm was utilized to address the multi-objective nature of the problem and to generate an efficient set of Pareto-optimal solutions. Subsequently, the TOPSIS multi-criteria decision-making method was applied to rank and prioritize the non-dominated solutions, thereby facilitating the selection of optimal scenarios for practical implementation.

The core structure of the problem was conceptualized as a two-level model. In the first level, decisions are made regarding the permissibility of straight, right-turn, and left-turn movements at designated nodes within the network. The second level subsequently addresses the traffic assignment problem based on the configuration of permitted movements established in the first level.

3. 1. Node Safety Performance Functions In network design problems, the primary objective is typically the minimization of travel time for users. This relationship is conventionally modeled using a travel time function, as shown in Equation 1, which defines the dependence of travel time on traffic flow. Similarly, the development of a safety performance function requires formulating a relational model that associates safety (denoted as s_{ij}) with traffic flow. This relationship is expressed through Equation 2.

$$t_{ij} = f(x_{ij}) \quad (1)$$

$$s_{ij} = g(x_{ij}) \quad (2)$$

This model is based on the Time to Collision (TTC) index as a surrogate safety measure. To support the modeling process, empirical data were collected from four unsignalized intersections within the urban road network of Dezful city. The relationship between traffic flow and safety performance was modeled using a linear regression approach, formally expressed in Equation 3. Table 1 provides a summary of the key features and statistical parameters of the linear regression model structure. Subsequently, the specific safety-traffic model developed for this study is presented in Equation 4.

$$Y = \beta_0 + \beta_1(X_1) + \beta_2(X_2) + \cdots + \beta_i(X_i) \quad (3)$$

$$Conflict\ Index = \beta_0 + \beta_1(Traffic\ Flow) \quad (4)$$

The delay function applied is presented in detail in Equation 5 (53). In this equation, V denotes the traffic flow volume, while C represents the intersection capacity. The parameters α, β, and γ serve as key coefficients within the model, with their corresponding values provided in Table 2.

$$D_m = 9.6 \times (\alpha + \beta \times (\frac{V}{7 \times C})^{\gamma}) \quad (5)$$

3. 2. Designing the Problem Structure The main objective of the Network Design Problem (NDP) is to determine an optimal solution under imposed constraints. It is typically addressed through a two-level framework, where the leader level solves the network design problem and the follower level handles the traffic allocation. The primary goal of the NDP is to optimize the assignment of limited resources by selecting the most efficient links from predefined candidates to enhance overall network performance. The structure of this two-level problem is presented in Equation 6, with key variables and parameters summarized in Table 3.

$$\begin{aligned} &\underset{m \in M, n \in N}{min} \quad F(m,n) \\ &subject\ to: G_i(m,n) \le 0\ for\ i \in \{1,2,\dots,I\} \\ &n \in argmin\left\{f(m,v): g_j(m,v) \le 0, j \in \{1,2,\dots,J\}\right\} \end{aligned} \quad (6)$$

TABLE 1. Linear Regression Model Structure

Y	Dependent Variable
X_i	Independent Variables
β_i	Model Parameters

TABLE 2. Delay model parameters (53)

	Intersection
α	3.5
β	4.53
γ	1.35

The main problem follows Equation 7.

$$\begin{aligned} &\underset{y}{Min} \ \sum_{i,j\in(A\cup A_y)} {x_{ij}}^* t_{ij}(x_{ij}^*) \\ &s.t: y_{ij} = 0 \ or \ 1 \quad \forall (i,j) \in A_y \\ &\sum_{i,j\in A_y} c_{ij} y_{ij} \le B \end{aligned} \tag{7}$$

x_{ij}^*: Represents the user's equilibrium flow obtained by solving the low-level problem (Equation 8) in N (V, $A \cup A_y$). given the vector of projects y:

$$\begin{aligned} &\underset{x}{Min} \ \sum_{i,j\in(A\cup A_y)} \int_0^{x_{ij}} t_{ij}(u)du \\ &s.t.: \quad \sum_{P\in P_{ks}} x_P^{ks} = d^{ks}, \ \forall (k,s) \in P \\ &x_P^{ks} \ge 0, \ \forall p \in p_{ks}, \ \forall (k,s) \in P \\ &x_{ij} = \sum \ \sum \ x_P^{ks}.\delta_{ij,p}^{ks} \quad \forall (i,j) \in A_y \end{aligned} \tag{8}$$

The complete formulation of the two-level optimization problem is presented in Table 4. At the upper level (leader level), the decision variable concerns the configuration of turns at network nodes. The problem simultaneously minimizes two objective functions: a congestion-related index (travel time), and a safety-related index (time-to-collision conflict measure). To solve the lower-level assignment problem, the full capabilities of Visum software were utilized, given its efficiency and accuracy in network assignment modeling. The formulation incorporates three primary constraints:

1) **Flow conservation** – the total demand between an origin-destination pair must equal the sum of flows assigned to the corresponding paths.
2) **Non-negativity** – demand values and flow volumes must remain non-negative.
3) **Link demand assignment** – if a link is shared among multiple O–D paths, the total link flow must equal the aggregate demand distributed across all relevant paths.

Furthermore, in the Python implementation of the model, the **win32com library** was used to establish a dynamic interface between Python and the **Visum environment**. This connection enabled intelligent exchange of network data and results, thereby allowing seamless integration of Visum's computational power with the optimization algorithm coded in Python.

This study adopts a similar framework, where the follower-level task follows the conventional assignment problem formulation with two key modifications: a node-oriented problem structure and the integration of a safety index into the objective function. In the model structure of this study, the upper level simultaneously minimizes two objective functions — the conflict index and the delay index — both dependent on the flow volume at the node.

TABLE 3. Variables and Parameters of Network Design Problem

$N(V, A)$	The network consists of a set of arcs (A) and nodes (V).
(k, s)	origin (k)-destination (s), O/D, pair;(k, s) ∈ P, where P is the set of O/D pairs, $P \subseteq V \times V$
y_{ij}	Project decision variable, taking values 0 or 1 depending on rejection or acceptance of project link (i,j), $(i,j) \in A_y$, where A_y is the set of project links.
y	vector of y_{ij}'s with dimension equal to the number of the elements of A_y.
d^{ks}	Demand from k to s, (k, s) ∈ P, assumed to be constant.
x_{ij}	Link flow (i,j), $(i,j) \in A$.
x_p^{ks}	path flow p from origin k to destination s, $p \in p_{ks}$, where p_{ks} is the set of paths from k to s, $(k,s) \in P$.
x	vector of x_{ij}'s with dimension equal to the number of elements of $A \cup A_y$
$t_{ij}(x_{ij})$	volume- delay function of link (i,j), $(i,j) \in A \cup A_y$, representing average travel time , which is assumed to be only a function of flow in link (i,j), continuous, differentiable, Riemann integrable, and convex, defined for $x_{ij} \ge 0$
B	Budget level.
c_{ij}	Construction cost of link (i,j), $(i,j) \in A_y$

3. 3. Solution Algorithm

To solve the proposed two-level model and extract the Pareto fronts, the NSGA-2 algorithm was employed. Recognized as one of the most widely used metaheuristic algorithms for multi-objective problems, it operates by ranking Pareto fronts and preserving population diversity through a crowding distance mechanism. For each individual in the population, the number of decision variables was set

TABLE 4. Formulation of the two-level optimization problem

$\underset{y}{Min} \ \sum_{i,j\in(A)} {x_{ij}}^* t_{ij}(x_{ij}^*)$	First Objective (Congestion)	**Leader level**
$\underset{y}{Min} \ \sum_{i(V_Y)} TTC_i(x_{ij}^*)$	Second Objective (Conflict Index)	**Follower level**
$\underset{x}{Min} \ \sum_{i,j\in(A\cup A_y)} \int_0^{x_{ij}} t_{ij}(u)du$	Objective Function of Follower level	
$s.t.: \ \sum_{P\in P_{ks}} x_P^{ks} = d^{ks}, \ \forall (k,s) \in P$	Constraint. 1	
$x_P^{ks} \ge 0, \ \forall p \in p_{ks}, \ \forall (k,s) \in P$	Constraint. 2	
$x_{ij} = \sum \ \sum \ x_P^{ks}.\delta_{ij,p}^{ks} \ \forall (i,j) \in A_y$	Constraint. 3	

equal to the number of movement-related decisions at the network nodes. Then, the FitnessMulti and Individual classes were defined using the DEAP library, with each individual represented as a binary list. The initial population was generated using random binary values (0 and 1) with varying population sizes of 50, 100, and 150 individuals.

In this study, the Two-Point Crossover operator and Bit Flip Mutation with a mutation probability of 5% for each decision variable were applied. Parent selection for the next generation was performed using the selNSGA2 method, which ranks individuals based on Pareto front order and crowding distance. For each individual, after determining the combination of access status decisions, the traffic allocation model was executed in VISUM, and the resulting network traffic volumes were extracted and incorporated into the high-level problem. To investigate the model's behavior and assess the effect of population size and number of generations on result quality, various combinations of population sizes (50, 100, and 150) and generation counts (10, 15, 20, 25, 30, 35, 40, 45, and 50) were tested. In total, 27 combination cases were examined, and for each, the Pareto fronts and optimization indices were extracted and analyzed. Figure 1 shows the left, straight, and right movements for each node in VISUM. Each movement is encoded as a string of 0s and 1s, representing whether it is open or closed at the node location. Within a Python loop, each configuration is parsed, the assignment model is executed in VISUM for every case, and the results are recorded for use in the higher-level model.

The NSGA-II algorithm is well-suited for addressing large-scale optimization problems, owing to its combined use of metaheuristic search techniques and Pareto front analysis. A distinctive feature of this study is the integration of NSGA-II with the specialized traffic

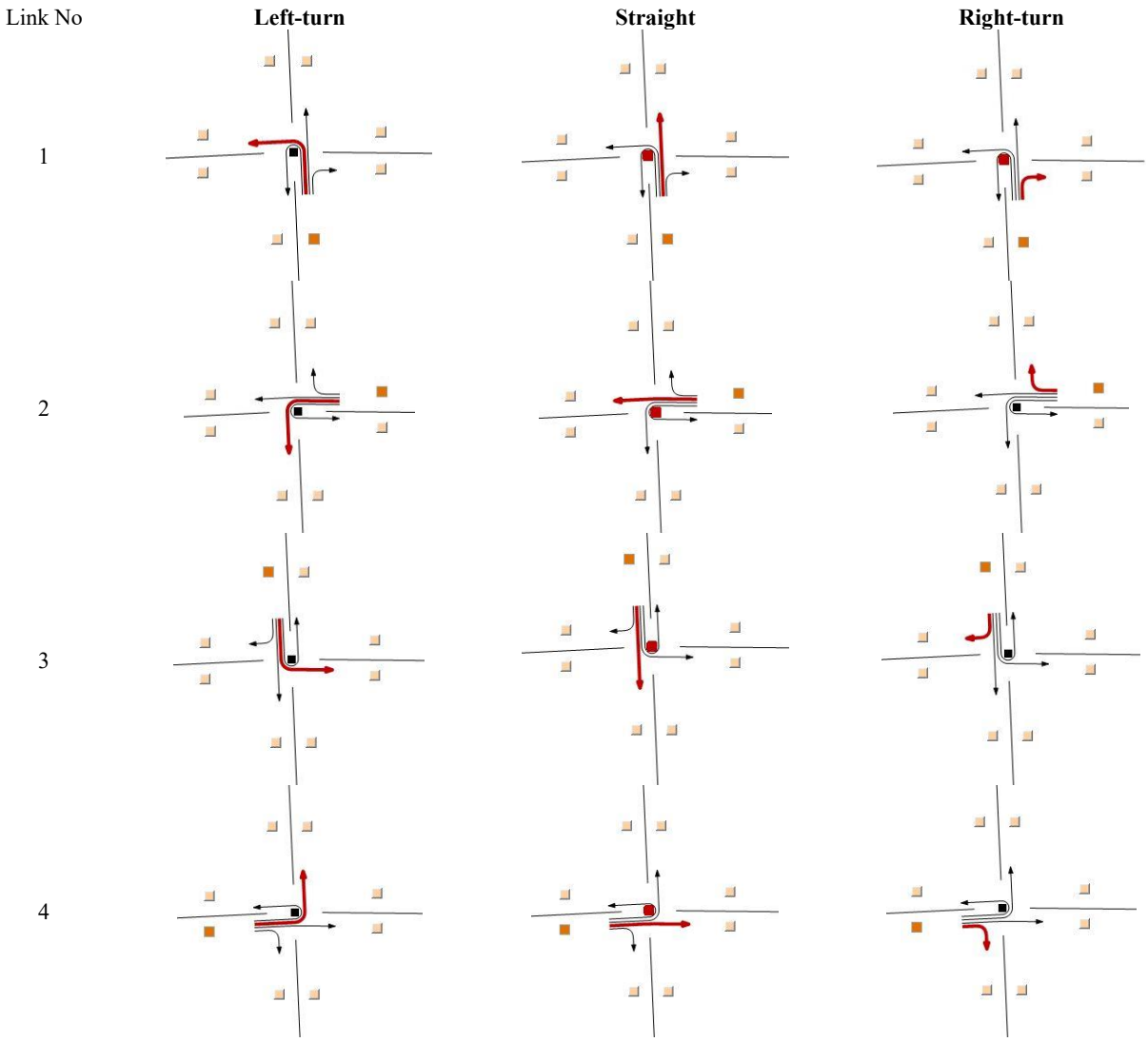

Figure 1. Left-turn, straight, and right-turn movements in Visum software

generation and evaluation was implemented in Python, enabling automated interaction with Visum through built-in connectivity functions. This setup allowed for seamless execution of assignment models and the direct transfer of results into the optimization framework, thereby ensuring both computational efficiency and methodological rigor. The logic of Pareto fronts is based on representing alternative scenarios in the coordinate system of two objective functions. When the horizontal axis is defined as the first objective function and the vertical axis as the second, the relative distribution of scenarios forms the basis for identifying dominant and non-dominated solutions. In a minimization problem, if the origin is defined as the point of reference, scenarios located in the first quadrant are considered non-dominated, those in the second and fourth quadrants are equivalent, and those in the third quadrant are dominated. A key feature of the NSGA-II algorithm lies in its reliance on evolutionary search principles. Similar to other metaheuristic algorithms, it begins by generating an initial set of solutions and iteratively progresses toward the global optimum, thereby reducing the risk of entrapment in local optima. The evolutionary operators form the core of this mechanism: the crossover operator combines chromosomes (scenarios) to explore promising solution spaces, while the mutation operator introduces variability, enabling the algorithm to escape local optima and preserve diversity across generations.

To address the lower-level assignment problem, Visum PTV 2023 software was employed, while the comprehensive solution algorithm was developed in Python 3.9.9. The main Python libraries utilized for writing and executing the algorithm are listed in Table 5. The overall workflow of the algorithm implementation is illustrated in Figure 2.

For the evolutionary operators, the two-point crossover (cxTwoPoint) was adopted for recombination, while the bit-flip mutation (mutFlipBit) was applied to introduce variability (54). Both operators are widely recognized in the genetic algorithm literature and are readily available through standard Python libraries, making them effective and reliable choices for this problem. Figure 3 show the a part of code written in Python.

3. 4. Scenario Analysis After generating the Pareto fronts, the TOPSIS method was applied to identify the best combination of decisions from the set of non-dominated solutions. In this method, the decision matrix

TABLE 5. Python libraries utilized for writing and executing the algorithm

No.	Library
1	win32com
2	numpy
3	pandas
4	random
5	time
6	pickle
7	matplotlib
8	deep

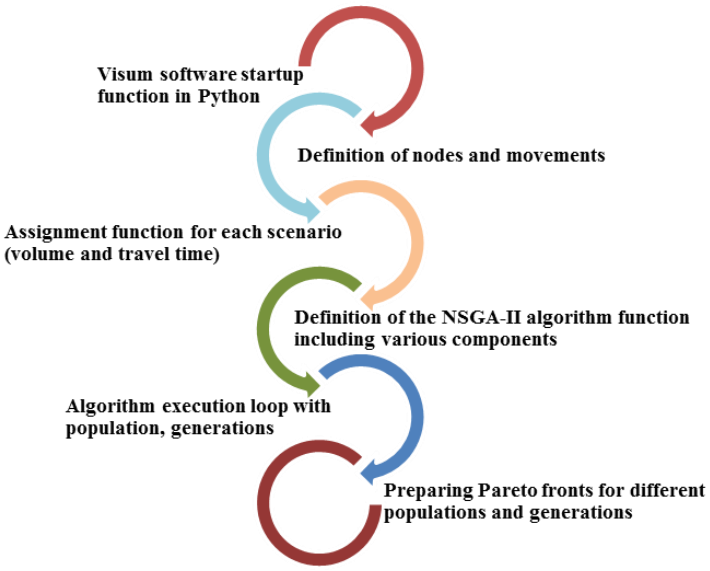

Figure 2. The overall workflow of the algorithm implementation

```python
def run_assignment(individual):
    index = 0
    binary_representation = ""
    for node, turns in turn_movements.items():
        for turn in turns:
            fromNode, toNode, _ = turn
            turn_obj = visum.Net.Turns.ItemByKey(fromNode, node, toNode)
            if turn_obj is not None:
                turn_obj.SetAttValue("TSysSet", "C" if individual[index] == 1 else "B")
            binary_representation += str(individual[index])
            index += 1

    visum.Procedures.Execute()

    results = []
    for link in visum.Net.Links:
        results.append({
            "FromNode": link.AttValue("FromNodeNo"),
            "ToNode": link.AttValue("ToNodeNo"),
            "Volume": link.AttValue("VolVehPrT(AP)"),
            "TravelTime": link.AttValue("TCur_PrTSys(C)"),
        })
```

Figure 3. A part of code written in Python

containing the Z1 and Z2 values for each solution was first extracted and normalized. Subsequently, the distance of each solution from the positive and negative ideal points was calculated, and a proximity index to the ideal solution was determined. The solution with the highest proximity index was selected as the optimal solution. Pareto front diagrams were plotted for all 27 combination cases, and the corresponding TOPSIS results were reported for each case.

It is important to emphasize that the Relevance Estimation and Value Calibration (REVAC) method—one of the fundamental approaches in parameter tuning—was employed to calibrate the parameters of the proposed problem (55, 56). This method not only determines the optimal parameter values but also evaluates the relative importance of each parameter. The REVAC procedure begins by assigning a probability distribution over the feasible range of each parameter.

The process is then iteratively updated by applying an evaluation function, selecting elite solutions, and shifting the distributions (bin distribution) toward regions associated with improved performance. The evolution of parameter distributions is further assessed using an entropy index, which captures the degree of concentration of parameter values. To refine the selection of optimal intervals, the differential entropy index was applied. The interpretation of this method is straightforward: A narrow, concentrated distribution (low entropy) indicates high parameter importance, as specific parameter values strongly enhance algorithmic performance. A wide distribution (high entropy) suggests low parameter importance, as variations in that parameter do not significantly influence outcomes. A notable strength of REVAC lies in its emphasis on identifying an optimal probabilistic model for parameters, rather than a single deterministic value, thereby offering a more robust foundation for algorithm tuning.

Unlike explicit intervalization, the REVAC method employs probability density models to identify a probability distribution centered within a subset of the initial parameter range. Over the course of the process, the mean of the distribution shifts toward the optimal region, while the variance decreases, thereby concentrating the search around the most promising parameter values. The iterative process of optimization and parameter tuning is illustrated in Figure 4.

4. CASE STUDY CHARACTERISTICS

The general layout of the Dezful case study network is illustrated in Figure 5. The data derived from this network form the foundation for developing the models in the design problem. Conflict indices were derived from a meticulous analysis of video data captured via drone surveillance, enabling the accurate identification and classification of potential traffic conflicts at each intersection. Data collection was performed on weekdays between 8:00 AM and 6:00 PM using a Phantom 4 Pro drone equipped with a 1-inch, 20-megapixel sensor, capable of recording ultra-high-definition 4K (4096×2160) video at 60 frames per second, stabilized by a 3-axis gimbal to ensure high-precision data acquisition.

Each drone flight session lasted approximately 30 minutes and maintained a minimum altitude of 150 meters to prevent any influence on driver behavior due to the drone's presence. The recorded video data were subsequently processed and analyzed using the DFS (Drone Footage Analysis System) and SSAM (Surrogate Safety Assessment Model) software tools. Within the modeling framework, the number of observed traffic conflicts served as the dependent variable, while the corresponding intersection flow rate was treated as the independent variable. Figure 6 illustrates the empirical data collected from the four observed intersections, providing a visual representation of traffic volumes and conflict occurrences during the study period.

An important feature of the geometric configuration of the study area is that each intersection node is connected to exactly four links, providing a uniform

structural foundation for the analysis (Table 6). The study concentrates on a set of unsignalized urban intersections, whose geometric and operational characteristics were derived from field data. The intersections were selected according to specific criteria, including geometric similarity, comparable traffic conditions, and the absence of traffic signals, thereby enabling a focused examination of the influence of geometric factors on both safety and traffic flow. The intersections analyzed in this study were all four-legged, unsignalized junctions without physical dividers. In all cases, the intersection angles were approximately 90 degrees, representing a near-perpendicular geometry. Lane widths on the secondary roads were measured at 10–12 meters, while those on the main roads ranged between 13 and 15 meters. This variation in main road width is particularly noteworthy, as it may reflect differences in traffic capacity and could influence driver behavior in maneuver selection. In total, four intersections were examined under field conditions, each selected to ensure broadly similar characteristics while maintaining slight geometric variations.

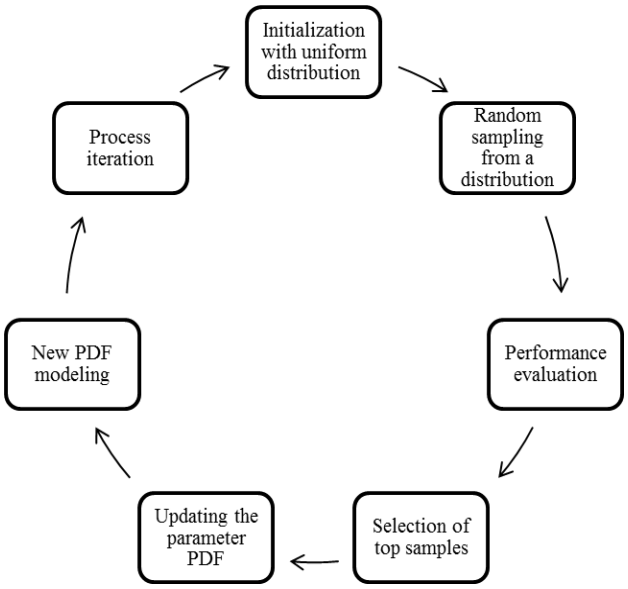

Figure 4. Iterative process of optimization and parameter tuning

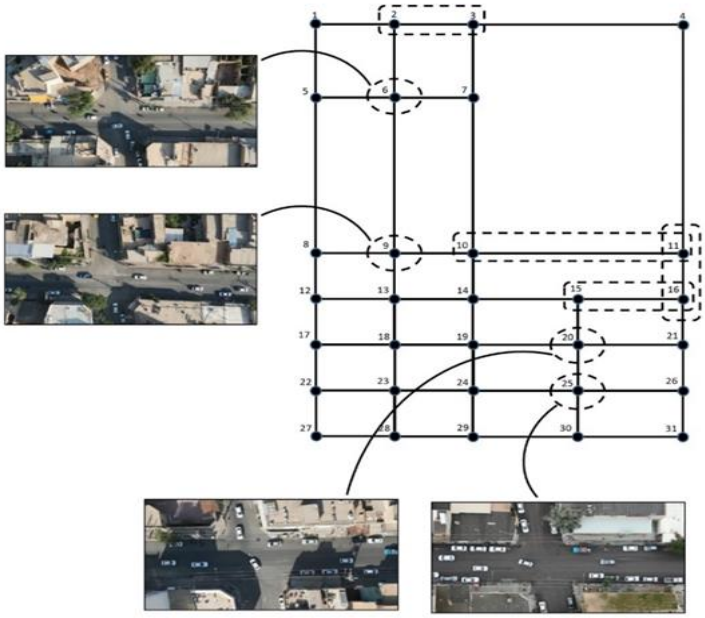

Figure 5. Overview of the study intersections within the Dezful city roads network

a. Node 6

b. Node 9

c. Node 20

d. Node 25

Figure 6. Data collection process at intersections and extraction of conflict indices

Specifically, Intersection No. 6 had a main road width of 15 meters, Intersection No. 9 measured 14 meters, and Intersections Nos. 20 and 25 measured 14 and 13 meters, respectively. The combination of comparable baseline conditions and modest geometric differences provides a valuable context for analyzing the influence of main road width on both safety outcomes and traffic performance at unsignalized intersections.

TABLE 6. Unsignalized urban intersections characteristics

node	Number of Legs	Type	Lane width (m)		Divider
			Major	Minor	
6	4-leg	Unsignalized	15	12	Undivided
9	4-leg	Unsignalized	14	12	Undivided
20	4-leg	Unsignalized	14	10	Undivided
25	4-leg	Unsignalized	13	10	Undivided

4. RESULTS

This section presents the results of implementing a two-level optimization model for the optimal management of turn movements at selected nodes within an urban network. The primary objective was to identify optimal configurations for opening or closing turn movements at nodes, aiming to simultaneously minimize travel time

cost (Z1) and safety-related cost (Z2). The multi-objective NSGA-2 algorithm was employed to solve the model, followed by the application of the TOPSIS multi-criteria decision-making method to analyze and select the most suitable scenarios. A key feature of this solution approach is its emphasis on the diversity of optimal responses, in contrast to the single-solution focus of previous network design studies.

In line with the node-based network design framework outlined in the preceding sections, the results of the proposed safety models for network configuration are presented. Table 7 summarizes the estimated parameters of the linear regression model developed for the network's nodes. Among the independent variables, traffic volume and speed were identified as statistically significant factors influencing safety outcomes. The corresponding t-values for traffic volume and speed were 16.387 and -1.542, respectively. The model demonstrated an R-squared value of 0.64, indicating a satisfactory level of explanatory power. As illustrated in Figure 7, the descriptive plots confirm a positive association between increasing traffic volume and the number of conflicts. Moreover, diagnostic plots validate that the assumptions underpinning linear regression are reasonably satisfied in this model.

By developing conflict-based safety models, the two-level problem was solved using the NSGA-2 algorithm. The main problem model was implemented across 27 different cases, comprising three population groups of 50, 100, and 150 individuals, each tested over 10, 15, 20, 25, 30, 35, 40, 45, and 50 generations. The resulting Pareto front diagrams for populations of 50, 100, and 150 are shown in Figures 8 to 10, respectively. The number of optimal fronts identified for these populations was 17, 25, and 31, respectively. For the population size of 50, both the first and last fronts contained a single solution, while the middle fronts included multiple optimal solutions. In the case of a population of 100, the first front

TABLE 7. Conflict-Traffic Model Estimated Parameters

Model	Unstandardized Coefficients		Standardized Coefficients	t	Sig.
	B	Std. Error	Beta		
(Constant)	1.904	4.126		0.461	0.645
Traffic Volume	1.033	.063	.798	16.387	0.000
Speed	-.258	.167	-.075	-1.542	0.125
R-square: 0.64					

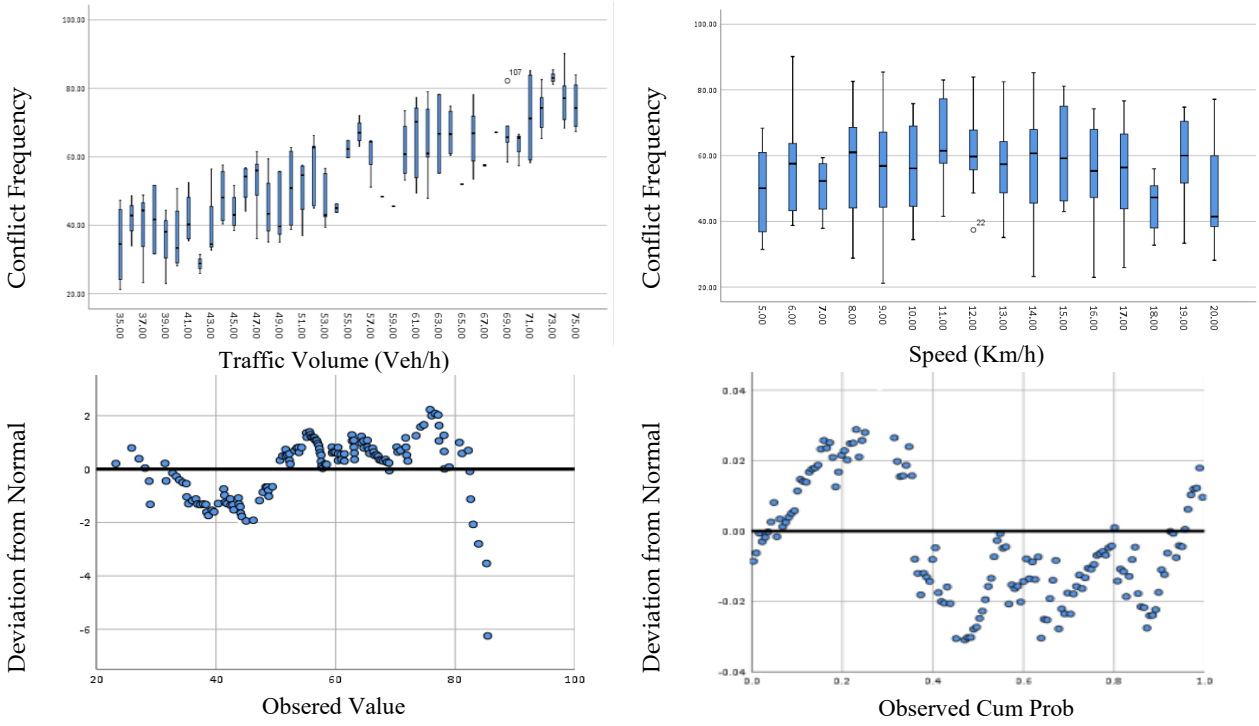

Figure 7. Descriptive statistics of Conflicts-volume models

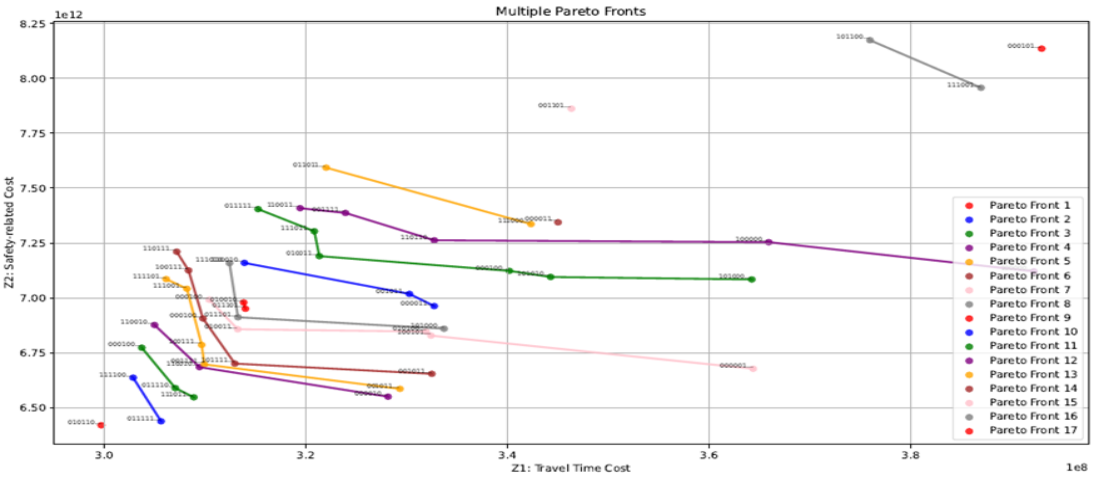

Figure 8. Pareto fronts diagram for a population size of 50 individuals

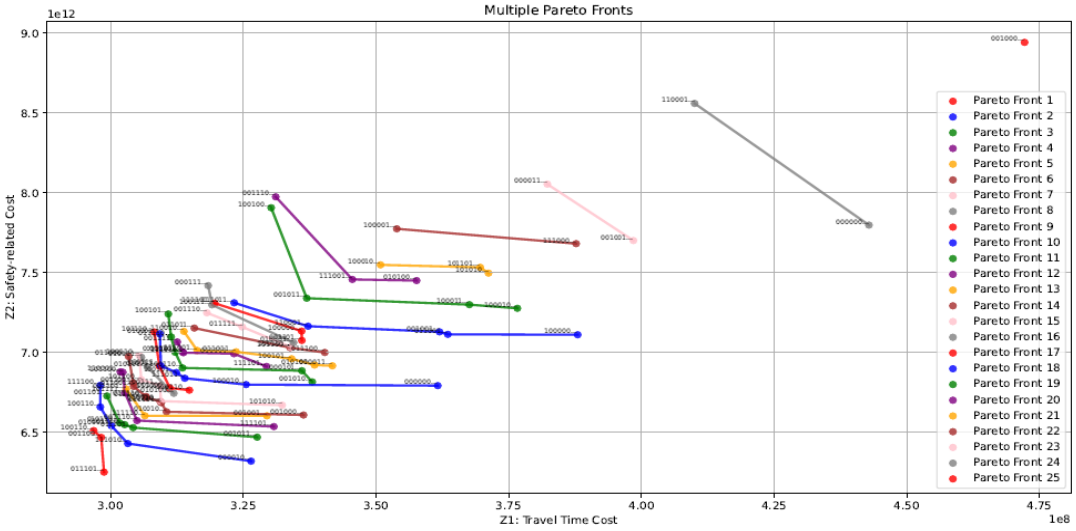

Figure 9. Pareto fronts diagram for a population size of 100 individuals

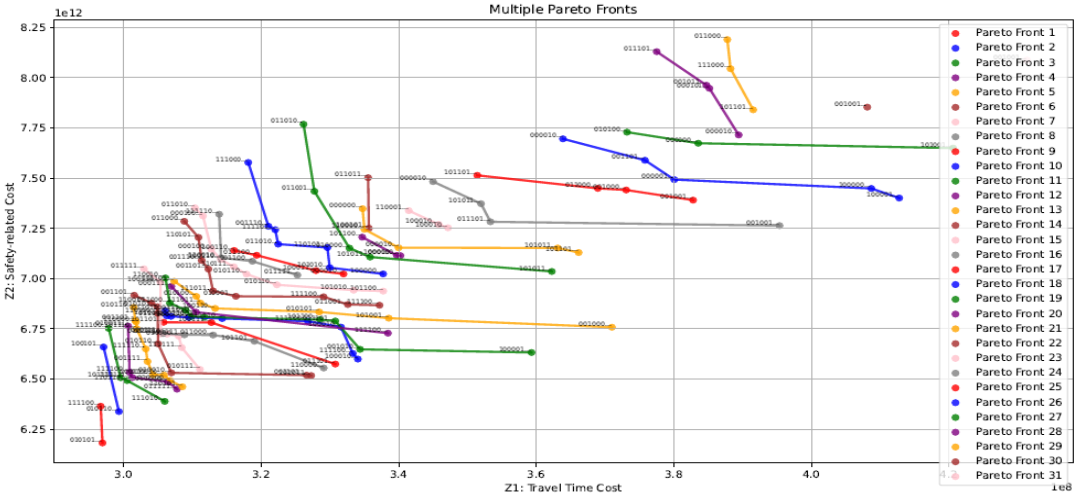

Figure 10. Pareto fronts diagram for a population size of 150 individuals

consisted of three solutions and the last front contained one. As the population increased to 150, the number of Pareto fronts rose accordingly; here, the first front contained two solutions, and the last front again contained a single solution.

Figure 11, for example, illustrates the distribution of Pareto fronts for a population size of 100 across generations 15 to 50. The number of fronts obtained in these nine cases is 26, 29, 26, 26, 25, 25, 24, and 24, respectively. To further assess the performance of the

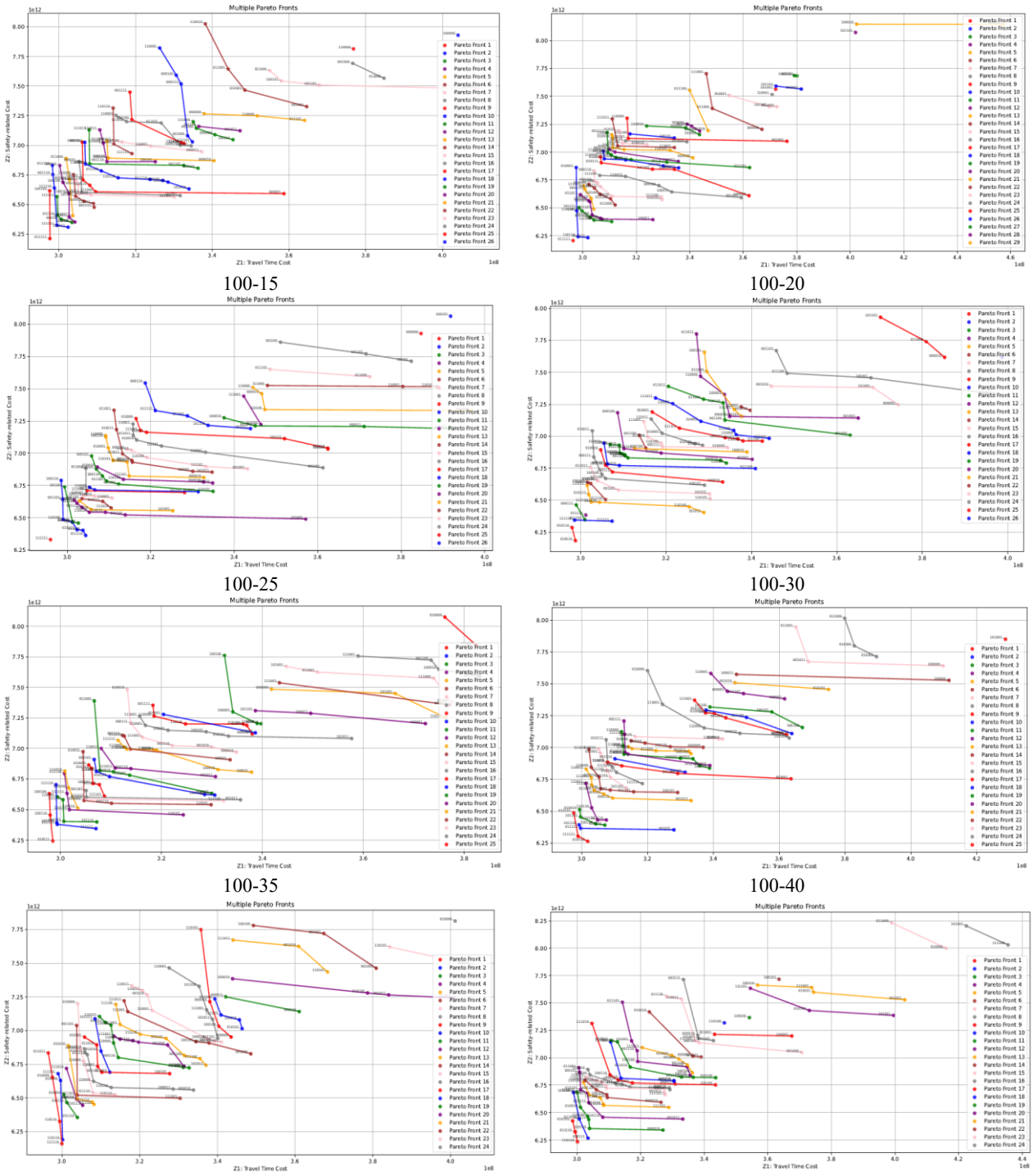

Figure 11. Distribution of Pareto fronts for a population size of 100 across generations 15 to 50.

TABLE 8. Running time and number of Pareto fronts for different populations and generations

Population	Generation	Fronts Frequency	1st front solutions	Last front solutions	Running time (s)
	10	25	3	1	6234
	15	26	2	1	9336
	20	29	1	2	12455
	25	26	1	1	15563
100	30	26	2	1	18675
	35	25	3	2	21777
	40	25	3	1	24895
	45	24	4	1	28001
	50	24	3	2	31108
	10	31	2	1	9357
	15	33	6	1	13990
	20	32	2	1	18667
	25	32	1	1	23328
150	30	29	3	2	27991
	35	31	4	1	32655
	40	34	4	1	37326
	45	31	3	1	42010
	50	29	3	1	46673

NSGA-2 algorithm, a sensitivity analysis was conducted based on two primary parameters: the initial population size and the number of generations. Three population sizes (50, 100, and 150) and nine generation counts (10, 15, 20, 25, 30, 35, 40, 45, and 50) were tested, resulting in a total of 27 different algorithm runs. The results indicate that increasing the population size has a negligible impact on enhancing the quality of the Pareto fronts. The fronts generated for population sizes of 100 and 150 show little difference compared to those obtained with a population of 50. In contrast, increasing the number of generations produced a gradual and modest improvement in the results. For each of the 27 runs, a corresponding Pareto front diagram was plotted, illustrating the trade-off relationship between the model's two primary objective functions (Z1 and Z2).

Selected figures from these 27 graphs illustrate the progression and enhancement in the dispersion and quality of solutions across higher generations. A summary of the model's running details for two population sizes — 100 and 150 — is provided in Table 8, where the running time for each scenario is also reported. The model's running time is primarily influenced by population size. Given the computational capabilities of the system used (Processor with 11th Gen Intel(R) Core (TM) i7 & 16 GB RAM), the average running time for a population of 100 — involving the generation of 100 scenarios and solving the assignment model 100 times — was approximately 622 seconds, equating to 6.22 seconds per assignment. For a population of 150, this time increased by roughly 1.5 times, with each assignment taking about 9.34 seconds. Based on the analysis results; achieving satisfactory optimal fronts appears feasible with a medium-sized population (around 100) and a generation count of at least 30. Additionally, the application of the TOPSIS method in the final decision-making phase proved valuable in clarifying the selection of the most suitable scenarios from the obtained Pareto points.

Subsequently, for a more detailed evaluation of each Pareto front, the TOPSIS method was applied to identify the most favorable scenario within each front. By calculating the TOPSIS score for each scenario, corresponding graphs were generated, highlighting the top-performing scenario in each front (marked in red). This approach facilitated multi-criteria decision-making even among non-dominated (Pareto optimal) solutions. Figure 12 illustrates the graph depicting the best scenario selection within each front for a population size of 100, evaluated up to the tenth generation, where the number of Pareto fronts reached 25. Detailed TOPSIS scores and their corresponding ranks are provided in Table 9. Furthermore, Figures 12 and 13 present the distribution of the TOPSIS-selected optimal scenarios across different generations of the model for a population of 100.

TABLE 9. TOPSIS scores and their ranks for different Pareto fronts

Pareto Front	Topsis Score	Topsis Rank	Pareto Front	Topsis Score	Topsis Rank
1	0.99	1	14	0.76	63
2	0.95	2	15	0.75	68
3	0.92	6	16	0.74	70
4	0.91	9	17	0.73	73
5	0.90	10	18	0.71	77
6	0.89	12	19	0.68	81
7	0.87	17	20	0.63	84
8	0.86	25	21	0.60	87
9	0.85	28	22	0.55	94
10	0.83	36	23	0.44	96
11	0.82	42	24	0.31	98
12	0.80	49	25	0.00	100
13	0.79	51			

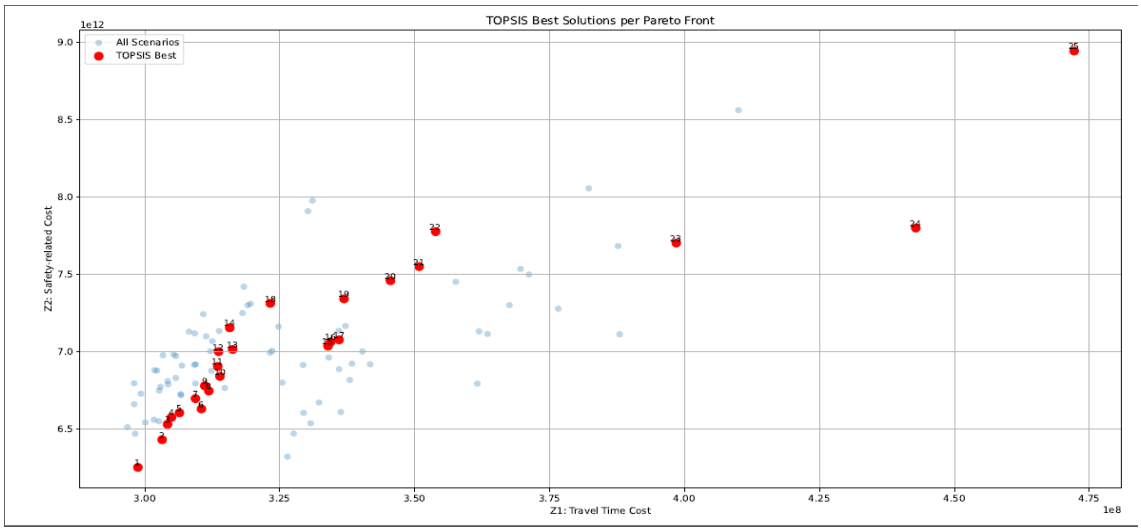

Figure 12. Distribution of TOPSIS-Selected Optimal Scenarios across Pareto Fronts for Generation 10 with a Population Size of 100

The graphs presented in Figures 12 and 13 are based on TOPSIS scores calculated using equal weights for the two objective functions (0.5–0.5). However, in practice, policymakers may assign different priorities to each objective depending on specific conditions. In such cases, the weights of the objective functions can be dynamically adjusted within the TOPSIS framework to reflect these priorities. Figures 14a and 14b illustrate the TOPSIS results under two extreme weighting scenarios: in Figure 14a, a weight of 1 is assigned to the safety cost objective and 0 to the travel time objective, causing the optimal solutions to cluster towards the horizontal axis, representing lower safety costs. Conversely, Figure 14b depicts the scenario where the travel time objective is fully prioritized (weight of 1), resulting in the optimal solutions shifting towards the vertical axis, indicating lower travel time costs.

According to the methodology described for algorithm parameter tuning, the REVAC process begins with a uniform distribution. For tuning the population size parameter, the initial search interval was set between 50 and 150. Assuming this range as the parameter space of the uniform distribution, the initial variance was calculated as 833, with corresponding differential entropy values of 6.89 (bit) and 4.78 (nat). The rationale for using a uniform distribution lies in ensuring complete neutrality and maximum coverage of the search space.

However, this approach inherently results in high variance, elevated entropy, and instability during the early search process, which in turn leads to a sharp decline in efficiency (Figure 15). To address this limitation, a truncated normal distribution, centered at the median with a controlled variance, was applied to refine the process (Figure 16). The rationale for using a uniform distribution lies in ensuring complete neutrality and maximum coverage of the search space. However, this approach inherently results in high variance, elevated entropy, and instability during the early search process,

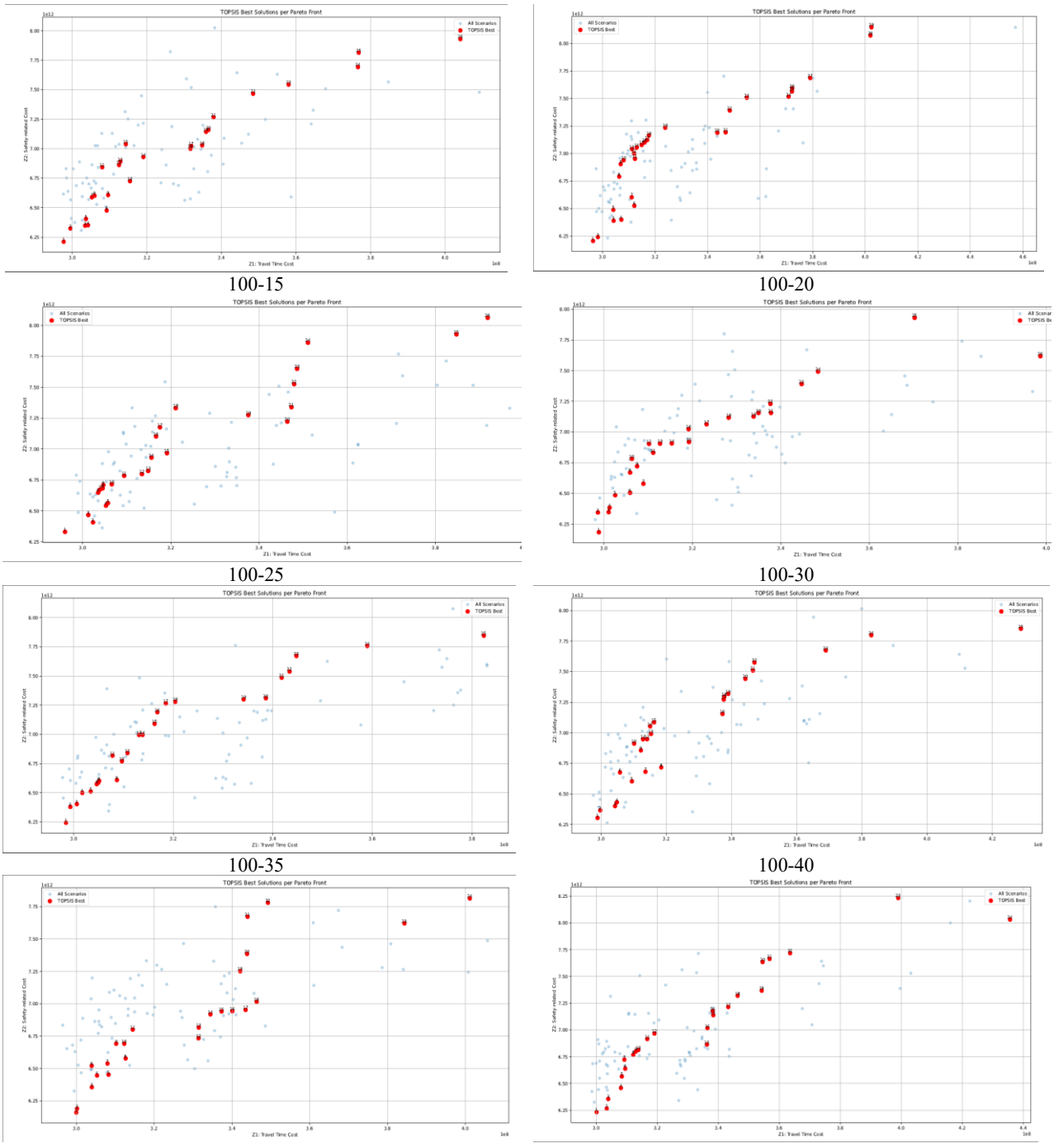

Figure 13. Distribution of TOPSIS-Selected Optimal Scenarios across Pareto Fronts for Generations 15 to 50 with a Population Size of 100

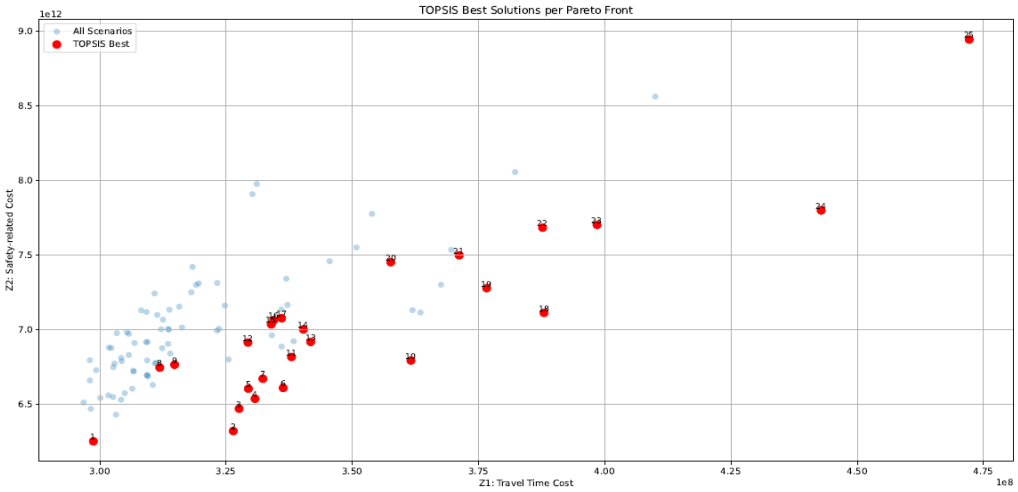

Figure 14a. TOPSIS-optimal scenarios with a weighting factor of 1 for safety and 0 for travel time

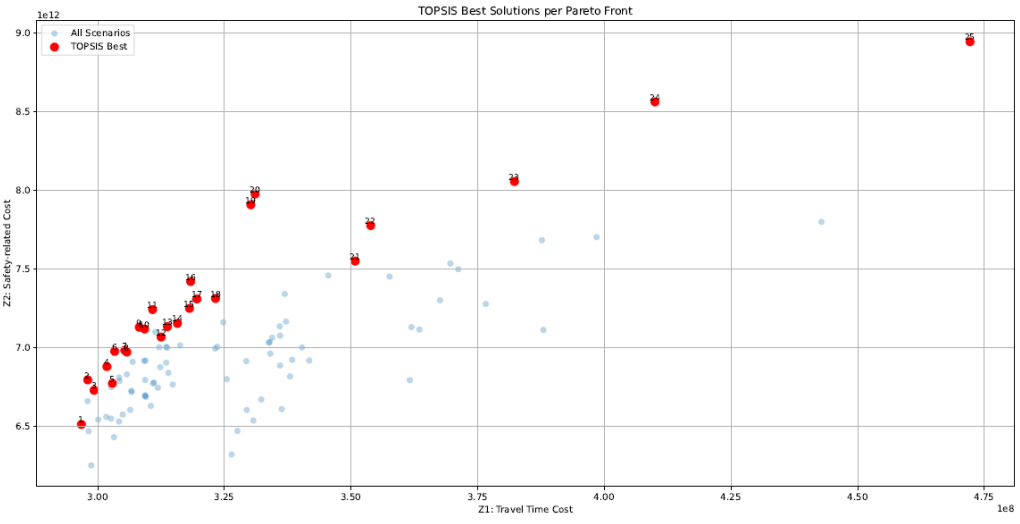

Figure 14b. TOPSIS-optimal scenarios with a weighting factor of 0 for safety and 1 for travel time

Figure 14. Distribution of TOPSIS-selected optimal scenarios across Pareto fronts under different weighting schemes for safety and travel time (delay) objectives

which in turn leads to a sharp decline in efficiency. To address this limitation, a truncated normal distribution, centered at the median with a controlled variance, was applied to refine the process (Figure 17).

5. DISCUSSION

The findings of this study underscore two pivotal dimensions in the context of network design problems. The first pertains to the explicit integration of safety considerations within the optimization framework—an aspect largely overlooked in previous studies, which predominantly prioritized congestion-related objectives through single-objective approaches. By embedding a safety performance function alongside congestion measures, and conducting a sensitivity analysis on the relative weighting of these objectives, this research advances a multi-objective perspective that offers a diverse set of optimal solutions. This stands in contrast to traditional methodologies, which typically culminate in a single recommended configuration, thereby limiting strategic insight for policymakers. The second significant contribution lies in the paradigm shift from link-based optimization strategies to a node-oriented network design approach. Rather than concentrating solely on the optimization of link capacities or configurations, this study emphasizes the strategic management of node-level movements (left, straight, and right turns) to influence overall network performance. This approach not only introduces greater flexibility in managing urban traffic systems but also enables more localized and safety-conscious interventions in critical network locations.

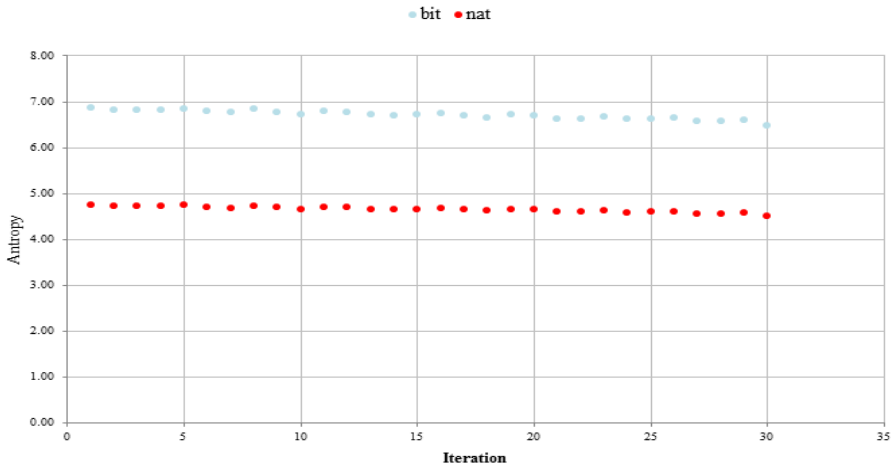

Figure 15. The dispersion of entropy values related to a population parameter with an initial uniform distribution

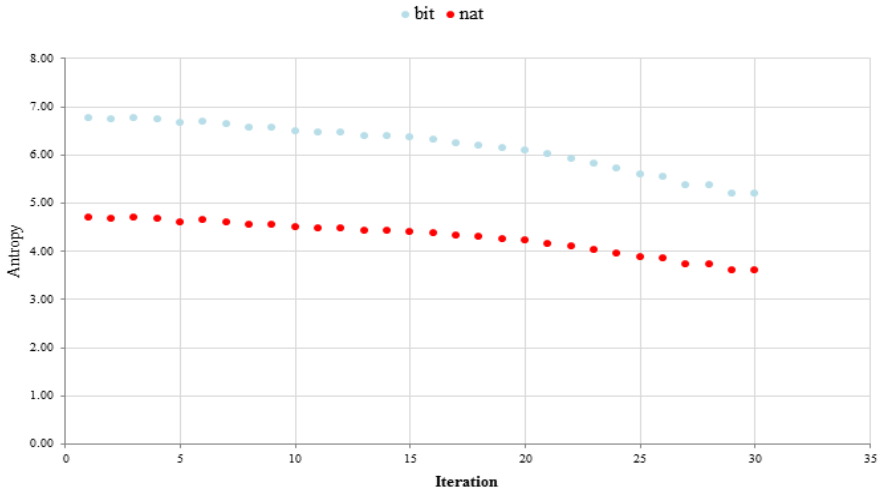

Figure 16. The dispersion of entropy values related to a population parameter with an initial truncated normal distribution

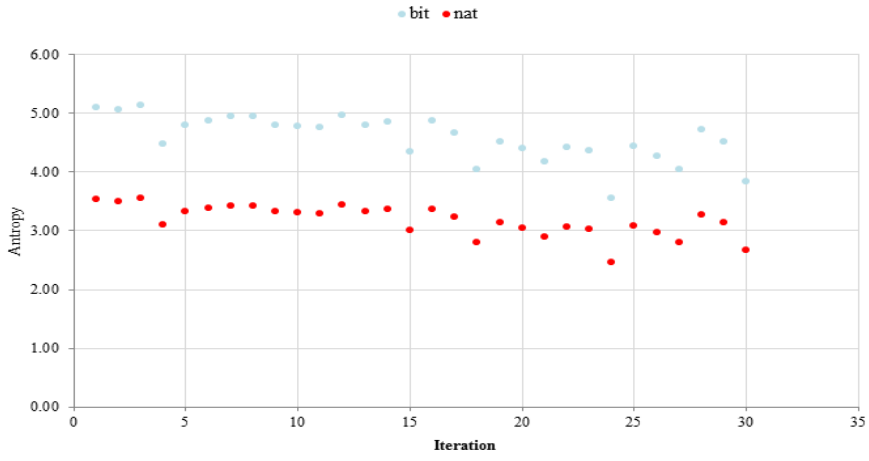

Figure 17. The dispersion of entropy values related to a generation parameter with an initial truncated normal distribution

Previous studies in the field of network design have predominantly adopted link-based optimization approaches, seeking to identify the most efficient set of links to enhance network performance. A classic example is the seminal work of LeBlanc (57) on the Sioux Falls network, comprising 24 nodes and 76 links, which employed a congestion-based, single-objective framework and ultimately recommended a single optimal solution—scenario 10110—for implementation. In his study, five candidate improvement projects were evaluated, with the first, third, and fourth projects selected based on their impact on network congestion. Gao et al. (23) also arrived at the identical solution of 10110 using the same network structure, as did Luathep et al. (31) in their analysis. With a developmental approach, the present study introduces a methodological advancement by shifting the focus from link-based interventions to node-level decision-making within the network design problem.

A second key innovation of this study lies in the explicit integration of a safety component into the network design problem. The detailed findings presented in the preceding sections demonstrate that a diverse set of optimal solutions can be identified, providing decision-makers with the flexibility to select configurations based on varying trade-offs between safety and congestion. This is particularly important in contexts where users may not consistently prioritize either safety or congestion reduction. Zhu et al. (58) highlighted this dilemma by illustrating that, from the users' perspective, the minimization of travel time delays often takes precedence over potential safety risks. This observation underscores the necessity for network planners and decision-makers to move beyond purely technical or optimization-based frameworks and incorporate behavioral insights into their strategies. The findings of this study emphasize the necessity of adopting a network-centric perspective in the analysis of node-level interventions, as opposed to a localized, point-specific approach. This research demonstrates that operational treatments implemented at a given node cannot be regarded as isolated adjustments, since their influence inevitably permeates through interconnected nodes within the network. Despite this, the majority of prior studies have predominantly concentrated on evaluating isolated node-specific treatments, often neglecting their broader systemic implications. For instance, Sun (59) examined vehicle interaction dynamics for right-turn maneuvers at individual intersections using conflict indices. Similarly, performance measures such as the Post Encroachment Time (PET) index have been employed to assess turning operations exclusively at singular node locations (60). Guo et al. (61) extended this line of inquiry by analyzing intersection safety based on specific treatments at node locations, relying on interaction indices for right-turning vehicles to gauge operational outcomes. Furthermore, a range of optimization models has been proposed to enhance turn control strategies, including the development of a mixed-integer linear programming model for optimizing left-turn geometries (62). Distinguishing itself from these conventional approaches, the present study integrates the Time to Collision (TTC) conflict index—a widely recognized time-based surrogate safety measure —within a comprehensive network optimization framework. This methodology enables the simultaneous evaluation of individual node performance and its interrelations with the operational states of other nodes across the network, thereby offering a more holistic and interconnected perspective on network safety and efficiency optimization.

Finally, it is essential to underscore the broader applicability of this study's findings to other transportation modes, including public transit and bus networks, positioning it as a foundational framework for addressing complex network design challenges. For instance, Loder et al. (63) introduced the Multimodal Urban Network Design Problem (MMNDP), a comprehensive framework aimed at supporting policymakers in formulating optimal pricing strategies and infrastructure investment decisions within multimodal transport networks. Their research demonstrated that increasing the cost of private vehicle usage and reallocating road space in favor of public transport can substantially reduce network-wide travel times. In the context of such multimodal optimization problems, incorporating node-based safety performance indices—an innovation advanced in the present study—can meaningfully influence decision-making processes in public transit network design by accounting for safety considerations alongside operational efficiency. Similarly, Canca et al. (64) proposed an integrated model combining strategic and tactical decision-making layers to optimize railway network design problem (RWNDP) and minimize associated costs. When integrated with the node-centric, safety-informed approach introduced in this study, such frameworks have the potential to enhance decision-support systems for railway and other multimodal networks, offering a more holistic and safety-conscious methodology for contemporary transportation network planning.

The findings of this study highlight that in the domains of policy-making, planning, and decision-making for improving urban indicators—particularly traffic infrastructure—traditional one-dimensional approaches may not only fail to deliver sustainable improvements but may, in some cases, result in the deterioration of key indicators despite substantial financial investment. Conventional approaches, which

rely primarily on single performance measures such as travel time (congestion), often produce solutions that diverge from those identified through the advanced, multi-dimensional framework employed in this study. For instance, an urban decision-maker may initially observe improvements in local travel time following the implementation of a treatment at a node; however, over time, safety indicators may deteriorate, or the travel time index itself may regress to pre-treatment congestion levels due to network-wide interactions.

6. CONCLUSIONS

This study demonstrates that the integration of safety considerations exerts a substantial influence on the design, configuration, and operational performance of transportation networks. The findings clearly indicate that a one-dimensional approach—centered exclusively on minimizing travel time as a proxy for congestion—is fundamentally insufficient for addressing the complexities of network design. By incorporating safety as a critical objective alongside travel time, the network design process transitions from producing singular, efficiency-driven solutions to generating a diverse set of balanced configurations. This underscores the necessity of adopting a holistic, multi-objective framework in which trade-offs between safety and travel time are systematically evaluated, ultimately yielding more robust, and operationally effective network designs.

In contrast to conventional network design problems, which are predominantly single-objective and congestion-focused, typically producing a singular optimal solution, this study demonstrates that the resulting solutions vary considerably depending on the relative prioritization of safety and congestion criteria. Addressing a critical gap in the literature, this research shifts the focus from traditional link-based decision-making—where optimization efforts have largely concentrated on identifying efficient link configurations within budgetary constraints—to a node-based network design framework. The study advances the methodological landscape by seeking the optimal configuration of flows at node locations, thereby capturing the interactive and system-wide effects of node-level interventions on overall network performance. Adopting a network-level perspective on node interventions enables decision-makers to enhance traffic capacity without necessarily compromising safety or exacerbating congestion, despite the potential associated costs. This finding underscores the notion that optimizing travel time improvements across a network does not inherently translate to enhanced safety outcomes. Conversely, interventions that improve safety or travel time at an individual node may fail to yield system-wide benefits. Additionally, the substitution of traditional crash data with conflict-based surrogate safety measures offers a valuable opportunity to develop multi-objective, two-level safety performance functions capable of balancing safety and travel time objectives within network design frameworks. Future research is encouraged to explore this potential by examining a broader array of conflict indices to refine these multi-criteria models.

The findings of this study hold significant implications for both the enhancement of existing transportation networks and the planning of future urban developments. Integrating safety considerations into network design necessitates a proactive, forward-looking strategy that not only aims to optimize travel times but also prioritizes the substantial reduction of crash risks and their associated consequences. This approach positions safety as a foundational criterion in network planning and design, rather than as a secondary outcome. Future research is encouraged to expand upon this proactive framework, applying it to the optimization of existing networks and embedding safety as a central principle in the design and adaptation of both current and emerging urban transportation systems.

7. REFERENCES

1. Jia W, Zhang K, Ma X, Li M. Resilience assessment for bus-metro multimodal networks considering various attacking scenarios. Multimodal Transportation. 2025:100238. https://doi.org/10.1016/j.multra.2025.100238
2. Chen A, Kim J, Lee S, Kim Y. Stochastic multi-objective models for network design problem. Expert Systems with Applications. 2010;37(2):1608-19. https://doi.org/10.1016/j.eswa.2009.06.048
3. Yang H, H. Bell MG. Models and algorithms for road network design: a review and some new developments. Transport Reviews. 1998;18(3):257-78. https://doi.org/10.1080/01441649808717016
4. Feng S, Wang A, Tian Z, Park S. Exploring the correlation between hard-braking events and traffic crashes in regional transportation networks: A geospatial perspective. Multimodal Transportation. 2024;3(2):100128. https://doi.org/10.1016/j.multra.2024.100128
5. Chen X, Jia Y. Sustainable traffic management and control system for arterial with contraflow left-turn lanes. Journal of Cleaner Production. 2021;280:124256. https://doi.org/10.1016/j.jclepro.2020.124256
6. Moinuddin M, Proffer L, Vechione M, Khanal A. Application of machine learning models to predict driver left turn destination lane choice behavior at urban intersections. International journal of transportation science and technology. 2024;13:155-70. https://doi.org/10.1016/j.ijtst.2023.12.005
7. Kan Z, Tang L, Kwan M-P, Ren C, Liu D, Li Q. Traffic congestion analysis at the turn level using Taxis' GPS trajectory data. Computers, Environment and Urban Systems. 2019;74:229-43. https://doi.org/10.1016/j.compenvurbsys.2018.11.007
8. Fan J, Li A, Ilahi A, Gao K. Emission impacts of left-turn lane on light-heavy-duty mixed traffic in signalized intersections: Optimization and empirical analysis. Heliyon. 2023;9(5). https://doi.org/10.1016/j.heliyon.2023.e16260

9. Autey J, Sayed T, Zaki MH. Safety evaluation of right-turn smart channels using automated traffic conflict analysis. Accident Analysis & Prevention. 2012;45:120-30. https://doi.org/10.1016/j.aap.2011.11.015
10. Foulaadvand ME, Belbasi S. Vehicular traffic flow at an intersection with the possibility of turning. Journal of Physics A: Mathematical and Theoretical. 2011;44(10):105001. http://dx.doi.org/10.1088/1751-8113/44/10/105001
11. Hu S, Jia Z, Yang A, Xue K, He G. Evaluating the sustainable traffic flow operational features of U-turn design with Advance Left Turn. Sustainability. 2022;14(11):6931. https://doi.org/10.3390/su14116931
12. Currie G, Reynolds J. Managing trams and traffic at intersections with hook turns: safety and operational impacts. Transportation research record. 2011;2219(1):10-9. https://doi.org/10.3141/2219-02
13. Hounsell NB, Yap YH. Hook turns as a solution to the right-turning traffic problem. Transportation science. 2015;49(1):1-12. https://doi.org/10.1287/trsc.2013.0482
14. Liu Z, Bie Y. Comparison of hook-turn scheme with U-turn scheme based on actuated traffic control algorithm. Transportmetrica A: transport science. 2015;11(6):484-501. https://doi.org/10.1080/23249935.2015.1018855
15. Guo Z, Sun D, Zhou L. Game Algorithm of Intelligent Driving Vehicle Based on Left-Turn Scene of Crossroad Traffic Flow. Computational intelligence and neuroscience. 2022;2022(1):9318475. https://doi.org/10.1155/2022/9318475
16. Lin W, Han H, Dong Y, Tayijiang D, Yu Q. Modeling of left-turn vehicle trajectories and exit lane selection at signalized intersections. 2023. http://dx.doi.org/10.21203/rs.3.rs-2586259/v1
17. Ahmed A, Sadullah AFM, Yahya AS. Field study on the behavior of right-turning vehicles in Malaysia and their contribution on the safety of unsignalized intersections. Transportation research part F: traffic psychology and behaviour. 2016;42:433-46. https://doi.org/10.1016/j.trf.2015.03.006
18. Paul M, Ghosh I. Post encroachment time threshold identification for right-turn related crashes at unsignalized intersections on intercity highways under mixed traffic. International journal of injury control and safety promotion. 2020;27(2):121-35. https://doi.org/10.1080/17457300.2019.1669666
19. Abhigna D, Ramees M, Ravishankar K. Effect of gap acceptance behavior of the right turning vehicles on the major road stream for uncontrolled three-legged intersections under mixed traffic conditions. International Journal of Engineering Transactions C: Aspects. 2018;31(6):870-6. https://doi.org/10.5829/ije.2018.31.06c.02
20. Farahani RZ, Miandoabchi E, Szeto WY, Rashidi H. A review of urban transportation network design problems. European journal of operational research. 2013;229(2):281-302. https://doi.org/10.1016/j.ejor.2013.01.001
21. Poorzahedy H, Abulghasemi F. Application of ant system to network design problem. Transportation. 2005;32(3):251-73. https://doi.org/10.1007/s11116-004-8246-7
22. Wang DZ, Liu H, Szeto WY. A novel discrete network design problem formulation and its global optimization solution algorithm. Transportation Research Part E: Logistics and Transportation Review. 2015;79:213-30. https://doi.org/10.1016/j.tre.2015.04.005
23. Gao Z, Wu J, Sun H. Solution algorithm for the bi-level discrete network design problem. Transportation Research Part B: Methodological. 2005;39(6):479-95. https://doi.org/10.1016/j.trb.2004.06.004
24. Drezner Z, Wesolowsky GO. Network design: selection and design of links and facility location. Transportation Research Part A: Policy and Practice. 2003;37(3):241-56. https://doi.org/10.1016/S0965-8564(02)00014-9
25. Poorzahedy H, Rouhani OM. Hybrid meta-heuristic algorithms for solving network design problem. European journal of operational research. 2007;182(2):578-96. https://doi.org/10.1016/j.ejor.2006.07.038
26. Solanki RS, Gorti JK, Southworth F. Using decomposition in large-scale highway network design with a quasi-optimization heuristic. Transportation Research Part B: Methodological. 1998;32(2):127-40. https://doi.org/10.1016/S0191-2615(97)00020-9
27. Friesz TL, Cho H-J, Mehta NJ, Tobin RL, Anandalingam G. A simulated annealing approach to the network design problem with variational inequality constraints. Transportation science. 1992;26(1):18-26. https://doi.org/10.1287/trsc.26.1.18
28. Abdulaal M, LeBlanc LJ. Continuous equilibrium network design models. Transportation Research Part B: Methodological. 1979;13(1):19-32. https://doi.org/10.1016/0191-2615(79)90004-3
29. Allsop RE, editor Some possibilities for using traffic control to influence trip distribution and route choice. Transportation and traffic theory, proceedings; 1974.
30. Wang DZ, Lo HK. Global optimum of the linearized network design problem with equilibrium flows. Transportation Research Part B: Methodological. 2010;44(4):482-92. https://doi.org/10.1016/j.trb.2009.10.003
31. Luathep P, Sumalee A, Lam WH, Li Z-C, Lo HK. Global optimization method for mixed transportation network design problem: a mixed-integer linear programming approach. Transportation Research Part B: Methodological. 2011;45(5):808-27. https://doi.org/10.1016/j.trb.2011.02.002
32. Cantarella GE, Vitetta A. The multi-criteria road network design problem in an urban area. Transportation. 2006;33(6):567-88. https://doi.org/10.1007/s11116-006-7908-z
33. Mesbah M, Sarvi M, Currie G. New methodology for optimizing transit priority at the network level. Transportation Research Record. 2008;2089(1):93-100. https://doi.org/10.3141/2089-12
34. Resat HG, Turkay M. Design and operation of intermodal transportation network in the Marmara region of Turkey. Transportation Research Part E: Logistics and Transportation Review. 2015;83:16-33. https://doi.org/10.1016/j.tre.2015.08.006
35. Yao B, Hu P, Lu X, Gao J, Zhang M. Transit network design based on travel time reliability. Transportation Research Part C: Emerging Technologies. 2014;43:233-48. https://doi.org/10.1016/j.trc.2013.12.005
36. Yu B, Kong L, Sun Y, Yao B, Gao Z. A bi-level programming for bus lane network design. Transportation Research Part C: Emerging Technologies. 2015;55:310-27. https://doi.org/10.1016/j.trc.2015.02.014
37. Nassrullah Z. Evaluating Traffic Performance on Basra City Urban Roads Network. International Journal of Engineering Transactions B: Applications. 2023;36(11):2063-72. https://doi.org/10.5829/ije.2023.36.11b.11
38. Cipriani E, Petrelli M, Fusco G. A multimodal transit network design procedure for urban areas. Advances in transportation studies. 2006;10:5-20.
39. Fan W, Machemehl RB. Tabu search strategies for the public transportation network optimizations with variable transit demand. Computer-Aided Civil and Infrastructure Engineering. 2008;23(7):502-20. https://doi.org/10.1111/j.1467-8667.2008.00556.x
40. Gallo M, Montella B, D'Acierno L. The transit network design problem with elastic demand and internalisation of external costs: An application to rail frequency optimisation. Transportation

Research Part C: Emerging Technologies. 2011;19(6):1276-305. https://doi.org/10.1016/j.trc.2011.02.008

41. Rashidi E, Parsafard M, Medal H, Li X. Optimal traffic calming: A mixed-integer bi-level programming model for locating sidewalks and crosswalks in a multimodal transportation network to maximize pedestrians' safety and network usability. Transportation research part E: logistics and transportation review. 2016;91:33-50. https://doi.org/10.1016/j.tre.2016.03.016
42. Jasiūnienė V, Ratkevičiūtė K, Peltola H, editors. Road Network Safety Ranking Using Accident Prediction Models. Conference Vision Zero for Sustainable Road Safety in Baltic Sea Region; 2018: Springer.
43. Fancello G, Carta M, Serra P. Data Envelopment Analysis for the assessment of road safety in urban road networks: A comparative study using CCR and BCC models. Case studies on transport policy. 2020;8(3):736-44. https://doi.org/10.1016/j.cstp.2020.07.007
44. Gomes SV, Cardoso JL, Azevedo CL. Portuguese mainland road network safety performance indicator. Case studies on transport policy. 2018;6(3):416-22. https://doi.org/10.1016/j.cstp.2017.10.006
45. Ewing R, Dumbaugh E. The built environment and traffic safety: a review of empirical evidence. Journal of Planning Literature. 2009;23(4):347-67. https://doi.org/10.1177/0885412209335553
46. Moeinaddini M, Asadi-Shekari Z, Shah MZ. The relationship between urban street networks and the number of transport fatalities at the city level. Safety science. 2014;62:114-20. https://doi.org/10.1016/j.ssci.2013.08.015
47. Rifaat SM, Tay R, De Barros A. Effect of street pattern on the severity of crashes involving vulnerable road users. Accident Analysis & Prevention. 2011;43(1):276-83. https://doi.org/10.1016/j.aap.2010.08.024
48. Marshall WE, Garrick NW. Does street network design affect traffic safety? Accident Analysis & Prevention. 2011;43(3):769-81. https://doi.org/10.1016/j.aap.2010.10.024
49. Tarko AP. Surrogate measures of safety. Safe mobility: challenges, methodology and solutions: Emerald Publishing Limited; 2018. p. 383-405.
50. Hayward J. Near misses as a measure of safety at urban intersections: Pennsylvania Transportation and Traffic Safety Center; 1971.
51. Sarkar DR, Rao KR, Chatterjee N. A review of surrogate safety measures on road safety at unsignalized intersections in developing countries. Accident Analysis & Prevention. 2024;195:107380. https://doi.org/10.1016/j.aap.2023.107380
52. Wang C, Xie Y, Huang H, Liu P. A review of surrogate safety measures and their applications in connected and automated vehicles safety modeling. Accident Analysis & Prevention. 2021;157:106157. https://doi.org/10.1016/j.aap.2021.106157
53. Shahpar AH, Aashtiani HZ, Faghri A. Development of a delay model for unsignalized intersections applicable to traffic assignment. Transportation planning and technology. 2011;34(5):497-507. https://doi.org/10.1080/03081060.2011.586119
54. Sampson JR. Adaptation in natural and artificial systems (John H. Holland). Society for Industrial and Applied Mathematics; 1976.
55. Rajabi-Bahaabadi M, Shariat-Mohaymany A, Babaei M, Vigo D. Reliable vehicle routing problem in stochastic networks with correlated travel times. Operational Research. 2021;21(1):299-330. https://doi.org/10.1007/s12351-019-00452-w
56. Smit SK, Eiben AE, editors. Beating the 'world champion'evolutionary algorithm via REVAC tuning. IEEE Congress on Evolutionary Computation; 2010: IEEE.
57. Leblanc LJ. An algorithm for the discrete network design problem. Transportation science. 1975;9(3):183-99. https://doi.org/10.1287/trsc.9.3.183
58. Zhu D, Sze N, Feng Z. The trade-off between safety and time in the red light running behaviors of pedestrians: A random regret minimization approach. Accident Analysis & Prevention. 2021;158:106214. https://doi.org/10.1016/j.aap.2021.106214
59. Sun M, editor Research on the Signal Control Design of Right-turn Vehicle in Urban Traffic. 2013 the International Conference on Remote Sensing, Environment and Transportation Engineering (RSETE 2013); 2013: Atlantis Press.
60. Jiang C, Qiu R, Fu T, Fu L, Xiong B, Lu Z. Impact of right-turn channelization on pedestrian safety at signalized intersections. Accident Analysis & Prevention. 2020;136:105399. https://doi.org/10.1016/j.aap.2019.105399
61. Guo Y, Liu P, Wu Y, Chen J. Evaluating how right-turn treatments affect right-turn-on-red conflicts at signalized intersections. Journal of Transportation Safety & Security. 2020;12(3):419-40. https://doi.org/10.1080/19439962.2018.1490368
62. Yang H, Zhao J, Wang M. Optimal control of automated left-turn platoon at contraflow left-turn lane intersections. Journal of intelligent and connected vehicles. 2022;5(3):206-14. https://doi.org/10.1108/JICV-03-2022-0007
63. Loder A, Bliemer MC, Axhausen KW. Optimal pricing and investment in a multi-modal city—Introducing a macroscopic network design problem based on the MFD. Transportation Research Part A: Policy and Practice. 2022;156:113-32. https://doi.org/10.1016/j.tra.2021.11.026
64. Canca D, De-Los-Santos A, Laporte G, Mesa JA. The railway network design, line planning and capacity problem: An adaptive large neighborhood search metaheuristic. Euro Working Group on Transportation: Springer; 2016. p. 198-219.

COPYRIGHTS
©2026 The author(s). This is an open access article distributed under the terms of the Creative Commons Attribution (CC BY 4.0), which permits unrestricted use, distribution, and reproduction in any medium, as long as the original authors and source are cited. No permission is required from the authors or the publishers.

Persian Abstract

چکیده

پیکربندی بهینه حرکات گردشی در تقاطع‌ها، یک راهبرد اساسی در حوزه مسائل طراحی شبکه حمل و نقل است. اکثر مداخلاتی که در تقاطع‌ها برای مدیریت ترافیک دنبال می‌گردد، معمولاً بر اساس تأثیر موضعی آنها در گره خاص ارزیابی می‌شوند. با این حال، یک سوال اساسی مطرح می‌شود: آیا هرگونه مداخله‌ای در یک گره واحد می‌تواند مستقل از شرایط و عملکرد سایر گره‌ها در شبکه حمل و نقل باشد؟ در حالی که روش‌های ارزیابی نقطه‌ای، اغلب نتایج محدود و جداگانه‌ای ارایه می‌کنند، پویایی ترافیک در رویکرد شبکه‌ای به شیوه‌ای کاملاً متفاوت تکامل می‌یابد، و در یک چهارچوب تعادلی و چند معیاره، راه‌حل‌های بهینه را پیشرفته‌تر و چندبعدی می‌کنند. این مطالعه سه رویکرد جدید برای پرداختن به این چالش پیشنهاد می‌کند: (۱) توسعه یک چهارچوب تصمیم‌گیری جامع مبتنی بر شبکه برای مدیریت حرکات گردشی؛ (۲) تغییر مفهومی از روش‌های مرسوم مبتنی بر لینک به الگوهای گره محور در طراحی شبکه؛ و (۳) اتخاذ شاخص‌های تداخل به عنوان اقدامات ایمنی جایگزین به جای داده‌های سنتی تصادف، که در نتیجه یک رویکرد یکپارچه‌تر، پیشگیرانه‌تر و ایمنی‌محورتر را برای برنامه‌ریزی شبکه حمل و نقل شهری تسهیل می‌کند. برای عملیاتی کردن این روش‌ها، یک چهارچوب بهینه‌سازی دو سطحی و چند هدفه توسعه داده شده است که الگوریتم NSGA-2 را برای تولید راه‌حل‌های بهینه پارتو و روش TOPSIS را برای پشتیبانی از تصمیم‌گیری ادغام می‌کند. فرمول‌بندی مدل و فرآیندهای بهینه‌سازی بر اساس داده‌های تجربی جمع‌آوری‌شده از شبکه جاده‌ای شهری دزفول، ایران، بنا شده‌اند. یافته‌ها طیف متنوعی از راه‌حل‌های بهینه را ارائه می‌دهند که بینش‌های ارزشمندی را برای بهبود سیستم‌های حمل‌ونقل موجود و اطلاع‌رسانی در برنامه‌ریزی راهبردی و طراحی شبکه‌های شهری آینده ارائه می‌دهند.

International Journal of Engineering

Journal Homepage: www.ije.ir

A Preference-based User Similarity to Construct a Collaborative Recommender System

B. Rahimpour Cami[a], H. Hassanpour*[b], H. Mashayekhi[b]

[a] *Faculty of Industrial and Computer Engineering, Mazandaran University of Science and Technology, Babol, Iran*
[b] *Faculty of Computer Engineering, Shahrood University of Technology, Shahrood, Iran*

PAPER INFO

Paper history:
Received 18 August 2025
Received in revised form 14 September 2025
Accepted 30 September 2025

Keywords:
Collaborative Filtering
User Similarity
Similarity Measure
User Preferences

ABSTRACT

Recommender systems have emerged as indispensable tools to overcome the information overload on the web. These systems provide personalization for users to select favorite resources. Collaborative Filtering is among the popular approaches is widely used to construct recommender systems. The main challenge of this approach is the effectiveness of its similarity measure to find similar users/items for providing recommendations. In this paper, we propose a novel measure to compute the similarity considering users' preferences. The proposed similarity measure improves the performance of recommender systems by incorporating high level latent factors instead of co-rated items by users, or common selection patterns. These latent factors are extracted via preference-based user modeling. It also provides a better recommendation when only a few ratings (sparse dataset) are available for similarity calculation. We implemented the proposed method and evaluated it using the MovieLens dataset. The evaluation results show that the proposed preference-based similarity measure considerably improves recommendation performance compared to other existing approaches.

doi: *10.5829/ije.2026.39.08b.17*

Graphical Abstract

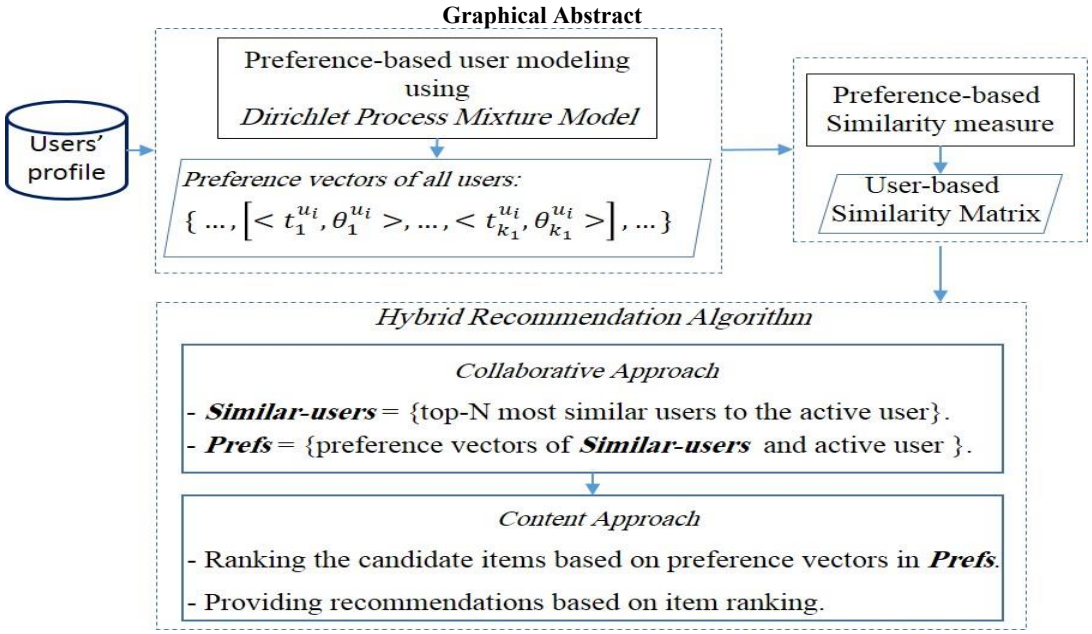

*Corresponding Author Email: h.hassanpour@shahroodut.ac.ir (H. Hassanpour)

Please cite this article as: Rahimpour Cami B, Hassanpour H, Mashayekhi H. A Preference-based User Similarity to Construct a Collaborative Recommender System. International Journal of Engineering, Transactions B: Applications. 2026;39(08):2012-21.

1. INTRODUCTION

Recommender systems have revolutionized online content discovery, helping users navigate the overwhelming information available on the web. By analyzing user profiles and interests, these systems predict items a user may desire, enhancing personalization and improving user experience. They are used in various online environments such as e-commerce and learning management systems (LMSs) (1, 2).

Three main approaches are available for constructing a recommender system: Collaborative Filtering (CF), content-based filtering, and hybrid methods (3). CF-based systems identify user communities with similar tastes and leverage their collective feedback for recommendations (4). Content-based systems, conversely, construct user profiles from item features and match them to new resources (5). Hybrid systems combine both approaches to improve performance (6).

Among these, CF remains particularly popular and successful (7, 8) employed by major platforms like Amazon (9) and Google News (10). Its core premise is that users with similar behavior share common interests. Modern CF implementations primarily employ neighborhood methods that compute user/item similarities (11, 12) and latent factor models that project users and items into shared feature spaces (13-15).

Despite its widespread adoption, CF's accuracy hinges on the ability of its similarity measure to discern meaningful user afinities, this is a challenge when relying solely on explicit ratings or selection patterns (16, 17). Conventional similarity measures like Cosine, Pearson, Jaccard, and mean squared difference primarily focus on users' selection patterns (16-18). Existing neighborhood-based CF methods often rely on raw co-ratings as numerical vectors for similarity calculation (18, 19), neglecting users' underlying interests and preferences. Furthermore, traditional methods struggle to perform effectively with sparse datasets, where only limited ratings are available (20, 21).

The major contribution of this work lies in using users' preferences as the main component of the similarity measure for building a collaborative filtering–based recommendation system. We incorporate users' preferences modeling (22) to construct the preference-based similarity measure. The preference-based similarity measure is the primary component of the proposed CF-based recommender systems. In this paper, we propose a new collaborative recommender system which employs both users' interests and preferences for clustering users into different groups. Users' preferences not only reflect latent factors but also prioritize them, offering a richer similarity measure for understanding users' behavior. Additionally, the proposed method uses the content information of items to construct the users' interests and to model the users' preferences. Therefore, the proposed method alleviates the sparsity and cold-start issues via using latent features more over numerical/non − numerical users' feedback. We used the MovieLens dataset to evaluate the accuracy of the proposed CF-based recommender systems which is empowered with the preference-based similarity measure. The experiments indicate that the preference-based similarity measure can improve the performance of CF-based recommender systems compared to other existing methods.

This paper is organized as follows: Section 2 provides an overview of previous research on collaborative filtering and similarity metrics. Section 3 introduces the proposed methodology. Section 4 describes the dataset, experimental setup, and comparative analysis. Finally, Section 5 provides conclusions for the paper and suggests directions for future research.

2. RELATED WORKS

In CF-based recommender systems, user profiles are represented as a rating matrix capturing user feedback (e.g., ratings or clicks) on items. Domain independency is the main advantage of collaborative filtering. As previously noted, CF systems primarily adopt two approaches: neighborhood-based methods and latent factor models.

In neighborhood-based CF methods, a similarity measure is applied to the entire rating matrix to identify neighbors of an active user or similar items to a candidate item (11, 21, 23). The most critical component of neighborhood based CF is the similarity measure's effectiveness in finding similar users. In other words, the core of neighborhood-based CF is to calculate similarities between users (user-based) (24) or items (item-based) (9). A list of popular similarity measures applicable for CF-based recommender systems along with their characteristics (advantages and disadvantages) can be found in literature (14, 21).

Bobadilla et al. (13) analyzed the rating matrix to extract significant users and items, and then applied a similarity measures (such as Pearson). Rahimpour et al. (22) presented a meta-heuristic optimization to gather a suitable subset of users' profiles, which is employed in similarity calculation to improve the performance of CF-based recommender systems. There are some modified versions of conventional similarity measures such as the constrained Pearson correlation coefficient (CPCC), weighed Pearson correlation coefficient (WPCC), and adjusted cosine measure (ACOS) which were briefly introduced by Bobadilla et al. (14) and Liu et al. (20). A combination of conventional similarity measures was discussed by Bobadilla et al. (14) and a hybrid method was presented using Jaccard and Mean Squared Differences (MSD) measures. Considering the

shortcomings of conventional similarity measures, a contextual similarity measure was presented by Liu et al. (20). This similarity measure is composed of three factors: Proximity, Significance and Singularity (PSS). Similar to conventional similarity measures, proximity is used to calculate the distance between ratings. The second factor determines the significance of two ratings based on their distance from the median rating. The singularity shows how the two ratings are different compared to other ratings.

Wang et al. (25) developed a hybrid method combining user-based and item-based similarities, using item similarity as a weighting factor to enhance user similarity accuracy. Patra et al. (21) calculated the average rate of each item is via a probability distribution. Then the Bhattacharyya distance is used to compute similarity between items. Cai et al. (26) constructed a typicality matrix instead of using rating matrix. The rows and columns of the typicality matrix show the users and cluster indices of items, respectively. Each element reflects the number of items selected by a user from the corresponding cluster. Conventional similarity measures are applied to the matrix, and neighbors are gathered according to their affinity to each cluster of items.

There are several heuristic techniques to alleviate the data sparsity (rating matrix sparsity) in CF-based recommender systems. Gazdar and Hidri (27) introduced a measure that addresses limitations such as data sparsity and cold-start problems. Their approach considers both user-item interactions and contextual information, leading to more accurate and personalized recommendations. Also, Abdalla et al. (19) introduced an innovative similarity metric that incorporated additional contextual information or advanced mathematical approaches to better reflect item similarities and boost the performance of item-based collaborative filtering. A hybrid similarity model was introduced by Guan et al. (28) that combines user-based and item-based CF with additional contextual or content-based information to improve recommendation accuracy in sparse datasets. By leveraging both user-item interactions and auxiliary data, the model mitigates the cold-start problem and enhances prediction performance, even when data is limited. Patra et al. (21) introduced a method based on the Bhattacharyya coefficient, a statistical measure that quantifies the overlap between two probability distributions. This approach captures the underlying statistical relationships between users or items more effectively, even when data is sparse. Anand and Bharadwaj (29) introduced a technique to compute both the direct similarity and transitive similarity (indirect similarity) between the two users who have common ratings. They designed a method to combine the direct and transitive similarities for finding neighbors. Lee et al. (24) introduced a hybrid method in which, the satisfaction of users with each item is embedded into the CF-based recommender systems. They infer the user confidence related to each rating and use it as a coefficient for the similarity computation. Khanian Najafabadi et al. (30) incorporated the rating matrix to cluster the items and constructed a user-clusters matrix. Instead of a user-items matrix, they used users-clusters matrix to calculate user similarity. Also, association rules mining was used to find favorite items (clusters) for the user.

In the latent factor models, the CF-based methods apply machine learning techniques to the rating matrix, and extract a model for prediction (11, 21, 23). Latent factor models are a well-known and successful method to create model-based collaborative recommender systems. This approach derives hidden features from the rating matrix, which reflect implicit associations between users and items in a latent representation space. Chen et al. (31) and Koren (32) utilized matrix factorization to obtain these latent features and apply them for ranking unseen items. The Author Topic Model (ATM) is another approach based on the latent factor model, which is used in collaborative filtering (33). In ATM, topics are extracted from user generated tags for items. Then, the user similarity is calculated via the extracted topics. Although latent factors are able to capture user interests, they cannot capture complex relations from user item ratings matrices. Deep learning has emerged as a powerful method to learn effective representatives from large-scale data. Fu et al. (34), Lei et al. (35) and Zhamg et al. (36) incorporated a deep learning method to construct a collaborative-based recommender system. A deep learning method can also be used to extract items' features. Then the features are integrated into the recommendation methods such as timeSVD++ (37).

Most CF-based recommender systems rely on low-level user ratings and co-rated items for similarity computation. While some methods identify user interests, they overlook interest prioritization. Our approach leverages preference-based user modeling introduced by Rahimpour et al. (22) and constructs a CF system using a preference similarity measure..

3. PROPOSED PREFERENCE-Based USER SIMILARITY

In this section, we first examine the existence of latent features and their influence on user behavior. These features not only capture user behavior but also provide shared factors for collaborative matching. Subsequently, we present the proposed similarity measure and its mathematical formulation. Finally, we describe the recommendation process.

3. 1. Motovation The **preference-based user similarity** approach addresses three key CF challenges:

sparsity , non − numericalfeedback, and latent feature. We examine each below.

Sparsity. Sparsity. Sparsity is one of the main challenges in CF, and there are several methods to alleviate this issue (38). Conventional similarity measures cannot find similar users to those with few ratings. To illustrate, we selected a subset of the MovieLens dataset (39) depicted in Table 1. The first column shows some randomly selected users. The movies and their genres are listed in the first row. The genre of each movie, in terms of the user's point of view, was brought in the second row. According to Table 1, user5 has few ratings. Therefore, it is impossible to calculate the similarity between user user5 and others. By means of the latent features approach, we can cluster users (or items) to alleviate the sparsity issue. We clustered the users in Table 1 considering the movies' genres. *Action*, *Crime*, and *Drama* are three distinct clusters of the movies. In terms of users clustering, we can find users (such as user1 and user2) who are similar to user5 and have same *Action* cluster. However, in item-based clustering, we can find movies such as *The Matrix* from the *Action* cluster. In other words, by extracting high-level features (instead of item level ratings), we are able to provide suitable features to find neighborhoods.

Non-numerical feedback. We need a numerical rating matrix to employ a similarity measure (or latent factor model) and construct a CF-based recommender system. When dealing with non-numerical feedback (e.g., clicks or views), we must define and extract latent features from the data. To illustrate the applicability of latent features in this context, a subset of the NewsTweet dataset[1] was considered and the selected tweets of all users were aggregated. As a convenient method, we used LDA (40) as a latent factor model to extract latent features. These latent features are the topics which the tweets are discussing. We analyzed the user behavior related to each latent feature. The results of two random samples of the dataset are depicted in Figure 1.

TABLE 1. A random subset of the MovieLens dataset. Movies and their genre are brought in the first row

	Movies				
	The Avengers **(Action)**	***Sherlok*** **(Crime)**	***Transformers*** ***(Action)***	***Matrix*** ***(Action)***	***Titanic*** ***(Drama)***
User1	2		2	4	5
User2	5		4		
User3			5		2
User4	1			5	
User5		2	4		
User6	4		5		1

[1] https://drive.shahroodut.ac.ir/index.php/s/rTvu6cidAiJdTaO

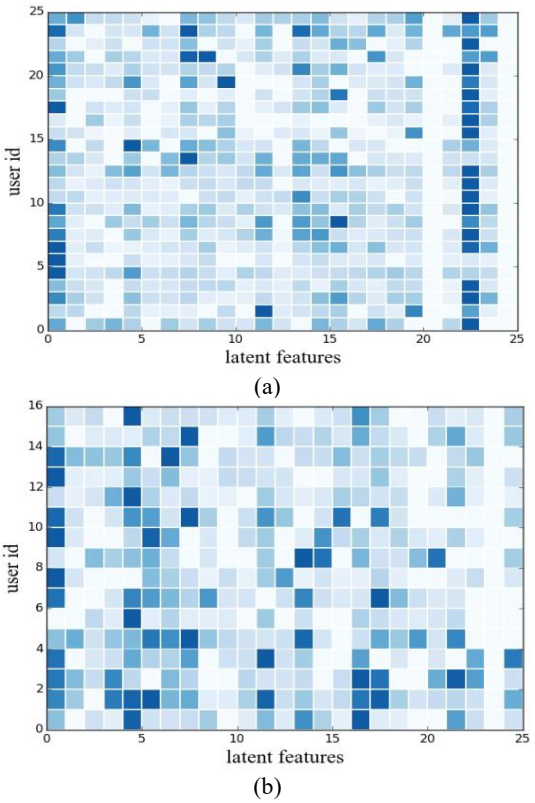

Figure 1. The latent features and their priority corresponding to the users for two random samples ((a) and (b)) from the NewsTweet dataset

The horizontal and vertical axes show the indices of latent features and users, respectively. Each row represents the influence of the latent features on the behavior of a particular user. Blocks with deeper shades represent features with greater influence. According to Figure 1, there are some latent factors that capture user behavior and can be considered as user interests. Some factors are more influential and affect users' preferences in selecting items.

Latent features. The main idea of the proposed method is to incorporate high-level latent features (which are extracted with latent factor modeling) instead of low-level item ratings. To further illustrate the latent features and their influence on user behavior, we applied the non-negative matrix factorization (NMF) (41) and timeSVD (32) on a subset of MovieLens dataset. In this experiment, we analyzed the users behavior via latent features. Figures 2(a) and 2(b) show the result of NMF and timedSVD, respectively. The horizontal and the vertical axes show the indices of latent features and users, respectively. The filled circles, depending on their sizes, indicate the priority of each latent feature for the users. As observed, the latent features capture users' item selection behavior across different interests, with certain

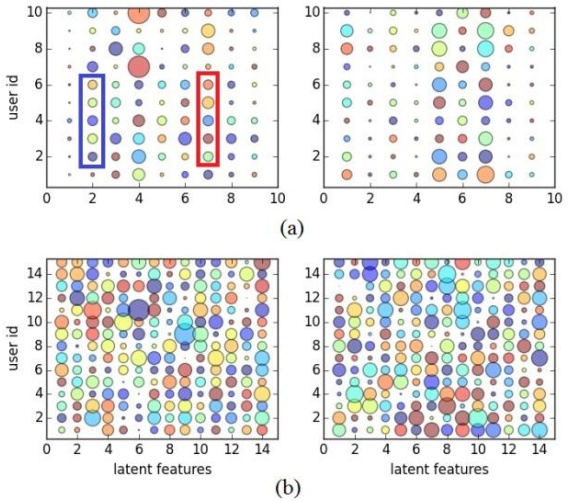

Figure 2. The extracted latent features from two random samples of the MovieLens dataset using (a) timedSVD and (b) NMF. Filled circles, depending on their size, indicate priority of the corresponding feature

features showing stronger user preference. Notably, the marked areas in the figures demonstrate shared latent features between users, enabling neighbor identification through feature similarity.

These results show that latent features effectively improve collaborative filtering. Our approach extracts them via preference-based user modeling, with the next section detailing the mathematical formulation of our preference-based similarity measure.

3. 2. Formulation of the Preference-Based Similarity Measure

We adapt latent features from user profiles (22)—originally used for content-based recommendation—to develop a novel preference-based similarity measure for collaborative filtering. Our hybrid approach integrates: 1) preference-based user modeling and 2) preference-aware similarity. Table 2 defines all notations used.

(1) Preference-based user modeling. Our preference-based user modeling approach assumes user behaviors are governed by latent factors (features), extracted using established techniques like matrix factorization and Bayesian non-parametric models (42). These latent factors indicate user interests. In the preference-based user modeling, the user preferences can be defined as the priority of interests (22). We use the Dirichlet Process Mixture Model (DPMM) as a Bayesian nonparametric framework to represent user preferences.

The graphical representation of DPMM for preference-based user modeling is depicted in Figure 3. According to this figure, the interest block and preference block are used to infer user interests and to calculate the priority of each interest, respectively. In this figure, the hyperparameter α determines the arrangement of clusters,

TABLE 2. outlines the notations for the proposed method

Notation	Description
r	An item
u	A user
A^u	Containing items selected by user (u) (user's profile)
a	Observed data
i,j,k	Used for indexing
t	The interest (cluster) identifier
θ	The preference distribution (interest priority)
$pref^u$	The preference vector over interests of user (u)
β	Dirichlet distribution parameter for the prior of preference distribution
α	Concentration parameter of Dirichlet Process (ddcrp)
G_0	Base distribution of Dirichlet Process
Ψ	A set of model parameters (α *and* β)

while the parameter G determines this distribution and is sampled from the distance dependent Chinese Restaurant Process (ddCRP) denoted as $G \sim ddCRP(\alpha)$ (43). The model parameter t acts as the cluster index (latent factor) for each data point, corresponding to the destination table of data in the ddCRP representation of the DPMM. Parameter a_i shows the observed data (items selected/rated by the user). The priority of latent clusters (θ_i) is characterized using the hyperparameter β along with the base distribution G_0. More details of the preference-based user modeling can be found in literature (22).

Through preference-based user modeling, each user u_x is represented by a preference vector of the form $(< t_1,\theta_1 >,...,< t_k,\theta_k >)$, where t_i denotes the i^{th} interest (a cluster of similar selected items) and θ_i represents its priority (quantifying the interest's influence). The generative process of user profile modeling is represented as follows:

- For each item a_i from user profile: draw interest assignment t_i: $t_i \sim ddCRP(.)$ (interest extraction block).
- For each interest k: calculate the distribution of latent clusters (θ) using $\{G_0, \beta\}$: $\theta \sim Dir(.)$ (preference inferring).
- For a new item a_x : $t_x \sim ddCRP(.)$ and $a_x \sim CategoricalDist(\Theta,t_x)$.

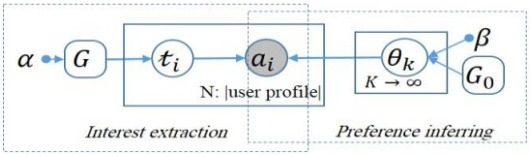

Figure 3. Graphical view of DPMM which is used for the preference-based user modeling.

(2) Preference-aware user similarity. Once the preference model is constructed, each user is represented by a preference vector, with the complete set visualized in Figure 4. Here, θ_i captures user preferences (priority weights), while t_i reflects user interests (feature vectors of selected items). For neighbor identification, we adopt a user-based CF approach that computes similarity between these vectors. Specifically, the similarity between users u_x and u_y, is derived from their preference vectors ($pref^u$) by evaluating two components: interest similarity and preference alignment. The former is calculated via *interestSim(..)*, which uses Jaccard similarity to quantify overlap be tween interest vectors t_i and the latter is calculated by *preferenceSim(..)*, a confidence term incorporating priority values θ_i of matched interests:

$$\begin{aligned} &Similarity(u_x, u_y) = \\ &Similarity(pref^{ux}, pref^{uy}) = \\ &\sum_{i=1}^{k_{ux}} \sum_{j=1}^{k_{uy}} \left(interestSim\left(t_i^{ux}, t_j^{uy}\right) \times \right. \\ &\left. preferenceSim(\theta_i^{ux}, \theta_j^{uy}) \right), \\ &preferenceSim\left(\theta_i^{ux}, \theta_j^{uy}\right) = e^{-|\theta_i^{ux}, \theta_j^{uy}|} \end{aligned} \quad (1)$$

Our dual-component measure weights similarity by both shared interests and their relative importance, ensuring high-priority preferences dominate.

3. 3. Recommendation The overall process of the proposed recommender system is depicted in Figure 5. The recommendation process is performed in three steps as follows. First, user profiles are incorporated into the Dirichlet Process Mixture Model (DPMM) to construct preference-based user models. Next, the preference based similarity measure (Equation 1) generates a user-user similarity matrix. Finally, this matrix drives the recommendation algorithm, which identifies the top-N neighbors of an active user *u* and calculates *u*'s preference for candidate items (e.g., item *r*) using Equation 2.

This equation integrates:

• $A^u = \{r_1, r_2, ..., r_{|A^u|}\}$, the set of items selected by u.

• Ψ, hyper-parameters (e.g. α and β in Figure 3).

• *prefs*, concatenated preference vectors of *u*'s neighbors.

• *interestAssignment*, the probability of assigning item *r* to interest *k*.

$$pref^{u_1} = \left[< t_1^{u_1}, \theta_1^{u_1} >, \dots, < t_{k_1}^{u_1}, \theta_{k_1}^{u_1} > \right]$$
$$\vdots$$
$$pref^{u_n} = [< t_1^{u_n}, \theta_1^{u_n} >, \dots, < t_{k_1}^{u_n}, \theta_{k_1}^{u_n} >]$$

Figure 4. The preference vectors of all users

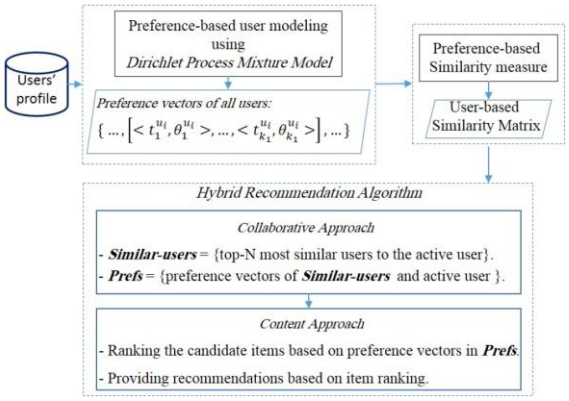

Figure 5. Components of the recommender system

• *interestPriority*, the priority of interest *k* from *prefs*.

Equation 2 ranks candidate items into u's recommendation list. Algorithm 1 implements this process, applying Equation 2 to all of u's neighbors to generate the ordered list..

$$\begin{aligned} &p(r|\, A^u, prefs, \Psi) = \frac{1}{p(A^u|\Psi)} \sum_{k=1}^{|prefs|} p(t_r = \\ &k|\Psi) * \mathrm{p}(\theta_k|\Psi) \times\ p(r, A^u|\, \theta_k, \Psi) \end{aligned} \quad (2)$$

4. EXPERIMENTAL RESULTS

We integrated our preference-based similarity measure into a hybrid CF system and validated it through extensive experiments against state-of-the-art algorithms. Below we detail the dataset, implementation, evaluation metrics, baselines, and experimental protocol, followed by a performance analysis showing our method's accuracy and robustness advantages.

We used the MovieLens[1] dataset for evaluation. To provide descriptive details about movies, we extracted storylines and genres from IMDb[2]. The movie information was then processed using text processing tools to construct feature representations corresponding to every movie.

Statistical parameters of the dataset are represented in Table 3.

We evaluate performance using standard accuracy metrics: precision, recall, and F1−measure (44), and employ the DCG@N[3] metric (4) to assess recommended resources according to their ranked positions. These metrics are calculated for varying recommendation list lengths (top@N = {3, 6, 9, 12}).

4. 1. Baselines We evaluated our approach against several existing techniques used to build recommender

[1] - https://grouplens.org/datasets/movielens

[2] - http://www.imdb.com

[3] - Discounted Cumulative Gain

Algorithm 1: the recommendation algorithm

Input: preference vectors, similarity matrix, active user *u*, and candidate_items

Output: An ordered list for recommendation

Initialization:

Similar_users = select top-N most similar users to *u*

Prefs = collect preference vectors of Similar_users and *u*

priority_list = {}

for each item in candidate_items, **do**: Iterates for each candidate item

p = Calculate the likelihood of item using Eq 2

priority_list = *priority_list* ∪ {item, p}

end for

Return *priority_list* in descending order of likelihood.

TABLE 3. Specifications of the dataset from MovieLens

Dataset	MovieLens
Number of users	4743
Number of movies	8787
Number of feedbacks	1 million

systems, utilizing the dataset presented in Table 3. These strategies involve item-based collaborative filtering (45), matrix factorization (SVD) (15), Funk-SVD (46), timeSVD (47), NMF (41), OS (27), AMI (48), and content-based filtering (5). SVD, timeSVD, Funk-SVD and NMF use latent factors to derive the user interests but do not prioritize them. OS (27) introduced a mathematically derived similarity metric. AMI (48) employed ratings to compute the statistical dependence between two users or two items.

The item-based filtering, fun-kSVD and content-based filtering were carried out using the LensKit[1] (49). The SVD and NMF were carried out using the Surprise[2] (50). Also, the timeSVD was carried out using the LibRec[3] (51-53).

4. 2. Experiments and Results

We carried out several experiments to assess the proposed recommender system (denoted as RS) equipped with our novel similarity measure.

Recommendation accuracy. We assessed our recommender system's accuracy on MovieLens using precision and DCG@N metrics across multiple trials. Compared to baselines under identical conditions (Table 4), our preference-based similarity measure achieved superior performance by effectively modeling user preferences. The results confirm that explicit preference modeling significantly improves recommendation quality over state-of-the-art approaches.

Hybrid vs. non-hybrid. The proposed method is, in fact, a hybrid approach that integrates collaborative filtering and content-based components, as illustrated in Figure 5. To illustrate the impact of the hybrid approach in providing more accurate recommendations, we constructed user models and performed several experiments on two methods, hybrid and content − based (non − hybrid) (21). First, we employed each user model separately and performed a content-based experiment. Our method recommends items matching the active user's preferences by employing a preference-based model in collaborative filtering to identify users with similar preferences. The results are depicted in Figure 6. According to this figure, the hybrid method (shown with the dotted bar) outperforms the content-based recommender system.

Sparsity. To test sparsity robustness, we randomly removed 35–40% of user profiles and compared results with baselines (see Table 5). Our method achieves higher precision and DCG@N for users with sparse histories by leveraging preference-based similarity, which relies on latent preferences rather than explicit ratings. It also addresses item cold-start by ranking new items via feature-vector-to-preference comparisons.

As reported in Tables 4 and 5, the baseline methods suffered a performance degradation of approximately 33%, whereas the proposed method showed only an 18% degradation. These results confirm that the proposed similarity measure is more resilient to sparsity and cold-start scenarios, demonstrating its effectiveness in maintaining recommendation quality compared to conventional approaches.

4. 3. Discussion

The primary focus of our work is to introduce a novel similarity measure that enhances collaborative recommender systems. It emphasizes the development of a preference-based similarity measure that improves the identification of user neighborhoods by incorporating latent factors and user preferences. As a result, the proposed method incorporating a preference-based similarity measure contributes to alleviating cold-start and sparsity as a natural by-product.

Our experiments (Tables 4 and 5) demonstrate clear improvements: for instance, our method improves precision and NDCG scores compared to the baseline methods (Section 4.1) that using conventional similarity measures. Moreover, Figure 6 shows improvement in F1 and NDCG over the non-hybrid approach (21).

[1] - http://lenskit.grouplens.org/

[2] - http://surprise.readthedocs.io/en/stable

[3] - https://www.librec.net/

TABLE 4. Comparison between the proposed RS and other methods in terms of the precision and NDCG metrics

top@N	Method	Precision	nDCG
3	Lenskit: item-item	0.212	0.219
	Lenskit: Funk-SVD	0.168	0.214
	Lenskit: Content-based	0.167	0.172
	Surprise: SVD	0.083	0.110
	Surprise: NMF	0.083	0.210
	LibRec: TimeSVD	0.342	0.360
	proposed RS	0.746	0.521
6	Lenskit: item-item	0.342	0.360
	Lenskit: Funk-SVD	0.331	0.348
	Lenskit: Content-based	0.267	0.253
	Surprise: SVD	0.217	0.233
	Surprise: NMF	0.256	0.253
	LibRec: TimeSVD	0.213	0.230
	proposed RS	0.747	0.670
9	Lenskit: item-item	0.436	0.464
	Lenskit: Funk-SVD	0.427	0.450
	Lenskit: Content-based	0.331	0.346
	Surprise: SVD	0.317	0.377
	Surprise: NMF	0.317	0.377
	LibRec: TimeSVD	0.280	0.300
	OS (27)	0.3	-
	AMI (48)*	0.25	-
	proposed RS	0.751	0.775

TABLE 5. Comparison of the precision and NDCG metrics for the proposed RS and baselines via a sparse dataset

top@N	Method	Precision	nDCG
3	Lenskit: item-item	0.149	0.154
	Lenskit: Funk-SVD	0.142	0.141
	Surprise: NMF	0.046	0.071
	proposed RS	0.615	0.398
6	Lenskit: item-item	0.234	0.247
	Lenskit: Funk-SVD	0.230	0.239
	Surprise: NMF	0.120	0.151
	proposed RS	0.607	0.503
9	Lenskit: item-item	0.298	0.320
	Lenskit: Funk-SVD	0.292	0.311
	Surprise: NMF	0.177	0.211
	proposed RS	0.616	0.586
12	Lenskit: item-item	0.352	0.380
	Lenskit: Funk-SVD	0.345	0.372
	Surprise: NMF	0.226	0.261
	proposed RS	0.617	0.652

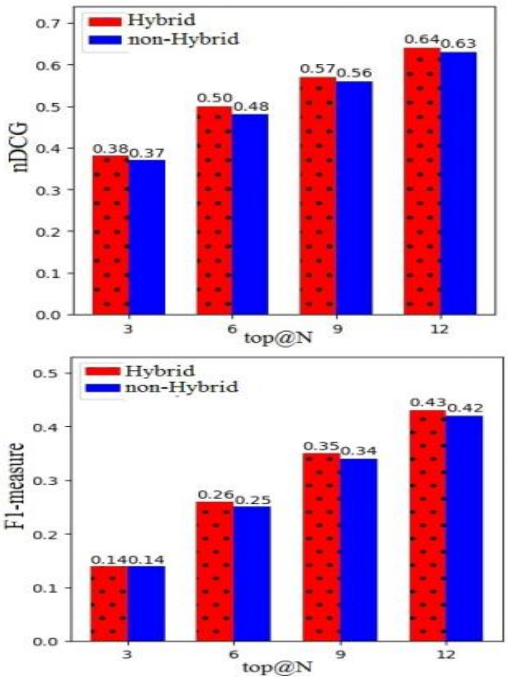

Figure 6. Comparison between the hybrid (the proposed RS) and non-hybrid (21) approaches in terms of the F1− measure and NDCG metrics

5. CONCLUSIONS

In this paper, we proposed a preference-based user similarity measure to construct a collaborative filtering recommender system. In addition to user interests, we used user preferences to calculate the similarity and find neighbors of the active user.

We implemented the preference-based user similarity and constructed a collaborative filtering system to provide recommendations.

The findings indicate that our method enhamces the performance of recommendation systems. Aaaitionally, the results indicate that, the preference-based similarity measure can alleviate the sparsity of users' profiles (rating matrix). For future research, incorporating preferences to construct item-item collaborative filtering could also be considered.

The proposed hybrid method can also be extended by incorporating contextual data (e.g., location, temporal events) for more adaptive user modeling, and by leveraging advanced deep learning models such as attention-based transformers to enrich user and item profiles.

6. REFERENCES

1. Lu J, Wu D, Mao M, Wang W, Zhang G. Recommender system application developments: a survey. Decision support systems. 2015;74:12-32. https://doi.org/10.1016/j.dss.2015.03.008

2. Zhao WX, Li S, He Y, Chang EY, Wen J-R, Li X. Connecting social media to e-commerce: Cold-start product recommendation using microblogging information. IEEE Transactions on Knowledge and Data Engineering. 2015;28(5):1147-59. https://doi.org/10.1109/TKDE.2015.2508816
3. Aljunid MF, Manjaiah D, Hooshmand MK, Ali WA, Shetty AM, Alzoubah SQ. A collaborative filtering recommender systems: Survey. Neurocomputing. 2025;617:128718. https://doi.org/10.1016/j.neucom.2024.128718
4. Wu H, Pei Y, Li B, Kang Z, Liu X, Li H. Item recommendation in collaborative tagging systems via heuristic data fusion. Knowledge-Based Systems. 2015;75:124-40. https://doi.org/10.1016/j.knosys.2014.11.026
5. Lops P, De Gemmis M, Semeraro G. Content-based recommender systems: State of the art and trends. Recommender systems handbook. 2010:73-105. https://doi.org/10.1007/978-0-387-85820-3_3
6. Burke R. Hybrid recommender systems: Survey and experiments. User modeling and user-adapted interaction. 2002;12(4):331-70. https://doi.org/10.1023/A:1021240730564
7. Cunha T, Soares C, de Carvalho AC. Metalearning and Recommender Systems: A literature review and empirical study on the algorithm selection problem for Collaborative Filtering. Information Sciences. 2018;423:128-44. https://doi.org/10.1016/j.ins.2017.09.050
8. Elahi M, Ricci F, Rubens N. A survey of active learning in collaborative filtering recommender systems. Computer Science Review. 2016;20:29-50. https://doi.org/10.1016/j.cosrev.2016.05.002
9. Linden G, Smith B, York J. Amazon. com recommendations: Item-to-item collaborative filtering. IEEE Internet computing. 2003;7(1):76-80. https://doi.org/10.1109/MIC.2003.1167344
10. Ricci F, Rokach L, Shapira B. Introduction to recommender systems handbook. Recommender systems handbook: Springer; 2010. p. 1-35.
11. Adomavicius G, Kwon Y. Improving aggregate recommendation diversity using ranking-based techniques. IEEE Transactions on Knowledge and Data Engineering. 2011;24(5):896-911. https://doi.org/10.1109/TKDE.2011.15
12. Adomavicius G, Tuzhilin A. Toward the next generation of recommender systems: A survey of the state-of-the-art and possible extensions. IEEE transactions on knowledge and data engineering. 2005;17(6):734-49. https://doi.org/10.1109/TKDE.2005.99
13. Bobadilla J, Hernando A, Ortega F, Gutiérrez A. Collaborative filtering based on significances. Information Sciences. 2012;185(1):1-17. https://doi.org/10.1016/j.ins.2011.09.014
14. Bobadilla J, Serradilla F, Bernal J. A new collaborative filtering metric that improves the behavior of recommender systems. Knowledge-Based Systems. 2010;23(6):520-8. https://doi.org/10.1016/j.knosys.2010.03.009
15. Koren Y, Bell R, Volinsky C. Matrix factorization techniques for recommender systems. Computer. 2009;42(8):30-7. https://doi.org/10.1109/MC.2009.263
16. Bag S, Kumar SK, Tiwari MK. An efficient recommendation generation using relevant Jaccard similarity. Information Sciences. 2019;483:53-64. https://doi.org/10.1016/j.ins.2019.01.023
17. He P, Shi J, Ma W, Zheng X. Broad collaborative filtering with adjusted cosine similarity by fusing matrix completion. Applied Soft Computing. 2024;165:112075. https://doi.org/10.1016/j.asoc.2024.112075
18. Abdalla HI, Amer YA, Nguyen L, Amer AA, Al-Maqaleh BM, editors. Numerical similarity measures versus Jaccard for collaborative filtering. International Conference on Advanced Intelligent Systems and Informatics; 2023: Springer.
19. Abdalla HI, Amer AA, Amer YA, Nguyen L, Al-Maqaleh B. Boosting the item-based collaborative filtering model with novel similarity measures. International Journal of Computational Intelligence Systems. 2023;16(1):123. https://doi.org/10.1007/s44196-023-00299-2
20. Liu H, Hu Z, Mian A, Tian H, Zhu X. A new user similarity model to improve the accuracy of collaborative filtering. Knowledge-based systems. 2014;56:156-66. https://doi.org/10.1016/j.knosys.2013.11.006
21. Patra BK, Launonen R, Ollikainen V, Nandi S. A new similarity measure using Bhattacharyya coefficient for collaborative filtering in sparse data. Knowledge-Based Systems. 2015;82:163-77. https://doi.org/10.1016/j.knosys.2015.03.001
22. Cami BR, Hassanpour H, Mashayekhi H. User preferences modeling using dirichlet process mixture model for a content-based recommender system. Knowledge-Based Systems. 2019;163:644-55. https://doi.org/10.1016/j.knosys.2018.09.028
23. Karabadji NEI, Beldjoudi S, Seridi H, Aridhi S, Dhifli W. Improving memory-based user collaborative filtering with evolutionary multi-objective optimization. Expert Systems with Applications. 2018;98:153-65. https://doi.org/10.1016/j.eswa.2018.01.015
24. Lee J, Lee D, Lee Y-C, Hwang W-S, Kim S-W. Improving the accuracy of top-N recommendation using a preference model. Information Sciences. 2016;348:290-304. https://doi.org/10.1016/j.ins.2016.02.005
25. Wang Y, Deng J, Gao J, Zhang P. A hybrid user similarity model for collaborative filtering. Information Sciences. 2017;418:102-18. https://doi.org/10.1016/j.ins.2017.08.008
26. Cai Y, Leung H-f, Li Q, Min H, Tang J, Li J. Typicality-based collaborative filtering recommendation. IEEE Transactions on Knowledge and Data Engineering. 2013;26(3):766-79. https://doi.org/10.1109/TKDE.2013.7
27. Gazdar A, Hidri L. A new similarity measure for collaborative filtering based recommender systems. Knowledge-Based Systems. 2020;188:105058. https://doi.org/10.1016/j.knosys.2019.105058
28. Guan J, Chen B, Yu S. A hybrid similarity model for mitigating the cold-start problem of collaborative filtering in sparse data. Expert Systems with Applications. 2024;249:123700. https://doi.org/10.1016/j.eswa.2024.123700
29. Anand D, Bharadwaj KK. Utilizing various sparsity measures for enhancing accuracy of collaborative recommender systems based on local and global similarities. Expert systems with applications. 2011;38(5):5101-9. https://doi.org/10.1016/j.eswa.2010.09.141
30. Najafabadi MK, Mahrin MNr, Chuprat S, Sarkan HM. Improving the accuracy of collaborative filtering recommendations using clustering and association rules mining on implicit data. Computers in Human Behavior. 2017;67:113-28. https://doi.org/10.1016/j.chb.2016.11.010
31. Chen B, Yang Z, Yang Z. An algorithm for low-rank matrix factorization and its applications. Neurocomputing. 2018;275:1012-20. https://doi.org/10.1016/j.neucom.2017.09.052
32. Koren Y, editor Collaborative filtering with temporal dynamics. Proceedings of the 15th ACM SIGKDD international conference on Knowledge discovery and data mining; 2009.
33. Jiang S, Qian X, Shen J, Fu Y, Mei T. Author topic model-based collaborative filtering for personalized POI recommendations. IEEE transactions on multimedia. 2015;17(6):907-18. https://doi.org/10.1109/TMM.2015.2417506
34. Fu M, Qu H, Yi Z, Lu L, Liu Y. A novel deep learning-based collaborative filtering model for recommendation system. IEEE transactions on cybernetics. 2018;49(3):1084-96. https://doi.org/10.1109/TCYB.2018.2795041

35. Dong X, Yu L, Wu Z, Sun Y, Yuan L, Zhang F, editors. A hybrid collaborative filtering model with deep structure for recommender systems. Proceedings of the AAAI Conference on artificial intelligence; 2017.
36. Zhang S, Yao L, Sun A, Tay Y. Deep learning based recommender system: A survey and new perspectives. ACM computing surveys (CSUR). 2019;52(1):1-38. https://doi.org/10.1145/3285029
37. Wei J, He J, Chen K, Zhou Y, Tang Z. Collaborative filtering and deep learning based recommendation system for cold start items. Expert systems with applications. 2017;69:29-39. https://doi.org/10.1016/j.eswa.2016.09.040
38. Hwangbo H, Kim Y. An empirical study on the effect of data sparsity and data overlap on cross domain collaborative filtering performance. Expert Systems with Applications. 2017;89:254-65. https://doi.org/10.1016/j.eswa.2017.07.041
39. Harper FM, Konstan JA. The movielens datasets: History and context. Acm transactions on interactive intelligent systems (tiis). 2015;5(4):1-19. https://doi.org/10.1145/2827872
40. Jelodar H, Wang Y, Yuan C, Feng X, Jiang X, Li Y, et al. Latent Dirichlet allocation (LDA) and topic modeling: models, applications, a survey. Multimedia tools and applications. 2019;78(11):15169-211. . https://doi.org/10.1007/s11042-018-6894-4
41. Luo X, Zhou M, Xia Y, Zhu Q. An efficient non-negative matrix-factorization-based approach to collaborative filtering for recommender systems. IEEE Transactions on Industrial informatics. 2014;10(2):1273-84. https://doi.org/10.1109/TII.2014.2308433
42. Gershman SJ, Blei DM. A tutorial on Bayesian nonparametric models. Journal of Mathematical Psychology. 2012;56(1):1-12. https://doi.org/10.1016/j.jmp.2011.08.004
43. Blei DM, Frazier PI. Distance dependent Chinese restaurant processes. Journal of Machine Learning Research. 2011;12(8). https://dl.acm.org/10.1007/978-3-031-40498-6_23
44. Avazpour I, Pitakrat T, Grunske L, Grundy J. Dimensions and metrics for evaluating recommendation systems. Recommendation systems in software engineering: Springer; 2013. p. 245-73.
45. Deshpande M, Karypis G. Item-based top-n recommendation algorithms. ACM Transactions on Information Systems (TOIS). 2004;22(1):143-77. https://doi.org/10.1145/963770.963776
46. Çoba L, Zanker M, editors. Replication and reproduction in recommender systems research-evidence from a case-study with the rrecsys library. International Conference on Industrial, Engineering and Other Applications of Applied Intelligent Systems; 2017: Springer.
47. Koren Y, Rendle S, Bell R. Advances in collaborative filtering. Recommender systems handbook. 2021:91-142. https://doi.org/10.1007/978-1-0716-2197-4_3
48. Fkih F. Similarity measures for Collaborative Filtering-based Recommender Systems: Review and experimental comparison. Journal of King Saud University-Computer and Information Sciences. 2022;34(9):7645-69. https://doi.org/10.1016/j.jksuci.2021.09.014
49. Ekstrand MD, Ludwig M, Konstan JA, Riedl JT, editors. Rethinking the recommender research ecosystem: reproducibility, openness, and lenskit. Proceedings of the fifth ACM conference on Recommender systems; 2011.
50. Hug N. Surprise: A Python library for recommender systems. Journal of Open Source Software. 2020;5(52):2174. https://doi.org/10.21105/joss.02174
51. Guo G, Zhang J, Sun Z, Yorke-Smith N, editors. Librec: A java library for recommender systems. CEUR Workshop Proceedings; 2015: RWTH Aachen University.
52. Spoorthy G, Sanjeevi S. Multi-criteria–recommendations using autoencoder and deep neural networks with weight optimization using firefly algorithm. International Journal of Engineering Transactions A: Basics. 2023;36(1):130-8. https://doi.org/10.5829/ije.2023.36.01a.15
53. Moeini M, Broumandnia A, Moradi M. A Personalized Web Recommendation System Based on a Weighted user Behavior Profile by Applying Extended Learning Method. 2025. https://doi.org/10.5829/ije.2025.38.04a.17

COPYRIGHTS

©2026 The author(s). This is an open access article distributed under the terms of the Creative Commons Attribution (CC BY 4.0), which permits unrestricted use, distribution, and reproduction in any medium, as long as the original authors and source are cited. No permission is required from the authors or the publishers.

Persian Abstract

چکیده

سیستم‌های توصیه‌گر به عنوان ابزارهای ضروری برای غلبه بر سربار اطلاعات در بستر وب توسعه یافته‌اند. این سیستم‌ها با فراهم کردن یک محیط شخصی‌سازی به کاربران امکان می‌دهند تا منابع مورد علاقه خود را انتخاب کنند. فیلترینگ مشارکتی از جمله رویکردهای موفق است که به طور گسترده برای ساخت سیستم‌های توصیه‌گر استفاده می‌شود. چالش اصلی این رویکرد، اثربخشی معیار شباهت آن برای یافتن کاربر/کالای مشابه برای ارائه توصیه است. در این مقاله، یک معیار جدید برای محاسبه شباهت با در نظر گرفتن تمایلات کاربران پیشنهاد می‌شود. معیار شباهت پیشنهادی، به جای استفاده از ماتریس امتیاز *کاربر*×*کالا*، با ترکیب فاکتورهای پنهان سطح بالا، عملکرد سیستم‌های توصیه‌گر مبتنی بر فیلترینگ مشارکتی را بهبود می‌بخشد. این فاکتورهای پنهان از طریق مدل‌سازی مبتنی بر تمایلات کاربر، استخراج می‌شوند. همچنین، زمانی که ماتریس بازخورد خلوت باشد (مجموعه داده‌های پراکنده) توصیه بهتری ارائه می‌شود. روش پیشنهادی با استفاده از مجموعه داده‌های MovieLens ارزیابی شده‌است. نتایج ارزیابی نشان می‌دهد که معیار شباهت پیشنهادی مبتنی بر تمایلات کاربر، عملکرد توصیه را در مقایسه با سایر رویکردهای موجود، بهبود می‌بخشد.

International Journal of Engineering

Journal Homepage: www.ije.ir

Influence of Load Eccentricity on Structural Response of Slender Hybrid Self-compacting Concrete Columns with Reactive Powder Concrete Shells under Uniaxial Loading

A. A. Salman Al-Taai*, W. A. Waryosh

Civil Engineering Department, College of Engineering, Mustansiriyah University, Baghdad, Iraq

PAPER INFO

Paper history:
Received 01 July2025
Received in revised form 17 August 2025
Accepted 28 August 2025

Keywords:
Hybrid Self-compacting Concrete
Slender Columns
Uniaxial Loading
Outer Shells
Reactive Powder Concrete

ABSTRACT

In this paper, a comprehensive investigation of the behavior of slender hybrid reinforced concrete columns consisting of self-compacting normal concrete (SC-NC) and reactive powder concrete (SC-RPC) shells with eccentric compression at different eccentricity ratios is presented. Three eccentricities (0.25, 0.65, and 0.9) were used to carry out these tests on six specimens, divided into three groups according to the eccentricity ratio. Each group included one reference specimen with a conventional SC-NC shell and one hybrid specimen with an RPC shell. The results showed that RPC contributed to the axial load capacity, and moment capacities. It is found that axial capacity increased by 57.8%, 21.1%, and 46.9% for small, medium, and large eccentricities, and moment capacity can increase by up to 56%. The RPC-reinforced specimens demonstrated higher absorption energy and lower lateral deflections. The results validate the effectiveness of RPC to improve the structural performance and behavior of hybrid columns subjected to eccentric uniaxial loading and the findings may offer relevant insights for applications in seismic-resistant and high-rise structures.

***doi**: 10.5829/ije.2026.39.08b.18*

Graphical Abstract

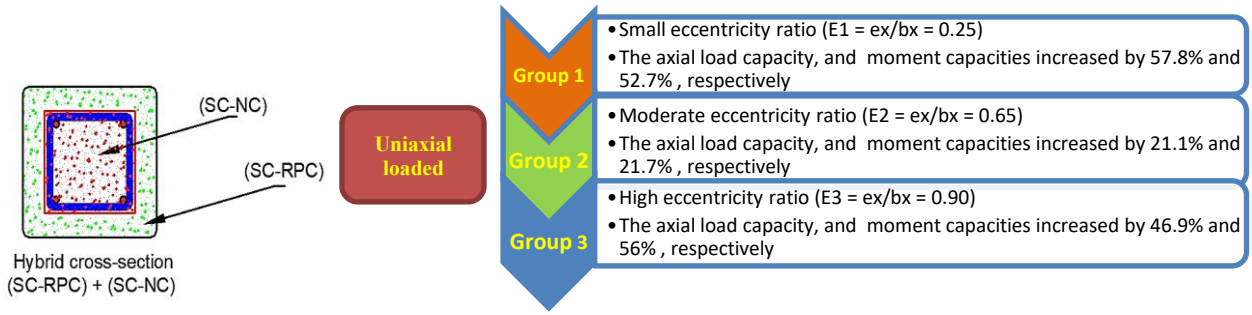

1. INTRODUCTION

RC columns are generally divided into two types in terms of their slenderness, namely slender and short columns, which are widely used in structural design of modern architectural buildings like high-rise buildings, large shopping malls, multilayer car parks, sports stadiums and so on. Being relatively small in transverse sectional dimension and having advantages of design flexibility and space saving, slender RC columns are prone to be more unstable because of the interaction of axial forces and bending moments (1-3). In order to overcome these structural drawbacks, there has been great effort to develop slender hybrid and composite columns by

*Corresponding Author Email: inm.ala@atu.edu.iq
(A. A. Salman Al-Taai)

Please cite this article as: Salman Al-Taai AA, Waryosh WA. Influence of Load Eccentricity on Structural Response of Slender Hybrid Self-compacting Concrete Columns with Reactive Powder Concrete Shells under Uniaxial Loading. International Journal of Engineering, Transactions B: Applications. 2026;39(08):2022-34.

combining different material characteristics for the improvement of the mechanical behaviors and the failure resistance.

A large number of studies have investigated on the structural behavior of composite column systems, especially those with embedded I-section steel profiles in concrete matrix (4-7). Meanwhile, extensive amount of research attention has also been directed to fill concrete-filled steel tube (CFST) columns, with a steel tube boundary and a concrete core (8-13). Furthermore, the mechanical properties of S-CFATCs have been studied extensively in recent years, Some experimental and analytical studies are introduced (14-19).

Hybrid columns (HC), which consist of ordinary concrete core encased with high strength concrete shell, ara an advanced structural form to improve the axial performance (20, 21). This type of hybrid column is considered an advanced structural configuration as it combines the benefits of high-strength concrete with the practicality and cost-efficiency of normal self-compacting concrete in a composite section, aiming to optimize both performance and material economy. The shell serves a two-fold purpose: structurally it can resist up to 40% of the overall axial load and functionally, it enables environmental protection for the embedded steel reinforcement, reducing the potential for corrosion and thermal stresses. As a result, any type of shell damage (whether in the form of surface cracking or material weakening) may adversely affect the strength and overall behavior of the column system (22).

The mechanical behavior of an outer high-strength concrete shell and an inner core may be developed to be full or partial bond in hybrid columns, and will perform differently. Early research work, for example that of Ali, and Mohammed (23), Ali (24), have scrutinized the effects of partial bonding on the ultimate behavior of short hybrid RC columns.

Ali and Mohammed (23) studied the effect of the RPC shell on axial capacity of hybrid columns under eccentric loading based on changing precast RPC shell with normal-strength concrete cover thickness. The results showed that the capacity of the load was improved by about 11% by increasing the shell thickness from 25 mm to 50 mm. The presence of both longitudinal and transverse steel reinforcement also enhanced the ductility and capacity at failure of the members, relative to the unconfined specimens. Also Ali (24) studied the behavior of hybrid columns as external energy-dissipating and self-centering systems by introducing the application of an epoxy layer for high-strength outer shells connected to the precast core. All of these columns were subjected to axial compression followed by eccentric compression, resulting in significant enhancements in ultimate capacity, varying from 28% up to 80% in concentric loading conditions (depending on the compressive strength of the shell). There were also comparable performance improvements with eccentric loading.

There has been a substantial literature published such as Ali and Mahdi (25), Resheq (20), Hamid et al. (26), Al-Zuhairi et al. (21), Mohammed et al. (27) and Mufja (28), studying the structural behavior of hybrid reinforced concrete columns with good bond quality between the high strength outer shell and the normal strength concrete core. The enhancement in axial capacity is attributed to the high strength of the outer shell, confinement effects, and stress redistribution due to full bonding between the core and outer layers.

Ali and Mahdi (25) also explored the effect of various outer shell concrete types—high strength concrete (HSC) and steel fiber reinforced concrete (SFRC) and e/h ratio on behavior of this type of structures. His conclusions were in favor of better shell quality as a noticeable improvement in strength and efficiency. The HSC-wrapped specimens showed a strength increase of 3.74% and 21.08% at eccentricity ratios of 1/3 and 1/2, respectively, whereas SFRC strengthened columns showed strength enhancement of 3.74% and 11.11%, respectively. Resheq (20) studied the axial behavior of hybrid concrete column subjected to axial loading by taking the diameter ratio of the concrete columns (NC) and (SCC) components. Results showed that the decrease of the NC core diameter along with the enlargement of the SCC shell can improve axial load capacity by about 70%. On the other hand, an increase in the NC shell with a decrease in the SCC core resulted in only ∼20% enhancement. Al-Zuhairi et al. (21) analyzed the structural performance of varying hybrid ratios in short columns under biaxial loading. Their study also found that hybrid CFT columns displayed a 33.5% increase in ultimate capacity compared to their nonhybrid counterparts. Moreover, the load-bearing capacity was increased by 38% at 0.16 hybrid ratio after the hybrid ratio was decreased from 0.36 to 0.16, and estimated axial strain also decreased significantly in the similar loading conditions. Hamid et al. (26) investigated the effects of core and transverse reinforcement diameters in short hybrid columns, which consist of ordinary concrete core located between 40 mm RPC layer. This combination enhanced the axial load capacity of the concrete specimens by an impressive 179 per cent compared to standard concrete blocks. Their results also showed that transverse reinforcement had a greater impact on structural strengthening than longitudinal reinforcement.

Previous studies have demonstrated that the mechanical response of hybrid columns with outer high-strength shells varies significantly depending on bonding conditions and shell configuration. These investigations primarily focused on enhancing axial capacity through shell thickness, reinforcement detailing, or interface

treatment, yet further exploration is still needed to evaluate composite performance under eccentric loading in vertically cast systems.

Recent studies have further confirmed that the structural performance of hybrid concrete columns is significantly influenced by the shell type, hybrid ratio, and reinforcement configuration. Improvements in axial strength across various configurations highlight the importance of shell-core interaction, yet comprehensive evaluations under biaxial or eccentric conditions remain limited.

Two commonly practiced methods of producing hybrid columns are widely referred to the literature. The first utilizes a core of plain or low-strength concrete concentrically surrounded by a layer of high-strength, fiber or non-fiber reinforced concrete. This results in a two-concrete cross section optimized for better structural effectiveness.

The hybridized sectioned variables also depend drastically on the rheology of both the concretes. They must, in fact, have been sufficiently fluid and cohesive to permit the outer shell to be cast effectively and remain continuously bonded. Shortcomings in these requirements may lead to chemical homogeneity loss and then structural integrity damage (29-31). Therefore, the use of SCC for the core and the shell could result in better homogeneity and interface compatibility. However, the axial deformation behavior of SCC-contained hybrid columns is not well addressed in the literature to date. A thorough experimental research is necessary to investigate the performance of such systems in axial loading, especially when both concretes meet the requirements of the SCC.

Although empirical work covering the biaxial behavior of long hybrid columns made with self-compacting concrete has been searched for, at the time of this writing there is no literature on their performance. This represents a substantial lack of knowledge of uniaxially loaded hybrid systems behavior, in particular when a complete bond between core and shell is supposed.

Thus, The aim of this study is to experimentally assess the structural performance of slender hybrid columns under eccentric loading, focusing on full-bond interlocking behavior. Recent investigations have highlighted the strategic role of advanced hybrid systems in enhancing structural resilience and controlling dynamic responses, particularly in seismic-prone and tall structures, motivating further exploration into their flexural and energy dissipation behavior (32, 33).

2. TEST SPECIMEN

The models used in this investigation were long RC columns of 140 × 140 mm cross-section and a total height of 1260 mm. Four 10 mm diameter longitudinal steel bars were placed throughout the length of each column, resulting in a reinforcement ratio (ρ) of 1.6%. The 22.5 mm thick on the concrete covers. This detailing adhered to the minimum reinforcement regulations specified in ACI 318-19 (1). The steel bars employed had a yield strength of 630 MPa and a modulus of elasticity of 200 GPa. Close links of 6 mm diameter were provided at 140 mm spacing over height of each column. A plan of the specimen with its dimensions and the reinforcement detailing is presented in Figure 1.

Uniaxial eccentric loading was applied by attaching a pair of corbels to the end of each column, as depicted in Figure 1. These corbels were arranged to carry the full load of the columns and to ensure that the failure takes place in the mid-span area. Corbel cross section was 260 × 260-mm square and 280-mm deep. In order to accomplish objectives of this study a particular test set-up has been developed to simulate the behavior of long columns under eccentric load. This arrangement was made to have load carried, and failure to occur on, the targeted test zone at the center height of the column. The specimens were positioned near the corbel edge to apply the required eccentricity (e/h). The center of gravity (CG) of each cross-section was calculated, and the load was aligned accordingly to ensure consistent eccentric loading.

3. TEST MATRIX

The test matrix of this study, conducted on six specimens, is given in Table 1 and specimens were bilaterally identical. Key parameters were the type of concrete of the

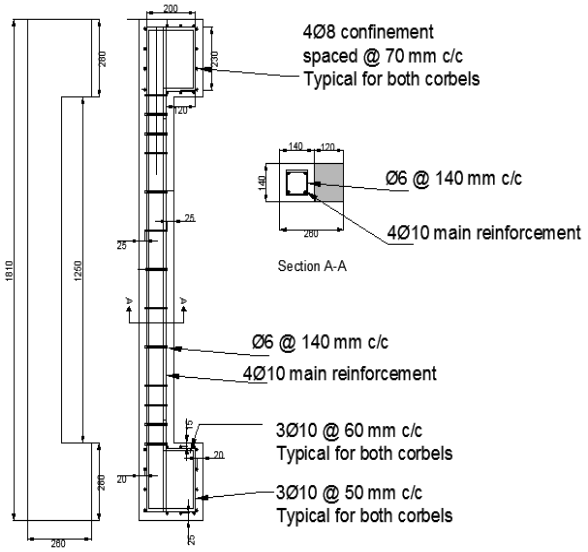

Figure 1. Details of reinforcement for hybrid self-compacting concrete columns

external shell and the degree of loading eccentricity. The specimens subjected to uniaxial eccentric loading were categorized into three groups according to the eccentricity ratio; small, intermediate and large. The types were also named as follows:

- UE1 for a small eccentricity ratio (E1 = ex/bx = 0.25)
- UE2 for a moderate eccentricity ratio (E2 = ex/bx = 0.65)
- UE3 for a high eccentricity ratio (E3 = ex/bx = 0.9)

where, (ex) is the eccentricity in millimeters and (bx) is the width of the column section. The symbol "U" signifies that the specimens were subjected to uniaxial eccentric loading.

Each group consisted of two samples; one reference and one hybrid sample. The control specimens were identified as NUE1, NUE2 and NUE3; and they were produced using self-compacting normal concrete. These served as control specimens. The hybrid elements with the RPC in the shell were denoted as RUE1, RUE2, RUE3, which represent minor, medium, large eccentric distance ratios, respectively. The letters "N" and "R" refer to normal self-compacting concrete and self-compacting reactive powder concrete for the outer section, respectively. Details and the test matrix are given in Table 1.

For future research, it is advisable to explore a larger number of concrete strengths and reinforcement densities, concrete cover sizes and eccentricities in the two principal directions of the section.

4. SPECIMEN INSTRUMENTATION

Specimens were tested under uniaxial eccentric loading in a 3000-kN-capacity testing machine. Loading tests were performed on all columns to failure under increasing load control. An instrumentation configuration per specimen is depicted in Figure 2.

Linear Variable Differential Transformers (LVDTs) were installed to record the lateral displacements, while electrical strain gauges were applied to record the longitudinal strains in the reinforcement located in the mid-height of the columns, as depicted in Figure 2.
The LVDTs were placed on the tension (long) side of the model at three locations: bottom (0), middle (½), and top (full effective length) of the member to record the lateral displacement along the longitudinal direction.

TABLE 1. The test matrix for uniaxial loading

Group	Eccentricity ratio	Self-compacting Hybrid concrete (SC-HC)				
		Outer Shell concrete		Inner Core concrete		designation
		Concrete type	Grade (Mpa)	Concrete type	Grade (Mpa)	Specimens
1	$e_x/b_x = 0.25$ (compression-controlled failure)	SC-NC	33.79	SC-NC	33.79	NUE1
		SC-RPC	88.86			RUE1
2	$e_x/b_x = 0.65$ (tension-controlled failure)	SC-NC	33.79			NUE2
		SC-RPC	88.86			RUE2
3	$e_x/b_x = 0.9$ (tension-controlled failure)	SC-NC	33.79			NUE3
		SC-RPC	88.86			RUE3

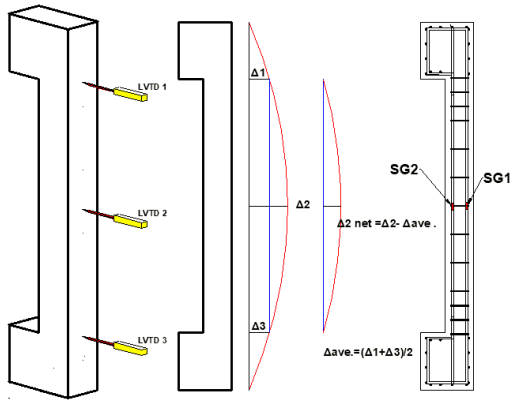

Figure 2. Arrangement of LVDTs and strain gage on longitudinal reinforcement for specimens

At mid-height, gauges SG #1 and SG #2 were pasted to measure strains in the steel bars at the tension and compression sides respectively.

Strain gauges were placed at mid-height where maximum axial strain is typically observed in slender columns. LVDTs were positioned at mid-span to capture the highest lateral deflection, and net readings were calculated by subtracting the middle LVDT value from the average of the other two to eliminate the effect of cross-section rotation and localize measurements between the corbels.

All LVDTs and strain gauges were calibrated according to the manufacturer's procedures prior to testing. The measurement uncertainty was within ±0.05 mm for LVDTs and ±1 με for strain gauges, ensuring

reliable data collection throughout the experiment.

Load was increased to failure in 10 kN increments. All recorded load, strain and displacement data during testing were stored on a computer by data acquisition systems (DAQ) incorporated in the testing machine.

5. TEST SETUP

Figure 3 Test setup for loading to each of the specimens. The load was applied by hydraulic jack through the two-loading caps with semicircular grooves. Hinged connections were used at each end of the columns. Each loading cap was comprised of a top plate (270 × 150 × 40 mm) attached to two side plates (270 × 150 × 10 mm) and two half side plates (150 × 150 × 10 mm). This model was developed in order to prevent stress concentration and early failure in the load path.

Eccentricity was applied and slip was prevented by seating a circular steel rod within semicircular grooves machined in the top loading plate. This configuration acted as a hinge, ensuring stable eccentric loading and allowing rotation. The setup is illustrated in Figure 3. Semicircular cuts were made in the top plates of the caps at defined locations. This resulted in the possibility of controlled uniaxial eccentric loading, depicted in Figure 3. The grooves facilitated the load transmission path only through the plate surfaces of the semicircular grooves, which was useful in the case of equal load transfer during testing.

6. MATERIAL

Multiple trial mixes were adopted to cast an appropriate self-consolidating concrete and the optimum mix design was chosen following EFNARC (33). Two of the original mixes were used in this experiment: Mix 1 is a reference mixture that is typical concrete having a 30 MPa compressive strength and Mix 2 is RPC6380, with 90 MPa in compressive strength.

Figure 3. Test setup and loading condition

The specific ingredients for the two mixes are given in Table 2. Type I ordinary Portland cement in accordance with ASTM type I and Iraqi standard (IQS 5/2019) was used in all mixtures. The coarse aggregate was crushed natural stone with a maximum size of 10 mm and a sulphate content of 0.06%. The fine aggregate used was crushed stone sand (of 3.5 FM) with sulphur content of 0.12 %.Silica fume (SiO_2 content:92%) was adopted as a cementitious replacement material. Straight steel fibers of 13 mm length and 0.2 mm diameter were utilized, which had an aspect ratio (l/df) of 65 and a tensile strength of 2500 MPa.

In order to make it workable and strong enough to be accepted as a self-compacting concrete all mixes were improved with superplasticizer of high efficiency based on modified polycarboxylic ether (Master Glenium 54) furnished by MBCC GROUP. The admixture is brown in colour and the specific gravity is 1.07 and the pH is between 5 and 8 as indicated by technical datasheet. It meets the requirements of ASTM C494 type F and G (34). The dosage was varied to ensure that each mix gave a slump flow of higher than 600 mm, which is the value required forself-compactingconcrete (33).

The 28-day compressive strengths of Mixes 1 and 2 were obtained as 33.79 MPa and 88.86 MPa, respectively. The longitudinal steel was deformed bars (Grade 520) of 10 mm diameter and a yield strength of 630 MPa. Shear reinforcement consisted of 6-mm-dia plain steel bars (i.e. with a yield strength greater than 520 N/mm^2). Mechanical properties of the reinforcement used in the tested specimens are summarized in Table 3.

TABLE 2. Mix proportions of self-compact concrete mixes

Material	Mixes	
	SC-NC	SC-RPC
Cement (Kg/m^3)	360	950
Sand (Kg/m^3)	780	1050
Gravel (Kg/m^3)	830	/
Water (Kg/m^3)	158.5	209.76
Water/Cement ratio	0.44	0.184
MasterGlenium 54 (Kg/m^3)	6.4	45.6
Silica fume (Kg/m^3)	/	190
Silica fume(%)	/	20%
Steel fiber (Kg)	/	78.5
Steel fiber (%)	/	1%
Compressive strength(28-days) (MPa)	33.79	88.86

TABLE 3. Mechanical properties of composite reinforcement

Reinforcement	Yield strength	Ultimate strength
Diameter (6 mm)	526	580
Diameter (8 mm)	354	561
Diameter (10 mm)	630	691

7. CASTING COLUMN SPECIMENS

All column specimens were cast in the vertical direction. For the hybrid reinforced concrete (RC) columns, a square aluminum tube (100 × 100 × 1.5 cm) was installed in the steel mold as a core form. This tube isolated the core concrete from the shell concrete during casting. At its top it was pressed against the steel mold edges to keep it from lateral movement and facilitate its breakaway once cast. The conventional RC columns, on the other hand, were cast at once and have no internal aluminum tube. Complete bonding between the core and the outer shell was ensured by casting both layers simultaneously in a fresh-to-fresh condition. Figure 4 explained cross-section in hybrid self-compacting concrete columns.

8. RESULTS

8. 1. Loads - Lateral Deflection Results From Figures 5 to 7, one can observe the influence of outer shell concrete type of the hybrid columns on the behavior under uniaxial eccentric loading in load-lateral deflection at mid-height. These are the first, second, and third sets of specimens with the eccentricity ratios (e/h = 0.25), (e/h = 0.65), and (e/h = 0.9), respectively. The outer shell material was per each group shifted from self-compacting normal concrete (SC-NC) to self-compacting reactive powder concrete (SC-RPC).

The lateral deflection was measured utilizing three LVDTs (two at the starting and ending point of the test area and one at center height). The net midpoint deflection was accordingly determined.

Experimental results for specimens with uniaxial eccentric loading are summarized in Table 4 and shown in Figure 8. The obtained Pu, Δu, and the percent of change of Pu in comparison to control specimens are displayed in the tabulated form. The findings revealed that the replacement of liner of normal concrete (NC) with reactive powder concrete (RPC) has significantly improved the axial load performance. With the small eccentricity (ex/bx = 0.25), the RUE1 was increased by 57.837% more than that of the control sample (NUE1).For moderate eccentricity (ex/bx = 0.60), RUE2 showed an enhancement of 21.052% relative to NUE2.For a large eccentricity (ex/bx = 0.9), a 46.89% increase in axial capacity compared to the reference sample NUE3 was achieved by RUE3.

Although each group included only two specimens, the percentage variation in peak load values ranged from approximately 19% to 45%, which is within acceptable experimental limits and supports the qualitative reliability of the results.

Although the specimen with e/h = 0.90 (RUE3) experienced the highest eccentricity, its performance in terms of flexural resistance was enhanced by the tensile strength and post-cracking behavior of the RPC shell. The embedded fibers within RPC contributed to stress redistribution by bridging micro-cracks, thereby improving ductility and sustaining load after cracking. In contrast, RUE2 (e/h = 0.65) was also subjected to tensile stresses but to a lesser extent, which may have limited the activation of fiber bridging mechanisms, resulting in earlier failure under a higher peak load (180.94 kN for RUE2 vs. 144.02 kN for RUE3). Meanwhile, RUE1 (e/h = 0.25) failed primarily due to compressive crushing, as the nearly concentric load induced high axial compressive stresses with minimal tension development.

TABLE 4. The experimental findings (ultimate load and displacement) for uniaxially loaded specimens

No.	Specimen	Pu (kn)	Δ_u (mm)	Increase in Pu %
1	NUE1	467.27	7.655	0
2	RUE1	737.52	6.281	57.837
3	NUE2	180.94	20.07	0
4	RUE2	219.04	20.64	21.052
5	NUE3	98.037	17.52	0
6	RUE3	144.02	26.03	46.898

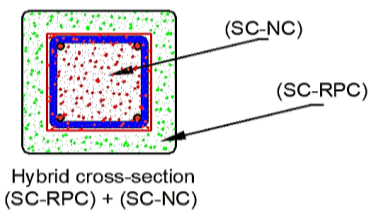

Figure 4. Explained cross-section in hybrid self-compacting concrete columns

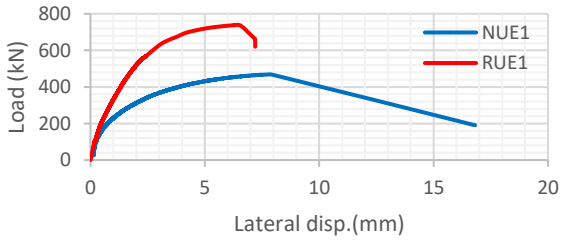

Figure 5. Loads-Lateral deflection curves for low eccentricity ratio (e/h=0.25)

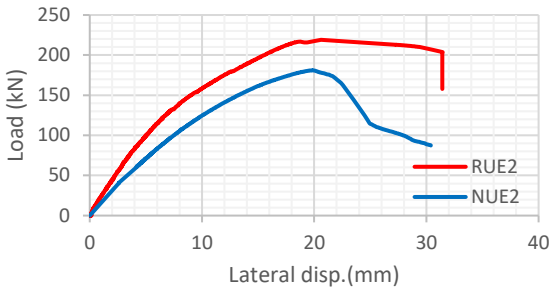

Figure 6. Loads-Lateral deflection curves for medium eccentricity ratio (e/h=0.65)

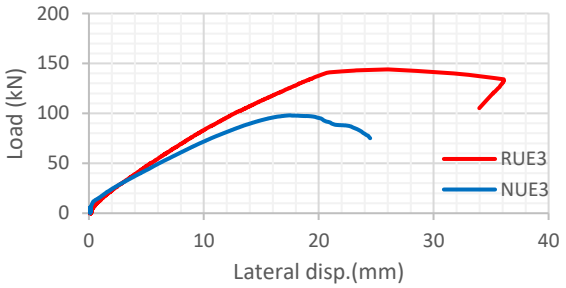

Figure 7. Loads-Lateral deflection curves for large eccentricity ratio (e/h=0.9)

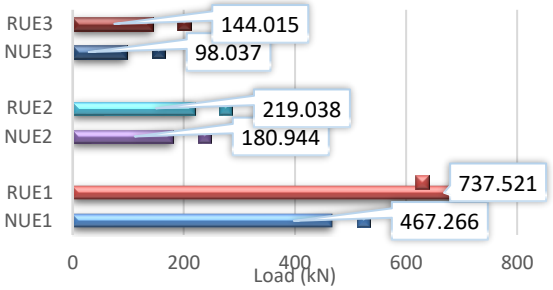

Figure 8. Ultimate load for column's specimens

8. 2. Longitudinal Steel Reinforcement Strains

Figures 9, 10, and 11 show how the longitudinal strain changed on both the compression and tension sides at the mid-height of the specimens in groups one, two, and three, respectively. These figures reveal that, in the uniaxial specimens, the tensile reinforcement reached yield before failure. For small eccentricity (e/h = 0.25), yielding happened at 92% of the ultimate load in specimen NUE1 and 97% in RUE1. This is because the applied eccentricity was small and below the balanced eccentricity of the section. At medium eccentricity (e/h = 0.65), the steel yielded at 87% of the ultimate load in NUE2 and at 88% in RUE2. This was due to increased section rotation, larger deflections, and an eccentricity higher than the balanced value. For large eccentricity (e/h = 0.9), yielding occurred at 81% of the ultimate load in NUE3 and 76% in RUE3. The lower values were caused by even more section rotation and significantly higher deflections, with the eccentricity well above the balanced level.

In all uniaxial specimens it was obvious that the compression reinforced concrete had not yielded. This means that the failure mode was controlled by tension, rather than un-restrained compression.

Thus the failure mode was ductile, and the influence of the level of eccentricity, the same as that for the tension reinforcement, and the position of the tension reinforcement near the outermost tension fiber were significant.

For uniaxially loaded columns, the maximum tensile stress generally occurs on the outer tension surface, leading to failure by yielding of the tensile steel prior to the occurrence of compressive concrete failure.

8. 3. Moment–curvature Relationship

All specimens were loaded under eccentric compression, resulting in uniaxial bending. The moment–curvature relationship was studied in the principal direction of the

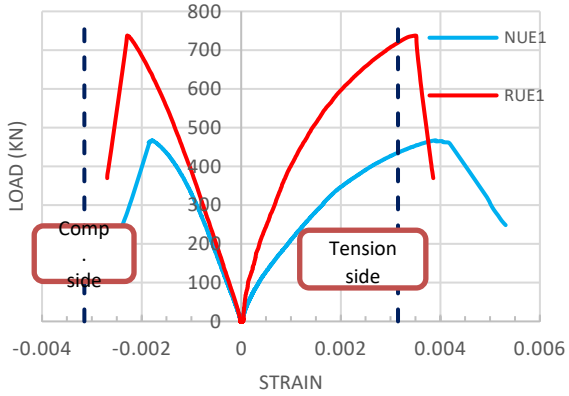

Figure 9. load -longitudinal steel strain curves for medium eccentricity ratio (e/h=0.25)

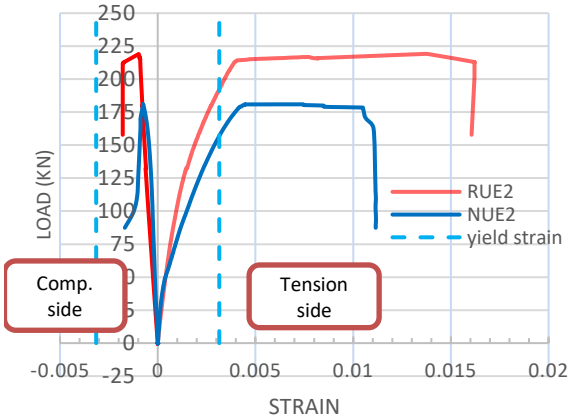

Figure 10. load -longitudinal steel strain curves for medium eccentricity ratio (e/h=0.65)

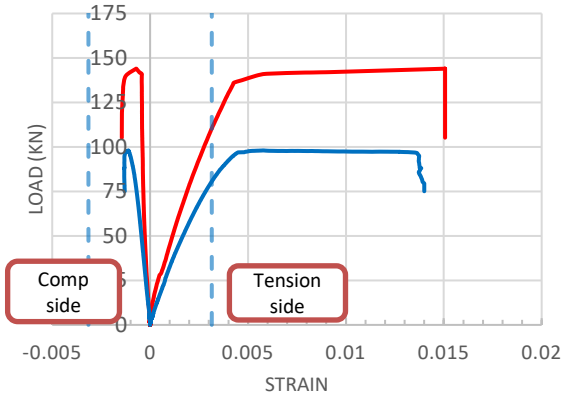

Figure 11. load -longitudinal steel strain curves for medium eccentricity ratio (e/h=0.90)

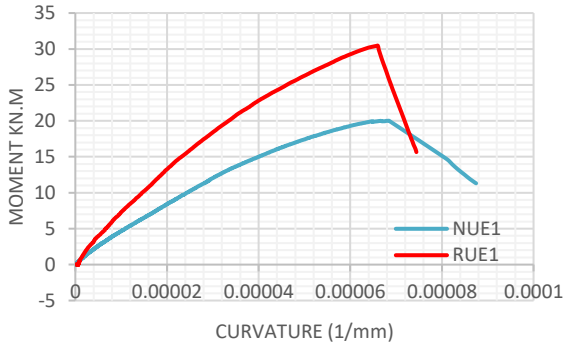

Figure 12. Moment-curvature curves for medium eccentricity ratio (e/h=0.25)

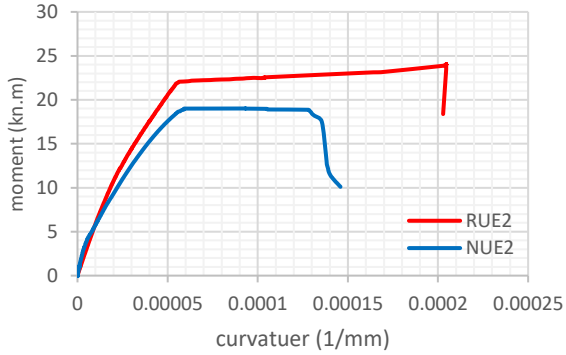

Figure 13. Moment-curvature curves for medium eccentricity ratio (e/h=0.65)

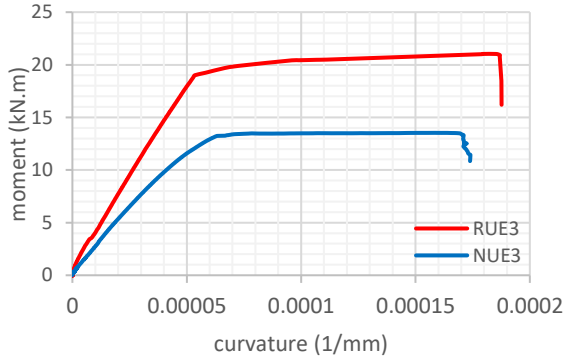

Figure 14. Moment-curvature curves for medium eccentricity ratio (e/h=0.9)

cross sections. Figures 12, 13 and 14 present the moment-curvature curves of the first and second groups of specimens and the third group of specimens respectively.

The bending moment (M) was given by the product of the applied load (P) and the true eccentricity. This true eccentricity was calculated by addition of the initial set eccentricity (e) to the critical net lateral deflection at mid-height (Δ) obtained in the prior stage. It is computed in Equation 1.

$$Mu= P(e+\Delta) \quad (1)$$

Curvature along the cross-sectional axis of the specimens was reported in a previous study. These curvatures were estimated using Equation 2,which assumes that plane sections remain plane after bending. Curvature (ϕ) was calculated as follows:

$$\Phi i = (\varepsilon_{sti}- \varepsilon_{sci})/d \quad (2)$$

Where (ε_{sti}) denotes the longitudinal strain in the tension reinforcement, (ε_{sci}) represents the longitudinal strain in the compression reinforcement, and (d) is the centre-to-centre distance of compression and tension reinforcements (114 mm for uniaxially loaded specimens).

A summary of the test results of the specimens subject to uniaxial eccentric loadings is also given in Table 5 and Figure 15. Data consist of the peak axial load (Pu), the lateral displacement at that peak load (Δu), and the ultimate bending moment, which is calculated as: Mu = Pu × (e + Δu). The table is also providing the percent increase or decrease in the bending moment (Mu).

The findings indicated that higher concrete strengths for the outer shell in hybrid sections resulted in enhanced flexural performance. In contrast, greater eccentricity ratios resulted in an appreciable decrease in the bending strength.

The substitution of the external shell veneer by reactive powder concrete (RPC) resulted in an evident increase of the flexural capacity. At low eccentricity ratio (ex/bx = 0.25), specimen RUE1 evidences an increase in resistance of 52.75% over the control specimen NUE1.

For the medium eccentricity (ex/bx = 0.65), RUE2 was 21.71% higher than NUE2. When the eccentricity ratio was large (ex/bx = 0.9), RUE3 was 55.99% higher than NUE3. These results are plotted in Figure 16. no analytical M–N interaction model was included due to

TABLE 5. Experimental findings (bending moment with curvature) for uniaxially loaded specimens

No.	Speci-men	Pu (kn)	Δ_u (mm)	Mu= Pu* (Δ_u+e) (kn.m)	Curvature (1/mm)	Increase in Mu (%)
1	NUE1	467.27	7.655	19.931	6.47E-05	0
2	RUE1	737.52	6.281	30.445	6.58E-05	52.751
3	NUE2	180.94	20.07	19.011	9.32E-05	0
4	RUE2	219.04	20.64	23.139	6.02E-05	21.713
5	NUE3	98.037	17.52	13.482	7.86E-05	0
6	RUE3	144.02	26.03	21.031	1.79E-04	55.993

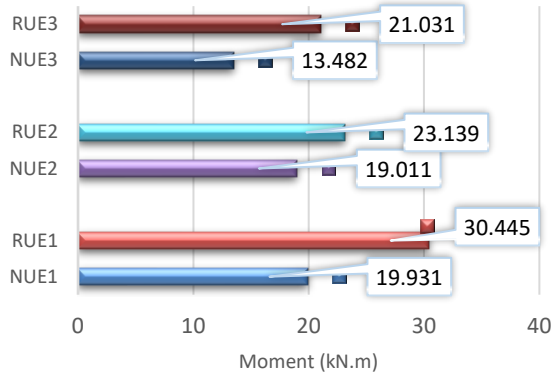

Figure 15. bending moments for column's specimens

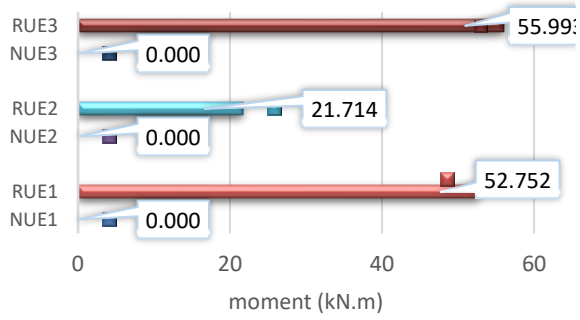

Figure 16. bending moments percentage according to reference specimens

the complex hybrid cross-section and the nonlinear behavior under high eccentricity.

8. 4. Evaluation of P–Δ Effectiveness To assess the impact of geometric nonlinearity in the tested slender columns, the second-order P–Δ moment was calculated as the product of peak axial load and the corresponding lateral displacement. This additional moment, arising from lateral instability, was compared with the primary eccentric moment to determine its relative influence.

As presented in Table 6, the P–Δ amplification ratio ranged between 12.21% and 18.49% across all specimens. These values confirm the noticeable effect of second-order behavior, especially in models subjected to higher eccentricities and larger deflections such as RUE2 and NUE2. In such cases, the additional moment significantly increased the internal moment demand, potentially accelerating failure due to lateral instability.

8. 5. FLEXURAL Energy Absorption The flexural energy absorption, estimated from the area under the moment–curvature (M–ϕ) curves, showed varied trends depending on the eccentricity ratio (e/h). For e/h = 0.25, the hybrid specimen (RUE1) absorbed more energy (2.423 kN) compared to the SC-NC specimen (NUE1: 1.725 kN). At e/h = 0.65, the SC-NC specimen (NUE2) exhibited greater absorption (3.850 kN) than its hybrid counterpart (RUE2: 2.389 kN). At the highest eccentricity (e/h = 0.90), the hybrid specimen (RUE3) again showed superior energy absorption (3.092 kN vs.

TABLE 6. P–Δ Moments and Amplification Ratios

Specimen	Pu (KN)	e (mm)	Δ (mm)	M_e	M_Δ	M_{total}	P-Δ ratio {%}
NUE1	467.27	35	7.66	16.35	3.58	19.93	17.95
RUE1	737.52	35	6.28	25.81	4.63	30.45	15.22
NUE2	180.94	91	20.07	16.47	3.63	20.10	18.07
RUE2	219.04	91	20.64	19.93	4.52	24.45	18.49
NUE3	98.037	126	17.52	12.35	1.72	14.07	12.21
RUE3	144.02	126	26.03	18.15	3.75	21.90	17.12

1.804 kN for NUE3). These findings highlight the influence of eccentricity on the flexural performance of hybrid sections, especially in enhancing post-cracking resistance. Figure17 show Energy of specimens.

8. 6. Mode of Failure Photographs of the tested columns under uniaxial eccentric loading are shown in Figure 18. A summary on observed failure modes and respective descriptions ara given in Table 7. In general, the tested sections presented flexural failure, that was strongly affected by the eccentricity also with respect to its value and position.

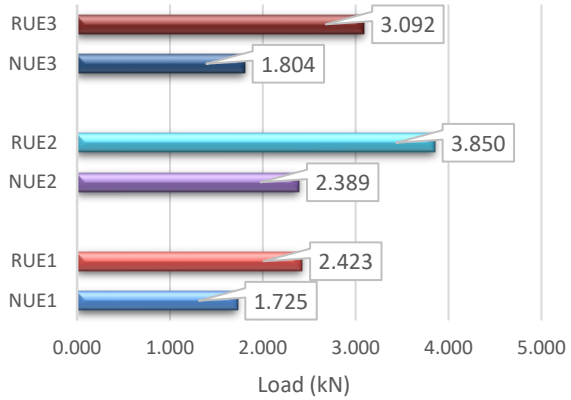

Figure 17. Energy for column's specimens

TABLE 7. Failure modes of specimens

Specimens	Failure modes	Description
NUE1	Compression failure	Suddenly concrete crushing in upper third of the column
RUE1	Compression failure	Suddenly concrete crushing in upper region of the column and a wide crack in upper third of the column.
NUE2	Flexural – compression failure	The appearance of cracks along the column in the tension zone, with gradual concrete crushing in the middle third in the compression zone.
RUE2	Flexural - ductile Buckling failure	The appearance of cracks along the column in the tension zone, with visible wide cracking in the mid-height of the column
NUE3	Flexural – compression failure	The appearance of cracks along the column in the tension zone, with gradual concrete crushing in the middle third in the compression zone.
RUE3	Flexural failure	Thin cracks are densely distributed along the length of the column.

Figure 18. Failure modes

9. CONCLUSION

This study experimentally investigated the structural behavior of slender hybrid reinforced concrete columns composed of a self-compacting core and outer shells made of either self-compacting normal concrete (SC-NC) or reactive powder concrete (SC-RPC), under uniaxial

and biaxial eccentric axial loads. Based on the obtained results and analysis, the following conclusions are drawn:

1. Substituting the SC-NC shell with SC-RPC significantly enhanced axial capacity. Compared to reference specimens, the axial load increased by 57.8%, 21.1%, and 46.9% for low (e/h = 0.25), moderate (0.65), and high (0.90) eccentricities, respectively, indicating the superior compressive performance of RPC in confined hybrid sections.
2. Moment capacity increased by 52.75%, 21.71%, and 55.99% at the respective eccentricities above. The improvement highlights RPC's significant contribution to flexural resistance, especially under high moment demands.
3. Second-order effects (P–Δ) became more pronounced with increasing eccentricity. The amplification ratio ranged from 12.21% to 18.49%, with hybrid columns (SC-RPC) exhibiting better control over lateral displacements, thus minimizing instability due to geometric nonlinearity.
4. The area under the moment–curvature (M–φ) curve showed enhanced energy dissipation in SC-RPC sections. Compared to SC-NC, the absorbed energy increased by 40.5% (RUE1), decreased in the mid-eccentricity case (RUE2), and peaked at +71.4% for RUE3, reflecting the efficient post-cracking performance of RPC in highly eccentric configurations.
5. With increasing eccentricity, failure shifted from compression-dominated to tension-controlled modes. RPC specimens exhibited higher curvature at peak loads, smoother softening behavior, and improved ductility. The failure pattern transformed from brittle crushing to more ductile flexural modes, ensuring more controlled and safer deformation.
6. Hybrid columns subjected to uniaxial eccentric loading maintained overall stability. Damage was more localized, and RPC-based sections exhibited superior lateral resistance compared to their SC-NC counterparts.
7. Load–deflection and M–φ curves confirmed that SC-RPC columns experienced reduced lateral deformation and more energy-dissipative behavior, especially under severe eccentricities.
8. The use of RPC in hybrid slender columns is promising for seismic-resistant and high-rise construction where ductility and energy absorption are vital. These findings underline the practical benefits of RPC beyond basic strength enhancement.

10. LIMITATIONS AND FUTURE WORK

This study was limited to an experimental investigation of the behavior of hybrid concrete columns under uniaxial eccentric axial loads. No numerical or analytical modelling was conducted as part of this study. While the results provide interesting data for structural performance, a predictive method is needed for more general use. Therefore, in the future, we are planning to construct finite element models and carry out analytical comparisons (such as M–N interaction analysis) to verify and generalize these observations to a broader parameter space.

11. REFERENCES

1. Committee A, editor Building code requirements for structural concrete (ACI 318-08) and commentary2008: American Concrete Institute.
2. Salman Al-Taai AA, Hassan SA, Hussein LF. Finite Element Analysis of Corner Strengthening of CFRP-Confined Concrete Column. 2018. https://doi.org/10.1088/1757-899X/454/1/012088
3. Al-Taai AAS. Finite Element Analysis of Concrete Filled Circular Steel Tube Short Columns Subjected to Axial Compression Load. Mathematical Modelling of Engineering Problems. 2025;12(5). https://doi.org/https://doi.org/10.18280/mmep.120523
4. Lai B, Liew JR, Venkateshwaran A, Li S, Xiong M. Assessment of high-strength concrete encased steel composite columns subject to axial compression. Journal of constructional steel research. 2020;164:105765. https://doi.org/https://doi.org/10.1016/j.jcsr.2019.105765
5. Lai B, Liew JR, Le Hoang A. Behavior of high strength concrete encased steel composite stub columns with C130 concrete and S690 steel. Engineering Structures. 2019;200:109743. https://doi.org/https://doi.org/10.1016/j.engstruct.2019.109743
6. Lai B, Liew JR, Wang T. Buckling behaviour of high strength concrete encased steel composite columns. Journal of Constructional Steel Research. 2019;154:27-42. https://doi.org/https://doi.org/10.1016/j.jcsr.2018.11.023
7. Begum M, Driver RG, Elwi AE. Behaviour of partially encased composite columns with high strength concrete. Engineering Structures. 2013;56:1718-27. https://doi.org/https://doi.org/10.1016/j.engstruct.2013.07.040
8. Mao W-J, Wang W-D, Zhou K, Du E-F. Experimental study on steel-reinforced concrete-filled steel tubular columns under the fire. Journal of Constructional Steel Research. 2021;185:106867. https://doi.org/10.1016/j.jcsr.2021.106867
9. Xie F, Chen J, Yu Q-Q, Dong X. Behavior of cross arms inserted in concrete-filled circular GFRP tubular columns. Materials. 2019;12(14):2280. https://doi.org/10.3390/ma12142280
10. Chen Z, Ning F, Song C, Liang Y. Study on axial compression bearing capacity of novel concrete-filled square steel tube columns. Journal of Building Engineering. 2022;51:104298. https://doi.org/10.1016/j.jobe.2022.104298
11. Liu J, Gao P, Lin X, Wang X, Zhou X, Chen YF. Experimental assessment on the size effects of circular concrete-filled steel tubular columns under axial compression. Engineering Structures. 2023;275:115247. https://doi.org/10.1016/j.engstruct.2022.115247
12. Hu H-S, Yang Z-J, Xu L, Zhang Y-X, Gao Y-C. Axial compressive behavior of square concrete-filled steel tube columns with high-strength steel fiber-reinforced concrete. Engineering Structures. 2023;285:116047. https://doi.org/10.1016/j.engstruct.2023.116047

13. Yuan F, Cao L, Li H. Axial compressive behaviour of high-strength steel spiral-confined square concrete-filled steel tubular columns. Journal of Constructional Steel Research. 2022;192:107245. https://doi.org/10.1016/j.jcsr.2022.107245
14. Patel VI, Liang QQ, Hadi MN. Numerical simulations of circular high strength concrete-filled aluminum tubular short columns incorporating new concrete confinement model. Thin-Walled Structures. 2020;147:106492. https://doi.org/10.1016/j.tws.2019.106492
15. Wang F-C, Zhao H-Y, Han L-H. Analytical behavior of concrete-filled aluminum tubular stub columns under axial compression. Thin-Walled Structures. 2019;140:21-30. https://doi.org/10.1016/j.tws.2019.03.019
16. Xu W, Zhang J, Liu F, Ma Z, Zhao G, Gu C, et al., editors. Axial compression behavior of assembled aluminum alloy-concrete-carbon steel double-skin tubular column. Structures; 2024: Elsevier.
17. Deng Z, Guo J, Yu J, Liu B. Axial compression performance of coral concrete-filled aluminium tube (CCFAT) square stub columns. Case Studies in Construction Materials. 2021;15:e00697. https://doi.org/10.1016/j.cscm.2021.e00697
18. Bu J, Liu Q, Yu Y, Qiu Q. Axial compression performance and bearing capacity calculation of round-ended concrete-filled aluminum tube column. Applied Sciences. 2023;13(13):7918. https://doi.org/10.3390/app13137918
19. Rong B, Zhai X, Li Z, Cheng H, Dong A, Zhang R. Study on axial compression behavior of 7A04-T6 concrete-filled aluminum tubular columns. Journal of Building Engineering. 2023;76:107118. https://doi.org/10.1016/j.jobe.2023.107118
20. Resheq A, editor Behaviour of hybrid concrete columns under axial compression loads. MATEC Web of Conferences; 2018: EDP Sciences.
21. Al-Zuhairi AH, Al-Ahmed AHA, Hanoon AN, Abdulhameed AA. Structural behavior of reinforced hybrid concrete columns under biaxial loading. Latin American Journal of Solids and Structures. 2021;18:e390. https://doi.org/10.1590/1679-78256640
22. Shariati M, Pourteymuri M, Naghipour M, Toghroli A, Afrazi M, Shariati M, et al. Evolution of confinement stress in axially loaded concrete-filled steel tube stub columns: study on enhancing urban building efficiency. Sustainability. 2024;16(17):7544. https://doi.org/10.3390/su16177544
23. Ali A, Mohammed Z. Strength evaluation of hybrid reinforced concrete columns under eccentric loads. Engineering and Technology Journal. 2018;36(4 Part A). https://doi.org/10.30684/etj.36.4a.12
24. ALI TKM. Experimental Behavior and Analysis of Hybrid Low-High Strength Reinforced Concrete Columns. Journal of Materials and Engineering Structures «JMES». 2020;7(2):203-14.
25. Ali AY, Mahdi WH. Experimental Investigation for Behavior of Reinforced Hybrid Concrete Corbel-Column System Subjected to Un-Symmetrical Vertical Loading. Journal of University of Babylon. 2017;25(2).
26. Hamid MM, Yassin LA, Mohammed AH, editors. Behavior of hybrid reinforced concrete columns. IOP Conference Series: Materials Science and Engineering; 2020: IOP Publishing.
27. Mohammed AH, Yassin LAG, Hamid MM. Experimental Investigation on the Ultimate Capacity of Rectangular Reinforced Hybrid Concrete Columns Under Axial Load. Geomate Journal. 2022;23(95):112-8. https://doi.org/10.21660/2022.95.3210
28. Hassan HF. Behavior of hybrid deep beams containing ultra high performance and conventional concretes. Engineering and Technology Journal. 2015;33(1):30-50. https://doi.org/10.30684/etj.33.1a.3
29. Danha L, Abdul-Hussien Z, Abduljabbar M, Yassin L, editors. Flexural behavior of hybrid ultra-high-performance concrete. IOP Conference Series: Materials Science and Engineering; 2020: IOP Publishing.
30. Hussein LF, Al-Taai AAS, Khudhur ID, editors. Sustainability achieved by using voided slab system. AIP Conference Proceedings; 2020: AIP Publishing LLC.
31. AYDIN E, OZTURK B, SAHIN E. Investigation of Behavior of Adjacent Planar Steel Frames Connected with Rigid Bars under Earthquake Effects.
32. Cetin H, Kebeli YE, Aydin E, Ozturk B, Ugu BA, editors. Experimental Evaluation of Tuned Mass Dampers for Seismic Vibration Control in Scaled Steel Structures. International Workshop on Energy-Based Seismic Engineering; 2025: Springer.
33. EFNARC S. guidelines for self-compacting concrete, English ed. European federation for specialist construction chemicals &concrete systems. 2005.
34. ASTM C. Standard specification for chemical admixtures for concrete. Annual book of ASTM standards. 2013.

COPYRIGHTS
©2026 The author(s). This is an open access article distributed under the terms of the Creative Commons Attribution (CC BY 4.0), which permits unrestricted use, distribution, and reproduction in any medium, as long as the original authors and source are cited. No permission is required from the authors or the publishers.

Persian Abstract

چکیده

در این مقاله، بررسی جامعی از رفتار ستون‌های بتن آرمه هیبریدی باریک ارائه شده است که از پوسته‌هایی از بتن خودتراکم معمولی (SC-NC) و بتن پودری واکنشی-(SC RPC)تحت فشار خارج از مرکز با نسبت‌های مختلف برون‌مرکزی تشکیل شده‌اند. سه نسبت برون‌مرکزی (۰.۲۵، ۰.۶۵، و ۰.۹) برای انجام آزمایش‌ها روی شش نمونه استفاده شد که بر اساس نسبت برون‌مرکزی به سه گروه تقسیم شدند. هر گروه شامل یک نمونه مرجع با پوسته SC-NC معمولی و یک نمونه هیبریدی با پوسته RPC بود. نتایج نشان داد که استفاده از RPC باعث بهبود ظرفیت باربری محوری و ظرفیت خمشی می‌شود. مشخص شد که ظرفیت محوری به ترتیب به میزان ۵۷.۸٪، ۲۱.۱٪، و ۴۶.۹٪ برای برون‌مرکزی‌های کم، متوسط و زیاد افزایش یافت و ظرفیت خمشی نیز تا ۵۶٪ قابل افزایش است. نمونه‌های تقویت‌شده با RPC انرژی بیشتری را جذب کرده و جابجایی جانبی کمتری از خود نشان دادند. نتایج به‌طور مؤثر کارایی RPC را در بهبود عملکرد سازه‌ای و رفتار ستون‌های هیبریدی تحت بار محوری خارج از مرکز تأیید می‌کنند و می‌توانند دیدگاه‌های ارزشمندی برای کاربرد در سازه‌های مقاوم در برابر زلزله و بلندمرتبه فراهم کنند.

IJE TRANSACTIONS B: Applications Vol. 39, No. 08, (August 2026) 2035-2048

International Journal of Engineering

Journal Homepage: www.ije.ir

Enhancing Smart Contract Access Control via Digital Identity Management and Machine Learning

R. Amiri, J. Karimpour*, H. Izadkhah

Department of Computer Science, University of Tabriz, Tabriz, Iran

PAPER INFO

Paper history:
Received 21 July 2025
Received in revised form 06 September 2025
Accepted 19 September 2025

Keywords:
Blockchain
Ethereum Blockchain
Digital Identity Management
Machine Learning

ABSTRACT

In the field of blockchain technology, ensuring secure and efficient access control for smart contracts remains a critical challenge. Traditional methods are often complex and resource-intensive, potentially hindering widespread adoption. This study proposes a novel machine learning-based approach to enhance access control mechanisms. Specifically, we classify users as either benign or potentially malicious based on transaction behavior and interaction patterns. A Support Vector Machine (SVM) classifier, combined with a Genetic Algorithm (GA) for dimensionality reduction, is applied to a dataset containing 50,000 transaction records from 1,000 blockchain addresses. The model achieved an accuracy of 94% on the test set and effectively distinguished users based on server interaction frequency and connection duration. Through visual analysis and comprehensive evaluation, we demonstrate that the proposed method improves both anomaly detection and operational efficiency. This approach has the potential to bolster trust and facilitate broader adoption of blockchain-based applications.

doi: *10.5829/ije.2026.39.08b.19*

Graphical Abstract

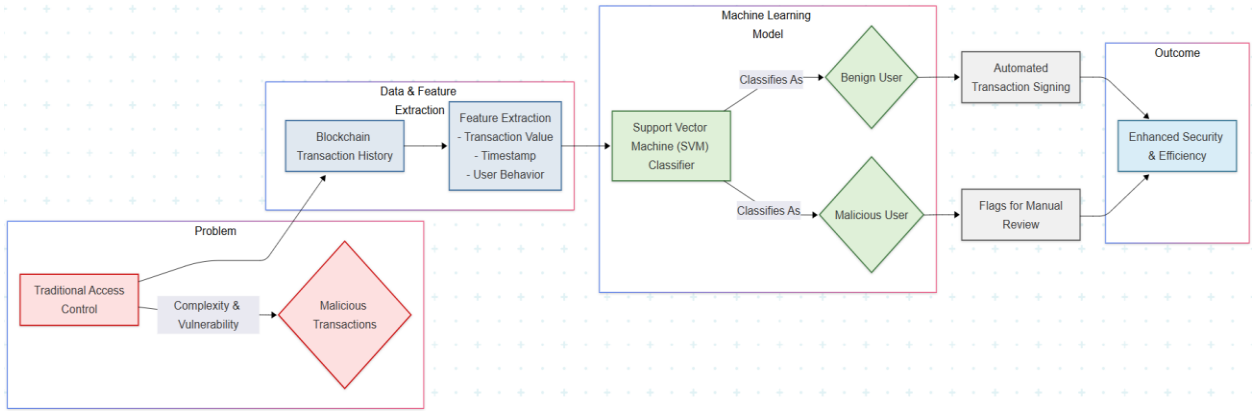

1. INTRODUCTION

Blockchain technology has introduced a transformative model for peer-to-peer digital transactions, creating novel financial ecosystems whose data patterns, such as cryptocurrency prices, can be forecasted using machine learning approaches (1, 2). Operating over a decentralized network, blockchain ensures transparency, integrity, and immutability of transaction data (3, 4). However, securing the endpoints and network layers of such decentralized systems remains a critical concern, similar to the security challenges faced in other emerging network paradigms like IoT-based 5G networks (5). Despite these advantages, many users find the process of

*Corresponding Author Email: karimpour@tabrizu.ac.ir (J. Karimpour)

Please cite this article as: Amiri R, Karimpour J, Izadkhah H. Enhancing Smart Contract Access Control via Digital Identity Management and Machine Learning. International Journal of Engineering, Transactions B: Applications. 2026;39(08):2035-48.

managing digital signatures—particularly the handling of cryptographic keys—complex and error-prone (6, 7). This complexity introduces potential vulnerabilities, creating an environment where users can be misled into authorizing malicious transactions, a challenge analogous to phishing in web applications where machine learning has been effectively used for detection (8, 9). Digital signatures tie directly to a user's blockchain account, managed through a digital wallet (10). This wallet helps users interact with the blockchain, with each account having a unique address that acts as the user's digital identity (11-13). For instance, during a transaction through a web application, if the application manipulates the transaction details, users could unknowingly approve a transfer of more funds than intended, resulting in financial loss (14-16). To address these challenges, this paper introduces a machine learning approach aimed at simplifying and securing the digital signature process. Specifically, our model serves as a dynamic access control mechanism that learns and enforces policies based on a user's evolving digital identity. By automating signatures and spotting transactions that do not look right, this method helps prevent problems before they happen. This is especially handy in blockchain apps like digital wallets, where it will automatically sign off on transactions for you. If the system spots a transaction that seems odd and might not be safe, it will ask for the user's okay before going ahead with the signature. When it comes to blockchain, a user's digital identity is not fixed; it's always changing based on the history of all their transactions. This transaction ledger is like a fingerprint for their account. We used this idea by using this transactional "fingerprint" as the basis for a user's identity profile. So, the machine learning model doesn't just find random problems; it also learns what normal, legal behaviour is for a certain digital identity. Then, access control is improved by marking transactions that do not fit this established identity-based pattern very well. This could mean that something has gone wrong.

2. LITERATURE REVIEW

In this section, a comprehensive research background of this study will be discussed. This will be followed by a related work section, where relevant works to this study and the novelty of our proposed methodology will be discussed.

2. 1. Research Background In this section, we dive into what others have found about spotting fraud within the blockchain network. They tried using a mix of tech tricks like k-means clustering, a thing called Mahalanobis distance, and a method known as support vector machine learning (SVM) to spot the odd ones out (17, 18). Researchers Pam and Lee tackled how to pick out which users and their transactions might not be on the up and up by looking at the patterns in the Bitcoin blockchain network. What stands out from these studies is that nobody has really thought about folding machine learning into the process of digitally signing blockchain transactions to make it automatic. While there has been some effort to detect weird transaction patterns before, none of the methods reviewed were made to work with how transactions are typically done, and nobody really looked into using data tagged by users to help with this. The fresh idea here is that the proposed method doesn't care about the type of transaction or its patterns; it just needs enough transaction history to work its magic and flag transactions that don't look right. Previous research has investigated machine learning for blockchain security, yet considerable deficiencies persist. Many current methods depend on static, rule-based systems that are not flexible, have problems with scaling, or need complicated setups that make them hard to use. This paper tackles these shortcomings by presenting an innovative, data-driven methodology for smart contract access control. This work makes three main contributions: A new machine learning framework, personalized anomaly detection, and real-world testing.

2. 1. 1. Blockchain Transactions We are going to focus on Ethereum because it's the digital currency that has the most people working on it – lots of developers and researchers are involved with Ethereum, and we'll also use it in our experiments later on. These blocks then link up one after the other in a chain, creating a ledger (19, 20). These signatures, and the transactions they verify, get shared across the entire network (21, 22). The term externally owned accounts (EOA) or user accounts refers to accounts that are owned and controlled by users outside of the company (23, 24). These accounts hold users' ether assets and are protected through asymmetric encryption and private keys (25). Also, each account in the Ethereum blockchain (or the blockchain of any other cryptocurrency) has a unique address that is used to perform transactions and receive and transfer ether (13, 26). On the other hand, smart contract-based accounts are accounts in which the smart contract code is placed (27, 28). This message activates the code of that account, and thus, the contract-based account can perform various actions, such as transferring tokens, writing something to the internal storage, creating new tokens, performing a series of calculations, and creating new contracts (27). This instruction is cryptographically signed, created by an EOA, and announced to the blockchain (22, 29).

2. 2. Related Work The convergence of blockchain technology, smart contracts, and machine learning has emerged as an expanding research domain. It is especially prominent in improving security, access control, and digital identity management. Previous

research has investigated diverse approaches that integrate these disciplines. Each of these studies has enhanced the security and efficiency of blockchain networks. In this section, we will discuss the relevant studies and how they are related to our research. Akbarfam et al. (30) presented DLACB, a system that enhances access control by abolishing predetermined regulations and diminishing management complexity via the amalgamation of deep learning and blockchain technology. This work aligns with our research, which aims to improve the administration of digital identities and access control in blockchain-based smart contracts.

Mounnan et al. (31) proposed a blockchain-based access control system that uses speech recognition for biometric authentication, employing an AutoEncoding Generative Adversarial Network (AE-GAN) model and smart contracts for secure storage and policy enforcement.

This work aligns with our research as both studies aim to improve security in blockchain systems through advanced access control techniques. Specifically, while our approach utilizes machine learning to classify users based on transaction behavior for smart contract access control, their method employs speech recognition as a biometric modality for user authentication in blockchain-based applications. Kim et al. (32) examined machine learning techniques that are designed to identify vulnerabilities in smart contracts. This paper is closely aligned with our study. The reason for that is that both studies stress the significance of digital identity management and the security of smart contracts. Gao (33) proposed a decentralized access control mechanism for IoT ecosystems using blockchain and smart contracts, with formal verification. In a domain-specific application, Ghaly et al. (34) explored the integration of blockchain-enabled smart contracts in the construction industry through a SWOT framework and social network analysis, highlighting benefits like transparency and challenges such as scalability. This complements our work by demonstrating real-world smart contract use cases, though it does not incorporate ML for user classification as in our proposed SVM-GA approach.

Gaur et al. (35) introduced an advanced architecture that utilizes machine learning and blockchain to improve authentication and security in Internet of Hospital Things (IoHT) systems. Similarly, Benaich et al. (36) proposed an immersive blockchain conceptual framework for securing Electronic Health Records (EHRs), emphasizing decentralized access control and privacy in healthcare. This aligns with our focus on digital identity management but lacks the ML-based anomaly detection we introduce for personalized smart contract access. Alizadeh et al. (37) employed a cryptographic approach to regulate permissions within blockchain networks. Conversely, our research introduces an innovative machine learning-based methodology to improve access control in blockchain smart contracts. In contrast to the static, rule-based system described in previous research, our approach utilizes data-driven insights to facilitate adaptive anomaly detection and minimize the burden of human rule upkeep. Liao et al. (38) presented a framework for Access Control (BIMAC). This proposed framework addresses the realm of open banking. This is done through confronting the issues of trust, digital identity management, and safe access control. It addresses the issue by utilizing blockchain technology to create a decentralized, user-focused system. There are several facilities provided by this study. The functions, such as decentralized third-party authentication, online bank account establishment, and meticulous data authorization. Works like DLACB (30) and speech recognition-based authentication (31) enhanced security but face adoption, scalability, and integration complexity issues. Similarly, machine learning for smart contract security (32) and IoHT systems (35) offers precision but is limited by platform specificity and scalability. Cryptographic approaches (37) ensure robust permissions yet lack adaptability, while identity management frameworks (38) required large datasets and risk false positives. Decentralized IoT access control (33) is secure but resource-intensive. These studies often rely on static rules or complex setups, neglecting dynamic adaptability. While not directly focused on blockchain (39), evaluate the usability of a mobile augmented reality app for PC hardware training across three countries, providing insights into user engagement with emerging technologies. DLACB (30) and formal verification methods for IoT (33) are two examples of how decentralised access control has improved by making it less dependent on centralized rules. However, they often make it harder to scale and require a lot of processing power, which makes them less useful in real-time blockchain environments.

Biometric-based systems like speech recognition by Mounnan et al. (31) improved authentication but have trouble with integration complexity and platform specificity. On the other hand, cryptographic permission models (35) offer strong security but don't have the adaptive flexibility that user behaviours need to change. Approaches focusing on machine learning for vulnerability detection (32) and IoHT security (34) demonstrate precision in static analyses, but they overlook personalized anomaly detection, resulting in higher false positives when applied to diverse transaction histories. Building on identity management frameworks like BIMAC (36), which emphasized user-centric decentralization, our proposed SVM-GA method synthesizes these elements into a dynamic, automated signature process that minimizes manual rule maintenance and improves efficiency by 19% over static baselines, as shown in our evaluations.

These studies all show a common problem with adaptive, user-specific modelling. Our new idea is to use transaction "fingerprints" for custom classification, which will make it easier for more people to use blockchain without putting security at risk. Our research introduces a novel machine learning-based approach for access control in blockchain smart contracts, leveraging data-driven adaptive anomaly detection. By dynamically classifying users based on transaction behavior, it reduces manual rule maintenance, offering a scalable, flexible solution that addresses these critical gaps. Table 1 reviews the papers in terms of their objectives and advantages, and disadvantages. Previous studies on blockchain, smart contracts, and machine learning have advanced security and access control, yet significant gaps remain.

3. A PROPOSED MACHINE LEARNING METHOD FOR AUTOMATIC DIGITAL SIGNATURE

In this part of our discussion, we introduce a new approach designed to automate and personalize the digital signing of blockchain transactions. This method

TABLE 1. Summary overview of previous studies

Ref.	Year	Objectives	Advantages	Disadvantages
(30)	2023	DLACB proposal, a deep learning-based access control system using blockchain.	Combining blockchain and deep learning for decentralized and transparent access control.	The newness of this system may pose problems in adoption and scalability.
(31)	2025	The paper aims to design, implement, and evaluate an access control system that integrates speech recognition as a biometric modality with blockchain technology for secure and private user authentication.	The system offers enhanced security and privacy through blockchain's decentralized and tamper-resistant nature, flexibility and ease of updates via smart contracts, and improved scalability and reduced blockchain overhead by delegating certain functions to an API.	Potential drawbacks include the complexity of integrating speech recognition with blockchain, possible new vulnerabilities, reliance on an API which could be a single point of failure, and performance issues due to the computational intensity of homomorphic encryption.
(32)	2023	Provides a comprehensive overview of machine learning techniques for identifying the security of smart contracts.	A detailed review of smart contract vulnerabilities and providing reliable solutions with machine learning.	Focused mostly on the Ethereum platform and limited generalizability to other platforms.
(33)	2025	To propose a decentralized IoT access control system using blockchain and smart contracts to enhance security and trust in dynamic environments.	The approach ensures secure and scalable execution of smart contracts through formal verification, mitigating security risks in IoT ecosystems.	The complexity and resource demands of blockchain technology and formal verification may present challenges for resource-constrained IoT devices and users without specialized expertise.
(34)	2024	To address the gap in understanding the impact of Blockchain-enabled Smart Contracts (BSC) on the construction sector through systematic keyword analysis, SWOT analysis of 174 peer-reviewed papers, identification of 72 factors, social network analysis (SNA), and clustering to evaluate adoption factors.	Enhances transparency, automation, and security in construction processes; provides a comprehensive evaluation of benefits like streamlined workflows and reduced management complexity; identifies opportunities for transformation in complex projects with multiple stakeholders.	Challenges in scalability, adoption barriers, integration complexity with existing systems; potential threats from regulatory issues and high implementation costs as per SWOT weaknesses and threats.
(35)	2022	Proposing a ML-based smart-contract system for an IoHT system	Boosting accuracy and computational performance in IoHT systems by combining machine learning	Scalability issues and uneven performance may arise
(36)	2025	To develop a conceptual framework for securing Electronic Health Records (EHRs) against traditional and quantum threats, improving system resilience, user experience, and operational efficiency using a hybrid blockchain with quantum-resistant cryptography, DAOs, AI, and metaverse integration.	Strengthens data protection with quantum-resistant algorithms (CRYSTALS-Dilithium, CRYSTALS-Kyber); decentralizes control via DAOs; enhances user engagement and efficiency through AI and metaverse; addresses interoperability and privacy in healthcare.	Potential complexity in implementation and integration; requires advanced technology adoption; may face challenges in scalability and user training for new interfaces like metaverse.
(37)	2022	Aims to enhance blockchain security by proposing a cryptographic access control mechanism	robust permission management through predefined rules and cryptographic keys	high computational resource demands and limited adaptability to dynamic user behaviors
(38)	2022	Creating a blockchain-based framework for secure identity management	Machine learning methods provide enhanced precision, adaptability, and efficiency.	Challenges include the requirement for datasets and the risk of false positives in vulnerability detection.

not only automates the review and signing of transactions suggested by decentralized apps but also brings in a tailored system for spotting unusual patterns in blockchain transactions. Transaction histories associated with an address are arranged in chronological order, much like a timeline. Our study concentrates on the transaction timestamp and its corresponding value in USD at the moment of the transaction. We considered the characteristics of time series data, and hence, a method by the name of rolling window analysis was utilized. This approach examines time series data in sequential parts, or "windows". By merging these technologies, our proposed system enhances the security and efficiency of blockchain transactions while introducing unprecedented levels of customization and automation in digital transaction management.

3. 1. Feature Extraction to Identify the Account

We examined the history of previous transactions for each blockchain address. We extracteed two essential pieces of information: the timestamp of each transaction and the transaction value converted into US dollars at that precise instant. We subsequently partition this data into discrete intervals or "time windows," each denoting a specific epoch. During these intervals, we consolidate the data. This approach to segmenting and analyzing transaction data enables the systematic identification of trends and anomalies, eventually yielding significant insights into transaction habits and patterns. Figure 1 presents the feature extraction within the blockchain platform for classification purposes. In our study, we chose to define the length of each moving window, denoted as m, based on a specific time duration rather than the count of transactions. Moreover, we set the step size, represented as h, in terms of individual transactions.

For each blockchain address, a set of behavioral and transactional features were extracted within each time window. While the primary transactional features were transaction timestamp and value in USD, we also engineered behavioral features critical for identifying malicious patterns. These include: Number of References to Server: Defined as the total count of transactions initiated by the address within a given time window. Duration of Connection: Approximated as the time delta between the first and last transaction within a window. This serves as a proxy for user session activity. Sent Data / Received Data: Calculated as the aggregate USD value of outgoing and incoming transactions for the address in that window.

Our objective was to develop a system that customizes the identification of anomalous transactions according to each user's activity profile. We developed such a system because transaction patterns might differ amongst blockchain addresses. Therefore, we utilized various approaches for each analytical period. This

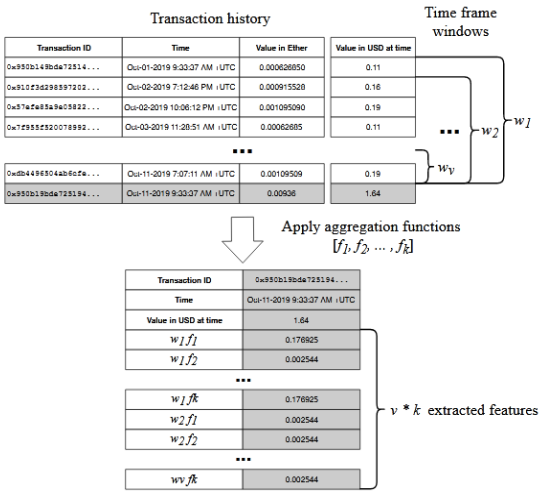

Figure 1. Feature extraction in the blockchain platform for classification

method enabled us to consolidate transaction data inside each interval. The process results in a dynamic moving window size that adjusts according to the varying amount of transactions in each period. Our research does not aim to provide a universal temporal frame for analysis; it concentrates on formulating a mechanism that ascertains the optimal analysis period for each blockchain address, providing a tailored solution for detecting anomalous transactions.

3. 2. Data Preprocessing

We preprocessed the raw transaction data to make sure the model was strong. The median value of the feature column was used to fill in the missing values in the transaction records. After that, Min-Max scaling was used to normalise all of the features to a range of [0, 1]. This step is very important to stop features with larger scales from having too much of an effect on how the model learns.

3. 3. Dimensionality Reduction

A Genetic Algorithm (GA) was used for feature selection to make the calculations less complicated and lower the chance of overfitting. The GA uses the SVM classifier's performance as the fitness function to look at different groups of features over and over again. This process finds the most useful features (like the number of server references and the length of the connection) and gets rid of the ones that are not useful or are too many, which makes the model work better and more efficiently. Here is how the process was carried out: A first group of "chromosomes" was made. In this case, each chromosome stands for a possible solution, which is a specific group of the available features (for example, Number of References to Server, Duration of Connection, Sent Data, etc.). Most of the time, each

chromosome is encoded as a binary string, with each bit representing a feature. A "1" means the feature is in the subset, and a "0" means it is not. Also, the "fitness" of each chromosome (or feature subset) was checked to see how well it worked. The performance of the Support Vector Machine (SVM) classifier was the fitness function. The SVM model was trained and tested on a validation set for each feature subset. The accuracy of the classification was used as the fitness score. A higher accuracy indicated a "fitter" chromosome. Moreover, the GA iteratively created new generations of feature subsets through three main operations, namely, selection, crossover, and mutation. Chromosomes with higher fitness scores were given a greater probability of being selected for "reproduction." Pairs of selected "parent" chromosomes exchanged parts of their binary strings to create new "offspring" chromosomes. This combines promising feature subsets, exploring new parts of the solution space. To maintain genetic diversity and avoid premature convergence to a suboptimal solution, random bits in the offspring chromosomes were flipped (e.g., a '1' changing to a '0').

3. 4. Categorization and Classification of Users

The Support Vector Machine (SVM) classifier was selected as the principal model for several significant reasons. First, SVM works very well in spaces with a lot of dimensions, which makes it a good choice for complex transaction data. Second, it is strong against overfitting, especially when you use a linear kernel and set the regularisation parameter just right. Finally, its ability to find a clear separating hyperplane makes the classification results easy to understand, which is very important for security applications. A later comparison with other models (see Section 4.4.2) showed that it worked better.D The goal of the learning system is to obtain a hypothesis that guesses the function or the relationship between the input and the output. Classes of healthy users spend most of their time referring to the server with a low to medium number, and also their connection time to the server is low to medium, and the amount of information sent to the server is medium, and the amount of information received is high. About the suspicious class, the number of references to the site is low, the received information is average, the connection time to the server is high, and the amount of information sent is also high. Discussing the class of hackers, the number of references to the site is high, the received information is average, the connection time to the server is high, and the amount of information sent is also high. The algorithm used in this article is shown in Figure 2.

In Figure 3, a general method of the user connection is illustrated.

3. 5. Proposed System Architecture

The suggested system is meant to be a security layer between a decentralised application (dApp) and the user's digital wallet. It will never be able to get to the user's private keys. This is how the process works: A user begins a transaction in a dApp. Before the transaction is sent to the wallet to be signed, we send its parameters (like the recipient and value) and any user behaviour metadata that goes with it to our ML model through an API. The SVM

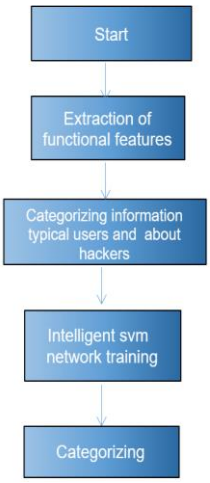

Figure 2. General process of the proposed method

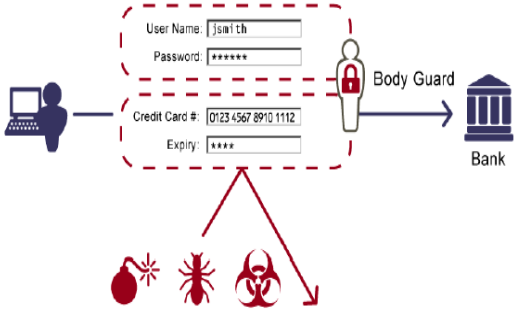

Figure 3. Overview of users connecting to the server

TABLE 2. The evaluated scenarios

Scenario	Description
The first scenario	Categorizing the characteristics of sent data according to received data
The second scenario	Classification of received data according to the duration of connection to the server
The third scenario	Classification of received data and the number of references to the server
The fourth scenario	Classification of sent data and duration of connection to the server
The fifth scenario	Classification of sent data and the number of references to the server
The sixth scenario	Classification of the number of references to the server and the duration of connection to the server

model examines the data and categorises the transaction as either "Benign" or "Potentially Malicious." If the transaction is benign, it goes right to the user's wallet with a standard confirmation message. If Potentially Malicious: The system marks the transaction and sends the user a high-alert warning to check it out before they sign. In Figure 4, a flowchart is designed to outline the transaction security workflow.

4. RESULTS

This section delineates the exhaustive findings of the study on improving access control for smart contracts on blockchain networks through machine learning techniques. The research employs a Support Vector Machine (SVM) classifier, together with dimensionality reduction methods, to classify users into healthy and suspicious/hacker categories based on transaction and behavioral characteristics. The results include a comprehensive dataset description, model development, and hyperparameter optimization. We also discuss classification performance and a comparative study with alternative machine learning models. The results are corroborated by visual representations obtained from the supplied scatter plots (Figures 5–9), which demonstrate the distinction of user classes across different feature pairings.

4. 1. Dataset Description The dataset is based on the publicly available 'Ethereum Fraud Detection Dataset' from Kaggle (40), which provides aggregated transaction histories for 9,841 unique Ethereum addresses, labeled as either valid (benign) or fraudulent (malicious). To align with our study's focus on time-series behavioral analysis, we sampled 1,000 addresses from this dataset (700 labeled as benign/Class 0 and 300 as malicious/Class 1, preserving an approximate 70/30 class distribution). For each selected address, we retrieved raw transaction histories via the Etherscan API (a public Ethereum blockchain explorer) over a three-month period. We then applied rolling window analysis (as described in Section 3.1) to generate multiple time-windowed records per address, resulting in a total of 50,000 records suitable for our machine learning framework.

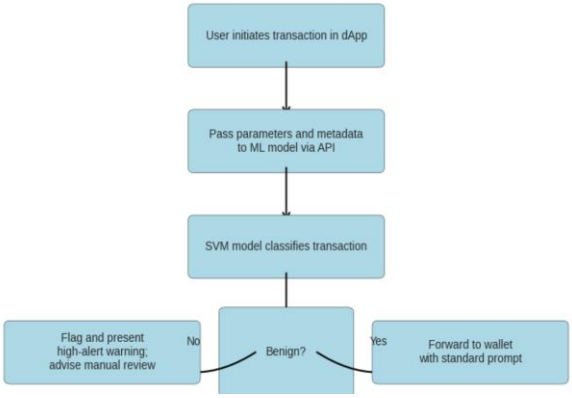

Figure 4. Transaction security workflow flowchart

The structure of the base dataset includes 51 columns per address: an index, the Ethereum address, a binary FLAG (0 for benign, 1 for malicious), and 49 behavioral features derived from transaction histories. Key features include time-based metrics (e.g., 'Avg min between sent tnx,' 'Time Diff between first and last (Mins)'), count-based metrics (e.g., 'Sent tnx,' 'Received Tnx,' 'Unique Received From Addresses'), and value-based metrics (e.g., 'total Ether sent,' 'total ether received,' 'avg val sent,' converted to USD using historical exchange rates from CoinMarketCap API). After sampling and windowing, our expanded dataset maintains this structure but generates multiple rows per address for chronological analysis. Fraud labels were assigned based on known illicit activities, such as addresses reported for phishing, scams, Ponzi schemes, or hacks, sourced from community reports, blockchain analysis platforms (e.g., Etherscan labels and Chainalysis reports), and public datasets. This labeling process ensures relevance to our classification of healthy users (low-to-moderate activity patterns) versus suspicious/hackers (high-frequency or anomalous patterns).

To verify authenticity, the base dataset has been used in multiple peer-reviewed studies on blockchain fraud detection, including ensemble learning approaches for transaction classification and machine learning models for illicit activity detection. The underlying blockchain data is publicly auditable on Ethereum explorers like Etherscan, confirming transaction integrity through cryptographic hashes. No synthetic data was added; all records reflect real-world Ethereum activity, with potential biases (e.g., class imbalance) mitigated through preprocessing.

4. 1. 1. Dataset Statistics The research employs a dataset consisting of 50,000 transaction records from 1,000 distinct blockchain addresses, with the data divided into 720 hourly intervals during a three-month period. The class distribution is categorized into two segments: Healthy Users (Class 0) represent 70% (35,000 records), whilst Suspicious Users/Hackers (Class 1) include 30% (15,000 records). For model development and evaluation, the dataset is split into 80% training (40,000 records) and 20% testing (10,000 records). The train/test split was performed using stratified random sampling to preserve the 70/30 class distribution, with 80% (40,000 records) allocated to training and 20% (10,000 records) to testing via scikit-learn's train_test_split function (random_state=42 for reproducibility). This ensures balanced representation of behavioral patterns across

splits, building on the verified structure of the source dataset.

4. 2. Model Implementation The primary classification model employed was a Support Vector Machine (SVM). The reason for this choice is its efficacy in high-dimensional areas and its ability to establish distinct decision boundaries via support vectors. The SVM was trained to classify users into two classes. The class 0, which includes healthy users. They are characterized by low-to-moderate server references, medium sent data, and high received data and class 1, which is suspicious users or hackers. They are characterized by high server references, high sent data, and average received data.

4. 3. Hyperparameter Tuning This study examines the hyperparameters, namely the regularization parameter C and the kernel type. The values examined for C were (0.01, 0.1, 1, 10, 100); diminished values of C emphasize a broader margin. This could increase bias. Conversely, elevated values diminish the margin to minimize training errors. This may augment variance. The kernel types analyzed included Linear, Polynomial (of degrees 2 and 3), and Radial Basis Function (RBF) with gamma values designated as (0.1, 1, 'scale').

The cross-validation results are summarized in Table 3:

The optimal configuration was to set the kernel as linear and the C parameter to 1.0. This configuration achieved the highest mean cross-validation accuracy (0.93) with low variance. This indicates a balanced trade-off between bias and overfitting. The linear kernel was preferred due to its simplicity and alignment with the linear decision boundaries observed in the scatter plots.

4. 4. Classification Results The SVM model was assessed on the test set utilizing the optimal hyperparameters. The categorization outcomes were evaluated using standard performance criteria and depicted through scatter plots. These charts illustrate the distinction between healthy users and suspect users/hackers across multiple feature pairings. The performance metrics on the test set are presented in Table 4:

Feature importance was assessed using a Random Forest classifier with 100 trees, trained on the same dataset. The top five features influencing classification, ranked by importance score (0–1), are listed in Table 5:

These features align with the behavioral patterns described in the methodology: healthy users and suspicious users/hackers exhibit the same pattern as discussed. To assess the effectiveness of a tailored approach, we delved into the specific transaction characteristics unique to each blockchain address. The goal was to discover if there's a universal set of transaction features that signal anomalies or if these indicators vary from one address to another. If transaction characteristics remain consistent across

TABLE 3. Cross-validation results for SVM hyperparameter tuning

Kernel	C Value	Mean CV Accuracy	Std. Deviation
Linear	0.01	0.87	0.02
Linear	0.1	0.90	0.01
Linear	1	0.93	0.01
Linear	10	0.92	0.02
Linear	100	0.91	0.03
Polynomial (d=2)	1	0.89	0.02
Polynomial (d=3)	1	0.88	0.03
RBF (γ=0.1)	1	0.91	0.02
RBF (γ=1)	1	0.90	0.02
RBF (γ=scale)	1	0.92	0.01

TABLE 4. SVM performance metrics on the test set.

Metric	Value
Accuracy	0.94
Precision	0.92
Recall	0.89
F1-Score	0.90
AUC-ROC	0.96

TABLE 5. Feature importance scores.

Feature	Importance Score
Number of References to Server	0.28
Duration of Connection	0.25
Sent Data	0.20
Received Data	0.18
Transaction Value (USD)	0.09

different addresses, it would suggest a uniform transaction pattern exists for all. However, if these characteristics vary, it would underline the need for a personalized anomaly detection strategy. We employed the random forest classification algorithm to analyze the transaction features. This is identical to the data inputs used in the isolation forest method for spotting anomalies. The criteria for abnormality were determined by the labels generated by the isolation forest. Our random forest model was built with 100 trees. This enables us to quantify the relevance of each feature on a scale from 0 to 1. A higher value denotes a more significant influence. Additionally, we compiled these findings in a table to rank the features. This provides a clear overview of their relative importance. This comprehensive analysis allowed us to determine whether a one-size-fits-all model suffices or if individualized anomaly detection models are essential for accurately identifying transaction irregularities across diverse blockchain addresses. Our first goal was to set a baseline for performance using simple, directly measurable metrics like the number of transactions and the amount of data. We could make a strong and easy-to-understand model by only focussing on these five main features, which would avoid the need for engineered metrics.

4. 4. 1. Visualizations The scatter plots (Figures 5-9) illustrate the SVM's classification performance across different feature pairs:

Distinct trends appear between healthy users and hackers in a series of data visualizations. Figure 5 demonstrates that healthy users (green stars) aggregate around medium sent data and elevated received data. Conversely, hackers (red plus signs) display high sent data and diminished received data. Figure 6 similarly illustrates hackers exhibiting elevated sent data and reduced connection durations. In contrast to healthy users who have moderate sent data and extended connection timings. Figure 7 substantiates this distinction, since hackers exhibit elevated references in conjunction with their transmitted data. In Figure 8, healthy users are defined by low-to-medium references and extended durations. On the other hand, hackers exhibit high references and reduced durations. Ultimately, Figure 9 verifies a constant distinction between the groups regarding sent data relative to the quantity of references, with support vectors situated around the decision boundary.

4. 4. 2. Comparative Analysis To evaluate the SVM's performance relative to other classifiers, three additional models were implemented and tested on the same dataset; they are Decision Tree, C4.5 (via Decision Tree with entropy criterion), and Naïve Bayesian. Hyperparameter tuning for these models was conducted: For the Decision Tree model Max_depth = (3, 5, 7, 10),

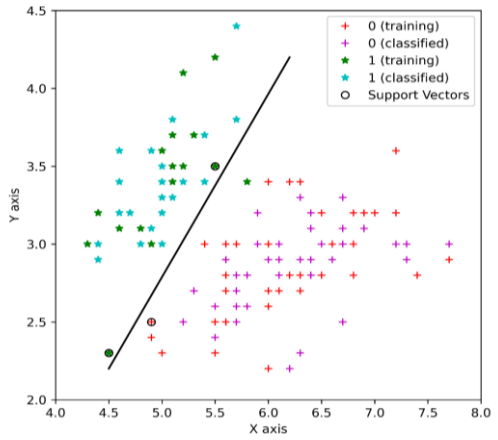

Figure 5. Showing the classification of the characteristics of the sent data according to the received data

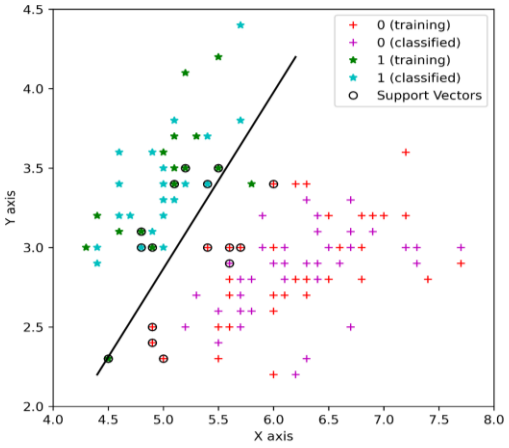

Figure 6. Classification of sent data according to the duration of connection to the server

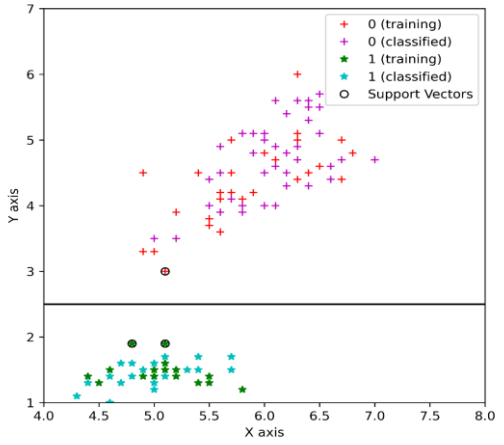

Figure 7. Categorization of sent data and the number of references to the server

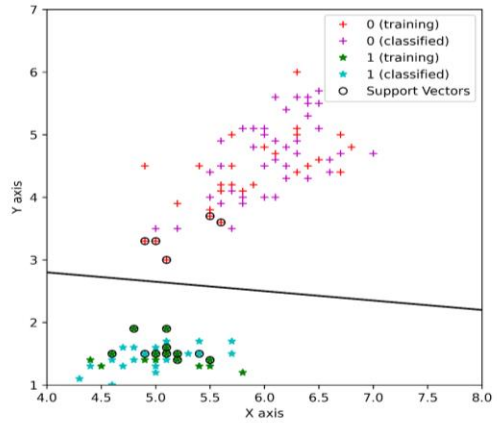

Figure 8. Classification of the number of references and duration of connection to the server

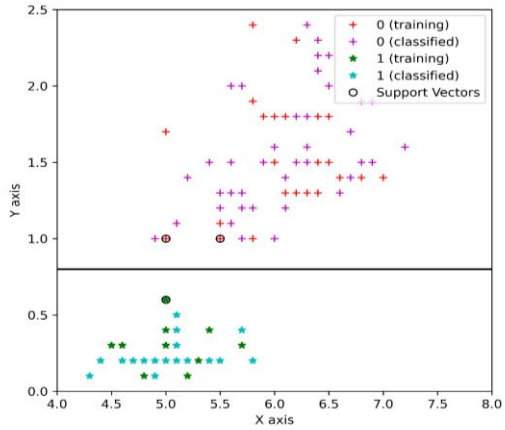

Figure 9. Categorization of sent data and the number of references to the server

tuned via grid search. For C4.5, the parameters were the same as for the Decision Tree, with the entropy criterion. For the Naïve Bayesian model, there are no significant hyperparameters; Gaussian NB was used.

The comparative results are presented in Table 6: The SVM surpassed all rival models on every metric, attaining an accuracy of 94%, precision of 92%, recall of 89%, F1-score of 90%, and AUC-ROC of 96% on the test set including 10,000 records. The SVM's exceptional performance is due to its effective management of high-dimensional data and its capacity to determine an ideal hyperplane that maximizes the margin between classes.

The Decision Tree and C4.5 models, however proficient in capturing feature interactions, were surpassed by the SVM because of their susceptibility to overfitting and intricate decision bounds. The Naïve Bayesian model had the least effective performance. It is mostly because to its presumption of feature independence. Compared to baselines, SVM improves efficiency by 19% over rule-based (static thresholds) and 9% over Isolation Forest. In Figures 10 and 11, the confusion matrix and ROC-AUC cruve are depicted, respectively.

Overall, our proposed work improves access control in smart contracts by providing an innovative SVM-based approach and dimensionality reduction. Our main innovation in automating digital signatures is detecting anomalies with 94% accuracy and reducing computational complexity, which simplifies the user experience and increases security.

4. 4. 3. Robustness Evaluation To check for robustness, we used the Fast Gradient Sign Method (FGSM) to simulate evasion attacks by changing the features of the test set (for example, adding or removing 10% noise from the connection duration) and adversarial examples. The SVM kept its accuracy at 92.5% with mild perturbation, but it dropped to 81% with severe perturbation (e.g., ±50% noise). This was better than Logistic Regression (83.5% and 82%, respectively). The baseline accuracy was 76.5%, while the accuracy of

TABLE 6. Comparative performance metrics of classifiers

Model	Accuracy	Precision	Recall	F1-Score	AUC-ROC
SVM (Linear, C=1)	0.94	0.92	0.89	0.90	0.96
Decision Tree (d=7)	0.88	0.85	0.83	0.84	0.87
C4.5 (d=7)	0.89	0.87	0.84	0.85	0.88
Naïve Bayesian	0.82	0.79	0.76	0.77	0.83
Random Forest	0.92	0.90	0.87	0.88	0.94
Gradient Boost	0.90	0.88	0.86	0.88	0.92
Logistic Regression	0.88	0.85	0.82	0.83	0.90
Rule-Based Baseline	0.75	0.70	0.65	0.67	0.78
Isolation Forest	0.85	0.82	0.80	0.81	0.88

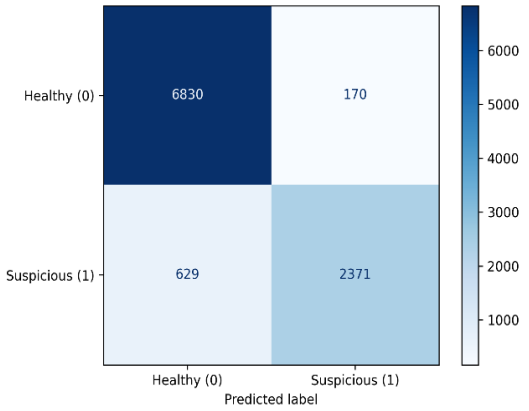

Figure 10. Confusion matrix of proposed SVM model

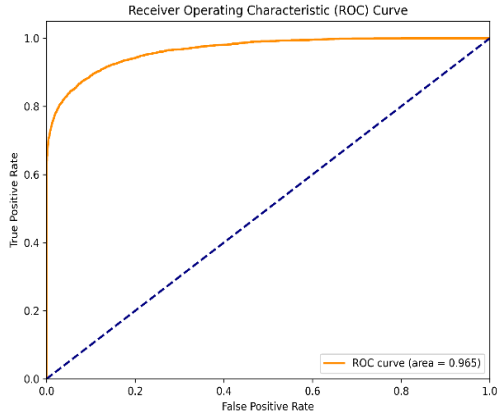

Figure 11. ROC-AUC curve of proposed model

SVM was 74.5% when FGSM attacks were used with ε=0.1. This shows that the system is strong, but it also shows that adversarial training is needed in future versions. The results of the evaluation is illustrated in Table 7.

TABLE 7. Comparative results of robustness evaluation

Model	Accuracy
SVM Base accuracy	94.00%
SVM Perturbed (10%)	92.50%
SVM Severe (50%)	81.00%
SVM Adversarial FGSM	74.50%
Baseline Base accuracy	84.50%
Baseline Perturbed (10%)	83.50%
Baseline Severe (50%)	82.00%
Baseline Adversarial FGSM	76.50%

5. DISCUSSION

The findings indicate that the SVM model, in conjunction with GA-based dimensionality reduction, significantly improves smart contract access control. The elevated accuracy (0.94) and AUC-ROC (0.96) demonstrate strong performance. Also, the precision (0.92) and recall (0.89) imply a well-balanced capacity enabling the detection of suspicious users with few false positives. The feature importance analysis validates the methodology's emphasis on behavioral indicators. These correspond with the established user classifications: Healthy Users and Suspicious Users/Hackers. For healthy users' characteristics, we can exemplify their low to medium referrals, medium transmitted data, and high received data. On the other hand, for suspicious users' characteristics, they exhibit elevated references, substantial transmitted data, and average received data. The scatter plots (Figures 5-9) illustrate the efficacy of the SVM, demonstrating distinct class separation and support vectors strategically located at the decision boundaries. The overlap shown in certain plots emphasizes the intricacy of the classification problem. It strongly emphasizes the need for individualized anomaly detection as specified in the methodology. In the comparative analysis section, we demonstrate the advantages of SVM relative to Decision Tree, C4.5, and Naïve Bayesian models. We can affirm its suitability for this application. The effectiveness of the linear kernel demonstrates that the diminished feature space is linearly separable. This conclusion is supported by the visual representations. Automated signing makes things faster, but it also raises important questions about usability and user trust. One major worry is what happens when a false positive happens, which is when a real transaction is wrongly flagged as malicious. In our proposed system, this kind of event would not stop the user. Instead, it would send the transaction back to a manual approval process, which would act as a security checkpoint. This is a small inconvenience, but it's a good trade-off because the risk of a false negative (approving a bad transaction) is much higher. To gain trust, a practical implementation could include an adjustable sensitivity threshold or a "learning period" during which the model's decisions are shown to the user for confirmation before full automation is enabled. This makes sure that users stay in control while also getting the extra layer of security that comes from machine learning. In terms of misclassification, the primary impact of a misclassification on a legitimate user is a temporary shift from a frictionless, automated experience to a traditional, manual one. The system is designed to fail safely; when in doubt, it requires explicit user consent, thereby prioritizing security over convenience in ambiguous situations.

6. LIMITATION

The proposed method has the following limitations

- Class Imbalance: The dataset contains 70% legitimate and 30% suspicious users, which may bias the classifier.
- Generalizability: The method was tested on Ethereum only; its applicability to other platforms needs exploration.
- Scalability: Rolling window analysis is computationally intensive and may require optimization for real-time use. There are also some limiations about optimizations all of which could result in much better model, namely, off-chain computation, parallel processing, incremental calculation, and hardware acceleration.

7. CONCLUSION

This research presents a machine learning-driven method for improving access control in blockchain smart contracts. By automating transaction signing and detecting anomalies, the system enhances both security and user experience. With a classification accuracy of 94%, the approach offers a reliable and efficient alternative to manual signature verification. Future work will focus on real-time deployment and extending the model to multi-blockchain ecosystems. Alos we will investigate sophisticated feature engineering to elucidate more intricate user behaviours. This could involve developing metrics such as the ratio of sent-to-received transactions, the Gini coefficient of transaction values to assess regularity, or time-delta features between consecutive transactions, potentially resulting in a more detailed classification.

In terms of optimizations, the off-chain computation is an off-chain server that keeps an eye on the blockchain could do the analysis. The smart contract would only get the final classification (benign/malicious), which would cut down on the amount of work that needs to be done on-chain. Another one is parallel processing. The analysis of different user accounts or time periods could be done at the same time on more than one processor core or server. Additionally, incremental calculation can be used. Instead of recalculating the whole window every time, you can use stream processing algorithms that can update feature calculations as new transactions come in. Lastly, hardware acceleration uses GPUs to speed up the steps of processing the ML model and extracting features. Regarding the importance of a personalized anomaly detection, the significance of a tailored anomaly detection model is most effectively demonstrated through the juxtaposition of user profiles. For instance, a bot that trades high-frequency might make hundreds of small trades every day. A global model that used average user data to train would probably see this normal bot activity as a very strange thing. On the other hand, a Decentralised Autonomous Organization (DAO) treasury might make one very large transaction every month to pay its contributors. This transaction would be very unusual for a normal user, but it is normal for the DAO's profile. In both cases, a one-size-fits-all model would fail, causing a lot of false alarms and making the system less useful. Our personalized method, which learns the unique "rhythm" of each address, is necessary to accurately tell the difference between normal and unusual behaviour in a variety of situations.

In terms of threat model, our method is meant to protect against a certain group of threats while making some assumptions. The main threat that this system protects against is transaction phishing, which is when a malicious dApp interface tricks a user into signing a transaction with wrong parameters, like an incorrect recipient address or a higher transfer amount. It also helps find automated transaction spam that comes from a hacked account and doesn't follow the user's normal behaviour. This ML system could cause two problems: 1) False Positives, where a real transaction is flagged as malicious, which makes things harder for the user; and 2) False Negatives, where a malicious transaction is missed and marked as benign. Our high precision (0.92) and recall (0.89) values show that we are doing a good job of reducing both types of errors.

Author Contribution Statement

Reza Amiri: Methodology, Conceptualization (Ideas), Investigation, Visualization, Analysis, Software (Programming and development), Writing – original draft, Writing – review & editing.
Jaber Karimpour: Supervision, Validation, Writing – review & editing.
Habib Izadkhah: Consultation, Validation, Writing – review & editing.

Conflicts of interest

The authors declare no conflicts of interest.

Supplementary Materials

The data that support the findings of this study are available on request.

8. REFERENCES

1. Nakonechnyi V, Toliupa S, Saiko V, Lutsenko V, Ghno GSN, Hussain AK, editors. Blockchain implementation in the protection system of banking system during online banking operations. 2024 35th Conference of Open Innovations Association (FRUCT); 2024: IEEE. 10.23919/FRUCT61870.2024.10516404

2. Khedmati M, Seifi F, Azizi M. Time series forecasting of bitcoin price based on autoregressive integrated moving average and machine learning approaches. International Journal of Engineering Transactions A: Basics. 2020;33(7):1293-303. 10.5829/ije.2020.33.07a.16
3. Alamsyah A, Muhammad IF. Unraveling the crypto market: A journey into decentralized finance transaction network. Digital Business. 2024;4(1):100074. 10.1016/j.digbus.2024.100074
4. Zheng Z, Xie S, Dai H-N, Chen X, Wang H. Blockchain challenges and opportunities: A survey. International journal of web and grid services. 2018;14(4):352-75. 10.1504/IJWGS.2018.095647
5. Dey A, Nandi S, Sarkar M, editors. Security measures in IoT based 5G networks. 2018 3rd International Conference on Inventive Computation Technologies (ICICT); 2018: IEEE. 10.1109/ICICT43934.2018.9034365
6. Anusha R, Saravanan R. Revolutionizing signature scheme: the enhanced Edward Elgamal extreme performance accumulate signature approach for IoT and blockchain applications. Soft Computing. 2025;29(3):1473-96. 10.1007/s00500-025-10426-0
7. Eskandari S, Clark J, Barrera D, Stobert E. A first look at the usability of bitcoin key management. arXiv preprint arXiv:180204351. 2018. 10.48550/arXiv.1802.04351
8. Hamidi H, Sayah A. Combining machine learning algorithms to detect phishing urls: a stacking approach. International Journal of Engineering Transactions B: Applications. 2025;38(8):1939-52. 10.5829/ije.2025.38.08b.18
9. Atzei N, Bartoletti M, Cimoli T, editors. A survey of attacks on ethereum smart contracts (sok). International conference on principles of security and trust; 2017: Springer. 10.1007/978-3-662-54455-6_8
10. Bamert T, Decker C, Elsen L, Wattenhofer R, Welten S, editors. Have a snack, pay with Bitcoins. IEEE P2P 2013 Proceedings; 2013: IEEE. 10.1109/P2P.2013.6688717
11. Kersic V, Vidovic U, Vrecko A, Domajnko M, Turkanovic M. Orchestrating digital wallets for on-and off-chain decentralized identity management. IEEE access. 2023;11:78135-51. 10.1109/ACCESS.2023.3299047
12. Ahmed MR, Islam AM, Shatabda S, Islam S. Blockchain-based identity management system and self-sovereign identity ecosystem: A comprehensive survey. Ieee Access. 2022;10:113436-81. 10.1109/ACCESS.2022.3215286
13. Babel M, Willburger L, Lautenschlager J, Völter F, Guggenberger T, Körner M-F, et al. Self-sovereign identity and digital wallets. Electronic Markets. 2025;35(1):1-14. https://doi.org/10.1007/s12525-025-00772-0
14. Albshaier L, Almarri S, Hafizur Rahman M. A review of blockchain's role in E-Commerce transactions: Open challenges, and future research directions. Computers. 2024;13(1):27. 10.3390/computers13010027
15. Krishnan LP, Vakilinia I, Reddivari S, Ahuja S. Scams and solutions in cryptocurrencies—A survey analyzing existing machine learning models. Information. 2023;14(3):171. 10.3390/electronics12061422
16. Chen T, Li X, Luo X, Zhang X, editors. Under-optimized smart contracts devour your money. 2017 IEEE 24th international conference on software analysis, evolution and reengineering (SANER); 2017: IEEE. 10.1109/SANER.2017.7884650
17. Ntousis O, Makris E, Tsanakas P, Pavlatos C. A dual-stage processing architecture for unmanned aerial vehicle object detection and tracking using lightweight onboard and ground server computations. Technologies. 2025;13(1):35. https://doi.org/10.3390/technologies13010035
18. Podgorelec B, Turkanović M, Karakatič S. A machine learning-based method for automated blockchain transaction signing including personalized anomaly detection. Sensors. 2019;20(1):147. 10.3390/s19245433
19. Ou W, Huang S, Zheng J, Zhang Q, Zeng G, Han W. An overview on cross-chain: Mechanism, platforms, challenges and advances. Computer Networks. 2022;218:109378. 10.1016/j.comnet.2022.109378
20. Tschorsch F, Scheuermann B. Bitcoin and beyond: A technical survey on decentralized digital currencies. IEEE Communications Surveys & Tutorials. 2016;18(3):2084-123. 10.1109/COMST.2016.2535718
21. Dominguez Anguiano T, Parte L. The state of art, opportunities and challenges of blockchain in the insurance industry: a systematic literature review. Management Review Quarterly. 2024;74(2):1097-118. https://doi.org/10.1007/s11301-023-00328-6
22. Decker C, Eidenbenz R, Wattenhofer R, editors. Exploring and improving BitTorrent topologies. IEEE P2P 2013 Proceedings; 2013: IEEE.
23. Chou C-C, Hwang N-CR, Schneider GP, Wang T, Li C-W, Wei W. Using smart contracts to establish decentralized accounting contracts: An example of revenue recognition. Journal of Information Systems. 2021;35(3):17-52. https://doi.org/10.2308/ISYS-18-028
24. Buterin V. A next-generation smart contract and decentralized application platform. white paper. 2014;3(37):2-1. https://ethereum.org/en/whitepaper/
25. Boneh D, Franklin M, editors. Identity-based encryption from the Weil pairing. Annual international cryptology conference; 2001: Springer.
26. Béres F, Seres IA, Benczúr AA, Quintyne-Collins M, editors. Blockchain is watching you: Profiling and deanonymizing ethereum users. 2021 IEEE international conference on decentralized applications and infrastructures (DAPPS); 2021: IEEE.
27. Lin S-Y, Zhang L, Li J, Ji L-l, Sun Y. A survey of application research based on blockchain smart contract. Wireless Networks. 2022;28(2):635-90. https://doi.org/10.1007/s11276-021-02874-x
28. Szabo N. Formalizing and securing relationships on public networks. First monday. 1997. https://doi.org/10.5210/fm.v2i9.548
29. Bodziony N, Jemioło P, Kluza K, Ogiela MR. Blockchain-based address alias system. Journal of Theoretical and Applied Electronic Commerce Research. 2021;16(5):1280-96. https://doi.org/10.3390/jtaer16050072
30. Akbarfam AJ, Barazandeh S, Gupta D, Maleki H. Deep learning meets blockchain for automated and secure access control. arXiv preprint arXiv:231106236. 2023. https://arxiv.org/abs/2311.06236
31. Mounnan O, Boubchir L, Manad O, El Mouatasim A, Daachi B. DBAC-DSR-BT: A secure and reliable deep speech recognition based-distributed biometric access control scheme over blockchain technology. Computer Standards & Interfaces. 2025;92:103929. https://doi.org/10.1016/j.csi.2024.103929
32. Jiang F, Chao K, Xiao J, Liu Q, Gu K, Wu J, et al. Enhancing smart-contract security through machine learning: A survey of approaches and techniques. Electronics. 2023;12(9):2046. https://doi.org/10.3390/electronics12092046
33. Guo Z. Blockchain-enhanced smart contracts for formal verification of IoT access control mechanisms. Alexandria Engineering Journal. 2025;118:315-24. https://doi.org/10.1016/j.aej.2022.03.064
34. Ghaly M, Elbeltagi E, Elsmadony A, Tantawy MA. Integration of Blockchain-Enabled smart contracts in construction: SWOT framework and social network analysis. Civil Engineering

Journal. 2024;10(05):1662-97. https://doi.org/10.28991/CEJ-2024-010-05-020

35. Gaur R, Prakash S, Kumar S, Abhishek K, Msahli M, Wahid A. A machine-learning–blockchain-based authentication using smart contracts for an IoHT system. Sensors. 2022;22(23):9074. https://doi.org/10.3390/s22239074
36. Benaich R, Gahi Y, El Mendili S. Pioneering the Security of EHRs Using an Immersive Blockchain Conceptual Framework. Emerging Science Journal. 2025;9(1):161-87. https://doi.org/10.28991/ESJ-2025-09-01-010
37. Alizadeh M, Koohi, S., Vahidi, V. A decentralized access control framework for the personal health records based on blockchain and smart contract. Journal of Information Security and Applications. 2023;72:103375. https://doi.org/10.1016/j.jisa.2022.103375
38. Liao C-H, Guan X-Q, Cheng J-H, Yuan S-M. Blockchain-based identity management and access control framework for open banking ecosystem. Future Generation Computer Systems. 2022;135:450-66. https://doi.org/10.1016/j.future.2022.05.015
39. Criollo S, Guerrero-Arias A, Arif YM, Samala AD, Jaramillo-Alcázar Á, Luján-Mora S. Usability Evaluation of a Mobile Augmented Reality App for PC Hardware Training: A Comparative Study in Three Countries. 2025. https://doi.org/10.28991/ESJ-2025-09-02-024
40. Aliyev V. Ethereum fraud detection dataset. Kaggle Retrieved March. 2021;13:2022. https://www.kaggle.com/datasets/vagifa/ethereum-frauddetection-dataset

COPYRIGHTS

©2026 The author(s). This is an open access article distributed under the terms of the Creative Commons Attribution (CC BY 4.0), which permits unrestricted use, distribution, and reproduction in any medium, as long as the original authors and source are cited. No permission is required from the authors or the publishers.

Persian Abstract

چکیده

در حوزه فناوری بلاکچین، تضمین کنترل دسترسی ایمن و کارآمد برای قراردادهای هوشمند همچنان یک چالش اساسی است. روش‌های سنتی اغلب پیچیده و منابع‌بر هستند و به طور بالقوه مانع پذیرش گسترده می‌شوند. این مطالعه یک رویکرد جدید مبتنی بر یادگیری ماشین را برای بهبود مکانیسم‌های کنترل دسترسی پیشنهاد می‌دهد. به طور خاص، ما کاربران را بر اساس رفتار تراکنش و الگوهای تعامل به عنوان خوش‌خیم یا بالقوه مخرب طبقه‌بندی می‌کنیم. یک طبقه‌بندی‌کننده ماشین بردار پشتیبان (SVM)، همراه با تکنیک‌های کاهش ابعاد، بر روی مجموعه داده‌ای حاوی ۵۰،۰۰۰ رکورد تراکنش از ۱۰۰۰ آدرس بلاکچین اعمال می‌شود. این مدل در مجموعه آزمایشی به دقت ۹٤٪ دست یافت و کاربران را بر اساس فرکانس تعامل با سرور و مدت زمان اتصال به طور مؤثر متمایز کرد. از طریق تجزیه و تحلیل بصری و ارزیابی جامع، نشان می‌دهیم که روش پیشنهادی هم تشخیص ناهنجاری و هم کارایی عملیاتی را بهبود می‌بخشد. این رویکرد پتانسیل تقویت اعتماد و تسهیل پذیرش گسترده‌تر برنامه‌های مبتنی بر بلاکچین را دارد.

International Journal of Engineering

Journal Homepage: www.ije.ir

Assessment of using Soybean Biodiesel Fuel on Performance and Exhaust Emission Characteristics of a Common-rail Diesel Engine (OM355)

S. Ojaghi, S. Jafarmadar*, S. Khalilarya

Department of Mechanical Engineering, Urmia University, Urmia, Iran

P A P E R I N F O

Paper history:
Received 16 August 2025
Received in revised form 25 September 2025
Accepted 02 October 2025

Keywords:
Biodiesel Fuel
Common Rail
Performance Characteristics
Emission Characteristics

A B S T R A C T

The impact of performance and exhaust emission features of a common-rail diesel engine OM355 using a biodiesel/diesel mix (volume ratios of B5, B10, and B15) was analyzed in this study. Between engine speeds of 1000 and 1500 RPM, there was an observed increase in power and torque, with enhancements of 5% and 0.5%, respectively. Conversely, at elevated engine speeds, specifically from 1800 to 2200 RPM, both power and torque exhibited a reduction ranging from 1 to 4% in comparison to conventional diesel fuel. The brake-specific fuel consumption (BSFC) decreased by 4 to 1% at low and medium speeds, particularly between 1000 and 1500 RPM, due to the reduction in energy content from using soybean biodiesel. However, at high speeds in the range of 1800 to 2200 RPM, BSFC increased by 1 to 3.5%. In addition, the results of the emissions test indicated that emissions from mixed fuels were significantly higher than those from regular fuel or diesel owing to the lack of any engine modifications. Based on the test results, despite the increase in pollutant emissions using mixed fuels, the emission levels of the aforementioned fuels were within the Euro 5 standard limits. Considering that diesel engines operate optimally at middle speeds, which is their maximum torque range, and considering the engine performance features, the utilization of biodiesel blends B5, B10, and B15 is acceptable for the engine performance. To reduce the adverse effects of biodiesel combustion, various methods, such as preheating the fuel, increasing the fuel rail pressure, decreasing the injection duration, using additives, and retuning electronic engine control (ECU) units based on the biodiesel characteristics, could be utilized as a viable replacement in diesel engines.

***doi**: 10.5829/ije.2026.39.08b.20*

Graphical Abstract

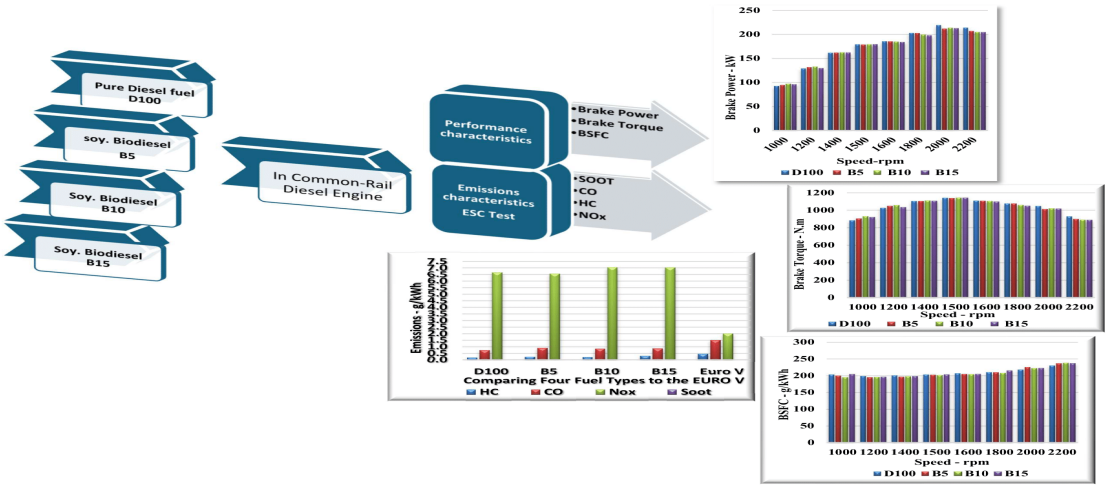

*Corresponding Author Email: s.jafarmadar@urmia.ac.ir (S. Jafarmadar)

Please cite this article as: Ojaghi S, Jafarmadar S, Khalilarya S. Assessment of using Soybean Biodiesel Fuel on Performance and Exhaust Emission Characteristics of a Common-rail Diesel Engine (OM355). International Journal of Engineering, Transactions B: Applications. 2026;39(08):2049-62.

NOMENCLATURE			
BSFC	Brake Specific Fuel Consumption	B5	Biodiesel 5%
BTE	Brake Thermal Efficiency	B10	Biodiesel 10%
CR	Common-Rail	B15	Biodiesel 15%
CI	Compression-Ignition	D100	Neat Diesel
PN	Particle Number	ESC	The steady-state European Stationary Cycle
PM	Particle Matter	(ΔX)	Uncertainty of a measured variable
LCV	Lower Calorific Value	σ	Standard deviation
SFC	Specific Fuel Consumption	Xi	Denotes an individual experimental reading
CO	Carbon monoxide	R	Function of the measured variables
UHC	Unburned Hydrocarbon	ΔR	Uncertainties of the calculated
NOx	Nitrogen Oxide	RMS	Root MNean Square
ECU	Electronic Control Engine	n	the total number of readings
TDC	Top Dead Center	λ	Air-Fuel equivalence Ratio
EGR	Exhaust Gas Recirculation (EGR)	PPM	Parts Per Million
RCCI	Reactivity Controlled Compression Ignition (RCCI)		

1. INTRODUCTION

Scientists continue to produce energy from renewable resources because of the depletion of fossil fuels and the increase in their prices. Biodiesel may be a potential replacement for diesel fuel because of its simple manufacturing method, compatibility with standard diesel engines, and low pollution. Biodiesel did not require any modifications. Utilizing animal fats and waste cooking oils as feedstock offers a cost-effective solution to the economic challenges associated with the raw material supply. Combustion of biodiesel derived from these sources has been shown to significantly decrease emissions of unburned hydrocarbons and carbon monoxide, while only causing a marginal increase in nitrogen oxide (NOx) emissions. Biodiesel fuel contains no sulfur; therefore, biodiesel is different from diesel (1). The cetane number, flash point, viscosity, and oxygen content in biodiesel are all greater than those of regular diesel fuel. All of these properties affected om the emissions of pollutants.

A study on particulate matter emissions from common-rail diesel engines indicated that biodiesel/diesel blends exhibited a similar geometric mean particle diameter but a lower particle number concentration compared with diesel fuel. Observations indicated that increasing engine speed and load led to a reduction in particle concentration, while the particle size exhibited no significant variation. The study also reported a reduction in both the total particle count and particle mass per unit volume when biodiesel was blended with diesel (2). An experimental investigation was conducted on a common-rail diesel engine fueled with biodiesel–bioethanol blends. Among the tested formulations, B20 and B20E5 demonstrated superior brake-specific fuel consumption (BSFC) and improved brake thermal efficiency (BTE) compared to conventional diesel. These blends also produced notable reductions in carbon monoxide (CO) emissions and particle number concentrations. Additionally, the incorporation of ethanol contributed to lower nitrogen oxide (NOx) emissions, a phenomenon attributed to ethanol's cooling effect, which reduces peak combustion temperatures during homogeneous exothermic reactions and thereby suppresses overall NOx formation (3). The behavior of a diesel engine equipped with a high-pressure common-rail (CR) injection system was investigated to evaluate the performance characteristics of biodiesel under advanced operating conditions, the results showed that higher viscosity delayed fuel injection and impaired atomization. The smaller droplet size of biodiesel contributed to lower CO_2 emissions compared with fossil fuels. In addition, biodiesel contained more oxygen than diesel; as a result, nitrogen oxide (NOx) emissions increased, whereas suspended particulate matter decreased (4). An investigation was carried out to analyze submicron particle emissions from compression ignition (CI) engines. The findings demonstrated that biodiesel reduced the particle number (PN) and particulate matter (PM) emissions. Moreover, the findings refuted the widespread belief that oxygen-rich fuels inevitably increase the nitrogen oxide (NOx) emissions. The oxygen present in the ester molecules lowered the NOx emissions and acted as an anti-knock agent. Increasing the load level caused the NOx emissions to decrease, whereas the other PM emissions increased. Furthermore, biodiesel content above 10% reduced soot particle formation and did not significantly affect the adsorbed mass of hydrocarbons (HC), thereby enhancing organic solubility under all operating conditions (5). According to an experimental study, the fuel-generated power was equal for both biodiesel and diesel under partial load operation. Under full-load operation, engine power experienced a slight decline attributable to the lower calorific value of biodiesel, although the magnitude of this reduction was minimal. Biodiesel's intrinsic oxygen content played a key role in lowering emissions of particulate matter, carbon

monoxide (CO), and unburned hydrocarbons. These results indicate that biodiesel represents a promising cleaner fuel alternative for diesel engine use (6). Several factors influence the emissions and performance of biodiesel. The proven factors were the biodiesel mixing ratio, biodiesel properties, engine type, operating circumstances, and addition of any type of additive. Because of the mixed fuel had a lower LCV and a higher BSFC than diesel, power reduction was observed in the blended fuel. A few problems associated with the use of an inline injection pump to inject fuel are that fuel injection is based on engine speed, the maximum fuel pressure is low, and multiple injections cannot be used in this case. The monophasic injection method restricts the mixing of two or more substances. As a result, zones of low and high richness were identified in the study area (7). In one study, bioethanol–gasoline mixtures were tested in a spark-ignition (SI) engine to reduce fossil fuel consumption. The thermal efficiency ($\eta_{th,b}$) decreased as the ethanol percentage increased, whereas the latent heat of evaporation increased with higher ethanol content. At a fixed equivalence ratio, raising the ethanol content led to a decrease in both air mass intake and volumetric efficiency. Consequently, the reduced volumetric efficiency combined with the higher latent heat of ethanol caused a drop in the air–fuel mixture temperature, resulting in increased instances of misfires and flame extinction (8). An experimental study reported that marine engines can use biodiesel from renewable sources as a substitute for petroleum diesel because it meets diesel fuel quality standards. Because marine engines operate on various fuels, biodiesel represents a valuable alternative for reducing harmful emissions (9). Research has shown that engines running on soybean biodiesel experience a decrease in torque and an increase in brake-specific fuel consumption (BSFC) relative to conventional diesel, primarily due to biodiesel's lower energy content. At the same time, the use of biodiesel significantly reduced emissions of unburned hydrocarbons and carbon monoxide (CO) by 28 to 46%. In contrast, nitrogen oxide (NOx) emissions increased, and CO_2 concentrations rose by 1.46 to 5.03%. Moreover, blending biodiesel with diesel was observed to shorten the ignition delay and reduce the intensity of the peak during homogeneous combustion (10). Experiments with water–biodiesel emulsions in a compression ignition (CI) engine demonstrated that soybean biodiesel blends significantly reduced smoke, carbon monoxide (CO), and hydrocarbon (HC) emissions compared to conventional diesel. Nevertheless, these blends did not achieve additional reductions in nitrogen oxide (NOx) emissions. The emulsified fuel exhibited a lower specific fuel consumption (SFC) at water concentrations of up to 10%, and the maximum CO and HC emissions also decreased. These reductions were significant but diminished at water concentrations of ≥ 10% (11). A study was carried out to assess how injection timing and pressure influence emissions in a compression ignition (CI) engine fueled with soybean biodiesel, with particular emphasis on soot and smoke production. Although using biodiesel in common-rail CI engines is commonly associated with higher nitrogen oxide (NOx) emissions, it may simultaneously contribute to increased smoke formation. However, simultaneous reductions in CO and HC under certain operating conditions have been reported. Experiments were performed at post-injection timings of 15°, 30°, and 45° after top dead center (TDC) and at injection pressures of 550 and 650 bar. The findings revealed that, in general, soybean biodiesel reduced CO, HC, and NOx emissions; however, specific combinations of injection timing and pressure led to increased smoke and NOx levels (12). The study investigated the effects of injection pressure on ignition behavior and pollutant emissions in a common-rail (CR) internal combustion engine fueled with palm oil biodiesel. The fuel's elevated cetane number and inherent oxygen content were found to improve ignition performance. At low engine speeds, biodiesel atomization was more difficult. However, the researchers demonstrated that atomization could be improved by increasing the injection pressure, even without engine modifications. The findings further showed that nitrogen oxide (NOx) emissions rose with increasing injection pressure. In addition, the application of exhaust gas recirculation (EGR) has been reported to mitigate pollutant formation (13). Additionally, the effects of blending graphene nanoparticles with soybean oil–based biodiesel on the performance and emission characteristics of compression ignition (CI) engines were investigated. When tested under a 12 kg load, the B60GNP100 blend outperformed conventional diesel, recording the minimum brake-specific fuel consumption of 12.58% and attaining the maximum brake thermal efficiency of 27.13% (14). Biodiesel blends were analyzed to determine their impact on the efficiency and pollutant features of common-rail CI engines. The study included both simulated and experimental tests under three loading conditions. An increase in the proportion of biodiesel within the fuel blend was found to reduce engine power output, while simultaneously leading to higher brake-specific fuel consumption (BSFC) and elevated nitrogen oxide emissions. The findings revealed that fuel blends with a higher share of biodiesel relative to gasoline produced comparatively lower emissions of smoke, unburned hydrocarbons (HC), and carbon monoxide (CO). This study suggests that biodiesel has the potential to improve the performance of compression ignition (CI) engines (15). For instance, one investigation employed a reactivity-controlled compression ignition (RCCI) approach, where a gasoline–diesel/biodiesel blend incorporating waste cooking oil was used to take advantage of the complementary characteristics of the different fuel components. The experiments showed that

unsaturated fatty acids burned faster than saturated fatty acids. The use of unsaturated lipids shortened the engine start time, whereas saturated fatty acids had no significant effect on fuel consumption (16). An experimental investigation was carried out to assess how castor oil–derived biodiesel influences both the emission characteristics and performance behavior of diesel engines. The B15 blend was the most effective in reducing particulate matter at 50% load, although the brake-specific fuel consumption (BSFC) increased for the B20 and B30 blends, along with higher nitrogen oxide (NOx) emissions. Under quarter-load operating conditions, noticeable decreases in nitrogen oxide (NOx) and particulate matter (PM) emissions have been reported (17). A study conducted three-dimensional modeling of split-injection schemes to evaluate their effects on pollutant formation and the performance characteristics of indirect injection (IDI) combustion engines. The main challenge in reducing diesel engine pollutants was identified as the inverse correlation between smoke and nitrogen oxide (NOx) emissions. The application of split injection has proven to be an efficient strategy for concurrently lowering soot and nitrogen oxide (NOx) emissions in diesel engines (18). A study examined the impact of adding diethyl ether (DEE) to diesel–biodiesel blends on engine performance and exhaust emission behavior. The study revealed that the addition of 5% DEE to diesel fuel resulted in a 5.9% decrease in fuel usage and a 9.6% boost in thermal efficiency, while lowering NOx emissions by 20.5% (19, 20). A study conducted consumption and emission tests on a single-cylinder, four-stroke diesel engine at various operating loads with biodiesel produced from the distillation of soybean and coconut oil. The addition of distilled biodiesel from soybean and coconut oil to all blends resulted in a maximum improvement in brake thermal efficiency of 56.08% and a reduction in specific fuel consumption of 18.33% compared to diesel fuel. Adding distilled biodiesel to diesel fuel resulted in a maximum reduction of 30% in carbon monoxide emissions in all blends (21).

An investigation was carried out to assess how the addition of titanium dioxide nanoparticles to biodiesel influences combustion dynamics and emission characteristics in a compression ignition engine. According to the study, titanium dioxide nanoparticles decreased CO emissions by 30% and HC emissions by 21.5% when the engine operated at higher speeds and concentrations. When the fuel burns more completely due to the titanium dioxide nanoparticles, there was a 15% increase of CO_2 emissions. The more the speed of the engine increased, the more NO_X emissions decreased by 20% when TiO_2 nanoparticles were added (22).

The mass-based fuel injection system in CR diesel engines requires precise air-fuel ratio control to reduce emissions. The onboard electronic control unit estimates the amount of fuel mass to be injected for combustion using the sensor data of the rail pressure, fuel temperature, engine speed, intake air mass and gas pedal position. In this system, the injector supplies fuel at high pressure only when the engine requires it to operate. Unlike other systems, CR technology separates the production pressure from the injection. In a CR diesel engine, the pump continues to supply fuel to the rail and behind the injectors depending on the engine control mode. Multi-stage injection can be performed during working cycles, unlike the linear injection fuel delivery system in the CR system. This implies that the primary injection stage is responsible for smooth engine operation, the main injection stage is responsible for producing the desired power, and the secondary injection stage is responsible for minimizing emissions.

Based on the above discussion, soybean biodiesel fuel reduced pollutants such as carbon monoxide and unburned hydrocarbons, except for nitrogen oxides, compared with conventional diesel fuel, without requiring fundamental changes to the engine under test. However, it adversely affects the performance characteristics of the engine under test, such as power, torque, and brake-specific fuel consumption.

Some studies on biodiesel did not inform the emission standards of the test engine, while others focused on engines with standards below Euro 5 standards. In contrast, studies examining the effects of biodiesel in engines compliant with Euro 5+ and Euro 6 emission regulations remain scarce. This gap is particularly significant, given the tightening of global emission frameworks that demand cleaner combustion strategies.

To fill this research gap, the current study assessed the performance and emission behavior of an OM355 diesel engine, produced by IDEM Co., after its fuel system was upgraded from an inline injection pump to a high-pressure common rail configuration. With the addition of after-treatment technologies, the engine's emission compliance improved from Euro 4 to Euro 5 Evv, a level situated between Euro 5 and Euro 6 standards. This study examined the effects of soybean biodiesel under Euro 5+ conditions, utilizing the steady-state European Stationary Cycle (ESC) protocol as a method for engine certification, without making any modifications to the engine.

In this study, an electronically controlled high-pressure common-rail diesel engine fueled with soybean biodiesel/diesel blends was tested on an engine bench to analyze the effects of different blend ratios on the combustion characteristics. The test fuels consisted of diesel and biodiesel blends, with pure diesel denoted as D100. The blends were prepared at volumetric ratios to produce three fuels with different B5, B10, and B15.

The study employed the European Stationary Cycle (ESC) testing method, in accordance with engine certification, to measure exhaust emissions from the

diesel engine. The evaluated performance and emission characteristics included power and torque output, brake-specific fuel consumption, and emission pollutants contained CO, HC, NOx, and soot with no adjustments made to the engine during the experiments.

2. MATERIAL AND METHODS

This study describes an experiment on a CR diesel engine utilizing 5%, 10%, and 15% volumetric biodiesel mixtures. The volumetric percentages of the mixtures were denoted as B5%, B10%, and B15%. The pollutants and performance characteristics of the diesel engines were measured at partial and complete loads using the selected fuel mixtures. The tests were performed at the engine laboratory of IDEM Company.

2. 1. Materials

2. 1. 1. The Engine Specifications A modern CR diesel engine (OM355) was used in this study, and its technical data are presented in Table 1.

2. 1. 2. Test Equipment The exhaust gases and performance features of the CR diesel engine were tested and evaluated at the Iranian Diesel Engine Manufacturing Co. (IDEM) engine test cell. The test equipment used, as shown in Figure 1, is described as follows:

- Hydraulic Dynamometer: A hydraulic brake was employed on the engine to monitor and quantify its key performance parameters.

TABLE 1. Engine OM355 Characteristics- courtesy of IDEM Co. brochure

Model	OM355
Engine type	A vertical, turbocharged diesel engine equipped with a CR fuel system
Number of Cylinders	6 in Line
Bore Diameter	128 mm
Number of Strokes	Four-stroke
Stroke Length	150 mm
Emission Standard	Euro 5 EEV with DOC + SCR
Compression Ratio	1 :16.82
Number of Valves	12 Intake + 12 Exhaust valves
Engine Displacement	11.580 Liter
Fuel Type	Diesel fuel
Engine Power/Rated Power	2000rpm /220 kW
Maximum Engine Torque	1500rpm /1145 N.m
Engine Type	205 g/kW.h
Direction of Rotation:	Counter-clockwise

- Various Sensors: Engine power, brake torque, and other variables are measured using the sensors available in the test cell. In addition, the main variables (temperature, pressure, etc.) essential for engine performance were measured.
- Fuel Consumption Meter: The BSFC was measured using the AVL 733S digital flowmeter with up to one-thousandth accuracy in kilograms per hour.
- Exhaust Emissions Measurement Device: Emissions from the engine were measured using AVL DiCom 4000, which was manufactured in Austria. The pollutants that were measured were NOx, HC, λ, CO_2, CO, and opacity (soot).
- Computerized data acquisition system: Data were acquired using a computerized data acquisition system.

2. 1. 3. Fuel Regular diesel fuel used in Iran was utilized as the base fuel, as well as soy. Biodiesel was used as the fuel in this investigation. This research analyzed the performance characteristics of the base fuel as well as soy-derived biodiesel, with their respective properties summarized in Tables 2 and 3. B5, B10, and B15 denote blended fuels with 5, 10, and 15% biodiesel in pure diesel fuel, respectively. D100 denoted base fuel.

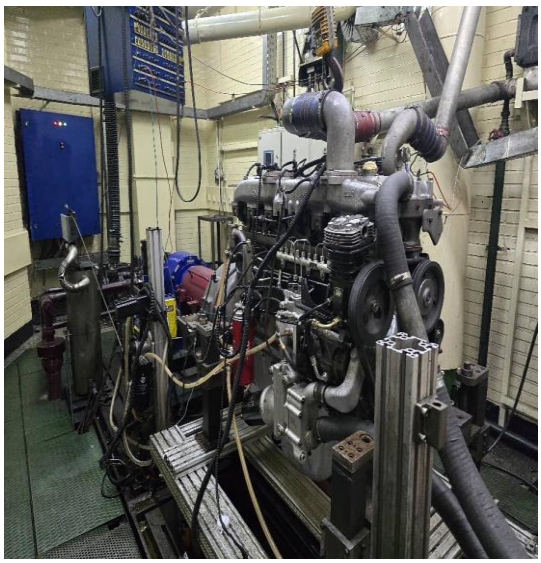

Figure 1. Engine Test Cell

TABLE 2. Test Results of Diesel Fuel Specification Used in Test

Property/ Characteristic	Diesel fuel Test results	Test Method	Unit
Flash Point	61	EN ISO 2719	°C
Viscosity	4.1	EN ISO 3104	mm^2/s
Calorific Value	42570	--------	kJ/kg
Density	839	--------	kg/m^3

TABLE 3. Test Results of Biodiesel Specification Used in Test

Property/ Characteristic	Biodiesel Test results	Test Method	Unit
Flash Point	170	EN ISO 3679	°C
Viscosity	4.81	EN ISO 3104	mm^2/s
Calorific Value	33810	--------	kJ/kg
Density	880	--------	kg/m^3

2. 1. 4. Error and Uncertainty Analysis Errors and uncertainties in measurements may arise from the choice and calibration of instruments, variations in environmental conditions, and intrinsic constraints of the experimental procedures and observational techniques. Measurement uncertainties are generally classified into two categories: systematic errors, which originate from calibration deficiencies and bias, and random errors, which result from measurement repeatability and data scattering. The uncertainty of a measured variable (ΔX) is typically evaluated assuming a Gaussian distribution, where a range of ±2σ corresponds to a 95% confidence interval for the observed values, as stated in Equation 1 (23).

$$\Delta X_i = \frac{2\sigma_i}{\bar{X}_i} \times 100 \quad (1)$$

In this context, Xi denotes an individual experimental reading, n is the total number of readings, and σ is the standard deviation. The uncertainties of the calculated parameters can be evaluated using Equation 3, where:

$$R = f(X1, X2, X3, \ldots\ldots\ldots\ldots Xn) \quad (2)$$

$$\Delta R = \sqrt{\left[\left(\frac{\partial R}{\partial X_1}\Delta X_1\right)^2 + \left(\frac{\partial R}{\partial X_i}\Delta X_2\right)^2 + \left(\frac{\partial R}{\partial X_3}\Delta X_3\right)^2 + \ldots\left(\frac{\partial R}{\partial X_n}\Delta X_n\right)^2\right]} \quad (3)$$

where R is a function of the measured variables. Consequently, ΔR was calculated using the root mean square (RMS) of the errors associated with the measured parameters. The uncertainties inherent to the measurement instruments are summarized in Table 4.

TABLE 4. Accuracies of the Measurements

Measured Parameter	Measurement Device	Accuracy	Uncertainty
Rpm	Tachometer	1 rpm	± 1 rpm
Torque	Dynamometer	1 N.m	± 1 N.m
$\dot{m}_f$	AVL -Fuel meter	0.1 kg/h	± 0.1 kg/h
HC, NOx	AVL DICOM4000	1 ppm	± 1 ppm
CO	AVL DICOM4000	0.01%	± 0.01 %
Opacity	AVL415 Smoke meter	0.1%	± 0.1 %

2. 2. Test Methodology and Procedure This study comprehensively assessed the effects of biodiesel blends on the operational performance and emission characteristics of a common-rail compression ignition (CI) engine. This study investigated the torque, power, and BSFC performance characteristics of the engine. The exhaust gas features examined included soot, CO, HC, and NOx, using two different base fuels and soybean biodiesel at volume percentages of B5%, B10%, and B15%, while varying the engine speed from 1000 to 2200 rpm in increments of 200 rpm. The investigations were implemented in full-load situations as well as four partial-load conditions: 25%, 50%, 75%, and 100%. The emission characteristics were studied for the partial load mode at three speeds: 1350, 1650, and 1950 rpm. Furthermore, to obtain better and more accurate results, every reading was duplicated three times, and the average measurements were used as the ultimate outcomes in the graphs.

3. RESULTS AND DISCUSSION

The test data for the base fuel and blended fuels at volumetric ratios of 5%, 10%, and 15% (indicated by the symbols B5, B10, and B15, respectively) are presented as follows:

3. 1. Brake Power

3. 1. 1. Interaction Impact of Fuel Type & Speed on Brake Power of Engine Owing to the correlation between power, torque, and speed under test conditions, the power variation also depends on the engine speed. Figure 2 shows the highest brake power, 219.1 kW which was obtained for the base fuel at a speed of 2000 rpm. The lowest brake power, 92.40 kW, was achieved at 1000 rpm for the base fuel. As depicted in the figure, brake power for the blended fuels increased with engine speed up to 1500 rpm, beyond which it declined at higher speeds. The relative power increased in blended fuels B5, B10, and B15 compared to that of the base fuel at 1000 rpm by +32.2%, +25.5%, and +20.4%, respectively. This relative increase showed a declining but positive trend up to 1500 rpm. The relative power changes for blended fuels B5, B10, and B15 compared to the base fuel at 1600 rpm were -10.0%, -40.0%, and -8.0%, whereas at 1800 rpm, they were -10.0%, -60.1%, and -4.2%, respectively. The magnitude of power reduction seen with the blended fuels, in relation to the calorific value of soybean biodiesel, depended on the particular composition of each fuel blend. The reduction in power associated with biodiesel's lower calorific value is partly alleviated by its inherent characteristics—namely, greater oxygen content, higher cetane number, and increased density—which together help compensate for the resulting performance loss. The higher density and cetane rating of

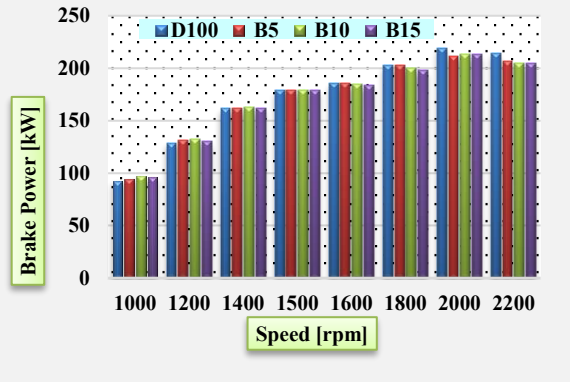

Figure 2. Effect of biodiesel on power at different speeds and full load

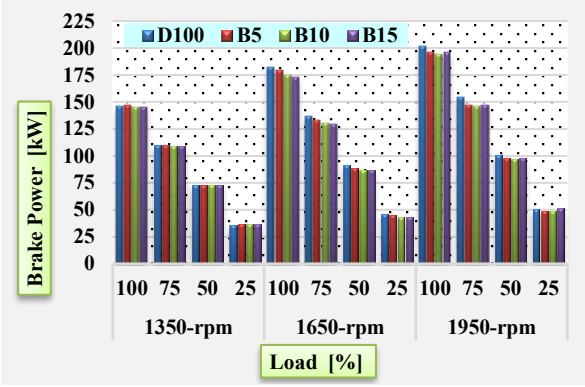

Figure 3. Effect of biodiesel on power at different speeds and partial load

the blended fuels partially offset the impact of their reduced calorific value compared to the base diesel, which diminishes and smooths the variations in brake power across the different blends. The increased density of biodiesel allows a larger mass of fuel to enter the combustion chamber per injection, while its intrinsic oxygen content and higher cetane number enhance combustion at lower engine speeds, resulting in a corresponding improvement in engine power.

For the above reasons, the difference in brake power between the blended fuels was negligible at medium speeds, and their performance coincided. The biodiesel content in the blended fuels increased at medium and high speeds because of its lower calorific value which led to a decrease in the brake power at these operating points. At high speeds, such as 2000 and 2200 rpm, blended fuels B5, B10, and B15 showed relative power reductions of -3.30%, -2.60%, -2.90%, -3.20%, -4.10%, and -4.30%, respectively, compared with the base fuels. At higher speeds, near the maximum power, the influence of fuel properties on the brake power became more pronounced. At such speeds, the adverse effect of their low calorific value is more evident owing to ineffective atomization because of the high viscosity of the blended fuel and less time available for mixing with air, which, in turn, adversely affects the combustion quality. The trend of the curve indicates that the brake power decreased as the share of biodiesel increased compared to that of the base fuel, which is attributed to the lower energy content of biodiesel. The blended fuel B10 indicated the highest brake power among the tested fuels at low to medium speeds, at which the engine reached its peak torque, with an average relative increase of 2.2%, indicating the suitability of this fuel for use at low and medium speeds.

3. 1. 2. Interaction Effect of Fuel Type and Load on Engine Brake Power The engine brake power is indicated at various loads, as shown in Figure 3. As shown in Figure 3, the brake power of the fuels examined in this study increased linearly with an increase in load from 25 to 100% at the aforementioned speeds. The relative changes in the brake power at full load and low speed for B5, B10, and B15 were -0.6%, +0.6%, and -0.4%, respectively, and the relative power drop was negligible.

The relative changes in brake power for B5, B10, and B15 at full load and intermediate speed were +2%, -2%, and -4.4%, respectively, whereas at high speed, they were +3%, -3%, and -4%, respectively. For B10 and B15 at maximum loads and intermediate and high speeds, the low heating value of biodiesel led to a relative decline in the brake power. A relative increase in power was observed for fuel B5 at partial loads and both intermediate and high speeds, which was attributed to the larger fuel mass injected per unit volume of biodiesel, owing to its high density and oxygen content.

3. 2. Engine Brake Torque

3. 2. 1. interaction Impact Fuel Type and Speed on Brake Torque Brake torque is an engine performance property and is a function of the fuel type and engine speed. The relative increase in the brake torque of blended biodiesel fuels 5B, 10B, and 15B at 1000 rpm, according to Figure 4, was +2.30%, +5.20%, and +4.20%, respectively, compared with that of diesel. Engine torque showed a relative rise up to 1500 rpm, but beyond this point, it decreased at higher speeds in comparison to the torque achieved with the base diesel fuel. The maximum torque generated by the engine owing to volumetric efficiency was correlated with a speed of 1500 rpm, at which a relative decrease occurred. The relative torque changes at 1500 rpm for blended fuels 5B, 10B, and 15B with respect to pure diesel were -0.20%, +0.10%, and +0.12%, respectively, which were not significant changes. At low and moderate engine speeds, the inherent oxygen content and elevated density of biodiesel helped offset the drawbacks of its lower calorific value, promoting more efficient combustion of the fuel blend.

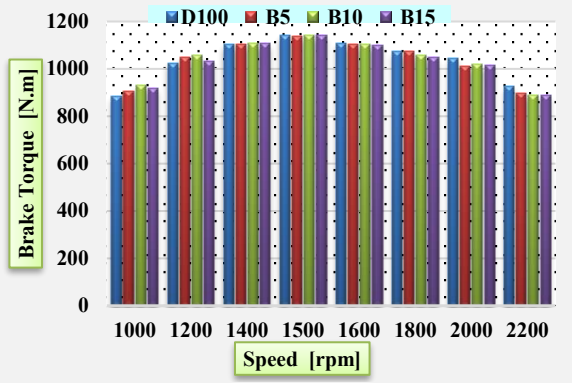

Figure 4. Impact of biodiesel on torque at different speeds

The relative decrease in torque of the blended fuels at high speeds of 2000 and 2200 rpm was -3.40%, -2.60%, -2.90%, -3.20%, -4.20%, and -4.30%, respectively. As the percentage of biodiesel increased at higher speeds, the amount of lost torque increased. The most important reasons for torque reduction at speeds higher than 1500 rpm, in addition to limited volumetric efficiency and increased frictional loss, are the low energy content and high viscosity of biodiesel. At these speeds, the high density of biodiesel changed the air-fuel ratio, and its high viscosity degraded the quality of fuel atomization and caused relative torque loss with respect to pure diesel fuel.

3. 2. 2. Interaction Impact Fuel Type and Load on Engine Brake Torque Brake torque is a key engine function influenced by the physicochemical properties and percentage of biodiesel, rotational speed, and engine load. Figure 5 shows a graphical representation of the brake torque values for the four fuels at three speeds and four loads.

The variation in the relative brake torque at 1350 rpm for partial and complete loads was less than 1% for an increased biodiesel share in the blends. This increase was attributed to the presence of oxygen in the biodiesel.

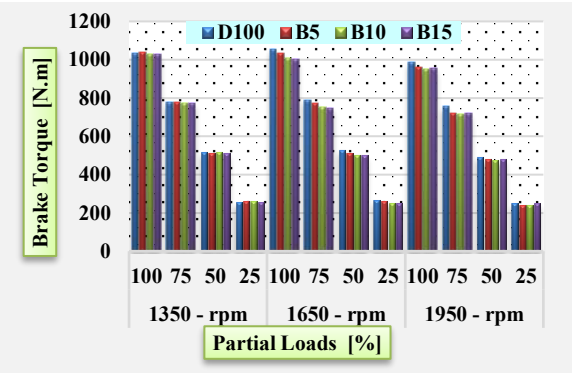

Figure 5. Impact of biodiesel on torque at varied speeds and loads

At the middle speed of 1650 rpm, the lowest torque disadvantages for B5, B10, and B15 were -0.2%, -4.5%, and -5.3%, respectively, under the full load conditions. At a 75% load, these decreases are -2.7%, -4.8%, and -5.3%; at a 50% load, they are -3%, 1.5%, and 2.3%; and at a 25% load, they are -1.1%, -4.5%, and -5%. The lower heating value of biodiesel, which is additionally associated with its high density, as well as the oxygen content in the biodiesel structure, partially compensates for its low calorific value and leads to a torque decrease at mid-range speeds. The power was reduced by a factor related to torque at a high-speed of 1950 rpm for the blended fuels of B5, B10, and B15 at full load by -2.7%, -3.5%, and -2.9%, respectively. This reduction for a 75% load is -4.8%, -6.5%, and -4.8%; for a 50% load it is -6.2%, -4.3%, and -6.2%; and for a 25% load it is -4.4%, 6.3%, and -4%. At higher engine speeds, torque exhibited a noticeable decline under both partial and full load conditions, primarily due to the combined effects of biodiesel's reduced energy content and its greater density relative to conventional diesel. Fuel-rich zones at high speeds and incomplete combustion caused a decline in torque only at this speed because of the direct injection of more fuel mass per unit volume, as biodiesel fuel is denser.

3. 3. Interaction of Fuel and Speed on BSFC BSFC is widely used to compare the thermal and economic efficiencies of internal combustion engines. BSFC is typically associated with the performance of an engine at different loads or with various fuels at a given load. BSFC measures how efficiently an engine converts fuel into usable power, indicating the amount of fuel required to generate a given brake power. It provides a comparative basis for evaluating biodiesel against conventional fuels in terms of energy efficiency. It is determined by relating the mass flux of the fuel through the cylinder to the brake-power output of the engine. As shown in Figure 6, brake-specific fuel consumption (BSFC) decreases at low and moderate engine speeds, while it rises at higher speeds. The BSFC at 1000 and 1200 rpm with B5, B10, and B15 changed by −1.7%, −0.4%, +0.6%, and −1.7%, −1.4%, and −1.1% compared to the base fuel, respectively. The differences in BSFC from the base fuel for biodiesel blends B5, B10, and B15 at medium speed were −0.34%, +0.34%, and +0.15%, respectively. At high speeds, the values were +3.2%, +0.2%, and +2.1%, respectively. The BSFC characteristics depend directly on the fuel density and inversely on the fuel calorific value. Fuel blends featuring lower density combined with higher calorific values achieved the lowest BSFC when operated at identical loads.

The elevated BSFC observed with biodiesel, relative to the base fuel, can be attributed to its lower energy content. The reduced calorific value of the blend

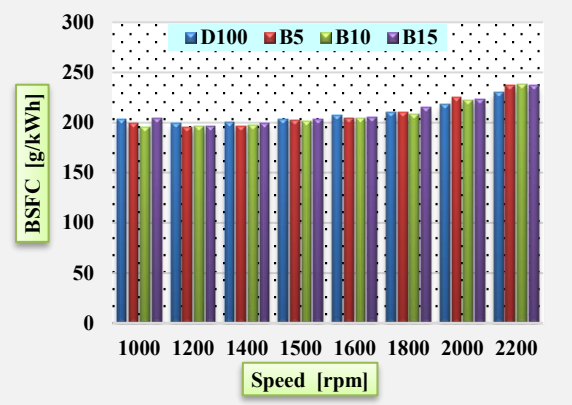

Figure 6. The effect of biodiesel on BSFC feature

consequently resulted in increased specific fuel consumption. Due to its higher density, biodiesel requires greater fuel volumes to generate an equivalent level of engine power. This decline occurred because the fuel contained less energy than that of diesel. Biodiesel fuel benefits from its high density and oxygen content, which improve combustion, and high cetane number, which counters the low calorific value, resulting in a reduced BSFC at low speeds. When operating at medium speeds, biodiesel produced BSFC values that were nearly equal to those of diesel fuel. At high speeds, the low calorific value and high viscosity of the biodiesel fuel resulted in poor atomization, which led to an increased BSFC.

3. 4. Effect of Biodiesel on Soot Emission Rate

Heywood (24) in his book "Internal Combustion Fundamentals," defined soot as a mixture of large solid particles and small liquid droplets in exhaust gases, mainly comprising carbon soot, unburned organic matter, and sulfate compounds. The non-uniform charge distribution in the cylinder creates areas where the fuel mixture is rich but lacks sufficient oxygen and experiences incomplete vaporization. In these regions, some of the fuel pyrolyzed, resulting in primary soot particles. These nuclei became larger particles when carbon and organic molecules were added. Because of the oxygen present in the fuel-rich portion of the flame, oxidation activities can produce carbon dioxide. Soot is created by incomplete combustion processes at locations far from the flame and with little oxygen. Soot formation is caused by incomplete combustion, poor fuel and air mixing, high engine load, low engine speed, aromatic compounds, and sulfur in fuel.

To reduce soot, a reasonable and possible fuel-air mixture quality, fuel/air ratio, and combustion condition, high injection pressure, and low-sulfur fuel are used. Moreover, soot production depends on the fuel type, biodiesel content, and engine load. Figure 7 illustrates the evolution of carbon for four distinct fuels under three engine speed conditions. The blended fuels (D100, B5, B10, and B15) emit full-load particulate emissions of 0.000, 0.000, 0.003, 0.005, and 0.007 g/kWh at average speed; 0.000, 0.008, 0.006, and 0.008 g/kWh at high speed; and 0.000, 0.022, 0.026, and 0.023 g/kWh at low speed. The soot emissions of D100 and its blends were 0.001, 0.001, 0.003, and 0.017 g/kWh at low load; 0.001, 0.001, 0.013, and 0.026 g/kWh at mid load; and 0.001, 0.051, 0.068, and 0.057 g/kWh at full load, all in the 25% load range.

The exhaust gas flow from vehicles using biodiesel produced more carbon particulates because biodiesel has higher density and viscosity. The atomization of viscous biodiesel is poor, resulting in large fuel droplets coexisting within the cylinder. This condition slows the mixing of fuel and air, ultimately leading to the formation of a "fuel-rich" mixture zone. Biodiesel also has a high vaporization temperature and can only partially vaporize under low-load and low-temperature conditions. At low and mid speeds and in part-load situations, the air-fuel ratio is higher, which leads to a lean mixture. The increase in the oxygen content in the biodiesel molecule increases the combustion efficiency, and if sufficient time for soot oxidation is available under these conditions, the increase in soot emissions can be small compared with that in diesel.

The experimental findings indicate that, while overall fuel consumption declined with higher biodiesel blend ratios, the rate of soot formation increased under identical engine conditions at both light and full loads, particularly at low and medium speeds. This effect is attributed to the higher viscosity of biodiesel, which impairs atomization and produces locally rich fuel zones near the injection spray, resulting in comparatively higher soot emissions than those observed with conventional diesel. The higher density of biodiesel at increased velocities complicates the air intake, elongating the zones of denser fuel and shortening the time available for soot oxidation due to faster processing. However, the quantity of oxygen present during fuel combustion is insufficient, resulting in a greater discharge of soot than the base fuel.

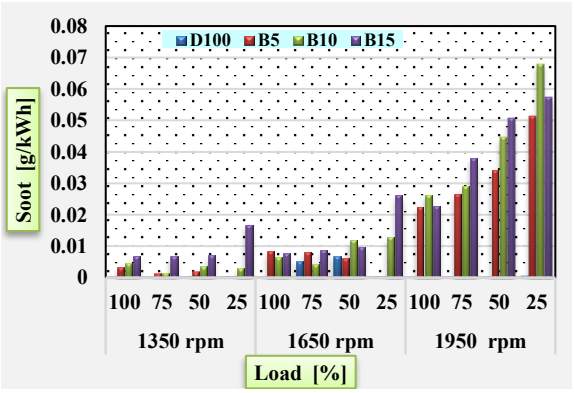

Figure 7. Effect of Biodiesel in Emission Test Modes on Soot

3. 5. Effect of Biodiesel on Carbon Monoxide Carbon monoxide emissions largely arise from incomplete combustion. In regions where the air–fuel ratio is fuel-rich ($\lambda < 1$), the limited availability of oxygen prevents the full conversion of carbon in the fuel to carbon dioxide (CO_2). Therefore, a portion of the carbon remained unoxidized and was released as CO emissions. As a diesel engine is always under lean combustion conditions (excess air; $\lambda > 1$), relatively little carbon monoxide is formed. High combustion temperatures enable the conversion of carbon monoxide to carbon dioxide through oxidation; however, low exhaust gas temperatures prevent this conversion.

The pollutant is formed because of two factors: the slow fuel vaporization process and the creation of a rich mixture during low-load and cold-start engine operations. In addition, at low speeds, owing to the sufficient time for fuel-air mixing, the amount of CO emissions decreased as the speed decreased. The maximum amount of carbon monoxide emissions for blended and base fuels was registered under no-load conditions. The high viscosity, poor atomization, and incomplete vaporization of biodiesel fuel cause local incomplete combustion and the formation of carbon monoxide emissions. As shown in Figure 8, with an increase in the load, the amount of carbon monoxide emissions for all fuels decreased owing to the high combustion temperatures at full load.

As illustrated in Figure 8, the relative changes in carbon monoxide emissions for blended fuels B5, B10, and B15, compared to the base fuel at full load and at low, middle, and high speeds, were (-0.13%, -0.02%, +0.37%), (+2.5%, +7.5%, +8.5%), and (+5%, +5.5%, +4.5%), respectively. For blended fuels at a partial load of 50% and low, middle, and high speeds, the relative changes in this pollutant were (+3.6%, +1.1%, +3.6%), (+22%, +16%, +15%), and (+7.5%, +5.2%, +6.7%), respectively. At a partial load of 25% and low, middle, and high speeds, the relative changes for blended fuels

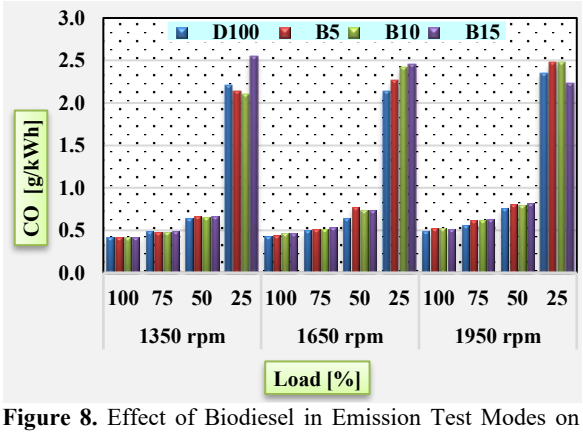

Figure 8. Effect of Biodiesel in Emission Test Modes on Carbon Monoxide

B5, B10, and B15 were (-3%, -4.4%, +15.5%), (+7.5%, +13.2%, +14.5%), and (+7.5%, +5.8%, -4.9%), respectively. For the blended fuels, at all speeds, the maximum carbon monoxide emissions were at a 25% partial load and the minimum at full load. The high combustion temperature and increased oxygen content in the biodiesel fuel were more effective at high loads because of the higher air-to-fuel ratio. At partial loads and low speeds, the increased air-to-fuel ratio resulted in excess air that reduced the combustion temperature, caused incomplete vaporization of the biodiesel fuel, and decreased the reaction rate of carbon monoxide oxidation to carbon dioxide. Specifically, increasing the proportion of biodiesel in the fuel blend results in elevated emissions of this pollutant. At full load and high speed, with an increase in the combustion temperature owing to improved combustion, the amount of this pollutant decreased. Previous investigations have demonstrated that carbon monoxide formation is primarily linked to incomplete combustion resulting from a low air-to-fuel ratio. Additional contributing factors include the physicochemical properties of the fuel, injection parameters, engine load, low operating temperatures, and insufficient residence time for complete oxidation. Elevated CO emissions indicate that a portion of the fuel's chemical energy is not effectively converted into useful work by the engine (25, 26).

3. 6. Effect of Biodiesel Fuel on Unburned Hydrocarbon Emissions HC emissions are primarily the result of incomplete combustion. If a fraction of the fuel is not oxidized in the combustion chamber, it is classified as an unburned hydrocarbon (UHC). The lowest combustion chamber loads produced the lowest temperatures, which prevented sufficient fuel oxidation. If the fuel and air are incorrectly mixed and create fuel-lean/fuel-rich zones, and if the biodiesel fuel is of poorer quality than diesel fuel owing to its higher viscosity, all these factors lead to incomplete combustion, which causes an increase in this pollutant. Fuel features such as viscosity, density, and engine operating conditions are effective in reducing this pollutant level. High-viscosity biodiesel fuels also allow the formation of large fuel droplets. If the fuel is not completely atomized, it will not burn. This process results in excess hydrocarbon production. From Figure 9, it can be observed that the increase in this pollutant for blends B5, B10, and B15 compared to pure diesel fuel at full load and low, mid, and high speeds were (-1.3%, +20%, +81%); (+122%, +97%, 171%); and (-4.6%, -13.7%, +23.4%), respectively. The changes in this pollutant at a partial load of 25% and low, middle, and high speeds for the B5, B10, and B15 blends compared to the base fuel were (+23%, +12.6%, +57.5%), (+48%, +35.8%, +94.6%), and (-16.9%, -16.9%, +22.3%), respectively. The viscosity of biodiesel fuel discharges

large fuel droplets, resulting in inadequate atomization at partial loads and low speeds. These factors suggest that the high boiling point of biodiesel, coupled with relatively low combustion chamber temperatures, can prevent complete fuel vaporization, ultimately resulting in incomplete combustion.

The elevated density of biodiesel promotes the formation of fuel-rich regions, leading to incomplete combustion under full-load conditions. Additionally, the available oxidation time is reduced. While the inherent oxygen content of biodiesel aids the combustion process, fuel-rich zones still result in an increase in unburned hydrocarbon emissions.

3. 7. Effect of Biodiesel-Blended Fuel on NOx Emissions In general, the reduction in fuel injection at partial loads causes the combustion temperature to be low, leading to a reduction in the generation of NOx. As a result of the NOx creation process, which is heavily reliant on temperature, the reactions involved in NOx formation proceed slowly at low temperatures. At low engine loads, the high viscosity of biodiesel impairs proper fuel–air mixing, leading to localized high-temperature regions in the combustion chamber and, consequently, elevated NOx formation. A decrease in the combustion temperature at partial loads reduces the NOx formation. The chemical composition of biodiesel increases its oxygen content. Such an increase causes more complete combustion at low temperatures and reduces the NOx formation at high temperatures. Biodiesel contains higher oxygen content in its chemical structure than fossil fuels, which results in elevated combustion temperatures when the biodiesel concentration increases, thus producing more nitrogen oxides (NOx).

The two-stage injection method includes pilot injection, which shortens the ignition delay and controls

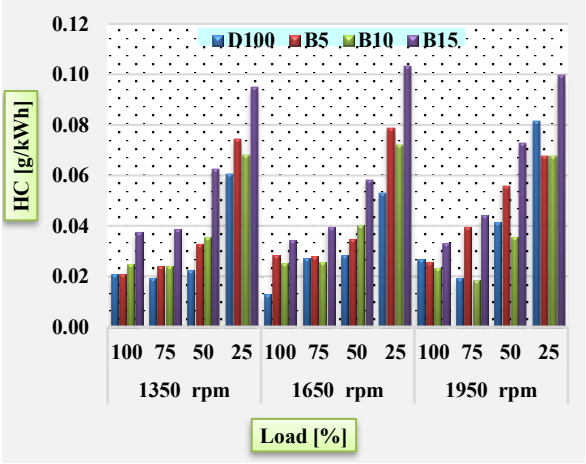

Figure 9. Effect of Biodiesel in Emission Test Modes on Unburned Hydrocarbons

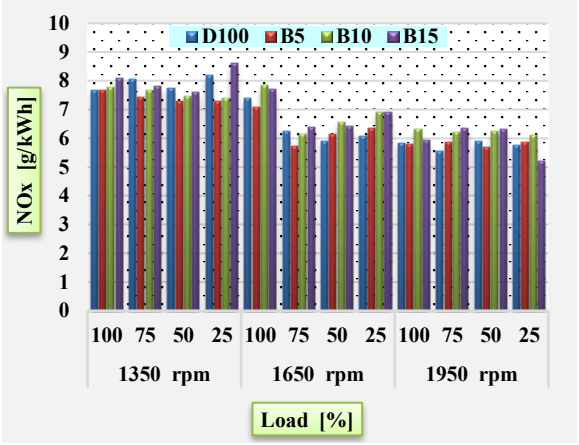

Figure 10. Effect of Biodiesel in Emission Test Modes on NOx

the initial combustion temperature, and main injection, which manages the temperature levels to prevent the formation of NOx. Rising combustion temperatures led to a corresponding increase in nitrogen oxide (NOx) emissions. Figure 10 illustrates the relative increase in NOx emissions for blended fuels B5, B10, and B15 compared to pure diesel fuel at full load across low, middle, and high speeds, with values of (-0.27%, +1.34%, +5.31%), (-4.40%, +6.25%, +4.16%), and (-0.71%, +8.12%, +1.19%), respectively.

At low speeds and partial loads, the NOx emissions were reduced because of the low temperature. Because of the enhanced oxygen content of the blended fuels, the combustion temperature increased at the maximum load and low speed, which in turn resulted in more NOx emissions. Modifying the temperature and pressure conditions for NOx formation increased the amount of NOx at an intermediate speed. At higher engine speeds, the reduced residence time of gases in the combustion chamber contributed to a decrease in NOx emissions. Nevertheless, the high temperature of the combustion chamber allows NOx pollutants to form, which are present in greater quantities than the base fuel.

Under full-load conditions at low and medium engine speeds, incorporating soybean biodiesel markedly elevated NOx emissions, primarily due to higher peak combustion pressures and temperatures, as well as a shortened ignition delay. The combustion process was further enhanced by the intrinsic oxygen content of biodiesel, which promotes more complete oxidation. This procedure resulted in more thorough burning at lower temperatures. Furthermore, at high temperatures, the NOx formation decreased. In addition, an increase in the biodiesel percentage because of its high oxygen content increased the combustion temperature and produced more NOx. Multistage injection strategies, such as pilot and main injections, significantly reduce ignition delay and control the temperature at the beginning and main

stages of combustion, which also reduces NOx. When the injection pressure is higher, the atomization of the fuel is finer. This improves combustion, which increases the combustion temperature. Consequently, more NOx was produced.

3. 8. Effect of Biodiesel-Blended Fuel on Pollutants

Table 5 presents the total emissions of HC, CO, NO_x, and soot measured over the 13-mode steady-state test cycle. The data in Table 5, together with Figure 11, show that biodiesel–diesel blends emitted higher levels of these pollutants than neat diesel; however, all values remained within the regulatory limits of the Euro 5 environmental standard. The units are expressed in g/kWh.

The higher viscosity of soybean biodiesel compared to diesel fuel causes poor spray atomization, resulting in poor combustion efficiency and higher pollutant emissions. The engine produced elevated emissions because it was operated without biodiesel optimization. The combustion process of biodiesel operates more efficiently because it contains built-in oxygen, has a high cetane rating, and has a short ignition delay, which minimizes some biodiesel-related negative effects.

At the conclusion of this section, Table 6 presents a summary of the results from both the studies included in the literature review in the introduction and the current study.

TABLE 5. Engine Emission Components in the ESC Test

Emissions	D100 g/kWh	B5 g/kWh	B10 g/kWh	B15 g/kWh	Euro V
CO	0.17	0.23	0.210	0.312	0.46
HC	0.741	0.912	0.857	0.861	1.50
NOx	6.639	6.544	7.029	7.016	2.00
Soot	0.002	0.013	0.015	0.017	0.02

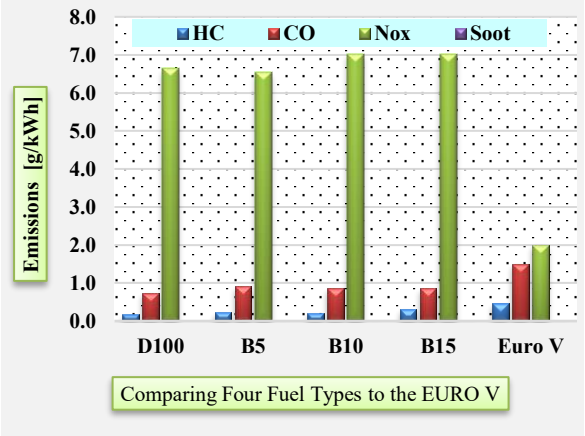

Figure 11. Comparison of Emission Results for Four Fuel Types with EURO V Standard

TABLE 6. Summary of Findings and Comparison from the Literature Review and present study

Author(s)	Key Findings
Wang et al. [2]	PN ↓; geometric mean diameter unchanged; PM ↓ with load/speed ↑
Ho et al. [3]	BSFC ↓, BTE ↑; CO ↓; PN ↓; NOx ↓ with ethanol (cooling effect)
Kim et al. [4]	Viscosity ↑ → delayed injection; droplet size ↓ → CO_2 ↓; NOx ↑, PM ↓
Chen and Wu [5]	PN ↓, PM ↓; oxygen esters ↓ NOx (anti-knock); soot ↓
Lapuerta, et al. [6]	Power ~ diesel (partial load); power ↓ at full load; CO, HC, PM ↓
Xue et al. [7]	LCV ↓, BSFC ↑; power ↓; blend ratio/additives matter; inline pumps limit injection strategies
Mostafavi et al. [8]	η_{th} ↓; latent heat ↑; air–fuel temp ↓ → misfires, flame quench
Eremeeva et al. [9]	Biodiesel met fuel quality; reduced harmful emissions
Özener et al. [10]	Torque ↓, BSFC ↑; CO & HC ↓ (28–46%); NOx & CO_2 ↑; ignition delay ↓
Vellaiyan et al. [11]	Smoke, CO, HC ↓; NOx ~ unchanged; SFC ↓ (≤10% water)
Fayad [12]	CO, HC ↓; NOx & smoke ↑ at certain timings/pressures
Kim et al. [13]	Cetane ↑, oxygen ↑ → ignition improved; injection pressure ↑ → atomization ↑ but NOx ↑
Kadam et al. [14]	B60GNP100 → BSFC ↓ (12.58%), BTE ↑ (27.13%)
Nguyen et al. [15]	Power ↓, BSFC ↑, NOx ↑; smoke, HC, CO ↓ vs. gasoline
Talesh et al. [16]	Unsaturated FA → faster burn, start time ↓; saturated FA little effect
Jafarmadar et al. [17]	B15 → PM ↓; B20/B30 → BSFC & NOx ↑; quarter-load → NOx & PM ↓
Jafarmadar et al. [18]	Soot & NOx ↓ simultaneously; soot–NOx trade-off mitigated
Youssef et al. [19] & Jafarmadar et al. [20]	Fuel use ↓ 5.9%; BTE ↑ 9.6%; NOx ↓ 20.5%
Rosiane et al. [21]	BTE ↑ 56.08%; BSFC ↓ 18.33%; CO ↓ 30%
Khujamberdiev and Che [22]	CO ↓ 30%; HC ↓ 21.5%; CO_2 ↑ 15%; NOx ↓ 20% at high speed
Present Study	- Power/Torque: slight ↑ at low–mid speeds; drop above 1500 rpm (viscosity & poor atomization). - BSFC: ↓ 1–4% at low–mid speeds; ↑ 1–3.5% at high speeds. - Soot: small ↑ at mid loads, sharp ↑ at high loads. - CO: max at 25% load, min at full load. - UHC: ↑ at low speeds & full load (fuel-rich zones). - NOx: ↓ at low load; ↑ at full load due to higher temps/oxygen; partly ↓ at high rpm.

4. CONCLUSION

The operational performance and emission characteristics of a six-cylinder OM355 common-rail diesel engine were assessed using soybean biodiesel–diesel blends (B5, B10, and B15) under both full- and partial-load conditions. The results show that at low to medium engine speeds, the higher density and oxygen content of biodiesel partially offset its lower heating value, leading to slight improvements in power and torque and a 1–4% reduction in BSFC. However, at speeds above 1500 rpm, the high viscosity and boiling point of biodiesel caused poor atomization and incomplete evaporation, resulting in decreased power and torque as well as a 1–3.5% increase in BSFC.

Emission analysis indicated that biodiesel blends slightly increased soot and CO emissions at low speeds due to incomplete vaporization but facilitated better combustion and soot oxidation at partial loads. At high speeds and full loads, soot emissions rose significantly because of fuel-rich zones. CO emissions peaked at 25% partial load, while the lowest values were recorded at full load. UHC emissions increased at low speeds and full load, mainly due to poor vaporization and the formation of fuel-rich areas. NOx emissions were reduced at low loads owing to lower combustion temperatures but increased under full load because of higher peak temperatures and pressures; at high speeds, shorter residence times limited NOx formation.

Overall, soybean biodiesel blends are compatible with common-rail diesel engines without structural changes, though penalties in BSFC, soot, and NOx emissions become evident at high-speed and high-load operation.

The authors suggested specific nonstructural modifications for soybean biodiesel properties to address these limitations, including preheating the fuel, raising rail pressure, shortening injection time, adding additives, and adjusting ECU settings. These performance optimization methods reduce combustion-related negative impacts while creating better engine operation stability. Biodiesel blends up to B15 demonstrate effective compatibility with Euro 5+ compliant diesel engines for complete fuel substitutions.

Future biodiesel research must investigate the complete range of engine performance and emission output variations that occur when the biodiesel concentration in the base fuel progresses from B20 to B100. Evaluating the effects of biodiesel on engine longevity and component wear is essential, alongside examining its compatibility with advanced emission control systems, including Selective Catalytic Reduction (SCR) and Diesel Particulate Filters (DPF), to effectively reduce NOx, soot, and other regulated pollutants.

5. REFERENCES

1. Wu G, Ge JC, Choi NJ. A comprehensive review of the application characteristics of biodiesel blends in diesel engines. Applied Sciences. 2020;10(22):8015. https://doi.org/10.3390/app10228015
2. Wang X, ZHAN Z, Hu T, Huang Z. Influence of biodiesel/diesel blends on particulate emissions in a turbocharged common rail diesel engine. SAE International Journal of Fuels and Lubricants. 2014;7(3):643-52. 10.4271/2014-01-2368
3. How H, Masjuki H, Kalam M, Teoh Y. Engine performance, emission and combustion characteristics of a common-rail diesel engine fuelled with bioethanol as a fuel additive in coconut oil biodiesel blends. Energy Procedia. 2014;61:1655-9. . https://doi.org/10.1016/j.egypro.2014.12.185
4. Kim J-W, Kim H-I, Kim Y-J, Lee K-H, editors. An experimental study on biodiesel characteristics in a common rail direct injection diesel engine. Proceedings of the FISITA 2012 World Automotive Congress: Volume 1: Advanced Internal Combustion Engines (I); 2012: Springer.
5. Chen Y-C, Wu C-H. Emissions of submicron particles from a direct injection diesel engine by using biodiesel. Journal of Environmental Science and Health, Part A. 2002;37(5):829-43. https://doi.org/10.1081/ESE-120003591
6. Lapuerta M, Armas O, Rodriguez-Fernandez J. Effect of biodiesel fuels on diesel engine emissions. Progress in energy and combustion science. 2008;34(2):198-223. http://dx.doi.org/10.1016/j.pecs.2007.07.001
7. Xue J, Grift TE, Hansen AC. Effect of biodiesel on engine performances and emissions. Renewable and Sustainable energy reviews. 2011;15(2):1098-116. https://doi.org/10.1016/j.rser.2010.11.016
8. A. Mostafavi RS, M. Yousefifard, O. Jahanian, . "Investigating the Performance and Pollutants of a Light Agricultural SI Engine with Gasoline-ethanol Fuel under Low Load Conditions and Constant Equivalence Ratio. International Journal of Engineering Transactions B: Applications. 2025 38(8):1793-808. 10.5829/ije.2025.38.08b.06
9. Eremeeva A, Khasanov A, Oleynik I, Kondrasheva N, Marinets A. Development of biofuel as Marine low-viscosity fuels with environmentally friendly components. International Journal of Engineering Transactions B: Applications. 2025;38:273-9. 10.5829/ije.2025.38.02b.02
10. Özener O, Yüksek L, Ergenç AT, Özkan M. Effects of soybean biodiesel on a DI diesel engine performance, emission and combustion characteristics. Fuel. 2014;115:875-83. https://doi.org/10.1016/j.fuel.2012.10.081
11. Vellaiyan S, Partheeban CA. Emission analysis of diesel engine fueled with soybean biodiesel and its water blends. Energy Sources, Part A: Recovery, Utilization, and Environmental Effects. 2018;40(16):1956-65. https://doi.org/10.1080/15567036.2018.1489911
12. Fayad MA. Investigation the impact of injection timing and pressure on emissions characteristics and smoke/soot emissions in diesel engine fuelling with soybean fuel. Journal of Engineering Research. 2021;9(2). https://doi.org/10.36909/JER.V9I2.9683
13. Kim HY, Ge JC, Choi NJ. Effects of fuel injection pressure on combustion and emission characteristics under low speed conditions in a diesel engine fueled with palm oil biodiesel. Energies. 2019;12(17):3264. https://doi.org/10.3390/en12173264

14. Kadam PM, Dolas DR, Pal S, Gajghate SS. Impact of Soybean Biodiesel Blends with Mixed Graphene Nanoparticles on Compression Ignition Engine Performance and Emission: An Experimental and ANN Analysis. International Journal of Automotive and Mechanical Engineering. 2024;21(3):11512. https://doi.org/10.15282/ijame.21.3.2024.5.0888
15. Nguyen TN, Khoa NX, Tuan LA. The correlation of biodiesel blends with the common rail diesel engine's performance and emission characteristics. Energies. 2021;14(11):2986. https://doi.org/10.3390/en14112986
16. Talesh Amiri S SR, Jahanian O, Alamian R. . Performance Simulation of an RCCI Engine Fueled with Gasolinediesel/Biodiesel Waste Cooking Oil with a Focus on Consumption Trends of Fuel Constituents. International Journal of Engineering, Transactions A: Basics. 2025;38(10):2208-19. 10.5829/ije.2025.38.10a.01
17. Jafarmadar S, Pashae J. Experimental study of the effect of castor oil biodiesel fuel on performance and emissions of turbocharged DI diesel. International Journal of Engineering-Transactions B: Applications. 2013;26(8):905-12. 10.5829/idosi.ije.2013.26.08b.12
18. Jafarmadar S, Zehni A. Multi-dimensional modeling of the effects of spilt injection scheme on performance and emissions of idi diesel engines. International journal of engineering-transactions C: Aspects. 2012;25(2):135. 10.5829/idosi.ije.2012.25.02c.07
19. Youssef A, Ibrahim A. A numerical investigation on enhancing the performance of a diesel engine fuelled with diesel-biodiesel blend using a diethyl ether as an additive. Engineering Reports. 2024;6(11):e12915. https://doi.org/10.1002/eng2.12915
20. Jafarmadar S, Khalilaria S, Saraee HS. Prediction of the performance and exhaust emissions of a compression ignition engine using a wavelet neural network with a stochastic gradient algorithm. Energy. 2018;142:1128-38. https://doi.org/10.1016/j.energy.2017.09.006
21. Rosiane de Almeida Andrade M, de Andrade Bezerra JK, Duarte LdJN, Lavoie J-M, de Barros Neto EL. Performance, evaluation and gas emission of diesel and distilled biodiesel blends in IC engine. Biofuels. 2024;15(10):1271-80. https://doi.org/10.1080/17597269.2024.2358564
22. Khujamberdiev R, Cho HM. Evaluation of TiO2 Nanoparticle-Enhanced Palm and Soybean Biodiesel Blends for Emission Mitigation and Improved Combustion Efficiency. Nanomaterials. 2024;14(19):1570. https://doi.org/10.3390/nano14191570
23. Appavu P, Venu H. Quaternary blends of diesel/biodiesel/vegetable oil/pentanol as a potential alternative feedstock for existing unmodified diesel engine: Performance, combustion and emission characteristics. Energy. 2019;186:115856. https://doi.org/10.1016/j.energy.2019.115856
24. Heywood J. Internal combustion engine fundamentals. 2018.
25. Behçet R. Performance and emission study of waste anchovy fish biodiesel in a diesel engine. Fuel Processing Technology. 2011;92(6):1187-94. https://doi.org/10.1016/J.FUPROC.2011.01.012
26. Ozsezen AN, Canakci M. Determination of performance and combustion characteristics of a diesel engine fueled with canola and waste palm oil methyl esters. Energy Conversion and Management. 2011;52(1):108-16. https://doi.org/10.1016/j.enconman.2010.06.049

COPYRIGHTS
©2026 The author(s). This is an open access article distributed under the terms of the Creative Commons Attribution (CC BY 4.0), which permits unrestricted use, distribution, and reproduction in any medium, as long as the original authors and source are cited. No permission is required from the authors or the publishers.

Persian Abstract

چکیده

دراین تحقیق تأثیراستفاده از سوخت های ترکیبی بیودیزل سویا/دیزل با نسبت های حجمی B۵ ،B۱۰ و B۱۵ را برمشخصه های عملکردی و آلایندگی یک موتور دیزل تجاری ریل مشترک (OM۳۵۵) بررسی شد. نتایج نشان داد که توان و گشتاور ترمزی در سرعت‌های پایین تا متوسط، در محدوده ۱۰۰۰ تا ۱۵۰۰ دور در دقیقه، نسبت به سوخت دیزل معمولی ۰.۵ تا ۵ درصد افزایش داشته ، اما در سرعت های بالا، به ویژه در محدوده ۱۸۰۰ تا ۲۲۰۰ دور در دقیقه، کاهشی بین ۱ تا ٤ درصد در مقایسه با سوخت دیزل معمولی مشاهده شد. مشخصه مصرف سوخت ویژه ترمزی، در سرعت‌های پایین و متوسط، به ویژه بین ۱۰۰۰ تا ۱۵۰۰ دور در دقیقه، به دلیل کاهش محتوای انرژی ناشی از استفاده از بیودیزل سویا، ٤ تا ۱ درصد کاهش یافت. با این حال، در سرعت‌های بالا در محدوده ۱۸۰۰ تا ۲۲۰۰ دور در دقیقه، این مشخصه افزایشی بین ۱ تا ۳/۵ درصد داشت. علاوه بر این، نتایج آزمون آلایندگی نشان داد که انتشار آلاینده ها از سوخت های ترکیبی به دلیل عدم اعمال اصلاحات در موتور، نسبت به سوخت دیزل معمولی به طور قابل توجهی افزایش یافته است. طبق یافته های آزمون حالت پایا، با وجود افزایش انتشار آلاینده های سوخت های ترکیبی ، اما میزان انتشار آلاینده های مذکور به جز آلاینده ناکس، در محدوده استاندارد یورو ۵ باقی ماند. با توجه به اینکه موتور دیزل در سرعت های متوسط، که محدوده بیشینه گشتاور خود می باشد، به طور بهینه عمل می کند، استفاده از مخلوط های بیودیزل B۵، B۱۰ و B۱۵ با توجه به ویژگی های عملکردی موتور مناسب قابل قبول است. برای کاهش اثرات انتشار آلایندگی سوخت بیودیزل، اصلاحات مختلفی از جمله پیش گرمایش سوخت، افزایش فشار ریل سوخت، کاهش زمان پاشش، استفاده از افزودنی ها و تنظیم واحد کنترل الکترونیکی موتور بر اساس ویژگی های بیودیزل سویا می توان از این سوخت به عنوان یک جایگزین عملی در موتورهای دیزلی استفاده کرد.

AIMS AND SCOPE

The objective of the International Journal of Engineering is to provide a forum for communication of information among the world's scientific and technological community and Iranian scientists and engineers. This journal intends to be of interest and utility to researchers and practitioners in the academic, industrial and governmental sectors. All original research contributions of significant value focused on basics, applications and aspects areas of engineering discipline are welcome.

This journal is published in three quarterly transactions: Transactions A (Basics) deal with the engineering fundamentals, Transactions B (Applications) are concerned with the application of the engineering knowledge in the daily life of the human being and Transactions C (Aspects) - starting from January 2012 - emphasize on the main engineering aspects whose elaboration can yield knowledge and expertise that can equally serve all branches of engineering discipline.

This journal will publish authoritative papers on theoretical and experimental researches and advanced applications embodying the results of extensive field, plant, laboratory or theoretical investigation or new interpretations of existing problems. It may also feature - when appropriate - research notes, technical notes, state-of-the-art survey type papers, short communications, letters to the editor, meeting schedules and conference announcements. The language of publication is English. Each paper should contain an abstract both in English and in Persian. However, for the authors who are not familiar with Persian, the publisher will prepare the latter. The abstracts should not exceed 250 words.

All manuscripts will be peer-reviewed by qualified reviewers. The material should be presented clearly and concisely:

- *Full papers* must be based on completed original works of significant novelty. The papers are not strictly limited in length. However, lengthy contributions may be delayed due to limited space. It is advised to keep papers limited to 7500 words.
- *Research* notes are considered as short items that include theoretical or experimental results of immediate current interest.
- *Technical notes* are also considered as short items of enough technical acceptability with more rapid publication appeal. The length of a research or technical note is recommended not to exceed 2500 words or 4 journal pages (including figures and tables).

Review papers are only considered from highly qualified well-known authors generally assigned by the editorial board or editor in chief. Short communications and letters to the editor should contain a text of about 1000 words and whatever figures and tables that may be required to support the text. They include discussion of full papers and short items and should contribute to the original article by providing confirmation or additional interpretation. Discussion of papers will be referred to author(s) for reply and will concurrently be published with reply of author(s).

INSTRUCTIONS FOR AUTHORS

Submission of a manuscript represents that it has neither been published nor submitted for publication elsewhere and is result of research carried out by author(s). Presentation in a conference and appearance in a symposium proceeding is not considered prior publication.

Authors are required to include a list describing all the symbols and abbreviations in the paper. Use of the international system of measurement units is mandatory.

- On-line submission of manuscripts results in faster publication process and is recommended. Instructions are given in the IJE web sites: www.ije.ir-www.ijeir.info
- Hardcopy submissions must include MS Word and jpg files.
- Manuscripts should be typewritten on one side of A4 paper, double-spaced, with adequate margins.
- References should be numbered in brackets and appear in sequence through the text. List of references should be given at the end of the paper.
- Figure captions are to be indicated under the illustrations. They should sufficiently explain the figures.
- Illustrations should appear in their appropriate places in the text.
- Tables and diagrams should be submitted in a form suitable for reproduction.
- Photographs should be of high quality saved as jpg files.
- Tables, Illustrations, Figures and Diagrams will be normally printed in single column width (8cm). Exceptionally large ones may be printed across two columns (17cm).

PAGE CHARGES AND REPRINTS

The papers are strictly limited in length, maximum 8 journal pages (including figures and tables). For the additional to 8 journal pages, there will be page charges. It is advised to keep papers limited to 3500 words.

Page Charges for Papers More Than 8 Pages (Including Abstract)	
For International Author ***	**$55 / per page**
For Local Author	**100,000 Toman / per page**

AUTHOR CHECKLIST

- Author(s), bio-data including affiliation(s) and mail and e-mail addresses).
- Manuscript including abstracts, key words, illustrations, tables, figures with figure captions and list of references.
- MS Word files of the paper.

International **J**ournal of **E**ngineering, P.O. Box 13145-1659, Tehran, I.R. Iran
Materials and Energy Research Center, 5 Ahuramazda St., Alvand Ave., Argentina Sq., Tehran, Islamic Republic of Iran
www.merc.ac.ir - www.emerc.ac.ir

THOMSON REUTERS

WEB OF SCIENCE

Scopus®

CAS®
A DIVISION OF THE
AMERICAN CHEMICAL SOCIETY

Google
Scholar